SHRP-H-643

Ice-Pavement Bond Disbonding--Fundamental Study

Robert R. Blackburn
Midwest Research Institute
Kansas City, Missouri

T. Ashworth
South Dakota School of Mines and Technology
Rapid City, South Dakota

Charles G. Schmidt
SRI International
Menlo Park, California

Barbara J. Kinzig
Surface Research and Applications, Inc.
Lenexa, Kansas

Strategic Highway Research Program
National Research Council
Washington, DC 1993

SHRP–H–643
Contract H-203

Program Manager: *Don M. Harriott*
Project Manager: *J. David Minsk*
Production Editor: *Cara J. Tate*
Program Area Secretary: *Francine Burgess*

May 1993

key words:
ice adhesion
ice-pavement bond
ice removal - chemical
ice removal - mechanical
interfacial shear strength
mathematical modeling
surface physics

Strategic Highway Research Program
National Academy of Sciences
2101 Constitution Avenue N.W.
Washington, DC 20418

(202) 334-3774

350/NAP/593

Acknowledgements

The research herein described was supported by the Strategic Highway Research Program (SHRP). SHRP is a unit of the National Research Council that was authorized by Section 128 of the Surface Transportation and Uniform Relocation assistance Act of 1987.

This final report was prepared by Midwest Research Institute (MRI) and the subcontractors, South Dakota School of Mines and Technology (SDSM&T), SRI International (SRI), and Surfaces Research and Applications (SRA) for the Strategic Highway Research Program (SHRP) under SHRP Contract No. H-203 (MRI Project No. 8977-S). The report covers the work performed and findings made during the multiyear, multitask activities of the contract.

Mr. L. David Minsk was the SHRP Research Manager for the contract.

The work reported was conducted under the administrative direction of Dr. William D. Glauz, Principal Advisor, and Dr. Charles F. Holt, Director of the Engineering, Environmental, and Management Systems Department.

The report was prepared by Mr. Robert R. Blackburn, Principal Investigator (MRI) with assistance from Mr. Howard W. Christie, Principal Chemist (MRI); Dr. T. Ashworth, Chairman of Physics Department (SDSM&T); Dr. Jack A. Weyland, Professor of Physics (SDSM&T); Dr. Charles G. Schmidt, Senior Materials Scientist (SRI); Dr. Richard W. Klopp, Research Engineer (SRI); Dr. Jeffrey W. Simons, Research Engineer (SRI); Dr. Jacques H. Giovanola, Senior Research Engineer (SRI); Mr. Paul R. Gefken, Research Engineer (SRI); Mr. David C. Erlich, Physicist (SRI); Dr. Barbara J. Kinzig, President (SRA); and Dr. Gordon T. Fujimoto, Senior Research Scientist (SRA). Other team members who assisted in the conduct of the research include Dr. Cecil C. Chappelow (MRI), Dr. A. D. McElroy (Consultant), Mr. Gordon E. Gross (Consultant), Ms. Rosemary E. Moran (MRI), Ms. Jean E. Pelkey (MRI), Messrs. William Cunningham (MRI), Gordon Shaw (MRI), Mark Blackburn (MRI), Mike Westphal (SDSM&T), and Jeffrey Wood (SDSM&T).

Several state highway officials lent their assistance in providing core samples of highway pavements for use in the experimental portion of the program. Special acknowledgement and appreciation are due for assistance given by key members of the highway or transportation department staffs of California, Connecticut, Montana, and New York.

Contents

List of Figures

List of Tables

Abstract

This fundamental study of the ice-pavement bond structure and the mechanics of its formation provides a basis for the development of techniques and devices for destroying or disrupting the ice-pavement bond once it has formed. The destruction process of the ice-substrate bond is explored. The report also characterizes the physical and chemical processes that cause deterioration in the bond formed between ice and asphalt and portland cement concretes. Finally, the report makes recommendations for further work to develop practical solutions for destroying the ice-pavement bond.

Executive Summary

The overall objective of the research was to conduct a fundamental study of the ice-pavement bond structure and the mechanics of its formation, in order to provide a sound basis for the development of techniques and devices for destroying or disrupting the ice-pavement bond once it has formed. Embedded within this overall objective were three specific objectives. These were to:

a. Explore the process by which the bond formed between ice and a solid substrate is destroyed, using the principles of surface and interfacial physics.

b. Characterize the physical and chemical processes that cause deterioration in the bond formed between ice and asphalt and portland cement concretes.

c. Identify techniques that can be used or noncorrosive and environmentally acceptable materials which can be introduced to destroy the bond between ice and pavement materials.

The scope of the research was both experimental and analytical in nature. The surface and interfacial properties of ice and various substrates were investigated in the laboratory at temperatures between 0° and –40°C. Analytical models were employed to extend the conditions examined in the laboratory investigation. Substrates investigated include model (artificial) substrates, pavement-component substrates, laboratory-produced pavement substrates, and samples of highway surfaces (dense-graded asphalt, open-graded asphalt, rubber-modified asphalt, and portland cement concrete) conforming to representative highway specifications.

The research objectives were met through a multiyear, multitask research approach. The activities, conducted during the first year of the contract, focused on exploratory studies of fundamental elements associated with the ice-pavement bond formation and destruction. After an exhaustive literature review was performed, various laboratory experiments were performed using ice samples grown under extremely well-controlled conditions on

homogeneous substrates. These experiments were aimed at investigating the properties of the intact ice-substrate interface and the properties of ice removed from substrates. The substrates used included model (artificial) surfaces and single-component samples of pavement materials. All materials and substrates used were carefully prepared and characterized.

Material and sample handling protocols were established for use throughout the study by the laboratory teams. This step was undertaken to help prevent uncertainties in the laboratory findings due to inadvertent contamination or sample handling differences. Finally, various mathematical models of ice-substrate disbondment were investigated for purposes of extending the laboratory findings.

The activities during the second year of the contract focused on investigations of techniques for the destruction of the bond between ice and highway pavement materials. The highway pavement materials used in this part of the investigation consisted of laboratory-produced substrates and core samples taken from several in-service highway pavements. Various laboratory tests were conducted in the investigation of the physical and chemical processes for disbonding ice on highway pavement materials. All of the highway materials were characterized and special handling and cleaning protocols were developed for the pavement cores and laboratory-produced specimens. Laboratory tests were conducted to investigate various physical processes for disbonding ice from various highway substrates. Additional laboratory tests were conducted to investigate the destruction of ice-substrate bonds by chemical undercutting. Finally, additional mathematical models were developed for examining physical processes for disbonding ice from pavement materials.

It was concluded that the bond established between ice and highway pavement materials is a complex function of many parameters including temperature, rate and direction of freezing, and the physical and chemical conditions of the substrate surface. The successful destruction of the bond between ice and highway pavement materials by either physical means, chemical means, or a combination of the two, requires an appropriate match of the bond destruction technique with the type and condition of the substrate surface and the conditions involved in the bond formation. Numerous other conclusions were developed from the research findings. These conclusions provide the basis for recommended further work to develop practical solutions for destroying the ice-pavement bond under a variety of operating conditions.

1

Introduction and Research Approach

Introduction

The impact of snow and ice storms has long been a concern to the traveling public. Prior to the development of the automobile, travel during the winter weather was somewhat limited. The advent of the automobile and, eventually, of all-weather roads resulted in the development of improved snow and ice removal techniques that replaced the slow and labor intensive use of hand tools so prevalent in the early 1900s.

The years between 1920 and 1929 witnessed the most rapid change in snow removal technology on highways. The demand for complete removal of snow from the all-weather roads grew yearly, and the need for bigger, more capable equipment and better removal techniques became apparent. During these years, blade plows became bigger and heavier, truck plowing speeds increased from something less than 5 mph to 30 mph or faster as truck power and weight increased, and trucks became the most important tool in snow removal (1).

Deicing salts, primarily sodium chloride, have been applied to highways for control of snow and ice since early in this century. Prior to 1941, very little straight salt was applied to the roadways; most was mixed with sand or other abrasives to freeze-proof stockpiles and to treat locally hazardous highway locations such as curves, hills, and intersections. Experiments were begun in New England in 1941 using NaCl alone as an ice preventative. The total amount of NaCl applied across the country remained relatively low until the mid-1950s when usage surged dramatically to around 1 million tons annually, partially in response to the public demand for better all-weather roadway conditions. This demand eventually led to the adoption of a bare pavement policy by the highway departments in the snow-belt states (2).

Currently, the economic well-being, livelihood, and strategic defense of the U.S. depends to a large extent on the year-round mobility of trucks, buses, and passenger cars on the nation's highway network. Winter conditions of ice and snow still cause serious disruptions in the economies of nearly all states. Our great dependence on highway transportation for the movement of goods, services, and people has resulted in the demand for more rapid and effective clearance of ice and snow from the highways. As a result, there has been an increased use of chemicals and abrasives by highway agencies to assist in providing a clear roadway. The current usage of salt is approaching a rate of 10 million tons per year (3).

Sodium chloride has become the chemical of choice because it is effective at subfreezing temperatures (eutectic temperature of –6°F), has low first costs, and is readily available. At temperatures not far below freezing, salt is effective for combating ice and light snow and greatly enhances the effectiveness of plowing under conditions of heavy snow conditions.

Concern has been steadily voiced over the last dozen years about the effects of heavy salt use on the roadside environment, water supplies, vehicles, and highway structures. The direct cost of the current national salt usage is about $350 million. However, the effective cost of its use is many times higher. A 1981 study report by the National Bureau of Standards and Battelle Laboratories (4) concluded that the automobile corrosion costs attributable to salt use were about $1.2 billion per year. Estimates made by Murray and Ernst (5) in 1976 indicated that the cost of salt damage to bridges is even larger than the cost of automobile corrosion. Thus, an apparently inexpensive highway deicing methodology is, in reality, extremely expensive, possibly more than 100 times the cost of the material itself.

In addition, the extent and cost of environmental pollution are now manifesting themselves. Although there has not yet been a nationwide estimate of the costs arising from environmental pollution (particularly the salination of water supplies), the number and cost of localized problems are beginning to paint an alarming picture. At a recent meeting of the Winter Maintenance Committee of TRB (6) presentations included reports of additional construction costs of $2.5 million for a ¼ mile segment of interstate from which direct salt run-off had to be avoided; $1.5 million to provide city water to a small community whose water supply had been contaminated by sodium; and $4 million to develop protection wells and drainage systems to safeguard another community's water wells. These are just a very few of the many environmental problems which are arising from the use of salt.

Removal of ice (and compacted snow) from highway surfaces has been accomplished in part by mechanical means (scraping) and in part by use of deicing chemicals or, in many locations, by a combination of these techniques. Neither the combination of these methods

nor their singular use is completely satisfactory. The chemical methods (salts) have problems already enumerated, and the mechanical method does not provide complete ice removal.

There is now clear need for practical methods of winter highway maintenance which are reasonable alternatives to chloride salts, but which do not have the attendant problems of corrosion and environmental damage. Unfortunately, there has been a paucity of basic research, so presently there is not available the body of necessary scientific information or ideas upon which to begin the development of new methods. This has occurred simply because of the small amount of funding that has been invested in basic studies.

This oversight is hard to understand in view of the over $1 billion spent annually on snow and ice control by all levels of government. Resources of all these government jurisdictions do not permit research beyond short-term, limited objective studies, most of which are focused on local problems with little transferability to other areas. Also, the snow removal/ice control industry is dispersed and fragmented. No individual equipment manufacturer has the resources or the incentive to conduct long-range studies to improve equipment performance or operational techniques. Finally, and most importantly, the majority of the total costs of snow and ice control, as noted earlier, are not borne by the agencies charged with providing the control, but by other agencies, affected communities, and the individual private citizens.

Realization of the need for a national approach to the problems of improved snow and ice control has now occurred. The Transportation Research Board (TRB) of the National Research Council, under sponsorship of the Federal Highway Administration and with the cooperation of the American Association of State Highway and Transportation Officials (AASHTO) undertook a thorough and probing study of the extent to which expanded R&D could make major contributions to improving highway transportation. That study recommended that a Strategic Highway Research Program (SHRP) be initiated to focus on the problem. The SHRP concept was originally proposed in a TRB Special Report 202: "America's Highways: Accelerating the Search for Innovation," published in 1984 (7). The report recommended a $150 million, five-year program of research focused on six high priority technical research areas (TRA), one of which was defined as TRA-6—Snow and Ice Control on Highways and Bridges. The recommendations provided in TRB Special Report 202 to initiate SHRP were approved by AASHTO in July 1984.

Under the guidance of the National Cooperative Highway Research Program (NCHRP) six separate SHRP contractors were selected by a SHRP Task Force in early 1985 to develop the specific research plans for the six TRAs. Several advisory group meetings were held to assist the research contractor during the development of the detailed research program. In addition,

a National SHRP Workshop was held in September 1985 to provide a preview and review of the preliminary research plans that were being developed within each TRA. A second introduction to SHRP's anticipated plans occurred at the 1986 Annual Meeting of TRB. Both these meetings increased the U.S. and foreign technical community's awareness of SHRP. The individual TRA research plans were finalized by February 1986 and later approved by the SHRP Task Force. The details of the research plans for each TRA are contained in a TRB publication issued in May 1986 (3).

Since the publication of SHRP's research plans, the 12 originally proposed study projects under TRA-6 have been consolidated into seven contracts. In addition, the seven contracts dealing with control of snow and ice have been combined with the contracts under maintenance cost effectiveness to provide a new technical area of SHRP called "Highway Operations."

With the passage of the Surface Transportation and Urban Relocation Assistance Act of 1987, Congress guaranteed SHRP's existence. Two fundamental studies in the area of snow and ice control were included in the first set of contracts signed under SHRP funding. One of these studies entitled "Ice-Pavement Bond Disbonding—Fundamental Study" was conducted by Midwest Research Institute under Contract No. SHRP-87-H203 and is reported here. This project was developed as a comparison to the fundamental study of ice-pavement bond prevention conducted under SHRP Contract H-201. In addition, it was designed to provide direct input to the SHRP Contract H-204 dealing with ice-pavement bond disbonding—surface modification and disbonding.

Past work aimed at the development of methods for removal of ice from pavement surfaces has been rather narrow in scope (8). There is a small quantity of basic data on the adhesive properties of ice, the mechanisms of adhesion, and the effects of different substrates on their adhesion. Proper application of existing technical information and the development of needed basic knowledge covering ice adhesion should provide a sound basis for the development of new, practical measures for ice removal. A much better understanding of the physical and chemical phenomenon observed at the ice-pavement interface is required before bond destruction can be achieved in an economical manner. The information presented in this report is to provide the fundamental knowledge needed by researchers pursuing the development of innovative and economically feasible processes for ice removal.

Research Objectives and Scope

The overall objective of the research was to conduct a fundamental study of the ice-pavement bond structure and the mechanics of its formation, in order to provide a sound basis for the development of techniques and devices for destroying or disrupting the ice-pavement bond once it has formed. Embedded within this overall objective were three specific objectives. These were to:

a. Explore the process by which the bond formed between ice and a solid substrate is destroyed, using the principles of surface and interfacial physics.

b Characterize the physical and chemical processes that cause deterioration in the bond formed between ice and asphalt or portland cement concretes.

c. Identify techniques that can be used or noncorrosive and environmentally acceptable materials which can be introduced to destroy the bond between ice and pavement materials, or alternatively, to reduce the tensile strength between ice and pavement materials to a value not exceeding 15 psi (0.10 MPa), without adversely affecting desirable pavement properties such as friction.

The scope of the research was both experimental and analytical in nature. The surface and interfacial properties of ice and various substrates were investigated in the laboratory at temperatures between 0° and –40°C. Analytical models were employed to extend the conditions examined in the laboratory investigation. Substrates investigated include model (artificial) substrates, concrete components, asphaltic concrete components, and samples of highway surface (dense-graded asphalt, open-graded asphalt, rubber-modified asphalt, and portland cement concrete) conforming to representative highway specifications.

The program was not a pure research study, but rather research of a fundamental nature directed toward a very specific goal: the development of practical methods for disbonding ice from pavements. Although techniques or materials for destroying the ice-pavement bond have resulted from the study, further investigation leading to practical application will be the responsibility of subsequent SHRP contracts.

The principal goal of the study was to provide an improved understanding of the ice-pavement bond structure and its formation sufficient to guide the development of techniques, materials, and equipment for weakening or eliminating the bond with low energy input without the use of environmentally undesirable physical or chemical energy sources.

The results of the research study include:

a. Development of methods for characterizing the destruction of the ice-pavement bond and for studying the mechanics of its formation and its change with time.

b. Identification of energetically favorable chemical or mechanical methods for disbonding ice from pavement surfaces.

c. Recommendations for further work to develop practical solutions for destroying the ice-pavement bond.

Research Approach

The research objectives were met through a multiyear, multitask research approach. The activities conducted during the first year of the contract focused on exploratory studies of fundamental elements associated with the ice-pavement bond formation and destruction. After an exhaustive literature review was performed, various laboratory experiments were performed using ice samples grown under extremely well-controlled conditions on homogeneous substrates. These experiments were aimed at investigating the properties of the intact ice-substrate interface and the properties of ice removed from substrates. The substrates used included model (artificial) surfaces and single-component samples of pavement materials. All materials and substrates used were carefully prepared and characterized.

Material and sample handling protocols were established for use throughout the study by the laboratory teams. This step was undertaken to help prevent uncertainties in the laboratory findings due to inadvertent contamination or sample handling differences. Finally, various mathematical models of ice-substrate disbondment were investigated for purposes of verifying and extending the laboratory findings.

The activities during the second year of the contract focused on investigations of techniques for the destruction of the bond between ice and highway pavement materials. The highway pavement materials used in this part of the investigation consisted of laboratory-produced substrates and core samples taken from several in-service highway pavements. Various laboratory tests were conducted in the investigation of the physical and chemical processes for disbonding ice on highway pavement materials. All of the highway materials were characterized and special handling and cleaning protocols were developed for the pavement core and laboratory-produced specimens. Laboratory tests were conducted to investigate the

physical processes for disbonding ice from various highway substrates. Additional laboratory tests were conducted to investigate the destruction of ice-substrate bonds by chemical undercutting. Finally, additional mathematical models were developed to examine the physical processes of disbonding ice from pavement materials.

The research approach followed in the study is outlined, as follows, together with a brief description of the activities in each step. The activities are discussed without reference to the project year in which they took place.

Research Review

A critical review was performed of past research findings relevant to ice adhesion and the chemical and physical processes that cause destruction or deterioration of the bond formed between ice and a solid substrate.

The purpose of the literature review was to define the limitations of knowledge concerning the process by which the bond formed between ice and a solid substrate is destroyed from a surface and interfacial physics standpoint. Another objective of the literature review task was to identify existing data on the characterization of the physical or chemical processes that cause deterioration in the bond strength formed between ice and real-world highway pavement surfaces, including asphalt and portland cement concrete. Also of interest was the identification of potential techniques that could be used, or noncorrosive and environmentally acceptable materials which could be introduced to destroy or sufficiently weaken the bond between ice and pavement materials.

Literature on the above issues were identified using computerized and manual literature searches. The major data bases searched included those associated with Chemical Abstracts (CA), Computerized Engineering Index (COMPENDEX), the U.S. Army Cold Regions Research and Engineering Laboratory (USACRREL), the National Technical Information Service (NTIS), the Transportation Research Information Service (TRIS), the International Information Services for the Physics and Engineering Communities (INSPEC), and the Educational Resources Information Center (ERIC). The first five data bases were specifically identified as being highly pertinent to the research effort. The INSPEC data base was searched because it covers several journals, including Physics Abstracts, in which physical properties of ice are reported. The ERIC data base was also searched because it covers both the atmospheric and glaciologic journals.

In the course of the computerized searches, well over 1,500 general citations were screened to yield about 750 citations of at least some value to the project objectives. The ERIC, CREEL, and INSPEC data bases produced about 80% of the citations of value.

In addition to the computerized literature searches, selective manual searches were conducted of the publications, reports, and books in the extensive holdings of the research team's libraries and in other local technical and university libraries.

The results of the research review were used to help identify some of the model substrates used in the laboratory investigations and to solidify the research plan for conducting the experimental and mathematical modeling portions of the study. An expandable reference data base was constructed to include the literature references found to be of interest to the project. The Pro-Cite bibliographic software package was used in constructing the data base. A copy of the data base was provided to SHRP on 5 ¼-in floppy discs.

Selection and Characterization of Materials Used in the Study

The substrates used in the study consisted of model (artificial) specimens, pavement component materials, and highway pavement samples. Six model substrates were used in the study: glass, FEB Teflon, mercury, Mylar®, perfluorinated oil, and a gold surface prepared by vacuum deposition on a polished glass substrate. Four pavement component substrates were used in the study: limestone, silica, portland cement mortar, and asphalt. The highway pavement samples consisted of laboratory-produced specimens and highway core samples. Portland cement concrete and dense-graded asphalt specimens were prepared in the laboratory from highway component materials. Core samples were collected from representative portland cement concrete, rubber-modified asphalt, and dense- and open-graded asphaltic concrete highway surfaces. All the substrate materials were subjected to selective characterizations. These included physical surface characterizations (optical micrographs, profilometer measurements, and repeated contact angle measurements with one liquid) and limited surface energetic characterizations (contact angle measurements using various liquids). Absorption isotherms and heats of wetting measurements were made using fine powders of selected substrates. Surface tension measurements were also made on all liquids used for contact angle measurements. Whenever possible, a history was obtained on the highway surfaces from which the core samples were obtained (i.e., location and date constructed, material and formulation specifications, traffic volume, and any other pertinent data). Details of the substrate characterization work, both from a physical surface standpoint and from a surface energetics standpoint, are discussed in Section 2 and in Appendix A.

Development of Handling, Cleaning, and Storage Protocols

The materials used in the study were divided into five major groups: liquids, solid model substrates, pavement component substrates, laboratory-produced specimens, and highway core samplings. Handling and storage protocols were developed for each material group used in the study. In addition, cleaning protocols were developed for glassware and the various substrates used in the laboratory investigations. A special diagnostic method was also developed for characterizing the surface condition of laboratory-produced specimens and highway pavement core samples after they were subjected to the cleaning protocol. The protocols, as well as general laboratory procedures, were established for use by the project teams to enhance reproducibility of data both within and between laboratories. Further details are given in Appendix B of the protocols developed and in Appendix C of the diagnostic method used to determine the surface condition of the substrates subjected to a cleaning process.

Investigation of Physical Processes for Disbonding Ice from Various Substrates

The investigation of physical processes for disbonding ice from various substrates fell into five major areas. The first area involved an investigation into the morphology of ice grown on four model substrates with different surface energetics. The second area involved the evaluation of the potential for using selective wavelengths of IR radiation to disbond ice at the ice-pavement interface. The third area involved measurements under low load rate conditions of the ice-substrate bond strength in sheer on untreated model substrates and on untreated and chemically-treated pavement component substrates. The fourth area involved the determination of the impact effects on ice bonded to composite substrates (laboratory-produced specimens and highway core samples). Finally, the fifth area involved an investigation of the effects of thermal stresses on the ice-pavement bond strength. Details of the findings achieved in each of the five areas are presented in Section 2 under the appropriate headings. Further details are given in Appendices D through H of the investigations of physical processes for disbonding ice from substrates.

Investigation into the Destruction of Ice-Substrate Bonds by Chemical Undercutting

Two sets of experiments were conducted to investigate the destruction of the ice-substrate bonds by chemical undercutting. The main objectives of these experiments were to determine the influence of temperature and substrate on the time-dependent characteristics of special common chemical deicers. The first set of experiments determined the undercut area, as a

function of time, of four deicers on six substrate materials under a variety of experimental conditions. The four deicers used were ethylene glycol, NaCl, $CaCl_2$, and calcium magnesium acetate (CMA). Of the six substrates used, three were model substrates (FEP Teflon, Mylar, and gold) and three were pavement component substrates (fused silica, portland cement mortar, and limestone). The experimental conditions included temperatures of 25°F (–4°C), 15°F (–9°C), 5°F (–15°C), and –40°F (–40°C); freezing rates of fast, medium, and slow; and freezing modes of bottom-up and top-down. The statistical analysis of the undercutting data was limited to ethylene glycol. The analysis was directed at determining the effects of temperature and substrates on the initial rate (i.e., at time zero) of the undercutting curve.

The second set of undercutting experiments determined the undercut area, as a function of time, of three deicers at three temperatures on highway core samples and laboratory-produced specimens. Tests were conducted at temperatures of 25°F (–4°C), 15°F (–9°C), and 5°F (–15°C) using all the substrates in the as-received, but cleaned condition. The three deicers—NaCl, $CaCl_2$, and ethylene glycol—were used in all temperature-substrate combinations. The substrates used in the experiments included portland cement concrete, dense-graded asphalt, open-graded asphalt, and rubber-modified asphalt core samples and laboratory-produced specimens made of portland cement concrete and dense-graded asphalt. Undercutting action was also investigated on smooth highway core samples and laboratory-produced specimens at selected temperatures. The results of the undercutting experiments are discussed in Section 2 under "Investigation into the Destruction of Ice-Substrate Bonds by Chemical Undercutting" and in more detail in Appendix I.

Mathematical Modeling of Physical Processes for Disbonding

During this part of the study, six mathematical models were developed to describe the stress environments at ice-concrete interfaces. The objectives of the modeling efforts were (1) to develop a better understanding of the mechanisms of ice disbondment in currently or potentially practical ice removal methods, and (2) to assist in the development of experimental methods and the interpretation of the experimental results of this investigation.

For the first model, a one-dimensional analysis was performed to determine the conditions required to disbond ice from a concrete substrate with a planar compressive shock load applied normal to the ice surface. The model assesses the magnitudes of the stresses at the ice-concrete interface from an idealized planar shock wave. The shock wave conditions were identified that optimize the interfacial stresses for ice disbondment. The practical considerations necessary to achieve optimal shock wave conditions are discussed.

For the second model, a three-dimensional analysis was performed to describe the stresses that result when an ice layer is struck by a wedge moving at high velocities parallel to an ice-concrete interface. This model simulates the velocity and geometry of the shear experiments performed in this study. The model also approximates the conditions that are present when an ice layer is struck by a conventional snow plow.

For the third model, a two-dimensional analysis was performed to assess the effects on an ice layer from the impact of a wedge traveling normal to the ice-concrete interface. The model is the two-dimensional analog of an axisymmetric penetrator that initiates ice disbonding and prepares the ice for deicing chemical injection.

For the fourth model, a fracture mechanics approach was used to describe the stresses ahead of a crack tip at an ice-concrete interface. The model provides a framework to relate the ice disbonding forces to interfacial energy characteristics.

For the fifth model, a finite element analysis was used to simulate the critical features of the quasistatic shear tests that were conducted during this program. The uniformity of the stress field that is produced by the test was determined and the effect of several modifications to the specimen design was studied.

For the sixth model, the finite element modeling approach was used to examine the effects of pavement surface topography on the ice-pavement interfacial stresses from shear loads applied to the ice.

Detailed description of the methods and the findings for each of the six modeling efforts are given in Section 2 and in Appendix J.

2

Findings

The findings of the study are presented below under the three major headings of: "Characterization of Substrates," "Properties of Ice Grown on Different Substrates," and "Investigation of Physical Processes for Disbonding Ice from Various Substrates." The first and third major headings are further subdivided. Additional details of the material presented in this section are given in Appendices A through L.

Characterization of Substrates

Selection and Description of Substrates

The materials selected for use in this project are described in this section. The materials used in this program can be divided into five categories. These categories are summarized below in Table 1. A full description of the source, preparation, and evaluation of these materials is presented in Appendix A. It was important that the nature of the surfaces of solid substrates and liquids be known to properly interpret the results of the other parts of the project. A complete description of the characterization procedures is also presented in Appendix A.

To ensure that impurities or surface morphology changes were not introduced by improper handling, protocols were established for the handling and storage of the diverse types of samples and other materials used in this project. A complete description of the standard laboratory procedures developed and utilized in this project is presented in Appendix B.

Table 1. Materials used in this study

Liquids	Pavement Core Samples
Liquid model substrates: fluorinated oil, mercury	Portland cement concrete
Water	Open-graded asphalt
Reference liquids for contact angle Measurements	Dense-graded asphalt
	Rubber-modified asphalt
Solid Model Substrates	Laboratory-Produced Pavement Substrates
Fluorinated ethylene propylene (FEP) Teflon	Portland cement concrete
Mylar	Dense-graded asphalt
Gold	
Pyrex glass	
Pavement Component Substrates	
Limestone	
Portland cement mortar	
Asphalt	
Fused silica	

To guarantee that the water used in the ice growth studies was free from surface-active contaminants, surface tension measurements were performed, and stringent water handling protocols were implemented, as described in Appendix B.

The model substrates were selected to provide a wide range of surfaces on which to perform preliminary ice growth experiments.

The FEP Teflon and fluorinated oil provided low surface energy substrates. Gold, mercury, and Pyrex glass provided substrates with high surface energy, and the Mylar provided an intermediate surface.

The results from these materials formed the basis for the ice growth experiments performed on the pavement component substrates and pavement samples.

Surface Energetics

Contact Angle Characterization of Substrates

The contact angle method was selected for primary surface energetic characterization of the solid substrates to be used in this program. Accurate surface energetic characterization at the beginning of the study of a sample permits subsequent measurements to monitor changes in the surface due to ice growth and removal and to the use of surfacants and/or undercutting materials. Once the values expected for the various liquids on a substrate were established, the method also provided a rapid and nondestructive determination of surface contamination or change in condition of substrates. The contact angle of a liquid on a solid surface is a direct indicator of the interfacial tension between the liquid/solid pair.

The equilibrium sessile drop method was used to measure the contact angles of liquids on the model substrates. The angle made by the edge of a fluid drop and the solid surface is measured optically. From the contact angles made by sessile drops of a series of liquids of differing liquid surface tensions, the critical surface tension of wetting, γ_c, is obtained, and the work of adhesion may be obtained.

The slowly advancing equilibrium drop method of Shafrin and Zisman (9) was employed in these measurements. Initially, a small (ca. 1 mm diameter) drop of liquid, selected by its surface tension to be only partially spreading so that it will stay intact on the surface, is carefully placed on the surface and its contact angle measured. An additional small amount of liquid is then added to the drop and the contact angle measured again. Additions are made until three successive measurements of the contact angle do not differ as the drop 'advances' on the surface. The slowly advancing equilibrium drop method eliminates any problems from initial instabilities. Angles reported are the average of readings taken on both sides of a drop after three or more successive additions. Initial measurements are not included in the average recorded. Typically three or more separate drops are measured on different regions of the surface under study. A full description of the method is given in Appendix A.

Contact angle measurements were made on the FEP Teflon and Mylar substrates used in this study. (These measurements were not made on the Pyrex and gold substrates.) The samples of both polymer films were prepared by cutting specimens to size, then cleaning according to the handling protocols established earlier. After initial rinses with ethanol and hexane, the film samples were extracted with ethanol in a Soxhlet extractor for 2 to 3 hr. A Ramé-Hart goniometer was used to measure contact angles made by liquids whose surface tensions had been previously measured. Contact angles on FEP Teflon and Mylar are reported in

Tables 2 and 3. Each angle reported is the result of measurements on at least three separate drops of the liquid.

A Zisman plot of cos θ vs liquid surface tension, γ_{LV}, is used to obtain γ_c, the critical energy of wetting, from the extrapolation to cos $\theta = 1$. At that point, θ will be equal to zero, and hence complete spreading will occur for any liquid with that value of surface tension and lower. A typical Zisman plot is shown in Figure 1 for the data from FEP Teflon in Table 2. Extrapolation leads to a γ_c value of 17 mN/m, in good agreement with the literature value for the fluoropolymer surface. The results from the contact angle measurements on FEP Teflon and Myler compare favorably with those previously reported in the literature (10,11).

The work of adhesion, W_a, is directly related to the interfacial tension (force) between a solid and a liquid. It is the work required to separate the two, thereby creating two new surfaces, one solid and one liquid. For the liquid surface component, $W_a = \gamma_{LV}$. The solid component is $\gamma_{LV} \cos \theta$. Thus $W_a = \gamma_{LV} (1 + \cos \theta)$. When $\theta = 0$, i.e., at the critical surface tension of wetting, γ_c, then cos $\theta = 1$ and $W_a = 2\gamma_c$. For other values of θ obtained with real liquids at their respective γ_{LV} values, W_a may either be the same as or greater than W_a at γ_c, indicating a linear or enhanced interaction of the liquid-solid pair. Higher W_a values mean the liquid is more difficult to remove. Using the value of γ_c obtained, as listed in Tables 2 and 3, the work of adhesion for FEP Teflon and Mylar is found to be 34.0 and 74.0 mN/m, respectively.

Contact angle measurements were obtained with water on the limestone pavement component samples. Visual observation shows that the limestone is not a homogeneous material. There were various bands through the samples. Despite this, the drops had circular symmetry and exhibited no "wings" at the water-limestone interface. However, when the water drop was removed from the limestone substrate surface, a wet circular area remained where some water had penetrated into the limestone. A contact angle of 28° for water on limestone was measured. Using this result with the value of 69.5 mN/m for the surface energy of water in air, the work of adhesion for water on limestone is computed to be 130 mN/m.

The porosity of the PCC mortar made contact angle measurements even more difficult on the PCC mortar than on the limestone. An approximate value of 22° was obtained, however, for the contact angle of water on PCC mortar. This yields a work of adhesion of 134 mN/m for water on PCC mortar.

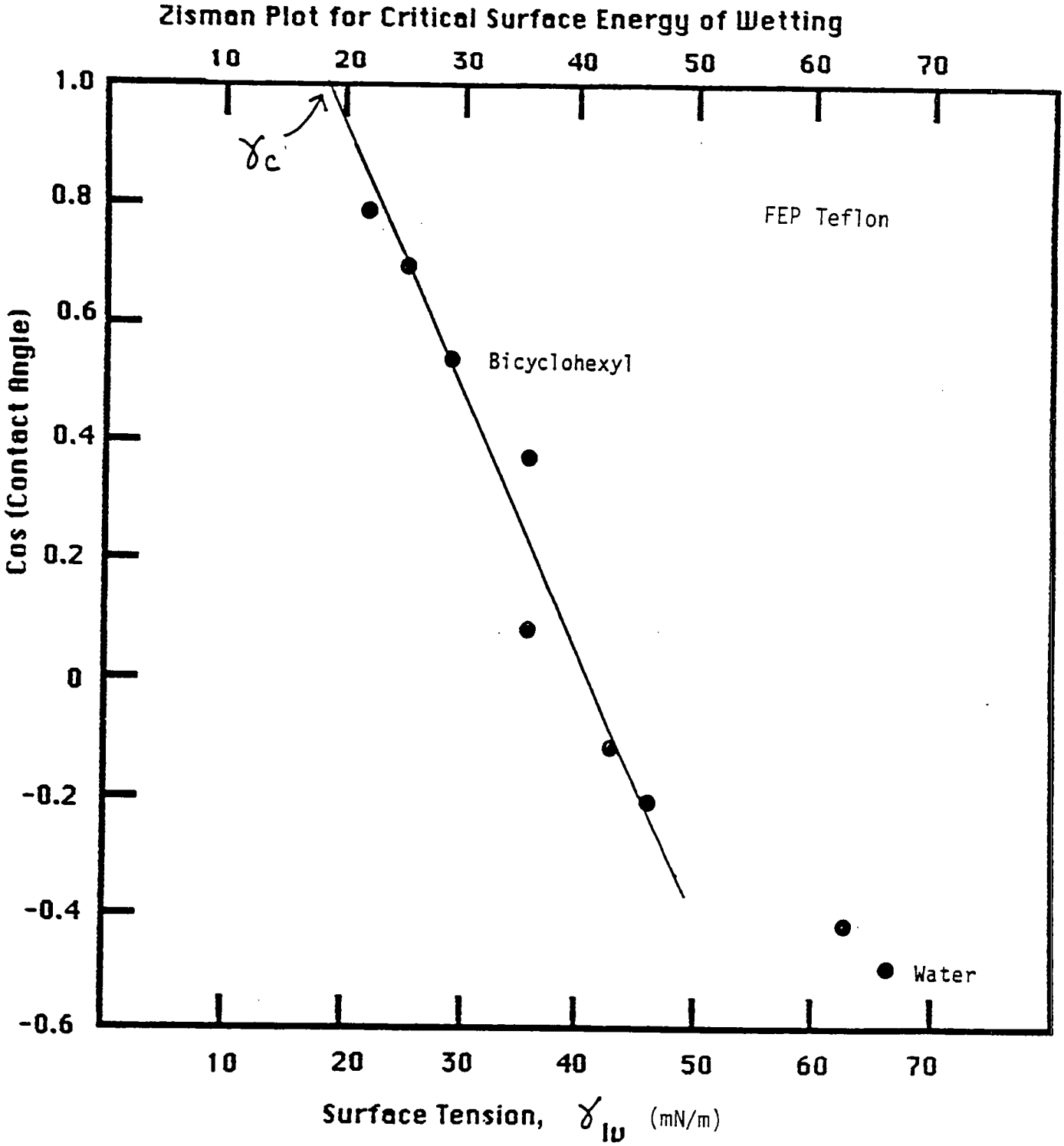

Figure 1. Zisman plot of cos θ vs γ_{LV} for various liquids on FEP Teflon

Table 2. Contact angles with various liquids on FEP Teflon surfaces[a]

Liquid	γ_{LV}	θ Degrees	Cos θ
2X distilled water	62.8	120	−0.50
Glycerol	62.5	115	−0.42
Ethylene glycol	45.6	102	−0.21
Methylene iodide	43.9	97	−0.12
n-Methyl formamide	35.9	85	0.08
Dibromoethane	35.8	68	0.37
Bicyclohexyl	29.0	57	0.54
Hexadecane	25.2	46	0.70

[a]Critical surface tension of wetting, γ_c = 17 mN/m.

Table 3. Contact angles with various liquids on Mylar surface[a]

Liquid	γ_{LV}	θ Degrees	Cos θ
2X distilled water	69.5	71	0.21
Glycerol	62.5	69	0.36
Ethylene glycol	46.6	58	0.54
Propylene carbonate	40.1	26	0.90
n-Methyl formamide	39.1	25	0.91
Dipropylene glycol	32.0	spreads	—
Bicyclohexyl	31.8	spreads	—
Hexadecane	25.2	spreads	—

[a]Critical surface tension of wetting, γ_c = 37 Mn/m.

This study also demonstrated the need for proper handling of specimens. Merely handling the specimens with ungloved hands was found to drastically increase the water contact angles from the 20° to 30° range for limestone and PCC mortar specimens up into the 60° to 70° range. Some limestone specimens were even found to have contact angles in excess of 90° for water. The results of the water contact angle measurements are summarized in Table 4.

Table 4. Work of adhesion of water from contact angle measurements

Substrate	Contact angle (degrees)	Work of adhesion (mN/m)
Teflon	120	34
Mylar	71	74
PCC mortar	22	134
Limestone	28	130
Asphalt	95	63.2

Contact angles were measured with water on asphalt samples prepared in the laboratory and used without further treatment. Asphaltic materials were isolated in storage and handling from concrete and other model components during this study. Water had a contact angle of 95° on asphalt. Using this result, together with the above value of the surface energy for water in air, the work of adhesion for water on asphalt is computed to be 63.2 mN/m. The water drops were round and exhibited no wings at the water-asphalt interface. However, when the water drop was removed from the asphalt substrate's surface, a slight ring, in the shape of the drop, remained where the water had been placed on the asphalt. The contact angle for asphalt is intermediate between that of FEP Teflon and Mylar. This is to be expected. Asphalt has a higher surface concentration of functional groups capable of hydrogen bonding to water than the FEP Teflon, but a lower concentration than that of Mylar. The ring feature left on the surface when the water drops were removed indicates that there is some additional interaction between the asphalt surface and water.

Surface Area and Absorption Isotherms

Surface area measurements and adsorption isotherms of water were obtained on powders derived from the limestone, silica, and portland cement mortar used in the other areas of this investigation. These were done to investigate molecular-scale interactions of the first layer of water with highway pavement surfaces of interest. Laboratory measurements were made to collect fundamental data related to the ice-substrate bonding mechanism. To measure these interactions involving such minute quantities, powders are typically used to increase the available area of a solid. The specific surface area (area per gram) must be known in order to evaluate the isothermal adsorption of the vapor of interest.

Surface area measurements: A fine powder was prepared by grinding small pieces of the substrate material with a mortar and pestle. The specific surface area was measured for each of the materials using reversible nitrogen adsorption with a Quantasorb area meter. A description of this equipment and its operation are given in Appendix A. The table below shows the results obtained for the three powders considered.

Sample material	Specific surface area (m^2/g)
Limestone	3.15
Silica	1.58
Concrete mortar	22.25

Adsorption isotherms: Generally, there are five types of adsorption isotherms, according to the BET system of classification (12). These types are shown in Figure 2 where $V_{adsorbed}$ is the volume of gas adsorbed at reduced partial pressure, P/P_o. A type I Langmuir (13) isotherm is usually adequate only for unimolecular adsorption on a flat surface with no pores or capillaries.

For multimolecular adsorption on a surface containing pores or capillaries, the BET (Brunauer, Emmett, and Teller) theory of multimolecular adsorption predicts a type II isotherm having a sigmoidal shape.

The gravimetric method was used for collecting adsorption isotherm data (14). Details of the apparatus and the operating procedure are given in Appendix A.

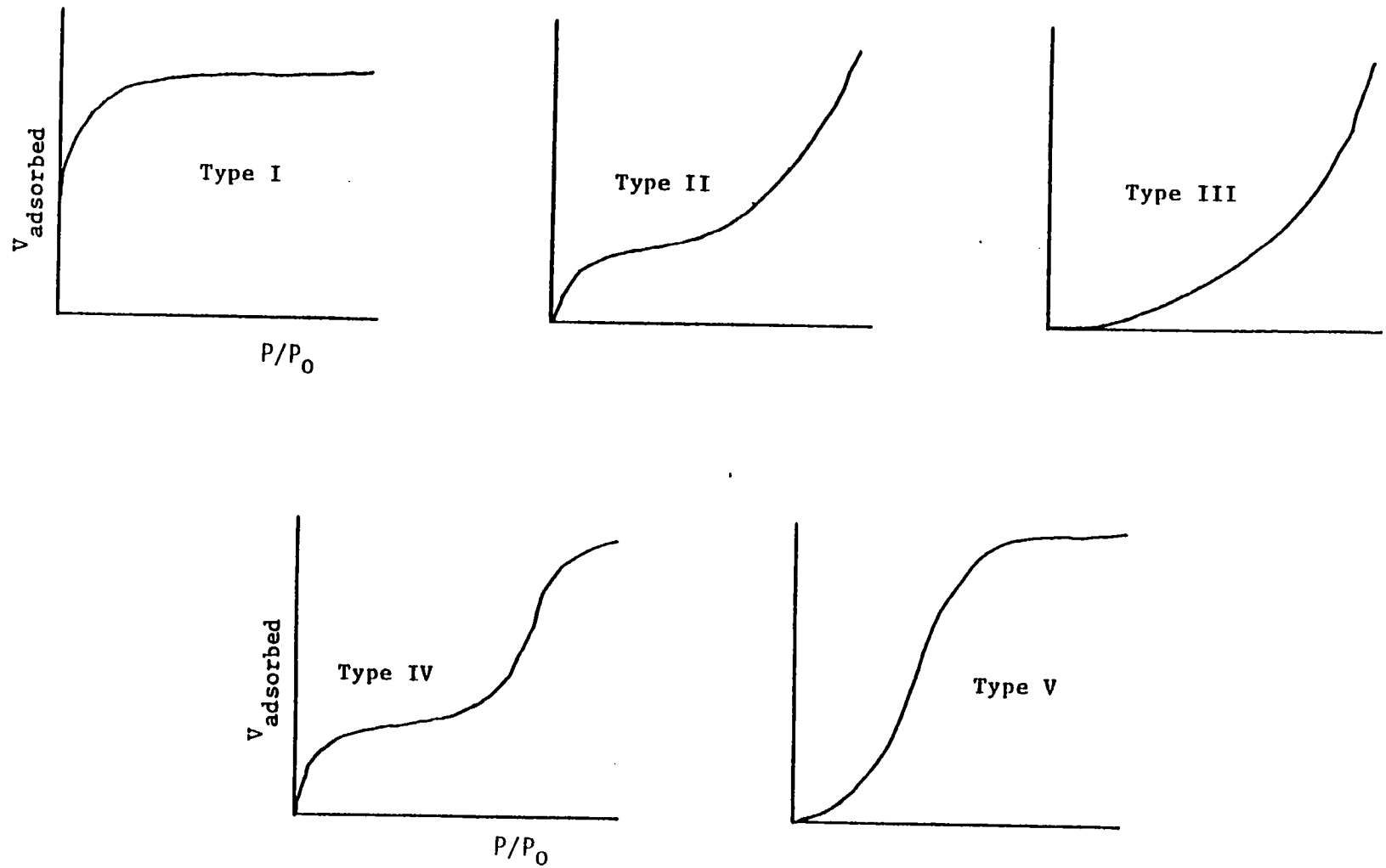

Figure 2. Five types of adsorption isotherms

Type II isotherms were obtained for the powders of all three pavement component substrates using water as the adsorbate. These isotherms shown in Figure 3 are characteristic of powders with cracks, pores, or capillaries in their surface. The presence of the knee in the adsorption isotherm at a partial pressure of about 0.1 indicates that the energy released during adsorption of the first layer of the adsorbate is significantly higher than the energy released during the adsorption of subsequent layers.

The data between a partial pressure of 0.05 and 0.35 were analyzed as described in Appendix A to obtain $E_1 - E_L$, where E_1 is the first layer heat of adsorption and E_L is the heat of liquefaction of the adsorbate (water in this case). From this the energy released per unit area and the bond energy of a single adsorption site were calculated. The results of this data analysis are presented in Table 5.

The energy released per unit area for silica and portland cement mortar are comparable, but the value for limestone is considerably lower. The adsorption site area per molecule for limestone is about double that of silica and mortar, which explains why the energy per unit area is about half. However, the bond energy of limestone is slightly higher than portland cement mortar and both are lower than silica, which was assumed to be a high energy surface at the beginning of the investigation. This suggests that the silica component of portland cement concrete makes a greater thermodynamic contribution to the ice-pavement bond than the other two pavement components.

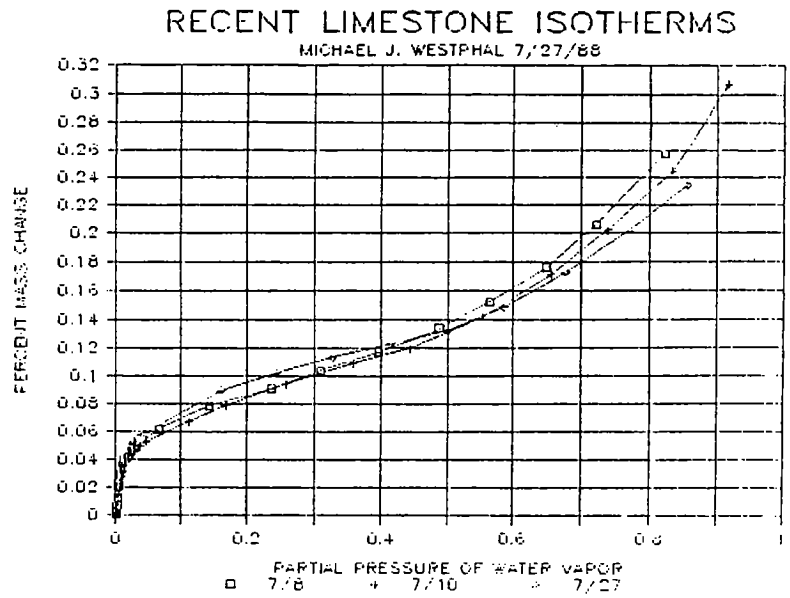

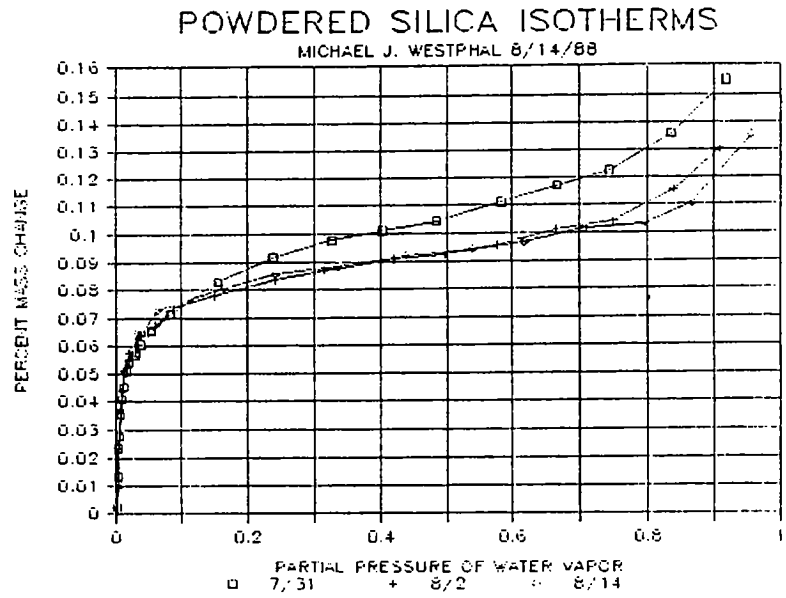

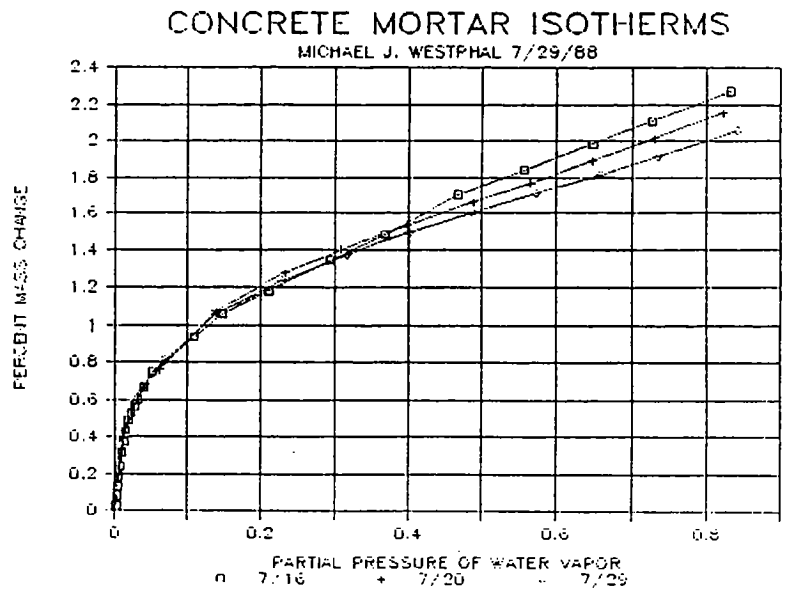

Figure 3. **Limestone isotherms (a), powdered silica isotherms (b), and portland cement mortar isotherms (c)**

Table 5. Adsorption isotherm analysis for water on pavement components.

Material sample No.		BET constant ($\times 10^2$)	Monolayer mass ($\times 10^{-2} mg^{-1}$)	$E_1 - E_L$ ($\times 10^2$ J/g)	Energy released/ unit area (J/m^2)	Adsorption Site area (A^2)	Bond energy (eV)
Silica	1	152.9	3.11	13.03	1.39	7.66	0.666
	2	13.89	3.18	9.82	1.27	7.62	0.604
	3	1.81	3.51	7.06	1.29	6.89	0.553
Portland cement mortar	1	0.571	50.8	5.49	1.24	6.77	0.524
	2	0.476	52.1	5.25	1.28	6.49	0.520
	3	0.472	50.9	5.22	1.25	6.64	0.519
Limestone	1	0.783	4.00	5.91	0.713	11.96	0.532
	2	0.587	3.68	5.49	0.640	13.07	0.522
	3	0.792	3.76	5.94	0.656	12.97	0.531

Properties of Ice Grown on Different Substrates

Understanding the influence of the surface properties of a solid on the structure of ice formed at the interface should provide a basis for developing better methods for ice removal from highway surfaces. An investigation was performed of the morphology (structure) of ice grown on model substrates with different surface energetics. The purposes of the interfacial ice growth study were twofold. The first was to determine the effect, if any, of the model substrate surface energies upon the morphology of ice found at the ice-substrate interface. The second purpose of the work was to investigate and establish, if possible, the existence of a liquid-like layer at the ice-substrate interface that has been postulated by other researchers.

Four model substrates—gold, mercury, fluorinated oil, and FEP Teflon—were tested to cover the high and low ranges of surface energies (i.e., gold is very high and FEP Teflon is near the lowest). Ice growth experiments were performed at temperatures of 25°F (–4°C), 5°F (–15°C), –10°F (–23°C), and –40°F (–40°C). Also, the freezing mode was varied so that the water either froze from the air down to the substrate or froze from the substrate upward.

In a typical experiment, five ice samples were grown on a particular substrate at one of the selected combinations of temperatures and freezing modes. The substrate was removed from the ice (leaving the ice intact) and the surface properties of the ice-substrate interface were investigated. The ice was removed from the gold substrate by amalgamation with mercury. Ice was removed from the mercury substrate by lifting the ice from the liquid mercury surface. Ice was removed from the fluorinated oil also by lifting the ice from the liquid oil surface. Finally, the ice was removed from the FEP Teflon substrate by pealing the film from the ice.

Evaluation of the morphology of the ice formed at the ice-substrate interface was made by replication of the ice surface with a thin plastic film. Replicas were made of the ice surface that was in contact with the substrate and of the ice surface generated by cleaving the ice specimen perpendicular to the ice-substrate interface. Contact angle measurements were made on the ice surfaces that were in contact with the substrate to measure the surface energetics and determine any changes the substrate may have caused.

A flowchart that summarizes the major aspects of this investigation is given in Appendix D. Also included in that appendix are details of the experimental design established for the investigations, the procedures followed in the replication of the ice surfaces, and the procedures followed and results obtained in making surface energy determinations.

A cold chamber capable of operating over the range of 32°F (0°C) to –40°F (–40°C) was constructed for the investigation. A complete description of the design, fabrication and checkout of the cold chamber is presented in Appendix E.

Sixteen formal experiments were planned which involved the four substrates (FEP Teflon, mercury, gold, and a fluorinated oil fluid) against which ice was formed at four temperatures (25°, 5°, –10°, and –40°F), then removed and examined. Twelve of the 16 runs were completed. Ice formed against a 1000-Å-thick layer of sputtered gold on clear glass could not be removed by the proposed mercury amalgamation process and was thus lost. Apparently, the gold layer was too thin to allow amalgamation to occur under the ice, although the surrounding exposed gold film was rapidly removed by the liquid mercury.

Determination of the presence or absence of the "liquid-like" layer of the complex interface layers at the substrate were planned using FTIR spectroscopy.

A mechanical problem coupled with time limitations prevented measurement of ice surface properties by FTIR spectroscopy, which was expected to yield structural information about the ice surfaces. The mechanical problem was the physical limitation in locating the sample at the fixed focal point of the FTIR microscope. No definite tests were conducted using FTIR to investigate the existence of a liquid-like layer at the ice-substrate interface.

Scanning electron microscopy (SEM) was used to examine thin film replicas formed against the ice surface. Both polystyrene and polyvinyl formal were found suitable for replication when dissolved in methylene chloride at 0.5 wt % concentration or less. Backing up the polyvinyl formal film with a thicker nitrocellulose layer produced a replica film that was less subject to collapse and wrinkle on removal by melting the ice in water and removing the film from the water-air surface. Examination of the photos from the SEM runs lead to the following observations.

- Ice formed on FEP Teflon, Mylar, fluorinated oil fluid, and mercury surfaces replicated those surfaces quite well to the 500-Å limit of observation.

- No noticeably different ice structure was noted on the substrate interface ice samples, except in the case of the Mylar film where some damage to the ice was found on removal of the film from the ice.

- The rather complex surface of fractured ice was truly replicated but polymer concentrations greater than 0.5 wt % lead to the entrapment of bubbles in the replica film. At 0.5 wt %, this phenomenon was nearly eliminated. Some surface structure

was visible in the fracture replicas at greater than 1,000X which may have been crystal ends or defects.

- No photograph showed the existence of an interphase layer. Observations of the edge of the ice fracture adjacent to the substrate interface were not obtained in all samples.

- About 25% of the fracture surface replicas were lost because of collapse of even the backed up replicas.

- The ice structure under the interface layers was readily demonstrated by allowing the ice to evaporate at test temperature. The ice saturating column was removed from the dry N_2 inlet to produce the desired evaporation. Progressive etching after 10 to 60 minutes created even deeper patterns of crystal structure.

There were many manipulative problems encountered in handling the complexly shaped replicas obtained from the cleaved ice surface, which unfortunately made observation of the replicates at the critical ice-substrate edge of the cleaved surface nearly impossible.

Examination of the ice-substrate interface by measurement of the contact angle was complicated because several of the contact angle test fluids also used for the characterization of solid substrates froze. The more polar and hydrogen-bonded fluids readily cut the ice as they quickly spread. It thus was not possible to measure the critical surface tension of ice using these fluids and techniques. A different set of fluids must be selected that have the required temperature range of fluidity and surface tension properties for successful determination of the critical surface tension. The only contact angle test liquid that did not wet and spread on the surface of the ice or freeze was α-bromonaphthalene. Mercury as a test liquid was also used and found to be partially satisfactory. The results of these measurements are given in Appendix D. Conclusions concerning the significance of these measurements are given below.

All of the contact angle measurements made on ice grown on FEP Teflon (low energy surface) and on mercury (high energy surface) gave similar results. Thus, the effect of these two substrates on the ice-substrate interface was not measurable using the sessile drop contact angle method.

The contact angle measurements made on ice grown against fluorinated oil varied widely. This variability was probably due to a residue of the fluorinated oil left on the ice. The variability in measurements also prevented any conclusions from being drawn about the effects of this substrate on the ice-substrate interface structure.

Investigation of Physical Processes for Disbonding Ice from Various Substrates

Presented below are the findings relative to several investigations of physical processes for disbonding ice from various substrate surfaces. The findings resulting from an investigation of selective heating of the ice-substrate interface by IR radiation are given first. These are followed by the results from a study of the ice-substrate bond shear strength under low rate shear conditions. The findings from an investigation into the destruction of ice-substrate bonds by chemical undercutting are then given. Next are presented the findings from an investigation of the impact effects of ice bonded to pavement materials. Finally, the results are given concerning the use of thermal stress to induce disbonding at the ice-substrate interface.

Investigation of Selective Heating of the Ice-Substrate Interface by IR Radiation

This area of investigation involved the evaluation of the potential for using selective wavelengths of IR radiation to disbond ice at the ice-pavement interface. This concept was rather speculative in nature but held a high potential for application of thermal energy selectively to the ice-substrate material. The investigation was organized in a series of four steps, each designed to provide either positive or negative decisions as to the potential of this approach to selective heating. The four steps were: literature survey, FTIR-IR evaluation, analytical evaluation, and proof of concept. If a negative decision was reached at any point, further work in this area was to be stopped.

The initial step involved a literature search of the infrared absorption characteristics of ice and water. A number of bulk ice measurements have been reported (15-17), but no reports of surface ice were found. All of the bulk ice reports dealt with transmission experiments in the O-H stretching region.

In the absence of definite evidence regarding the spectrum of surface ice, it was decided to conduct a series of experiments using an Analect Fourier Transform Infrared Spectrophotometer. The purpose of these experiments was to compare the infrared spectrum of surface ice (thin ice coating) with that of bulk ice and water. The rationale behind the experiments was that surface ice is more representative of the ice-pavement interface than is bulk ice. If the infrared absorption properties of the surface ice are sufficiently different from bulk ice, a window may result allowing a selective irradiation of the ice-pavement interface.

The spectra necessary to characterize the IR absorption were made using a prism reflectance cell (18). Both liquid and solid samples are accessible using the method. Because the cell sample attenuated total reflectance (ATR-IR) of the infrared radiation, it was ideally suited to highly absorbing substances such as water and ice. Use of a 45° ZnSe crystal results in an effective pathlength of 0.9 μm at 3300 cm^{-1}. Thus, the cell samples the first 1 micron of ice in contact with the ZnSe substrate.

Figure 4 shows the ATR-IR spectrum of liquid water in the prism cell. The spectrum is characterized by a broad absorption band near 3300 cm^{-1} (OH stretching modes) and a weaker band near 1650 cm^{-1} (water bending mode). The spectrum is in good agreement with the published data (18). To obtain the spectrum of ice, the ZnSe crystal was cooled gradually with liquid nitrogen followed by the condensation of liquid water onto the surface. The resulting ATR-IR spectrum of ice is shown in Figure 5. The O-H stretching region is observed to narrow somewhat and shift to lower frequency. The spectra are plotted together in Figure 6. The water (ice) bending mode is unshifted, but decreases in intensity broadens somewhat. The spectra were reproducible over a period of 30 minutes, and a considerable amount of ice was observed to melt off the crystal at the end of the experiment.

The absorption characteristics of the ice spectrum in Figure 7 with an expanded wave-length scale are very similar to the band shape and position of amorphous ice (15). This result demonstrates the similarity of bulk and surface ice (when sampled to a depth of 1 μm). Because of this similarity and the similarity of amorphous and crystalline ice reported in the literature (15), it was concluded that an appropriate window for selective surface irradiation does not exist. Consequently, further work on selective heating of the ice-substrate interface by IR radiation was abandoned.

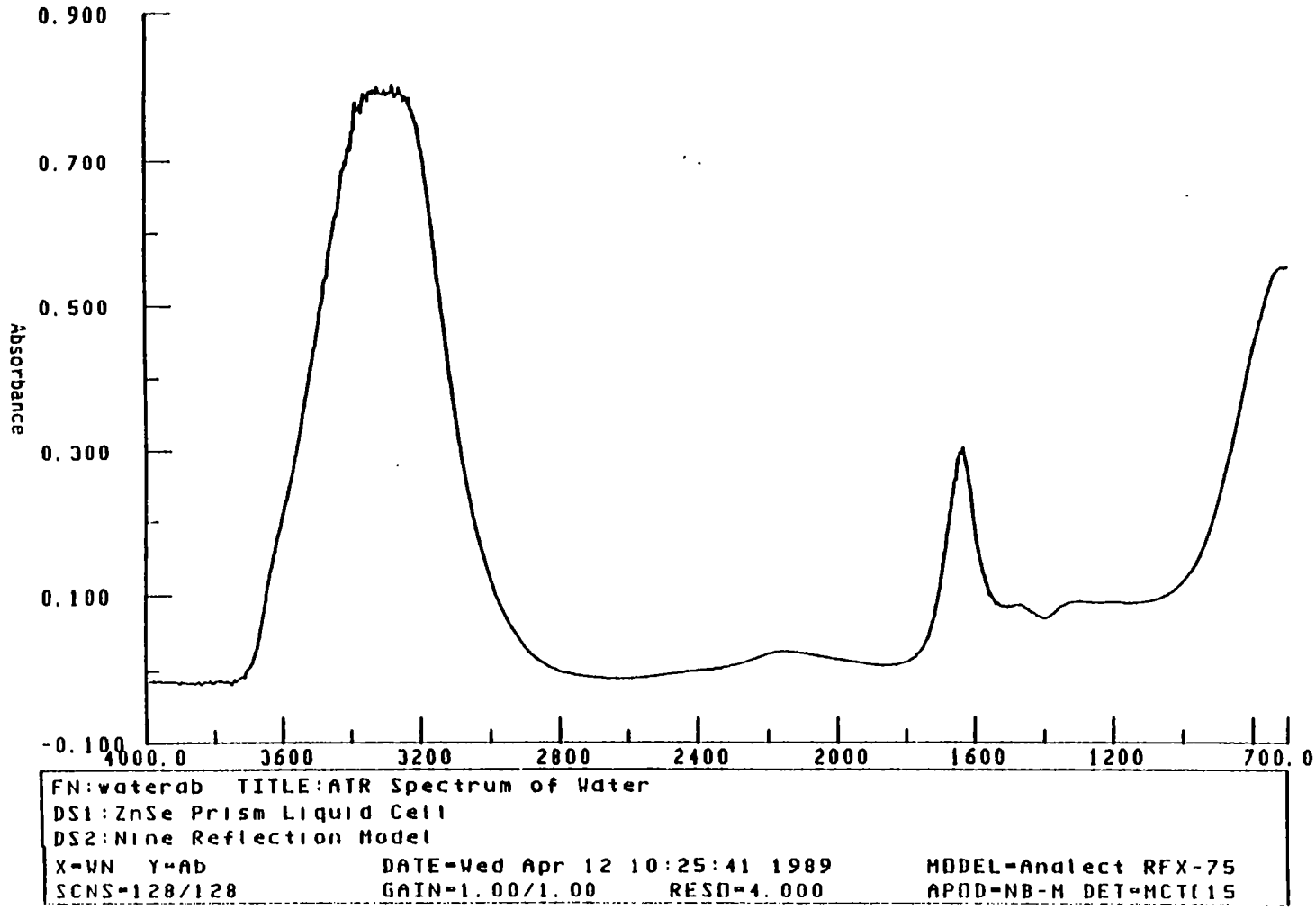

Figure 4. ATR-IR spectrum of water

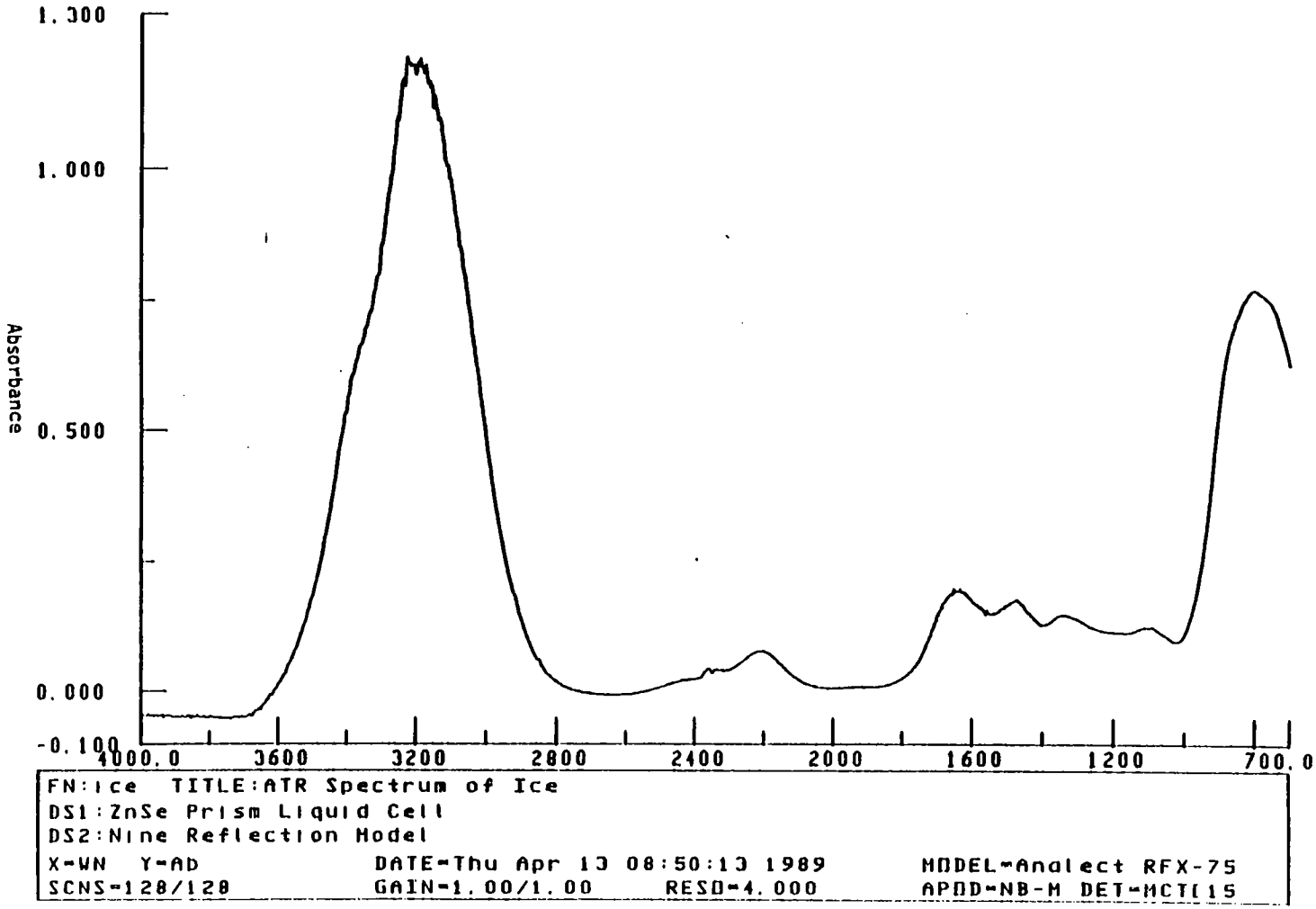

Figure 5. ATR-IR spectrum of ice

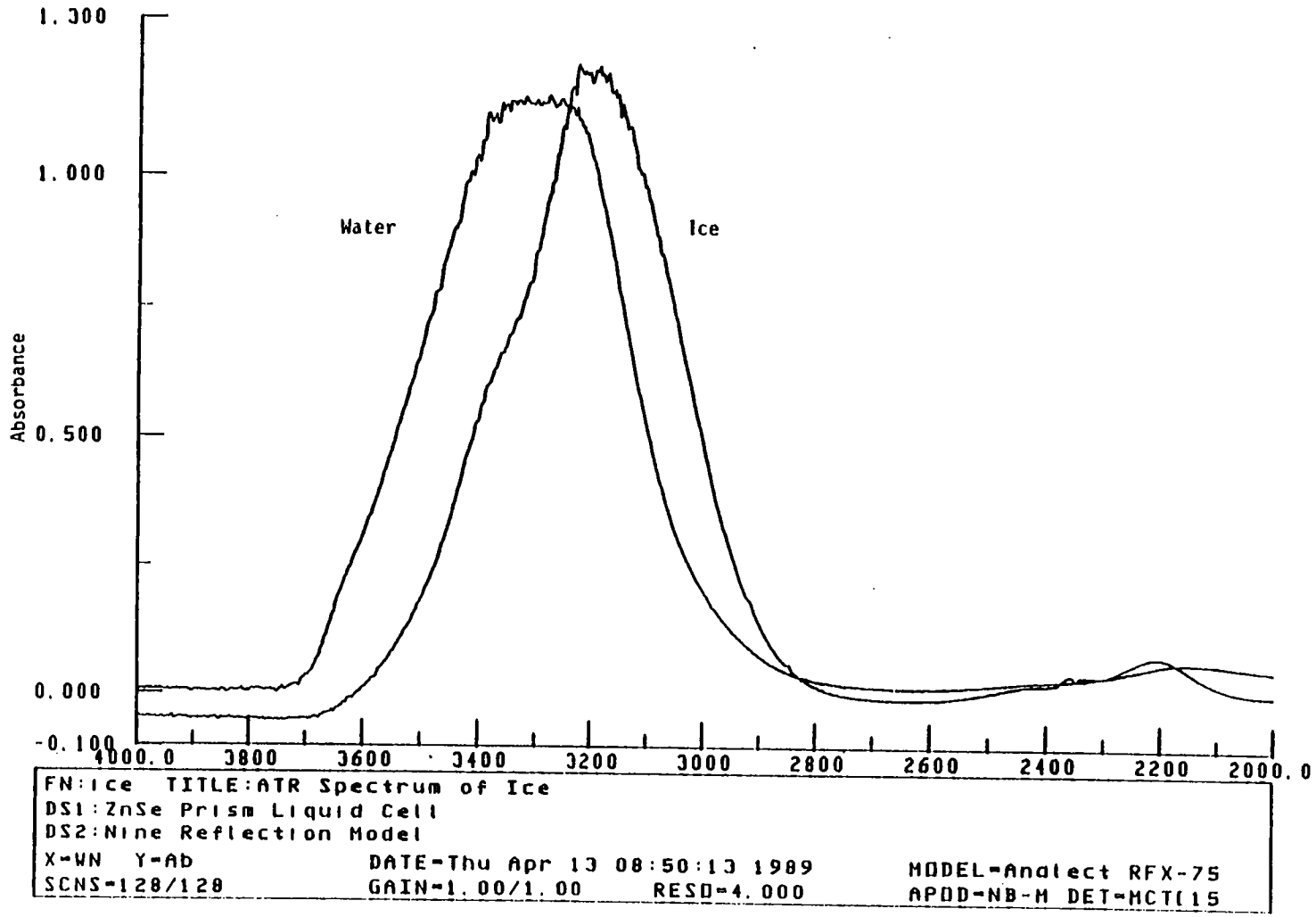

Figure 6. ATR-IR spectrum of ice and water

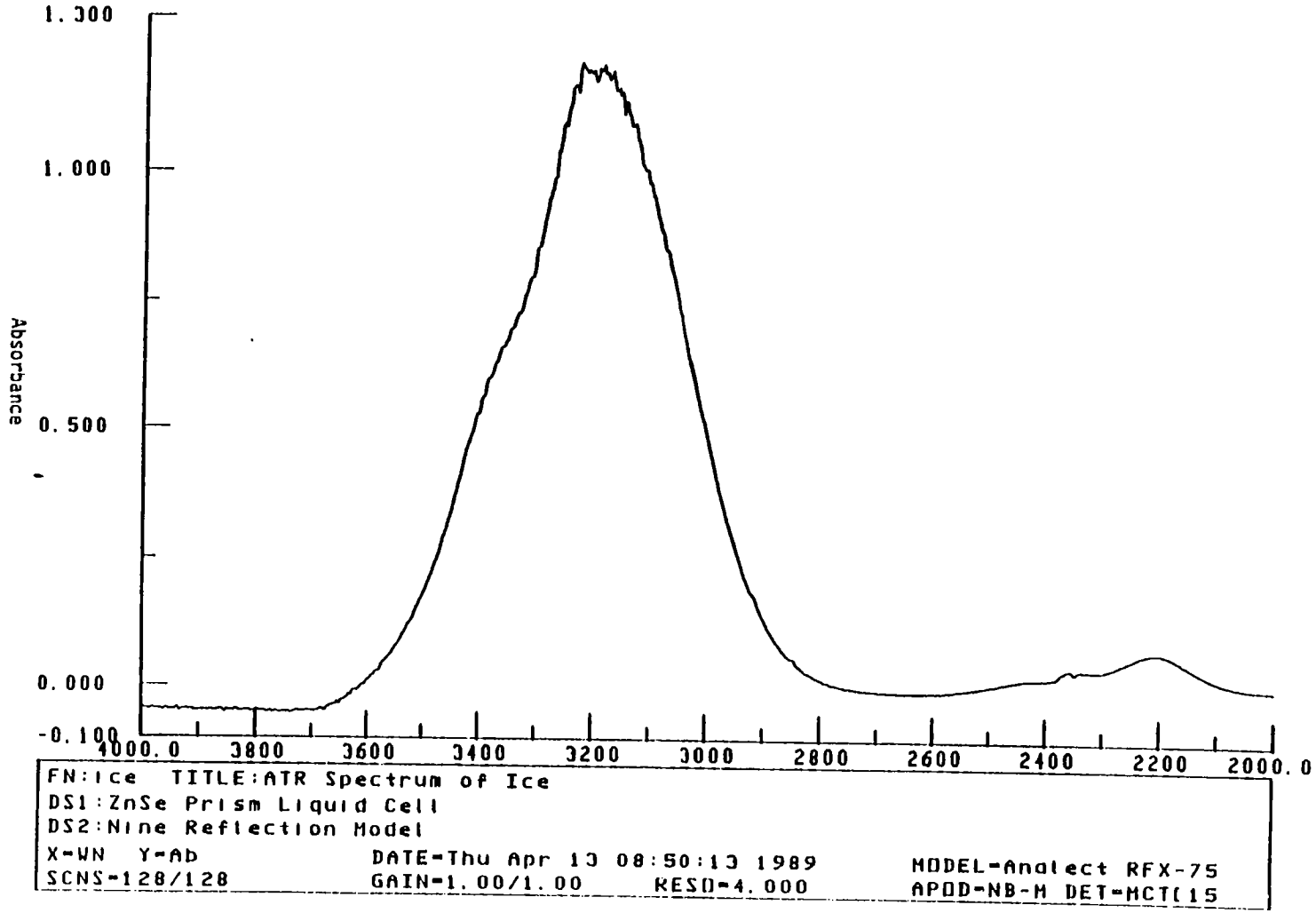

Figure 7. Adsorption characteristics of the ice spectrum

Ice-Substrate Bond Shear Strength Under Low-Rate Shear Conditions

This section presents the results of measurements made under low load rate conditions of the ice substrate bond strength in shear on untreated substrates. Shear strength measurements of ice on various substrates were performed in order to give a direct measure of adhesional bonding strength. Such tests give insight into bonding mechanisms and are also relevant to the direct mechanical removal of ice from highway surfaces.

Experimental Conditions

A statistically valid experimental design was developed for guiding the shear test experiments. The design called for testing six substrates—two model substrates (Pyrex and Teflon) and four substrates which represent components of highway surfaces (limestone, silica, portland cement mortar, and asphalt) under combinations of test temperature, freezing rates, and modes of freezing. Four temperature conditions were used: 25°F (–4°C), 15°F (–9°C), 5°F (–15°C), and –9°F (–23°C). Three freezing rates were used during the testing (slow, medium, and fast) along with two modes of freezing. Freezing from the substrate upward was referred to as the bottom-up (BU) freezing mode. Freezing from the top surface of the water downward to the substrate was referred to as the top-down (TD) mode.

The shear rate used in all the tests was approximately 4,000 lb/minute (1,814 kg/min)—the fastest rate that could be achieved with the testing apparatus. A description of this test apparatus and the details of the test procedures are presented in Appendix F.

Measuring the shear strength of ice on Teflon necessitated some major changes in the shear test methods and procedures used for the other substrates. A "Stair-Case Testing Facility" was developed to address the unique problems associated with testing the Teflon substrate. This testing facility is described in Appendix G.

Results and Statistical Analysis of the Shear Strength Data

The results of the interfacial shear testing of chemically untreated substrates are included in Tables 6 through 11. The complete data obtained, including sessile drop measurements, are given in Appendix D. Between five and eight replicate shear tests were run for each set of conditions. All of the tabulated data except that for limestone code number 4100 were used in the analysis. The data for limestone code number 4100 were discarded as outliers. These data were found to be high and the test runs were then replicated three times in test runs 4100B, 4100C, and 4100D. The results from the 4100 test run were replaced by those from 4100B, 4100C, and 4100D.

Two experimental designs were developed for conducting the shear tests: one for the pavement components of limestone, asphalt, and portland cement (PC) mortar, and one for the substrates of silica, Pyrex, and Teflon. Generally, the shear strength results were analyzed separately for these two sets of substrates. The shear strength results for silica under fast freezing rate and bottom-up freezing mode conditions were also combined with the results from limestone, asphalt, and PC mortar in performing the analysis of the pavement component substrates. This was done because silica is truly a component of highway pavements.

Figure 8 shows the results of tests performed on silica limestone, asphalt, and PC mortar. All of the ice specimens tested were subjected to bottom-upward freezing at a fast rate. Average shear strength values in Figure 8 have standard deviations of between 0.37 and 1.78 kg/cm^2 and associated standard errors of between 0.13 and 0.63 kg/cm^2 (see Tables 6, 7, 8, and 9). The curves in Figure 8 and subsequent figures of shear strength measurements are drawn to show general trends of the plotted data; they are not statistically based.

A total of 176 individual tests run on the component substrates at 16 different combinations of experimental conditions was available for analysis. The test runs considered were all tests with the four pavement components run at the four temperatures of –4°, –9°, –15°, and –23°C. An analysis of variance (ANOVA) with two main factors, substrate and temperature, and their interaction was performed. The interaction term was not statistically significant ($p = 53\%$), that is, the effect of changing test temperatures on shear strength does not vary between substrates. Consequently, the interaction term was deleted in a subsequent ANOVA.

Table 6. Shear test of ice on limestone

Code number	Freeze freeze mode[a]	Test rate F,M,S[b]	Mean shear temp. (°C)	Shear strength (kg/cm^2)	Deviation (kg/cm$^{2)}$
4100	BU	F	–4	7.61	2.30
4100B	BU	F	–4	3.46	0.81
4100C	BU	F	–4	3.64	0.97
4100D	BU	F	–4	3.80	0.61
4200	BU	F	–9	5.10	1.23
4300	BU	F	–15	5.29	1.28
4300B	BU	F	–15	5.68	1.52
4400	BU	F	–23	4.00	0.93

[a] BU = Bottom-upward freezing
TD = Top-downward freezing

[b] F = Fast rate of freezing
M = Medium rate of freezing
S = Slow rate of freezing

Table 7. Shear test of ice on asphalt

Code number	Freeze freeze mode	Test rate F,M,S	Mean shear temp. (°C)	Shear strength (kg/cm^2)	Deviation (kg/cm^2)
5100	BU	F	–4	1.88	0.40
5200	BU	F	–9	3.38	1.16
5300	BU	F	–15	2.84	0.99
5400	BU	F	–23	1.55	0.50

Table 8. Shear test of ice on portland cement mortar

Code number	Freeze freeze mode	Test rate F,M,S	Mean shear temp. (°C)	Shear strength (kg/cm^2)	Deviation (kg/cm^2)
6100	BU	F	–4	4.34	1.72
6100B[a]	BU	F	–4	5.76	1.78
6200	BU	F	–9	6.09	1.37
6200B[a]	BU	F	–9	6.82	1.62
6300	BU	F	–15	6.20	0.81
6300B[a]	BU	F	–15	5.88	1.14
6400	BU	F	–23	5.97	1.41

[a] A second series of measurements was made for 6100B, 6200B, and 6300B because sessile drop testing was not conducted beforehand.

Table 9. Shear test of ice on silica

Code number	Freeze freeze mode	Test rate F,M,S	Mean shear temp. (°C)	Shear strength (kg/cm^2)	Deviation (kg/cm^2)
3112	TD	S	–4	3.85	2.15
3131	BU	F	–4	1.45	0.37
3212	TD	S	–9	3.34	1.58
3212B[a]	TD	S	–9	4.57	1.67
3231	BU	F	–9	3.37	1.41
3312	TD	S	–15	2.64	1.56
3331	BU	F	–15	3.22	1.20
3412	TD	S	–23	2.51	0.77
3412B[a]	TD	S	–23	2.59	1.19
3431	BU	F	–23	1.96	0.62

[a] Set of measurements was repeated because no sessile drop test was conducted prior to shear strength testing.

Table 10. Shear test of ice on Pyrex

Code number	Freeze freeze mode[a]	Test rate F,M,S[b]	Mean shear temp. (°C)	Shear strength (kg/cm²)	Deviation (kg/cm²)
1121	BU	M	–4	2.19	1.26
1132	TD	F	–4	2.40	1.15
1221	BU	M	–9	2.41	0.63
1232	TD	F	–9	2.51	1.31
1321	BU	M	–15	1.92	0.53
1332	TD	F	–15	2.44	0.56
1421	BU	M	–23	1.53	0.47
1432	TD	F	–23	2.18	0.91

[a] BU = Bottom-upward freezing
TD = Top-downward freezing

[b] F = Fast rate of freezing
M = Medium rate of freezing
S = Slow rate of freezing

Table 11. Shear test of ice on Teflon

Code number	Freeze freeze mode	Test rate F,M,S	Mean shear temp. (°C)	Shear strength (kg/cm²)	Deviation (kg/cm²)
2111	BU	S	–4	0.19	0.08
2122	TD	M	–4	0.23	0.12
2211	BU	S	–9	0.09	0.03
2211B	BU	S	–9	0.20	0.05
2211C	BU	S	–9	0.13	0.07
2222	TD	M	–9	0.32	0.10
2311	BU	S	–15	0.23	0.08
2322	TD	M	–15	0.30	0.06
2411	BU	S	–23	0.18	0.04
2422	TD	M	–23	0.30	0.07

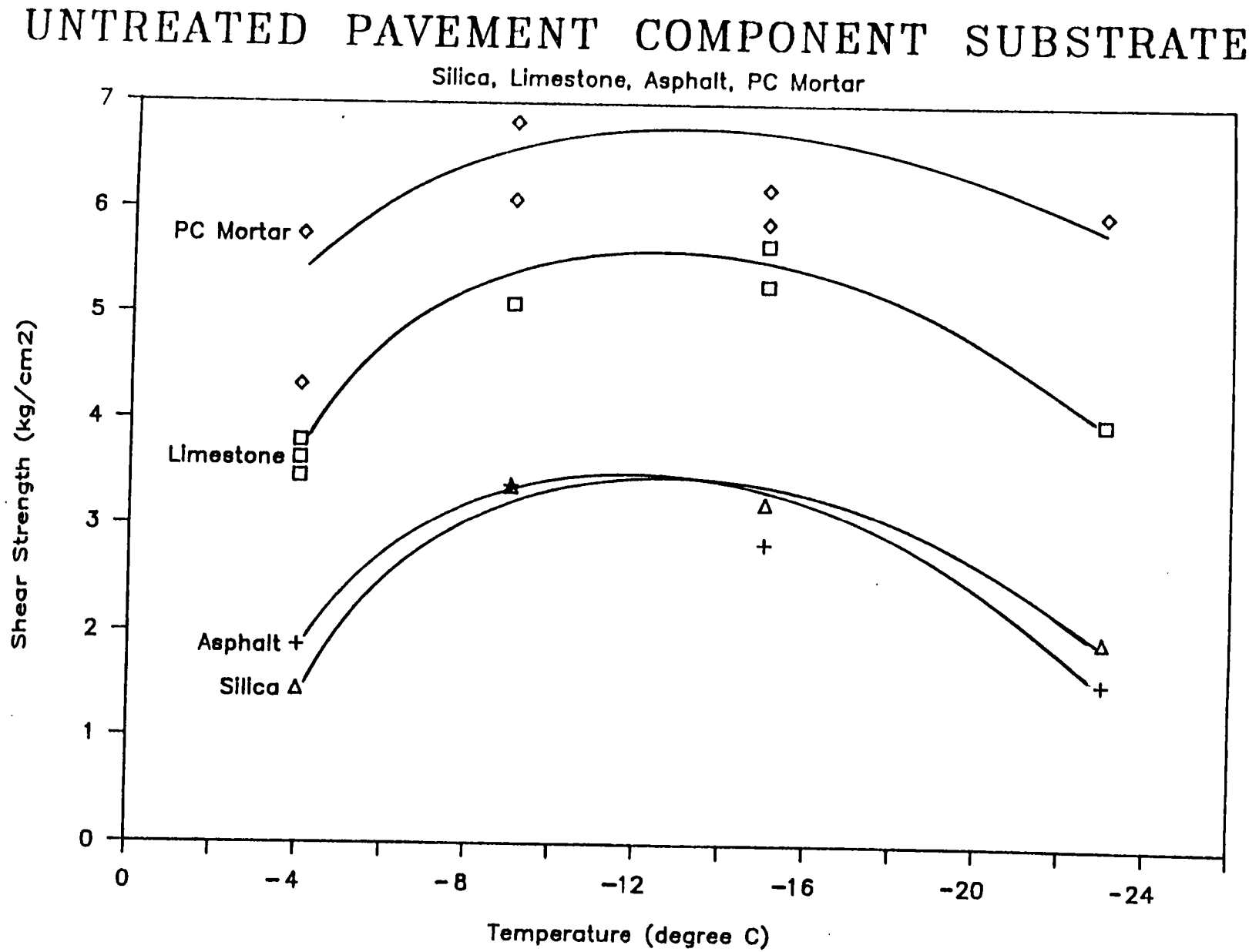

Figure 8. Bond shear strength of ice on pavement components

The overall mean shear strength for silica, limestone, asphalt, and PC mortar is 4.17 kg/cm^2 with an experimental error (root mean square error) of 1.17 kg/cm^2.

Most of the variation in the shear strength data is due to the substrate effect (F value of 83.9) and some to the temperature effect (F value of 17.5), both being significant at the 0.001 level. Shear strength least square means and standard errors (se) at each level of the two factors are given below.

Substrates (significant at the 99.9% confidence level)

Limestone:	shear strength = 4.58, se = 0.16 kg/cm^2
Asphalt:	shear strength = 2.41, se = 0.21 kg/cm^2
PC mortar:	shear strength = 5.80, se = 0.16 kg/cm^2
Silica:	shear strength = 2.50, se = 0.21 kg/cm^2

All pair-wise comparisons except the silica versus asphalt comparison are statistically significant. In order, the shear strength results are highest for PC mortar, then limestone, then silica and asphalt. The multiple comparisons were performed at the 5% experiment-wise error rate.

Temperature (significant at the 99.9% confidence level)

–4°C:	shear strength = 2.98, se = 0.16 kg/cm^2
–9°C:	shear strength = 4.56, se = 0.19 kg/cm^2
–15°C:	shear strength = 4.39, se = 0.17 kg/cm^2
–23°C:	shear strength = 3.37, se = 0.21 kg/cm^2

Of the six possible comparisons of average shear strength values between the four temperature levels, all but two are statistically significant. Shear strength is significantly higher at –9° than at –4°C; significantly higher at –9° than at –23°C; significantly higher at –15° than at –23°C; and significantly higher at –15° than at –4°C. Results at –9° and –15°C are not statistically different from each other, neither are those between –4° and –23°C. All comparisons were made at the 5% experiment-wise error rate.

Substrate by temperature interaction (not significant at the 95% confidence level): It was noted that this term was not statistically significant at the 95% confidence level. The least square means with their standard error are presented nonetheless for the 16 categories determined by the four substrates and the four temperature levels.

Limestone @	–4°C:	shear strength = 3.63, se = 0.24 kg/cm^2
Limestone @	–9°C:	shear strength = 5.10, se = 0.41 kg/cm^2
Limestone @	–15°C:	shear strength = 5.48, se = 0.29 kg/cm^2
Limestone @	–23°C:	shear strength = 4.00, se = 0.41 kg/cm^2
Asphalt @	–4°C:	shear strength = 1.88, se = 0.41 kg/cm^2
Asphalt @	–9°C:	shear strength = 3.38, se = 0.41 kg/cm^2
Asphalt @	–15°C:	shear strength = 2.84, se = 0.41 kg/cm^2
Asphalt @	–23°C	shear strength = 1.55, se = 0.41 kg/cm^2
PC mortar @	–4°C:	shear strength = 5.05, se = 0.29 kg/cm^2
PC mortar @	–9°C:	shear strength = 6.45 se = 0.29 kg/cm^2
PC mortar @	–15°C:	shear strength = 6.04, se = 0.29 kg/cm^2

PC mortar @	−23°C:	shear strength = 5.97, se = 0.41 kg/cm^2
Silica @	−4°C:	shear strength = 1.45, se = 0.41 kg/cm^2
Silica @	−9°C:	shear strength = 3.37, se = 0.41 kg/cm^2
Silica @	−15°C:	shear strength = 3.22, se = 0.41 kg/cm^2
Silica @	−23°C:	shear strength = 1.96, se = 0.41 kg/cm^2

Figure 9 is a plot of shear strength versus temperature results for tests performed on silica for two freezing rates (slow and fast) and two freezing modes (bottom-up and top-down). Average shear strength values in Figure 9 have standard deviations of between 0.37 and 2.15 kg/cm^2 and associated standard errors of between 0.13 and 0.76 kg/cm^2 (see Table 9).

Figure 10 is a plot of shear strength versus temperature results for tests performed on Pyrex at two freezing rates (medium and fast) and two freezing modes (bottom-up and top-down). Average shear strength values in Figure 10 have standard deviations of between 0.47 and 1.31 kg/cm^2 and associated standard errors of between 0.17 and 0.46 kg/cm^2 (see Table 10).

Figure 11 is a plot of shear strength versus temperature results for tests performed on Teflon at two freezing rates (slow and medium) and two freezing modes (bottom-up and top-down). Average shear strength values in Figure 11 have standard deviations of between 0.03 and 0.12 kg/cm^2 and associated standard errors of between 0.01 and 0.04 kg/cm^2 (see Table 11).

A total of 209 individual tests run on silica, Pyrex, and Teflon at 24 different combinations of experimental conditions, were available for analysis. The experimental design was a modified Latin-square design, replicated at each temperature level. An analysis of variance with four main factors—substrate, temperature, freezing rate, and freezing mode—and all two-way interactions with temperature was performed.

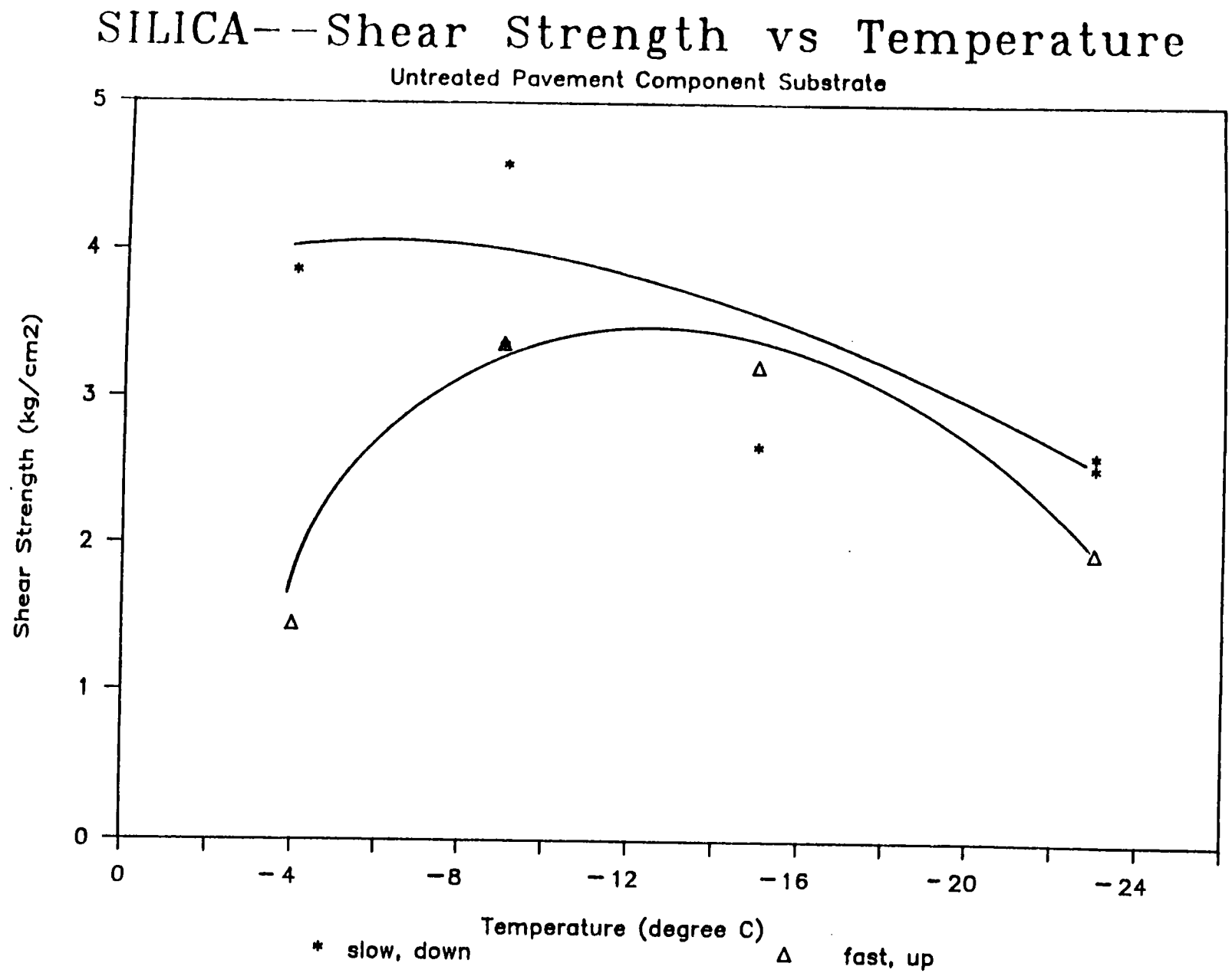

Figure 9. Bond shear strength of ice on fused silica

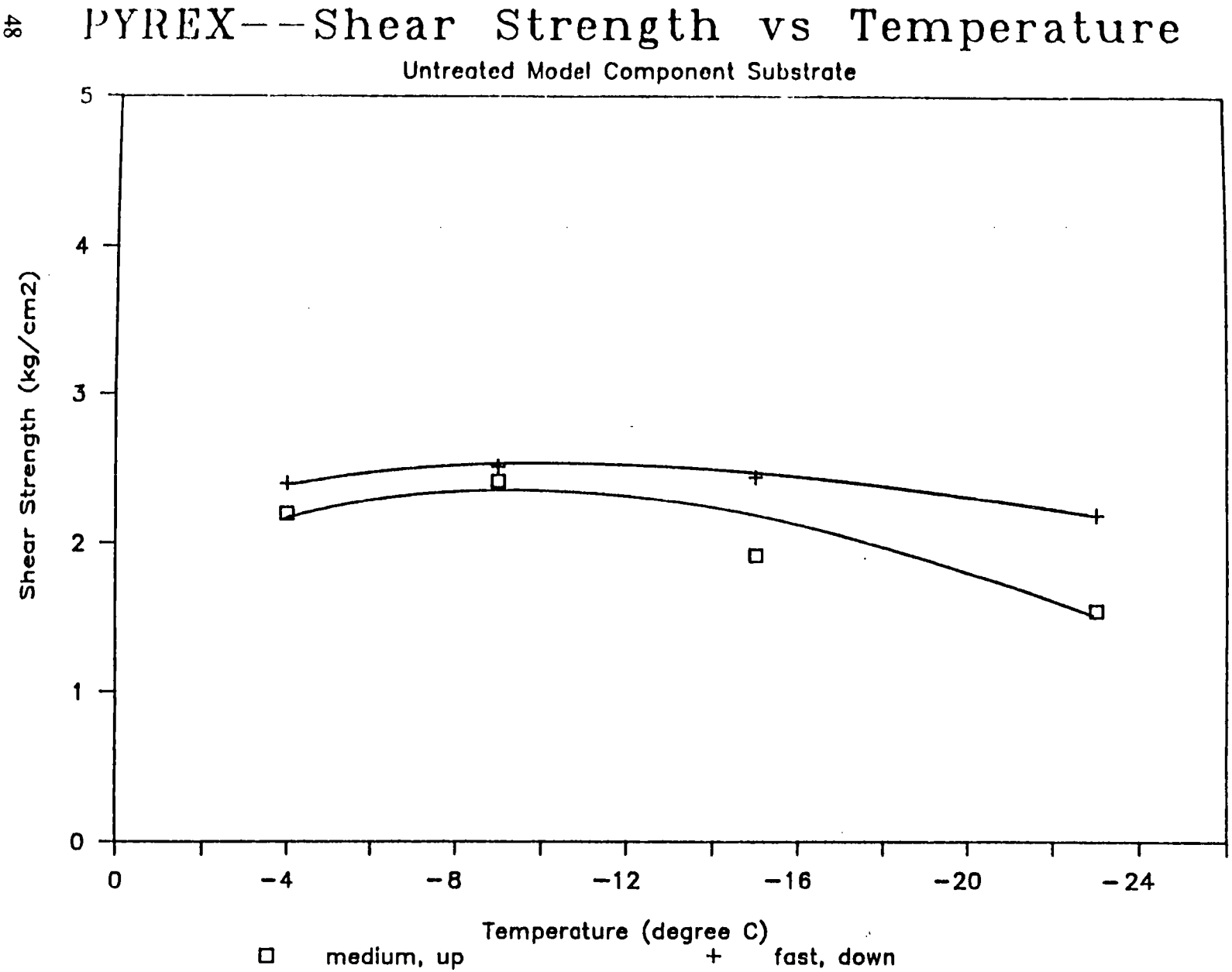

Figure 10. Bond shear strength of ice on Pyrex glass

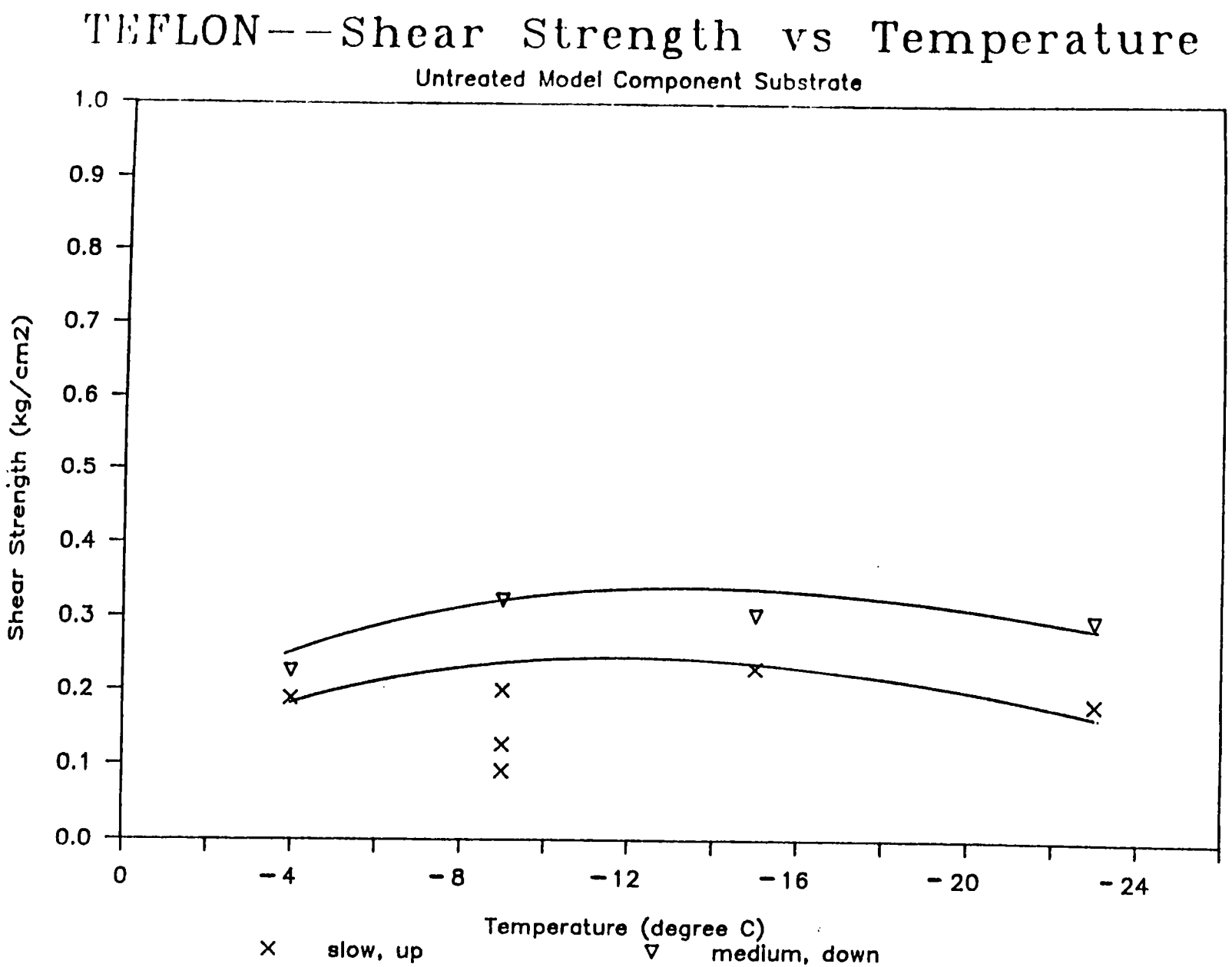

Figure 11. Bond shear strength of ice on Teflon

The overall mean strength for silica, Pyrex, and Teflon is 1.83 kg/cm^2 with an experimental error (root mean square error) of 0.97 kg/cm^2. These results are considerably lower than those for the pavement components, and with smaller error terms.

Of all the main effects and two-way interactions in the analysis, freezing rate and the temperature-by-freezing mode interaction were not statistically significant at the 95% confidence level. Again, the differences among substrates contributed most to the variation in the shear strength (F of 107.4), while all other statistically significant terms contributed relatively little to the variation in the test results (largest F is 8.9).

Shear strength least square means and their standard error (se) for all factors and two-way interactions are given below.

Substrates (significant at the 95% confidence level)

Pyrex:	shear strength = 2.31, se = 0.13 kg/cm^2
Teflon:	shear strength = 0.17, se = 0.14 kg/cm^2
Silica:	shear strength = 2.84, se = 0.13 kg/cm^2

All three pair-wise comparisons are statistically significant at the 5% experiment-wise error rate. Shear strength decreases significantly from silica, to Pyrex, to Teflon.

Temperature (significant at the 95% confidence level)

–4°C:	shear strength = 1.72, se = 0.14 kg/cm^2
–9°C:	shear strength = 2.13, se = 0.13 kg/cm^2
–15°C:	shear strength = 1.79, se = 0.14 kg/cm^2
–23°C:	shear strength = 1.45, se = 0.14 kg/cm^2

Of all six possible pair-wise comparisons of average shear strength between the four temperature levels, all but one comparison is not significant at the 5% experiment-wise error rate. As temperature decreases from –4° to –23°C, shear strength increases to a maximum value and then decreases as the temperature approaches –23°C. This pattern has been observed throughout this data base.

Freezing rate (not significant at the 95% confidence level)

Slow	shear strength = 2.00, se = 0.13 kg/cm^2
Medium	shear strength = 1.69, se = 0.14 kg/cm^2
Fast	shear strength = 1.64, se = 0.13 kg/cm^2

No pair-wise comparison is statistically significant, that is, overall, the rate of freezing has no effect on shear strength for these three substrates. However, there is a significant temperature by freezing rate interaction as shown below, which indicates that overall, the freezing rate effect is washed out by the temperature effect.

Freezing mode (significant at the 95% confidence level)

Up	shear strength = 1.57, se = 0.10 kg/cm^2
Down	shear strength = 1.98, se = 0.10 kg/cm^2

The mode of ice freezing on the three substrates has a significant effect on shear strength.

Substrate by temperature interaction (significant at the 95% confidence level)

Pyrex @	–4°C:	shear strength = 2.69, se = 0.28 kg/cm^2
Pyrex @	–9°C:	shear strength = 2.54, se = 0.26 kg/cm^2
Pyrex @	–15°C:	shear strength = 2.07, se = 0.27 kg/cm-^{2}
Pyrex @	–23°C:	shear strength = 1.94, se = 0.27 kg/cm^2
Teflon @	–4°C:	shear strength = 0.00, se = 0.28 kg/cm^2
Teflon @	–9°C:	shear strength = 0.13, se = 0.24 kg/cm^2
Teflon @	–15°C:	shear strength = 0.45, se = 0.28 kg/cm^2
Teflon @	–23°C	shear strength = 0.25, se = 0.29 kg/cm^2
Silica @	–4°C:	shear strength = 2.63, se = 0.27 kg/cm^2
Silica @	–9°C:	shear strength = 3.72 se = 0.24 kg/cm^2
Silica @	–15°C:	shear strength = 2.86, se = 0.27 kg/cm^2
Silica @	–23°C:	shear strength = 2.17, se = 0.24 kg/cm^2

The temperature effect on shear strength varies by substrate. This is best depicted in the plot of these results in Figures 9, 10, and 11.

Freezing rate by temperature interaction (significant at the 95% confidence level)

Slow rate @	–4°C:	shear strength = 2.51, se = 0.28 kg/cm^2
Slow rate @	–9°C:	shear strength = 2.29, se = 0.21 kg/cm^2
Slow rate @	–15°C:	shear strength = 1.58, se = 0.28 kg/cm^{-2}
Slow rate @	–23°C:	shear strength = 1.61, se = 0.26 kg/cm^2
Med. rate @	–4°C:	shear strength = 1.66, se = 0.28 kg/cm^2
Med. rate @	–9°C:	shear strength = 2.16, se = 0.27 kg/cm^2
Med. rate @	–15°C:	shear strength = 1.64, se = 0.27 kg/cm^2
Med. rate @	–23°C	shear strength = 1.27, se = 0.27 kg/cm^2
Fast rate @	–4°C:	shear strength = 0.99, se = 0.27 kg/cm^2
Fast rate @	–9°C:	shear strength = 1.94 se = 0.26 kg/cm^2
Fast rate @	–15°C:	shear strength = 2.16, se = 0.27 kg/cm^2
Fast rate @	–23°C:	shear strength = 1.47, se = 0.27 kg/cm^2

Freezing mode by temperature interaction (not significant at the 95% confidence level)

Bottom-up @	–4°C:	shear strength = 1.28, se = 0.21 kg/cm^2
Bottom-up @	–9°C:	shear strength = 1.97, se = 0.18 kg/cm^2
Bottom-up @	–15°C:	shear strength = 1.79, se = 0.20 kg/cm-^{2}
Bottom-up @	–23°C:	shear strength = 1.23, se = 0.21 kg/cm^2
Top-down @	–4°C:	shear strength = 2.16, se = 0.20 kg/cm^2
Top-down @	–9°C:	shear strength = 2.29, se = 0.19 kg/cm^2
Top-down @	–15°C:	shear strength = 1.80, se = 0.20 kg/cm^2
Top-down @	–23°C	shear strength = 1.68, se = 0.19 kg/cm^2

The four pavement components were not tested at all freezing mode and freezing rate combinations because of practical constraints. Consequently, no direct assessment of these effects on shear strength results can be made for all these substrates.

However, an assessment of these effects can be made based on the results for silica, Pyrex, and Teflon. Based on the results for these three substrates, only the freezing mode had a statistically significant effect on the shear strength. However, the difference between the top-down results, 1.98 kg/cm^2, and the bottom-up results, 1.57 kg/cm^2, is of little practical consequence.

Some overall comments can be made relative to the shear strength data presented in the figures. The shear strength of the ice-substrate bond is a maximum around –9°C and exhibits a nonlinear behavior with temperature for all substrates. A possible explanation for this behavior is as follows:

1. At –4°C, the ice-substrate bond is weak, and most breaks occur at this interface.

2. At –9°C, the ice-substrate bond has increased. Some of the breaks are clean; others leave ice on the interface.

3. At –15°C and certainly at –23°C, the ice has become brittle, and the interface bond is still strong. Most breaks at these temperatures occur within the bulk ice where the shear strength is less than at the interface.

Investigation of the Effects of Chemical Undercutting on Ice-Substrate Bond Shear Strength

A series of tests was performed to investigate the effects of chemical undercutting on the ice-substrate bond shear strength under extremely low load rate conditions. The tests involved the determination of time, after initiation of chemical undercutting, to shear failure of the ice-substrate interface under a fixed load condition. The shear tests were performed using the "Stair-Case Testing Facility" described in Appendix G. The combination of undercutting/ shear tests were conducted at two temperatures (–4°C and –9°C) using one substrate (limestone) and two deicing chemicals (NaCl and ethylene glycol).

The substrate preparation procedure was the same as was used for the limestone in the low load rate shear tests up to the point where ice was grown on the substrate. The procedure unique to undercutting was as follows. Two Teflon rings were laid on each limestone substrate and a small Teflon plug with a base diameter of 3/8 in (0.95 cm) was placed in the center of each ring. Two rubber bands were fastened around the limestone and on each side of the Teflon plug in order to maintain the position of the plug as well as apply sufficient force to keep water from leaking out under the ring during the freezing process. The substrates were then placed in a freezer maintained at –20°C and then allowed to reach thermal equilibrium. Triply-distilled water was placed in the freezer until ice crystals began to form, at which time 8 mL of this ice-water was transferred to each Teflon ring. The ice samples were grown from the substrate upward using a fast freezing rate. One hour was allowed to pass and then the Teflon plugs were twisted and removed from the ice. Because of the low adhesion of ice to Teflon, the plugs could be easily removed. It should be noted, however, that we often noticed ice cracks being propagated due to the action of removing the plugs.

The limestone substrates were then transferred to the testing freezer. At least 4 hours were allowed to pass to enable the samples to reach thermal equilibrium at the desired testing

temperature. Then, beginning at the lowest limestone substrate in the stair-case, we introduced 0.50 mL of a saturated deicer solution at 0°C into the hole created by the small Teflon plugs, using a 1-mL syringe.

Initially, it was decided to apply a constant shear force to each ring that was equivalent to a shear stress of 15 psi (0.10 MPa). Calculations indicated this would require nearly 30 lb (13.6 kg) of weight hung from each ring. Because this would be difficult with the shear test apparatus, it was decided instead to hang a 3-kg weight on each ring.

Only one substrate could be tested at a time. The substrate mounted on the lowest tier of the stair-case facility was tested first, followed by the substrate on the next highest tier, and so forth. This testing arrangement prevented the deicing solution released during shear failure of one sample from contaminating the other ice samples.

The results obtained in the combined undercutting/shear tests are presented in Table 12. Each value of "time to failure" is an average of eight tests. No tests were conducted to determine time to failure without chemical undercutting because the required shear force was larger than could be produced by the test apparatus.

The extremely large times to failure recorded for the combined undercutting/shear tests indicate that the bond strength of the ice-substrate interface cannot be overcome with the desired level of static shear stress until a sizeable portion of the bond area has been chemically undercut. The test results also suggest that combined undercutting/shear tests conducted under dynamic conditions would yield more informative results that could be used in designing a ice removal system.

Table 12. Combined undercutting/shear tests of ice grown on a limestone substrate

Code number	Deicing chemical	Test temperature °C	Time to failure (min)	Standard deviation (min)
4112	NaCl	–4	71.9	22.2
4121	NaCl	–9	> 120	-
4411	Ethylene glycol	–4	30.8	10.3
4421	Ethylene glycol	–9	77.6	35.7

Impact Effects of Ice Bonded to Pavement Materials

This section represents the results of a study to determine the disbonding effects of impacts to ice bonded to pavement materials. Both shear and normal loading were to be investigated. Test equipment and procedures were developed to investigate impact loading applied in shear at the ice-substrate interface. It was hoped that the equipment and procedures would be applicable also to the case of impact loading applied normal to the interface. However, such was not the case. A few preliminary normal impact tests were performed. These tests involved dropping a 60 degree wedge onto a 3-mm thick ice sheet grown on a portland cement mortar at 25°F (–4°C). The drop height was about 12 in (30.5 cm) above the ice. Neither the exact drop height or impact forces were recorded. These tests gave disappointing results in that the substrate surface was damaged, and even cracked, by the impact. Consequently, no results were obtained for tests of impact applied normal to the ice surface. The following data are the results of tests in which the impact loading was applied in shear at the ice-substrate interface.

Details are given in Appendix H of the substrates used in the impact shear tests, along with a description of the impact test apparatus. Also presented in Appendix H is an example of the data generated during impact testing and the associated data analysis. The appendix concludes with general remarks concerning the impact shear test results.

Selective impact shear tests were performed at temperatures of 25°F (–4°C) and 15°F (–9°C) using laboratory-produced specimens and core samples taken from in-service highway surfaces. The laboratory-produced specimens were made of portland cement concrete and dense-graded asphalt. The core samples were taken from portland cement concrete, dense-graded asphalt, open-graded asphalt, and rubber-modified asphalt pavements. The results are given in Table 13 of the kinetic energy change resulting from a nominal 5 mph (8.1 km/h) impact shear of ice bonded to cleaned pavement materials at the two temperature levels. More energy is required for impact shearing of ice bonded to open-graded asphalt at 15°F (–9°C) than at 25°F (–4°C). The opposite is true for rubber-modified asphalt at the two temperatures. At 25°F (–4°C) more energy is required for impact shearing of ice bonded to rubber-modified asphalt than for open-graded asphalt at the same temperature. At 15°F (–9°C), more energy is required for impact shearing of ice bonded to open-graded asphalt than the other three types of core samples used. The order of the other three core samples in terms of decreasing energy required for impact shearing at 15°F (–9°C) is: dense-graded asphalt, portland cement concrete, and rubber-modified asphalt.

Table 13. Kinetic energy change (Joules resulting from 5 mph (8.1 km/h) impact shear testing of ice bonded to clean pavement materials at two temperature levels

Pavement materials	Test temperature	
	25°F (–4°C)	15°F (–9°C)
Core samples		
Portland cement concrete	–	1.16
Dense-graded asphalt	–	1.20
Open-graded asphalt	1.04	1.34
Rubber-modified asphalt	1.52	1.00
Laboratory-produced specimens		
Portland cement concrete	–	0.46
Dense-graded asphalt	–	0.82

The energy required for impact shearing of ice bonded to the laboratory-produced specimens at 15°F (–9°C) is less than the energy required for the core samples of the same materials. Of the two laboratory-produced specimens, less energy is required for impact shearing of ice bonded to portland cement concrete at 15°F (–9°C). The same difference is noted for the core samples of the two materials (portland cement concrete and dense-graded asphalt). However, the magnitude of the difference is less for the core samples than for the laboratory-produced specimens.

Impact shear tests were also performed to obtain an estimate of the effects of speed on the kinetic energy change during disbonding. The results are given in Table 14 of the kinetic energy change resulting from a nominal 5 mph (8.1 km/h) and 10 mph (16.1 km/h) impact shear of ice bonded to cleaned pavement materials at 15°F (–9°C). The dependence on speed of removal is very pronounced in the speed range considered.

Table 14. Kinetic energy change (Joules) resulting from 5 and 10 mph (8.1 and 16.1 km/h) impact shear testing of ice bonded to clean pavement materials at 15°F (–9°C)

Pavement materials	Impact speed	
	5 mph (8.1 km/h)	10 mph (16.1 km/h)
Core samples		
Open-graded asphalt	1.34	2.59
Rubber-modified asphalt	1.00	3.13
Laboratory-produced specimens		
Portland cement concrete	0.46	1.72

More energy is required for disbonding at 10 mph (16.1 km/h) than at 5 mph (8.1 km/h) for all the materials considered. Almost two and three times the energy required for disbonding ice at 5 mph (8.1 km/h) is required at 10 mph (16.1 km/h) for open-graded asphalt and rubber-modified asphalt, respectively. Almost four times the energy required for disbonding ice at 5 mph (8.1 km/h) is required at 10 mph (16.1 km/h) for the laboratory-produced portland cement concrete specimen. Of the two core samples tested, less energy was required at 5 mph (8.1 km/h) for disbonding ice from rubber-modified asphalt than from open-graded asphalt. However, at 10 mph (16.1 km/h), more energy was required to disbond ice from rubber-modified asphalt than from open-graded asphalt.

Finally, impact shear tests were performed at 15°F (–9°C) on two types of core samples to determine the effects of substrate surface contaminants on the kinetic energy change during disbonding. Impact shear tests at a nominal speed of 5 mph (8.1 km/h) were performed first on the core samples in the as-received and uncleaned state. The impact shear tests were then repeated after the substrate surfaces were cleaned following the procedure described in Appendix B. The results of these tests are displayed in Table 15. The energy required for disbonding is less for the contaminated (uncleaned) surfaces than it is for the cleaned surfaces. The difference in energy required for disbonding ice from a contaminated and a cleaned surface is greater for rubber-modified asphalt than for open-graded asphalt.

Table 15. Kinetic energy change (Joules) resulting from 5 mph (8.1 km/h) impact shear testing of ice bonded to uncleaned and clean pavement materials at 15°F (–9°C)

Highway pavement core samples	Kinetic energy change (Joules)	
	As-received and uncleaned	Cleaned
Open-graded asphalt	1.24	1.34
Rubber-modified asphalt	0.76	1.00

Use of Thermal Stress to Induce Disbonding

The objective of this subtask was to conduct an investigation to determine if a method of enhancing ice removal can be based on the concept of thermally-induced stress. The effort began with a search of the literature for work of a closely-allied nature, for mechanical and thermal parameters of the materials of the ice-pavement interface, and for interfacial heat transfer coefficients. This was followed by simple modeling to estimate the potential for thermally-induced stress for ice bonding.

It was surprising to find that there was little relevant material in the literature. Very few references exist which deal with thermal shock and ice. Several references deal with the equivalent problem for ceramics; these were useful in suggesting approaches, but did not provide guidance for the problem at hand.

A preliminary mathematical analysis was conducted to predict the temperature difference which must exist in order for ice to fracture. For simplicity, consider a spherical ice cube for which, at t = 0, a small spherical element in the center suddenly cools down.

The temperature decrease should result in a decrease in volume given by:

$$\Delta V = B\ V\ \Delta T$$

where B is defined as the volume coefficient of expansion.

Suppose now that a tensile (hydrostatic) stress was applied to the original sphere. The sample should then increase its volume according to:

$$\Delta V = -K\ V\ \Delta P$$

where K is called the isothermal compressibility.

Now if the sphere, subject to both cooling and tensile stress, is not allowed to change volume, one concludes that:

$$BV\ \Delta T + K\ V\ \Delta P = 0$$

from which the relationship follows:

$$\Delta P = -B/K\ \Delta T.$$

Although this has been obtained using a phenomenological approach, it is also derived in most thermodynamics textbooks. It can be used to predict the temperature difference ΔT which must exist in order for ice to fracture due to thermal shock. From *Ice Physics* by Hobbs (19), the following values for B and K are found:

$B = 150 \times 10^{-6}\ (°C)^{-1}$
(value reported for −10°C)
$K = 19 \times 10^{-6}\ (bar)^{-1}$
(value reported for −10°C)

This leads to: $\Delta P = 7.89$ bar/°C ΔT

In 1963 Gold (20) reported subjecting ice plates to thermal shock by bringing them into contact with colder ice blocks. He noted a preference for cracks to form either parallel or perpendicular to the basal face. The ultimate strength of a smooth ice surface was found to be between 30 and 40 bar and the surface temperature shock required to produce this stress was found to be about 6°C.

If the value of 35 bar is used for the pressure difference, then one finds from the relationship above the change in temperature necessary to cause thermal fracture in ice. When this is done, one obtains a value of 4°C, which is in good agreement with Gold's results. Thus, these estimates indicate that a sudden thermal shock which leads to a temperature difference of 4°C can lead to fracture.

The estimate of the temperature difference necessary to induce fracture depends of course on the values of B and K, which are themselves functions of temperature. Although Hobbs gives the temperature variation of these quantities, three sets of results are given, and agreement is not good among the three. It does appear, however, that B is roughly 150 x 10^{-6} $(°C)^{-1}$ at warmer temperatures and decreases as the temperature drops. At −180°C, for instance, B = 51 x 10^{-6} $(°C)^{-1}$. Values for K are even more incomplete. Results reported in 1914 are given in Hobbs' book for five temperatures as shown below.

Temperature (°C)	K x 10^{-6} bar
0	33
−5	23
−10	19
−15	18
−70	21

Although complete data are lacking, an attempt was made to indicate how the temperature difference necessary to induce fracture varies with the temperature of the ice. Assuming that the pressure required for fracturing remains relatively constant, an estimate for the required temperature difference for fracture as a function of temperature can be obtained. The results are tabulated in Table 16 and shown in Figure 12. One notes that from 0°C to approximately −120°C, the temperature difference required to produce fracture appears to be nearly independent of temperature.

Table 16. Thermal shock temperature differences

$\Delta T = \Delta P\ K/B$

T	B	K	B/K	ΔT
10	156	19	8.21	4.3
50	129	20	6.45	5.4
90	155	20	7.75	4.5
110	124	20	6.20	5.6
130	81	20	4.05	8.6
150	42	20	2.10	16.7
170	28	20	1.40	25.0
190	17	20	0.85	41.2
210	11	20	0.55	63.6
230	8	20	0.40	87.5
250	5	20	0.25	140.0

T of ice in degrees C (negative temperature).
B = Coefficient of volume expansion in 10^{-6} per degree C.
K = Compressibility in 10^{-6} per bar.
ΔP = 35 bar from *Ice Physics* by Hobbs, page 335 (19).

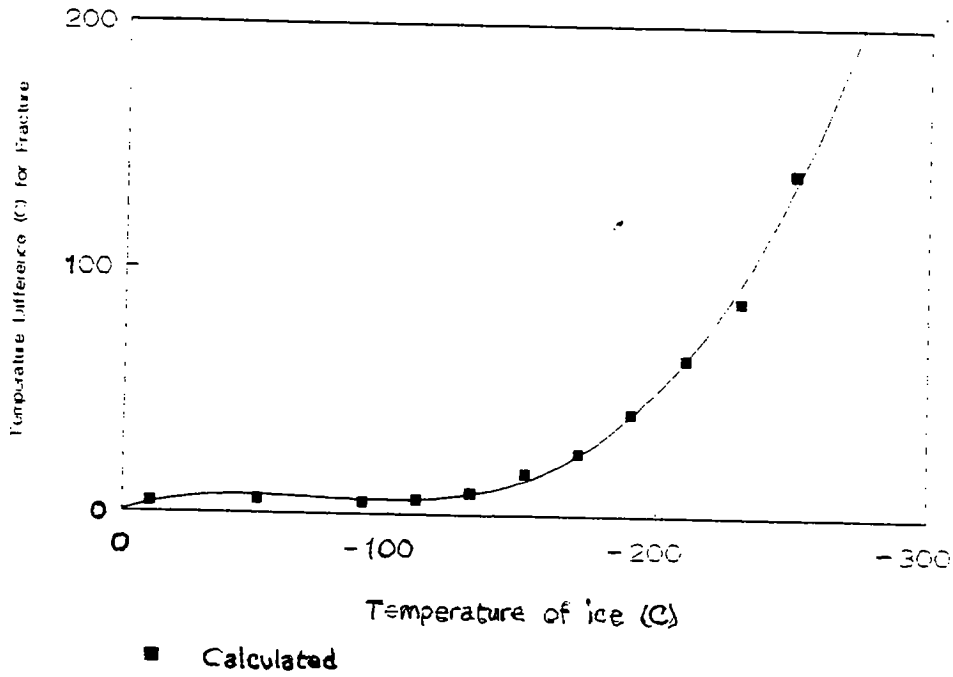

Figure 12. Temperature difference for fracture vs. temperature of the ice

From this graph one might conclude that dropping liquid nitrogen on ice might not be effective since the temperature difference is so large. However, the ice will crack before it gets to liquid nitrogen temperature. That is, if a 10° temperature difference will cause fracturing, then even if liquid nitrogen is poured on the ice, the ice will crack when there is a 10° temperature difference between its surface and part way into its interior.

Although this estimate is subject to error, it appears that the temperature difference to cause thermally-induced fracture might be reasonably constant over a wide enough range of temperatures. This would make a technique based on thermal fracture feasible.

The problem of thermal shock fracture was also considered from the point of view of the energy associated with the development of additional surface area and of crack propagation. It was much more difficult to make simple estimates by these approaches, but the indications were either supportive of the above conclusion or not contrary to it.

The next step of this investigation was a preliminary laboratory examination of the effects of thermal stress. Two experiments were carried out. The first of these tests involved pouring liquid nitrogen directly onto the surface of ice formed in a shallow metal pan. Although this was an extreme test, it was important in that a negative result would have indicated that the premise was not viable. However, the results were spectacular. The ice shattered into many pieces and the bonding to the metal surface was completely destroyed.

The second preliminary test was more representative of a highway situation. Layers of ice of varying thickness (up to a quarter of an inch) were formed on concrete slabs. Liquid nitrogen was then poured onto the ice surface. In all cases there was adequate stress developed to cause fragmentation of the ice as a result of cracking normal to the ice-concrete interface. This suggested that the bonding to the concrete was probably also affected.

These preliminary test results guided the follow-on work which proceeded to a more complete evaluation of the thermal effect including direct measurement of the interfacial strength in the presence of thermal shock.

Questions which needed to be considered in evaluating the potential of thermally-induced stresses for interfacial strength reduction included:

- Is the interfacial strength reduced by the presence of thermal gradients, and by how much?

- Are any effects related to the existing temperature gradients, to temperature differences, or to some combination of these parameters?

- Are there other parameters which are of importance?

- How can optimum effect be achieved?

- How can any effects be optimally utilized in the application to ice-bond reduction on actual highway surfaces?

It was not possible to perform a complete study of all of these facets of the problem. However, an experiment was designed to give specific interfacial strength data for two heat transfer cases. The time length of shock treatment was also used as a parameter in the experiment. The two heat transfer cases chosen were the direct application of liquid nitrogen to the surface, and heat transfer to an aluminum foil cup containing liquid nitrogen placed directly on the ice. Although it would appear that direct application of liquid nitrogen is a very extreme case, it should be remembered that, as a liquid bead boils by heat transfer from the surface below it, the liquid is converted to nitrogen gas. The gas layer forms an effective thermal insulator. Heat transfer from surfaces immersed in liquid nitrogen has been studied previously (21).

High values of heat transfer coefficient [in excess of 10,000 W/(m^2–K)] are seen in the boiling heat transfer regime, but the value drops abruptly as the stable film boiling regime is entered. This is the mode encountered between a liquid drop and a solid surface, and the transfer coefficient is down to 1,000 W/(m^2–K) or lower. Heat transfer between solid surfaces is very complex, but in most cases it is determined by the total load force between them. Thus, the transfer between a light aluminum cup and an ice surface will be characterized by a very low accommodation coefficient.

The thermal shock tests were performed in the shear apparatus previously used for low load-rate interfacial strength studies. Ice was grown from the substrate upward at a fast rate, accomplished by placing the substrate directly on an aluminum plate which was on the bottom of a freezer at –25°C. When the substrate cooled to the temperature of the plate, water at 0°C was poured into the Teflon ring used to contain the water until the ring was nearly full. One hour after setting the testing chamber to the desired temperature, the substrates to be tested were transferred from the specimen preparation freezer (typically at –20°C) to the testing chamber used in previous tests. At that time the first substrate was mounted in the test apparatus, and 4 hours were allowed for the substrates to come to thermal

equilibrium at the test temperature. The shear rate used in all these tests was approximately 4,000 lb/minute (1,814 kg/minute).

The results of these thermal shock/shear tests are quite dramatic, as shown in Figure 13. When liquid nitrogen was poured directly onto ice grown on a concrete substrate and left on for 30 sec, the interfacial shear strength was reduced to approximately 20% of its value without the thermal shock. A further series of tests was performed using the foil cup to contain the liquid nitrogen, with the length of time the cup was on the ice surface as a parameter. As can be seen from the figure, the shear strength was also greatly reduced for a 30-sec thermal shock exposure. For 15- and 5-sec exposures, the extent of the reduction decreases, but even for the shortest exposure there is still a significant reduction of the interfacial strength.

These results are encouraging since they suggest a possible ice removal scheme which is environmentally safe and which could be nondestructive to the pavement surface. Further studies of this effect are clearly justified. To this end, an attempt was made to gain more understanding of the mechanisms involved by investigating closed-form solutions of the transient heat flow from a surface.

Cooling of an ice layer on a concrete substrate can be modeled by a heat sink (of infinite heat capacity and hence constant temperature) connected to the ice surface by a fixed thermal resistance (and no heat capacity). The ice and concrete can be considered as having homogeneous, isotropic thermal conductivities which are independent of temperature. Although this may seem to be a rather idealized model, it is in fact quite close to conditions which can be realized in practical configurations. It is also reasonable to consider initially the temperature of the ice-concrete interface as being at a fixed temperature. Thus, the problem becomes equivalent to conduction along a one-dimensional bar of material from which there is no heat transfer from the sides.

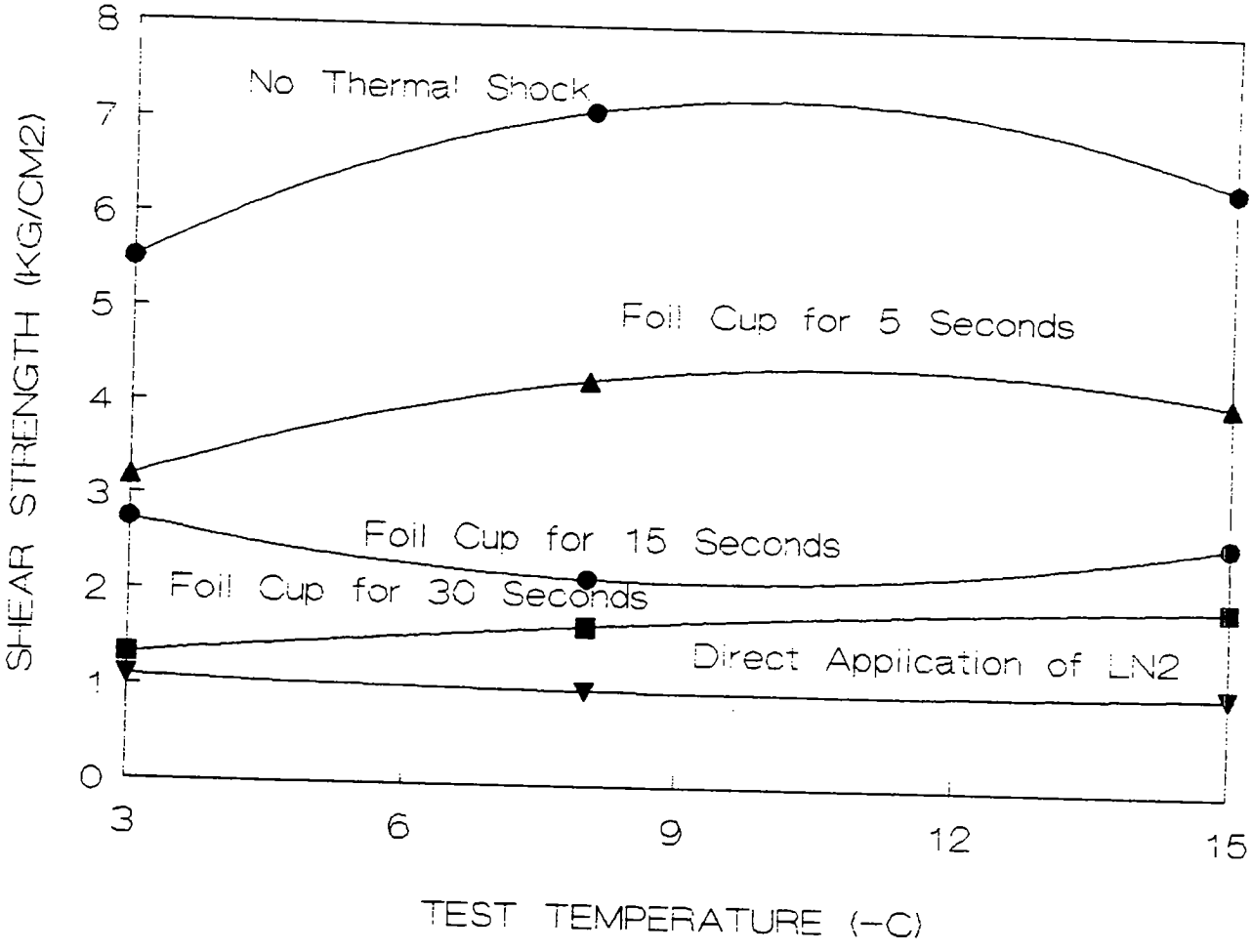

Figure 13. Effects of LN_2 thermal shock on the shear strength of ice bonded to clean concrete substrates

Consider initial conditions in which the material is at a constant temperature. If the temperature at one end is now raised instantaneously while the temperature at the other end is held constant, the solution of the heat-flow equation (where α is the thermal diffusivity of the material) may be expressed as the sum of the steady-state solution and a transient solution. Hence

$$\frac{d^2T}{dx^2} = \frac{1}{\alpha}\frac{dT}{dt} \tag{1}$$

$$T(x,t)=T_s(x)+T_t(x,t) \tag{2}$$

where $T_s(x)$ is a linear function. The product solution of the heat-flow equation can be obtained in the form

$$T_t = a_n \sin\frac{nTx}{L} \exp\left(\frac{-n^2t}{D}\right) \tag{3}$$

where

$$D = \frac{L^2\delta C_p}{\pi^2 K}$$

Thus, by combining the steady-state solution and a superposition of this type, the required solution T(x,t) may be assumed in the form

$$T(x,t)=T_1+(T_2-T_1)\frac{x}{L}+\sum_{k=0}^{\infty} a_n \sin\frac{n\Pi x}{L}\exp\left(\frac{-n^2t}{D}\right) \tag{4}$$

where the coefficients a_n are determined as Fourier coefficients such that the initial conditions are satisfied. L = thickness of ice layer; K, C_p, and δ are the thermal conductivity, specific heat, and density of ice, respectively.

The parameter D has the units of time. For ice, the thermal diffusivity has the value of about 0.0000015 m^2/sec. Thus, for a layer of ice 1-mm thick, D has a value of 0.07 sec, and for a layer of ice 1-cm thick as used in the shear tests, D has a value of 7.0 sec.

Use of Dirichlet boundary conditions is equivalent to the case of a large heat transfer coefficient. To model a small heat transfer coefficient, Neumann conditions are appropriate for one end of the material. This configuration results in a solution which also contains terms like those in equation (3), i.e., decaying exponentials with the same time constraints. Thus, it can be concluded from the data in Figure 13 that the fracturing process and the attendant reduction of interfacial strength is associated with the existence of a significant temperature difference across a significant thickness of the ice. Otherwise, if the effect were associated with the existence of a large temperature gradient, the fracture would occur in the fraction of a second when very large temperature gradients exist in the fraction of a millimeter of ice just below the surface. It is also likely that the process is controlled mainly by the heat transfer coefficient between the cooling agent and the ice surface. This is inferred by the fact that the maximum interfacial strength reductions we have observed occur after 30 sec of cooling. This is a longer time than is required for significant modification of the temperature profile through a 1-cm layer of ice.

There are a number of tests which should be performed to complete this initial investigation to develop practical means of disbonding ice from substrates using thermal shock principles. These include:

- Direct measurement of the heat transfer coefficient between ice and a range of surfaces to determine the range of values which can be obtained. Applied pressure should be used as a parameter in these tests.

- Measurement of interfacial strength for a range of thicknesses of ice on concrete and other substrates using a range of heat transfer coefficients.

- Numerical modeling of transient temperature profiles should be performed for configurations for which closed-form solutions can be obtained and which can be achieved experimentally. When the accuracy of the modeling has been confirmed, it could be used to investigate a wide range of parameter variations in the search for optimization of effectiveness and practical implementation procedures.

Investigation into the Destruction of Ice-Substrate Bonds by Chemical Undercutting

Two sets of experiments were conducted to investigate the destruction of the ice-substrate bond by chemical undercutting. The main objective of these experiments was to determine the influence of temperature and substrate condition on the time-dependent undercutting characteristics of several common chemical deicers. The first set of experiments involved chemical undercutting of ice on model and pavement component substrates. The second set of experiments involved chemical undercutting of ice on highway pavement materials. The findings obtained from each set of experiments are given below and in more detail in Appendix I. Details of the experiments conducted and procedures followed during these experiments are also given in that appendix.

Chemical Undercutting of Ice on Model and Pavement Component Substrates

The first set of undercutting experiments consisted of determining the time-dependent undercut area produced by four deicers at an ice-substrate interface under a variety of experimental conditions. The four deicers used were ethylene glycol ($HOCH_2CH_2OH$), sodium chloride (NaCl), calcium chloride ($CaCl_2$), and calcium-magnesium-acetate (CMA). Seven substrates were used in the tests and consisted of three model substrates (FEP Teflon, Mylar, and gold) and four pavement component substrates (fused silica [representing sand], portland cement mortar, limestone, and asphalt). Measurements of the undercutting action of saturated solutions of the deicers were made at the four test temperature levels of 25°F (–4°C), 15°F (–9°C), 5°F (–15°C), and –40°F (–40°C). Three freezing rates (slow, medium, and fast) were also employed in combination with two modes of freezing (bottom-up and top-down).

A statistical design was developed for the undercutting testing because of the large number of tests of possible combinations that could have been conducted. The statistical design plus other physical considerations (deicers were not tested at temperatures close to or below their eutectic temperature) resulted in 504 undercutting tests, each performed in triplicate.

The undercutting tests were performed in the cold chamber described in Appendix E. Appendix I presents the details of the materials used, and procedures followed during the undercutting experiments. The procedure used to measure the undercutting area as a function of time from 35-mm photographic records is also described in Appendix I.

Prior to the statistical analysis of the data, the undercutting results were adjusted to account for the surface area, at time zero, that a Teflon plug used during the ice growth was in contact with the substrate. This initial area, created when the plug was removed just before the experiment, was subtracted from all measured undercut areas obtained from the 35-mm photographic records. The resulting differences were then normalized by dividing them by the appropriate weight of the deicer. In the text below, these final results are referred to as adjusted undercut areas.

In order to show the maximum information in tabular and plotted form, a new variable, "Freezing Code," was constructed as shown in Table 17. There are a total of six levels of this combined variable (3 freezing rates x 2 freezing modes).

Table 17. Freezing mode/rate codes

Freezing code	Freezing rate	Freezing mode
A	Fast	Bottom-up
B	Fast	Top-down
C	Medium	Bottom-up
D	Medium	Top-down
E	Slow	Bottom-up
F	Slow	Top-down

Up to three replicate runs were performed for each unique combination of substrate, deicer, temperature, freezing rate, and freezing mode. The replicate results were averaged prior to all statistical analysis.

No attempt was made to correlate the freezing point lowering capability of the deicer solutions because the concentration of the solutes continuously varied during the undercutting process.

The results obtained from the undercutting tests at –40°C (–40°F) and with the asphalt substrate were of marginal usefulness and were excluded from the analysis. Only two deicers were tested at –40°C (–40°F): ethylene glycol and $CaCl_2$. The undercutting activity of $CaCl_2$ was nil at that temperature, and only neat ethylene glycol showed a very slight undercutting action on one substrate. The undercutting areas on the asphalt substrates could not be reliably determined from the photographic records because of the lack of contrast between the undercut area and the black asphalt.

Plots were developed of the average adjusted undercut area versus time for each of the 24 deicer x substrate combinations (4 deicers x 6 substrates). These plots are shown in Figures 2 through 25 in Appendix I. The data points are coded by the freezing mode/rate code. The key given in the plots indicates the temperature corresponding to the freezing mode/rate codes for each undercutting equipment.

Each of the 24 plots was examined to determine whether, for each substrate and deicer combination, there is an apparent temperature effect and/or an apparent freezing mode/rate effect on the undercut area. The conclusions are summarized in Table 18.

The temperature and freezing mode/rate patterns found with ethylene glycol are consistent for the six substrates. The adjusted undercut area for 25°F is greater than that for 15°F which is greater than that for 5°F at all times. There is no apparent freezing mode/rate effect for any of the six substrates for this deicer.

The temperature and freezing mode/rate patterns found with NaCl vary among the six substrates. The adjusted undercut area for 25°F is greater than that for both 5° and 15° for all substrates at all times. However, the areas for 15°F are greater than those for 5°F for FEP Teflon and fused silica only. The results for 5° and 15°F are not different for Mylar, gold, portland cement mortar (PCM), and limestone.

For NaCl, there is no freezing mode/rate effect on the adjusted undercut area for Mylar, fused silica, and limestone. There is, however, a freezing mode/rate effect for the other three substrates. The effect is not consistent within the three substrates.

The temperature and freezing mode/rate patterns found with $CaCl_2$ vary among the six substrates. The adjusted undercut area for 25°F is greater than that for both 5° and 15°F for all substrates, at all times. However, the areas for 15°F area greater than those for 5°F for FEP Teflon, fused silica, and limestone. The results for 5° and 15°F do not differ for Mylar, gold, and PCM.

For $CaCl_2$, there is no freezing mode/rate effect on the adjusted undercut area for fused silica. There is a freezing mode/rate effect for the other five substrates. The effect is not consistent within the five substrates. The undercutting data obtained for CMA showed very erratic results. The data were examined to determine whether temperature has an effect on the undercutting area. However, no temperature pattern was found with CMA for any of the six substrates.

Table 18. Apparent temperature and freezing rate/mode effect for various deicer and substrate combinations

Deicer	Substrate	Apparent Temperature Effect?	Apparent Freezing rate/mode effect?
Ethylene Glycol	FEP Teflon	Yes; data curves distinct for all three temperatures	No
	Mylar	Yes; data curves distinct for all three temperatures	No
	Gold	Yes; data curves distinct for all three temperatures	No
	F. Silica	Yes; data curves distinct for all three temperatures	No
	PCM	Yes; data curves distinct for all three temperatures	No
	Limestone	Yes; data curves distinct for all three temperatures	No
NaCl	FEP Teflon	Yes; data curves distinct for all three temperatures	Possible difference between freezing code 'D' and 'E' at 5 deg F
	Mylar	Data curve for 25 deg F higher than curves for 5 and 15 deg F	No
	Gold	Data curve for 25 deg F higher than curves for 5 and 15 deg F	Possible difference between freezing code 'D' and 'E' at 25 deg F
	F. Silica	Yes; data curves distinct for both temperatures	No
	PCM	Data curve for 25 deg F higher than curves for 5 and 15 deg F	Possible difference between freezing code 'B' and 'C' at 25 deg F Possible difference between freezing code 'D' and 'E' at 15 deg F
	Limestone	Data curve for 25 deg F higher than curves for 5 and 15 deg F	No

Freezing Code Legend		
Freezing Code	Freezing Rate	Freezing Mode
A	Fast	Bottom-Up
B	Fast	Top-Down
C	Medium	Bottom-Up
D	Medium	Top-Down
E	Slow	Bottom-Up
F	Slow	Top-Down

Table 18. Apparent temperature and freezing rate/mode effect for various deicer and substrate combinations (concluded)

Deicer	Substrate	Apparent Temperature Effect?	Apparent Freezing rate/mode effect?
CaCl2	FEP Teflon	Yes; data curves distinct for all three temperatures	Possible difference between freezing code 'A' and 'F' at 25 deg F
	Mylar	Data curve for 25 deg F higher than curves for 5 and 15 deg F	Possible difference between freezing code 'A' and 'D' at 15 deg F
	Gold	Data curve for 25 deg F higher than curves for 5 and 15 deg F	Possible difference between freezing code 'A' and 'F' at 15 deg F
	F. Silica	Yes; data curves distinct for both temperatures	No
	PCM	Data curve for 25 deg F higher than curves for 5 and 15 deg F	Possible difference between freezing code 'D' and 'E' at 15 deg F
	Limestone	Yes; data curves distinct for all three temperatures	Possible difference between freezing code 'B' and 'E' at 15 deg F
CMA	FEP Teflon	No	Possible difference between freezing code 'A' and 'F' at 25 deg F
	Mylar	No	Possible difference between freezing code 'C' and 'F' at 25 deg F
	Gold	No	Possible difference between freezing code 'D' and 'E' at 25 deg F Possible difference between freezing code 'A' and 'F' at 15 deg F
	F. Silica	No	No
	PCM	No	Possible difference between freezing code 'D' and 'E' at 15 deg F
	Limestone	No	No

Freezing Code Legend		
Freezing Code	Freezing Rate	Freezing Mode
A	Fast	Bottom-Up
B	Fast	Top-Down
C	Medium	Bottom-Up
D	Medium	Top-Down
E	Slow	Bottom-Up
F	Slow	Top-Down

For CMA, there was no freezing mode/rate effect on the adjusted undercut area for fused silica and limestone. There is a freezing mode/rate effect for four of the six substrates. The effect is not consistent within the six substrates.

The statistical analysis of the undercutting data was limited to ethylene glycol. The analysis was directed at determining the effects of temperature and substrates on the initial rate (i.e., at time zero) of the undercutting curve.

Linear regression analysis was used to fit a quadratic equation to the ethylene glycol data. The adjusted undercut area was regressed on time and time.^{2} A separate analysis was performed for each substrate-temperature combination. If the factor time^2 was not statistically significant at the 10% significance level, then a first-order linear regression was performed regressing the adjusted undercut area on time. In all cases, the regression lines were forced through the origin.

The results of the regression analyses are presented in Table 19. Columns 1 and 2 denote the temperature and the substrate, respectively. The shape of the fitted curve, quadratic or linear, is given in column 3. Columns 4 and 5 list the rate of undercutting at time = 0 (initial slope) of the equation and its corresponding standard error, respectively. Here, the undercutting rate is given in units of adjusted undercut area per unit time. The boxes shown on the right of the table contain the average (avg), standard deviation (std), and coefficient of variation (CV) of the undercutting rate at time = 0 for each temperature.

The fitted equations obtained from the regression analyses for ethylene glycol are shown with the adjusted undercut area and plotted in Figures 14 through 19. No freezing codes are shown since there was no apparent freezing mode/rate effect for any of the six substrates. Instead, the data are encoded by temperature.

Next, to determine whether the initial slopes differ by temperature and by substrate, a two-way analysis of variance (ANOVA) was performed on these slopes. The two factors considered are temperature (3 levels) and substrate (6 levels). The results of the ANOVA are presented in Table 20.

Table 19. Ethylene glycol on six substrates (tests at 3 freezing rates and 2 freezing modes)

Temperature	Substrate	Shape of fitted curve	Rate @ time = 0	Std error of rate @ time = 0	Statistics for rate @ time = 0
25 deg F	FEP Teflon	quadratic	0.778	0.037	
	Mylar	linear	0.799	0.025	
	Gold	quadratic	1.105	0.069	
	F. Silica	linear	0.640	0.018	avg = 0.809
	PC Mortar	linear	0.715	0.040	std = 0.159
	Limestone	linear	0.815	0.009	CV = 20%
15 deg F	FEP Teflon	quadratic	0.537	0.026	
	Mylar	quadratic	0.346	0.017	
	Gold	quadratic	0.474	0.041	
	F. Silica	quadratic	0.363	0.031	avg = 0.450
	PC Mortar	quadratic	0.471	0.032	std = 0.078
	Limestone	quadratic	0.506	0.013	CV = 17%
5 deg F	FEP Teflon	quadratic	0.228	0.020	
	Mylar	quadratic	0.284	0.032	
	Gold	quadratic	0.274	0.025	
	F. Silica	NA			avg = 0.257
	PC Mortar	linear	0.215	0.011	std = 0.033
	Limestone	quadratic	0.285	0.035	CV = 13%

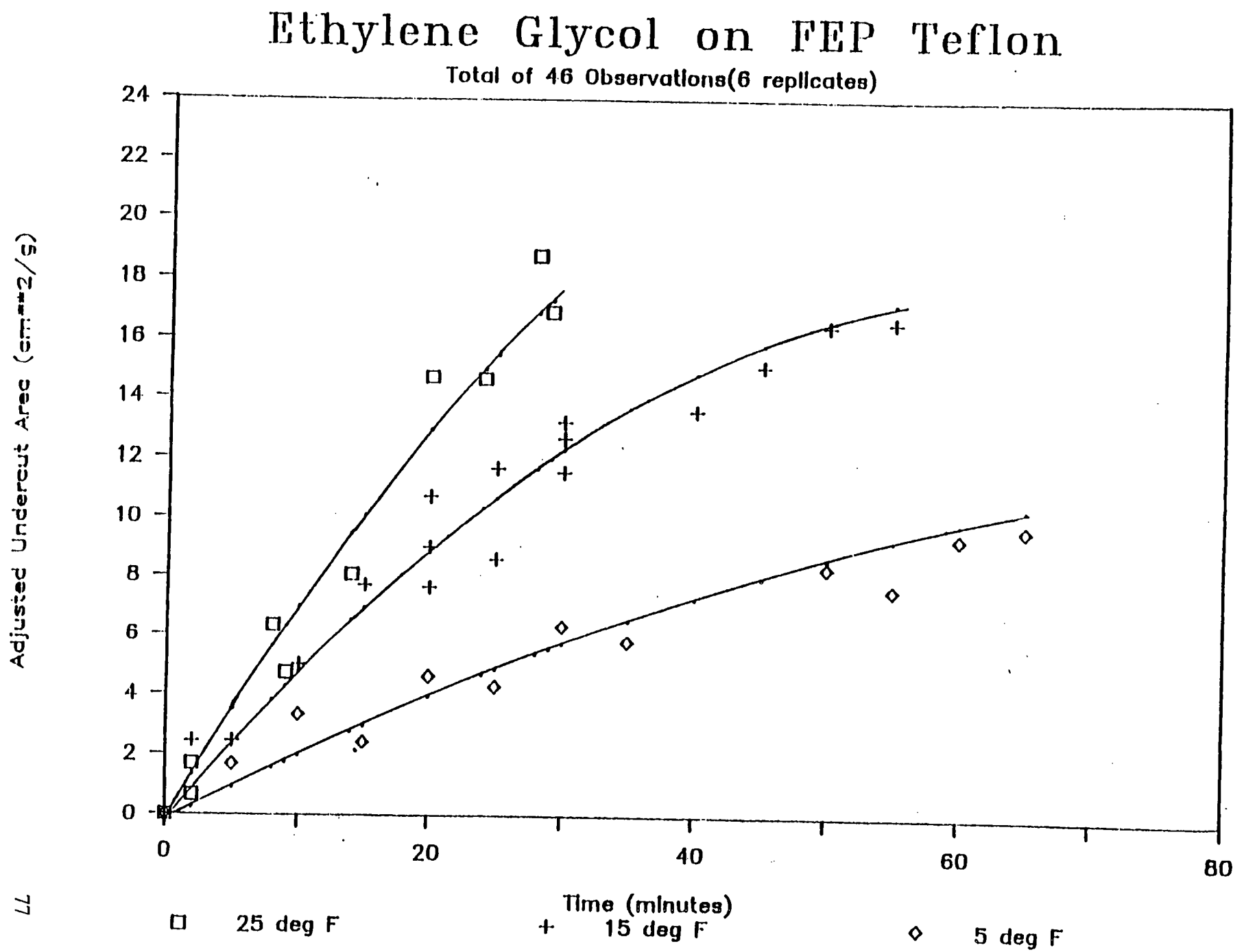
Ethylene Glycol on FEP Teflon
Total of 46 Observations(6 replicates)
Adjusted Undercut Area (cm**2/s)
24
22
20
18
16
14
12
10
8
6
4
2
0
0
20
40
60
80
Time (minutes)
25 deg F
15 deg F
5 deg F

Figure 14.

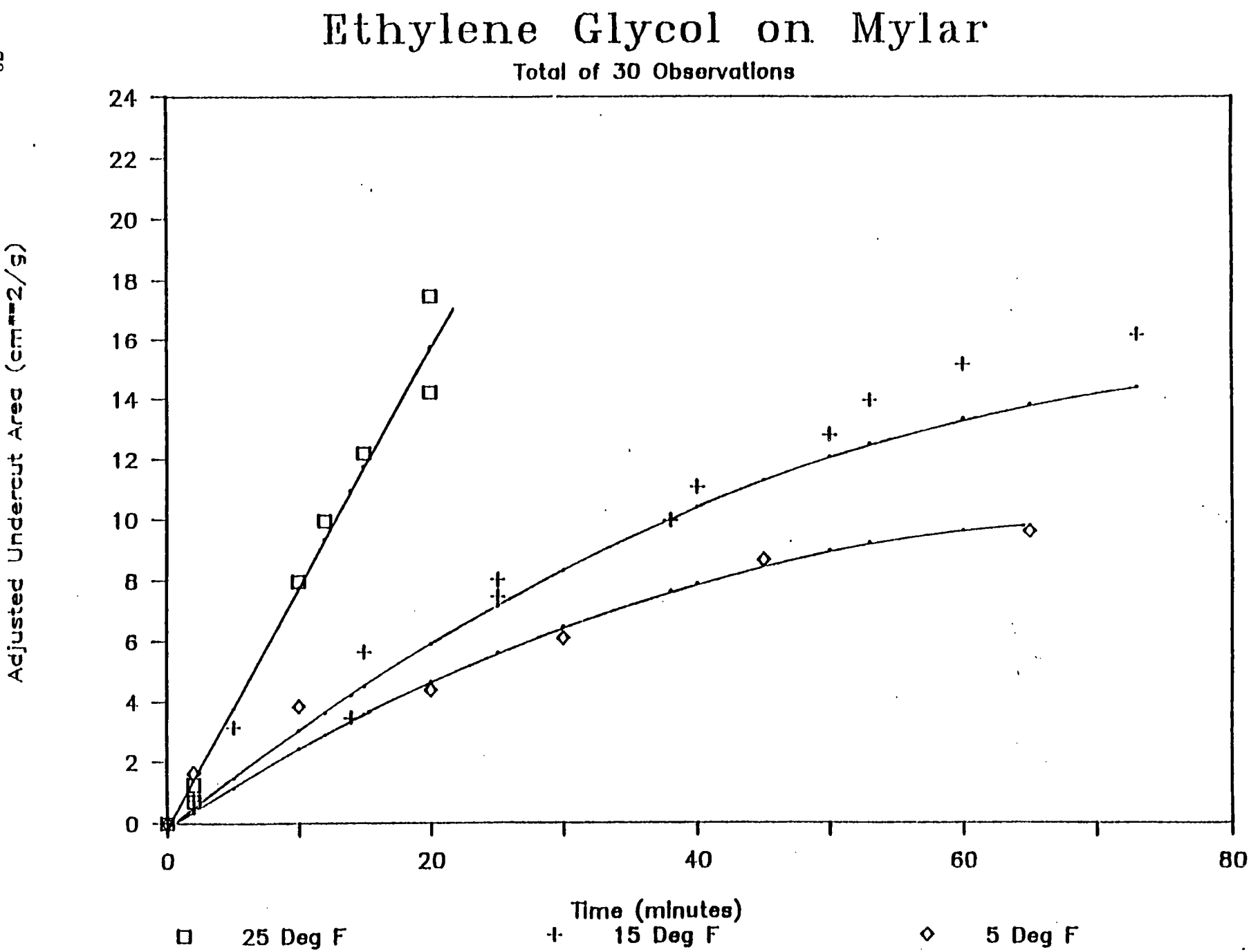
Ethylene Glycol on Mylar
Total of 30 Observations
Adjusted Undercut Area (cm**2/s)
24
22
20
18
16
14
12
10
8
6
4
2
0
0
20
40
60
80
Time (minutes)
25 Deg F
15 Deg F
5 Deg F

Figure 15.

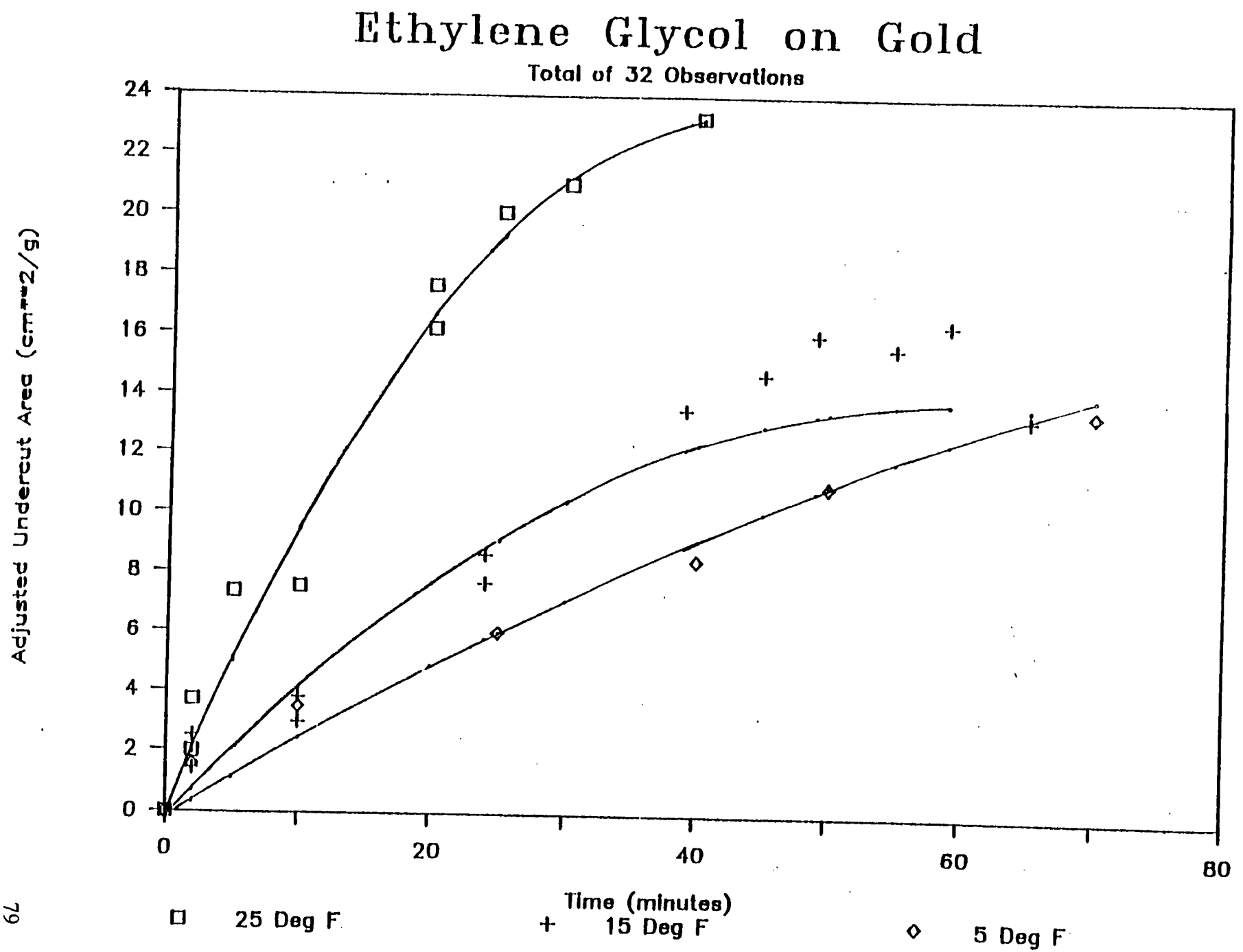
Ethylene Glycol on Gold
Total of 32 Observations
Adjusted Undercut Area (cm**2/g)
24
22
20
18
16
14
12
10
8
6
4
2
0
0
20
40
60
80
Time (minutes)
25 Deg F
15 Deg F
5 Deg F

Figure 16.

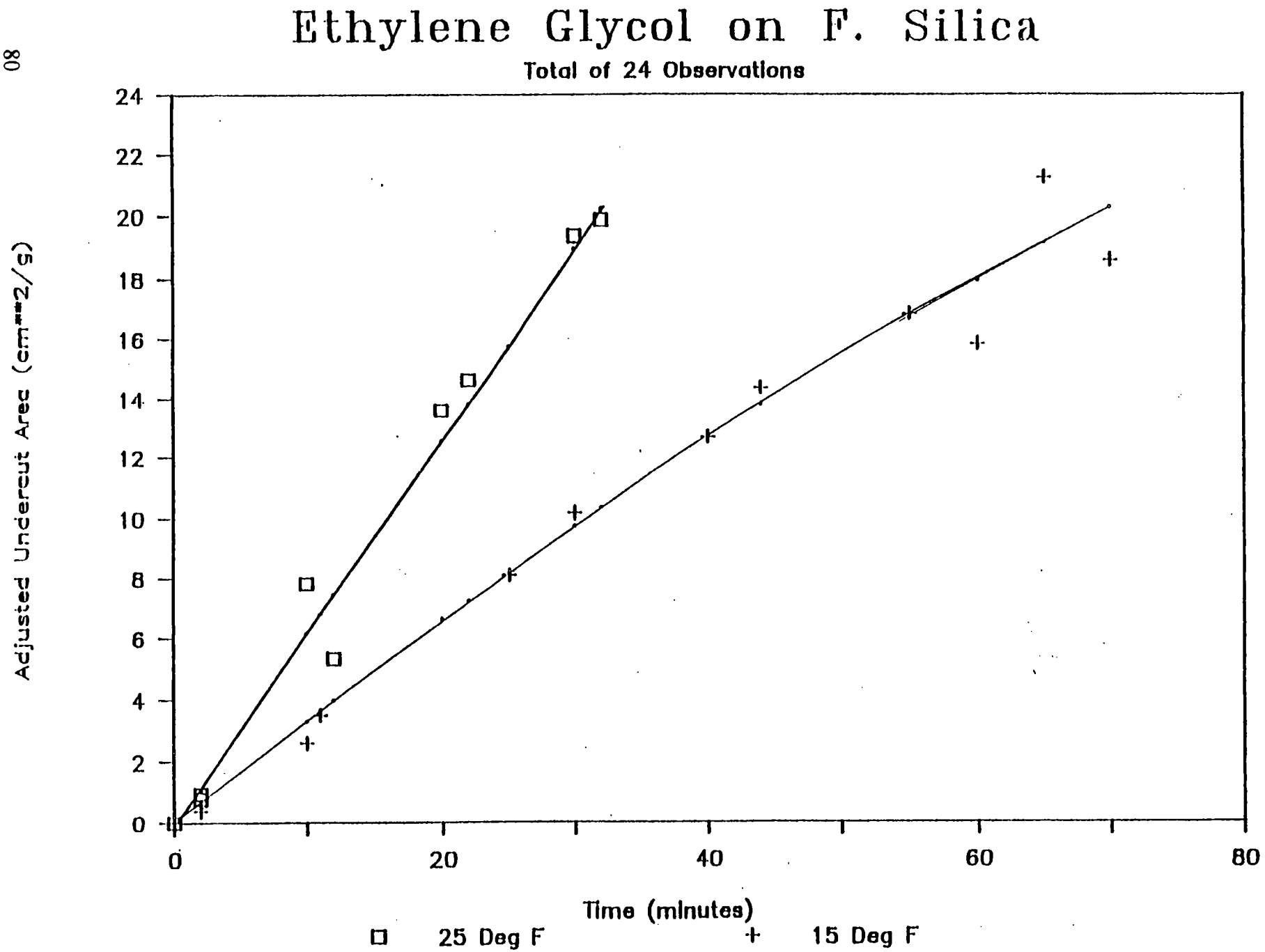
Ethylene Glycol on F. Silica
Total of 24 Observations
Adjusted Undercut Area (cm**2/g)
24
22
20
18
16
14
12
10
8
6
4
2
0
0
20
40
60
80
Time (minutes)
25 Deg F
15 Deg F

Figure 17.

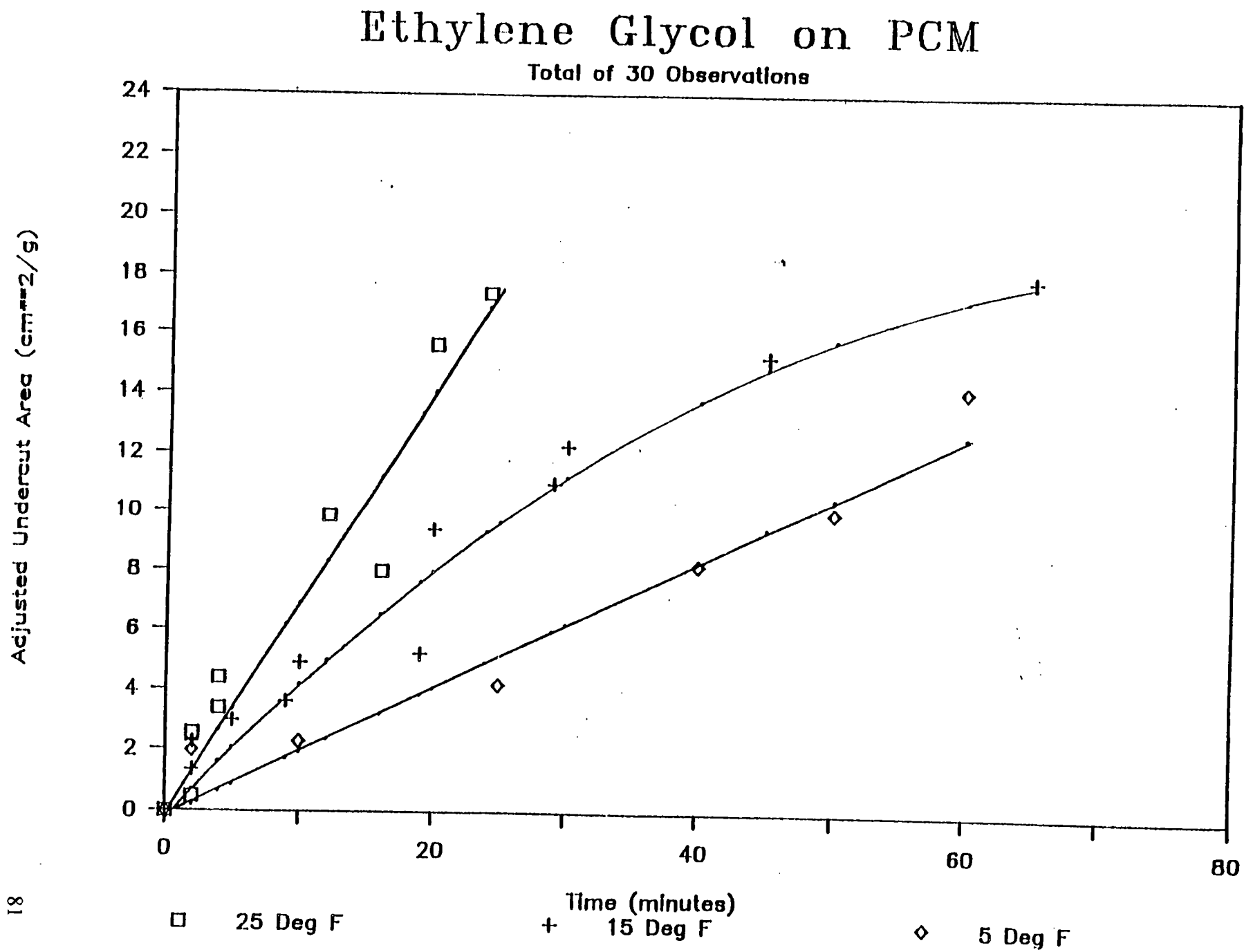
Ethylene Glycol on PCM
Total of 30 Observations
Adjusted Undercut Area (cm**2/g)
24
22
20
18
16
14
12
10
8
6
4
2
0
0
20
40
60
80
Time (minutes)
25 Deg F
15 Deg F
5 Deg F

Figure 18.

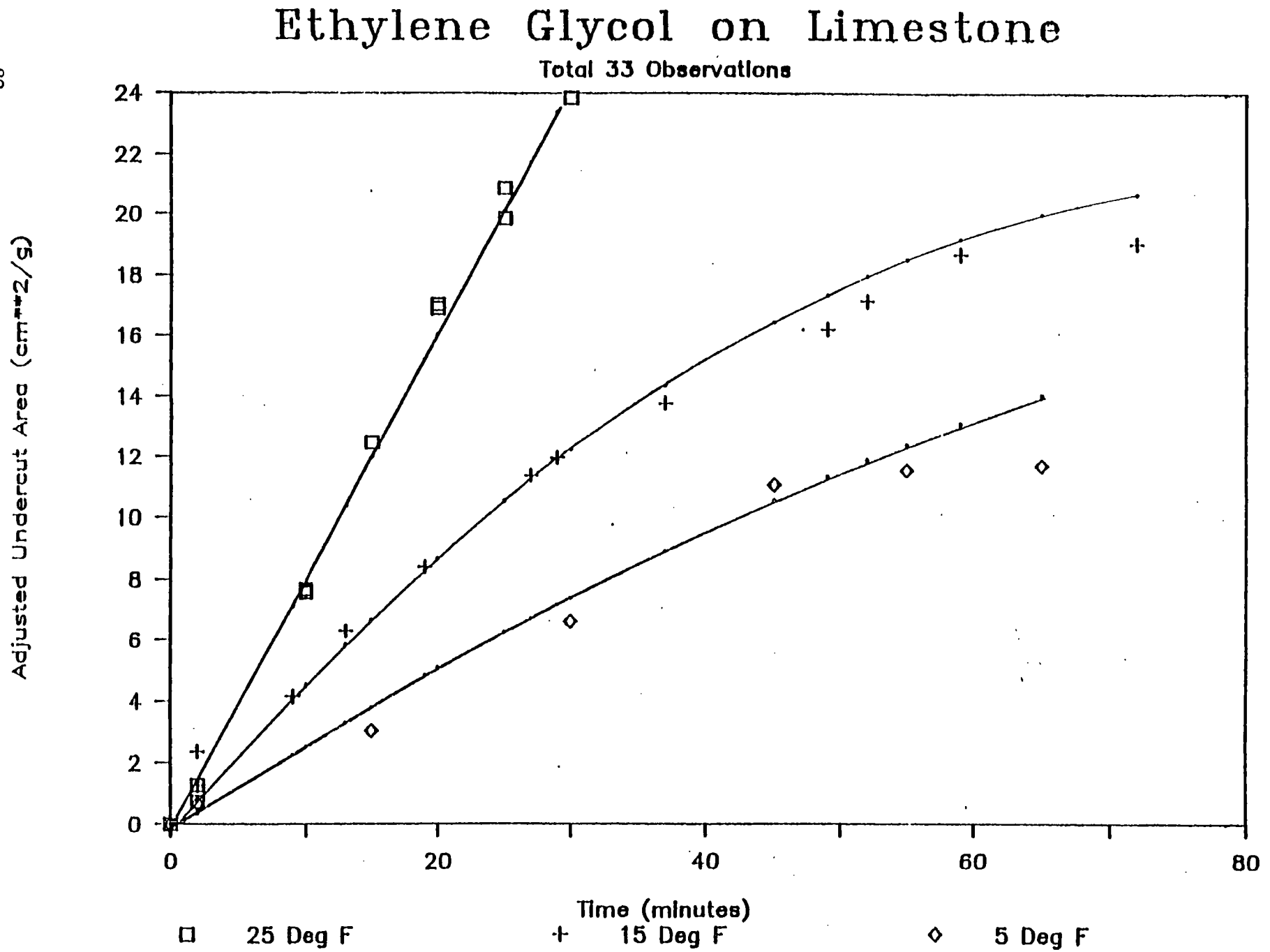
Ethylene Glycol on Limestone
Total 33 Observations
Adjusted Undercut Area (cm**2/g)
24
22
20
18
16
14
12
10
8
6
4
2
0
0
20
40
60
80
Time (minutes)
25 Deg F
15 Deg F
5 Deg F

Figure 19.

Table 20. Results of two-way ANOVA

Source of variation	Sums of squares	Degrees of freedom	Mean squares	F-ratio	p
Temperature	0.911	2	0.456	50.494	< 0.0001
Substrate	0.083	5	0.017	1.849	0.199
Error	0.081	9	0.009		

Table 20 shows that for ethylene glycol, temperature has a significant effect ($p < 0.0001$) on the initial slope of the regression equation. However, the type of substrate has no significant effect ($p = 0.199$) on the initial slope of the fitted equation.

Additional statistical analysis of the undercutting data for NaCl, $CaCl_2$, and CMA were not undertaken because of budgetary and time constraints. It is considered worthwhile to repeat the above statistical analysis for NaCl and $CaCl_2$ to determine the temperature, substrate, and freezing mode/rate effect for these two commonly used deicers. These analyses can be accomplished using the experimental data presented in Appendix I.

Chemical Undercutting of Ice on Highway Pavement Materials

The second set of undercutting experiments consisted of determining the time-dependent undercut area produced by three deicers at the ice-substrate interface on highway core samples and laboratory-produced specimens. Tests were conducted at temperatures of 25°F (–4°C), 15°F (–9°C), and 5°F (–15°C) using all the substrates in the as-received, but cleaned condition. The substrates were cleaned using the procedure described in Appendix B. The three deicers—NaCl, $CaCl_2$, and ethylene glycol—were used in all temperature-substrate combinations. The substrates used in the second set of undercutting experiments included portland cement concrete, dense-graded asphalt, open-graded asphalt, and rubber-modified asphalt core samples and laboratory-produced specimens made of portland cement concrete and dense-graded asphalt. Undercutting action was also investigated on smooth highway core samples and laboratory-produced specimens at 25°F (–4°C) and 5°F (–15°C). The undercutting tests were performed in a walk-in cold room.

The ice samples were grown on the highway pavement materials using a slow freezing rate and in a bottom-up direction. The same Teflon plugs used to form cavities in the ice grown on the model and pavement component substrates were also used to form cavities in the ice grown on the highway pavement materials.

Fluorescein disodium salt was added to the deicing solutions before they were inserted into the cavities formed by the Teflon plugs. Photographs were then taken with the aid of a UV-light source at eight predetermined time points over a 1-hour period during the undercutting action. The 35-mm negatives used in the photographic process showed a good contrast between the undercutting areas and the substrate material. The undercutting patterns observed on the highly textured surfaces, such as on the open-graded asphalt cores and laboratory-produced portland cement concrete specimens, were irregular in shape and followed the surface voids around the exposed surface aggregate. The undercutting patterns on the smoother substrates tended to be circular patterns. Appendix I presents the details of the materials used, and procedures followed during the undercutting experiments with the highway materials.

Plots were developed of the average adjusted undercut area versus time for each of the 18 deicer x substrate combinations (3 deicers x 6 substrates). These plots are shown in Figures 26 through 43 in Appendix I. Also shown in these figures are the results achieved for the smooth substrate surfaces. The data used to generate these figures are also presented in that appendix, along with the data recording and reduction procedures.

The tests conducted with each deicer involved primarily an evaluation of the effects of different types of substrates and their physical surface characteristics (particularly surface roughness) on the undercutting characteristics. All substrate surfaces were cleaned before testing by standardized procedures. Thus, the chemical properties of the substrate surfaces in all cases, including the core samples, do not reflect the chemical contamination which accompanies highway uses. The undercutting results should, however, reflect the chemical properties of the substrate material (i.e., asphalt or portland cement concrete). Potential differences might exist between core samples and laboratory-produced substrates of the same type of material. The core samples were exposed to long-term weathering and use effects; the laboratory-produced specimens were not exposed to these environmental impacts.

Effects of Substrate Surface Texture

Comparisons were made of the undercutting results obtained for as-received and smooth substrate pairs of the same material. The smooth substrate surfaces were obtained by sawing the substrate material with a fine tooth saw blade. These comparisons were made at 25°F (–4°C) and at 5°F (–15°C). Ratios of undercutting results for as-received substrate surfaces to results for smooth substrate surfaces were formed for each time point for a given substrate-deicer-temperature combination. An average value of this ratio over time was then determined for each substrate-deicer-temperature combination. The results at 25°F (–4°C) and 5°F (–15°C) are given in Tables 21 and 22, respectively, for the six substrates and three deicers. From Table 21 it can be seen that the extent of undercutting at 25°F (–4°C) on as-received substrates was considerably less than that on smooth substrates in a majority of the cases (14 out of 18). This difference for the 14 cases varied by factors ranging from 0.5 to about 0.9.

At 5°F (–15°C), no clear cut conclusions can be drawn from comparisons of undercutting results for as-received and smooth substrate surfaces. The inconsistencies of the ratios in Table 22 are due, in large part, to the fact that the undercut areas are quite small at 5°F (–15°C) and are subject to more error in measurement than those at 25°F (–4°C). In addition, the small undercutting patterns at 5°F (–15°C) are approximately of the same dimensions as the surface irregularities (surface voids or aspirates) of some of the as-received samples. The undercutting patterns at 5°F (–15°C) may thus reflect behavior over one or two surface irregularities rather than behavior over an average population of irregularities. At 25°F (–4°C), the larger undercutting patterns should more closely reflect the average surface condition.

Effects of Substrate Material

The determination of the effects of substrate material on the undercutting characteristics of the three deicers is best shown by the results at 25°F (–4°C) and 15°F (–9°C). The undercutting results for the core samples and laboratory-produced specimens for a given substrate condition-deicer-temperature combination were normalized with the corresponding undercutting results from the laboratory-produced portland cement concrete specimens. Averages of the ratios over the three deicers were then computed for each substrate condition-temperature combination.

Table 21. Ratios of undercutting results for as-received substrates to results obtained for smooth substrates at 25°F (–4°C)

Substrate material	As-received/smooth ratio x 100		
	$CaCl_2$	NaCl	Ethylene glycol
Core samples			
Portland cement concrete	100	69	82
Dense-graded asphalt	69	78	70
Open-graded asphalt	71	50	60
Rubber-modified asphalt	78	114	89
Laboratory-produced specimens			
Portland cement concrete	69	62	68
Dense-graded asphalt	61	172	128

Table 22. Ratios of undercutting results for as-received substrates to results obtained for smooth substrates at 5°F (–15°C)

Substrate material	As-received/smooth ratio x 100		
	$CaCl_2$	NaCl	Ethylene glycol
Core samples			
Portland cement concrete	260	118	94
Dense-graded asphalt	125	168	81
Open-graded asphalt	74	158	192
Rubber-modified asphalt	83	63	87
Laboratory-produced specimens			
Portland cement concrete	73	93	145
Dense-graded asphalt	163	134	199

The results of these undercutting comparisons are given in Table 23 for the as-received substrates at 25°F (–4°C), the as-received substrates at 15°F (–9°C), and the smooth substrates at 25°F (–4°C). The results in Table 23 are referenced to a value of 100 for the laboratory-produced substrate of portland cement concrete. This material was chosen for convenience because most of the other numbers in Table 23 are less than 100. Another substrate could just as easily have been chosen as the basis for comparison.

Table 23. Undercutting comparisons over three deicers at 25°F (–4°C) and 15°F (–9°C) based on a value of 100 for laboratory-produced specimen of portland cement concrete

Substrate material	25°F (–4°C) as-received	15°F (–9°C) as-received	25°F (–4°C) smooth
Core samples			
Portland cement concrete	97	86	78
Dense-graded asphalt	86	70	82
Open-graded asphalt	58	42	63
Rubber-modified asphalt	82	70[a]	63[b]
Laboratory-produced specimen			
Portland cement concrete	100	100	100
Dense-graded asphalt	122	98	80

[a] Data based on California core samples.

[b] Data based on Montana core samples.

Comparisons involving the smooth substrates should reflect the differences due to physical chemical properties of the substrate material (i.e., asphalt compared to portland cement concrete). However, the comparisons of the results from the smooth substrates given below tend to indicate other operating effects.

- The laboratory-produced smooth portland cement concrete specimen was undercut more readily than the smooth portland cement concrete core sample (100 vs. 80).
- The laboratory-produced smooth dense-graded asphalt specimen was undercut to about the same extent as the smooth dense-graded asphalt core sample (80 vs. 82).

- The smooth dense-graded asphalt core sample was undercut more extensively than the smooth open-graded asphalt core sample (82 vs. 63).

- The smooth rubber-modified asphalt core sample was undercut to about the same extent as the smooth open-graded asphalt core sample (63 vs. 63), but considerably les than the smooth dense-graded asphalt core sample (63 vs. 82).

Comparison of the undercutting results for the four as-received core samples should be indicative of undercutting to be expected under field conditions without contamination effects. The order of decreasing undercutting for these four materials at 25°F (–4°C) is as follows:

Portland cement concrete (97)
Dense-graded asphalt (86)
Rubber-modified asphalt (82)
Open-graded asphalt (58)

The two laboratory-produced specimens in the as-received condition appeared to be undercut more extensively at 25°F (–4°C) than the four core samples at that temperature.

At 15°F (–9°C), the order of decreasing undercutting for the four as-received core samples is as follows:

Portland cement concrete (86)
Dense-graded asphalt (70)
Rubber-modified asphalt (70)
Open-graded asphalt (42)

Again, the two laboratory-produced specimens in the as-received condition were undercut more extensively at 15°F (–9°C) than the four core samples at that temperature.

Mathematical Modeling of Physical Processes for Disbonding

Introduction

During this investigation, six mathematical models were developed to describe the stress environments at ice-concrete interfaces. The objectives of the modeling efforts were (1) to develop a better understanding of the mechanism of ice disbondment in currently or

potentially practical ice removal methods, and (2) to assist in the development of experimental methods and the interpretation of the experimental results of this investigation.

The following discussion provides a detailed description of the methods and the findings for each of the six modeling efforts. The figures cited in this discussion are given in Appendix J.

Simulation of Planar Shock Waves on the Ice-Concrete Bond

The objective of the planar shock wave modeling effort was to determine if a planar shock wave could cause ice to disbond from a concrete substrate. The model shows the magnitude of the normal interfacial stresses and the effect that impactor impedance has on those stresses under ideal loading conditions.

Modeling Approach

The model employs a one-dimensional stress-wave analysis program (22) (SWAP) as modified by D. C. Erlich and B. Lew of SRI International. The program uses the method of characteristics to describe all shock wave shapes with a series of shock waves. It is especially suitable for problems that involve true shock fronts.

In the present case, an impact-generated stress wave is simulated in a uniaxial strain geometry. All simulations consist of a 0.635-cm-thick ice layer and a 0.3-cm-thick impactor. Impactors were given mechanical impedance properties of steel, nylon, or ice, so that the effect of higher, lower, and identical impactor impedances could be observed. The ice layer was assumed to lie on a concrete substrate that is either semi-infinite or 2.54 cm thick.

The properties of the materials involved in the analysis are as follows:

Sound velocity (m/s):

- ice = 3,000
- concrete = 2,110
- steel = 5,180
- nylon = 1,800

Density (g/cm^3):

ice = 0.917
concrete = 2.85
steel = 7.896
nylon = 1.14

A mechanical equation of state for ice obtained from CRREL (23) shows the following features (1) elastic behavior to about 75 MPa (indicating a shock wave velocity of about 3,000 m/s), (2) a fairly sharp transition to a low shock wave velocity regime (about 750 m/s) that suggests a change of state of the ice, and (3) a return to a higher shock wave velocity regime that coincides with the Hugoniot curve for water. Impact velocities were selected so that the maximum compressive stress in the ice did not exceed the crush strength in CREEL's mechanical equation of state for ice (i.e., 75 MPa). In the simulations that permitted the ice-concrete interface to fracture, the bond was assumed to have a strength level that is typical of monolithic ice in tension (i.e., 10 MPa).

For all simulations, the stress histories were recorded within the ice layer at depths of 0.2, 0.4, and 0.63 cm (i.e., at two locations in the ice and at one location near the ice-concrete interface. The stress history was also recorded for the concrete at a depth of 0.317 cm from the ice-concrete interface.

Results

Figure J-1 shows the stress measuring location (or "stress gage locations") and the locations of the impacter, ice, and concrete substrate in the form of an x-t diagram (i.e., a diagram showing the stress wave front locations with time). In the simulation in Figure J-1, the impacter is made of steel, the concrete is semi-infinite, and the ice and the ice-concrete interface are infinitely strong (see Table 24 for additional details about the boundary conditions for the simulation in Figure J-1 and for all of the simulations). In Figure J-2, the stresses at the stress gage locations in the ice and concrete are shown as a function of time. For times less than about 15 μs, the stresses at all locations are comprehensive. From about 15 to 23 μs, tensile stresses arise because of the impedance mismatch between the steel impacter and the ice.

Table 24. Planar shock wave simulation condition and results

Simulation run desig. number	Impactor material	Impact velocity (ms)	Concrete thickness (cm)	Ice spall strength (MPa)	Ice/concrete disbonding strength (MPa)	Peak compressive stress at the impact plane (MPa)	Peak compressive stress at the interface plan (MPa)	Peak tensile stress at the ice-concrete interface (MPa)	Time after impact of peak tensile stress (μs)
1A1	Steel	20	∞	∞	∞	52	73	5	18
1D	Steel	20	2.54	∞	∞	52	73	42	29
1D1	Steel	20	2.54	10	10	52	73	disbonded	29
2D1	Ice	35	∞	∞	∞	48	66	0	--
3D	Ice	35	2.54	∞	∞	48	66	41	29
4D	Ice	35	2.54	10	10	48	66	disbonded	29
1B1	Nylon	35	2.54	∞	∞	46	62	first peak at 25, second peak at 40	first peak at 6, second peak at 29
1B2	Nylon	35	2.54	∞	10	46	62	disbonded	6
1B3	Nylon	35	2.54	10	10	46	62	disbonded	6

In Figure J-3, an x-t diagram is presented for a simulation run the same way as that shown in Figures J-1 and J-2, with the exception that the concrete is 2.54 cm thick in Figure J-3. Wave reflections from the underside of the concrete produce very large tensile stresses (up to 42 MPa at the ice-concrete interface) as shown in Figure J-4. Attenuation of the stress in the concrete was not included in the analysis so increasing the concrete thickness to a value greater than 2.54 cm has no effect on the results other than to increase the time required for the reflected waves to reach the ice-concrete interface. Consequently, results from simulations with different concrete thicknesses are not shown.

Figure J-5 shows the stress history for a simulation that was run the same way as the simulation shown in Figures J-3 and J-4, except that the strengths of the ice and the ice-concrete interface were finite (10 MPa). The value of the strength of the ice-concrete bond is roughly typical of the impact strength of ice (24). A comparison of Figures J-4 and J-5 shows that the effect of the tensile stresses produced by the impedance mismatch of the steel impactor and the ice is sufficient to cause disbonding of the ice. Failure at the ice-concrete interface is apparent in Figure J-5 from the lack of stress near the ice-concrete interface and within the ice after about 30 μs.

Figures J-6, J-7, and J-8 show the stress-time histories for simulations with an ice impactor. These simulations, although perhaps not of direct practical significance, were performed to determine the effects of using an impactor with the same mechanical impedance as ice. Figure J-6 shows the stress-time history for semi-infinite concrete with an infinitely strong ice layer and ice-concrete interface. The impact produces no tensile stress in the ice because of the matched impedance with the impacter and lack of a free surface to reflect the compressive wave on the underside of the concrete. Figure J-7 shows that 2.54-cm-thick concrete produces substantial tensile stresses in the ice and at the ice-concrete interface when the reflected wave from the bottom surface of the concrete arrives (about 30 μs after impact). Figure J-8 shows that when a fracture stress for the ice and the ice-concrete interface is 10 MPa, disbonding occurs.

Figures J-9, J-10, and J-11 show the stress-time histories for simulations with a nylon impactor. Nylon was selected for these simulations because its impedance is significantly lower than ice. In Figure J-9, the simulation is for semi-infinite concrete with ice and an ice-concrete interface with an infinite failure stress. The tensile stress that is induced at the interface due to the impedance mismatch produced by a nylon impactor is substantially higher than the tensile stress achieved with the steel impactor (i.e., 25 MPa versus 5 MPa, respectively). Figure J-11 shows that the tensile stresses produced by the nylon impactor are sufficient to fracture the ice at the interface about 6 μs after impact when a bond strength of 10 MPa is included in the simulations. The nylon impacter produced the highest tensile

stresses at the interface in the semi-infinite concrete in spite of a slightly lower compressive stress that was produced on impact. Consequently, from the standpoint of producing the highest possible tensile stress at the ice-concrete interface, a low impedance impactor (i.e., lower than ice) appears to be the most efficient. Furthermore a low impedance impactor is also most likely to produce a tensile stress at the interface that is sufficient to disbond ice from concrete without crushing the ice on impact.

Three-Dimensional Analysis of the Stresses at an Ice-Concrete Interface by a Wedge Moving Parallel to the Interface

The objective of this modeling effort was to assist in the interpretation of the high rate shear tests that were performed during the study. To do this, the finite element analyses performed in this study simulate the experimental conditions of those experiments as closely as possible. The simulations correlate the removal measured stresses in the loading device (i.e., a wedge attached to a shaft) with the behavior of an ice sample that is sheared from a pavement substrate. By comparing the simulations with experimental results, we assess the relative importance of ice-concrete bond strength and of experimental parameters such as the ice material properties and the mechanics of the test apparatus.

Modeling Approach

Finite element computations were performed using DYNA-3D (25), a three-dimensional dynamic nonlinear finite element program. Figure J-12 shows the finite element mesh used in the analysis. It conforms to the geometries and dimensions of the experimental apparatus used. The model includes the ice block, concrete substrate, and brass scraper with aluminum lead shaft. A lumped mass was added to the end of the load shaft to represent the mass of the support plate used in the experiments.

The ice block was 3.56 cm square and 1.27 cm in thickness. The scraper was 6.35 cm wide and had an inclination of 30 degrees. The 1.91-cm-diameter load shaft was 38.1 cm in length. Details of the load shaft counterbore and its location within the blade were modeled explicitly; however, a set screw that was used to attach the scraper to the load shaft was not modeled.

The elastic moduli used were 8.27, 20.7, 100, and 69 GPa for the ice, concrete, brass scraper, and aluminum load shaft, respectively. These materials had corresponding densities of 0.898, 2.67, 8.5, and 2.8 g/cm,^{3} respectively. The masses of the scraper-shaft assembly and ice

block were 4.19 and 0.014 kg, respectively. The scraper-shaft assembly was given a velocity at impact of 6.94 or 2.48 m/s and was constrained to move only along the z-axis as shown in Figure J-12.

To gain an understanding of the effects of the various experimental parameters, a reference computation was performed. In the reference computation, all materials remained elastic, the scraper was rigidly fixed to the load shaft, the ice-concrete bond was given zero strength, and the impact velocity was 6.94 m/s. In the following sections we show the influence of variations in these parameters.

Effects of Ice Material Properties. To examine the effects of ice material properties, simulations with an elastic-perfectly plastic material model for the ice were compared with results using elastic ice properties. In the elastic-perfectly plastic ice material mode, an effective yield stress of 7.5 MPa was used. This value roughly corresponds to the value for fragmentation in compression tests (24). For simplicity, the ice-concrete bond was assumed to have zero strength and the load shaft was assumed to be rigidly fixed to the scraper. The impact velocity was 6.94 m/s.

Figure J-13 shows the axial stress in the load shaft versus time at the location of the experimental strain measurements (i.e., on the load shaft approximately 7 cm from the tip of the wedge). The finite element results for the two material models (dashed lines) are shown with two experimentally measured results (solid lines). The elastic material model resulted in a maximum effective stress in the ice of 30 MPa (not shown in the figure) which is considerably higher than the experimentally measured fragmentation stress of 7.5 MPa. As shown in Figure J-13, a large axial compressive stress was produced in the load shaft. Using the elastic-perfectly plastic material model reduced the maximum compressive stress by 37% and produced a more favorable comparison with experimental results.

Figure J-14 shows a comparison of the kinetic energy change in the scrapper-shaft assembly for the two ice material models. The elastic ice model reduces the kinetic energy 40% more than the elastic-perfectly plastic model. This suggests that the nonelastic properties of ice can have a significant effect on the kinetic energy calculations for a high initial kinetic energy (i.e., at an initial impact velocity of 6.94 m/s). Later, we will see that the elastic and elastic-perfectly plastic material models for ice produce similar kinetic energy changes for a low initial kinetic energy changes for a low initial kinetic energy (i.e., at an initial impact velocity of 2.48 m/s).

Effects of Impacting Blade Mechanics. In the experiment, a set screw secured the compression shaft to the blade. To determine the possible effects of the set screw, computations were performed with the load shaft fixed to the scraper at all points and with the load shaft only attached to the scraper at nodes that are in line with the axis of the set screw. In the latter computation, a gap between the compression load shaft front surface and scraper of 0.159 cm was introduced. In both computations an elastic material model for the ice was used with an impact velocity of 6.94 m/s.

Figure J-15 shows a plot of the load shaft axial stress versus time. In comparing the two finite element results (dashed lines), a 19% reduction in the peak stress was observed when the load shaft was attached to the scraper at the set screw position. The two experimental results (solid lines) are shown for comparison.

There are many ways that the load shaft could be attached to the scraper. The case presently examined probably represents a situation that is close to the lower bound with respect to the amplitude of the stress wave transmitted from the blade to the load shaft. The results indicate that the method of attachment can significantly affect the stress measurements.

Effects of Ice-Concrete Bond Strength. Figure J-16 shows a comparison of the kinetic energy change in the scraper-shaft assembly for simulations with ice that is not attached to the substrate and for simulations with an ice-concrete bond strength of 0.75 MPa. The tension and shear strength values of the interface were assumed to be the equal in these simulations. The 0.75-MPa value of the ice-concrete bond strength is typical for the quasistatic shear strength of an ice-concrete bond (26). The kinetic energy change in the scraper-shaft assembly was not affected by the bond strength in the range of bond strengths that were investigated. This suggests that, in the simulations for the high impact velocity (6.94 m/s), the energy required to break the ice-concrete bond is small compared to the kinetic energy transmitted to the ice block.

Effects of Impact Velocity. To assess the effect of impact velocity, simulations were performed at two impact velocities (2.48 and 6.94 m/s). Figure J-17 shows a comparison of kinetic energy change in the scraper-shaft assembly for elastic and elastic-perfectly plastic ice material models. Unlike the results obtained at an impact velocity of 6.94 m/s, the results shown in Figure J-17 indicate that the impact between the scraper-shaft system and ice is, for the most part, an elastic impact (i.e., there is little effect from the incorporation of the elastic-perfectly plastic constitutive model).

Figure J-18 shows a comparison of the kinetic energy change from simulations with several different ice-concrete bond strengths for an elastic-perfectly plastic ice material model (dashed lines) for an impact velocity of 2.48 m/s. As observed for simulations with an impact velocity of 6.49 m/s, there is little difference between no bond strength and a bond strength of 0.75 MPa. The solid horizontal line corresponds to the kinetic energy change measured in an ice disbonding experiment conducted at a velocity of 2.48 m/s. To match this change in our computations we required an ice-concrete bond strength of 3.5 MPa. This value is unrealistically high which suggests that other effects are likely to be responsible for the reduction of kinetic energy of the scraper-shaft assembly. Those other effects may include contact between the scraper and concrete before or during impact.

Figures J-19 and J-20 show contour plots of shear and tensile stress distributions, respectively, in the concrete near the ice-concrete interface for a simulation of a test with a 3.5 MPa bond strength. The contour plots represent stress conditions when disbonding begins. The ice-concrete interface bond stress distribution is complex due to the combination of both shear and tension between the ice and concrete substrate. However, qualitatively, we see that the shear and tensile stresses are largest near the ice impact face and decay towards the distal end of the specimen.

Two-Dimensional Analysis of the Stresses at an Ice-Concrete Interface by a Wedge Moving Perpendicular to the Interface

The objective of this modeling effort was to improve our understanding of the effects on an ice layer from the impact of a wedge traveling normal to the ice-concrete interface. In this analysis, we examine (1) the propensity for a crack to initiate or propagate along the ice-concrete interface, (2) whether a path can be opened from the ice surface to the ice-concrete interface to allow access for deicing chemicals, and (3) the potential for a wedge indenter to damage the pavement.

The finite element method is used to determine the stress and deformation fields in the ice layer and the supporting pavement. From the nature of the shear and normal stresses acting across the ice-concrete interface, we can examine the tendency for interface cracks to form and grow. From the stress field in the vicinity of the indentor, we can examine the tendency for the wedge to open a path for deicing chemicals through the ice to the pavement. Finally, from the magnitude of the stresses in the pavement, we can make a preliminary assessment of pavement damage resulting from a wedge that impacts an ice layer on the pavement.

Modeling Approach

The model simulated the effect of an indentor with a $2\theta = 60°$ included angle wedge traveling at a constant velocity of $V_0 = 5$ m/s penetrating an h = 0.3-cm-thick ice layer bonded to a concrete substrate (see Figure J-21). Plane strain deformation was enforced. The dynamic, explicit finite element code, DYNA-2D (27) was used for this analysis. The finite element mesh is shown in Figure J-22. Because of symmetry, only one half of the problem was modeled. The mesh was rezoned periodically during the calculations to avoid numerical difficulties associated with badly distorted elements. To further avoid numerical difficulties, the tip of the wedge was bunted slightly to a radium of h/10 = 0.03 cm.

The ice was modeled as elastic-plastic using the von Mises yield criterion. We used a density of 0.898 g/cm^3, Young's modulus of 8.27 GPa, and Poisson's ratio of 0.35. The yield stress of the ice, Y, was assumed to be 100 MPa and the results for stress were scaled by this stress level. The tangent modulus was chosen to be very small relative to Young's modulus so as to approximate an elastic-perfectly plastic material. We chose a tangent modulus of 8.27 MPa. The concrete was modeled as an elastic solid with a density of 2.67 g/cm^3, Young's modulus of 20.7 GPa, and Poisson's ratio of 0.20. The wedge was assumed to be rigid. A verification of the results presented below is given in Appendix K.

Results

Deformed finite element mesh patterns at various depths of wedge penetration, p, are shown in Figure J-23. The penetration is normalized by the ice thickness. The mesh was rezoned periodically, so mesh displacements are not necessarily the same as material displacements. Since penetration occurred at a constant velocity, time, t, and the normalized penetration, p, are equivalent and related by $t = ph/V_0$. Contour plots of the horizontal normal stress component, s_{xx}/Y, the vertical normal stress component, s_{yy}/Y, and shear stress component, s_{xy}/Y, in the ice layer are shown for selected penetration depths in Figures J-24 through J-26. All stresses are normalized to the yield stress of ice that was assumed from this analysis ($Y = 100$ MPa). The stresses on the ice side of the ice-concrete interface are shown as a function of distance along the interface for selected penetrations in Figures J-27 through J-29. Plots of the horizontal normal stress component, s_{xx}/Y, on the concrete side of the ice-concrete interface are shown for selected penetrations in Figure J-30. Plots of the vertical normal and shear stress components on the pavement side of the interface are nearly identical to those for the ice side shown in Figures J-28 and J-29 because shear and normal tractions must be continuous across the interface. A plot for the maximum principal stress along the pavement side of the ice-concrete interface is shown in Figure J-31.

In Figures J-24 through J-26, the stresses in the ice on the vertical axis below the tip of the wedge are compressive over half the distance to the pavement interface. Nearer the interface, the horizontal normal stress component is tensile, and is maximum at a value of $s_{xx}/Y \approx 0.4$ when the normalized penetration is 0.1. For greater penetrations, the magnitude of the tension decreases and the maximum occurs closer to the interface. The normal vertical stress component, s_{yy}/Y, remains compressive along the vertical axis.

Shear stresses s_{xy}/Y are elevated along a line running from the tip of the wedge downward and outward at about 45°. See, for example, Figure J-26(c). Along the same line, s_{xx}/Y and s_{yy}/Y are compressive, which might tend to discourage the development of a shear crack. However, near the ice-concrete interface, the magnitudes of s_{xx}/Y and s_{yy}/Y are reduced relative to s_{xy}/Y, which might favor nucleation of a shear crack. Cracks running downward at approximately 45° with respect to the surface of the ice would be analogous to the Hertzian cone cracks that form in axisymmetric indentation.

As shown in Figures J-27 through J-29, the horizontal normal stress component, s_{xx}/Y, in the ice at the interface is low, but the vertical normal stress component, s_{yy}/Y, and the shear stress component, s_{xy}/Y, are high. Because s_{yy}/Y is compressive, interfacial crack nucleation and propagation are not favored; however, at $x/h > 0.8$, s_{yy}/Y is reduced and s_{xy}/Y is elevated, which will tend to promote shear cracking.

The stress contour plots suggest that fracture is likely to appear as a shear crack that extends upward from the interface at 45° to meet the punch and horizontally outward along the interface, leaving an "island" of damaged ice below the penetrator. The situation is shown schematically in Figure J-32. We are not able to determine whether such cracks would propagate through the compressive stress field near the wedge, nor are we able to determine from the present analysis how far the crack would propagate out along the interface.

The blunted 60° wedge examined in the present analysis produces considerable compressive stresses that might not be optimal for fracturing the ice in preparation for the injection of deicing chemicals. A wedge with a more acute angle might produce smaller compressive stresses that would more readily propagate cracks in the ice. However, a blunt 60° wedge induces considerable yielding and displacement of the ice that reduces the ice thickness which might assist in getting deicing chemicals near the interface. Yielding of the ice occurs over an extensive region around the penetrator which might also assist the deicing chemicals to reach the ice-concrete interface.

If the yield strength and stiffness of the ice are much less than the yield strength and stiffness of the pavement, the results of the present analysis will scale with the ice yield strength.

Furthermore, since the penetration velocity is slow relative to elastic wave speeds in the ice and pavement materials, and since the material models are rate independent, these computed deformations will be the same for any lower penetration velocity. Thus, the results presented in this section can be scaled to other ice thicknesses, penetration velocities, and strengths as long as penetration is slow relative to wave speeds, the ice is thin relative to other dimensions of the problem, and the ice is relatively weak.

Fracture Mechanics Analysis of a Crack at the Ice-Pavement Interface

In most cases, the interface between ice and a substrate does not rupture simultaneously at all points, given uniform loading. Instead, disbonding begins at the weakest location first and spreads from there. This is the case whether the weakening is caused by a bubble in the ice, a geometrical irregularity at the substrate surface, a preexisting crack, or a locally contaminated zone. Even the most minute bond strength variations will force disbonding to begin at the lowest strength locations. To study such problems, we turn to the principles of fracture mechanics. Using these principles, we can attempt to relate surface energy measurements provided by surface chemists to the loads required to disbond ice from a substrate.

Modeling Approach

According to linear elastic fracture mechanics (LEFM) theory, the stresses at the tip of a sharp crack are singular, that is, they go to infinity as the crack tip is approached. Intuition tells us that this is wrong; real materials will not sustain infinite stresses. However, LEFM is useful in the analysis of real materials even though stresses are not infinite at a crack tip. This is because the stresses in the vicinity of the tip of a crack in a real material increase as if they are going off to infinity as the crack tip is approached. Nearer the crack tip, material nonlinearities dominate and the analysis is much more difficult. However, there is an annular region surrounding the crack tip that is sufficiently far away such that an elastic analysis is accurate. The stresses and strains inside the nonlinear region are uniquely determined by the stresses on its boundary, given by the elastic analysis. therefore, even if the onset of fracture is governed by processes inside the nonlinear crack tip region, these processes are uniquely determined by the elastic stresses further from the crack tip. The assertions that LEFM is accurate in an annular region and that LEFM uniquely determines the nonlinear fields are true under fairly broad restrictions on material properties, nearness of flaws to boundaries, and rate of loading. Thus, we can use LEFM theory to analyze real materials in general and the disbonding of ice from substrates in particular.

In the present analysis, we use LEFM to determine the magnitude of the crack tip stress singularity (the so-called stress intensity) for the shear test specimen geometry and load configuration used in the quasistatic shear test experiments. We can also use LEFM to relate the stress intensity to the energy required to extend the crack (the so-called energy release rate), that is, the energy required to disbond ice. The energy required to disbond ice as determined from the shear tests can then be correlated to surface energies measured by independent means.

Analytical solutions using LEFM have been reported in the literature for many configurations of cracks, specimens, and applied loads (28,29). Unfortunately, the interface crack problem with the geometry of the shear test is not among these. Thus, we turn to the finite element method (FEM) in combination with LEFM to compute the stress and strain fields near the crack tip. In the present discussion, we present a test problem for which an asymptotic analytical solution is known. The finite element mesh is shown in Figure J-33 for a crack at the ice-concrete interface of a large ice-concrete panel pulled in tension. The corresponding asymptotic problem for the FEM mesh is a finite crack at the interface between two infinite half spaces. The asymptotic analysis (30) yields the following description of the tensile stresses σ_{22} along the bond line (at the interface) ahead of the crack tip:

$$\sigma_{22} = \frac{1}{2}\,\sigma_{22}^{\infty}\sqrt{\frac{a}{r}}\left[\cos\left(\varepsilon \ln\frac{r}{a}\right) - 2\,\varepsilon \sin\left(\varepsilon \ln\frac{r}{a}\right)\right] \qquad (1)$$

Here r is the distance from the crack tip, a is the crack length,

$$\varepsilon = \frac{1}{2\pi}\left[\ln\frac{k_1\,\mu_2 + \mu_1}{k_2\,\mu_1 + \mu_2}\right]$$

$k = 3 - 4\nu$, μ is the shear modulus, ν is Poisson's ratio, σ_{22}^{∞} is the tensile stress far from the crack, and subscripts 1 and 2 refer to material above and below the bond plane, respectively. Values for σ_{22} determined for the FEM and asymptotic analyses are shown in Figure J-34.

The agreement between the finite element and asymptotic solutions is excellent over distances ranging from 3 x 10^{-4} crack lengths to about one crack length ahead of the tip. Therefore, we can accurately compute energy release rates and stress intensities within this range with the FEM analysis.

It is a simple matter to compute the energy release rate using the J integral, given by

$$J = \int_{\Gamma} \left(W n_i - \sigma_{ij} \frac{\delta u_i}{\delta x_1} \right) ds \qquad (2)$$

where Γ is any contour (on which the solution is known to be accurate) surrounding the crack tip, σ_{ij} are the stresses, u_i are the displacements, W is the strain energy density such that $\sigma_{ij} = \partial W/\partial \varepsilon_{ij}$, ε_{ij} are the strains, and $\underline{n} = n_1\underline{i} + n_2\underline{j}$ is the outward normal to the contour. See Figure J-35(a). For FEM computations, it is convenient to recast the J integral as an area integral (31) (i.e., a summation over elements) between two contours,

$$J = \int_{A} \left(\sigma_{ij} \frac{\partial u_i}{\partial x_1} - W\delta_{1j} \right) \frac{\partial q_1}{\partial x_j} \, dA \qquad (3)$$

See Figure J-35(b). Here q_1 is an arbitrary smooth function which varies from 1 on the inner contour to 0 on the outer contour, and $\delta_{ij} = 1$ for i = j, $\delta_{ij} = 0$ otherwise. The energy required to create a unit area of crack extension is equal to J. This quantity will be computed from the forces required to cause disbonding in the shear tests and it will be compared to the surface energy characteristics determined in Task 4.

It is quite possible that the single parameter $\underline{J}$ (or a single surface energy) will be insufficient to characterize ice disbonding. We might find that different amounts of energy are required for disbonding by lifting and disbonding by shearing. For this reason, it is useful to know separately the opening mode and shearing mode stress intensities.

When a crack in a homogeneous body is opened by forces normal and symmetrical to the crack plane, the crack responds by opening in a symmetric mode. No shear stresses develop ahead of the crack tip. Furthermore, the opening mode stress intensity is proportional to $\sqrt{J}$ as computed above. Conversely, forces on a homogeneous body that are transverse and symmetrical to the crack plane lead to a crack shearing mode. No crack opening occurs, and the shear mode stress intensity is proportion to $\sqrt{J}$ (the shearing mode J is different than the opening mode J).

Pure normal or shear stresses do not occur in symmetric loading of an interface crack between two different media. Consider the extreme example of a finite crack in the interface between a rigid and an incompressible material. As the bodies are pulled apart normal to the crack plane, the incompressible material (Poisson's ratio = 1/2) tries to contract perpendicular to the loading direction, whereas the rigid material cannot. This leads to shear stresses parallel to the interface, and thus the crack loading is a coupled symmetric opening mode and a shearing mode. This coupling implies that the opening and shearing mode stress intensities cannot be obtained from only knowledge of J. The effects of shearing and lifting ice from a substrate must be separated in another manner.

To uncouple and determine the stress intensities, we use the method employed by Shih and Asaro (32). The area integral in Equation (3) is modified to be

$$G_{int} = \int \left[(\sigma_{ij})_{aux} \frac{\delta u_i}{\delta x_i} + \sigma_{ij} \left(\frac{\delta u_i}{\delta x_1} \right)_{aux} - \sigma_{ij} \, (\varepsilon_{ij})_{aux} \delta_{1j} \right] \frac{\delta q_1}{\delta x_j} \, dA \qquad (4)$$

where $()_{aux}$ are taken from the known asymptotic solution, evaluated first for an opening mode asymptotic field, both with unit loading. The actual opening and shear mode stress intensities, which will be examined to see if they can be correlated with the results of the shear tests, are proportional to the G_{int} values calculated from (4).

Results

We now have available the tools to analyze the shear test and relate the failure loads to the energy required to disbond ice from a substrate. In addition, we can separate the effects of shearing and lifting. The remaining tasks are to perform FEM analyses to simulate the shear tests with an interface crack that will be run under Task 5, and to compute the required area integrals. Ultimately, the force required to disbond ice from a substrate will be correlated with the interface energy characteristics.

The energy release rate *(J)* and the stress intensity [(Q_I) for crack opening and (Q_{II}) for shear] have been determined for two geometries of ice bonded to homogeneous concrete using the area integral analysis outlined above. The first geometry is the same as that presented in the discussions above (i.e., a finite crack at the interface between infinite half spaces of ice and concrete). We examined this geometry because an analytical solution exists which can be used to validate the FEM analysis. The second geometry is similar to the loading conditions in the shear test experiments. Using this analysis, we will relate the failure load values measured in the shear tests with surface energy measurements.

The stress intensities are computed from the following expressions:

$$Q_I = G_{int}^{(1)} \frac{2\cosh^2(\pi\varepsilon)}{\frac{(1-\nu_1)}{\mu_1} + \frac{(1-\nu_2)}{\mu_2}} \tag{5}$$

$$Q_{II} = G_{int}^{(2)} \frac{2\cosh^2(\pi\varepsilon)}{\frac{(1-\nu_1)}{\mu_1} + \frac{(1-\nu_2)}{\mu_2}} \tag{6}$$

where: μ_1 and μ_2 are the shear moduli for ice and concrete, respectively, ν_1 and ν_2 are Poisson's ratios for ice and concrete, respectively, and

$$\varepsilon = \frac{1}{2\pi} \ln \left[\frac{3\mu_2 - 4\mu_2 \nu_1 + \mu_1}{3\mu_1 - 4\mu_1 \nu_2 + \mu_2} \right]$$

For the problem with an analytical solution, values for G_{int} in Equations (5) and (6) are computed from Equation (4). Expressions for the asymptotic stress and strain terms in Equation (4) have been derived by Shih and Asaro (32) and the displacement gradients and displacement gradient terms have been derived by Lee and Choi (33). We note that several errors were noted in their analysis; corrected versions of their equations are presented in Appendix L. In the FEM analyses, values for G_{int} were computed from a summation equation that is analogous to Equation (4). The strain energy release rate *(J)* was computed from Equation (3) for the analytical solution or, in the FEM analyses, from the analogous summation equation.

Table 25 compares the values of J, Q_I, and Q_{II} for the test problem from the analytical equations and from FEM computations. The two procedures are in very good agreement with respect to the values for J and Q_I. Values for Q_{II} are very small and, as a result, could not be accurately computed by FEM computations.

Table 25. Strain energy release rate (J) and stress intensity factors (Q_I and Q_{II}) computed from an analytical solution and FEM simulations of a finite crack at the interface between infinite half spaces of ice and concrete under a tensile load of 1,000 Pa

	J (Nm/m^2)	Q_I ($Pa\ m^{1/2}$)	Q_{II} ($Pa\ m^{1/2}$)
FEM computations*	2.67×10^{-5}	590	5
Analytical solution	2.66×10^{-5}	591	18

* Values from the FEM computations are mean values computed from eight integration domains ranging in size from 6.3×10^{-4} to 1.4 mm.

Table 26 shows the values of J, Q_I, and Q_{II} for FEM simulations of the shear test geometry shown in Figure J-36.

Table 26. Strain energy release rate (J) and stress intensity factors (Q_I and Q_{II}) from FEM simulations of a shear test under a load of 1,000 PA

J (Nm/m^2)	Q_I ($Pa\ m^{1/2}$)	Q_{II} ($Pa\ m^{1/2}$)
8.54×10^{-7}	72	77

* Values are means computed from eight integration domains ranging in size from 6.3×10^{-4} to 1.4 mm.

In this example, a uniform pressure of 37 N/m (corresponding to a load of 1,000 Pa) was applied parallel to the ice-concrete interface. Values of J, Q_I, and Q_{II} can be obtained from any applied load by scaling. Q_I and Q_{II} are proportional to the applied load, and J is proportional to the square of the applied load.

The model was compared to experimental data that describe the nominal quasistatic shear stress required to disbond ice from ground Pyrex glass, ground silica, limestone, asphalt, and portland cement mortar. The experimental procedure and test results that were used in this comparison are described earlier in this section of the report and in Appendix F. The "nominal quasistatic shear stress" for each test was obtained by dividing the force required to disbond a cylinder of ice by the total area of bonding between the ice and the substrate (i.e., 12.08 cm^2). A measure of the energy required to disbond the ice from each substrate was obtained from the contact angle measurements described earlier in this section of the report under "Surface Energetics." Contact angle measurements were made on each substrate at the location of the ice-substrate bond of each shear test. The "work of adhesion" for each shear test was computed from the contact angle measurements as follows (9).

$$W_A = \gamma_{LV}(1+\cos\theta)$$

where: W_A = work of adhesion
γ_{LV} = the surface energy for water in air = 69.5 dynes/cm (+ 69.5 mN/m)
θ = the contact angle

The data from the shear tests at temperatures ranging from −23° to −4°C and under various freezing rates are shown in Figure J-37. The data fall into two groups: high work of

adhesion bond data (Pyrex glass, silica, limestone, and portland cement mortar) and low work of adhesion bond data (asphalt).

It should be noted that these results are preliminary in nature. The contact angle data used to generate estimates of the work of adhesion are considerably lower than they should be due to the large drop size used. The resultant work of adhesion are consequently higher than would be expected. The separation of the asphalt results from the results of the other substrates is yet to be explained.

The model was compared to these data by equating the force required to generate an energy release rate *(J)* equal to the work of adhesion. The finite element analysis of a rigid substrate with a horizontal force applied to a rectangular ice sheet of unit thickness produced a value of J equal to 8.54×10^{-7} N/m for an applied force of 37 N/m. Because J is proportional to the square of the applied load, we have the following relationship:

$$J = \frac{(\ 8.54\ x\ 10^{-7}\ N/m\ )\ (\ A\ )\ (\ L^2\ )}{(\ 37 N/m\ )^2} \tag{8}$$

where: J = energy release rate in N/m
A = bond area = 0.001207 m^2
L = applied load in N

In terms of a nominal applied shear stress, we have the following:

$$S = 0.372\ \sqrt{J'} \tag{9}$$

where: S = nominal shear stress in kg/cm^2
J' = energy release rate in dynes/cm

Figure J-37 compares the model given by Equation (9) to the shear test data.

We note that the model was developed entirely independently of the shear tests. The only materials data used by the model are the elastic properties of ice and the surface contact angle wetting measurements.

Rather poor agreement between the data and the simplistic model is evident. It is clear that additional factors affect the experimentally measured nominal shear stress. Further analysis of the mode of failure observed in the experiments and adjustments to the experimental techniques are necessary to determine unequivocally the nature and importance of these additional factors; however, likely explanations are immediately evident. In most tests, the portland cement mortar and the limestone substrates exhibited higher nominal shear stresses than the model predictions. The high surface porosity of these substrates may have produced a high strength ice-substrate bond by allowing water to penetrate into the substrate. A high strength ice-substrate bond did not develop on the asphalt, Pyrex glass, and silica substrates. Apparently, these surfaces either did not have significant porosity or water did not enter the pores (which is likely for the asphalt substrates due to the high water asphalt surface tension). The Pyrex glass and silica substrates generally produced shear stress values that were lower than the predictions of the model. This could be due to flaws in the ice-substrate interface that were larger than those assumed by the simplistic model or because the loads applied during the experiments were not precisely parallel to the substrate. Further work is needed to construct experiments that are more amenable to FEM simulation (e.g., by using rectangular rather than disc-shaped ice specimens to make the experiments more two-dimensional) and that are better characterized in terms of initial crack size. The latter experiments could be accomplished by intentionally introducing large flaws at the interface of controlled dimensions.

Finite Element Analysis of the Ice-Substrate Shear Tests

The objective of the analyses described below was to assist in the interpretation of the quasistatic shear test results performed in this investigation and to suggest improvements in the mechanical aspects of the test design.

Modeling Approach

Finite element analyses were performed to investigate the stress environment at the ice-substrate interface of the shear test experiments. The calculations were performed using NIKE–2D, a general purpose nonlinear finite element program developed at Lawrence Livermore National Laboratory (34). The effects on interfacial stresses from variations in tests specimen geometry, mold material (Teflon or aluminum), and load application direction have been examined through several cases. These cases were examined to identify the most important shear test configuration variables for the quasistatic ice-substrate shear experiments

performed in this investigation. Implications of the model for the interpretation of the shear test results are described below.

Discussion

The geometry of the first case considered is represented by the baseline conditions shown in Figure J-38. An ice block is loaded by a uniform pressure of 100 psi (0.69 MPa) distributed over a 0.125 in (0.318 cm) length centered 0.125 in (0.318 cm) above the substrate. The substrate is modeled as a rigid surface. The ice block is rectangular with a length of 1.5 in (3.8 cm), unit depth, and a thickness of 0.5 in (1.27 cm). The load is applied to a Teflon or aluminum mold that is 0.25 in (0.635 cm) thick. For simplicity, we assumed that the ice is bonded to the substrate with no friction and to lift freely off the substrate. A rectangular specimen geometry has been used in the simulations (rather than the circular specimen geometry used in the shear tests) so that a two-dimensional analysis could be used.

Figure J-39 shows the shear and normal stresses at the interface of the ice from an applied load on aluminum and Teflon mold materials. For both materials, the shear stresses show a sharp peak at the mold-ice interface that decays rapidly with distance from the model [Figure J-39(a)]. The sharp gradient in shear stress makes it difficult to quantify the strength of the interface. However, there is an advantage with the Teflon mold because the peak shear stress is about 50% higher in the aluminum than in the Teflon [105 psi (0.724 MPa) versus 70 psi (0.48 MPa)]. Regardless of the mold material, Figure J-39(a) shows that the shear stresses are not uniformly distributed across the specimen surface. This is an unavoidable consequence of Saint-Venant's Principle that states that localized applied tractions to a body give rise to localized stresses and strains within the body.

The interface normal stresses are shown in Figure J-39(b). The normal stresses for aluminum show a very sharp tensile peak at the mold interface and small compressive stresses away from the mold. The normal stresses in the Teflon show a region of tension that extends about 0.4 in (1.0 cm) from the mold. The mold reacts in the following ways when a load is applied: (1) the mold tends to lift the ice off the substrate in response to the couple that develops when the ice is bonded to the substrate and the mold is not, and (2) a tensile normal stress in the ice balances the compressive normal stress in the mold which causes the mold to bulge under the applied compressive load (i.e., the Poisson effect in which a negative strain in one orientation produces positive strains in the orthogonal directions). The difference in these two effects is that the normal stresses are highly concentrated near the applied load when the first effect dominates and the normal stresses are more evenly distributed when the second effect dominates. With a Teflon mold, the second effect dominates because its low elastic

modulus produces a large Poisson effect. With an aluminum mold, the first effect dominates because of aluminum's high elastic modulus.

In the second case considered, the load is applied through a mold of Teflon or aluminum with a chamfer on the inner edge (see Figure J-40). The chamfer cuts away the mold surface adjoining the ice at a 45° angle. Two chamfer sizes were investigated; a small chamfer with a dimension of 0.0625 in (0.159 cm) along the substrate, and a large chamfer with a dimension of 0.1875 in (0.4763 cm) along the substrate. Chamfered mold geometries were investigated to determine if a more uniform shear stress distribution and a reduced normal stress could be produced near the edge of the ice.

The resulting stress distributions along the ice-substrate interface for a chamfered Teflon mold are shown in Figure J-41(a) and J-41(b). The chamfer reduces the peak shear stress. The small chamfer reduces the peak about 30% from 70 psi (0.48 MPa) to 50 psi (0.34 MPa) and the large chamfer reduces the peak about 40% from 70 psi (0.48 MPa) to 44 psi (0.30 MPa). It is clear that a sharp shear stress gradient persists despite chamfering; however, the chamfer improves the normal stress distribution by removing the sharp singularity at the mold interface [Figure J-41(b)]. The normal stresses for the for the large chamfer models are all less than about 10 psi (0.069 MPa).

The effect of a chamfer on the shear and normal stress distribution at the interface in the aluminum is shown in Figure J-41(a) and J-42(b). Qualitatively, the effect is the same as for the Teflon. As shown in Figure J-42(a), the peak shear stress is reduced 28% from a maximum of 105 psi (0.72 MPa) with no chamfer to 76 psi (0.52 MPa) with a large chamfer. The effect on the normal stresses, shown in Figure J-42(b) is not obvious. In both chamfer cases, there is a sharp peak at the mold-ice interface. The peak shear and normal stresses for a mold with a large chamfer are less than the peaks for the molds with small chamfers, but both chamfered conditions produce peaks that are greater than those for the molds with no chamfer. Because the stress gradients for molds with no chamfers are sharp, the calculations may not accurately represent the peak.

The final calculation investigated the effects of angling the applied load. As shown in Figure J-43, the load was angled down 30° from horizontal. For this case, we used a Teflon mold with a large chamfer. The stresses induced by an angled load are compared to those for a horizontal load in Figure J-44(a) and J-44(b). The shear stresses shown in Figure J-44(a) are not greatly affected by the angled load. The peak stress is nearly the same for angled and horizontal loads, but the stress away from the mold is less for the angled load. The major effect of angling the applied load on the normal stress, shown in Figure J-44(b), is to add a compressive stress in the ice near the mold.

Finite Element Analysis of the Effect of Surface Roughness on the Stresses at the Ice-Pavement Interface

Finite element analyses were performed to investigate the effects of surface roughness on the distribution of shear stress at a homogeneous, crack-free ice-pavement interface. Surface roughness features that are effective in concentrating stresses at the interface are presumed to be effective in initiating cracks at the interface which, in turn, will promote disbonding. Two-dimensional surface roughness features with varying height, wavelength, and shape were investigated. In addition, the effect of two load geometries was investigated. The results of the calculations and their implications for the effectiveness of surface roughness on pavements are discussed below.

Modeling Approach

Two-dimensional static analyses of the behavior of ice on a rigid substrate were performed using the finite element code NIKE-2D (34). A sheet of ice 0.5 in (1.27 cm) thick and 4 in (10.16 cm) long was modeled as a homogeneous linear plastic material with a value of Young's modulus of 300 psi (2.07 GPa) and Poisson's ratio of 0.40. The interface between the ice and substrate was modeled as a rigid boundary.

Results

Two types of loading were applied in this investigation: a uniform shear load on top of the ice and a pressure load on one side of the ice. The first loading case shows the effect of a uniformly applied shear stress on the interfacial shear stress of a smooth substrate (see Figure J-45). As shown in Figure J-46, the interfacial shear stress is nearly uniform in the center portion of the ice and equal to the shear stress that is uniformly applied to the top surface of the ice. The second loading case, shown in Figure J-47, is designed to simulate the stresses induced by the edge of a plow loading the ice. It is represented by a uniform pressure of 100 psi (0.69 MPa) distributed over an area 0.1 in (0.25 cm) high centered at 0.2 in (0.51 cm) above the substrate. The resulting interfacial shear stress distribution is shown in Figure J-48.

Virtually all the applied load is resisted by the ice-pavement interface within 1 in (2.5 cm) of the applied load. This result is consistent with the findings of the ice shear test simulations described in the previous section which show that forces applied to the edge of ice bonded to a substrate induce significant interfacial stresses near the region of load application.

To investigate the effects of surface roughness, we varied the geometry of the interface surface and compared the resulting interfacial shear stress distributions. For the first loading case (uniform shear stress applied to the top surface of the ice), we investigated the five surfaces shown in Figures J-49 through J-53. The first surface profile we investigated is shown in Figure J-49; it has a sinusoidal profile with a wavelength of 1 in (2.5 cm) and a peak amplitude of 0.125 in (0.318 cm) (one-fourth of the ice thickness). The second surface profile is shown in Figure J-50 and has a sinusoidal profile with the same wavelength as the first surface but with half the amplitude [0.067 in (0.17 cm)] but half the wavelength [i.e., a wavelength of 0.5 in (1.3 cm)]. The fourth surface profile is shown in Figure J-52; it has the same amplitude and wavelength as the first surface but has a triangular shape. The fifth surface profile is shown in Figure J-53; it has the same amplitude and wavelength as the first surface but with a square profile.

The effect of surface roughness on the shear stress in the ice on a substrate with a sinusoidal surface profile is shown in Figure J-54. Contours of shear stress produced by a uniformly applied shear stress on the top surface of the ice show that the highest stress concentrations exist at the peaks of the interface and the lowest stresses exist in the valleys. The highest stresses occur at the interface which indicates that surface roughness could help initiate cracks at the interface under the loading conditions used in this simulation; however, the low interfacial stresses in the valleys of the substrate surface profiles suggest that substantial ice will remain between the peaks after the top layer has been removed.

The effect of surface profile amplitude on the interfacial shear stress is shown in Figure J-55. The interfacial shear stress for the surfaces with nonzero amplitudes oscillate about the interfacial shear stress level for the smooth substrate. The peak stress increases with increasing surface profile amplitude such that the highest stress is about 168, 146, and 106 psi (1.16, 1.01, and 0.73 MPa) for a surface roughness amplitude of 0.125, 0.067, and 0.0 in (0.318, 0.152, and 0.0 cm), respectively.

These results indicate that increasing the amplitude will enhance ice fracture initiation at the interface near the surface feature peaks; however, it is also apparent that interfacial disbonding will be more difficult in the valleys of the surface features.

The effect of surface profile wavelength is given in Figure J-56 which shows the interfacial shear stress for a uniformly applied shear stress to the top of the ice on surfaces with sinusoidal profiles. Decreasing the profile wavelength increases the number of peaks in the interfacial shear stress pattern and reduces the peak stress slightly [from 146 to 138 psi (1.00 to 0.95 MPa)]. The decrease in wavelength also reduces the minimum interfacial shear stress [from 64 to 26 psi (0.44 to 0.18 MPa)].

The effect of surface profile waveform is given in Figure J-57 which shows the interfacial shear stress for sine wave, triangular wave, and square wave profiles of equal amplitude and wavelength. For these calculations, there is little difference between the interfacial shear stresses for the sine and triangular wave profiles. For the square wave profile, the peaks in the interfacial shear stress are reduced and spread over a larger area and the shear stress along the valleys is nearly zero. This result indicates that the square wave substrate profile is likely to require a higher applied shear stress to initiate interfacial cracking than the other waveforms investigated. Furthermore, because the interfacial shear stresses in the valleys of the square wave substrate profile are very low, it is likely that a substantial amount of ice will remain in these valleys after the top layer of ice has been removed.

In the discussion that follows, we describe the results from a parameter study of the effect of surface roughness on the interfacial shear stresses produced by uniform pressure applied to the edge of ice on a rigid surface. For this loading geometry, we modified our calculational mesh as shown in Figures J-58 and J-59 to give more resolution near the loaded edge.

The effects of substrate roughness depend on the surface features near the edge of the ice because the interfacial shear stresses are highly concentrated near the loaded edge (see Figure J-59). For the case of a sine wave surface profile, the effect of the surface roughness depends strongly on the phase of the roughness feature wave at the loaded edge. For example, when the roughness feature is downward sloping at the loaded edge (as in Figure J-59), the interfacial shear stress near the loaded edge is greatly reduced. Figure J-60 shows the interface shear stress for a smooth surface and sinusoidal surface profiles with different phase angles. The overall effect of surface roughness is the same as for the case of uniformly applied stresses for a smooth surface. Where the roughened surface slopes up initially, the peaks hear stress is about 70% greater than for the case with no roughness. For the case where the surface slopes down, the peak shear stress is about 50% less than for a smooth surface. This result indicates that substrate surface roughness has a highly variable effect on the interfacial stresses produced by pressure on the edge of the ice (e.g., like the loading of a plow blade). Interfacial stresses could be higher or lower than those for a smooth surface depending on the surface geometry in the immediate vicinity of the edge of the ice.

The effects of surface roughness amplitude on the interfacial shear stresses is shown in Figure J-61. For this loading case, the peak interfacial shear stress does not change over roughness amplitudes of 0.067 to 0.125 in (0.17 to 0.318 cm).

The effects of wavelength on the interfacial shear stresses that develop from edge loading the ice are shown in Figure J-62. As for the case of uniformly applied shear stress on the top of

the ice, increasing the wavelength increases the number of peaks in the interfacial shear stress. However, for this loading case, the peak stress is slightly higher for the shorter wavelength surface [31.6 vs. 31.2 (0.218 to 0.215 MPa)].

The effects of substrate waveform on the interfacial shear stress from edge loading of the ice are shown in Figure J-63. In this example, the peak for the sine wave is higher than for the triangle wave [28.8 vs 26.4 psi (0.199 to 0.182 MPa)].

The role of surface roughness in enhancing crack initiation for edge loaded ice is difficult to assess due to the highly localized stress patterns that develop. It appears that the details of substrate surface roughness in the immediate vicinity of the applied stress dominate the long-range surface roughness effects. Future investigations of the effect of surface roughness will concentrate on smaller scale surface features which appear to be more likely to influence the efficiency of ice disbonding.

3

Interpretation, Appraisal, and Application of Findings

The findings reported in Section 2 are the results of a fundamental study of ice-pavement bond disbonding. This section discusses and interprets these findings.

Background

Characterization of Substrates

The proper selection, handling, and characterization of substrates for use in this project were critical to the proper evaluation of the results of ice-growth tests. Four classes of substrates were selected. These classes were model substrates, pavement-component substrates, pavement core samples, and laboratory-produced pavement substrates.

The model substrates were selected to provide surfaces with a wide range of surface energies on which to perform preliminary ice-growth experiments. These ranged from low energy surfaces such as FEP Teflon and fluorinated oil to the high energy surfaces of mercury, gold, and Pyrex glass. Mylar was chosen as a representative surface for intermediate surface energy. For the pavement-component substrates, samples of limestone, portland cement mortar, fused silica, and asphalt were obtained. The pavement core samples were of open- and dense-graded asphalt, rubber-modified asphalt, and portland cement concrete. The laboratory-produced pavement substrates consisted of samples of portland cement concrete and dense-graded asphalt.

Protocols were established for the proper handling, cleaning, and storage of the substrates used in this program (see Appendix B). The extensive laboratory practices already in place at several of the team member institutions were used as the basis for these protocols. This approach ensured that uniform protocols were used throughout this program, thus eliminating uncertainties in the findings due to variations in laboratory practices or due to surface contamination.

Contact Angle Measurements

Contact angle measurements were performed on the pavement-component substrates before testing. The limestone and portland cement mortar substrates were found to have low water contact angles, which is characteristic of high energy surfaces. The asphalt was found to have a water contact angle intermediate between the water contact angles obtained for FEP Teflon, which is a low energy surface, and Mylar, an intermediate energy surface.

As a result of this pre-testing activity, the following conclusion was drawn: ice would be expected to have a higher adhesion strength on the limestone and portland cement mortar substrates than on the asphalt. This conclusion was confirmed by the low rate shear tests that are discussed below.

The drop diameter method, which is described fully in Appendix C, was developed to measure contact angles on surfaces whose roughness made it impossible to view the liquid substrate interface accurately. A drop of liquid of a known volume was placed on the substrate of interest. The diameter of the drop was measured from above rather than the contact angle being measured from the side. With the diameter and volume of the drop known, the contact angle of the liquid drop with the surface of the substrate could be calculated.

The drop diameter method can be used on substrates in place and thus provides a quick and easy method for surface contamination testing. With heterogeneous samples, a number of liquid drops can be used to obtain an average assessment of the surface. These drops can be placed on depressed areas of rough samples that are not normally accessible by sessile drop measurements made with a goniometer. Drop diameter measurements ensure that a series of rough substrates, of a given type, all have the same surface characteristics and thus allow for meaningful comparison of results obtained from tests on the different substrates.

Determining Properties of Ice Grown on Different Substrates

SEM micrograph studies were performed on replicated ice surfaces to investigate, first, the effect of the different substrates on the morphology of the surface of the ice at the interface. Second, these studies were aimed at obtaining information on the "liquid-like" layer that is postulated to occur at the ice-substrate interface. Third, tests at varying temperatures investigated the effects of the freezing mode.

Two different freezing modes were used. These freezing modes were "top-down," in which the water on the substrate froze from the top surface down to the substrate, and "bottom-up," in which the water froze from the substrate-water interface upward. Ice was grown on model substrates and then removed. SEM replicas were obtained and contact angle measurements were performed on the surface of the ice that had been against the model substrate. SEM replicas were also obtained from the surface of fractured ice.

Ice formed on FEP Teflon, Mylar, fluorinated oil, and mercury replicated those surfaces to within the 500 Å resolution limit of the SEM. No noticeably different ice structures were found. The replication also failed to show any differences between the ice immediately adjacent to the substrate and ice in bulk. The contact angle measurements showed no differences in the ice surfaces depending on the various substrates. Thus, it was determined, within the resolution limit of the SEM, that the interfacial ice structure was not influenced by the substrate surface energetics. This means that substrate surface energetics cannot be used to determine interfacial ice structure, especially energetics that would be susceptible to specific disbonding processes.

Investigation of Selective Heating of the Ice-Substrate Interface by IR Radiation

An attenuated total reflection (ATR) infrared spectrum of ice was obtained to investigate the thin layer of ice (1 μm thick) that is in contact with a substrate. A ZnSe crystal was used for the substrate. The ATR spectrum indicates that this layer of ice at the substrate-ice interface has a similar absorption spectrum to that of bulk ice and water. This result was found with both the strong 3,300 cm^{-1} OH stretching band and the weaker 1,650 cm^{-1} water bending absorptions. Although the absorption spectra were not identical, they overlapped enough so that there was no region in the infrared spectrum in which radiation would be absorbed only by the ice at the ice-substrate interface. The conclusion that can be drawn is that it is not

possible to use the IR frequency range in a physical disbonding process to selectively destroy the bond at the ice-pavement interface.

Ice-Substrate Bond Shear Strength Under Low-Rate Shear Conditions

To gain insight into the bonding mechanism of ice and its relevance to the direct removal of ice from highway surfaces, shear strength measurements were performed to give a direct measure of adhesional bond strength.

Shear strength tests were performed on the model substrates and the pavement-component substrates. These tests were performed at four temperatures: 25°F (–4°C), 15°F (–9°C), 5°F (–15°C), and –10°F (–23°C). The effects of freezing rate and the effects of freezing mode on the shear strength were also investigated. Two different freezing modes were used. These freezing modes were "top-down," in which the water on the substrate froze from the top surface down to the substrate, and "bottom-up," in which the water froze from the substrate-water interface upward.

As expected, the lowest ice-substrate bond was found on FEP Teflon, which has the lowest surface energy of any of the substrates used in this program. In tests on the pavement component substrates, the ice-substrate bond strength was highest for portland cement mortar, followed in decreasing order by limestone, silica, and asphalt. The Pyrex glass had an ice-substrate bond that was slightly lower than the fused silica samples. The bond strengths were consistent with the results of the work of adhesion determined from the earlier contact angle measurements.

All of the pavement-component substrates had ice-substrate bonds that were stronger at –9°C and –15°C than the bond strengths at either –4°C or –23°C. The results obtained at –9°C and –15°C were not significantly different from each other. There was a similar temperature effect for silica and Pyrex glass ice-substrate bond strengths. In general, only at warmer temperatures (i.e., –4°C) was ice broken primarily along the interface. At lower temperatures, some ice remained on the substrate after the shear test, indicating that crack propagation is the mechanism that leads to failure at lower temperatures. From a practical standpoint, these results suggest that it is possible to shear most of the ice from the substrate at temperatures just below freezing. At lower temperatures, however, some ice will remain on the substrate after shearing. Additional effort (either physical or chemical) will be required to remove the residue of ice.

Impact Effects of Ice Bonded to Pavement Materials

Experiments were performed to investigate the effects of impact shearing at the ice-substrate interface. The impact tests were conducted at 25°F (–4°C) and 15°F (–9°C) on pavement core samples and on laboratory-produced pavement substrates. The impact studies measured the kinetic energy change of a scraper mechanism when the scraper struck an ice sample in a motion parallel to the ice-substrate interface. these impact studies were conducted with the scraper moving at 5 mph (8.1 km/hour) and at 10 mph (16.1 km/hour).

The impact studies found that more energy is required for impact shearing of ice bonded to open-graded asphalt at 15°F (–9°C) than at 25°F (–4°C). More energy is required, however, for rubber-modified asphalt at 25°F (–4°C) than at 15°F (–9°C). The low-speed shear test results show a stronger ice-substrate bond at 15°F (–9°C) than at 25°F (–4°C) on all of the pavement-component substrates.

Further investigation will be needed to determine why the rubber modification has such an effect on the impact energy needed to remove ice from this type of substrate at 25°F (–4°C).

At 15°F (–9°C), more energy is required for impact shearing of ice bonded to open-graded asphalt than the other three types of core samples. The order of the other pavement types in terms of decreasing energy required for impact sharing at 15°F (–9°C) are: dense-graded asphalt, portland cement concrete, and rubber-modified asphalt. These results would suggest that rubber-modified asphalt might have an advantage over the other pavement types at lower temperatures by requiring less energy for ice disbonding by blading.

For impact shearing of ice bonded to contaminated (uncleaned) pavement core surfaces, less energy is required at 15°F (–9°C) than for cleaned surfaces. These results are expected. Since the contaminants are probably oils and other hydrocarbons, these types of contaminants lower the surface energy and the work of adhesion of the substrate, thus weakening the ice-substrate bond.

Finally, it was found that more energy is required for impact disbonding at 10 mph (16.1 km/hour) than at 5 mph (8.1 km/hour) for all the materials considered. Almost two to three times the energy required for impact disbonding at 5 mph (8.1 km/hour) is required at 10 mph (16.1 km/hour) for open-graded asphalt and rubber-modified asphalt. Almost four times the energy required for disbonding ice at 5 mph (8.1 km/hour) is required at 10 mph (16.1 km/hour) for the laboratory-produced portland cement concrete. This finding, that ice removal is more energy efficient at lower speeds, may be an important consideration in the design and operation of future ice removal systems.

Effects of Thermal Stresses on Ice-Pavement Bond Strength

Application of a thermal stress to the ice-substrate interface was found to drastically decrease the shear strength of the ice on the substrate. Experiments were performed in which a thermal stress in the form of rapid cooling was applied to ice grown on a portland cement concrete substrate. The rapid cooling was achieved by placing an aluminum cup containing liquid nitrogen in contact with the ice or by directly applying liquid nitrogen to the ice.

A decrease in the shear strength by a factor of 5 could be achieved by the direct application of liquid nitrogen to the ice for 30 sec before the shear test was performed. Even placing the liquid-nitrogen-filled cup in contact with the ice for as little as 5 sec resulted in a decrease of 40% in shear strength. Calculations were performed which indicate that a rapid cooling of even 4°C may be enough to cause a significant decrease in the ice-substrate bond strength.

The results achieved with the thermal stress investigation are encouraging. The results suggest a possible ice removal scheme that would consist of rapidly cooling the surface of the ice bonded to a pavement with something like liquid nitrogen and then removal of the fractured ice with a blade after a small time interval. However, to develop a practical application of this technique would require further investigation of several aspects. For example, the actual process used to conduct heat away from the ice needs further refinement. While this is not a problem when using rapid cooling to induce thermal stress, the problem still exists of providing good thermal conduction from the ice to the heat sink. Even a 5–sec contact time with the heat sink material may be too long to implement in actual highway pavement applications.

Investigation into the Destruction of Ice-Substrate Bonds by Chemical Undercutting

An extensive set of chemical undercutting tests was performed with four chemicals (NaCl, $CaCl_2$, CMA, and ethylene glycol) and six model and pavement component substrates (FEP Teflon, Mylar, gold, fused silica, portland cement concrete mortar, and limestone). These tests were conducted to determine if the substrates, or particularly, the surface energetics of substrates had an influence on the rate and extent of chemical undercutting.

Examination of the undercutting data generated with the model and pavement component substrates revealed a lot of differences. The varied differences noted for the chemical

undercutting of the four deicers on the six substrates suggests that parameters other than surface energetics are controlling the undercutting action. Consequently, the chemical undercutting characteristics cannot be predicted from surface energetics.

The temperature and freezing mode/rate patterns found during chemical undercutting tests with NaCl and $CaCl_2$ mostly varied among the six different substrates used. The undercut areas produced by NaCl and $CaCl_2$ at 25°F (–4°C) were greater than those for both 15°F (–9°C) and 5°F (–15°C) for all the substrates, at all times. In some instances, however, the 15°F (–9°C) and 5°F (–15°C) undercut data for each deicer did not differ for the various substrates. Sometimes there was a freezing mode/rate effect on the chemical undercutting area produced by NaCl and $CaCl_2$, but the effect was not consistent within the substrates tested.

The undercutting data obtained with CMA showed very erratic results. No temperature pattern was found with this deicer for any of the model or pavement component substrates. This suggests that the use of CMA as a deicing agent may have limited value when applied to ice-covered roads.

Temperature had a significant effect on the initial slope of the undercutting area versus time curve for ethylene glycol and all the substrates. However, the type of substrate had no significant effect on the initial slope of the undercutting area versus time curve for ethylene glycol.

The examination of the undercutting data generated with pavement core samples and laboratory-produced substrates revealed some practical considerations. In a majority of the cases investigated, the extent of chemical undercutting by NaCl, $CaCl_2$, and ethylene glycol at 25°F (–4°C) on as-received (textured) highway core samples and laboratory-produced substrates was considerably less than that on smooth substrate surfaces of the same materials. Also, at 25°F (–4°C) and 15°C (–9°C), the order of the pavement materials in terms of decreasing undercutting action on as-received, but cleaned surfaces, was as follows:

- Portland cement concrete
- Dense-graded asphalt
- Rubber-modified asphalt
- Open-graded asphalt

These results would suggest that the rate of chemical application should be varied by pavement type and condition to achieve a desired undercut area at a selected time interval after application of a chemical.

The laboratory-produced specimens of portland cement concrete and dense-graded asphalt in the as-received and cleaned condition were undercut more extensively at both 25°F (–4°C) and 15°F (–9°C) than the four pavement core samples in the as-received and cleaned condition. These results would indicate that care should be used when trying to estimate undercutting characteristics on in-service highways from data resulting from undercutting tests performed with laboratory-produced specimens.

Mathematical Modeling of Physical Processes for Disbonding

The mathematical modeling results achieved during the study have several practical implications.

- There is a good possibility that a nylon impactor can produce tensile stresses at the ice-concrete interface of sufficient magnitude to disbond the ice from the concrete.

- There is a possibility that the impact of a wedge, with an included angle less than 60°, traveling normal to an ice-concrete interface can promote ice fracture at the interface.

- If ice cracking does not occur, substantial indentation and damage of the ice layer by a wedge can significantly assist in applying deicing chemicals at or near the ice-concrete interface.

- Increasing the surface roughness amplitude of a pavement can increase the interfacial shear stresses at the peaks of the pavement surface topography. Crack initiation in the ice will be enhanced at these locations. However, ice removal from the pavement in regions between the peaks will be more difficult as the surface roughness amplitude increases.Interpretation, Appraisal, and Application of Findings

4

Conclusions and Recommendations

This section of the final report presents conclusions and recommendations that the authors have developed after considering all the information obtained during this fundamental study of ice-pavement bond disbonding.

Conclusions

1. The bond established between ice and highway pavement materials is a complex function of many parameters including temperature, rate and direction of freezing, and the physical and chemical conditions of the substrate surface.

2. The successful destruction of the bond between ice and highway pavement materials by either physical means, chemical means, or a combination of the two, requires matching appropriately the bond destruction technique with the type and condition of the substrate surface and the conditions involved in the bond formation.

3. The number of substrate types selected for investigation was adequate to cover the range of surface energies of interest, as well as the components of highway surface materials.

4. The sample handling and storage protocols developed were adequate to ensure reliable determination of substrate surface properties.

5. Contact angle measurements using the equilibrium sessile drop method were found to adequately characterize the surface energetics of all nonporous substrates measured.

The method was not suitable, however, for use with the porous limestone and portland cement mortar substrates.

6. Contact angle measurements, either by the sessile drop method or by the drop diameter method, allow for a quick nondestructive means of testing for surface contaminants on materials. The drop diameter method can be used on substrates in place.

7. Thin film replication failed to show the presence of differentially structured layers of ice-water immediately adjacent to the low energy substrate. Replication of the edge formed at the substrate interface was accomplished but handling problems of the complexly shaped replicas made observations of the ice-substrate edge of the cleaved surface nearly impossible.

8. The infrared absorption spectra characteristics of ice and water are very similar. Also, the infrared absorption spectra characteristics of surface ice (to a depth of 1 μm) are very similar to that of bulk ice. This suggests that the IR frequency range cannot be used to selectively destroy the bond at the ice-pavement interface.

9. Substrate and temperature have a significant effect on the ice-substrate bond strength for the pavement component substrates of portland cement mortar, limestone, silica, and asphalt.

10. In order, the ice-substrate bond strength results for the pavement component substrates are highest for portland cement mortar, then limestone, then silica and asphalt.

11. The results from shear strength tests indicate, in general, that only at warmer temperatures (i.e., –4°C) is the ice broken primarily along the interface. For colder temperatures, the breakage leaves ice on the interface. This leads to the tentative conclusion that crack propagation is the mechanism leading to failure at lower temperatures.

12. More energy is required for impact disbonding at 10 mph (16.1 km/hour) than at 5 mph (8.1 km/hour) for all the materials considered. This suggests that it is more efficient from an energy standpoint to disbond ice from pavement materials at a slow speed.

13. Less energy is required at 15°F (–9°C) for impact shearing of ice bonded to contaminated (uncleaned) pavement core surfaces than it is for the cleaned surfaces. This suggests that weaker ice-pavement bonds are present on contaminated highway

surfaces, particularly those surfaces between the wheel paths that are exposed to petroleum products discharged by vehicles.

14. The interfacial shear strength of ice bonded to portland cement concrete substrates can be greatly reduced by thermal shock resulting from the application of LN_2 to the free surface of the ice.

15. The effects of the model and pavement component substrates on the chemical undercutting characteristics of NaCl and $CaCl_2$ are not readily apparent.

16. At 25°F (–4°C) and 15°F (–9°C), the order of pavement materials in terms of decreasing undercutting action on as-received, but cleaned surfaces, is as follows:

    - Portland cement concrete
    - Dense-graded asphalt
    - Rubber-modified asphalt
    - Open-graded asphalt

    This suggests that a higher deicing chemical application rate would be required for dense-graded asphalt, rubber-modified asphalt, and definitely open-graded asphalt, to achieve the same undercutting action observed with portland cement concrete.

17. An impactor with an impedance that is lower than ice is more effective at producing a high tensile stress at the ice-concrete interface than is an impactor with an impedance that is higher or equal to ice.

18. Tensile stresses produced at the ice-concrete interface by the difference in impedance between a nylon impactor and ice are sufficient theoretically to disbond the ice from the concrete. These tensile stresses can be produced without ice crushing from the compressive impact stress.

19. Wave reflections from the bottom surface of the concrete are not needed theoretically to produce disbonding. This suggests that the effectiveness of a plane wave for disbonding ice from concrete will not be a strong function of the properties of the concrete.

20. Including a planar shock wave in a realistic (i.e., nonuniform) ice layer on a concrete substrate will present substantial practical difficulties.

21. Finite element modeling (FEM) simulations of the impact mechanism response during shearing of ice from a concrete substrate showed it was difficult to determine the ice-substrate bond strength from the response characteristics. The impact mechanism response is complicated because of the influence of several factors.

22. FEM simulations of the ice-concrete bond strength revealed that the shear and tensile stress distribution near the ice-concrete interface was not uniform. Thus, caution should be taken in relatively relating changes in an impact mechanism response to a uniform ice-concrete bond stress.

23. The impact of a 60° wedge traveling normal to an ice-concrete interface produces considerable compressive stress under the wedge near the interface that will reduce the tendency for ice fracturing. A narrower wedge is likely to decrease the compressive stresses in the ice and promote ice fracture.

24. Even if ice cracking does not occur, the substantial indentation and damage of the ice layer by a wedge can be of significant assistance in applying deicing chemicals at or near the ice-concrete interface.

25. As long as the ice is weak relative to the pavement, and the indenter wedge does not penetrate all the way through the ice, pavement damage is expected to be low.

26. A comparison was made between experimental measurements of the force required to shear ice from various substrates and computed values of the force required to generate an energy release rate equal to the work of adhesion. It is clear that there are other factors that influence the bond strength between ice and pavement besides the work of adhesion. High surface porosity (characteristically found in substrates such as portland cement concrete and limestone) may substantially increase the strength of the mechanical bond between an ice layer and a substrate.

27. The influence of the surface roughness of the pavement on ice disbonding is dominated by the surface features near the point of load application (i.e., near the blade of a snow plow) because interfacial shear stresses are concentrated near the loaded edge of the ice.

28. Increasing the surface roughness amplitude of a pavement can increase the interfacial shear stresses at the peaks of the pavement surface topography. Crack initiation in the ice will be enhanced at these locations. However, ice removal from the pavement in regions between the peaks will be more difficult as the amplitude of the surface roughness increases.

Recommendations

- The design and operations of future ice removal systems need to incorporate both chemical and mechanical means in the destruction of the ice-pavement bond. The rate of chemical application should be varied by pavement type and condition to achieve a desired undercut area at a selected time interval after application of a chemical. The speed at which ice is removed from the pavement should be as slow as possible. Ice removal is more energy efficient at 8.1 km/hour than at 16.1 km/hour. Finally, the design of the cutting edge of the plow blade should be such that crack propagation at the ice-pavement interface is promoted at lower temperatures. Also, the design of the cutting edge should recognize a stronger ice-substrate bond exists at −9°C and −15°C than at −4°C and −23°C.

- A prototype ice removal system should be built that can deliver a vertical impact force to the ice-pavement interface before a scraping force is applied to the interface region. Preliminary analytical results indicate there is a good possibility that a nylon impactor can produce tensile stresses at the ice-concrete interface of sufficient magnitude to disbond the ice from the concrete.

- Additional impact shear testing of ice bonded to pavement materials needs to be conducted at various temperatures and speeds to confirm conclusions drawn relative to the significance of these independent variables. These should be confirmed further with limited field experiments to determine the appropriate speed for efficient ice-disbonding under various operating conditions.

- Selective impact shear testing of ice bonded to pavement materials needs to be conducted using different cutting configurations. The results of these tests would be used to determine the optimum cutting edge configuration for minimum impact load under a variety of operating conditions.

- A number of laboratory and limited field tests should be performed to complete the initial investigation to develop practical means of disbonding ice from pavement substrates using thermal shock principles.

- Limited field experiments need to be conducted to determine if different deicing chemical application rates should be used with different pavement types to achieve the same chemical undercutting effects.

- Combined undercutting/impact shear tests need to be conducted for a range of pavement materials, temperatures, and deicing materials.

- Selective impact shear testing of ice bonded to pavement materials treated with deicing chemicals needs to be conducted to determine appropriate anti-icing application rates.

- Selective tests involving impact loading applied normal to the ice-substrate interface need to be conducted to confirm conclusions drawn from FEM relative to the impactor geometry needed for favorable ice fracture.

- The influence of the surface roughness of various pavement materials on ice disbonding under wheel passages needs to be investigated in controlled laboratory tests.

- The undercutting data generated with model and pavement component substrates need to be further analyzed to determine if any of these substrates had an effect on the initial slope of the undercutting area versus time curves for NaCl, $CaCl_2$, and CMA.

Appendix A

Selection and Surface Characterization of Materials Used in the Study

The materials selected for use in this project are described in this appendix. This appendix has two sections. First, the materials selected for use are described, and methods of characterization of surface physical properties and cleanliness are described. Next, experimental details of three methods used to determine surface properties of these materials are given.

Materials

The materials used in this program are divided into five major groups: liquid materials, solid model substrates, pavement component substrates, pavement core samples, and laboratory-produced pavement substrates. Each of these groups is discussed below, considering the sources of the materials, the preparation of the materials prior to their use, and any evaluation of the materials performed prior to their use.

Liquids

The liquids used fall into three categories. In the first category are the liquids employed as model substrates on which ice growth was studied. Two liquid model substrates were used: fluorinated oil (Krytox 1514) and mercury. The second category contains liquids that were selected for use in contact angle determinations on solid substrates. These are listed in Table A-1. The last category contains the water used to produce ice for the various experiments and deicing solutions used in the undercutting experiments.

Table A-1. Surface tension values measured on liquids selected for contact angle determinations

Chemical	Surface tension mN/m	Large polar component	Purification technique
Water	69.5	p	Doubly distilled
Glycerol	62.5	p	–
Ethylene glycol	57.5	p	–
Methylene iodide	46.8	–	Silica gel
α-Bromonaphthalene	42.1	–	Alumina/silica gel
1,2-Dibromoethane	40.4	–	Silica gel
Tricresyl phosphate	40.2	p	Alumina/silica gel
Propylene carbonate	40.1	p	Silica gel
n-Methyl formamide	39.0	p	Silica gel
Dipropylene glycol	32.0	p	–
Hexadecane	25.2	–	Silica gel

Sources

Liquid chemicals were obtained from reliable suppliers and were of reagent grade or higher.

Krytox 1514, obtained from Du Pont, is a perfluoroalkylpolyether oil developed for use in vacuum pumps. It has the formula of $F\text{-}[CF(CF_3)\text{-}CF_2\text{-}0]_n\text{-}CF_2CF_3$, where n is between 10 and 60 and has an average molecular weight of 3500. The vapor pressure at 20°C is negligible (4×10^{-7} torr), and at 25°C it has a surface tension of 18 mN/m (18 dynes/cm). It is chemically inert, should provide few sites for interaction with water, and thus was used as a low energy liquid substrate.

Preparation

All the liquids for contact angle determination were purified prior to use by passing them through columns of activated solid absorbents. Chromatographic purification is particularly effective for removing surface active polar contaminants from organic liquids. Tricresyl phosphate (TCP) and 1-bromonaphthalene (alpha-bromonaphthalene) were chromatographically purified through columns packed with activated silica gel and alumina. Chromatographic purification of all other liquids was done with silica gel. Purified liquids

were stored in acid-cleaned, all-glass, custom containers for subsequent use in contact angle studies.

The mercury was obtained in triply-distilled form and stored in the original sealed containers. Just prior to use, the mercury was passed through a pinhole filter to remove any oxides that might have formed.

Doubly distilled water was prepared with a final distillation in an acid-cleaned all-glass, high-purity still of an alkaline permanganate solution from commercially distilled water. Some of the SDSM&T experiments made use of water that was redistilled twice from distilled water produced in a Barnsted still and passed through a Barnsted deionizing column. This triply-distilled water had a conductivity that was consistently between 0.70 to 0.75 michrohms.

A discussion of the preparation of the deicing solutions is given in the section on "Investigation into the Destruction of Ice-Substrate Bonds by Chemical Undercutting" in the main text of this report.

Evaluation

Interpretation of the contact angle measurements which were used for the surface energetic studies on solids relies on a series of liquids of known surface tensions. Surface tension values of all liquids used in contact angle measurements were obtained just prior to use.

In Phase I, the initial surface tension measurements were completed on all of the liquids to be used for contact angle measurements on the substrates. A series of fluids were selected to cover the range of surface tensions of interest from 25 to 72 mN/m. Surface tension values are reported in milliNewtons per meter (mN/m), a unit numerically equivalent to the previously used dynes/cm. Liquids of both polar and nonpolar character were selected, as a degree of polar interactions at a solid/liquid interface can often be detected by the use of liquids with similar surface tensions but different potential polar interactions.

The surface tensions of the fluids were obtained using a DuNuoy ring tensiometer. In this measurement, a freshly flamed platinum ring is raised through the surface of a fluid, and a torsion wire balance is used to indicate the force that was applied to "break" the ring from the surface. The lifting force is directly related to the surface tension of the fluid. The values of the surface tensions are used for assessing the purity and condition of the fluids, and are required for contact angle measurements by these liquids on solids, as described in a

subsequent section. Periodic measurement of the surface tension was used for rapid assessment of surface chemical quality of the fluids prior to each later use in the program.

Table A-1 summarizes the results of the surface tension measurements.

Solid Model Substrates

Four solid model substrates were used in the study: fluorinated ethylenepropylene (FEP) Teflon® (type A), Mylar, gold, and glass. These substrates are described below.

Sources

Sheets of FEP Teflon and Mylar samples in the range of 0.05 to 0.25 mm thick (2 to 10 mil) were obtained from commercial sources. The gold substrates were prepared by vapor deposition of gold to about 1000 Å thickness onto borosilicate glass plates. The plates were acid-cleaned prior to coating with gold using the procedure described in the next section dealing with preparation procedures.

Two types of glass substrates were used in this program. They were Pyrex and fused silica glass. Both were obtained from Dow Corning and were approximately 2.5 x 6 x 0.22 in thick rectangular plates. Pyrex, a borosilicate glass, was used as a model substrate in this study. The fused silica glass was used as a pavement component substrate and not a model substrate. It is discussed here for convenience because its source, preparation, and evaluation are identical to those of the Pyrex substrates. The fused silica was Corning's product 7940 and is a synthetic amorphous silicon dioxide, whose total impurities other than water, as stated by Corning, do not exceed 0.01%.

Preparation

The Mylar and Teflon were prepared for study using the following procedure. Both materials were cut to sizes required using a sharp blade and being careful not to increase the samples. The samples were rinsed with hexane and ethanol to remove any grease and then rinsed in a Soxhlet extractor for 2 to 3 hours in cyclohexane or ethanol. The samples were handled only with stainless steel forceps which were also cleaned in the Soxhlet extractor. If more than one sample was being cleaned, glass or stainless steel spacers were used to separate the samples.

The glass and fused silica samples were ground with silicon carbide grit, with the final grinding utilizing 600 grit silicon carbide compound. The grinding procedure used is similar to that used with the limestone substrate samples and is described in the section following on Pavement Component Substrates. After grinding, the samples were rinsed several times with distilled water to remove the grit and then prepared using the following acid-cleaning procedure.

The ground glass and fused silica samples were rinsed when necessary with a saturated or 6 M KOH ethanol solution to remove any grease. The grease-free glass samples were then acid-cleaned with a 10:1 sulfuric acid to nitric acid bath mixture heated to 100°C. The glass and fused silica samples were left for 1-2 hours in the heated bath, or if the samples were too large, the hot acid bath was repeatedly poured over the glassware. The glass and fused silica samples and the acid bath were allowed to cool to room temperature. The acid was then drained off and the samples rinsed with distilled water. The samples were soaked in distilled water overnight. The soaking liquid was floated off with more doubly-distilled water to prevent surface active substances from redepositing.

Glass and fused silica samples were dried in air with Al dust covers, then stored in closed Pyrex containers until studied. The gold samples were stored in acid-cleaned glass containers and used without further preparation.

Evaluation

The model substrate samples were characterized using contact angle measurements as described in the section on "Surface Energetics."

Pavement Component Substrates

Four pavement component substrates were used in the study. These were limestone, portland cement mortar, asphalt, and fused silica. The fused silica substrates were described in the earlier section; the other three are discussed below.

Sources

Limestone samples were obtained from various sources within South Dakota. Some of the sources produced samples that had a wide variety of porosity and color. It was decided to

use the limestone obtained from the quarry at the South Dakota State Cement Plant in Rapid City, as this source gave samples with a minimum variance in composition and porosity. This quarry produces rock from the Minnekahta formation. Samples from this quarry produced two types of limestone that differed in color, one somewhat reddish and one with yellow-colored layers. The one with yellow-colored layers in the formation produced samples that were much softer than the red limestone and contained many small voids. To avoid these problems, only samples of the red limestone were used in this study. The red limestone had fine veins of a white mineral that proved to be weak points in the rock. These white veins were avoided whenever possible.

Portland cement mortar samples were prepared according to ASTM C 109-86. The mortar consists of 1 part cement and 2.75 parts sand proportioned by weight. These formulations and material sources are listed in Table A-4. A water/cement ratio of 0.485 was used as is specified in the ASTM standard. Twenty cylindrical samples were prepared, having a radius of 4 in (10.2 cm) and a length of 8 in (20.3 cm). After being stored in limewater for 28 days, three of the samples underwent destructive compressive testing. The results of these tests gave a compressive strength of about 6,600 psi (45.5 MPa).

The asphalt samples were made from a paving asphalt base which is produced by the Shell Oil Company. According to the company-provided analysis it had the following properties:

Product: AC-20 (VAC-20)
Specific Gravity at 60°F: 1.039
Flash Point: 600°F
Viscosity at 140°F: 1862 poise
Viscosity at 275°F: 391 cs
Penetration at 77°F: 66 dmm
Solubility in trichlorethylene: 99.89%
TFOT Residue: Loss on heat: 0.03%
Viscosity at 140°F: 4742 poise
Ductility at 77°F: 150+ cm

Preparation

The limestone samples were cut to approximately 2.5 x 6 x 0.75 in sizes with a diamond saw. To finish the samples, each limestone sample was placed on a lapping wheel and ground with 220 grit silicon carbide grinding compound to remove the saw grooves. The samples were then hand-lapped on a glass plate to 600 grit finish using the following procedure.

The grinding stations utilized in this program consisted of clean glass plates, one for each grinding grit specification (220 grit, 400 grit, and 600 grit silicon carbide). Before each use, the grit was cleaned by rinsing with cyclohexane followed by two rinses with doubly distilled water. After grinding, each station was cleaned first with tap water to remove most of the excess grit, then cleaned twice more with distilled water and finally cleaned with triply distilled water. Operators wore disposable gloves during the grinding procedure to prevent hand-contamination of the specimens.

After grinding, the limestone samples were rinsed twice with singly distilled water and then finally rinsed with triply distilled water and stored in a covered Pyrex container. Prior to use, each sample was rinsed with cyclohexane, followed by two rinses with distilled water and a final rinse with triply distilled water. The samples were then air-dried under a drying cover.

The portland cement mortar cylinders were cut in half lengthwise to produce a planar surface for testing. The exposed surface was ground using the same grinding procedure as was used on the limestone samples. The mortar samples used in this study also received the same surface preparation and cleaning treatments as did the limestone samples.

Asphalt samples were prepared by heating the asphalt base to 140°F and pouring it onto a support substrate. For the undercutting experiments, this was a glass plate. For the interfacial shear tests, a portland cement mortar specimen similar to those prepared for the shear tests was used as the support substrate.

Characterization of Pavement Component Substrates

In order to make the data collected from undercutting tests, interfacial shear strength tests, etc., of the greatest possible value, substrates used for these tests were carefully characterized. Optical micrographs and profilometer measurements were taken to evaluate the physical characteristics of the surfaces; sessile drop measurements on each substrate prior to use in interfacial shear strength tests were used to confirm the cleanliness of the surfaces. Sessile drop studies, adsorption isotherms, and heats of immersion were obtained to evaluate the surface energetics. the results of the physical surface characterizations are presented first, followed by a discussion of the surface energetics evaluation.

Optical microscopy: The morphological character of the surfaces was recorded by taking optical micrographs. On surfaces such as silica and Pyrex, whose preparation (grinding with #600 grit) left them in a relatively uniform condition, these pictures simply record an impression of the roughness of the surface. For other substrates which have "structure," such

as the portland cement mortar, the micrographs provide a record of the size and distribution of the sand particles, and also indicate the size and distribution of surface imperfections such as pores and cavities.

Profilometer evaluation: A parameter of the surface quality is also obtained from profilometer evaluation. With this device one obtains information which is "orthogonal" to the information from the micrographs, that is, an indication of the height of small-scale surface undulations (microtexture).

The profilometer used was a Clevite Corporation SURF-INDICATOR, Model 21-0100-00. It is possible to discriminate between small scale surface variations and larger-scale undulations by observing the response as the stylus is moved at different speeds and different amplitudes. The microtexture values, representing a peak to peak average of several passes over the surface, were measured for the six selected substrates and presented below.

Material	Average microtexture (micro-inches)
Pyrex, as received (polished)	1
Pyrex, #600 grit polished	10
Silica, #600 grit polished	20
Limestone, #600 grit polished	35
Teflon, as received	30-50
Mortar, #600 grit polished	200

With the polished Pyrex, it was possible to detect additional long-range undulations of approximately 50 micro-inches, but over a small region it was very smooth. Clearly, the polishing with #600 grit silicon carbide powder does not produce exactly the same results on all surfaces. Microtexture values verify, as expected, that the finish obtained is best on the hardest surface, and deteriorates as the hardness of the material decreases. Teflon was expected to be very smooth, but as can be seen, the profilometer considers it otherwise. Here the microtexture is more in the form of undulations which are either wavelike or steplike. The spatial characteristics of the Teflon samples are somewhere between those of the ground surfaces and those of the variations on the polished Pyrex. The large variations on the portland cement mortar specimens are due to the variations in the component materials. When the surface is ground, the harder components such as the quartzite in the sand are left protruding above the areas of softer material, which are more easily removed.

Sessile drop characterization of each substrate prior to shear testing: As part of the measurement procedure for interfacial shear strength tests, modified sessile drop studies were performed to ensure that there was no surface contamination prior to conducting the shear test. The results of these measurements made on each substrate just before shear testing are presented in Appendix D along with the shear strength values. These sessile drop measurements used only a single drop of water. The contact angles measured in these tests were generally lower than those measured in equilibrium sessile drop measurements (advancing angle measurements). This is to be expected, as single drops usually spread out on a surface, to a larger extent, and have a lower contact angle than those drops formed in the advancing drop method.

Specimen contamination sensitivity test: It was of interest to find out how sensitive the modified sessile drop test was in detecting traces of contamination. A specimen contamination sensitivity test was performed that indicates it is indeed very effective in detecting contamination on mortar and limestone specimen surfaces resulting from contact with human skin. The specimens used for this test were a little smaller in size than the actual pavement component substrates used for shear testing, measuring 3.0 x 3.0 x 0.4 in. They were representative samples taken from the same bulk material as the substrates. Their surfaces were prepared and cleaned by the same procedures used to prepare the pavement component substrates.

A 63.0 ± 3.5 mg drop of triple distilled water was dropped from a height of approximately 1 mm onto the substrate surface and 1 minute* was allowed to pass before measuring the contact angle. The image was projected onto paper at a distance of 10 meters from the projection lens.

After contact angles were obtained for the clean substrates, the surfaces were contaminated by rubbing them lightly and uniformly for 10 sec with clean, dry bare hands. The contact angles were then remeasured with the results shown in Table A-2.

---

* The justification for only waiting 1 minute before measuring contact angles is based upon a side study involving Pyrex and silica polished with #600 grit. The study showed no significant effects of time (up to 30 minutes in a high humidity box) on the values of the contact angles.

Table A-2. Effect of contamination on contact angle

Drop location	Clean mortar contact angle	Contam. mortar contact angle	Clean limestone contact angle	Contam. limestone contact angle
1	22.3	48.8	20.8	60.5
2	22.3	73.5	22.5	64.5
3	26.3	78.5	32.0	70.8
4	21.0	67.5	35.3	71.5
5	17.5	75.0	29.0	55.5
Mean angle	21.9	68.7	27.9	64.6
Std. dev.	3.2	11.8	6.2	6.8

The clean mortar and limestone specimens had mean contact angles of 21.9 and 27.9° with standard deviations of 3.2 and 6.2°, respectively. After contamination, the mortar and limestone specimens had mean contact angles of 68.7 and 64.6° with standard deviations of 11.8 and 6.8°, respectively. It is concluded that the modified sessile drop test with distilled water is indeed a sensitive test for this type of contamination.

Pavement Core Samples

Core samples were taken from representative portland cement concrete, rubber-modified asphalt, and dense- and open-graded asphaltic concrete highway surfaces. Core samples were obtained from California, Connecticut, Montana, and New York.

Sources

A history was obtained of the highway surfaces from which the core samples were taken (i.e., location and date constructed, material and formulation specifications, traffic density and type, and any other pertinent data). A summary of the core samples obtained and used in this project is presented in Table A-3. The abbreviations used for the materials listed in Table A-3 are: DGA = dense-graded asphalt; OGA = open-graded asphalt; RMA = rubber-modified asphalt; and PCC = portland cement concrete.

Table A-3. Pavement core samples

Material	Test code	Average daily traffic	Source and history
DGA 4-in cores	CT101	8,000 (1983)	Wethersfield, Connecticut, east-bound Route 175, 1 1½-in overlay 1972, original pavement 1938, taken 2 ft from the white line
	CT102	8,000 (1983)	
	CT103	8,000 (1983)	
	CT104	8,000 (1983)	
	CT105	8,000 (1983)	
	CT106	8,000 (1983)	
	CT107	8,000 (1983)	
	CT108	8,000 (1983)	
	CT109	8,000 (1983)	
OGA 6-in cores	NY301	3,650 (1986)	New York DOT, paved 1985
	NY303	3,650 (1986)	
	NY305	3,650 (1986)	
	NY306	3,650 (1986)	
	NY309	3,650 (1986)	
	NY310	3,650 (1986)	
OGA 6-in cores	NY302	2,450 (1987)	New York DOT, paved 1987
	NY304		
	NY308		
	NY311		
RMA-Plus Ride 4-in cores	CA405	Not available	California DOT (LAS 395), Station 97.86
	CA406		
	CA407		
	CA408		
	CA409		
	CA410		
	CA412		
	CA413		
	CA414		
RMA-Plus Ride 6-in cores	CA401	Not available	California DOT (LAS 395), Station 97.86
RMA-Plus Ride 12 4-in cores	MT401	2,000 (1988)	Montana DOT, MacDonald Pass on U.S. 12, approximately 12 mi west of Helena, paved 1983, taken on outside wheel path
	MT402	2,000 (1988)	
	MT403	2,000 (1988)	
	MT404	2,000 (1988)	

Table A-3 (Continued)

Material	Test code	Average daily traffic	Source and history
PCC 4-in cores	CT503	a	Connecticut DOT, Route 2, Colchester, Connecticut, 4-lane divided, 9-in reinforced concrete (mesh 6 x 6 in), 40-ft slabs, paved 1964. Cores taken 3 ft from the shoulder and 10 ft apart in the westbound outside lane
	CT504	a	
	CT505	a	
	CT506	a	
	CT507	a	
	CT508	a	
	CT509	a	
	CT510	a	
	CT511	a	

[a]Average daily traffic was: 8,200 in 1984 (westbound)
17,000 in 1985 (2-way)
19,600 in 1987 (2-way)

Preparation

The core samples were cleaned, handled, and stored using the protocols discussed in Appendix B.

Evaluation

Since contact angle measurement has been used extensively in the studies of interfacial phenomena, it would be desirable to apply it to the study of ice adhesion on road surfaces. Several procedures exist for measuring contact angles, with the sessile drop method being the most widely used because of its ease of implementation.

In this program, both single point measurements with large sessile drops and multiple measurements with small droplets were used to evaluate interactions of the solid substrates with water. The development in this project of the drop diameter method was most useful, as it permitted the measurements to be made on very small regions of samples. Thus, the very different regions of mortar and aggregate can be separately measured with different drops. Single sessile drops, as were used in contamination detection tests, are not usually interpretable on heterogeneous and rough surfaces.

A sessile drop measurement entails placing a drop of liquid (water in our study) on the surface of the substrate. The angle that the fluid makes with the solid surface is then measured. This contact angle value can then be used to determine various interfacial quantities such as critical surface tension which then would lead to energy and adhesion characteristics. Although the procedure is simple, problems arise in trying to obtain reproducible results on heterogeneous substrates. It has been shown that factors, such as surface roughness, contamination, and inhomogeneities, can drastically influence contact angle measurements. These factors lead to contact angle hysteresis, a difference between advancing and receding contact angles. For most cases surface roughness can be treated mathematically through the relationship developed by Wenzel, but it is more difficult to account for contamination and inhomogeneities.

Thorough cleaning procedures need to be used to ensure consistent contact angle measurements. In working with PCC mortar and limestone, this has been difficult to obtain. A comparison of two cleaning procedures (next section) has shown that the effect of cleaning on contact angle can be large.

Since PCC mortar is a composite material, its inhomogeneities affect the contact angle. Since the drop size is much larger than the small aggregate size (sand in this case), this effect can probably be "averaged out" statistically. The limestone samples also have inherent inhomogeneities, but in the localized area of a sessile drop, these are normally small.

Another problem is porosity. A sessile drop will soak into PCC mortar relatively quickly making consistent contact angle measurement difficult, since the contact angle will become smaller with time. On very porous materials the receding contact angle is unstable and not reproducible.

Photographic techniques could be used to capture the contact angle immediately after drop placement and before soaking in takes place, but this approach is also very labor-intensive.

Reference books on this subject (35-37), as well as several journal publications, do not provide much direction to finding solutions to these problems, since none have examined PCC mortar or limestone. More controllable surfaces, such as glass or polytetrafluoroethylene (PTFE), are normally used in which proven cleaning procedures have been established. The applicable information obtained from these deals with the experimental setup of sessile drop apparatus, and then once the drop is measured, what information can be derived from it. Preparation and maintenance procedures will have to be determined for PCC and limestone if this information is to be a true indication of the surface energetics involved. Since the literature suggests that parameters such as surface roughness, contamination, and

inhomogeneities need to be severely controlled, these become the most immediate problems to address. Already, cleaning procedures are being investigated as are techniques to reduce the soaking in of the sessile drop. Since this apparently has never been done for these materials, this information will be important for future interfacial studies utilizing sessile drop measurements.

The pavement core samples (PCC and asphalt) have not only the problem of an inhomogeneous surface due to the large aggregate size, but also have the problem of surface roughness. This roughness often makes it impossible to get a clear view of the surface of drop at the spot where it comes in contact with the surface to measure the contact angle.

To evaluate the pavement core samples, the drop diameter method, described in Appendix C, was utilized. While this method does not yield the rigid quantitative results potentially available from the sessile drop contact angle method, the drop diameter method does yield a semiquantitative measure of surface properties and ensures that all samples of a given type have the same surface energetics. This allows for a meaningful comparison of ice growth tests performed under different conditions on samples of the same type, while sessile drops alone are not as useful.

In the drop diameter method, a drop of liquid with a known volume is placed on the source of the substrate. The diameter of the drop is measured from above, thereby negating the surface roughness problem. Using the procedure described in Appendix C, the contact angles of the drop on the substrates were determined.

SDSM&T performed sessile drop measurements on the three pavement samples listed below for comparison to the drop diameter method.

Test Code	Description
NY310	New York State DOT, open-graded asphalt
NY311	New York State DOT, open-graded asphalt
CA414	CALTRAN, Plus Ride, rubber-modified asphalt

The rough texture of the surfaces of these samples made contact angle measurements impossible except for a few high points on each sample. The New York DOT OGA samples had a contact angle of 77° ± 3° for water, while the Caltrans RMA had a contact angle of 57° ± 20° for water. Both of these values are high for pure aggregate materials, as seen in Table A-2. This is to be expected, since there are probably traces of asphalt and oil on these samples. The hydrocarbon nature of the asphalt oil will yield a lower energy surface and consequently higher contact angles. No comparison data were obtained using the drop diameter method because of the uncertainty assosciated with the measurement locations on the core sample surfaces. Consequently, the drop diameter method has not been validated.

Laboratory-Produced Pavement Substrates

PCC and asphalt specimens produced in laboratories were obtained for this study. These samples were handled according to the same protocols used for the pavement core samples.

Laboratory-Produced Portland Cement Concrete Substrate

For this project, SDSM&T produced 13 portland cement concrete slabs in the laboratory with approximate dimensions of 6.5-in x 8.5-in x 1-in deep. These specimens were made in accordance with the mix design used by the South Dakota Department of Transportation (DOT) for highway (nonbridge deck) pavement construction. Table A-4 summarizes the PCC pavement mix design and source of aggregate used.

The limestone coarse aggregate used in the mix design was obtained from the same source as were the limestone substrates that were used in our Phase I study.

In the first batch (the PW series) SDSM&T prepared, no super-plasticizing agent was used, which caused the mixture to be difficult to work with. After consulting with concrete mix engineers for South Dakota DOT, SDSM&T prepared a second batch, designated as the SP series. In the second batch, plasticizing agent was used and made the batch much easier to work with. The samples used in this project are listed in Table A-4.

Table A-4. Sources and composition of laboratory concrete samples

Sources of Material	
Fine aggregate	Birdsall Sand and Gravel Oral, South Dakota
Coarse aggregate	Pete Lien and Sons, Rapid City, South Dakota
Portland cement	Dacotah Type II
Air-entraining admixture	Any approved brand

Cement factor = 5.64 cwt

	Mix/cwt (lb)	Mix/yard^3 (lb)	Absolute volume (ft^3)
Cement	100	564	2.82
Water	43.8	247	3.96
Sand*	241	1,360	8.29
Rock*	306	1,724	10.31
Air content			1.62
Total		3,895	27.00

* Saturated surface dry basis.

An air content of 6.0% was used for calculations.

Laboratory-Produced Asphalt Specimens

Asphalt specimens were obtained from two laboratories.

1. Michigan Technological University (MTU) through SHRP Contract No. H-204. Fourteen, 4-in-diameter, dense-graded asphalt specimens were provided. These specimens had been made in a Marshall test mold using AC-20 asphalt and aggregate obtained from the SHRP Materials Reference Library in Austin, Texas. The aggregate gradation and the chemical composition of the asphalt binder were not specified by MTU. One end of each specimen was ground smooth, with a final grinding with 440-grit powder.

2. Springborn Laboratories through SHRP Contract No. H-204. Eight, 4-in-diameter, dense-graded asphalt specimens were obtained as a set of backup specimens for those obtained from MTU.

The samples used in this project are listed in Table A-5.

Surface roughness evaluations: Evaluation of surface roughness at SDSM&T was performed using three methods. In the first method two photographs were taken of each substrate, one with overhead lighting and one with the light source at 45° from vertical. Analysis of the difference in shadows cast by surface features in the two photographs allowed for comparison of the different samples.

For the second surface roughness evaluation, a "Surface Profile Evaluation" was performed. In this procedure a straight edge was placed edgeways on the surface of a substrate. The number of places that "high spots" came in contact with the straight edge was counted. The average distance between high spots gave a rough indication of surface texture. Small wires of various diameters were also used as "feeler gauges" to determine the depth of some of the depressions. The diameters of the wires in millimeters were as follows: 0.245, 0.250, 0.313, 0.337, 0.550, 0.606, 0.615, 0.643, 0.801, 0.945, 1.09, 1.15, and 1.28. Variations of less than 0.245 mm were not measured by this procedure. Variations recorded in the surface profile were then plotted.

Table A-5. Laboratory-produced pavement substrates

Material	Test code	Source and comments
PGA 4-in diameter	MI201 MI202 MI203 MI204 MI205 MI206 MI207 MI208 MI209 MI210 MI211 MI212	Michigan Technological University; made in accordance with specifications received from SHRP and per ASTM D 1554-82 and ASTM C 136-84a One side of each 2-in section was polished using the technique referenced by Huang and Ebrahim Zadeh in ASTM Technical Publication No. 530
PCC 6– x 9-in slab	SD601 SD602B SD602C[a] SD603B SD603C[a] SD603[a] SD604 SD605 SD606 SD607 SD608 SD609 SD611 SD612 SD613	South Dakota School of Mines and Technology; cement factor = 5.64 cwt Mix/cwt Cement 100 Dacotah type II Water 43.8 Sand (SSD) 241 Rock (SSD) 306 With superplasticizing agent added

[a] SD602C, SD603C, and SD613 were produced without the plasticizing agent and were polished before testing. The other SDSM&T PCC samples were used "as constructed."

Three examples of "Surface Profile Evaluations" are presented in Figure A-1. The photographs and evaluations found that all of the PCC samples with exposed aggregate were similar making them a suitable set of specimens for ice studies. The third surface roughness evaluation was performed using a profilometer to characterize the surfaces of the three polished portland cement concrete specimens. The values of the surface roughness as determined by the profilometer are given in Table A-6.

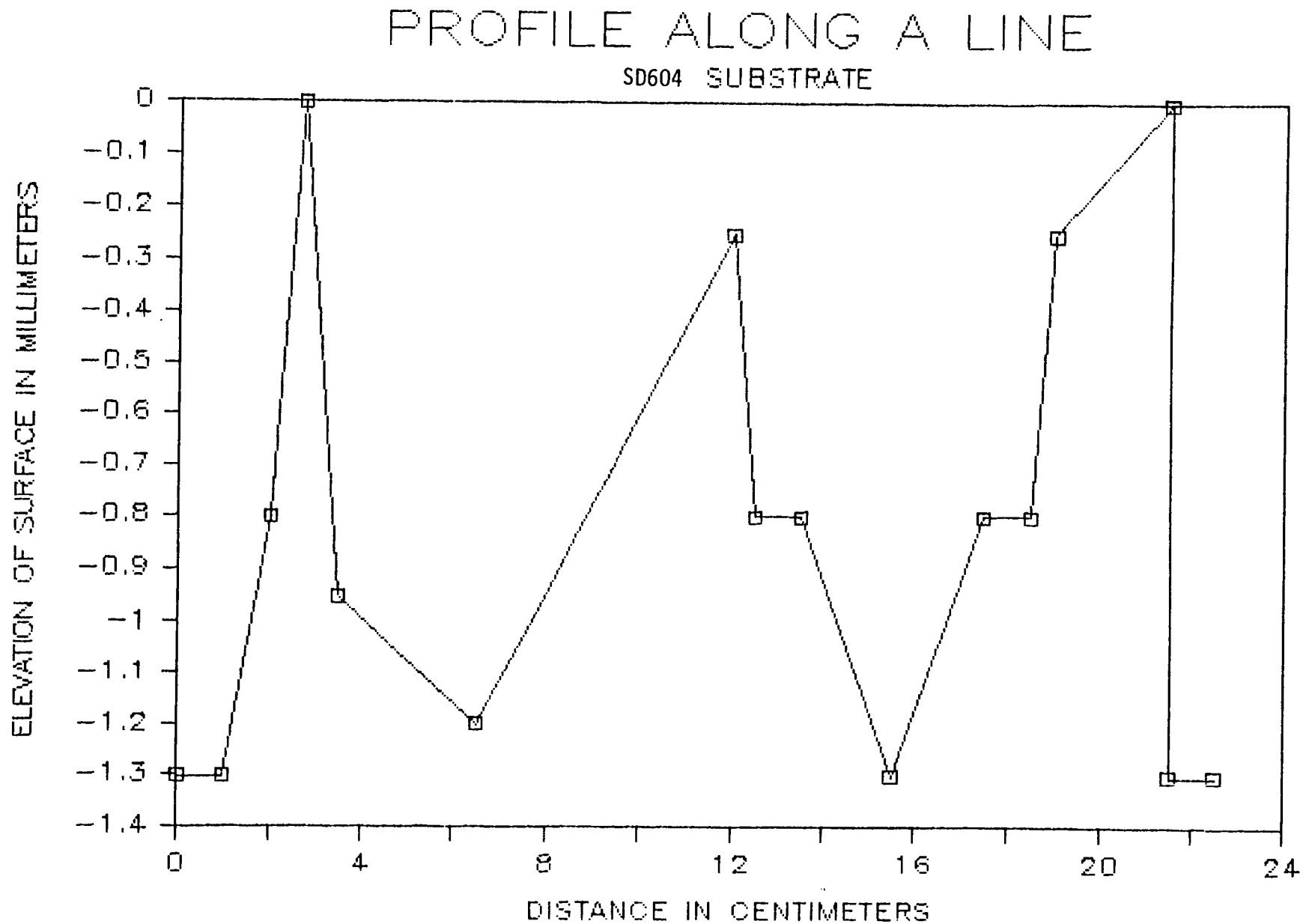

Figure A-1. Profile along a line

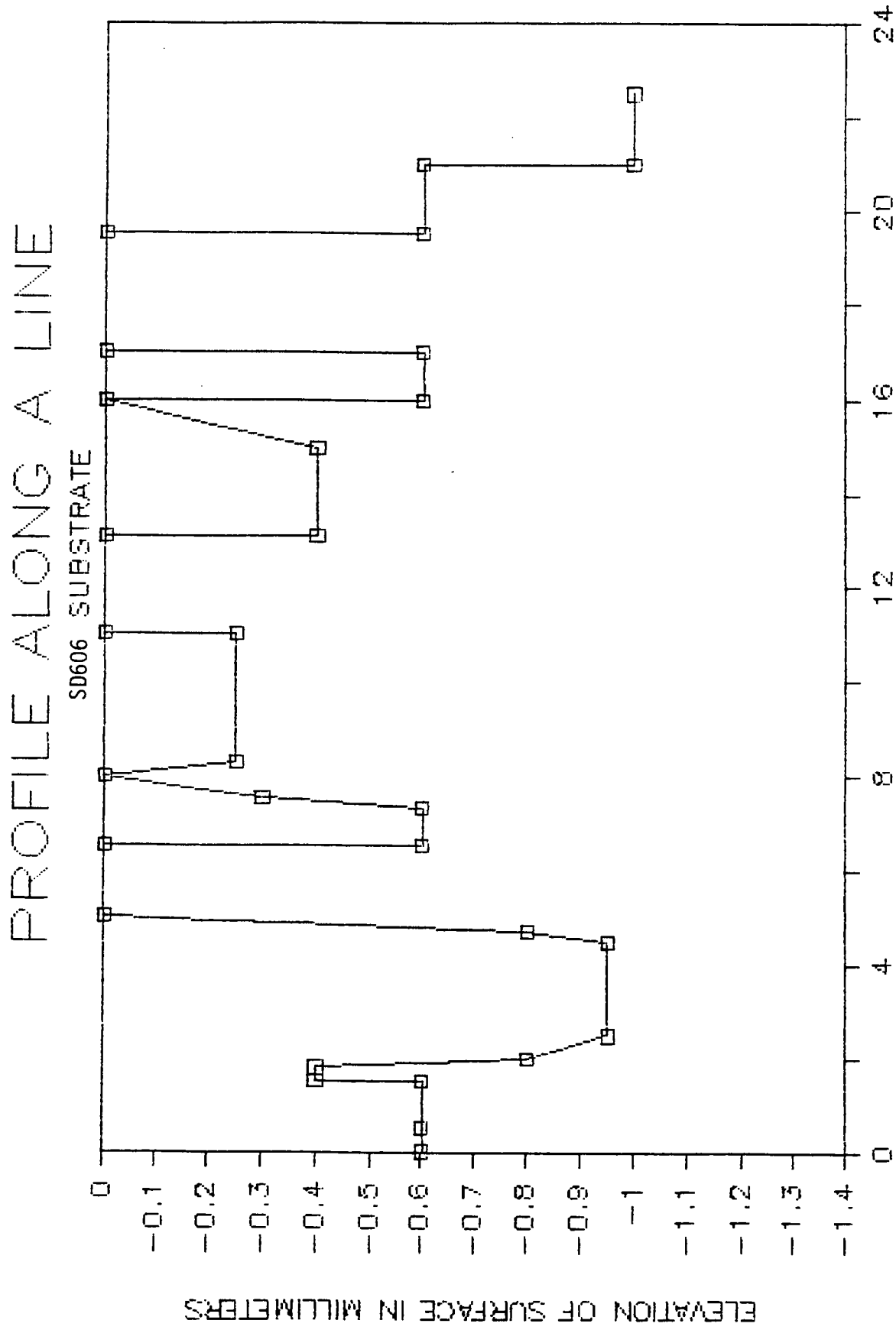

Figure A-1 (Continued)

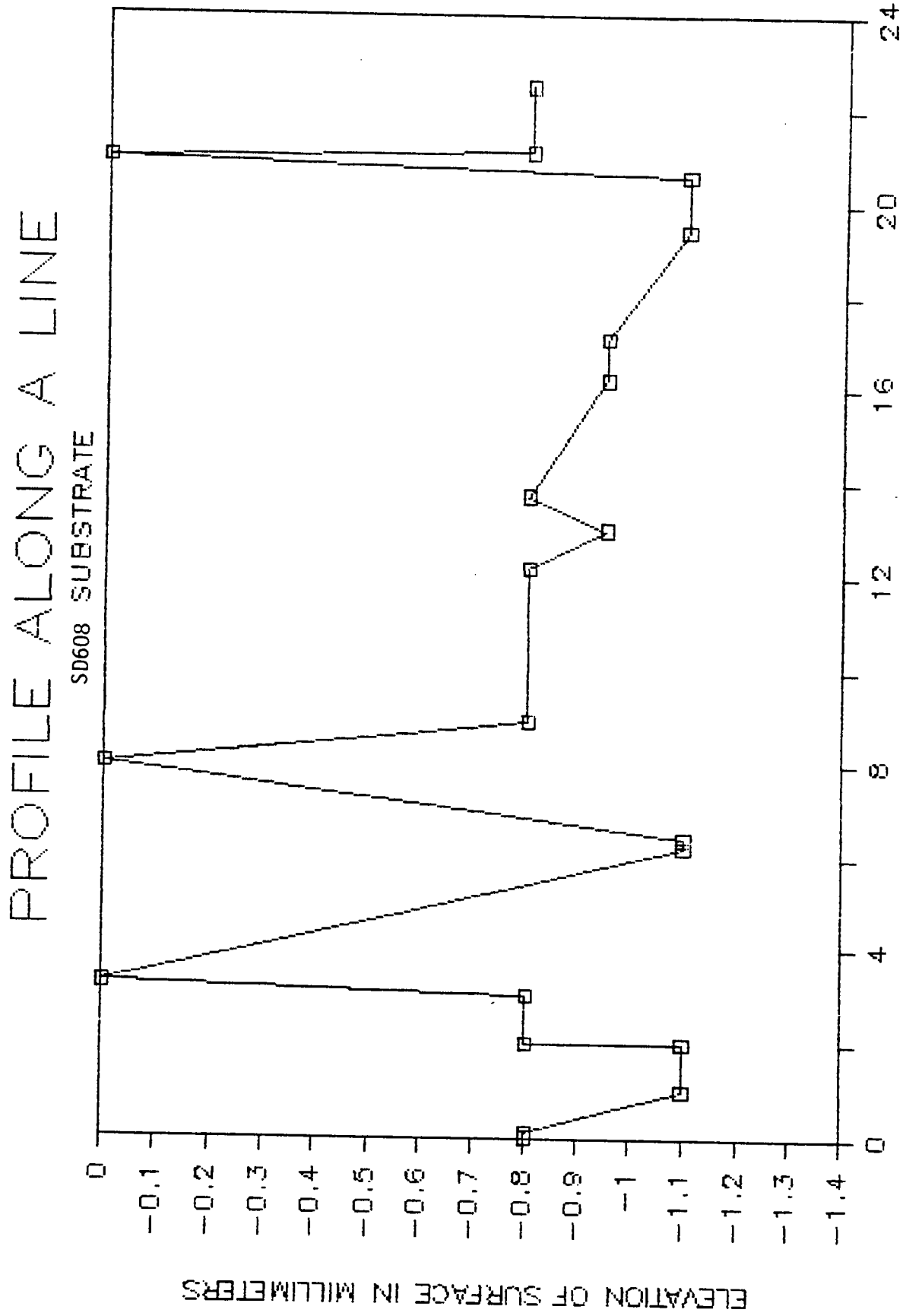

Figure A-1 (Continued)

Table A-6. Surface roughness determined by profilometer measurements

	Sample specification	Surface roughness (micro inches)
SD613		
(a)	On segment of limestone aggregate	30-60
(b)	On segment of mortar and sand	60-100
(c)	At transitions from mortar to large aggregate	Highly variable usually 100-200 but some greater than 300
SD602C		
(a)	On segment of limestone aggregate	30-60
(b)	On segment of mortar and sand	50-100
(c)	At transitions from mortar to large aggregate	Highly variable usually 100-200 but some greater than 300
SD603C		
(a)	On segment of limestone aggregate	30-60
(b)	On segment of mortar and sand	60-100
(c)	At transitions from mortar to large aggregate	Highly variable usually 100-200 but some greater than 300

Surface Characterization Methods

This section of the appendix describes experimental aspects of methods used to characterize the surfaces of the materials used in this study. These include equilibrium contact angles of sessile drops, modified sessile drops, surface area measurements, and adsorption isotherms.

Contact Angle Characterization of Substrates

The contact angle method was selected for surface energetic characterization of the solid substrates to be used in this program. The angle of repose formed by the edge of a sessile drop of liquid on a solid surface is a direct indicator of the interfacial tension between the liquid/solid pair. From the contact angles made by sessile drops of a series of liquids of differing liquid surface tensions, the critical surface tension of wetting, γ_c, is obtained, and the work of adhesion is a direct result. Accurate surface energetic characterization at the beginning of the study of a sample will allow subsequent measurements to monitor changes in the surface due to ice growth and removal and to the use of surfactants and/or undercutting materials. Once the values expected for the various liquids on a substrate are established, the method also provides a rapid and nondestructive determination of surface contamination or change in condition.

The equilibrium sessile drop method was used to measure the contact angles of liquids on the model substrates. In this method, a drop is placed on a region of the surface to be studied. The fluids are chosen to have a high enough surface tension that the drop does not spread out over the whole surface. The angle between the edge of the fluid.drop and surface of the material is measured optically.

The slowly advancing equilibrium drop method of Shafrin and Zisman (9) was employed in these measurements. Initially, a small (ca. 1-mm diameter) drop of liquid, selected by its surface tension to be only partially spreading so that it will stay intact on the surface, is carefully placed on the surface and its contact angle measured. An additional small amount of liquid is then added to the drop and the contact angle measured again. Additions are made until three successive measurements of the contact angle do not differ as the drop advances on the surface. The slowly advancing drop method eliminates any problems from initial instabilities. Angles reported are the average of readings taken on both sides of a drop after three or more successive additions. Initial measurements are not included in the high average recorded. Typically three or more separate drops are measured on different regions of the surface under study. Measurements at SRA were made with a standard NRL-type Ramé-Hart goniometer and NRL techniques.

A modified sessile drop procedure was utilized at SDSM&T to confirm the absence of surface contamination on the surfaces of substrates prior to their use in ice interfacial shear tests.

Sessile drop contact angle measurements with water were also made on the three polished PCC substrates. The substrates were first scrubbed with a brush under running tap water to remove any grinding grit, then rinsed with distilled water, allowed to air dry, and then tested. The contact angle measurement results are shown in Table A-7.

Table A-7. Sessile drop contact angle measurement results for three polished portland cement concrete specimens

	Contact angle (degrees)			
Substrate	Left	Right	Average (degrees)	Standard deviation
SD613	14.5	10.5		
	7.0	10.5		
	9.0	13.5		
	13.0	9.5		
	10.5	7.0		
			10.50	2.6
SD602C	4.5	4.5		
	9.0	6.0		
	9.5	9.5		
	7.5	9.5		
	11.0	5.0		
			7.60	2.4
SD603C	6.0	8.5		
	12.0	12.0		
	9.0	10.0		
	10.0	9.0		
	7.5	8.0		
			9.20	1.9

The low contact angles are characteristic of the contact angles obtained on the PCC mortar and limestone pavement component substrates as seen in Table A-2. Thus, the polishing process exposed a surface on which valid ice growth tests could be run.

Since the sessile drop method was included as part of the "surface energetics" evaluation, discussed in Section 2, a modified version of this test was used with only distilled water to check each surface for contamination after it had gone through the prescribed cleaning process. Initially, this measurement was to take place only once but, as described below, this approach was modified to include an evaluation between each cleaning and ice specimen fabrication.

The modified sessile drop apparatus used at SDSM&T, where the interfacial shear strength tests were performed, was constructed from a Bausch and Lomb Balopticon Model D lantern-type projector. The projector was modified by adding an adjustable diaphragm to control the illumination of the drop and by replacing the standard bulb with a clear glass, single filament 200-watt bulb. An adjustable gimbal stage was mounted just below the optic axis and between the condenser and projecting lenses. This stage allowed the height of the substrate to be adjusted and the surface to be inclined to the angle at which the image was clearest. Figure A-2 is a schematic of the sessile drop apparatus and shows the details of the optical system. A high humidity box with transparent walls was used during contact angle measurements. Only the advancing contact angle was measured.

Surface Area Measurement of Substrates

The surface area of powdered solids was measured using adsorption of a gas from a carrier stream with a Quantasorb area meter. The amount of nitrogen adsorbed at liquid nitrogen temperature and the amount subsequently desorbed at room temperature from an N_2/He mixture are used to calculate the surface area of the sample.

Gravimetric Adsorption Isotherms

The adsorption of vapors onto powdered solids is an informative method to determine the extent of interaction of the liquids/solid pair. In this study, water vapor was studied as the adsorbate onto limestone, PCC mortar, and fused silica.

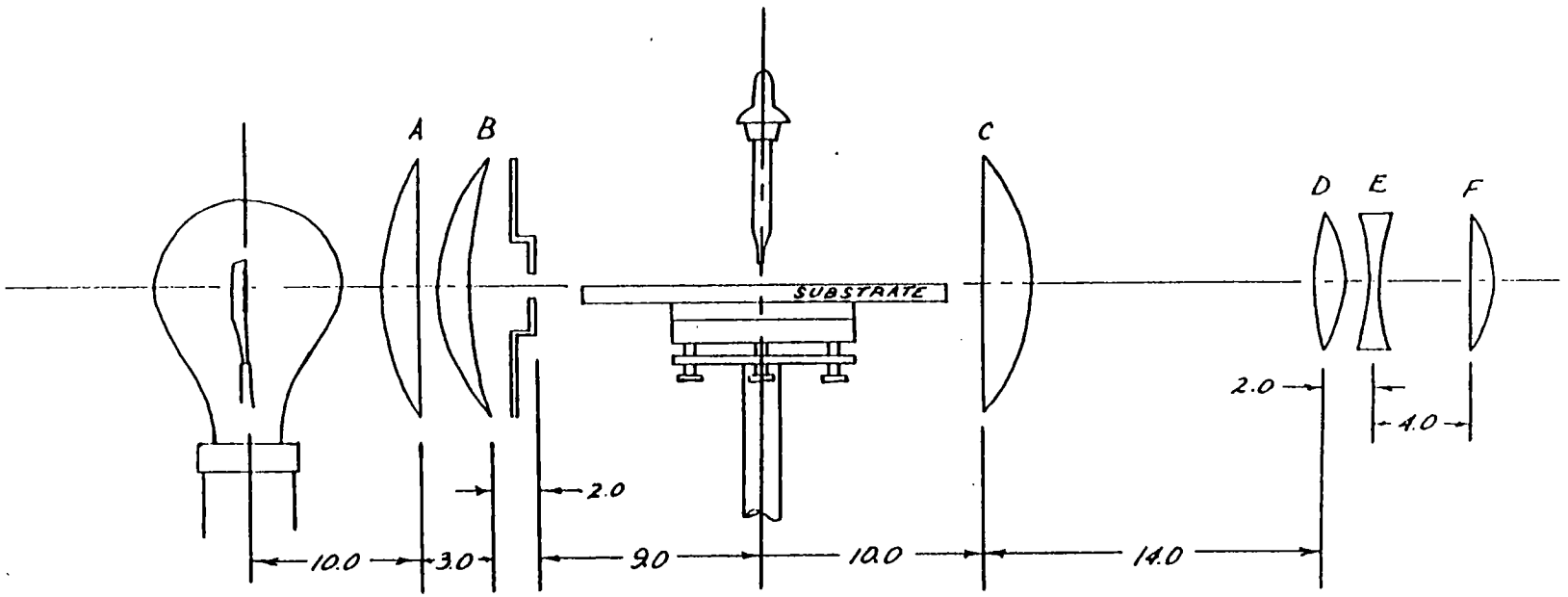

All Dimensions in cm

LENS	FOCAL LENGTH
A	180
B	800
C	75
D	120
E	-100
F	185

Figure A-2. Sessile drop apparatus

The gravimetric method of measuring adsorption isotherms was used. This method utilizes a microbalance contained in a vacuum chamber into which the adsorbate (water vapor) is admitted and the corresponding increase in adsorbent sample mass is noted. A typical isotherm involved the collection of over 20 data points along the curve from a partial pressure of about 0.002 to 0.9. The data can be plotted as $P/M(P_o-P)$ versus P/P_o, where P is the pressure of the adsorbate gas, P_o is the partial pressure of the gas at temperature T, and M is the mass of the adsorbed gas. This is the linearized form of the BET equation of multimolecular adsorption.

An example of a Type II isotherm is presented in Figure A-3, from experiments on PCC mortar. Type II isotherms were obtained for the powders of all three pavement component substrates using water as the adsorbate. These isotherms were characteristic of powders with cracks, pores, or capillaries in their surface.

Details of Experimental Procedure

A Cahn Model 2000 electrobalance with a sensitivity of 10^{-7} g is used for all mass measurements. The electrobalance is mounted in a vacuum chamber. The electrobalance output is connected to a Keithley nanovoltmeter to monitor the sample mass. The electrobalance and vacuum chamber are mounted on a special vibration isolation block in order to protect the system from vibrations which could degrade the electrobalance accuracy (See Figure A-4). The electrobalance and its vacuum chamber are enclosed in a thermal insulating box to minimize temperature fluctuations due to room temperature changes. The cell temperature is monitored with a mercury thermometer to within 0.05°C.

To begin an adsorption isotherm measurement, a sample of about 50 mg of freshly ground material is placed on the sample pan of the electrobalance. The samples are ground with a mortar and pestle.

The electrobalance is evacuated to about 10 mTorr and maintained at this pressure for 48 hours to allow the sample to outgas. By careful manipulation of a microvalve, water vapor is admitted into the system, allowing adsorption of water vapor onto the sample, as indicated by an increase in mass. It typically takes 10 min for the sample mass to stabilize at any given pressure after the introduction of water vapor. The process of admitting water vapor and allowing the sample mass to stabilize is repeated for vapor pressures from 10 mTorr through 18 Torr. A graph is generally produced of the percent mass change of the sample as a function of the partial pressure of water vapor in the system at room temperature.

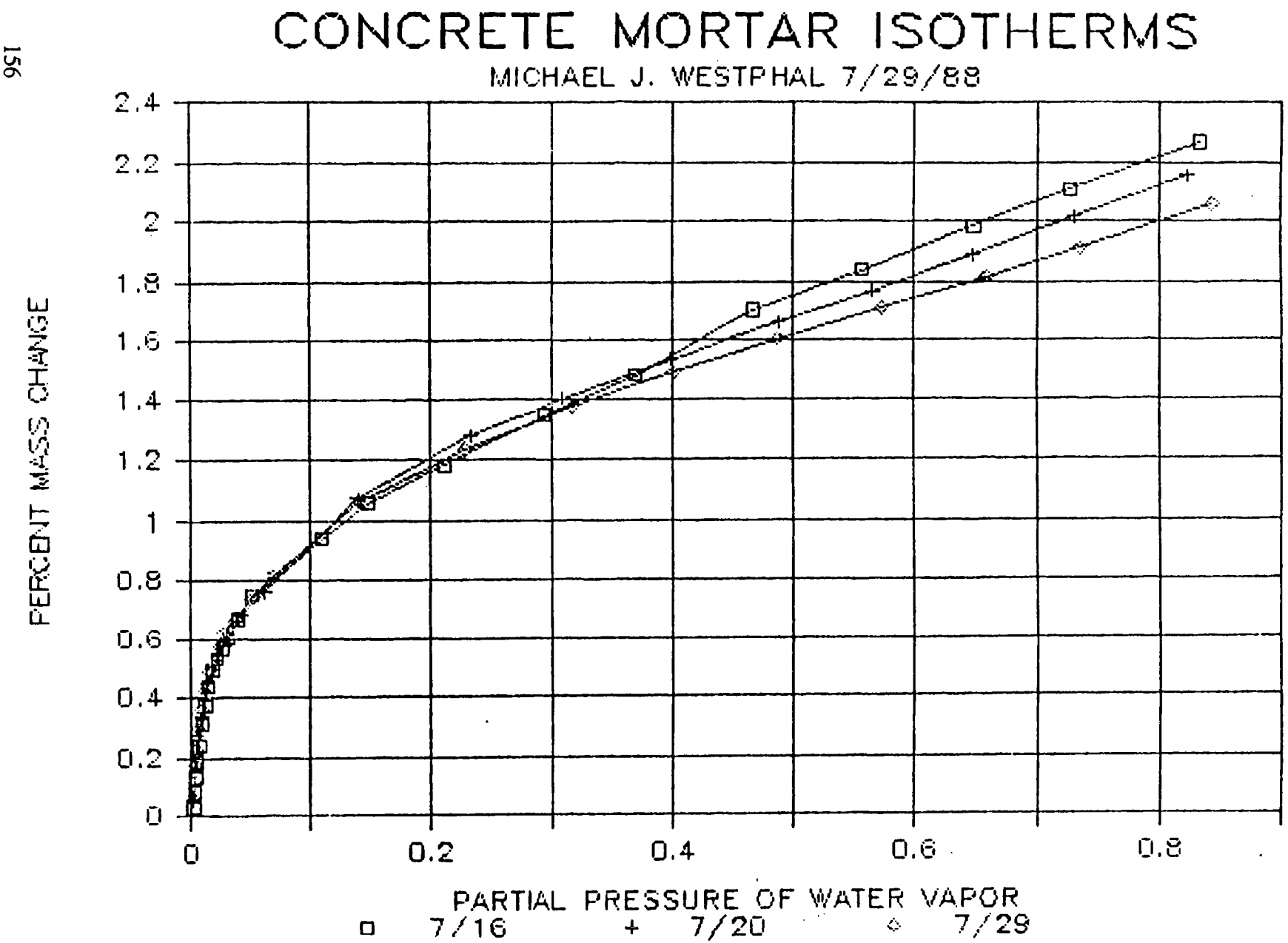

Figure A-3. Portland cement mortar isotherms

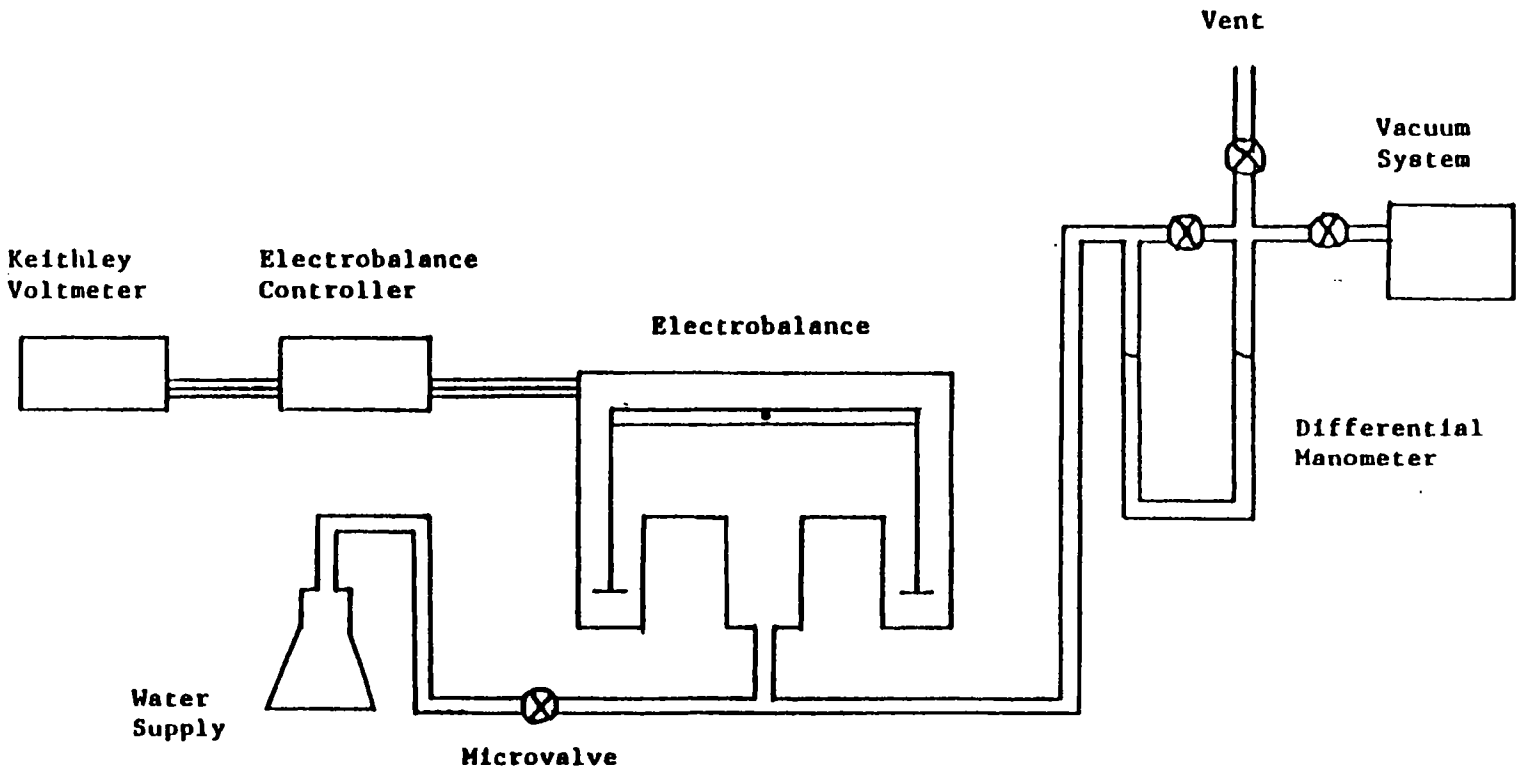

Figure A-4. Adsorption isotherm equipment schematic

The presence of the knee in the adsorption isotherm at a partial pressure of about 0.1 indicates that the energy released during adsorption of the first layer of the adsorbate is significantly higher than the energy released during the adsorption of subsequent layers. The data between a partial pressure of about 0.05 and 0.35 was plotted in the linear form to obtain the slope and intercept of the curve. The slope and intercept were then used to calculate the monolayer mass, M_m, and the BET constant, c, using the following expressions:

$$M_m = \frac{1}{(\text{slope} + \text{intercept})}$$

and

$$c = \frac{(\text{slope} + \text{intercept})}{\text{intercept}}$$

The following relationship is used to calculate the first layer heat of adsorption.

$$E_1 - E_L = kT \ln (C)$$

where: k = Boltzmann constant
T = temperature
E_L = heat of liquefaction (water)
E_1 = first layer heat of adsorption

Independent nitrogen measurements were used to calculate the total surface of the sample to obtain a heat of adsorption per unit area.

From the monolayer mass and the first layer heat of adsorption, the bond energy of a single adsorbate (water) molecule can be calculated. These values were given in Section 2.

Appendix B

Sample Handling and Cleaning Protocols

Establishment of Protocols

It is very important that the nature of the surfaces of solid substrates and liquids be known. Impurities or surface morphology changes introduced by improper handling cannot be tolerated. The importance of proper handling procedures for samples used in surface studies was shown in a study of metal cleaning techniques (9). Major differences were found in surface energy and bonding on materials that were cleaned by several procedures, all of which conformed to the relevant Military Specification. Further, these differences persisted through shipping and storage, and could be detected by contact angle, FTIR, and Auger spectroscopies. The establishment of coordinated protocols of this type was the only way to ascertain the uniform validity of results obtained with the diverse laboratory methods required for the successful completion of the present program.

To ensure the proper handling of materials, laboratory standard procedures for handling the diverse types of samples and materials were established. The extensive laboratory practices already in place at the four team member institutions were used to identify the protocols that were selected for use in this program. Analytical methods such as contact angle measurements were used to monitor the conditions of samples from the various sources.

Listed below are the handling procedures, which were used to ensure that the surface and interfacial measurements were of the highest accuracy. A uniform protocol throughout this program eliminated any uncertainties in our findings due to the ordinary variations present in individual laboratory practices.

Separate sections are included for the protocols specifically designed for the handling and cleaning of the pavement core samples and the laboratory-produced pavement substrates.

The last section of this appendix deals with tests of the water used in the ice growth studies. These tests ensured that the results obtained were free of effects from contaminants in the water.

Handling Protocols

Solid Substrates

Whenever possible the solid substrates were handled with clean stainless steel forceps or Teflon-coated tongs. The large size of the specimens used by SDSM&T in their interfacial shear tests (6.5 cm x 15 cm) made the use of forceps or tongs impractical. In these cases the samples were handled only on the edges using disposable rubber gloves.

Liquid Materials

Mercury: The mercury was used in a well-ventilated area. Provisions were made to easily clean up any inadvertent mercury spills. All of the mercury was used directly from the container. No metal objects were allowed to come in contact with the mercury. The mercury was passed through a pin-hole filter to remove any oxides just before its use and was discarded immediately after its use. All discarded mercury was collected for return to the manufacturer.

Fluorocarbon oil: The Krytox 1514 was used fresh out of its container.

Contact angle reference liquids: After purification these liquids were removed from their storage containers using only a platinum wire. The wire was cleaned and placed in a gas flame to remove all contamination just prior to being placed in the reference liquid. This platinum wire was the only item, outside of the container, to come in contact with the liquids before their use. Triply distilled water was used by SDSM&T to make sessile drop measurements on each substrate.

Storage

Solid Substrates

Solid substrate samples were stored in Teflon containers. Samples of one type of pavement component were stored separately from the other types of pavement components and from the Mylar and Teflon samples. This was particularly important in the case of the asphalt, which was stored separately immediately after its preparation, to prevent contamination of the other samples from volatiles that were released by the asphalt. The limestone and portland cement

mortar samples were stored in a manner to insure that the surfaces on which the ice experiments were to be performed came in little contact with anything else. This procedure not only prevented surface chemical contamination but also preserved the smooth finish that was achieved on those samples that were polished.

Liquid Materials

Liquids were stored in containers as received until further purification or use.

The mercury was stored in its original container up to just prior to its use. No sample of mercury was ever returned to its original container.

The fluorocarbon oil, Krytox 1514, was stored in its original container until it was needed.

The contact angle reference liquids, after their purification, were stored in all glass, greaseless containers that had been acid cleaned as described below. As some of them are sensitive to light, they were stored in a closed cabinet.

Additional General Laboratory Procedure

Glassware Used in Program

The glassware used in this program had to be clean to prevent unwanted contamination of the materials used. All glassware was cleaned using the following procedure, which is similar to that used for cleaning the glass and fused silica substrates.

The glassware had to be free of grease. If necessary, a saturated or 6 M KOH ethanol solution was used to remove any grease. The grease-free glassware was then acid-cleaned with a 10:1 sulfuric acid to nitric acid bath mixture heated to 100°C. The glassware was left for 1 hour, or if the glassware was too large, the hot acid bath was repeatedly poured over the glassware. The glassware and the acid bath were allowed to cool down to room temperature. The acid was then drained off and the glassware was then rinsed with distilled water. Standard acid cleaning safety procedures were followed during the acid bath cleaning of the glassware.

The larger glassware was allowed to air-dry in the laboratory after the acid bath. Necks of large vessels were loosely covered and some of the smaller items were dried under a drying

cover. Most of the smaller glassware was soaked in distilled water overnight. Any contaminants that came free usually formed a film on top of the water. To keep the film from redepositing on the samples, the soaking liquid was floated off with more doubly distilled water to wash away any film that may have formed.

Water

Water used in this program was either double- or triple-distilled, deionized water. Final rinses of all materials and handling instruments was with this purified water. Double-distilled water is distilled water to which a potassium hydroxide and potassium permanganate is added and then distilled again.

Other Utensils

All other utensils, such as forceps and Teflon-coated tongs, were cleaned before their use in handling the materials. Whenever possible, the utensils were placed in a Soxhlet extractor for the final cleaning.

Sample Handling Protocol for Pavement Core Samples and Laboratory-Produced Pavement Substrates

1. **Receipt.** Upon receipt, samples should be examined for integrity, edge condition, and overall appearance. Samples with large amounts of surface irregularity such as grooving or extraneous marking should be rejected if possible.

2. **Plastic Bags.** Plastic bags are to be avoided once the surfaces are cleaned because the bags contain surfactant release and antistatic agents designed to maintain a high concentration on the polyethylene surface. No contact of test surfaces with polymer of any kind should be permitted. Poly sheet or bags may be used as a "dust cover" so long as there is no contact of poly and test surfaces, especially during placement and removal of samples.

3. **Moisture**. It is important to allow samples to dry to equilibrium with the room humidity. High moisture levels can foster bacterial growth. This requires that samples be removed carefully from plastic bags or left with bags opened and untouching the top surface.

4. **Relative Humidity**. Room humidity should be recorded at least nominally during sample storage and handling. Any major changes in room condition (e.g., relative humidity level) should also be recorded. Humidity levels higher than 50% relative humidity or lower than 25% relative humidity should be noted. Samples stored under more extreme conditions should have an opportunity to equilibrate at a humidity value within the range above for several hours just prior to ice growth. This is more important if chemical adjuvants are to be used in the study, less so if ice from pure water is to be grown.

5. **Transport**. Transport in this sense means sample handling within a laboratory (e.g., from storage to experimental setup or from one laboratory area to another). Samples should be carried from each location with the top surface protected but not touched by any other materials. Cores should be maintained in an upright position if at all possible. This may be accomplished by support around the lower region. If the sample is to be transported and cannot be kept upright, then it should be arranged so that the upper surface is not touched by the carrying surfaces or by hands upon removal. A suitable arrangement would be the protrusion of the upper face from a rack with the core lying on its side, with enough clearance so that adjacent samples did not come into contact, and that the core did not rub against other materials during its transfer.

Sample Cleaning Protocol

The examination and testing of the cores and laboratory-produced specimens also resulted in the development of the following sample cleaning protocol.

Procedure for Cleaning Pavement Core Samples and Laboratory-Produced Pavement Substrates

USE DISTILLED WATER OR DEIONIZED WATER FOR ALL PROCESSES. DO NOT USE TAP WATER FOR ANY CONTACT WITH SAMPLES.

SAMPLES SHOULD BE CLEANED AS CLOSE AS POSSIBLE TO THE TIME OF TESTING. ETHANOL STEP MAY BE DONE IN ADVANCE.

1. **Dry Brush.** Brush any loose materials from the surface of the sample. If there is enough loose material that the brushing has exposed a significant amount of unweathered, untraveled area, this should be noted and, if possible, the sample should be rejected.

2. **Test with Droplets.** Test surface with water droplets in various regions. Pay attention to those with high contact angles (water standing up, as these will be areas with organic materials). Note the pattern, if any, of water wetting (i.e., if in a specific region of the sample, the water appears more nonwetting). Note the differences from aggregate inclusions and the mortar.

3. **Ethanol Treatment.** Rinse with ethanol. Brush using a medium-stiff natural or nylon brush. Rinse loose material. Let ethanol run off sideways. Collect ethanol. Note if there is any discoloration (more likely) or film on its surface.

4. **Dry.** Allow to dry to damp or dry condition, so that there is no visible liquid and color of sample has returned to its original state—at least 10 minutes.

5. **Hot Water Flash.** Flood with DD or DI water. Use hot water (– 40°C). Agitate with brush during the first wash. Any surface-active materials will tend to rise to the top of the pool of water. Continue adding water to the pool so that the water flood off rather than redeposits.

6. **Repeats.** Wash two more times, using 50 to 100 cc of water or more per wash.

7. **Fourth and Final Water Wash.** This should be done with core specimen surface vertical and rotated during wash so that water is immediately drained away from center in all directions.

8. **Drain.** Let sample drain dry with surface vertical for a few minutes. Return to normal position. Stand sample on a clean substrate.

9. **Retest for Contact Angle.** Test with water droplets. Contact angle should be lower in any areas where it was high. Repeat cleaning if contact angles are still unusually high.

10. **Use Specimen as Soon as Possible.** Sample is now ready for ice growth or other testing. If chemical deicing adjuvants are to be applied prior to ice growth, or if ice is to be grown from surface upward, dry it in air in a dust-free environment. Otherwise sample should be tested as soon as draining is complete.

Water for Ice Growth Studies

Tests were performed to ensure that the water used for ice growth studies itself be pure and not contain any surface contaminants. The water used at MRI was obtained from an in-house deionized water supply. Filters on this system are monitored and changed regularly.

Surface tension measurements were made on the deionized water using a Cenco-DuNuoy ring tensiometer. The deionized water used at MRI in this program was found to have a surface tension of 67.1 ± 0.3 mN/m (dynes/cm). This may be compared to a literature value of 72.0 mN/m at 25°C. While 5 mN/m lower, it is not so far off that the water cannot be used. (Values above 70 mN/m cannot usually be achieved without extreme means.) The appearance of the water, obtained and brought back to SRA in an acid-cleaned bottle, does not indicate excessive surface contaminants, empirically evidenced by observation after vigorous shaking of water in a bottle.

We concluded that MRI's deionized water, as tested, is pure enough that any contaminants should not have a significant effect on the results of MRI's ice growth experiments.

Water of higher purity could be obtained only upon stringent laboratory procedures such as distillation in an all glass system and special storage requirements. The parameters of the experiments on ice growth and removal on real substrates do not indicate that there would be any advantage to this special effort.

The following water handling procedures were used in this program.

Water Handling Procedures

1. Water should be examined periodically by shaking and permitting contents to settle. The presence of foam or bubbles is contraindicative of use of that supply.

2. Care must also be exercised in the containers used in the laboratory for collection, transfer and temporary storage of the deionized water so as to not introduce extraneous contaminants into the water from them.

3. In general: Use the same container.

4. If a bottle, do not let water come in contact with a paper bottle cap liner.

5. Allow a clean or new container to stand full of water at least overnight, then discard it and use a new supply.

6. It is better to store the container wet and full of water than dry. Unless water of dubious quality is placed in it, it will stay cleanest by being full of water at all times.

7. Do not use laboratory detergent to clean out the bottle after its initial conditioning.

8. During ice sample formation and ice growth, the water supply be contacted by as few materials as possible. Plastic or rubber gloves, for example, should not be in the pool of water, and water should not be poured over them, as surface-active agents on the polymer glove surfaces can migrate along the water both to the supply and to the mold.

9. If the maintenance schedule for the MRI in-house system can be determined, it may be possible to insure that water is not drawn just prior to or just after scheduled maintenance when quality may temporarily be lowest.

10. At other locations, e.g., SDSM&T, water quality may be monitored by the same methods. Shaking and the absence of surface active components in the water should be the most useful indicator. Conductivity measurements are not a good measure of water purity since it is the bulk water value being measured. Water with an acceptably low conductivity may have an appreciable amount of surface active material on its surface.

11. SRA should check the water surface tension periodically, and especially if there is any suspicion at any given time about the water quality. A lower limit of 64 mN/m for water quality is suggested. Any water supply having a surface tension value measured or suspected to be lower than 64 for pure water should not be used for ice growth studies in this program.

Appendix C

Development of Drop Diameter Method for Surface Condition of Pavement Samples

The wettability of a solid surface by a liquid can provide a great deal of information about the surface even without the derivation of exact "surface energetics." The assessment of surface properties of highway pavement cores and related samples is difficult in that traditional methods for measurement of wettability (e.g., with a laboratory goniometer) are not practical at all for these sample sizes, shapes, and locations. Accordingly, a method was devised to work with pavement and related samples with these variables that will provide a means to monitor and assess the surfaces both as-received and in the course of ice removal experiments.

To obtain this assessment of the surface of highway pavement samples, a method was developed to obtain contact angle measurements based on the diameter of a drop of test liquid.

The main aspects of this method are the following: A small drop of a known volume is placed on a locally homogeneous region of the surface to be measured. Since the volume of the drop is known, the only measurement that is required is the drop diameter. The drop diameter at its widest point is recorded. For asymmetric drops, the smallest diameter is also recorded and the two averaged to yield an average drop diameter.

Any method to measure the surface of an inhomogeneous solid must take into account the different regions of the solid as well as the net average value that may be representative of the solid as a whole. In this new method, the droplets to be measured are to be small enough to be confined to one type of area on the pavement such as on the aggregate, the asphalt, a rubber piece (in Plusride) or a mortar region. The values obtained for each type of region (e.g., on a rubber particle in Plusride) may be used independently, or may be combined to yield a net value for the surface being evaluated.

The drop-diameter method is based on the derivation shown below. It makes use of the well-established observation that a sessile drop on a surface will take the shape of a segment of a sphere. This will be true for all small drops until the drop size is great enough that gravitational effects are involved. Gravity is not a factor unless the drop is large enough to have a flattened central region like a "pool" of fluid.

Figure C-1 is a representation of a liquid drop on a solid surface shown in the cylindrical coordinate system. The drop is a section of a sphere whose center is located at $z = a$ and whose radius is c.

The mathematical surface at the interface between the liquid and the air in cylindrical coordinates is given by

$$z = \sqrt{c^2 - r^2} - a \tag{1}$$

The radius, r_o, of the lower edge of the section (representing the contacting interface of the drop at the liquid/solid interface) is given by

$$r_o = \sqrt{c^2 - a^2} \tag{2}$$

The volume, V, of the drop, is obtained by integrating over the surface at the air/liquid interface:

$$V = \int_0^{2\pi} \int_0^{\sqrt{c^2 - a^2}} \left(\sqrt{c^2 - r^2} - a \right) r \, dr \, d\theta \tag{3}$$

to obtain

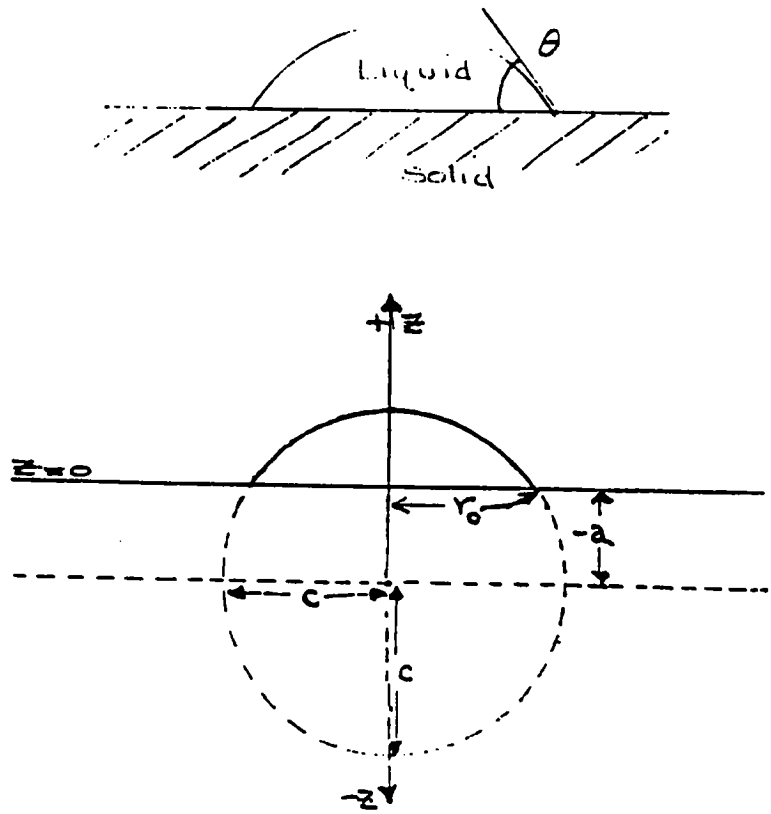

Figure C-1. Representation of a small sessile drop in cylindrical coordinates for calculations of drop sizes

$$V = (2\pi/3)\ (c^3 - 3\ a\ c^2/2 + a^3/2) \tag{4}$$

If a drop of known volume is placed on a surface and its diameter is measured, then equations (2) and (4) can be numerically evaluated to obtain values for a and c. These values then define the surface of the liquid/air interface.

The derivation of equation (1) will give the slope of the liquid/air interface at any point on the surface

$$dz/dr = -2\ r/\sqrt{c^2 - r^2} \tag{5}$$

When evaluated at z=0, dz/dr is the angle at which the liquid meets the solid surface, which is the contact angle, θ.

$$-(dz/dr)_{z=0} = \tan\ \theta \tag{6}$$

At z=0, the drop is defined to have a radius of r_o as given in eq. (2). This value for r_o yields

$$\tan\ \theta = 2\ \sqrt{c^2/a^2 - 1} \tag{7}$$

Thus, a measurement of the drop diameter equal to 2x radius, can be related to the drop volume and thus to the contact angle, for drops small enough to be spherical sections. The result is single-valued and unambiguous.

Because all liquids interacting by physical adsorption will form drops of spherical section when they are small, the tabulated calculations will be valid for all liquids, to determine the contact angle in lieu of direct measurement. Values of contact angle obtained this way are then plotted with the known surface tension of the spreading liquid(s) to obtain wettability information in the usual manner. Table C-1 presents sample calculations for drops of 1 µL volume.

Table C-1. Contact angles derived from drop diameter method

Drop Volume = 1.0 μL			
r_o (mm)	a (mm)	c (mm)	θ, degrees
0.782	0.0	0.782	90
0.872	0.2	0.895	83
0.944	0.4	1.025	78
1.004	0.6	1.170	73
1.057	0.8	1.326	69
1.104	1.0	1.490	66
1.203	1.5	1.923	58
1.283	2.0	2.376	52
1.410	3.0	3.315	42
1.555	4.5	4.761	35
1.701	6.5	6.719	28
1.890	10.0	10.177	21

Two reference look-up tables were established for various combinations of drop volumes and drop diameters. This allowed for the rapid measurement of contact angles on samples that are too rough to use a goniometer or are situated such that normal contact angle methods are not feasible. It will also permit different drop sizes to be delivered by any means available such as microsyringe or a micropipet, and allow different liquids, in some cases, to be used for measurement.

To obtain the reference tables Equation (7) was rewritten as

$$c^2 = r_o^2 q^2 \tag{8}$$

where

$$q = 4/\tan^2\theta + 1$$

substitution of this into equation (4) yields the drop radius is given by

$$r_o = \left[\frac{3V/2}{q^3 - \left(\sqrt{q^2 - 1}\right)(q^2 + 1/2)} \right]^{1/3}$$

Using this relation for the drop radius, drop diameters were calculated and are presented in Table C-2.

Table C-2. Diameter of drops (mm) versus contact angle (θ, degrees)

	Volume of drop (μL)				
θ (degrees)	0.50	1.00	1.50	2.00	2.50
90	1.24	1.56	1.79	1.97	2.12
85	1.35	1.70	1.95	2.14	2.31
80	1.46	1.83	2.10	2.31	2.49
75	1.56	1.97	2.25	2.48	2.67
70	1.66	2.10	2.40	2.64	2.85
65	1.77	2.23	2.55	2.80	3.02
60	1.87	2.35	2.70	2.97	3.20
55	1.97	2.49	2.85	3.13	3.37
50	2.08	2.62	3.00	3.30	3.56
45	2.20	2.77	3.17	3.49	3.76
40	2.32	2.92	3.35	3.68	3.97
35	2.46	3.10	3.54	3.90	4.20
30	2.62	3.29	3.77	4.15	4.47
25	2.80	3.53	4.04	4.45	4.79
20	3.04	3.83	4.39	4.83	5.20
15	3.37	4.24	4.85	5.34	5.76
10	3.87	4.87	5.58	6.14	6.61
5	4.88	6.15	7.04	7.75	8.35

For the second reference table, contact angles were calculated for drops with varying volumes and diameters. Two other algebraically equivalent forms for the volume of a contact angle drop are given by

$$V = \pi h\ (3\ r_o^2 + h^2)\ /\ 6 \tag{9}$$

$$V = \pi h^2\ (3c - h)\ /\ 3 \tag{10}$$

where h is the height of the contact angle drop or

$$h = c - a$$

Using the form of the volume given in equation (9), a function of the variable h can be defined as

$$f(h) = h^3 + (3r_o^2)\ h - 6V/\pi \tag{11}$$

Setting $f(h) = 0$ and solving for the roots provides three solutions, one of which is the height of the drop which can be used with the relations in equations (5) and (4) to obtain the other drop parameters of a and c. These are used with the relation in equation (1) to calculate the contact angle.

To solve for the roots of the function in equation (6), the Newton-Raphson Method was employed to numerically solve for h.

For this method, the first derivative of this function is needed and given by

$$f'(h) = 3\ h^2 + 3\ r_o^2$$

The Newton-Raphson Method is an iterative method that needs an initial estimate of the root. For this calculation, an initial estimate was obtained using the height of a drop with a contact angle of 90 degrees which is a hemisphere. The iterative formula for the i+1 iteration is given by

$$h_{i+1} = h_i - f(h_i) / f'(h_i)$$

Contact angles were calculated by the above described method and are presented in Table C-3. The diameter of a drop with a 90-degree contact angle is given in Table C-4 as a function of the drop volume.

Table C-3. Contact angle of drop (θ, degrees) versus diameter of drops (mm)

Diameter (mm)	Volume of drop (μL)				
	0.50	1.00	1.50	2.00	2.50
1.0	138.0	–	–	–	–
1.1	107.4	–	–	–	–
1.2	94.0	–	–	–	–
1.3	84.5	123.2	–	–	–
1.4	75.5	105.5	–	–	–
1.5	66.8	95.1	120.6	–	–
1.6	58.7	87.3	105.8	133.1	–
1.7	51.4	80.0	96.4	112.9	143.1
1.8	44.9	72.9	89.3	102.1	117.2
1.9	39.2	66.1	82.9	94.4	105.5
2.0	34.3	59.7	76.6	88.2	97.5
2.1	30.1	53.7	70.5	82.4	91.2
2.2	26.4	48.3	64.7	76.7	85.8
2.3	23.3	43.4	59.1	71.1	80.4
2.4	20.7	39.0	53.9	65.8	75.1
2.5	18.4	35.0	49.1	60.7	70.0
2.6	16.4	31.5	44.7	55.8	65.1
2.7	14.7	28.4	40.7	51.3	60.3
2.8	13.2	25.7	37.1	47.1	55.9
2.9	11.9	23.3	33.8	43.3	51.7
3.0	10.7	21.1	30.9	39.8	47.8
3.1	9.7	19.2	28.2	36.5	44.1
3.2	8.9	17.5	25.8	33.6	40.8
3.3	8.1	16.0	23.7	30.9	37.7
3.4	7.4	14.7	21.7	28.5	34.8
3.5	6.8	13.5	20.0	26.3	32.2
3.6	6.2	12.4	18.4	24.3	29.9
3.7	5.8	11.4	17.0	22.5	27.7
3.8	5.3	10.6	15.8	20.8	25.7
3.9	4.9	9.8	14.6	19.3	23.9
4.0	4.6	9.1	13.6	17.9	22.2
4.2	3.9	7.9	11.7	15.6	19.3
4.4	3.4	6.8	10.2	13.6	16.9
4.6	3.0	6.0	9.0	11.9	14.8
4.8	2.6	5.3	7.9	10.5	13.1
5.0	2.3	4.7	7.0	9.3	11.6
5.5	–	3.5	5.3	7.0	8.7

Table C-4. Diameter of contact angle drops (mm) with 90 and 180 degree contact angles (θ)

	Volume of drop (μL)				
θ	0.50	1.00	1.50	2.00	250
90	1.24	1.56	1.79	1.97	2.12
180	0.98	1.24	1.42	1.56	1.68

Appendix D

Investigation of the Properties of Ice Removed From Substrates

A brief description is presented in this appendix of an investigation of the morphology (structure) of ice grown on model substrates with different surface energetics. The purposes of the interfacial ice growth study were twofold. The first was to determine the effect, if any, of the model substrate surface energies upon the morphology of ice found at the ice-substrate interface. The second purpose of the work was to investigate and establish, if possible, the existence of a liquid-like layer at the ice-substrate interface that has been postulated by other researchers. This layer has been proposed to explain some of the behavior of ice frozen on metal substrates when placed under shear forces at low load levels.

Four model substrates—gold, mercury, fluorinated oil, and FEP Teflon—were tested to cover the high and low ranges of surface energies (i.e., gold has a high energy surface and FEP Teflon has a low energy surface). Experiments were performed at temperatures of 25°F (–4°C), 5°F (–15°C), –10°F (–23°C), and –40°F (–40°C). Also, the freezing mode was varied so that the water either froze from the air down to the substrate or froze from the substrate upward. A flowchart that summarizes the major aspects of this investigation is given in Figure D-1.

A cold chamber capable of operating over the range of 32°F (0°C) to –40°F (–40°C) was constructed for the investigation. A complete description of the design, fabrication, and checkout of the cold chamber is presented in Appendix E.

In a typical experiment, five ice samples were grown on a particular substrate at one of the selected combinations of temperatures and freezing modes (see Figure D-2). The substrate was removed from the ice (leaving the ice intact) while still in the cold chamber, and the surface properties of the ice-substrate interface were investigated in accordance with the procedures given in the following sections. Evaluation of the morphology of the ice formed at the ice-substrate interface was made by replication of the ice surface with a thin plastic

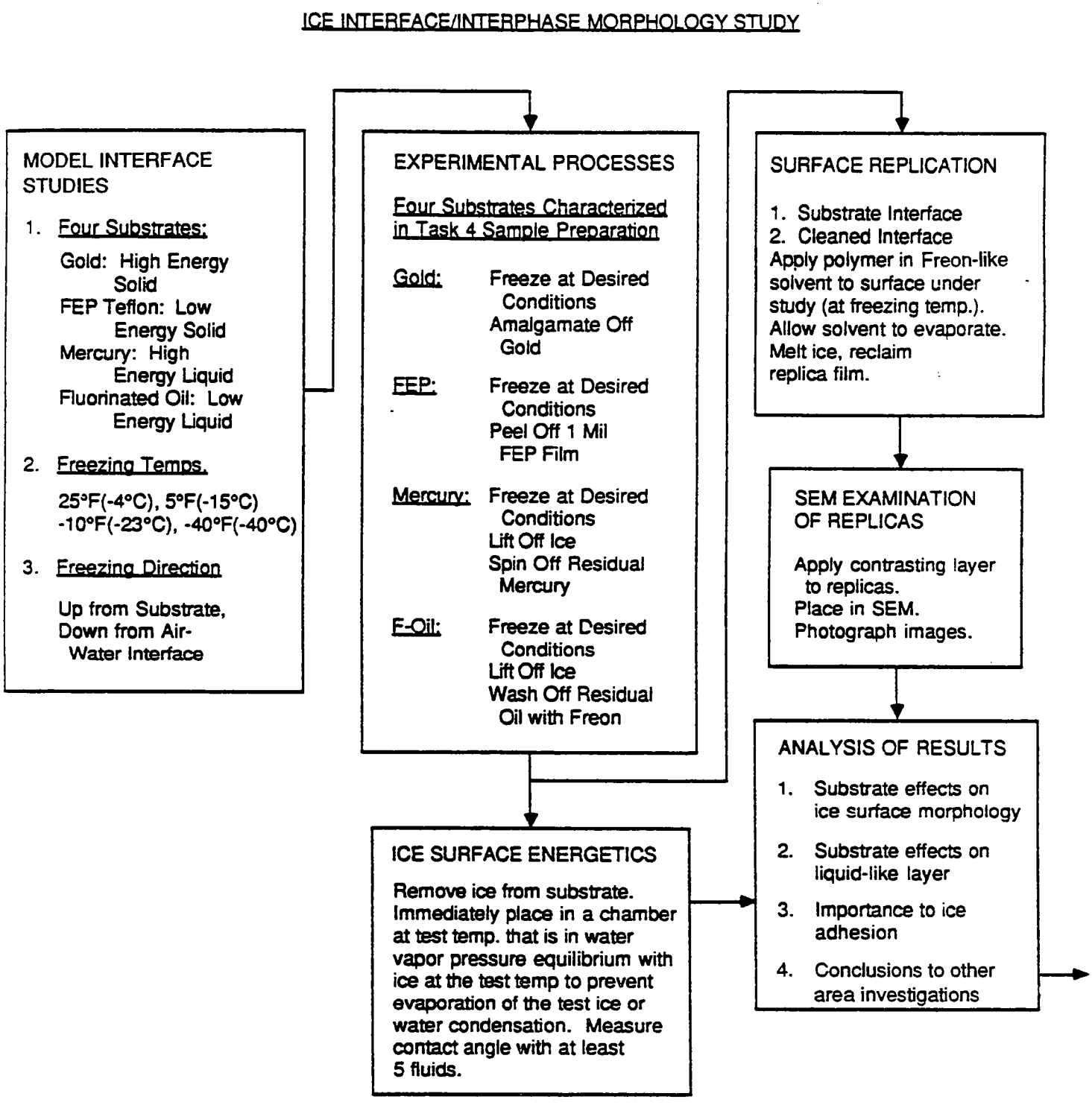

Figure D-1. Flowchart of ice interface/interphase morphology study

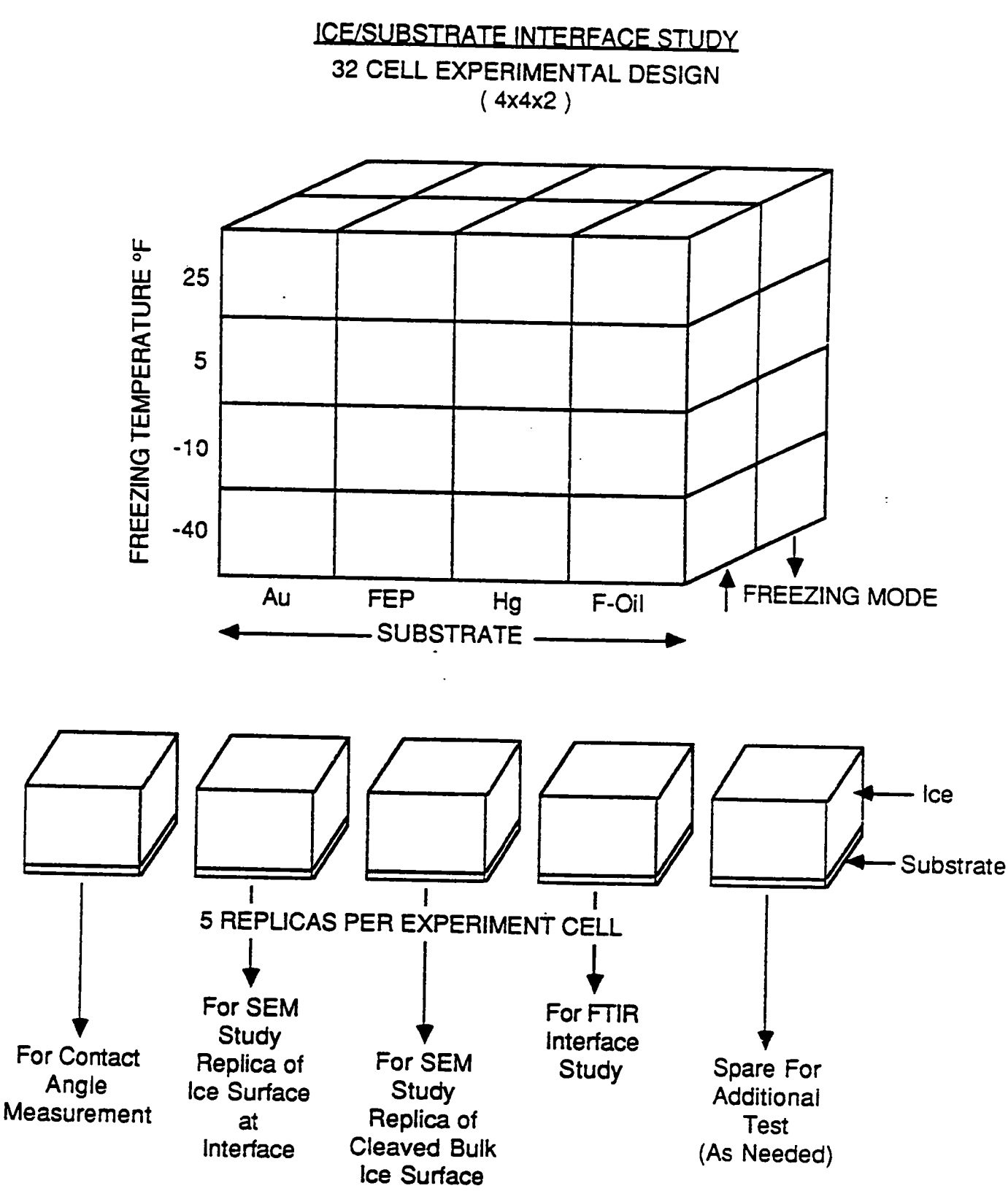

Figure D-2. Test matrix for interfacial ice growth studies

film. Replicas were made of the ice surface that was in contact with the substrate and of the ice surface generated by cleaving the ice specimen perpendicular to the ice-substrate interface. Contact angle measurements were made on the ice surfaces that were in contact with the substrate to measure the surface energetics and determine any changes the substrate may have caused. Determination of the presence or absence of the "liquid-like" layer of the complex interface layers at the substrate was planned using FTIR spectroscopy.

Brief descriptions are presented next of the experimental design established for the investigation, the planned output from the experiments, and the mold design developed for the substrates. These are followed by a discussion of the procedures used in the replication of the ice surfaces and a discussion of the procedures followed and results obtained in making surface energy determinations. Finally, a brief description is given of the spectroscopic measurements that were planned using a FTIR spectrometer. These measurements did not materialize because of logistic problems.

Experimental Design, Experimental Output, and Substrate Mold Configuration

A full experimental design matrix for the interfacial ice growth studies consisted of 32 individual cells (4 substrates x 4 temperatures x 2 freezing directions). A graphical representation of the test cells is given in Figure D-2.

A half replicate of this design was performed with all temperature-substrate combinations and one-half of each of the freezing direction permutations being involved. As shown in Figure D-2, the arrows adjacent to the front row cells of the design indicate the direction of freezing—bottom-up or top-down. The half replicate contains 16 cells.

The planned output of this series of experiments consisted of three sets of observations of the ice formed at the substrate-water interface. These three measurements included: (1) scanning electron microscope (SEM) examination of thin film replicas of the subject ice surface and of the surface formed when the ice specimen is cleaved, (2) determination of the contact angle of selected fluid(s) on the substrate-generated ice surface to describe the ice surface energetics, and (3) if possible a Fourier transform infrared (FTIR) spectroscopic examination, by reflection of the substrate-generated ice surface.

A simple mold design was chosen to accommodate all four substrates. The molds consist of 2-in (5.1-cm) square pieces of 0.25-in (0.64-cm) thick PTFE (polytetrafluoroethylene)

containing a 1.325-in (3.37-cm) mean diameter center hole. The diameter of the hole was 1.5 in (3.8 cm) on the lower surface and 1.25 in (3.18 cm) on the upper surface of the PTFE square. Thus, the interior mold walls were tapered to allow easy removal of the ice sample for examination. Trial runs of freezing and sample handling were made using the FEP Teflon, Mylar, mercury, and fluorinated oil (Du Pont Krytox 1514) with no difficulties being encountered in separation of the ice from the substrate. Impact with a chisel chilled to 0°C was found to be quite effective in producing the cleaved ice surface required for this study.

Replication of Ice Surfaces

It was found possible to form a replicating film of polystyrene on both the flat ice/substrate interface and the cleaved ice surface. A 0.5-wt % solution of polystyrene in methylene chloride (CH_2Cl_2) was applied dropwise from a fine tip dropper to the surface under study in the cold chamber at test temperature by making use of the large insulating extension. The drop rapidly wet and spread on the ice surface and was dry within 30 to 40 minutes at 5°F (−15°C). This thin film could be removed from the ice by use of pressure-sensitive tape placed directly on the cold ice to provide a transfer base. The film and tape were readily removed by a peeling force from the ice. The ice could also be immersed in room temperature water and the replica film floated free as the ice melted. The free film could then be picked up on a microscope slide by careful manipulation or again on pressure-sensitive tape placed directly on the water surface.

These thin films were quite fragile and tended to collapse on themselves on the water surface. An alternate method was developed that provides a much stronger film. This method made use of a 0.5-wt % polyvinyl formal (Formvar) solution and a 5.0-wt % parlodion solution in ethyl acetate. The polyvinyl formal solution was applied to the surface under investigation and allowed to dry at test temperature. A second and much thicker film of the parlodion was then formed on top of the first film. The polyvinyl formal film was insoluble in the ethyl acetate solvent carrying the parlodion and retained its replication on the ice surface. This composite replica was readily picked up from a water surface onto a microscope slide.

The replica films from 12 of the 16 runs of the four substrates and four temperatures were prepared, shadowed, and examined in the SEM at magnifications up to 20,000X. The gold substrate would release the ice by amalgamation with mercury, thus the gold-ice samples were lost. Examination of the photos from these SEM studies lead to the following conclusions and observations.

- Ice formed on FEP Teflon, Mylar film, and mercury surfaces replicated those surfaces quite well to 500 Å limit of observation.

- Both the 0.5-wt % polystyrene and 0.5-wt % polyvinyl formal solution provided replication of the ice surface to fine detail. That is, the appearance of the replica film from ice corresponded to a replica taken directly from the substrate surface.

- No unusual ice structure was noted on the substrate interface ice samples, except in the case of the polyester (Mylar) film where some damage to the ice was found on removal of the film from the ice.

- The rather complex surface of fractured ice was truly replicated but polymer concentrations greater than 0.5-wt % lead to the entrapment of bubbles in the replica film. At 0.5 wt %, this phenomenon was nearly eliminated. Some surface structure was visible in the fracture replicas at greater than 1,000X which may have been crystal ends or defects.

- No photograph showed the existence of an interphase layer. Observations of the edge of the ice fracture adjacent to the substrate interface were not obtained in all samples.

- About 25% of the fracture surface replicas were lost because of collapse of even the backed up replicas.

- The ice structure under the interface layers was readily demonstrated by allowing the ice to evaporate at test temperature. The ice saturating column was removed from the dry N_2 inlet. Progressive etching for 10 to 60 minutes created even deeper patterns of crystal structure.

Surface Energies

Contact angle measurements were utilized to describe the surface energetics of ice removed from substrates. For these measurements ice was grown on various substrates in Teflon molds. These molds consisted of square pieces of Teflon, 50 mm on a side and 6 mm thick, through which a 34-mm diameter hole had been bored. The molds were placed on the substrate of interest and 4.1 mL of doubly distilled water was placed in the hold in the mold. When frozen, a circular piece of ice ~ 30 mm in diameter and ~ 5 mm thick was produced in these molds. These molds were the same as were used in the interface replication experiments. The weight of the mold was sufficient to keep the water from seeping between

the substrate and the mold. The substrate with the mold and water, all at 0°C, was placed in the cold chamber at a preselected temperature. The water was frozen in either of two directions. To freeze the water up from the water-substrate interface down to the water-substrate interface, a piece of corrugated cardboard was placed under the substrate to insulate it on the bottom. This procedure was the same as that used in morphology study.

To study the ice interface, the mold and the ice it contained were inverted and the substrate removed exposing the surface of the ice that was against the substrate. It is on this surface that the interface experiments were performed. The manipulation of the mold containing the ice was done through a small 5- x 10-cm opening in the cold chamber. The cold chamber was kept under slightly positive pressure to keep room air from entering the chamber which would have allowed moisture in the room air to condense as frost on the samples.

Contact angle measurements were performed on ice grown against FEP Teflon, Krytox 1514 oil, and mercury substrates. For the FEP Teflon substrates, 2.5-cm-square samples were cut from a 0.05-mm thick sheet and placed on top of a glass plate for support. The fluorinated oil substrates were created by placing a drop of the Krytox 1514 oil on one of the before-mentioned FEP Teflon samples and spinning the piece on a rotating table to spread the oil. The oil-coated FEP sample was then placed on top of a glass plate for support. Ice was grown on mercury by placing the Teflon mold on the mercury.

Maintaining a clean surface on the ice was one of the major problems encountered in these experiments. In some cases, water vapor in the air condensed and froze on the surface of the ice sample. Ice crystals that had formed on the walls of the cold chamber sometimes became loose and deposited themselves on the surface of the ice sample. Both of these situations created an ice specimen that was no longer a sample of the ice-substrate interface. Even when a position on the ice sample could be found that was free of extraneous ice on which to run a contact angle measurement, excess ice crystals often blocked the optical path in the Rame-Hart goniometer making accurate measurements difficult. Data had to be discarded when excess ice crystals or a layer of frost deposited on the ice sample.

All of the liquids used in the contact angle measurements for the characterization of solid substrates were investigated for use in the contact angle measurements on ice. Glycerol, methylene iodidie, 1,2-dibromoethane, tricresyl phosphate, hexadecane, and *n*-methyl formamide all froze before a drop could fully form and a contact angle measurement could be taken.

All other liquids except one were found to wet and spread on the surface of the ice. The only liquid that did not wet and spread on the surface or freeze was α-bromonaphthalene in the

series reported. These results were found on ice grown at all of the temperatures tested (–4°C, –15°C, –23°C, and –40°C), on the three substrates tested (FEP Teflon, fluorinated oil, and mercury), and for both directions of freezing.

Mercury as a test liquid was additionally investigated. It was chosen because it was expected to not wet the ice surface and to remain liquid at all but the lowest temperatures. Contact angle measurements were made with mercury on ice surfaces at –40°C. The mercury formed discrete droplets, but the very high contact angles with the ice, imperfections in the ice surfaces, and vibrations in the experimental apparatus made exact measurements impossible. The contact angles measured with mercury were in the range of >120° to >140°.

Results of the α-bromonaphthalene and mercury experiments are summarized in Table D-1. Each contact angle reported was for a drop in which 2 to 4 additions of liquid were made. After 2 to 4 additions, the drop often became too large to measure accurately or grew too large and overran imperfections in the ice. If the contact angle of the drop had not stabilized in 2 to 4 additions, the measurements on the drop were discarded. After the contact angle had been measured, the drop was removed with a pipet. A ring was left at the outer edge of the drop, but no depression was left in the ice, indicating that the liquid had not melted the ice underneath it.

Contact angle measurements on ice grown against a mercury substrate were particularly difficult. Early experiments confined the mercury to a container approximately the size of the ice mold. The mercury formed a meniscus that the water and the subsequent ice conformed to, thereby forming a concave surface. This curvature of the surface was large enough to prevent a goniometer measurement of the contact angle. Attempts to get a rough estimate of the contact angle by tilting the goniometer so that it no longer sighted along the surface were unsuccessful. Later experiments on mercury were performed by floating the mold on the surface of a pool of mercury. This minimized the meniscus to ~ 0.5 mm and made approximate contact angle measurements possible with a tilted goniometer. This method had additional problems, however, in ice grown down from the water-air interface towards the water-mercury interface. The ice as it grew expanded unevenly and pushed itself down into the mercury, leaving a very uneven surface on which to measure contact angles.

Contact angle measurements were made on ice surfaces grown at the ice-air interface. Problems were encountered in growing a sample that was flat enough to perform a contact angle measurement. Samples grown in molds produced ice surfaces that were too irregular for contact angle measurements.

Table D-1. Contact angle measurements with α-bromonaphthalene and mercury on ice surfaces grown against various substrates[a]

Temperature	Substrates			
	FEP Teflon	Krytox 1514	Mercury	Air
−4°C	[b] Down	54,54,70,60,59 Down	[d] Up	–
−15°C	36,38,40,41 Up	54,47,47,40,41 Up	[e] Down	40,43,38
−23°C	40,38,40 Down	42,39,41,30 Down	35,30,39,30 Up	40,41,42
−40°C	(Hg >120)[c] Up	(Hg > 120)[c] Up	48,45 (Hg > 140)[f] Down	–

[a] The contact angles are reported in degrees. The direction "Up" or "Down" indicates the direction in which the ice was grown. All of the contact angles shown in the mercury column are approximate due to difficulties in obtaining a flat ice surface with the mercury substrate.

[b] Frost on these samples made measurements impossible.

[c] These sets of conditions need to be repeated to improve the accuracy of the reported measurements. The mercury measurements (Hg > 120) indicate approximate contact angle measurements made using mercury as the liquid. Only rough estimates could be made of the contact angles due to optical difficulties.

[d] This set of conditions was not attempted.

[e] Curvature of the ice due to the mercury meniscus made contact angle measurements impossible.

[f] The mercury measurement (Hg > 140) indicates approximate contact angle measurement made using mercury as the liquid.

To solve this problem, ice was grown in a mold against a piece of FEP Teflon mounted on a glass plate to get a flat surface to work with. This part of the procedure was similar to that used in the ice-FEP Teflon interface measurements. After removal of the FEP Teflon, two applications of water were made to the surface to remove any influence the FEP Teflon may have had on the surface. The sample was frozen after each application of water. Each application produced a film of water that was ~0.5 mm thick. The sample was then transferred to the cold chamber. Just before introduction into the cold chamber, the sample was brought in contact with a glass plate that was at room temperature. This recreated a water film on the surface of the ice. This procedure did not produce perfectly flat ice samples, as some irregularities were still observed, but areas of the samples were level enough for the contact angle measurements. Measurements on these samples produced results similar to that of ice grown at the FEP-, Krytox 1514-, and mercury-ice interfaces. These results were also presented in Table D-1.

In the case of the contact angle measurements made on ice grown against a Krytox 1514-covered substrate, widely varying values were obtained, probably due to residue of the fluorinated oil on the ice. These ice specimens were often visually more reflective in appearance. If enough of the oil remained on the surface of the ice, liquids placed on the ice would see a fluorinated hydrocarbon type surface and act accordingly. In some cases, an initial drop would have a contact angle as high as ~ 70°, and as liquid additions were made to the drop, the contact angle would drop to the 40° range. This was probably due to the drop being initially placed on a part of the ice that had a large residue of the Krytox 1514 on the surface. As the drop advanced, it spread into areas where the film was thinner and the α-bromonaphthalene then came in direct contact with the ice and acted accordingly. In measuring with other liquids, dipropylene glycol and ethylene glycol wetted the surface and spread, penetrating the oil film to come in direct contact with the ice.

Attempts to wash the ice surface with methylene chloride before the contact angle measurements resulted in a surface that visually appeared rougher. A close comparison could be made to a smooth cut, but unpolished piece of silica. The methylene chloride wash may have removed the Krytox 1514, but it also altered the surface, as the α-bromonaphthalene was now wet and spread on the ice surface.

In summary, with the exception of the contact angle measurements made on ice grown on Krytox 1514, all of the contact angle measurements gave similar results. The effect of the substrate on the ice-substrate interface was not measurable using the sessile drop contact angle method employed in these studies.

Fourier Transform Infrared (FTIR) Spectroscopy

Spectroscopic measurements using the Analect FTIR spectrometer were planned to investigate the ice-substrate interface. It was initially planned to obtain a reflectance measurement using the microscope attachment on the Analect FTIR spectrometer. Reflectance measurements were selected over transmittance measurements for the initial study because of the increased sensitivity of the reflectance measurement to surface properties. Jellinek has postulated and reported evidence for a liquid-like layer on the ice interface that is ~ 1 nm thick.[25,26] Even with an ice sample of only 1-mm thickness, this would indicate that differences in the spectra due to the ice at the interface would be only on the order of 1 part in 10^6.

The Analect FTIR spectrometer microscope attachment was configured for samples of 9 mm or less in thickness. It was impossible with the experimental apparatus to position the sample at the focal point of the microscope attachment. The cooling plate on which the ice sample had to rest was over 12 mm in thickness alone. If the cooling plate could have been reduced to 6 mm in thickness and samples of ice of 3 mm in thickness could have been grown and manipulated on the microscope stage, then it might have been possible to make a measurement. However, this would have left no room for insulation or for any irregularities in sample thickness. The mechanical problems cited, coupled with other limitations, prevented measurement of ice surface properties by FTIR spectroscopy.

Appendix E

Cold Chamber Operational Requirements, Design, Fabrication, and Checkout

Operational Requirements for Cold Chamber

Listed below are the major operational requirements for the cold chamber required for the ice growth and initial undercutting studies conducted in the program:

1. Temperature range: 0° to –40°C (32°to –40°F)

2. Humidity: At equilibrium with ice at the test temperature to avoid evaporation and/or condensation on the ice test surface.

3. Cool-down rate: No more than 1 hour for chill plate to reach equilibrium and 2 hour for air temperature.

4. Temperature control: ±1°C (±1.8°F).

5. Window: At least 12- x 12-in (30.5- x 30.5-cm) triple-glazed window to allow color photographs to be made of the test specimens. Window must not fog.

6. Infrared observation port: A port suitable for allowing use of an Analect Model XTR FTIR Microscope for IR spectra determination of ice structure at test conditions.

7. Chamber: Must operate at slight positive air pressure to prevent room air (and humidity) ingress. This requires injection of precooled and humidity controlled air.

8. Sample selector: A remote mechanical means for moving and rotating samples in the chamber without changing chamber environment.

9. Portability: Entire unit must be portable to allow transport to the FTIR microscope and to the Rame-Hart Goniometer for measurements.

10. Liquid injector: A method for injection of test fluids and water onto the test specimens.

The above list contained only the major requirements, which were rather awesome. It indicated that a freezing chamber must be fabricated because no commercial units were available that would be satisfactory even with extensive modification.

Prototype Chamber Fabrication

The test requirements call for –40°C (–40°F) operation. If two-stage electromechanical refrigeration units were used, they would be large and bulky and difficult to make portable. Therefore, liquid nitrogen was selected as a chilling source because it can be stored in a wide range of Dewar capacities and is relatively low in cost. A heat exchanger consisting of a foam-insulated 2-gal (7.6-L) capacity cylinder; two 3/8-in (0.95-cm) diameter copper tubing coils; an insulated cover; and a stirrer motor was assembled. The larger coil, which just clears the interior diameter of the cylinder, was the chill coil through which the discharge from a Du Pont Model DMA 50-L liquid nitrogen storage tank was passed. The smaller, interior tubing coil was used as a means for chilling a secondary coolant fluid flow. The heat exchanger was also fitted with a set of tubing ports that allowed transfer of the primary fluid coolant from, and return to, the bulk exchanger fluid. For this preliminary trial, manual control of liquid nitrogen flow was used to control temperature.

A 1-ft^3 interior (30.5-cm x 3.5-cm x 3.5-cm) insulated prototype chamber was fabricated from 2-in (5.1-cm) thick polyurethane foam board stock that was coated on each side with heat reflective aluminum foil. Three layers of this board were used, thus making the wall of the trial chamber 6 in (15.2 cm) thick. A window 16 x 16 in (40.6 x 40.6 cm) square was made which consisted of three layers of 1/8-in (0.32-cm) thick polymethylmethacrylate separated by 2-in (5.1-cm) thick layers of the foil-faced urethane foam with foil surfaces facing the exterior and interior of the window edges. Paper tubing about 1 in (2.5 cm) diameter was filled with a desiccant (anhydrous calcium sulfate) and placed around the interior periphery of the two layers of the window to absorb moisture and prevent interior window fogging at low temperature. Assembly of these pieces of insulation and the window produced a cube of 24-in (61-cm) dimension externally with a 12-in (30.5-cm) interior cube dimension.

A 12-in x 12-in (30.5-cm x 30.5-cm) chill plate, consisting of 1/4-in (0.64-cm) thick copper plate fitted with flattened [to 1/4-in (0.64-cm) height] 3/8-in (0.95-cm) diameter copper tubing soldered to its lower surface, was placed in the bottom of the interior chamber. The input-output tubing passed through a vertical wall of the chamber. A 100-ft^3/minute (2,832-L/minute) "pancake" fan was placed on an interior vertical wall with a 2-in (5.1-cm) standoff present to supply positive air circulation. A planar air cooling coil of 3/8-in (0.95-cm) copper tubing was placed on the interior vertical wall opposite the "pancake" fan. The window was covered with an additional layer of the foam insulator board that could be readily removed when photographs are required.

For the initial test, a commercial chill bath (Haake) was used to supply a flow of chilled water-glycol through the plate and air coil. Slow shipment of a solenoid-operated liquid nitrogen control valve forced the use of this bath instead of the heat exchanger. It was found that the chill plate would reach equilibrium in less than 2 hours but not in 1 hour at an operating temperature of −15°C (4°F), indicating that higher fluid flow was required than supplied by this bath (≡ 1 L/minute). By using other commercial chill bath (Forma Sci. Model No. 2095) with a 1.8-L/minute pump rate and a low temperature limit of −19°C (−2°F), it was possible to obtain a plate temperature of −11°C (12.2°F) and an air temperature of −4°C (25°F). This showed that an increased pump rate was required as well as increased air cooling coil area and exchange capacity.

Upon receipt of the solenoid-operated, liquid nitrogen service-rated valve, the heat exchanger was plumbed to the liquid nitrogen storage tank. A 9-L/minute centrifugal pump was used to transfer the 44 vol. % water, 56 vol. % ethylene glycol fluid from the heat exchanger through the plate and coil of the freezing chamber. Several runs were made to determine operational capabilities. The heat exchange fluid was found to form a slush at −49°C (−56°F) stopping the pumping action. At a heat exchanger temperature of −45°C, the lowest obtainable plate temperature was −30°C (−23°F), and an air temperature of −22°C (−8°F) was reached with the prototype chamber, which is still well above the −40°C (−40°F) goal. It was found that the increased viscosity of the glycol-water mixture at these temperatures reduced pumping speed to ≡ 0.3 L/minute).

Criteria for Working Cold Chamber

Fabrication of the simple prototype freezing chamber provided sufficient information to develop a workable final design for the freezing chamber. The following specifications were developed:

1. Three layers of 2-in (5.1-cm) thick, double foil coated urethane foam board is satisfactory. Warm up rate for the prototype was only 1°C/10 minutes with pump off.

2. The glycol-water mix must be replaced with a low viscosity fluid [i.e., propylene glycol monoethyl ether, pour point −130°F (−90°C), flash point 110°F (43°C)].

3. Three sets of air cooling coils are needed in the freezing chamber.

4. The 9-L/minute pump is probably adequate for low fluid viscosities.

5. The triple-glazed window design was workable. (No fogging was observed with the prototype at the lowest obtainable air temperatures of −22°C (−8°F).

6. The heat exchanger capacity was more than adequate because the liquid nitrogen valve open time was quite low (≅ 10%).

7. The interior space should be expanded to 18 x 18 x 12 in (45.7 x 45.7 x 30.5 cm) high to accommodate a 16-in diameter rotating chill plate, to allow movement of samples to then FTIR-contact angle port.

8. An Omega Model 4201 RTD-type temperature controller was obtained for controlling the heat exchanger bath temperature through the solenoid-operated liquid nitrogen control valve.

Fabrication of Working Cold Chamber

The working cold chamber was constructed so that it encompassed all of the above requirements and design criteria. An additional feature was added to the final configuration that allows movement of ice samples to three different, removable ports for sample manipulation and ice surface characterization by FTIR and contact angle measurements while the samples were kept chilled to the desired temperature and in the chamber environment.

Major Components and Design Configuration

The five major components of the final cold chamber configuration are described below.

Chamber Shell

Three layers of 2-in (5.1-cm) thick polyurethane foam board stock form the four walls and base of the chamber, which is 18 x 18 x 12 in (45.7 x 45.7 x 30.5 cm) high inside and 30 x 30 x 22 in (76.2 x 76.2 x 55.9 cm) high outside.

Top Window

Three layers of 1/8-in (0.32-cm) thick Lucite polymethylmethacrylate (55.9 x 55.9 cm) separated by 1 7/8-in (4.8-cm) dry dead air space. The two dead air spaces contain, in filter paper tubes, anhydrous calcium chloride desiccant to ensure that no clouding of the window occurs at low temperatures. This window provided an 18 x 18 in (45.7 x 45.7 cm) optical opening into the cold chamber for ready illumination and photographing of ice samples being evaluated at low temperatures.

Rotating Chill Plate Assembly

A sketch of this assembly is shown in Figure E-1. This assembly consists of a 16 in (40.6 cm) diameter by 0.25 in (0.64 cm) thick circular copper plate with a 3 in (7.6 cm) wide by 14.5 in (36.8 cm) long side arm. Copper tubing with 3/8-in (0.95-cm) OD was formed into a special coil shape with a single 14 in (35.6-cm) long loop 2.5-in (6.4-cm) wide. This shaped tubing was then pressed flat to a 0.25-in (0.64-cm) thickness and soldered to the copper chill plate with a lead/tin eutectic solder. Approximately 24 ft (732 cm) of copper tubing was used in this chill plate assembly, which is placed on the bottom interior of the chamber shell.

A 16-in (40.6-cm) diameter by 0.25-in (0.64-cm) thick circular aluminum plate was fitted with a 0.5-in (1.3-cm) diameter centered Teflon shaft and pulley. The shaft passed through a corresponding hole in the copper plate. Two 16-in (40.6-cm) diameter by 0.005-in (0.13-cm) thick sheets of Teflon were placed between the upper surface of the copper plate and the bottom of the aluminum plate to act as a lubricant for easy rotation. The 6-in (15.2-cm) diameter pulley wheel was attached to the shaft on the reverse side of the copper plate. Pull wires were attached to the pulley wheel. This assembly was placed in the interior bottom of the chamber shell with 2 in (5.1 cm) of the insulating foam removed to accommodate the pulley wheel. the 30 gauge pull wire cable passed through plastic tubing bushings in the chamber wall. A tapered brass steel ram about 4-in (10.2-cm) long was placed next to the rotatable aluminum plate on the copper sidearm to allow easy movement of ice samples on

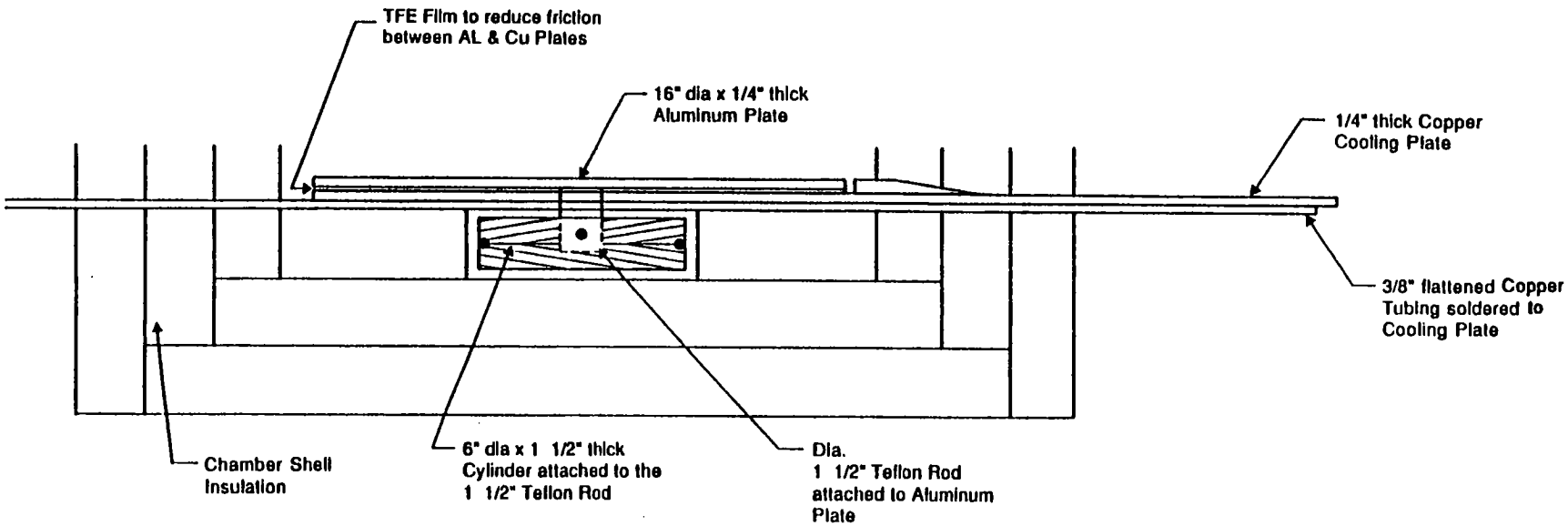

Figure E-1. Side view of turntable

the chill plate and sidearm. The top aluminum plate could readily be rotated in excess of 360°, thus providing the desired sample location flexibility.

Temperature Control System

Liquid nitrogen was chosen as the basic heat sink for reaching the required –40°F (–40°C) low temperature limit. A 50-L Dewar was mounted in a special cart that held the cold chamber and ancillary equipment. This cart was 30 in (76.2 cm) wide by 60 in (152 cm) long with the top surface 30 in (76.2 cm) from the floor. It consisted of a steel box frame, four swivel wheels, a top surface and a bottom shelf 19 in (48.3 cm) below the top surface. This arrangement was necessary to meet the portability requirements stated previously.

Liquid nitrogen was fed, under control of an Omega Model 4201 RTD-type temperature controller to a fluid-filled heat exchanger via 3/8-in (0.95-cm) copper tubing. The chilled fluid (propylene glycol monomethyl ether) was circulated to the air cooling coils and then to the chill plate and sidearm as shown in Figure E-2. The fluid was then returned to the heat exchanger. The air cooling coils consist of four loops of 3/8 in (0.95-cm) copper tubing soldered to three 10- by 16-in 20-gauge copper plates. These plates cover three of the four interior walls of the chamber. A 100 ft^3/minute (2,832 L/minute) "muffin" type fan was mounted on the fourth wall, as shown in Figure E-2, to provide a high air circulation rate.

In order to prevent moisture condensation on the ice held in the chamber or evaporator, it is necessary that the water vapor pressure of the atmosphere in the chamber be identical to that of ice at the chamber temperature. The ice surface characterization experiments to be performed demand a stable surface for at least 1 hour at test temperature. This requirement was met by installing an ice-packed saturator in the cold chamber. Dry air or nitrogen is passed through a coil of copper tubing immersed in the heat exchanger to bring it to approximate chamber temperature. This cooled gas was then passed through the chamber wall, by 1/4-in (0.64 cm) diameter copper tubing, and its final temperature was brought to the chamber temperature as it passed through 2½ turns of tubing on the inside wall of the cold chamber. This temperature-normalized gas was then passed through a 2 in (5.1 cm) diameter by 10 in (25.4 cm) high column of packed ice cubes held in a length of plastic pipe, and then to the chamber interior. This scheme assures the proper water vapor pressure for any operating temperature.

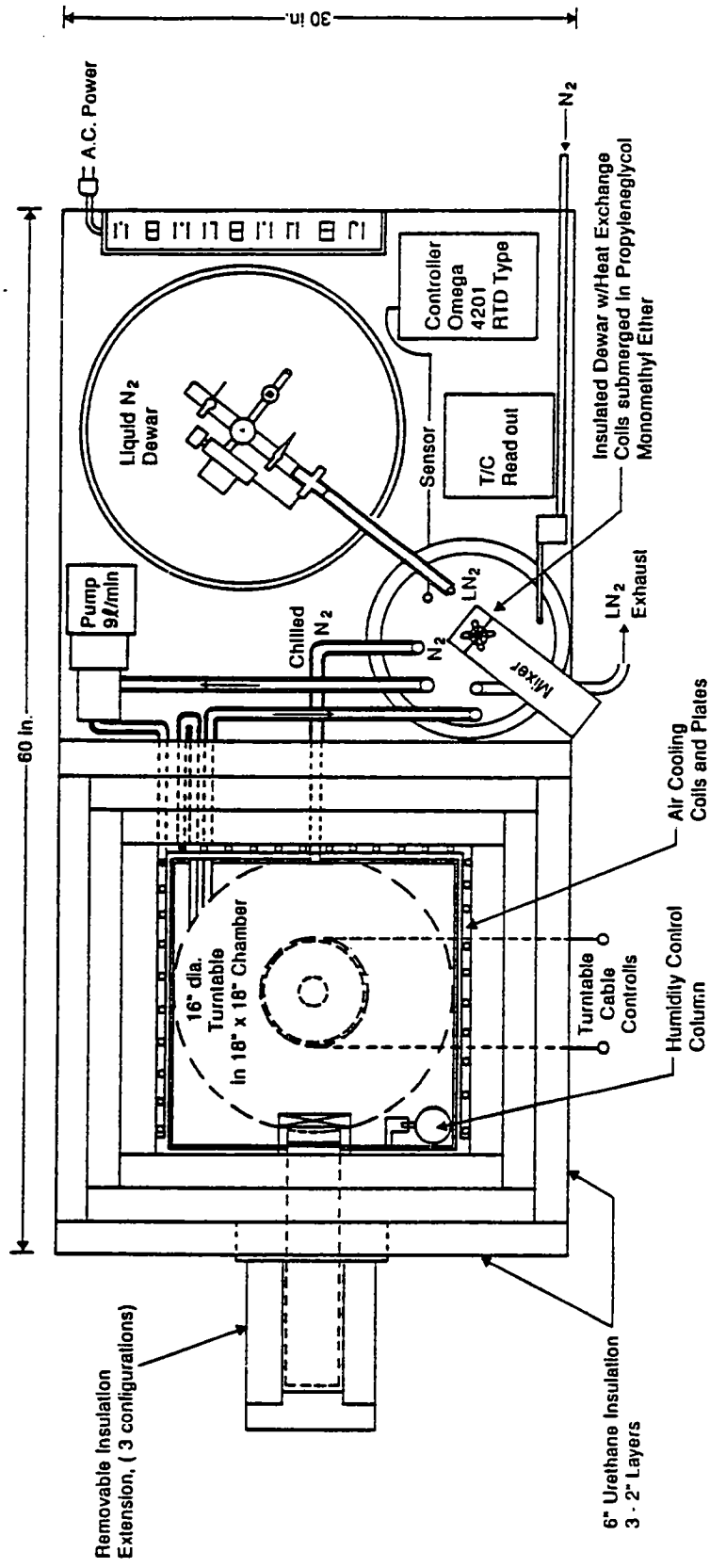

Figure E-2. Top view of cold chamber

Sidearm Insulation and Instrument Porting

The copper sidearm extends 7.5 in (19.1 cm) past the external wall of the cold chamber shell. Three different insulative cover sets were fabricated, each one to serve a different purpose, as described below. The extensions were designed for removal and exchange as required by the work underway.

Sample Manipulation and Undercutting Extension. The manipulation extension shown in Figure E-3A had an interior space that was large enough to allow handling of the 4- x 8-in (10.2- x 20.3-cm) undercutting samples as well as the 2- x 2-in (5.1- x 5.1-cm) molds used to form the ice for the interface studies. The end opening allowed movement of these samples by hand-held insulated probes. The opening on the top of this extension allowed additional handling by chilled plastic forceps for removal of ice samples from their molds and addition of the chilled undercutting solutions into the preformed holes in the ice/substrate test plate.

Contact Angle Extension. As shown in Figure E-3B, this extension was smaller, in order to fit on the Rame-Hart Goniometer. The side windows were of triple glass construction to provide insulation, freedom from clouding, and suitable optical properties to allow measurement of the drop contact angle. The drop was fed onto the surface under study through a microsyringe.

FTIR Extension. This extension, shown in Figure E-3C, had quite thin walls as dictated by the space available in the Analect Model XAD FTIR unit. An additional insulating slip-over box was kept in place until just prior to the 2-minute long IR scan of the subject ice surface. The silver chloride (AgCl) window consisted of an internal window and an external window mounted on a length of plastic tubing containing dry air. The IR beam that passed through these windows was reflected back into the microscope from the ice surface under study and was digitally processed by the FTIR unit.

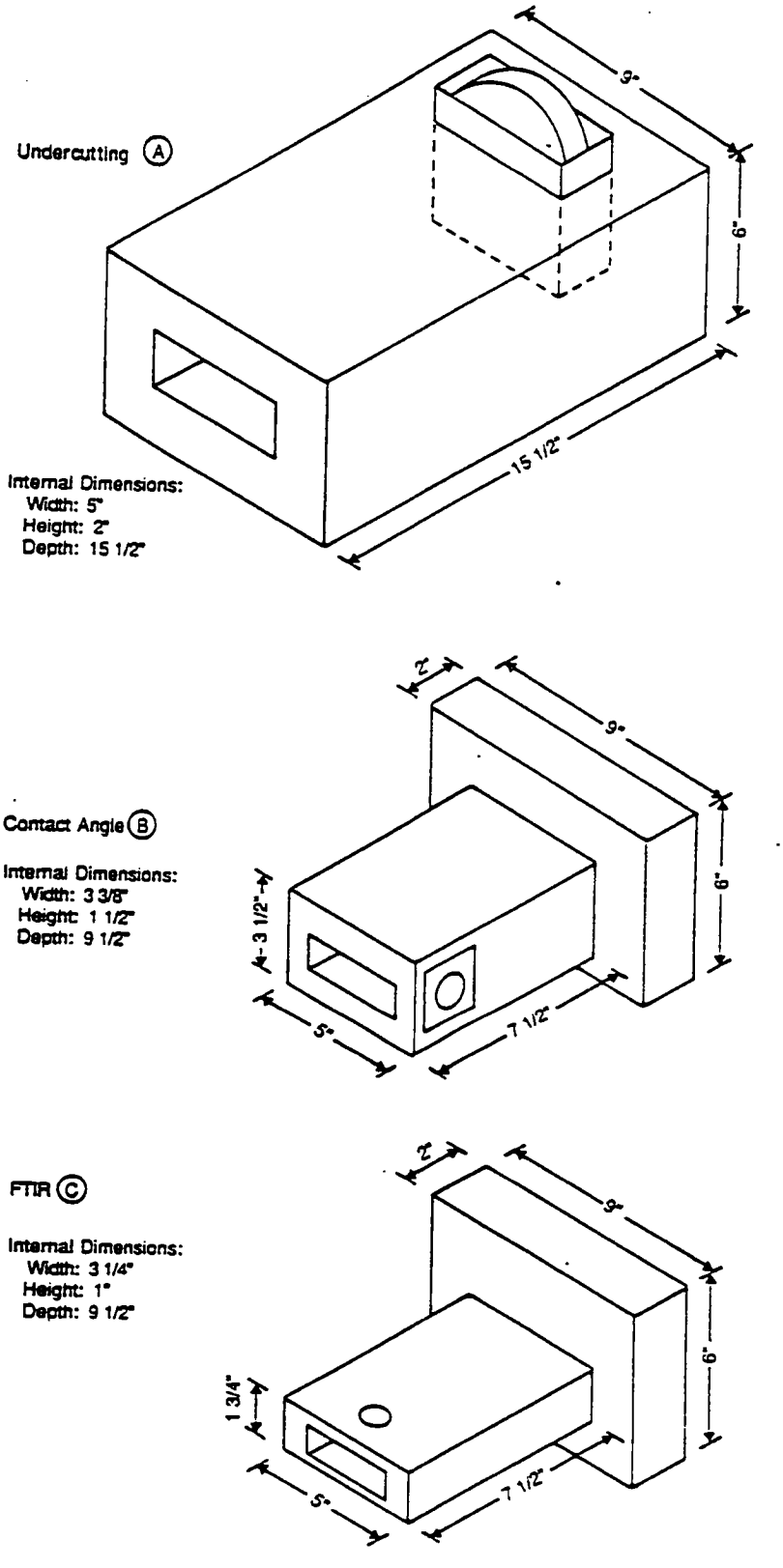

Figure E-3. Extension insulation sleeves

Chamber Trial Operations

The initial runs were done to determine the circulating fluid temperature required to produce the desired chamber temperature of 25°F (–4°C), 5°F (–15°C), –10°F (–23°C), and –40°F (–40°C). An additional requirement was created by the fact that the proportional control off-set range of the Omega Model 4201 RTD controller-indicator was not large enough to accommodate the response characteristics of this rather complex system. Thus, it was necessary to make the "set" temperature point of the controller higher than the desired fluid temperature. A series of runs were made to determine what actual set and fluid temperature were required. Type "E" thermocouples were installed at the bottom of the copper plate adjacent to the center shaft hole, 1 in from the far end of the extension plate, and in the interior of the cold chamber to determine the air temperature, and an additional thermocouple was used to monitor other points as needed.

The analog outputs of the four digital thermometers were continuously monitored by two twin-pen strip chart recorders. A summary of the results obtained are shown in Table E-1. Performance of the chamber was quite good as temperature equilibrium from room temperature start-up was reached in less than 2 hours, even at the –40°F (–40°C) operating condition. The largest temperature differential between the air and plate occurred at the –40°F operating condition and was 2°C (3.6°F); at higher temperatures the differential was less. This difference was sufficiently small to allow the testing to proceed. The top window showed no fogging at any of the test temperatures over an 8-hour operating time. Only a very light coating of frost was collected on the cold metal surface and this did not increase or decrease visually with time. The observation showed that the water pressure control scheme worked as planned.

Table E-1. Operating set points for the cold chamber

Desired operating temp. °C (°F)	Controller set temp. °C (°F)	Extension plate temp. °C (°F)	Center plate temp. °C (°F)	Chamber air temp °C (°F)	Controller read out temp. °C (°F)
–4(25)	–4.0(25)	–4(25)	–5(23)	–4(25)	–8.1(17.4)
–15(5)	–14.9(5.2)	–15(5)	–16(3)	–14(7)	–19.1(–2.4)
–23(–10)	–23.0(–9.4)	–22(–8)	–23(–10)	–21(–6)	–27.3(–17.1)
–40(–40)	–40.0(–40.0)	–41(–42)	–41(–42)	–39(–38)	–44.9(–48.8)

Appendix F

Interfacial Shear Strength Test Procedures and Results

General Description of Shear Test Apparatus

The basic system for interfacial shear testing was developed as part of a previous research project, "Investigation of the Basic Forces Involved in the Adhesion of Ice to Highway Surfaces" sponsored by the Federal Highway Administration. It consisted of a Cal-Tester Model TH-5 5,000-lb tester mounted outside a freezer with the loading members passing through the side of the freezer into an insulated, temperature controlled box as shown in Figure F-1. Plastic bushings through the freezer wall allowed for smooth operation of the tester without significant moisture infiltration. The sample holder was mounted to the frame of the testing machine. Temperature control was achieved with a thermistor temperature sensor, an on/off regulator controlling the supply of power to an electric light bulb, and an air circulation fan. When the box remained closed, the temperature could be regulated to within one tenth of a degree Celsius. Further details of the system can be found in Reports DOT/RSPA/DPB-50/79/28 (38), DOT/RSPP/DPB-50-82-5 (39), and the SDSM&T M.S. Thesis of Louie L. Lu and Anthony P. Ewing (40).

Details of Procedure—Substrate Preparation and Evaluation

Six substrates were used in the shear test experiments. Two of these substrates were referred to as model substrates (Pyrex and Teflon) and the remaining four substrates represented components of highway surfaces (limestone, silica, portland cement mortar, and asphalt). The tests were conducted under a combination of temperature (–4°, –9°, –15°, and –23°C), three freezing rates (slow, medium, and fast), and two modes of freezing (bottom-up and top-down).

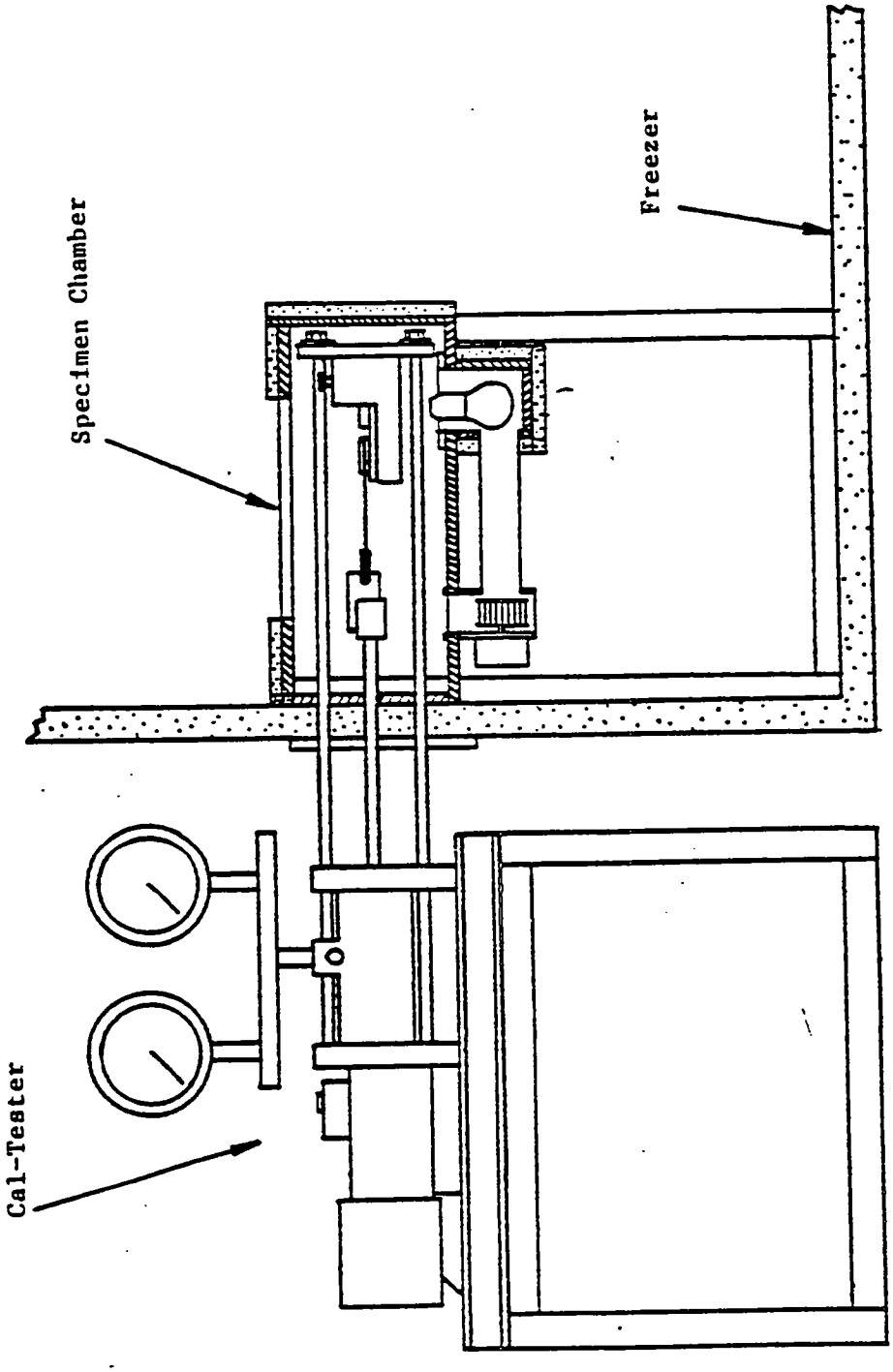

Figure F-1. Shear testing system

The preparation and initial cleaning of the silica and Pyrex glass substrates are described in Appendix B. The cleaning procedure for the other substrates is also described in that appendix. In order to ensure cleanliness, we opted to carry out the cleaning on silica and Pyrex substrates before each use. This was decided when it was found that the cleanliness of the substrate appeared to be deteriorating as testing proceeded (see below for details). After being cleaned and then rinsed in triply distilled water, the specimens were air-dried in the drying container previously mentioned. In order to maintain cleanliness the substrates were handled with rubber gloves each step of the way.

Before fabrication of a shear-test specimen, each substrate was evaluated by a sessile-drop contact angle measurement. This provided information about the particular substrate and a check for possible contamination. The apparatus and procedure for these measurements are described elsewhere. In order to determine the sensitivity of this procedure, it was shown that deliberately running a finger over a Pyrex substrate introduces a 10° change in the contact angle of water. By monitoring the contact angle, it was determined that there was a change occurring on a ground silica substrate as the testing proceeded. For test sequence codes 3312 and 3131, the contact angle with distilled, deionized water was found to increase from about 3° to 23°. It was then determined that cleaning of the silica and Pyrex substrates with hot acid before each test should be performed to ensure contamination-free tests. All but three sets of shear strength tests were conducted following the revised pretest cleaning procedures. These three sets only involved the silica substrate.

Once the substrate was approved for testing, it then had two Teflon rings placed on top of it and water poured into it and frozen. This procedure is discussed below in some detail.

For a number of years, Teflon rings were used in shear test studies[19,20] to contain the water frozen onto substrates. However, it was necessary to add refinements to these rings to make it possible to freeze either from the bottom-up (BU) or from the top-down (TD) over a wide range of freezing rates as called for in the experimental design.

The designs for these Teflon rings are shown in Figure F-2. Standard-size Teflon rings have an inside diameter of 1.572 in (4.0 cm) with a height of 0.435 in (1.1 cm); this provides for a volume of ice of 0.84 in^2 or 17.5 mL. On the outside surface of the ring was a circular depression around which the testing cable fits. For tests using the previously developed standard procedure of pouring water on cold substrates, the rings needed to be held on the substrate only with a rubber band. A small amount of water froze immediately on contact with the cold substrate and formed a seal between the ring and the substrate and thereby prevented leakage. However, even with careful grinding of the substrate surface and machining of the bottom face of the ring, it was not possible to prevent total leakage when

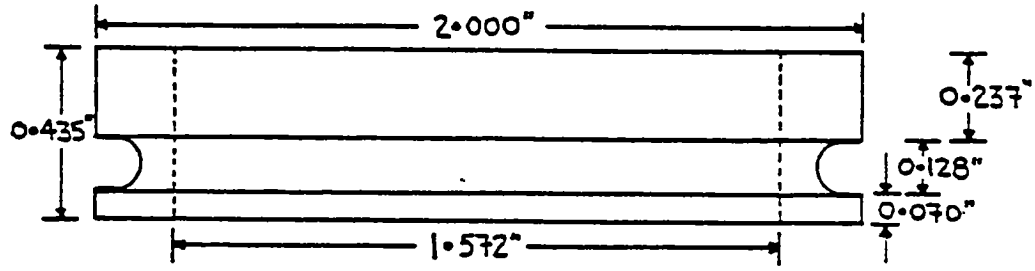

(a) Original type

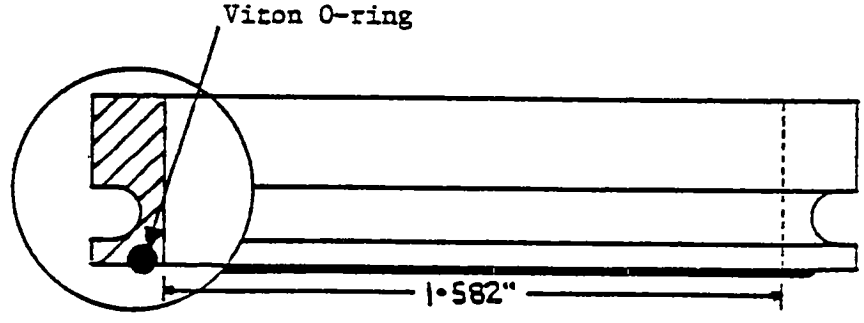

(b) O-ring type

Figure F-2. Teflon ring designs

water and substrate were both at 0°C. Significant amounts of water leaked, especially when freezing was made to occur from the top-down. It was necessary to incorporate an O-ring in the ring as shown in Figure F-3. Tests showed that this design allowed ice to be frozen from the top-down or bottom-up at either fast, medium, or slow rates without leakage problems.

Teflon rings were rinsed with cyclohexane and air-dried before each test. After rinsing they were handled only by the outer surface with rubber gloves in order to reduce the possibility of contamination. Before water was to be poured into the Teflon ring, the ring was first clamped onto the substrate. To ensure even seating of the O-ring type rings, the aluminum clamping jig shown in Figure F-4 was fabricated. The clamp had four wing nuts which were adjusted to supply just the right amount of pressure on the O-ring to achieve a good seal and a consistent inside diameter of the circle of contact.

The exact methodology used in freezing the triply distilled water in the Teflon rings was governed by freezing mode (TD or BU) and the rate of freezing desired. Details of this procedure are as follows.

Details of Procedure—Freezing Mode Procedure

One of the challenges faced during the experiments was to develop two reproducible procedures by which ice could be frozen: (1) from the substrate upward, hereafter referred to as the bottom-up mode, and (2) from the top surface of the water downward to the substrate, which we refer to as the top-down mode. In addition, for each of these two modes, three freezing rates, slow, medium, and fast, were required.

In order to obtain bottom-up freezing, one needs to ensure that the substrate provides the best heat loss path from the water. The fastest rate of freezing was accomplished by placing the substrate directly on an aluminum plate which was on the bottom of a freezer at –25°C. When the substrate cooled to the temperature of the plate, water at 0°C was poured into the Teflon ring until it was nearly full (alternatively, a small amount of water could have been placed in the Teflon ring, and additional water added after this had frozen). A styrofoam lid was placed over the entire assembly to prevent heat loss from the top of the water. Freezing began instantaneously at the substrate and proceeded upward at an approximate rate of 1.0 mm per minute.

The medium rate of freezing was obtained by having the substrate at 0°C and then placing it on an aluminum plate and immediately pouring water at 0°C into the Teflon ring. The styrofoam lid was again placed on top to insure downward heat transfer and thus freezing

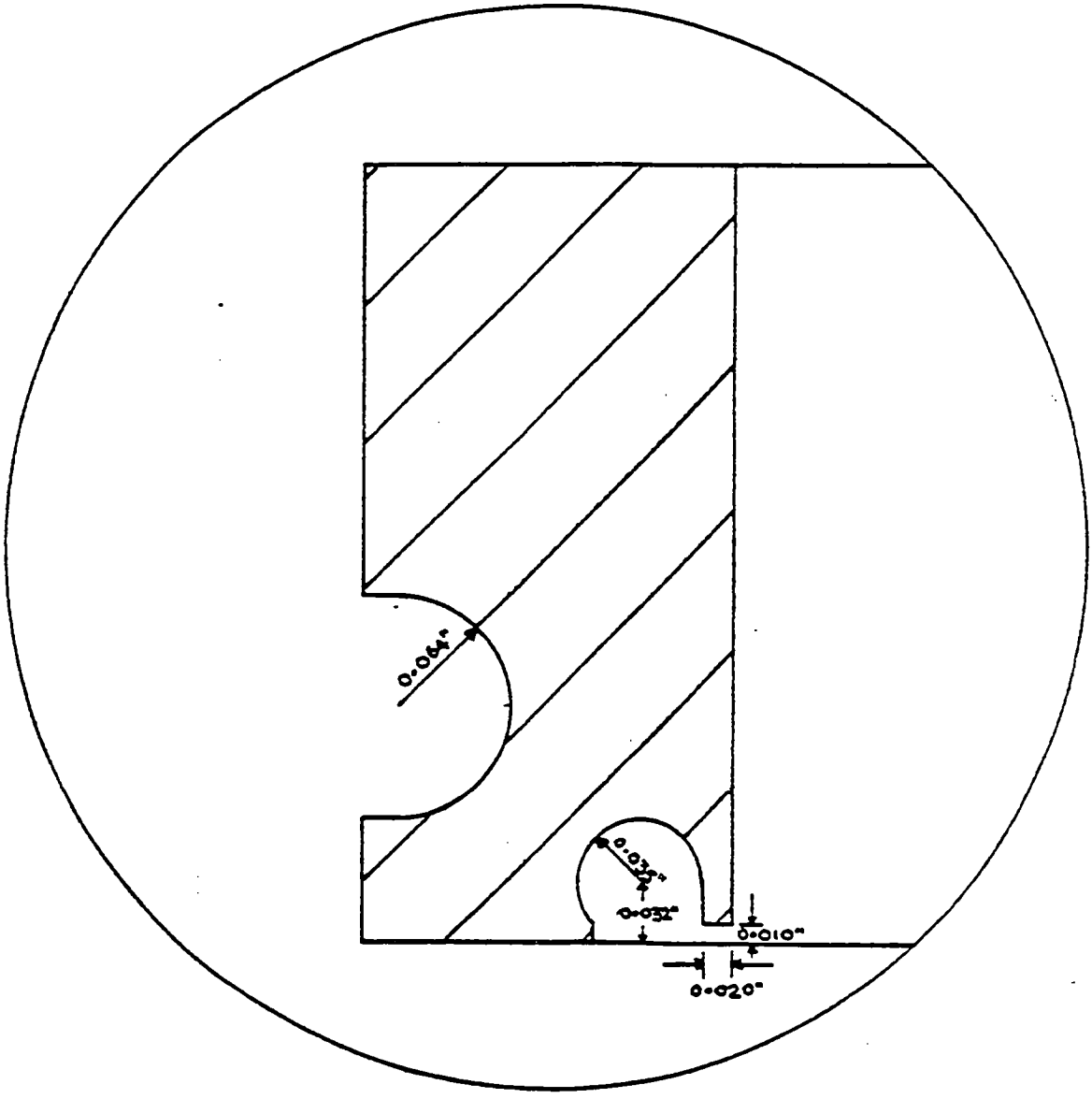

Figure F-3. O-ring type Teflon ring

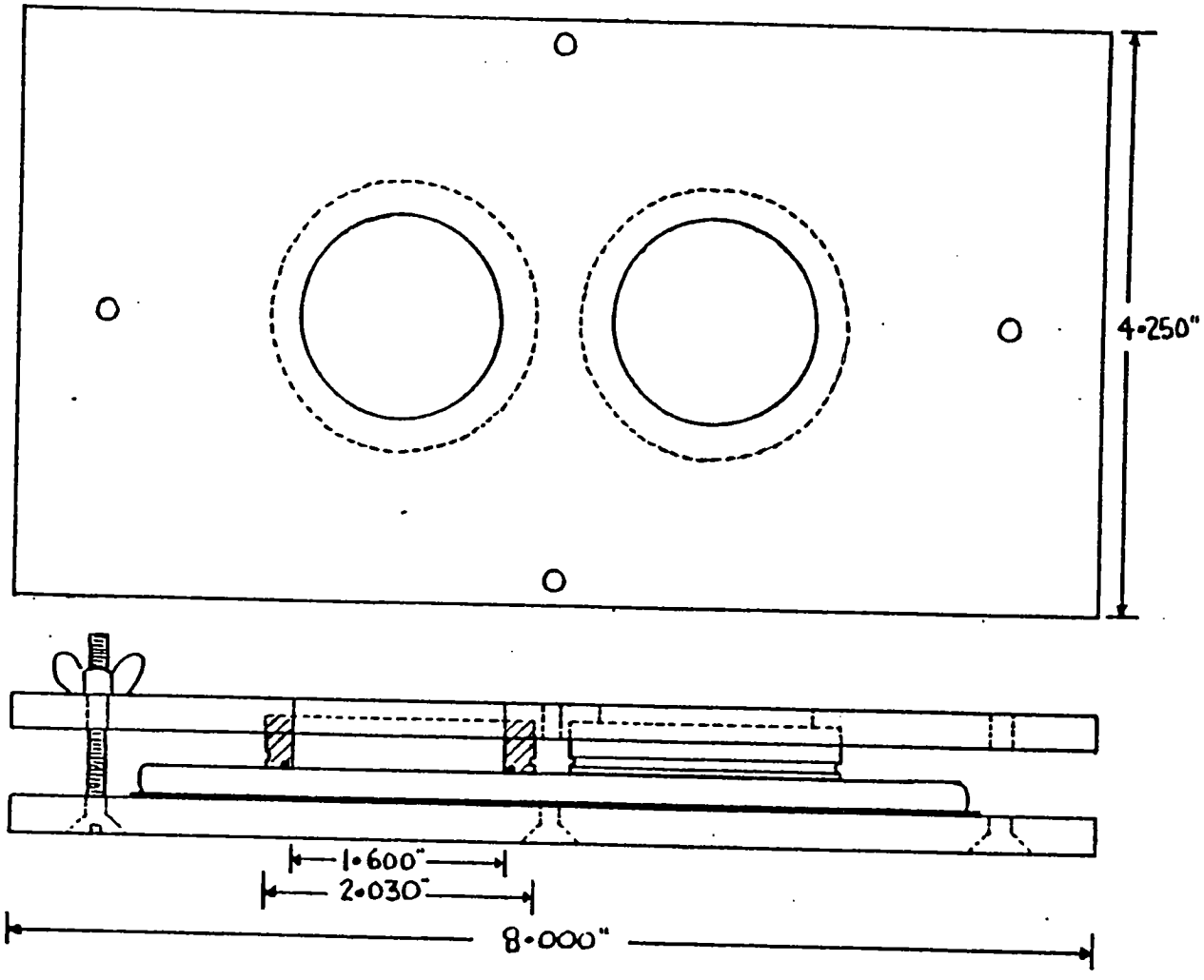

Figure F-4. Aluminum clamping jig

from the bottom-upward. In this case the freezing rate was approximately 0.25 mm per minute.

To achieve a slower freezing rate, the procedure was identical to that for the medium rate with the exception that a nylon spacer, 2.5 mm thick, was placed between the substrate and the aluminum plate. Measurements indicate that the freezing rate in this case was about 0.07 mm per minute.

Details of Procedure for Bottom-Up Freezing

Rate 1 (Slow)

(1) Place clean substrate with O-ring type Teflon rings (cleaned before use in cyclohexane and allowed to dry) into aluminum clamping jig ensuring alignment with holes in top plate. Tighten wing nuts until snug. NOTE: use PVC gloves when handling substrates and Teflon rings.

(2) Place entire assembly in 0°C freezer.

(3) Put 150 mL of triply distilled water in a clean covered glass container and place in 0°C freezer.

(4) After at least ½ hour, transfer jig assembly and water to –25°C freezer.

(5) Place jig onto nylon sheet which is on top of the aluminum plate at the bottom of the –25°C freezer.

(6) Add 13 mL of the 0°C triply distilled water to each Teflon ring using the 25-mL graduated pipette.

(7) Cover with insulating cover and allow to freeze for 1 hour.

(8) Remove prepared sample from aluminum clamping jig carefully and store in –25°C freezer until testing.

(9) Repeat with remaining substrates.

Rate 2 (Medium)

(1) Place clean substrate with O-ring type Teflon rings (cleaned before use in cyclohexane and allowed to dry) into aluminum clamping jig ensuring alignment with holes in top plate. Tighten wing nuts until snug. NOTE: use PVC gloves when handling substrates and Teflon rings.

(2) Place entire assembly in 0° freezer.

(3) Put 150 mL of triply distilled water in a clean covered glass container and place in 0° freezer.

(4) After at least ½ hour, transfer jig assembly and water to –25°C freezer.

(5) Place jig directly (no nylon) onto the aluminum plate at the bottom of the –25°C freezer.

(6) Add 13 mL of the 0°C triply distilled water to each Teflon ring using the 25-mL graduated pipette.

(7) Cover with insulating cover and allow to freeze for 1 hour.

(8) Remove prepared sample from aluminum clamping jig carefully and store in –25°C freezer until testing.

(9) Repeat with remaining substrates.

Rate 3 (Fast)

(1) Place clean substrate with O-ring type Teflon rings (cleaned before use in cyclohexane and allowed to dry) into aluminum clamping jig ensuring alignment with holes in top plate. Tighten wing nuts until snug. NOTE: use PVC gloves when handling substrates and Teflon rings.

(2) Place entire assembly in –25°C freezer.

(3) Put 150 mL of triply distilled water in a clean covered glass container and place in 0°C freezer.

(4) Allow entire assembly to cool to −25°C for at least ½ hour.

(5) Add 13 mL of the 0°C triply distilled water to each Teflon ring using the 25-mL graduated pipette.

(6) Cover with insulating cover and allow to freeze for 1 hour.

(7) Remove prepared sample from aluminum clamping jig carefully and store in −25°C freezer until testing.

(8) Repeat with remaining substrates.

Top-down freezing was accomplished by placing insulation under the substrate and leaving the top water surface open to allow heat removal by convection. The top aluminum plate of the clamping jig had holes which allowed the water to be exposed to the freezer air at about −20°C.

To obtain the slowest rate of freezing, a substrate at 0°C was placed in a styrofoam container which was on the bottom of the freezer. Water at 0°C was poured into the Teflon rings and allowed to freeze by natural convection. The freezing rate thus obtained was approximately 0.05 mm per minute.

The same scheme was used to produce an intermediate rate of freezing except that a fan was used to provide forced convection. The freezing rate obtained was about 0.25 mm per minute.

Since interest was primarily in the freezing rate of the water when it was immediately adjacent to the substrate, the highest freezing rate was achieved from the top-down by the following modification of the intermediate rate procedure. With the substrate at 0°C, only the minimum amount of water needed to cover the substrate was placed in the rings. Now heat which was removed as freezing approaches the water-substrate interface had to be conducted only through a thin layer of ice and the maximum possible freezing rate by convective heat removal from the upper surface was achieved. Soon after the initial water was frozen, more water was added. The substrate was then placed on the aluminum plate and the added water allowed to freeze from the bottom-up.

Details of Procedure for Top-Down Freezing

Rate 1 (Slow)

(1) Place clean substrate with O-ring type Teflon rings (cleaned before use in cyclohexane and allowed to dry) into aluminum clamping jig ensuring alignment with holes in top plate. Tighten wing nuts until snug. NOTE: use PVC gloves when handling substrates and Teflon rings.

(2) Place entire assembly in 0°C freezer.

(3) Put 150 mL of triply distilled water in a clean covered glass container and place in 0°C freezer.

(4) After at least ½ hour, transfer jig assembly and water to −25°C freezer.

(5) Place jig into inverted insulated cover (to insulate from bottom-up freezing) and place at the bottom of the −25°C freezer.

(6) Add 4 mL of the 0°C triply distilled water to each Teflon ring using the 5-mL graduated pipette.

(7) Allow to freeze for 1 hour (no fan, only natural convection).

(8) Remove prepared sample from aluminum clamping jig carefully and add remaining 9 mL of water and allow to freeze. This allows the aluminum clamping jig to be freed up for the next sample while finishing the current sample.

(9) Store prepared sample in −25°C freezer until testing.

(10) Repeat with remaining substrates.

Rate 2 (Medium)

(1) Place clean substrate with O-ring type Teflon rings (cleaned before use in cyclohexane and allowed to dry) into aluminum clamping jig ensuring alignment with holes in top plate. Tighten wing nuts until snug. NOTE: use PVC gloves when handling substrates and Teflon rings.

(2) Place entire assembly in 0°C freezer.

(3) Put 150 mL of triply distilled water in a clean covered glass container and place in 0°C freezer.

(4) After at least ½ hour, transfer jig assembly and water to −25°C freezer.

(5) Place jig into inverted insulated cover (to insulate from bottom-up freezing) and place at the bottom of the −25°C freezer.

(6) Add 4 mL of the 0°C triply distilled water to each Teflon ring using the 5-mL graduated pipette.

(7) Allow to freeze for 1 hour (use fan to provide forced convection). Fan is set on front of inverted cover with airflow directed over the top of the aluminum clamping jig (Variac set at 100%).

(8) Remove prepared sample from aluminum clamping jig carefully and add remaining 9 mL of water and allow to freeze. This allows the aluminum clamping jig to be freed up for the next sample while finishing the current sample.

(9) Store prepared sample in −25°C freezer until testing.

(10) Repeat with remaining substrates.

Rate 3 (Fast)

(1) Place clean substrate with O-ring type Teflon rings (cleaned before use in cyclohexane and allowed to dry) into aluminum clamping jig ensuring alignment with holes in top plate. Tighten wing nuts until snug. NOTE: use PVC gloves when handling substrates and Teflon rings.

(2) Place entire assembly in 0°C freezer.

(3) Put 150 mL of triply distilled water in a clean covered glass container and place in 0°C freezer.

(4) After at least ½ hour, transfer jig assembly and water to −25°C freezer.

(5) Place jig into inverted insulated cover (to insulate from bottom-up freezing) and place at the bottom of the –25°C freezer.

(6) Add 2 mL of the 0°C triply distilled water to each Teflon ring using the 5-mL graduated pipette.

(7) Allow to freeze for 1 hour (use fan to provide forced convection). Fan is set on front of inverted cover with airflow directed over the top of the aluminum clamping jig (Variac set at 100%).

(8) Remove prepared sample from aluminum clamping jig carefully and add remaining 11 mL of water and allow to freeze. This allows the aluminum clamping jig to be freed up for the next sample while finishing the current sample.

(9) Store prepared sample in –25°C freezer until testing.

(10) Repeat with remaining substrates.

Details of Procedure—Substrate Mounting

The mount for the substrates of Pyrex, silica, and Teflon required that the substrates remain stationary when subjected to up to 250-lb shear load without breaking. Previously concrete substrates were mounted by clamping them at one end in a jig; this required that a significant amount of pressure be applied at the edge of the specimen.

With the use of the larger (10.2 cm diameter) mortar substrates and with the fragile substrates of the various sizes and thicknesses of Pyrex, silica, and limestone, it was necessary to design and fabricate new specimen holders for the shear testing. For the larger half-cylinders an improved design was found which allowed easy insertion and required them to be clamped only lightly at the back end; resistance to the sharing force was provided by a bar across the front of the specimen. Since the need for tight clamping was removed, this allowed us to fix the cement half-cylinders with very little possibility of damaging the mortar. The new holder design is shown in Figure F-5.

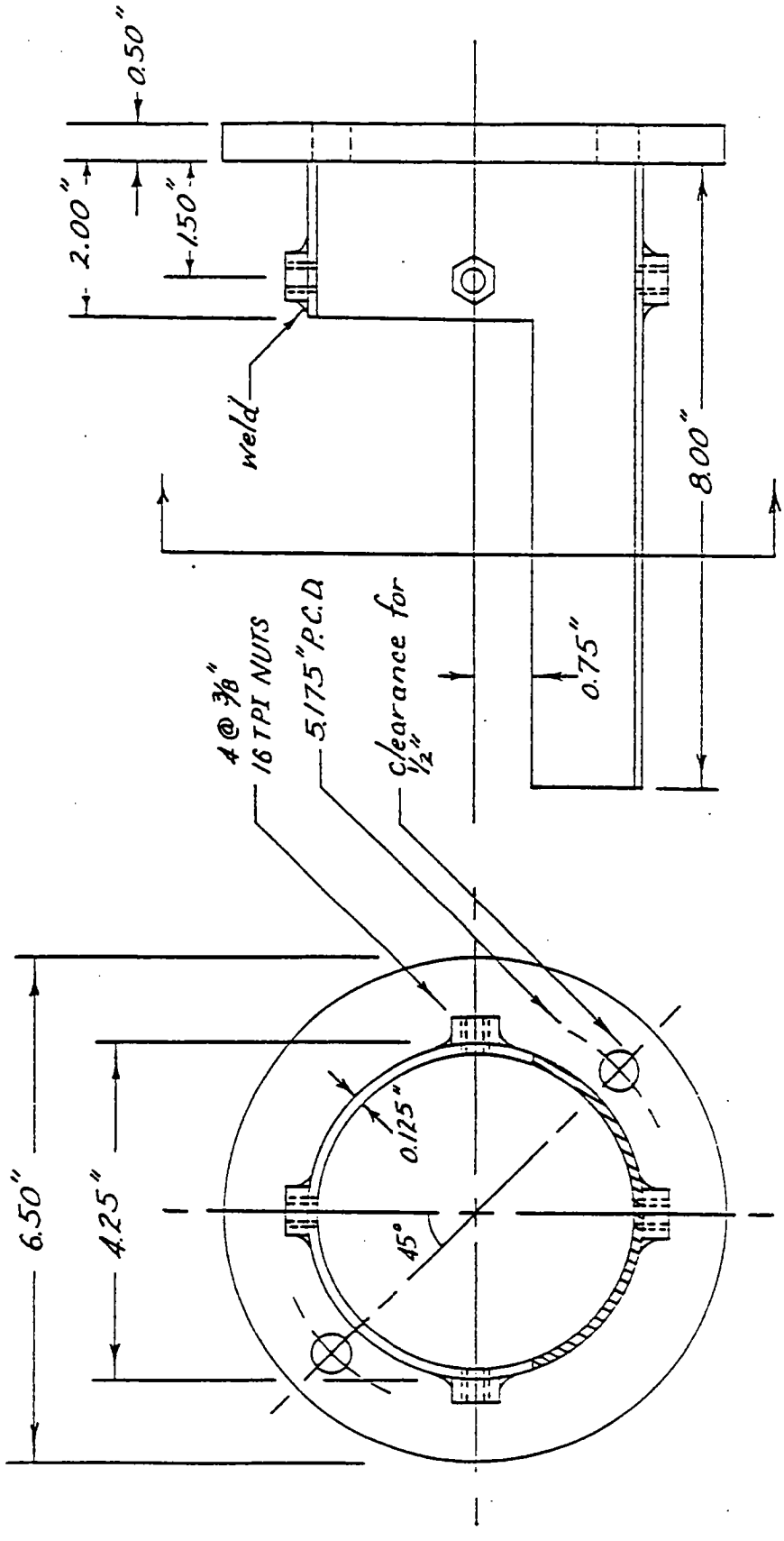

Figure F-5. Substrate holder

Inserts were then made to fit into the holder so that the different substrates were mounted at the correct height and could also be secured with only light clamping at the back end. This was particularly advantageous for the glass substrates. To further reduce the risk of damage to these substrates the mounting incorporated a thin layer (0.0625 in [0.16 cm]) of neoprene rubber; details of this insert are shown in Figure F-6. Inserts of this design were made to accommodate the Pyrex, silica, and limestone substrates. Teflon substrates were mounted on top of pieces of glass of the same size as the Pyrex substrates; they are mounted in similar holders which had extra clamps to secure the thin (0.010-in [0.025-cm] thick) Teflon sheet. An adapter to accommodate the smaller concrete half-cylinders onto which the asphalt had been cast was fabricated from 0.5-in (1.3-cm) steel rods as shown in Figure F-7.

It was necessary to make special provisions for mounting of the limestone substrates. Even with the best limestone available, the specimens often had veins of inclusion material which made the thin slabs of material rather weak. In particular, we found that they would break easily when subjected to the type of thermal cycling experienced in the shear test procedure. Our first attempt to overcome this problem was to epoxy the limestone onto a 0.125-in (0.32-cm) thick aluminum plate. However, the different contraction between the two materials was sufficient to set up enough internal shear to cause cleavage along the bedding planes. Subsequently several schemes were tried, and we found that epoxying a 0.0625-in (0.16-cm) x 6.0-in (15.2-cm) steel strip to each side of the limestone appeared to be effective in maintaining physical integrity. These reinforced substrates were mounted in the specimen holder using an adapter similar to those made for the glass substrates.

Details of Procedure—Testing Sequence

It was possible to control the temperature in the testing chamber to within 0.05°C. However, measurements indicate that the ice-substrate interfacial temperature changed as much as 0.5°C in the 2 minutes it took to change samples. In order to reduce the amount by which the freezer temperature rises during substrate changing, a large sheet of aluminum-faced insulation was inserted near the top of the freezer so that when the freezer opened only the sample chamber was subjected to room temperature. This tended to speed up the cool-down recovery time of the test chamber.

The temperature control system typically took about 2 hour to reach a given temperature within the range −5° to −15°C within the specimen test chamber. However, a much longer time was needed to get down to a temperature of −20°C, and it had to be left overnight to get below −20°C.

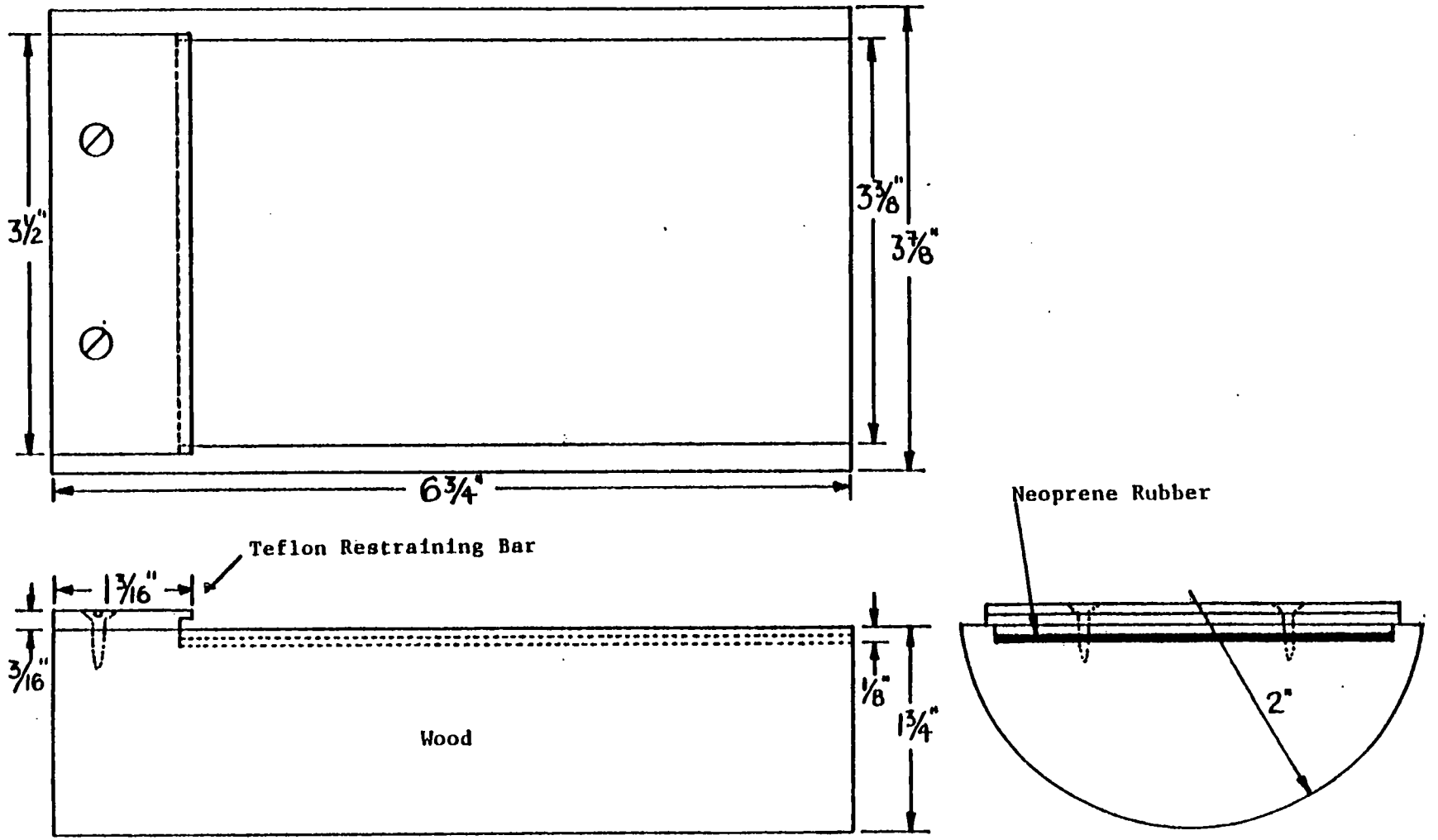

Figure F-6. Insert to support glass substrate

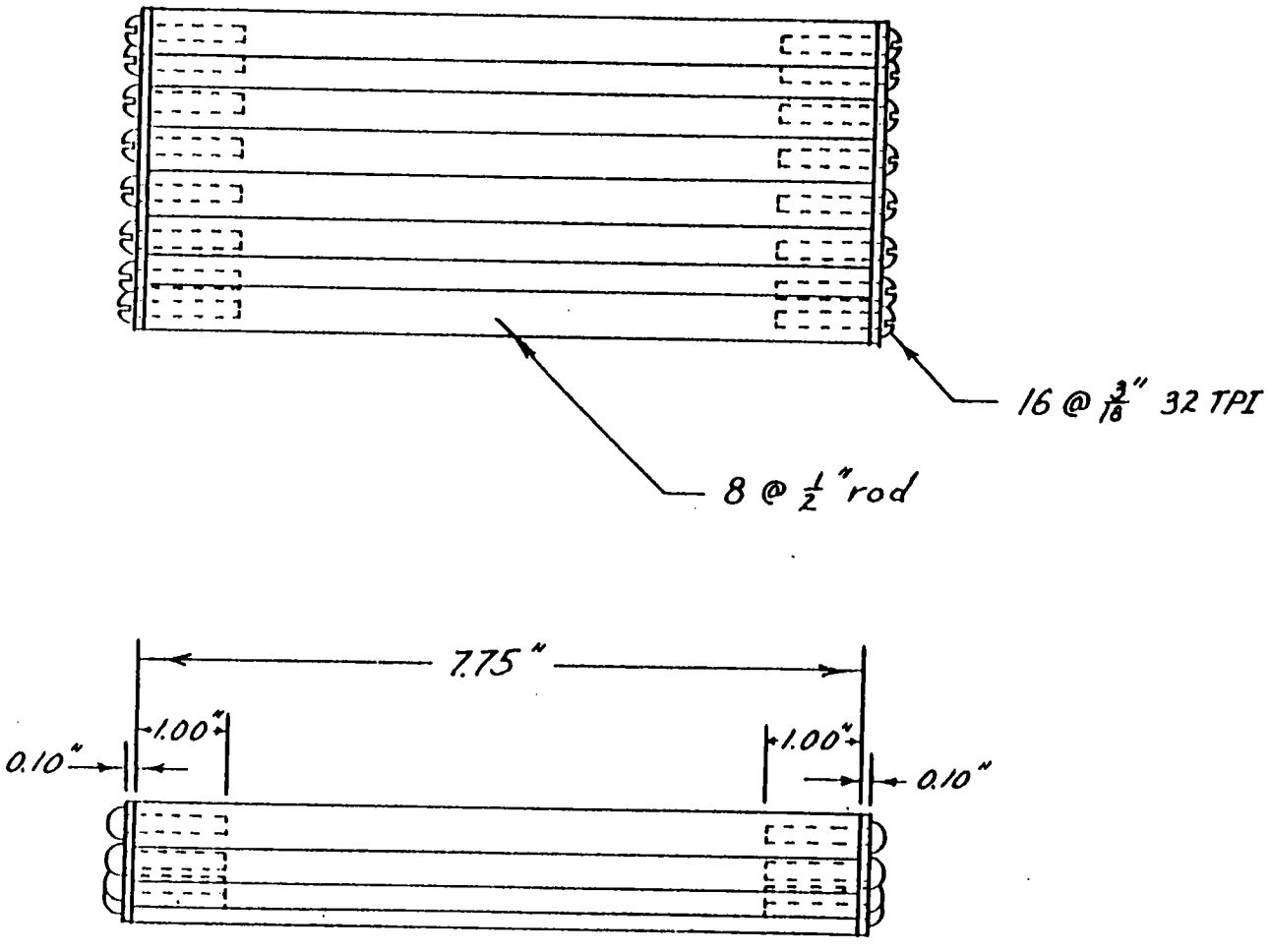

Figure F-7. Adapter for 3-in cylinders

One hour after setting the testing chamber to the desired temperature, the substrates to be tested were transferred from the specimen preparation freezer (typically at −20°C) to the testing chamber, and the first substrate was mounted in the test apparatus. Two pull cables were used, one to each Teflon ring. This made it possible to test both samples on a substrate without having to open the testing chamber. The arrangement is shown in Figure F-8.

Four hours were allowed for the substrates to come to thermal equilibrium at the test temperature. Measurements on a test specimen with a thermocouple embedded at the interface showed this to be more than adequate. We then conducted two tests on the first substrate, opened the test chamber, removed the first substrate and mounted the second substrate. One hour was then allowed for reestablishment of thermal equilibrium before the second substrate was tested. The same procedure was followed for testing the third and fourth substrates.

The shear rate used in all these tests was approximately 4,000 lb/minute—the fastest rate that could be achieved with the current configuration of the Cal Tester. The ice broke off the substrate typically with a shear force of 50 to 300 lb. The force exerted at failure was recorded by the auxiliary pointer on the pressure gauge.

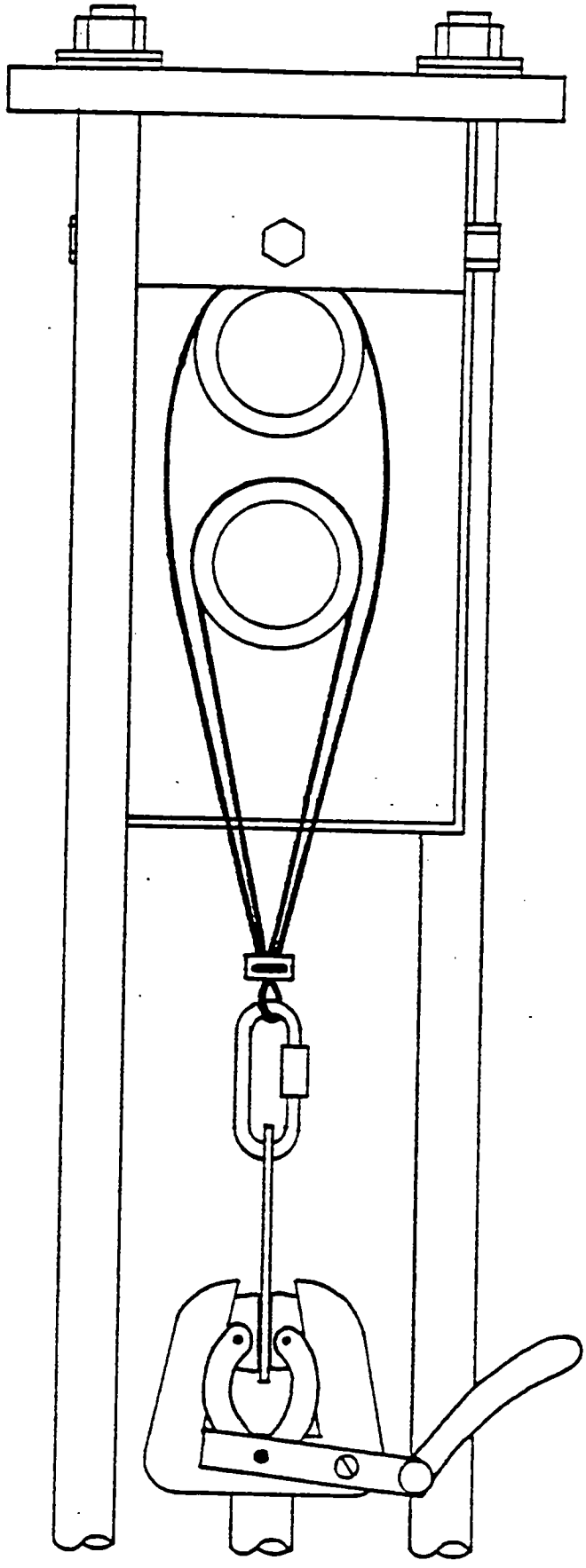

Figure F-8. Specimen/cable arrangement

Results of Interfacial Shear Strength Measurements

DATA FILE NAME: APE06D88
TEST SERIES: GPG 28JUN88-
TREATMENT: NONE (GROUND PYREX GLASS MODEL SUBSTRATE)
TEST CONSTANT: N/A
CALIBRATION: based on 04JAN88 data and sample area of 12.07 cm2
0.038701 * GAUGE - 0.15029 = TRUE Kg/cm2

MRI CODE	TEST TEMP (C)	SHEAR STRENGTH (KG/CM2)	STAND DEV (KG/CM2)	CONVERTED DATA 1	2	3	4	5	6	7	8
1121	-4	2.19	1.26	3.99	3.95	1.08		1.66	2.09	1.24	1.35
1132	-4	2.40	1.15	3.33	3.13	1.55	2.05	4.53	1.28	1.93	1.39
1221	-9	2.41	0.63	1.35	1.78	2.63	3.21	2.55	2.94	2.05	2.79
1232	-9	2.51	1.31	3.10	3.52	1.59	1.78	2.86	1.16	1.20	4.88
1321	-15	1.92	0.53	1.93	1.04	1.78	2.24	2.13	2.09	1.39	2.75
1332	-15	2.44	0.56	3.52	2.71	2.32	2.01	2.01	1.90	2.86	2.17
1421	-23	1.53	0.47	1.39	1.93	0.81	1.55	2.09	1.97	0.93	1.59
1432	-23	2.18	0.91	1.59	1.97	1.47	1.55	2.82	3.95	1.39	2.71

			SESSILE DROP ANGLE							
1121			6.8	6.8	10.3		4	4	9.3	9.3
1132			21.3	28.5	22.5	21.3	15.3	18.3	19.5	21.3
1221			8.3	10	19	22.5	9.5	6.8	22.8	25
1232			6	9.5	9.8	10.8	6.8	10.3	9.8	17.8
1321		AFTER TEST	35	17.8	30.5	25.8	17	25.3	19.5	39.5
1332			6.8	15.3	12	16.8	10.5	8	13	15
1421			5	7.3	11.5	17	9.3	6.8	10	14.3

MRI CODE	TEST DATE	COMMENTS ON TEST
1121	29JUN88	CLEAN BREAK
1132	09JUL88	CLEAN BREAK
1221	06JUL88	SOME ICE LEFT ON MOST
1232	26JUL88	MUCH ICE ON ONE, SOME ON REST
1321	13JUL88	SOME ICE ON ALL
1332	09AUG88	SOME ICE ON ALL
1421	20JUL88	SOME ICE ON ALL

DATA FILE NAME: APE11D88
TEST SERIES: TEF 19AUG88-
TREATMENT: NONE (TEFLON MODEL SUBSTRATE)
TEST CONSTANT: N/A
CALIBRATION: based on 04JAN88 data and sample area of 12.07 cm
0.0087 * GAUGE - 0 = TRUE Kg/cm2
(NOTE: the above calibration equation is different for the Teflon and includes an additional 0.2248 lb/Nt multiplicative factor)

MRI CODE	TEST TEMP (C)	SHEAR STRENGTH (KG/CM2)	STAND DEV (KG/CM2)	CONVERTED DATA 1	2	3	4	5	6	7	8
2111	-4	0.09	0.03		0.05	0.08	0.10	0.11	0.14	0.07	

2111 SESSILE DROP ANGLES

MRI CODE	TEST DATE	COMMENTS ON TEST
2111	19AUG88	#1,#8 CAME OFF BEFORE TEST

DATA FILE NAME: APE07D88
TEST SERIES: GSG 8JUN88-
TREATMENT: NONE (GROUND SILICA GLASS MODEL SUBSTRATE)
TEST CONSTANT: N/A
CALIBRATION: based on 04JAN88 data and sample area of 12.07 cm2
0.038701 * GAUGE - 0.15029 = TRUE Kg/cm2

MRI CODE	TEST TEMP (C)	SHEAR STRENGTH (KG/CM2)	STAND DEV (KG/CM2)	CONVERTED DATA 1	2	3	4	5	6	7	8
3112	-4	3.85	2.15	7.16	4.76	5.07	5.50	1.86	3.29	2.52	0.66
3131	-4	1.45	0.37	0.89	1.62	1.16	1.04	1.59	1.93	1.62	1.78
3212	-9	3.34	1.58	4.64	4.84	2.17	1.16	2.55	4.68		
3212B	-9	4.57	1.67	5.73	6.46	3.37	4.30	6.23	5.57	2.13	2.75
3231	-9	3.37	1.41	2.48	1.82	3.37	2.94	3.02	3.17	6.58	3.56
3331	-15	3.22	1.20	1.97	2.40	4.95	1.93	2.79	4.68	4.10	2.94
3312	-15	2.64	1.56	1.12	0.89	3.71	1.04	3.91	3.75	1.93	4.80
3412	-23	2.51	0.77	4.26	2.28	2.21	2.71	1.86	2.59	2.21	1.93
3412B	-23	2.59	1.19	2.36	1.55	2.09	4.95	1.39	3.21	1.82	3.33
3431	-23	1.96	0.62	1.28	2.59	1.97	2.94	1.47	1.90	1.24	2.32

	SESSILE DROP ANGLES							
3112	16.8	17.5	9.8	11	16.5	17.5	12.5	10
3131	23	23	20.3	20.3	19.5	19.5	14.3	14.3
3212	not available (redone)							
3212B	9	6	6.5	7.5	5.5	4.5	11.5	12.5
3231	not available							
3331	not available							
3312	5	5	6.8	6.8	7.8	7.8	3.3	3.3
3412	not available							
3412B								
3431	9.5	8.8	8.3	6.8	7.5	3.3	5.8	3

MRI CODE	TEST DATE	COMMENTS ON TEST
3112	11JUL88	MUCH ICE ON LAST, OTHERS CLEAN BREAK
3131	14JUN88	CLEAN BREAK
3212	07JUL88	LEAKAGE AND NO SESSILE DROP - REDONE
3212B	15JUL88	CLEAN BREAK (THIN ICE LAYER)
3231	10JUN88	SOME ICE ON HALF, OTHERS CLEAN BREAK
3331	12JUN88	SOME ICE ON ALL
3312	30JUN88	SOME ON TWO, OTHERS CLEAN BREAK (THIN ICE)
3412	28JUL88	CLEAN BREAK, NO SESSILE DROP - REDONE
3412B	03AUG88	CLEAN BREAK (THIN ICE LAYER)
3431	21JUL88	CLEAN BREAK (THIN ICE LAYER)

DATA FILE NAME: APE09D88
TEST SERIES: LIM 23JUL88-
TREATMENT: NONE (LIMESTONE MODEL SUBSTRATE)
TEST CONSTANT: N/A
CALIBRATION: based on 04JAN88 data and sample area of 12.07 cm2
0.038701 * GAUGE - 0.15029 = TRUE Kg/cm2

MRI CODE	TEST TEMP (C)	SHEAR STRENGTH (KG/CM2)	STAND DEV (KG/CM2)	CONVERTED DATA 1	2	3	4	5	6	7	8
4100	-4	7.61	2.30	7.20	3.71	4.68	7.89	8.98	8.90	9.52	10.0
4200	-9	5.10	1.23	6.19	5.88	3.87	7.35	4.49	4.45	4.10	4.49

	SESSILE DROP ANGLES							
4100								
4200	22.8	24.5	17.5	14.3	18.3	13.8	18.3	24.3

MRI CODE	TEST DATE	COMMENTS ON TEST
4100	23JUN88	CLEAN BREAK (THIN ICE LAYER)
4200	16AUG88	SOME ICE ON MOST

DATA FILE NAME: APE10D88
TEST SERIES: ASP 24JUL88-
TREATMENT: NONE (ASPHALT MODEL SUBSTRATE)
TEST CONSTANT: N/A (NOTE: EACH TEST IS A NEW SET OF SUBSTRATES)
CALIBRATION: based on 04JAN88 data and sample area of 12.07 cm2
0.038701 * GAUGE - 0.15029 = TRUE Kg/cm2

MRI CODE	TEST TEMP (C)	SHEAR STRENGTH (KG/CM2)	STAND DEV (KG/CM2)	CONVERTED DATA 1	2	3	4	5	6	7	8
5100	-4	1.88	0.40	2.40	2.21	1.66	1.16	1.78	1.62	2.17	2.01
5200	-9	3.38	1.16	2.67	3.95	2.75	3.41	1.16	4.30	4.76	4.06
5300	-15	2.84	0.99	2.13	2.90	4.41	1.28	2.55	3.91	2.40	3.13

	SESSILE DROP ANGLES							
5100								
5200								
5300	80	86	86.3	79	87	78	87.8	88.8
	83.8	83.3	86.8	87.3	88.3	85.3	83.8	82

MRI CODE	TEST DATE	COMMENTS ON TEST
5100	08AUG88	NO BREAKAGE OF ASPHALT, CLEAN BREAK
5200	02AUG88	BROKE ASPHALT
5300	24JUL88	BROKE ASPHALT

DATA FILE NAME: APE08D88
TEST SERIES: PCM 4JUL88-
TREATMENT: NONE (PC MORTAR MODEL SUBSTRATE)
TEST CONSTANT: N/A
CALIBRATION: based on 04JAN88 data and sample area of 12.07 cm2
0.038701 * GAUGE - 0.15029 = TRUE Kg/cm2

MRI CODE	TEST TEMP (C)	SHEAR STRENGTH (KG/CM2)	STAND DEV (KG/CM2)	CONVERTED DATA 1	2	3	4	5	6	7	8
6100	-4	4.34	1.72	3.64	1.90	6.77	2.94	5.42	4.10	6.46	3.48
6100B	-4	5.76	1.78	5.50	3.91	8.75	4.84	7.16	7.35	4.41	4.18
6200	-9	6.09	1.37	5.53	5.57	7.82	6.58	3.71	5.07	7.43	6.97
6200B	-9	6.82	1.62	7.31	7.66	8.71	6.19	6.81	4.64	8.71	4.53
6300	-15	6.20	0.81	6.31	5.88	6.81	6.42	6.23	5.34	7.58	4.99
6300B	-15	5.88	1.14	5.69	4.68	7.39	6.08	6.66	4.49	7.20	4.84
6400	-23	5.97	1.41	4.26	4.02	6.11	8.59	6.04	6.31	6.27	6.15

	SESSILE DROP ANGLES							
6100B	15.5	12.3	15.5	14.5	14.8	14.5	14	9
6200B	12.3	12	17.5	13.3	15.8	12.3	19.5	11
6300B	17.3	23.5	16.5	19.5	18.3	16.8	22.3	13
6400								

MRI CODE	TEST DATE	COMMENTS ON TEST
6100	05JUL88	NO SESSILE DROP - REDONE
6100B	18JUL88	CLEAN BREAK (THIN ICE LAYER)
6200	06JUL88	NO SESSILE DROP - REDONE
6200B	22JUL88	CLEAN BREAK (THIN ICE LAYER)
6300	10JUL88	NO SESSILE DROP - REDONE
6300B	29JUL88	CLEAN BREAK (THIN ICE LAYER)
6400	12AUG88	CLEAN BREAK (THIN ICE LAYER)

Appendix G

Facility for Shear Strength Testing of Ice on Teflon and Undercutting Study

Measuring the shear strength of ice on Teflon necessitated major changes in the methods used for other substrates because of the following:

- The Teflon substrate provided was only 0.010 in thick. Consequently, it needed to be supported fully at all times.

- Ice doesn't stick well to Teflon. Therefore, instead of measuring a typical shear force in the range of 50 to 200 lb with the Cal-Tester shear test facility, preliminary tests with this substrate indicated a shear force of less than 10 lb was required for disbondment.

In order to address these problems and to provide a facility which can also be used in undercutting tests, we developed another test facility, the "Stair-Case Testing Facility," (see Figures G-1 and G-2). The "stair-case" platform was used to mount four Teflon substrates. The Teflon rested upon Pyrex for support and was held in place by the use of wing nuts, as shown. Monofilament fishing line was used to transfer the applied force from outside the freezer to the samples. The force was applied at a rate consistent with the other tests by simply pulling by hand through a spring balance on the monofilament line. Each substrate had two Teflon rings with ice frozen within it, so that two tests could be obtained from each substrate.

In preliminary tests on a polyethylene bag, the measured shear strength varied between 0.7 and 10 lb. In order to have sufficient sensitivity in this range of measurements, we connected two spring balances in "series." The first spring balance measured forces up to 4.5 lb with an uncertainty of 0.1 lb. When it reaches full scale, the second spring balance continues on. The second balance had a full-scale capability of 33 lb with an uncertainty of 0.4 lb. Through this procedure we generated data of sufficient precision for both high and low shear strength values.

Note: Each step arrangement has similar wing nut clamp as the one shown

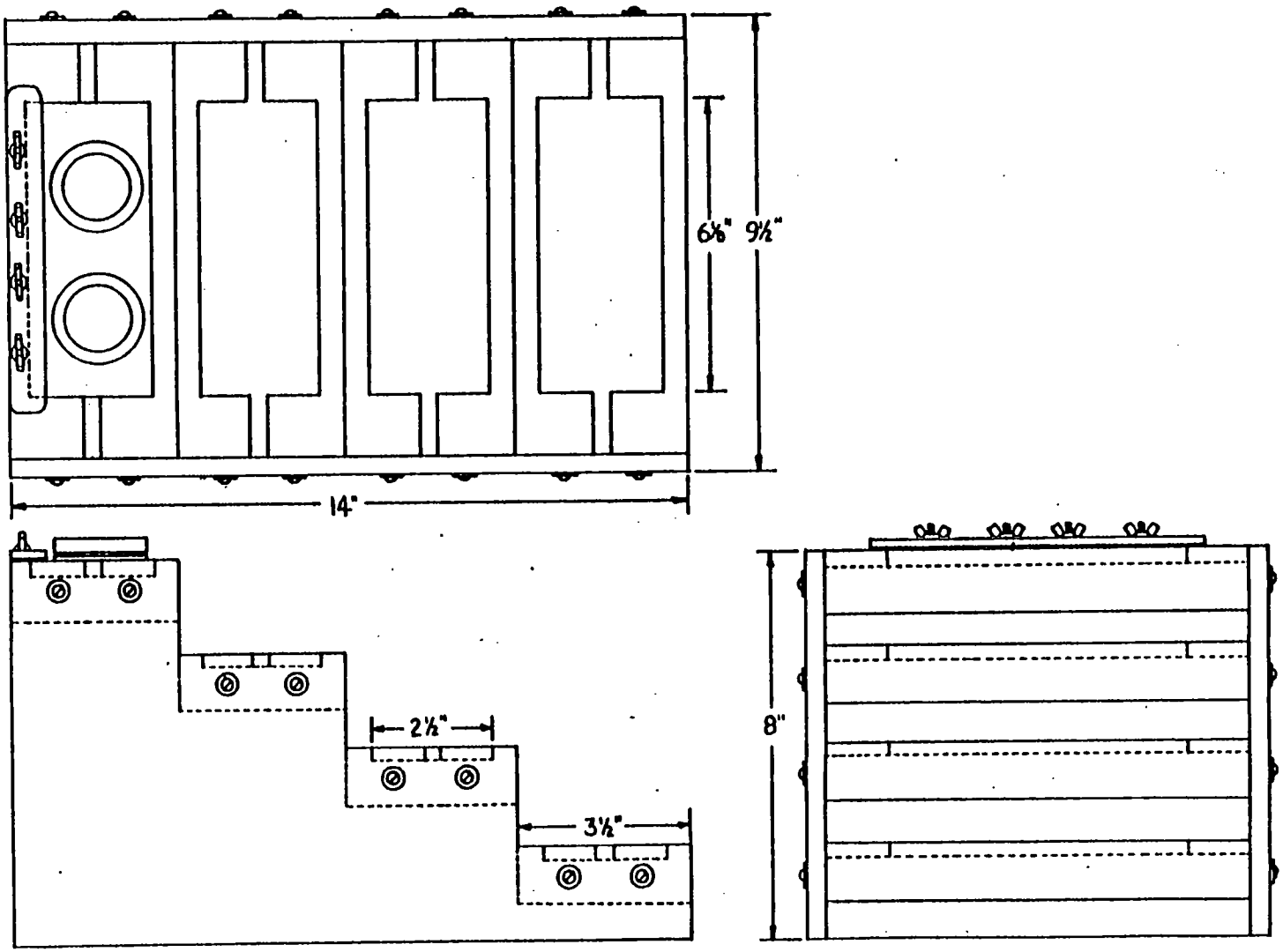

Figure G-1. Stair-case testing facility

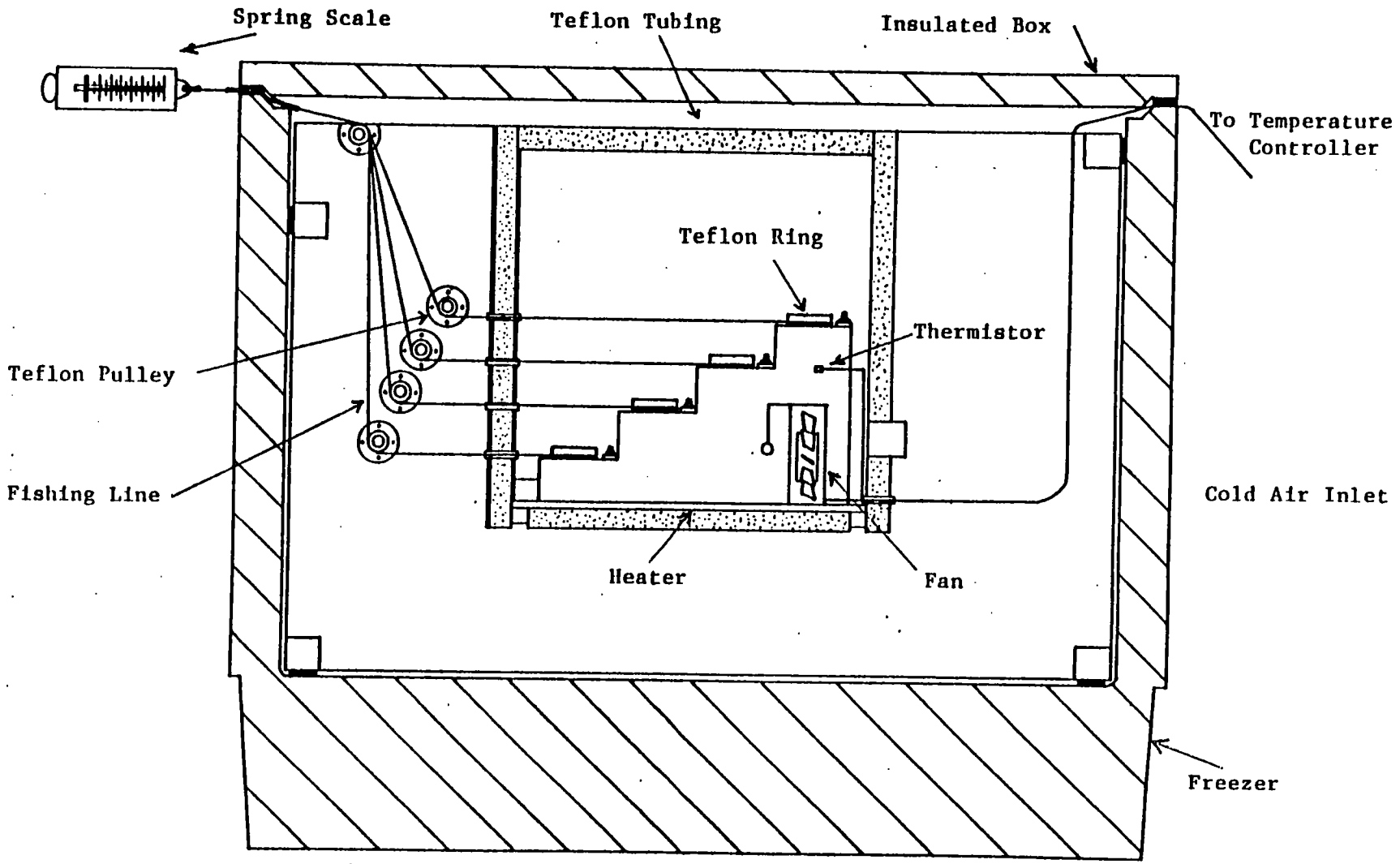

Figure G-2. Teflon shear strength testing configuration

The temperature of the Teflon samples was controlled by use of a resistance heating circuit as shown in the diagram in Figure G-3. A fan provided sufficient air circulation to minimize temperature stratification. This allowed control of the temperature within the sample chamber to within one hundredth of a degree Celsius.

The same procedure was used for growing ice on Teflon as was used for Pyrex and silica, with the exception that the ice was grown upon the Teflon substrate which was itself resting on Pyrex. When four substrates were prepared, the four Pyrex-Teflon-ice substrates were transferred to the Stair-Case Facility for testing.

The Teflon rings with O-ring inserts were used in the ice sample preparation. Also, the jig prepared for the Pyrex and silica substrates was used to keep sufficient pressure on the O-ring in order to prevent water from leaking out before the ice began to form. Much care was used in the handling of the ice-Teflon-Pyrex combination because the ice could fall off the Teflon with the slightest jarring or torsional action. It should be noted that the Pyrex used as a support while growing ice on the Teflon was also transferred to the testing chamber.

This facility was also used in the investigation of chemical undercutting on the bond shear strength described in Section 2.

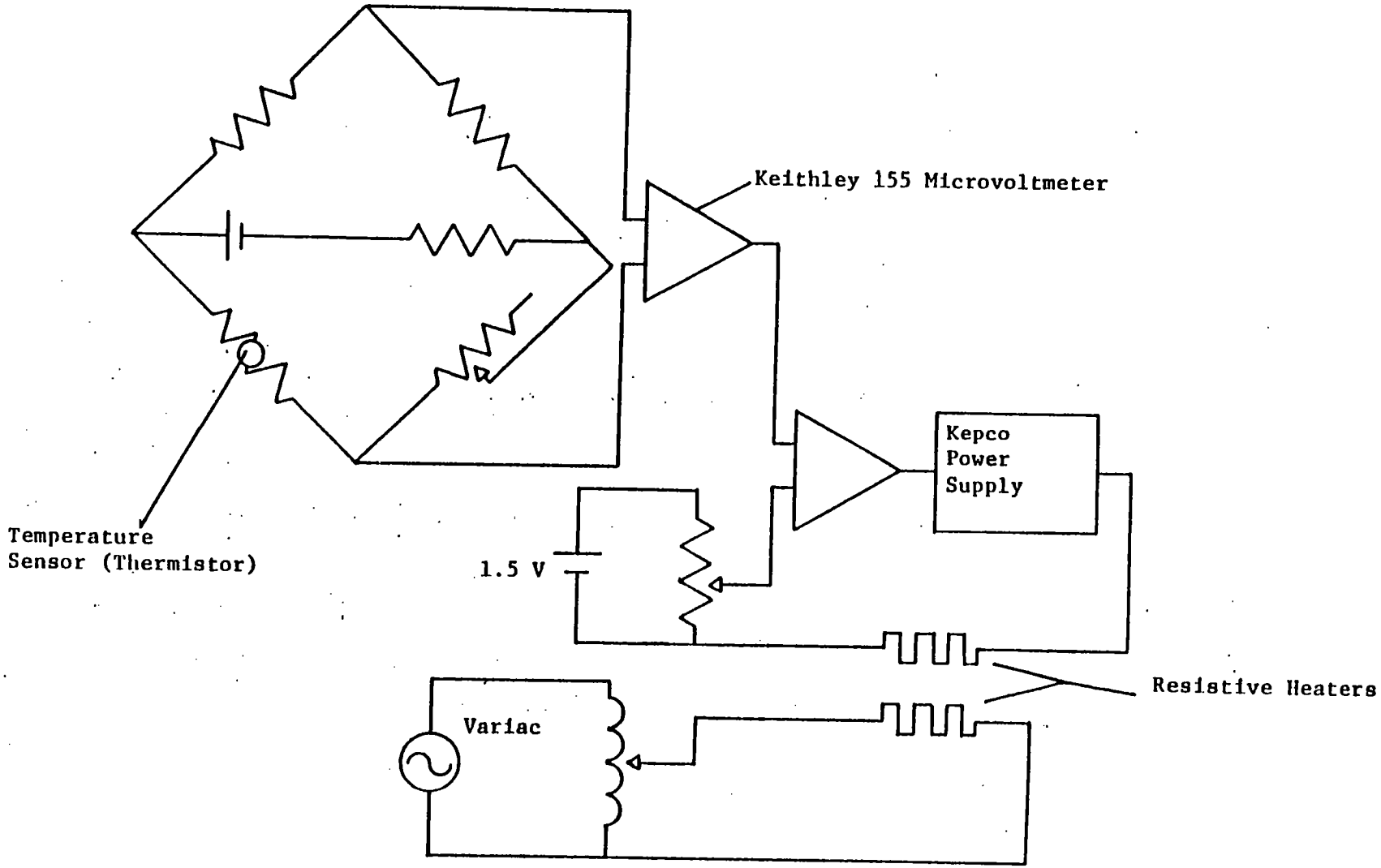

Figure G-3. Temperature control circuit design

Appendix H

Determination of Impact Effects on Ice Bonded to Pavement Materials

Shear strength measurements of ice on various untreated model and pavement component substrates were performed under low-rate shear conditions to provide basic data on a measure of the adhesional bonding strength. Discussions of the tests conducted and results obtained are given in Appendix F and in Section 2 under "Ice-Substrate Bond Shear Strength Under Low-Rate Shear Conditions." These shear tests were performed with a shear load applied parallel and as close as possible to the ice-substrate interface. The shear rate used in these tests was approximately 4,000 lb/minute (1,814 kg/minute)—the fastest rate that could be achieved with the configuration of the testing machine. This rate was extremely slow compared to the very high rates typical of snowplow operations. Therefore, it was considered important to generate additional shear strength measurements of ice on various composite substrates under higher loading rates. Interest was also directed at the generation of data concerning the effects of a high rate of loading of ice by penetration applied normal to the ice-substrate interface. Consequently, test equipment and procedures were developed to investigate the effects on disbonding of impact loading applied in shear at the ice-substrate interface. It was hoped the equipment and procedures would be applicable also to the impact loading applied normal to the interface.

The details given in this appendix are of work performed to determine the impact effects on ice bonded to pavement materials. The substrates used and procedures followed in preparing the test specimens are presented first, followed by a description of the development of the impact test apparatus. This is followed by an example of the data generated during impact testing and the associated data analysis. Finally, concluding remarks are given concerning the impact shear test results.

Substrate Configurations and Test Specimen Preparation

Two types of substrates were used in the impact tests. The first type consisted of laboratory-produced specimens made of portland cement concrete and dense-graded asphalt. The second type consisted of field (core) samples taken from portland cement concrete, dense-graded asphalt, open-graded asphalt, and rubber-modified asphalt highway pavement surfaces. The sizes and sources of each type of substrate are described in Appendix A. The substrates were cleaned using the procedures described in Appendix B.

The ice samples used during the impact shear testing were approximately 1.4 in long x 1.4 in wide x 0.5 in high (3.6 cm x 3.6 cm x 1.3 cm). The value of the cross-sectional area was chosen to match the cross-sectional area of the ice samples used in the low-rate shear tests. Two ice samples were grown on each laboratory-produced portland cement concrete specimen. One ice sample was grown on each of the other substrates. Special molds were designed for growing the ice using chilled deionized water. Closed cell rubber weather stripping of ¼-in (0.64-cm) thickness was used to form the ice sample and prevent the water from escaping from the intended cross-sectional area of the ice sample. The procedure followed in growing the ice samples is described in Appendix I and was the same as was used for growing ice in the second set of chemical undercutting tests.

Development of Impact Test Apparatus and Associated Test Procedures

A search was made for equipment that could be used for impact shear strength and impact force penetration measurements over a range of load application intensity and speed. The search revealed that test devices for impact loading were available, but there were no devices totally acceptable for impact testing of ice on highway specimens.

An Izod-type impact machine was borrowed from another firm for potential use in conducting initial impact shear and impact penetration tests and for the initial development of test procedures. These devices deliver an impact load through a pendulum motion of a striking head. Terminal speeds of 7 to 8 mph (11.3 to 12.9 km/hour) and delivery energies of up to 16 ft-lbf (12.7 J) are typical. Drawings were made of parts of the machine in preparation for designing specimen holding fixtures and force measurement pickup attachments. The borrowed Izod-type machine had very limited clearance for holding specimens of the size needed. Consequently, it was decided to postpone a decision to use the machine until it was determined if a simplified impact mechanism could be designed that would deliver higher energy levels at higher terminal speed.

Several designs were developed for the simplified impact mechanism. The designs were based upon suggestions received from researchers in the field of impact loading. One of the preliminary designs looked very promising and had the capacity of producing theoretical impact speeds of up to 18.7 mph (30.2 km/hour). The concept consisted of a falling weight that was constrained to vertical motion by channel tracks. The falling weight consisted of a top, or striking head assembly, that permitted the use of strain gages for measuring transient loads during impact.

A small mockup of the favorable design was constructed to check out alignment conditions. The mockup showed the preliminary design to be adequate for our needs, so a complete design of the preferred impact test fixture was developed. Further investigation of the Izod-type impact machine was halted, since the device had limited capabilities.

The impact mechanism developed and constructed is shown in Figure H-1. The design consisted of a 9.5 lb falling weight that was constrained to vertical motion by four nylon wheels that traveled inside of two vertically aligned channel tracks. The falling weight consisted of a frame, the four nylon wheels, and a tup, or striking head assembly, that permitted the use of strain gages for measuring transient loads during impact. Two rubber bumper pads were used to stop the falling weight before the scraper head contacted the specimen holder fixed to the floor of the cold room.

A small portion of the cold room ceiling was extended to allow installation of a release mechanism and provide a maximum drop height of 139.5 in (354.3 cm). The minimum delivery energy from the maximum drop height is 110.4 ft-lb (149.7 J).

All the major components of the impact test fixture except the blade head, nylon wheels, bumper pads, and specimen holder, were made of aluminum. The blade head was made of brass and the specimen holder was constructed of steel. A full bridge, consisting of four strain gages, was attached to a machined section of the tup.

Three Hall effect sensors were mounted on the track, and their leads were connected to a Fluke/Phillips digital storage oscilloscope. One of the sensors was used to trigger the oscilloscope, and the other two sensors, placed 2 in apart, were used to determine the velocity of the tup, just before it struck the ice sample on the substrate sample.

The strain gages, a signal amplifier, and the oscilloscope were all connected by wiring. A plotter was also connected to the oscilloscope. The signal amplifier, oscilloscope, and plotter

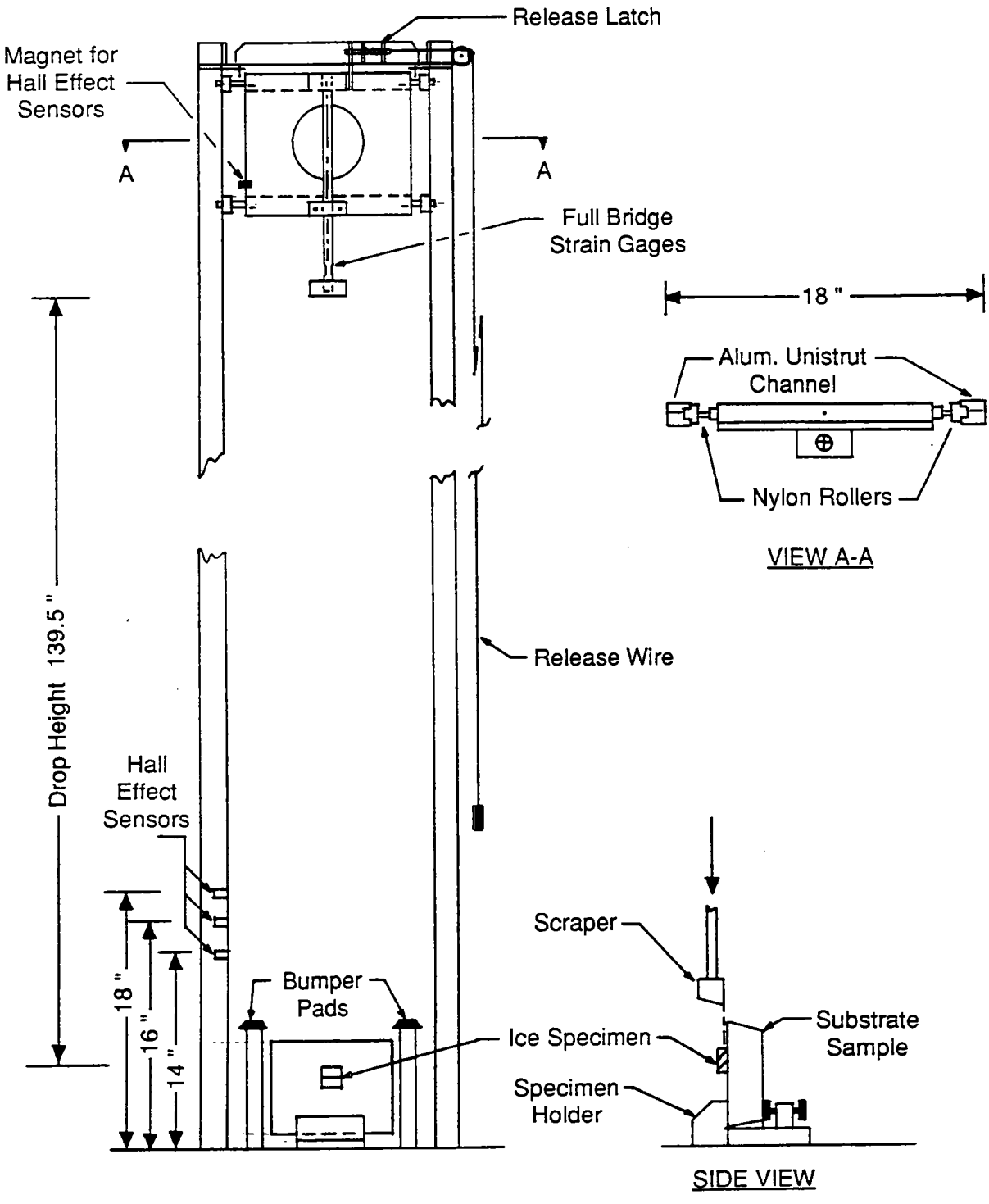

Figure H-1. Impact mechanism

were mounted outside the cold room. The output from the oscilloscope was fed directly to the dedicated plotter for making a hard copy of the signals from the two Hall effect sensors used to determine drop velocity and of the transient load trace immediately after a shear or penetration test.

A large number of drop tests were performed to correct the alignment of the tracks and to further check out the strain gages and recording instrumentation. After a realignment of the tracks, a number of drop tests were made from a height of 139.5 in (354.3 cm) to determine the maximum impact speed achievable. A typical plot made during a velocity check is given in Figure H-2. The two square waves were generated as the magnet passed by two Hall effect sensors. The vertical (ordinate) scale is a measure of the voltage output from the sensors (1 VDC/division) and the horizontal (abscissa) scale is a measure of time (2 ms/division). The speed was determined by measuring the time interval between the two square waves (7.32 ms in Figure H-2) and dividing this interval by 2 in (5.1 cm) (the separation between the two Hall effect sensors used to determine speed). The speed recorded for the traces displayed in Figure H-2 is 15.5 mph (25 km/hour). (This compares with a theoretical value of 18.7 mph [30.2 km/hour]). The system appears to produce reproducible maximum speed valves of about 15.5 mph (25 km/hour).

A number of shear tests of ice samples grown on 5 3/4-in x 8 3/4-in x 1 7/8-in (14.6-cm x 22.2-cm x 4.8-cm) portland cement mortar samples were conducted. These samples were surplus substrates remaining from a previous contact at MRI. These tests were performed at −10°C and were intended to provide a check of the strain gages and instrumentation. The first set of shear tests showed a disturbance problem in the transient response of the strain that was finally traced to contact bounce of the lead wires at two connections. This problem was corrected by hard-wiring the electrical contacts on all moving parts and using stiffer electrical lead wires.

Subsequent shear tests of ice revealed additional problems with the transient response of the strain. Figures H-3 and H-4 show typical curves of strain recorded during two impact shear tests of ice at −10°C on portland cement mortar substrates. In both figures, the vertical (ordinate) scale is a measure of the voltage output from the strain gages (0.2 VDC/division) and is related to the force (through voltage-strain-stress relationships) experienced by the scrapper-shaft assembly during the impact testing. The region of the curves above a neutral line (before impact is experienced) is a compressive strain/force indication. Tensile strain/force is exhibited below the neutral line. The horizontal (abscissa) scale is a measure of time (1 ms/division).

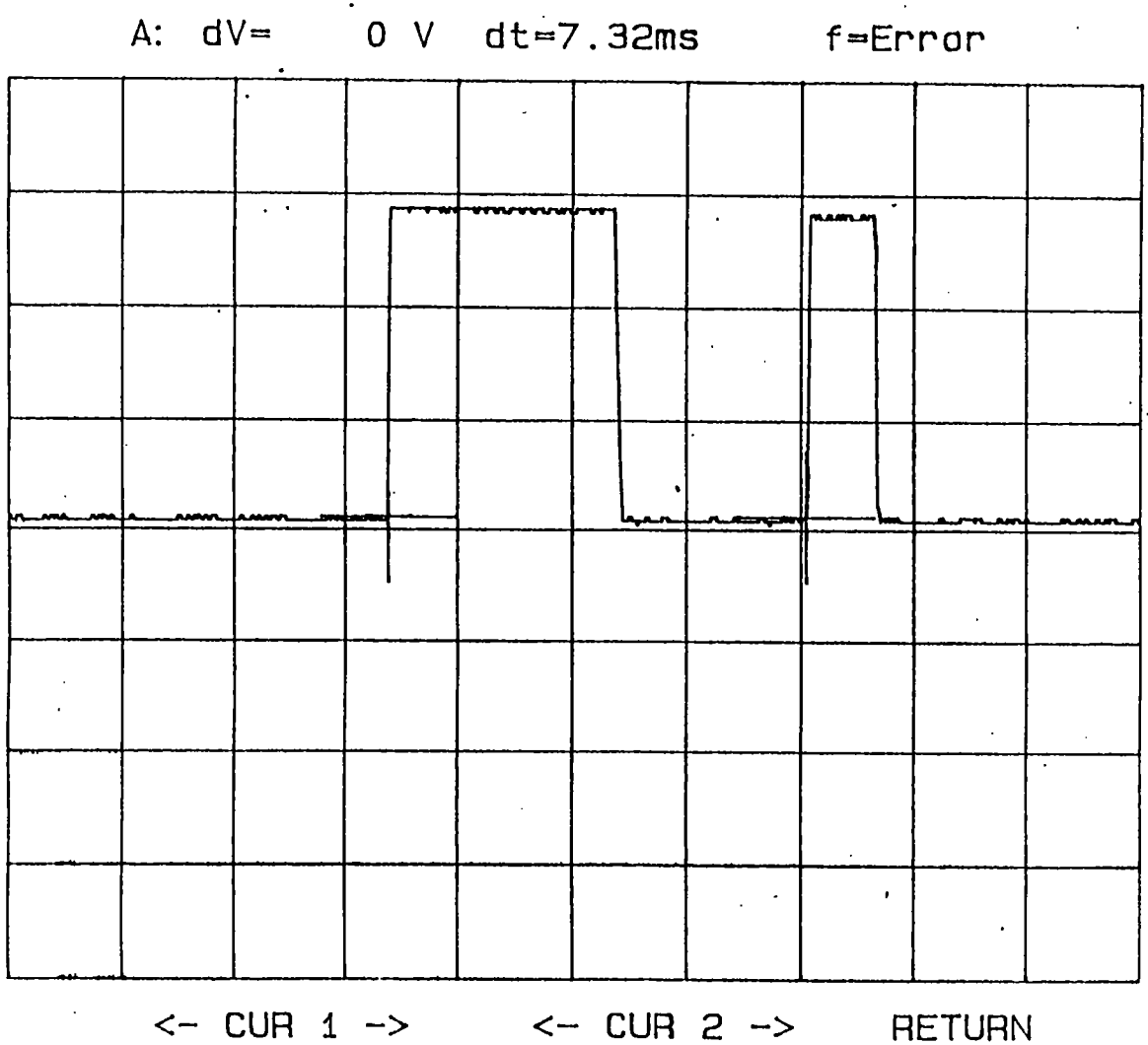

TEST: VELOCITY CHECK

NO. 5

DATE September 14, 1989

TIME 4:30 PM

SUBSTRATE N/A

DROP DISTANCE 139.5 in

DROP VELOCITY 22.769 FT/SEC.

15.525 MPH.

273.2 IN/SEC.

SCOPE PARAMETERS

EXCITATION VOLTAGE 5 VDC

VOLTAGE SCALE 1 VDC/DIV

TIME BASE SETTING 2 MS/DIV

TB TRIGGER MODE SINGLE

TRIGGER-X SOURCE EXT DC

TRIGGER COUPLING DC

FORMAT SETTING 1.8

SPECIMEN PREPARATION HISTORY

MOLD PRE-COOLED FOR N/A HRS

@ N/A °C - °F

COLD ROOM TEMP. -10 °C - °F

COLD PLATE TEMP N/A °C - °F

AIR TEMP. OF RREEZING CHAMBER °C °F

TIME: IN FREEZING CHAMBER N/A

OUT OF FREEZING CHAMBER N/A

OPERATOR

Figure H-2. Oscilloscope trace used to calculate the velocity of the falling weight

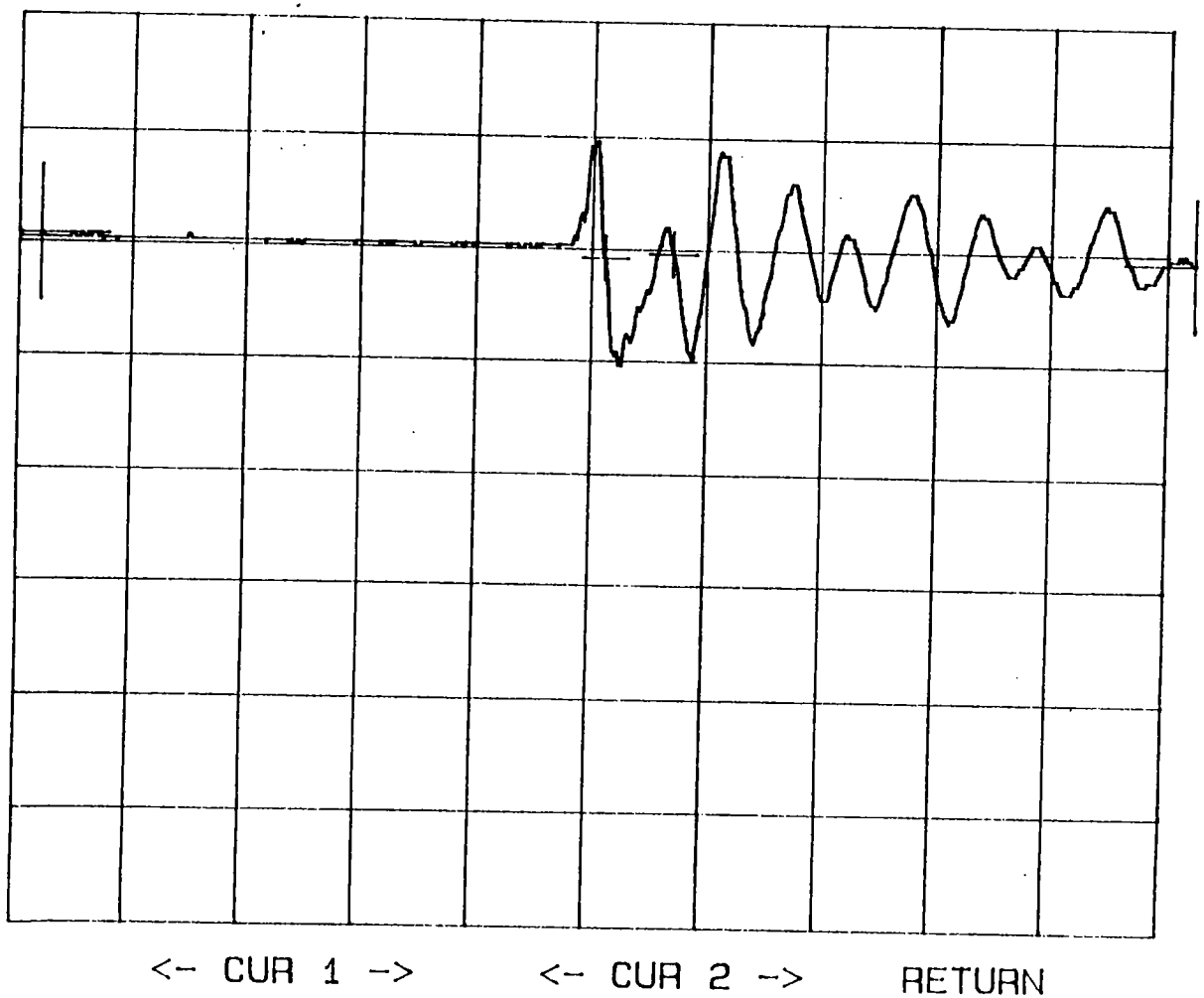

TEST: SHEAR IMPACT

NO. 5A-1

DATE September 14, 1989

TIME 4:45 PM

SUBSTRATE MORTAR

DROP DISTANCE 139.5 in

DROP VELOCITY 22.769 FT/SEC.
15.525 MPH.
273.2 IN/SEC.

SCOPE PARAMETERS

EXCITATION VOLTAGE 5 VDC

VOLTAGE SCALE 0.2 VDC/DIV

TIME BASE SETTING 1 MS/DIV

TB TRIGGER MODE SINGLE

TRIGGER-X SOURCE EXT DC

TRIGGER COUPLING DC

FORMAT SETTING 1.8

SPECIMEN PREPARATION HISTORY

MOLD PRE-COOLED FOR 16 HRS
@ -9 °C - °F

COLD ROOM TEMP. -10 °C - °F

COLD PLATE TEMP -9 °C - °F

AIR TEMP. OF RREEZING CHAMBER +2 °C - °F

TIME: IN FREEZING CHAMBER 0800 - 9/8/89

OUT OF FREEZING CHAMBER 1200 - 9/8/89

OPERATOR

Figure H-3. Transient response of strain recorded during disbondment test 5A-1 of ice on the portland cement mortar substrate

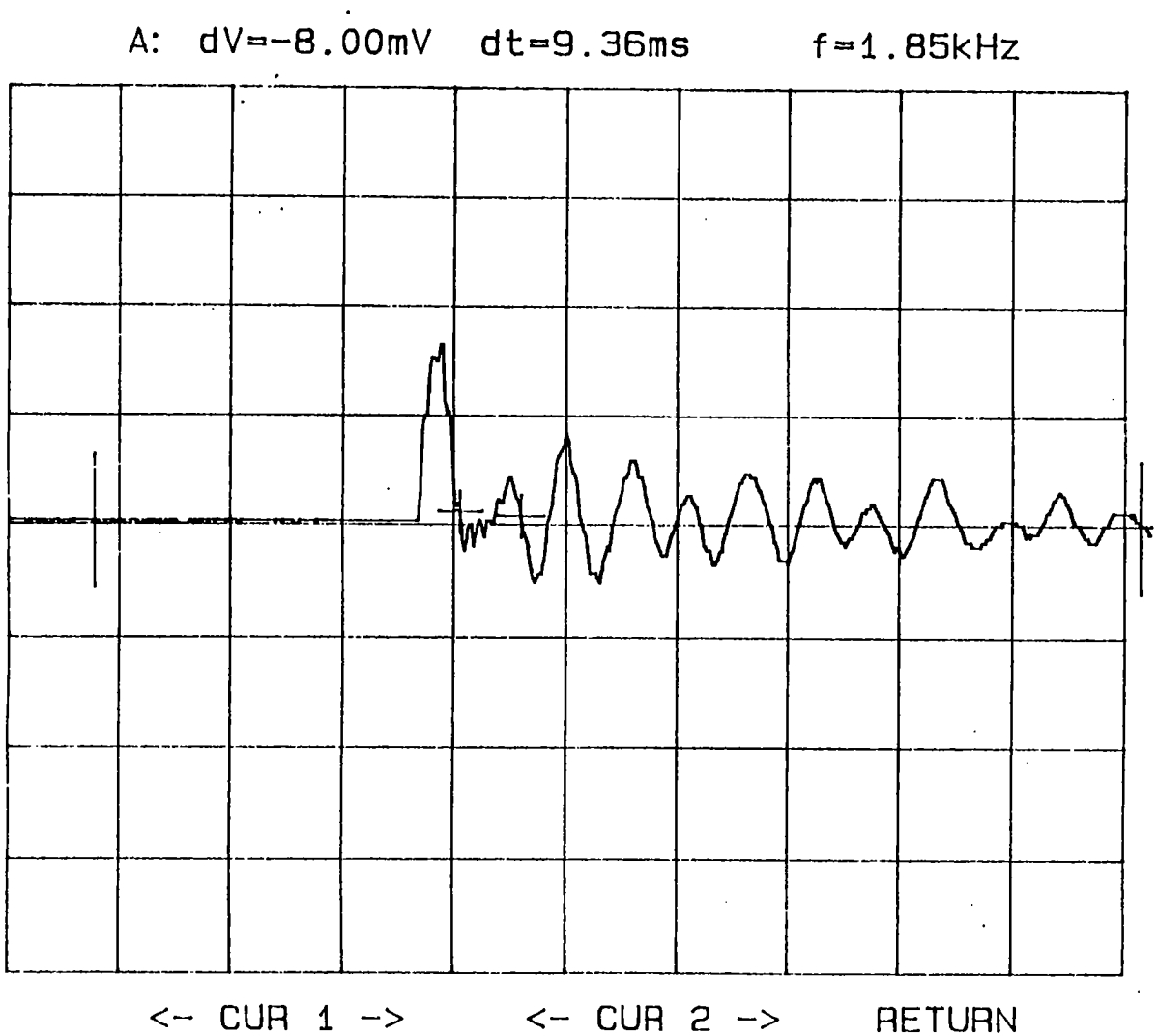

TEST: SHEAR IMPACT

NO. 5A-2

DATE September 14, 1989

TIME 5:05 PM

SUBSTRATE MORTAR

DROP DISTANCE 139.5 in

DROP VELOCITY 22.769 FT/SEC.

15.525 MPH.

273.2 IN/SEC.

SCOPE PARAMETERS

EXCITATION VOLTAGE 5 VDC

VOLTAGE SCALE 0.2 VDC/DIV

TIME BASE SETTING 1 MS/DIV

TB TRIGGER MODE SINGLE

TRIGGER-X SOURCE EXT DC

TRIGGER COUPLING DC

FORMAT SETTING 1.8

SPECIMEN PREPARATION HISTORY

MOLD PRE-COOLED FOR 16 HRS

@ -9 °C - °F

COLD ROOM TEMP. -10 °C - °F

COLD PLATE TEMP -9 °C - °F

AIR TEMP. OF RREEZING CHAMBER +2 °C - °F

TIME: IN FREEZING CHAMBER 0800 - 9/8/89

OUT OF FREEZING CHAMBER 1200 - 9/8/89

OPERATOR

Figure H-4. Transient response of strain recorded during disbondment test 5A-2 of ice on a portland cement mortar substrate

There appear to be two general regions to the response curves. The first region covers the first ½ to 1½ cycles. The curve in this region seems to be a combination of response due to disbondment and energy absorption plus a transient response of the apparatus. The transient response after the first ½ to 1½ cycles is very typical of an indicial response (mechanical response) of a single degree-of-freedom spring-mass-damper system. There appears to be no response to disbondment and energy absorption in this second region. The damped frequency of oscillation in the second time region is very close to the longitudinal frequency of oscillation of a cantilever shaft that is excited at the free end and in-line with the shaft longitudinal axis.

This ringing motion of the scraper-shaft assembly during impact testing is also present during impact testing is also present during the first region of the response curve. The complex strain response during the first ½ to 1½ cycles makes it very difficult to determine, with any certainty, the impact force due to disbondment and energy absorption of the ice sample.

A conservative (large) estimate of the peak compressive force can be obtained from the first ½ cycle of the response trace. In Figure H-3 the first peak corresponds to a compressive load of 4.4 kg/cm^2. In Figure H-4 the first peak corresponds to a compressive load of 7.9 kg/cm^2. These shear strength values are in the same numerical range as the low speed shear test results (6.09 and 6.83 kg/cm^2) reported in Section 2 of this report for ice on portland cement mortar specimens at –9°C. there is some uncertainty, however, in how accurate our impact shear force values are in light of the complex strain response over the first ½ cycle of the transient response curve.

The above results were shared with several researchers and no simple solution to the interpretation of the response curves was available.

An alternative approach to determining energy levels during impact testing was tried to avoid the apparent difficulty in interpreting the strain responses. The alternate approach involved measuring the velocity of the scraper before it impacted the ice sample, as it proceeded through the ice, and after it exited the region of the ice sample. The equipment used to make the velocity determinations was assembled from components on hand and consisted of a light-emitting diode, a phototransistor, and an interrupter. In principle, the amount of kinetic energy absorbed during the ice disbondment can be computed from the entering and exiting velocities and the mass of the falling mechanism. Also, it was envisioned that the velocity distribution during the deceleration portion could be differentiated and combined with the falling mass to give a rough estimate of the force.

Some simple tests were performed with a breadboard arrangement of the equipment needed to make repeated velocity measurements of the falling weight. The results looked encouraging; consequently, a prototype unit was assembled and installed in the cold room. Additional free-fall tests and some disbonding tests using ice grown on mortar specimens were conducted to refine the system, to decide how to obtain meaningful data, and to develop a way of analyzing and interpreting the data. The results of these additional tests and associated data analysis indicated that the concept appeared to work and should be applicable to impact shear tests. Consequently, production shear tests of ice grown on the substrates began using a hardwired version of the equipment.

Selective impact shear tests were performed at temperatures of 25°C (–4°C) and 15°F (–9°C) using the two types of laboratory-produced specimens and the core samples taken from four types of in-service highway surfaces. Impact shear tests were also performed at two levels of impact speeds (nominally 5 mph [8.1 km/hour] and 10 mph [16.2 km/hour] at 15°F (–9°C) to obtain an estimate of the effects of speed on the kinetic energy change during disbonding. Two types of core samples and one type of laboratory-produced specimen were used in these speed tests. Finally, impact shear tests were performed at 15°F (–9°C) on two types of core samples to determine the effects of substrate surface contaminants on the kinetic energy change during disbonding. Tests were performed first on the core samples in the as-received and uncleaned state. The shear tests were repeated after the substrate surfaces were cleaned following the procedure described in Appendix B. The results of these tests are presented in Section 2 of this report.

The scraper used during all the impact shear tests had a cutting edge that was perpendicular to substrate surface. In other words, the angle of attack of the leading edge of the cutter was zero.

A few preliminary impact penetration tests were performed. These tests gave disappointing results in that the substrate surface was damaged, and even cracked, by the impact. Considering the difficulty and time-consuming aspects in developing an impact shear test, it was decided to abandon the work on the development of an impact penetration test. Consequently, no results were obtained for tests of impact penetration applied normal to the ice surface.

Example of Data Generated During Impact Shear Testing and the Associated Data Analysis

An example is given below of the data generated during the impact shear testing and the associated data analysis. The example is presented for five impact shear tests conducted using the falling weight cutting apparatus and ice grown on the PCC laboratory-produced substrates received from SDSM&T. These substrates were the nonpolished specimens. Two free-fall tests were made before the impact runs, and one free-fall test was conducted after the runs. In the remaining test, three impact shear tests were conducted with each substrate under a given set of conditions. Again, two free-fall tests were made before the impact runs, and one free-fall test was conducted after the runs.* The free-fall tests were conducted to check that the apparatus did not change properties during use. The drop height for these eight tests was held constant at 12.375 in (31.433 cm), which produced a velocity near the impact point of about 5.5 mph (8.9 km/hour).

The velocities of the falling cutter were measured through use of an interrupter strip with opaque stripes that interrupt an optical beam as the cutter falls. The strip appears somewhat as in Figure H-5.

Figure H-5. Drawing of the interrupter strip

Table H-1 is a tabulation of data obtained in the described tests. Column 1 gives the data point numbers. Column 2 shows the readings obtained on a toolmaker's microscope for the trailing edges of the stripes on the interrupter strip used to measure the velocity of the cutter. The trailing edges were measured as they produce the signal spikes recorded by the recording oscilloscope. Column 3 shows the distance increments between the measured marks. It can be seen that the markings vary somewhat in separation. This variation is not a cause for concern because the actual distances are used in the velocity computations.

---

* In the remaining test, three impact shear tests were conducted with each substrate under a given set of conditions. Again, two free-fall tests were made before the impact runs, and one free-fall test was conducted after the runs.

Table H-1

:This is a chart of data taken by Gordon E. Gross and Wm. Cunningham on December 29,1989. :
:The data show measurements of the locations of markers used to measure the fall velocity :
:of the cutter and measurements of the time intervals between passage of those marks. :
:These data are used to compute the velocity of the cutter during its fall to the ice and :
:throughout the cutting process. :

Ice shearing study. Dec. 29,1989 G. Gross & Wm. Cunningham
Raw data
Bar strip measurements = M ; Time intervals = DT

Data Point Number	Observed M (in.)	Increment (in.)	Free fall DT(fsec)	Free fall DT(fsec)	Run 1 DT(fsec)	Run 2 DT(fsec)	Run 3 DT(fsec)	Run 4 DT(fsec)	Run 5 DT(fsec)	Free fall DT(fsec)
1	0.0608	0.0608	662	650	662	650	650	650	637	662
2	0.1848	0.1240	1320	1320	1330	1300	1310	1320	1310	1330
3	0.2457	0.0609	615	637	650	637	650	650	625	662
4	0.3070	0.0613	662	650	650	637	650	650	637	650
5	0.3702	0.0632	662	662	675	662	662	662	650	675
6	0.4304	0.0602	650	637	650	637	637	650	637	662
7	0.4927	0.0623	650	637	650	637	650	637	637	650
8	0.5539	0.0612	650	650	650	625	637	650	637	650
9	0.6157	0.0618	650	637	650	637	650	637	625	662
10	0.6767	0.0610	637	637	637	637	637	637	625	637
11	0.7407	0.0640	675	662	675	650	662	675	662	675
12	0.8011	0.0604	637	637	637	625	625	625	625	650
13	0.8635	0.0624	637	637	650	637	637	650	625	650
14	0.9243	0.0608	637	625	625	612	637	625	612	647
15	0.9866	0.0623	637	637	650	625	650	637	637	650
16	1.0473	0.0607	625	625	637	662	637	625	612	625
17	1.1110	0.0637	650	637	650	675	650	637	637	650
18	1.1719	0.0609	637	625	650	675	637	637	625	650
19	1.2349	0.0630	637	637	650	700	650	650	637	650
20	1.2957	0.0608	625	612	637	675	612	625	625	625
21	1.3563	0.0606	625	625	637	687	637	637	625	625
22	1.4176	0.0613	637	625	637	687	637	637	625	650
23	1.4796	0.0620	612	612	637	662	637	625	612	612
24	1.5421	0.0625	637	637	650	687	650	637	637	650
25	1.6041	0.0620	625	625	637	675	637	637	612	625
26	1.6648	0.0607	625	612	637	650	625	625	612	625
27	1.7278	0.0630	637	625	650	687	650	650	637	637
28	1.7889	0.0611	612	612	625	662	625	612	600	625
29	1.8506	0.0617	625	612	625	675	625	637	625	625
30	1.9120	0.0614	600	612	625	662	612	625	600	612
31	1.9747	0.0627	612	600	625	675	612	625	625	625
32	2.0358	0.0611	625	625	625	687	637	625	612	625
33	2.0976	0.0618	612	612	625	687	625	625	612	612
34	2.1597	0.0621	612	600	612	662	625	612	600	612
35	2.2214	0.0617	625	612	637	700	637	625	612	625
		Total times (fsec)----------	22876	22697	23149	23740	23001	22963	22563	23097

Columns 4 and 5 show time intervals for the first two free-fall tests. Columns 6 through 10 show time intervals for five shearing tests. The results in Column 7 (Run 2) show effects of a misalignment which resulted in contact of the cutter with the pavement sample, and they were not used in the analyses. Finally, Column 11 shows the time intervals for the final free-fall tests.

Table H-2 covers the analysis of the free-fall data. The first three columns are in Table H-1. Column 4 shows the total distance the cutter fell. The distances shown were computed based on the fact that the cutter would fall 12.375 in (31.43 cm) at the point of contact with the ice sample which would occur at data point 17. The distances on either side of the contact point were computed using the distances measured for the interrupter strip.

Columns 5, 6, and 7 represent raw data. Column 8 shows the mean values of the time intervals of Columns 5 through 7. The interval velocities shown in Column 9 are based on the average time intervals and on the distances shown in Column 3. The cumulative times shown in Column 10 were computed by adding the average time intervals to an initial time based on free-fall to the height of the first data point. The projected velocities shown in Column 11 result from a linear regression analysis of the data in Columns 9 and 10. The velocity is expected to be a linear function of the time as the acceleration should be nearly constant. The value of the gravity acceleration shown at the bottom of the regression chart is 29.25 ft/s/s (8.92 m/s/s). This value is below the normal value of 32.2 ft/s/s (9.8 m/s/s) and thus suggests drag due to friction and air resistance.

Table H-3 shows data and results of analyses for the shearing tests. The columns are similar to those discussed above for Table H-2 except as indicated in the following remarks. The columns of particular interest in this table are Columns 9 through 12. Column 9 shows the mean velocity of the cutter as it falls to the sample and proceeds on through the cutting process. There is too much scatter in the data to allow easy observation of the change in velocity at the point of impact. That change is readily observable in the graphical presentation of Figure H-6. Columns 11 and 12 show results of linear regression analyses of the velocity data of Column 9. In carrying out the regression analysis for the precutting range, data prior to point 14 (the earliest known impact point for the data set) were used even though the illustrated regression line is extended beyond that point. The regression analysis for the postcutting range was limited to data after point 17 for similar reasons even though the illustrated line is extended to earlier points.

Table H-2

This chart show calculations of the free-fall velocities and the acceleration of the cutter. The information shown is used to check on the performance of the apparatus. The distance increments shown were measured on a tool makers microscope. The time intervals were measured using the cursor timing marks on the storage oscilloscope used to record the signals from an optical coupler which detected the passage of marks on a transparent strip attached to the cutter. The measured intervals shown are between the trailing edges of those marks. The time intervals shown are averages of the three observatiions shown in Table I.

Data Bar strip measurements = M ; Time intervals = DT

Point Number	Observed M (in.)	Increment (in.)	Cum. Dist. (in.)	Free fall DT(fsec)	Free fall DT(fsec)	Free fall DT(fsec)	Average interval DT(fsec)	Interval velocity (in/sec)	Cum. time T(fsec)	Projected velocity (in/sec)
1	0.0608	0.0608	11.3248	662	650	662	658	92.40	242767	93.12
2	0.1848	0.1240	11.4488	1320	1320	1330	1323	93.70	244090	93.59
3	0.2457	0.0609	11.5097	615	637	662	638	95.45	244728	93.81
4	0.3070	0.0613	11.5710	662	650	650	654	93.73	245382	94.04
5	0.3702	0.0632	11.6342	662	662	675	666	94.85	246049	94.27
6	0.4304	0.0602	11.6944	650	637	662	650	92.66	246698	94.50
7	0.4927	0.0623	11.7567	650	637	650	646	96.49	247344	94.73
8	0.5539	0.0612	11.8179	650	650	650	650	94.15	247994	94.96
9	0.6157	0.0618	11.8797	650	637	662	650	95.13	248644	95.18
10	0.6767	0.0610	11.9407	637	637	637	637	95.76	249281	95.41
11	0.7407	0.0640	12.0047	675	662	675	671	95.43	249951	95.64
12	0.8011	0.0604	12.0651	637	637	650	641	94.18	250593	95.87
13	0.8635	0.0624	12.1275	637	637	650	641	97.30	251234	96.09
14	0.9243	0.0608	12.1883	637	625	647	636	95.55	251870	96.32
15	0.9866	0.0623	12.2506	637	637	650	641	97.14	252512	96.54
16	1.0473	0.0607	12.3113	625	625	625	625	97.12	253137	96.76
17	1.1110	0.0637	12.3750	650	637	650	646	98.66	253782	96.99
18	1.1719	0.0609	12.4359	637	625	650	637	95.55	254420	97.21
19	1.2349	0.0630	12.4989	637	637	650	641	98.23	255061	97.44
20	1.2957	0.0608	12.5597	625	612	625	621	97.96	255682	97.65
21	1.3563	0.0606	12.6203	625	625	625	625	96.96	256307	97.87
22	1.4176	0.0613	12.6816	637	625	650	637	96.18	256944	98.10
23	1.4796	0.0620	12.7436	612	612	612	612	101.31	257556	98.31
24	1.5421	0.0625	12.8061	637	637	650	641	97.45	258197	98.54
25	1.6041	0.0620	12.8681	625	625	625	625	99.20	258822	98.76
26	1.6648	0.0607	12.9288	625	612	625	621	97.80	259443	98.97
27	1.7278	0.0630	12.9918	637	625	637	633	99.53	260076	99.20
28	1.7889	0.0611	13.0529	612	612	625	616	99.13	260692	99.41
29	1.8506	0.0617	13.1146	625	612	625	621	99.41	261313	99.63
30	1.9120	0.0614	13.1760	600	612	612	608	100.99	261921	99.84
31	1.9747	0.0627	13.2387	612	600	625	612	102.40	262533	100.06
32	0.0611	0.0611	11.3251	625	625	625	625	97.76	263158	100.28
33	0.1229	0.0618	11.3869	612	612	612	612	100.98	263770	100.49
34	0.1850	0.0621	11.4490	612	600	612	608	102.14	264378	100.71
35	0.2467	0.0617	11.5107	625	612	625	621	99.41	264999	100.92

Regression Output:

Constant	7.909914
Std Err of Y Est	1.311255
R Squared	0.759305
No. of Observations	35
Degrees of Freedom	33
X Coefficient(s)	0.000351
Std Err of Coef.	3.44E-05

"G" = 29.25 f/s/s

"G" value indicates some drag.

Table H-3

This chart show calculations of the velocities and the acceleration of the cutter during cutting tests. The velocities are computed for each run, then are averaged to produce estimates of the velocity change due to cutting.

The points of impact of the cutter on the ice varied from point 13 to point 16. Therefore the regression analyses are made for points 1 to 13 as free fall, and for points 18 to 35 for ice cutting. The projections depicted in the matching graph extend beyond the times used in the regression analyses to emphasize the velocity change at impact.

Time intervals = DT

Point Number	Increment (in.)	Cum. Dist. (in.)	Run 1 DT(fsec)	Run 3 DT(fsec)	Run 4 DT(fsec)	Run 5 DT(fsec)	Mean interval (fsec)	Mean velocity (in/sec)	Cumulative time T(sec)	Pre-cut Proj. velocity (in/sec)	Post-cut Proj. velocity (in/sec)
1	0.0608	11.3248	662	650	650	637	650	93.57	0.242759	93.68	
2	0.1240	11.4488	1330	1310	1320	1310	1318	94.12	0.244077	94.18	
3	0.0609	11.5097	650	650	650	625	644	94.60	0.244720	94.43	
4	0.0613	11.5710	650	650	650	637	647	94.78	0.245367	94.67	
5	0.0632	11.6342	675	662	662	650	662	95.43	0.246029	94.92	
6	0.0602	11.6944	650	637	650	637	644	93.55	0.246673	95.16	
7	0.0623	11.7567	650	650	637	637	644	96.81	0.247316	95.41	
8	0.0612	11.8179	650	637	650	637	644	95.10	0.247960	95.65	
9	0.0618	11.8797	650	650	637	625	641	96.49	0.248600	95.89	
10	0.0610	11.9407	637	637	637	625	634	96.21	0.249234	96.13	
11	0.0640	12.0047	675	662	675	662	669	95.74	0.249903	96.39	
12	0.0604	12.0651	637	625	625	625	628	96.18	0.250531	96.63	
13	0.0624	12.1275	650	637	650	625	641	97.42	0.251171	96.87	95.17
14	0.0608	12.1883	625	637	625	612	625	97.32	0.251796	97.10	95.38
15	0.0623	12.2506	650	650	637	637	644	96.81	0.252439	97.35	95.61
16	0.0607	12.3113	637	637	625	612	628	96.69	0.253067	97.59	95.83
17	0.0637	12.3750	650	650	637	637	644	98.99	0.253711		96.05
18	0.0609	12.4359	650	637	637	625	637	95.57	0.254348		96.27
19	0.0630	12.4989	650	650	650	637	647	97.41	0.254995		96.49
20	0.0608	12.5597	637	612	625	625	625	97.32	0.255619		96.71
21	0.0606	12.6203	637	637	637	625	634	95.58	0.256253		96.93
22	0.0613	12.6816	637	637	637	625	634	96.69	0.256887		97.15
23	0.0620	12.7436	637	637	625	612	628	98.77	0.257515		97.37
24	0.0625	12.8061	650	650	637	637	644	97.13	0.258159		97.59
25	0.0620	12.8681	637	637	637	612	631	98.30	0.258790		97.81
26	0.0607	12.9288	637	625	625	612	625	97.16	0.259414		98.03
27	0.0630	12.9918	650	650	650	637	647	97.41	0.260061		98.25
28	0.0611	13.0529	625	625	612	600	616	99.27	0.260676		98.46
29	0.0617	13.1146	625	625	637	625	628	98.25	0.261304		98.68
30	0.0614	13.1760	625	612	625	600	616	99.76	0.261920		98.90
31	0.0627	13.2387	625	612	625	625	622	100.84	0.262542		99.11
32	0.0611	11.3251	625	637	625	612	625	97.80	0.263166		99.33
33	0.0618	11.3869	625	625	625	612	622	99.40	0.263788		99.54
34	0.0621	11.4490	612	625	612	600	612	101.43	0.264400		99.76
35	0.0617	11.5107	637	637	625	612	628	98.29	0.265028		99.97

Regression Output:

Constant	1.793658
Std Err of Y Est	0.768195
R Squared	0.642585
No. of Observations	13
Degrees of Freedom	11
X Coefficient(s)	378.52
Std Err of Coef.	85.12

"G" = 31.543567 f/s/s

Regression Output:

Constant	8.07906509
Std Err of Y Est	1.12301258
R Squared	0.53247045
No. of Observations	18
Degrees of Freedom	16
X Coefficient(s)	346.73
Std Err of Coef.	81.23

"G" = 28.894396 f/s/s

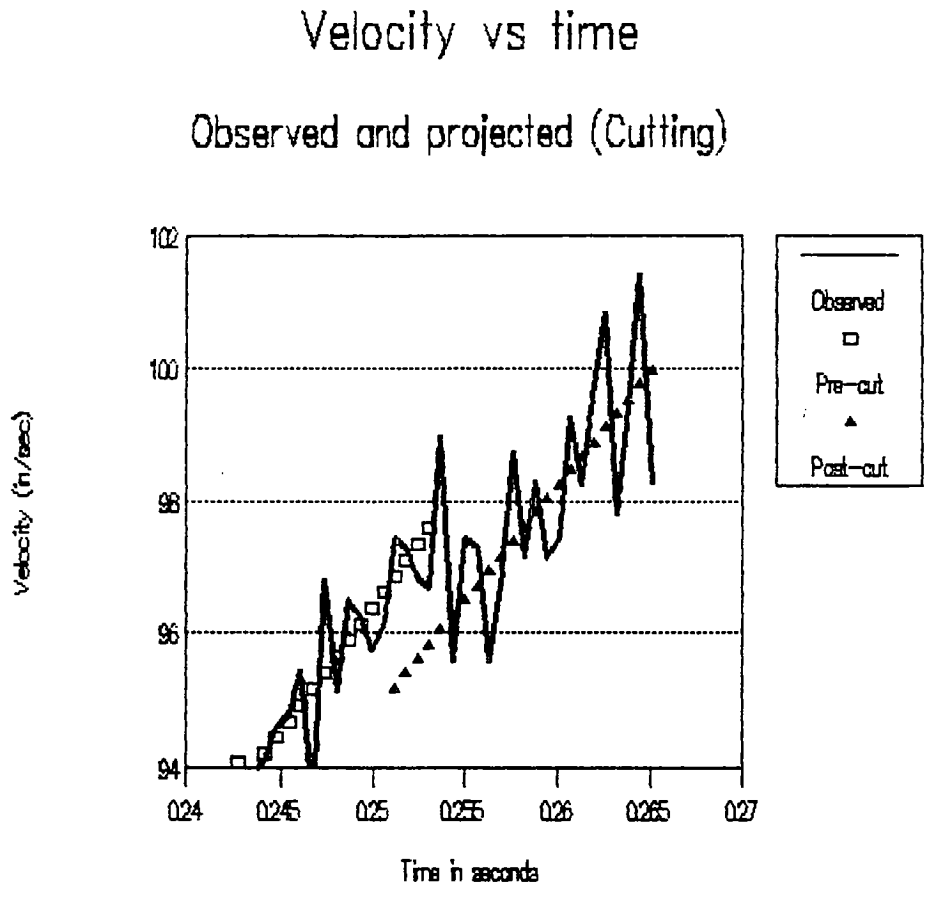

Figure H-6. Graphs of observed and projected velocities for an ice shearing test. Results are based on averages of four test runs

Table H-4 shows the computed results of the tests for those points near the impact point. Here, the last three columns are of interest. The third column from the right shows the differences in the projected, squared velocities, and the last two columns show the differences between the pre- and postcutting kinetic energies projected by the regression analyses. The small variation in the differences shown for points 13 through 16 indicates that the results are not very sensitive to errors in estimating the actual point of impact. This latter result requires that the regression analyses exclude all data from points in which the impact point might lie. The energy difference of about 0.44 J (0.34 ft-lb) is similar to a value of 0.7 J reported in an earlier test and is similar to estimates made in conversations with SDSM&T.

Concluding Remarks Concerning the Impact Shear Test Results

One source of concern that might be raised in the shear tests deals with the error that might be produced by the kinetic energy carried away by the sheared ice. The limit of that energy may be calculated as follows:

The maximum kinetic energy to be carried away by the flying ice would occur if the ice left the cutter after impact with no energy being lost in the cutting process (i.e., a perfectly elastic collision of the cutter on the ice). The energy thus carried can be estimated through a model in which a massive object (the cutter) strikes a light object (the ice) in an elastic impact. In that case, both energy and momentum are conserved, and the resulting velocity of the lighter object can be shown to be:

$$v = (2 \cdot M \cdot V) / (m + M)$$

where:
- v is the final velocity of the light object,
- V is the initial velocity of the heavy object,
- M is the mass of the heavy object, and
- m is the mass of the light object.

It can be seen here that, if the heavy object is very much heavier than the light object, the velocity of the light object after the impact will be about twice the velocity of the heavy object before impact.

Table H-4

This chart show calculations of the change in kenetic energy at the time of cutting of the ice by the falling cutter.
The changes in the average velocity in the range from point 13 to point 18 are used to compute the kinetic energy change represented by the difference in the projected velocities at those points.
It can be seen that the energy difference is about 0.46 Joules (0.34 ft-lbs) in that area.
The small variation in the energy computed at the points chosen gives some confidence that the result is not sensitive to errors in estimating the exact point of impact.

	Time intervals = DT					Pre-cut	Post-cut	Difference	Kinetic	Kinetic
Point Number	Increment (in.)	Cum. Dist. (in.)	Mean interval (/sec)	Mean velocity (in/sec)	Cumulativ time T(sec)	Proj. velocity (in/sec)	Proj. velocity (in/sec)	in squared velocities (m}/s})	energy change (Joules)	energy change (ft-lbs)
11	0.0640	12.0047	669	95.74	0.249903	96.39				
12	0.0604	12.0651	628	96.18	0.250531	96.62				
13	0.0624	12.1275	641	97.42	0.251171	96.87	95.17	0.2105	0.45	0.33
14	0.0608	12.1883	625	97.32	0.251796	97.10	95.38	0.2135	0.45	0.33
15	0.0623	12.2506	644	96.81	0.252439	97.35	95.61	0.2166	0.46	0.34
16	0.0607	12.3113	628	96.69	0.253067	97.58	95.82	0.2196	0.47	0.34
17	0.0637	12.3750	644	98.99	0.253711	97.83	96.05	0.2227	0.47	0.35
18	0.0609	12.4359	637	95.57	0.254348	98.07	96.27	0.2257	0.48	0.35
19	0.0630	12.4989	647	97.41	0.254995		96.49			
20	0.0608	12.5597	625	97.32	0.255619		96.71			

In the tests reported here, the maximum velocity of the ice can be calculated to be about 5.0 m/s (about 196 in/s or twice the velocity of the cutter). If the ice sample measured about 1 x 2.5 x 2.5 cm (about 3/8 x 1 x 1 in), it would have a mass of about 0.00625 kg (about 0.014 lb). At a velocity of 5.0 m/s, the kinetic energy of the ice would be about 0.08 J (0.06 ft-lb). Even in this extreme case, it can be seen that the kinetic energy loss does not mask the 0.44 J energy change shown in the tests.

While it is recognized that the tests and results presented here are limited in scope, it does seem clear that the system used was capable of measuring the energy requirements of ice removal with usable accuracy. In the example case presented, the maximum error appears to be less than 18%. This error limit is based on the extreme assumption of an elastic impact of the cutter on the ice. That the impact is far less than elastic is shown by the fact that the energy loss from the cutter on impact (about 0.44 J) is about 5.5 times that to be carried away by the ice in a purely elastic impact.

Based on the foregoing discussions, it is believed that the apparatus, as used, can show the effects of cutter speed and of substrate surface condition on the energy needed for ice removal.

Some improvement in the accuracy of the tests might be achieved by increasing the mass and cross-section area of the ice sample. For example, if the ice sample were to be made twice as thick and twice as wide and high, then its mass would be increased eightfold and the removal energy increased fourfold. These changes would have two benefits. First, the cutting energy would be four times as large as in the present tests (i.e., about 1.76 J or 1.3 ft-lb) while the maximum kinetic error would be reduced slightly. Where the maximum kinetic error at present is about 18% of the total measured energy loss, the larger sample would reduce that error to about 5%. Unfortunately, the remaining time and funds in the contract did not permit this extension of the investigation.

Appendix I

Details of Chemical Undercutting Experiments

The details are given in this appendix of two sets of experiments conducted to investigate the destruction of the ice-substrate bonds by chemical undercutting. The materials used and procedures followed during each set of experiments are presented below, along with the details of the experimental results obtained.

Chemical Undercutting of Ice on Model and Pavement Component Substrates

The first set of experiments consisted of determining the time-dependent undercut area produced by four deicers at an ice-substrate interface under a variety of experimental conditions. The four deicers used were saturated solutions of ethylene glycol ($HOCH_2CH_2OH_2$), sodium chloride (NaCl), calcium chloride ($CaCl_2$), and calcium-magnesium-acetate (CMA). Seven substrates were used in the tests and consisted of three model substrates (FEP Teflon, Mylar, and gold) and four pavement component substrates (fused silica, portland cement mortar, limestone, and asphalt). Measurements of the undercutting action of saturated solutions of the deicers were made at the four test temperature levels of 25°F (–4°C), 15°F (–9°C), 5°F (–15°C), and –40°F (–40°C). Three freezing rates (slow, medium, and fast) were also employed in combination with two modes of freezing: (1) from the ice-substrate interface up to the free surface of the ice, and (2) from the free surface of the ice down to the ice-substrate interface.

A statistical design was developed for the undercutting tests because of the large number of tests of possible combinations that could have been conducted. A full factorial design would

have required 672 tests,* each to be performed in triplicate. The number of required tests was reduced to 504, with each being performed in triplicate.

Substrate Configurations and Undercutting Test Specimen Preparation

The undercutting tests involving the model and pavement component substrates were performed in a specially constructed cold chamber. The chamber is described in Appendix E. The chamber was designed to accommodate 4- x 8-in (10.2- x 20.4-cm) sizes for the model and pavement component substrates. After the chamber was well along in its construction, it was found not possible to produce limestone substrates this large. Only 3- x 3-in (7.6- x 7.6-cm) limestone samples could be conveniently cut. The other substrate sizes remained at the 4- x 8-in (10.2- x 20.4-cm) dimensions.

Twelve undercutting test sites were made on each 4- x 8-in (10.2- x 20.4-cm) substrate. The spacings between the undercutting fluid injection sites for these substrates were 1.25 in (3.2 cm). Six test sites were made on each 3- x 3-in (7.6- x 7.6-cm) limestone substrate. The spacings between the undercutting fluid injection sites for these latter substrates were 1.1 in (2.8 cm). Thus an undercutting radius of 0.55 in (1.4 cm) could be accommodated on all the substrates tested.

Ice of 3/16-in (0.48-cm) thickness was formed on the substrates under the desired freezing conditions. Doubly distilled, deionized water was used to grow the ice samples. Tapered holes were produced in the ice during the freezing by use of Teflon plugs resting on the substrate surface. The configuration of a plus is shown in Figure I-1A. It was necessary to hold the plugs in the correct relative position on the substrate. A 3-in (7.6-cm) square, 1/4-in (0.64-cm) thick acrylic sheet was prebored to accept six of the plugs. A sketch of this arrangement is presented in Figure I-1B.

Double-distilled water was poured over the substrate, with the edges dammed with aluminum tape to a height of ¼ in (0.64 cm) above the substrate surface, in an amount calculated to produce a 3/16-in (0.48-cm) thick layer. The plug-holding fixtures (one for a 3- x 3-in [7.6- x 7.6-cm] size, two for a 4- x 8-in [10.2- x 20.4-cm] size) were centered on the substrate. This assembly was then placed in the cold chamber and frozen at the desired temperature freezing rate and direction.

---

* 4 deicers x 7 substrates x 3 freezing rates x 2 modes of freezing x 4 temperatures = 672 tests.

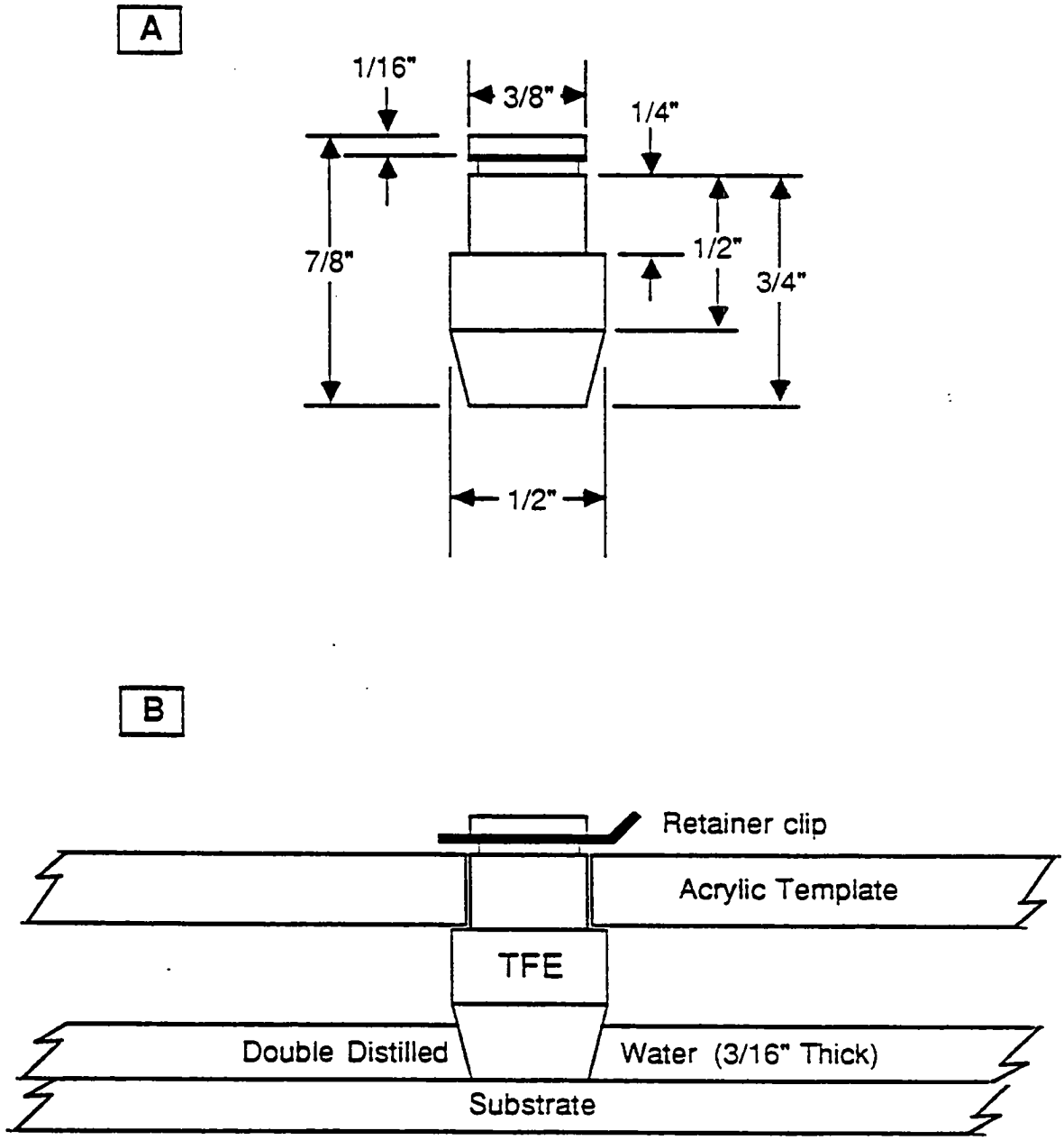

Figure I-1. Undercutting test specimen preparation

After the ice was completely frozen, the assembly was removed from the freezing chamber. The holding plate, pins removed, and the plugs were pulled out. These plugs nearly fell out in most cases. Applying a light torque to the plug removed any stubborn area with very rare damage to the ice structure. Once the plugs were removed, the substrate-ice sample was returned to the ice chamber and allowed to reequilibrate for 45 to 60 minutes. When the samples were at equilibrium temperature, they were moved to the filling port in the large insulated extension for injection of the required undercutting solution.

Injection of the Undercutting Solution

It is necessary that these solutions be saturated with the dissolved salt (or the compound) at the test temperature. Solutions were prepared in bulk at the test temperature and stored at that temperature in an ancillary cold chamber or in the working chamber. The salt solutions were dyed with sufficient "Bullseye Dye" (a product of Dow Chemical Company) to yield an intense blue. Crystal violet dye was found quite suitable for neat ethylene glycol.

The required number of 1-mL capacity plastic disposable syringes was loaded into three 0.5-in (1.3-cm) thick by 7-in (17.8-cm) long by 4-in (10.2-cm) wide aluminum plates that each contained twelve 3/8-in (0.95-cm) diameter holes through the width of the plate that just cleared the syringes. The syringe loaded plates were placed in the cold chamber and chilled to the test temperature and then loaded with the test solution (chilled to O°C in an ice bath) and returned to the cold chamber along with a chilled polyurethane foam insulating holder. When they were chilled to the test temperature, they were loaded into cold urethane foam insulating holders and removed from the cold chamber.

The ice-substrate sample was placed at the filling port of the test chamber, and the 0.25-mL solutions placed in their respective sites. The fluid added was sufficient to fill the injection site to a 1/8-in (0.32-cm) height. The sample was returned to the rotating cold plate and the next sample moved into place for filling, etc.

Photographs were taken of each 4- x 8-in (10.2- x 20.4-cm) test specimen (or two 3- x 3-in [7.6- x 7.6-cm] specimens) at regular intervals by a 35-mm camera mounted directly above the cold chamber. Two sets of flood lamps are used to illuminate the samples. The photo schedule was such that each test sample was photographed at 0-, 10-, 20-, 30-, 45-, and 60-minute intervals. As the undercutting occurred, the dye made the increased diameter of the initial cavity quite visible. The color slides were projected onto a screen to make measurement of the area of the undercut possible by tracing onto a vellum paper sheet and making subsequent area determination by the planimeter method of area determination. A

LCD digital clock and a standardized area grid were placed on the rotating disk prior to these experiments to provide a photographic record of the time lapsed during the tests and a standard reference area for use in determining the area of undercut.

Trial Undercutting Experiments

Several trial runs of the undercutting experiments were made using a plate of glass as the substrate. The purposes of these trial runs were to check out the processes and procedures and to develop the expertise required to properly time, photograph, and valuate the experimental results. Saturated sodium chloride (NaCl) solution and neat (undiluted) ethylene glycol were used as the undercutting agents. All tests were performed at 5°F (−15°C). It was found that three freezing rates (slow, medium, and fast) could be obtained by use of both top and bottom insulating materials to reduce the heat transfer rate. The actual freezing rate range was dependent upon the heat capacity of the different substrates and the cold chamber operating temperature. Direction of freezing (bottom-up or top-down) was also controlled by placement of the insulation.

The dyes used were very effective and undercutting patterns were highly visible to the eye. The 35-mm color slides clearly showed the undercutting action on all the substrates except asphalt. It was not possible to obtain photographs of the undercutting on the asphalt substrate because of the dense black background produced by the material. Consequently, no undercutting data are presented for this material. Procedures were later developed so that undercutting action on asphalt cores and laboratory-produced specimens could be obtained. These procedures are described later in this appendix.

Up to three replicate runs were performed for each unique combination of substrate, deicer, temperature, freezing rate, and freezing mode. The replicate results were then averaged prior to all statistical analyses.

The undercutting action by the four deicer solutions tended to produce nearly perfect circular patterns at the ice-substrate interface which was relatively smooth. In some instances at 25°F (−4°C), the undercut areas produced by ethylene glycol overlapped each other. The intersecting regions retained their circular patterns.

During the analysis of the undercutting data, the measured areas were adjusted to account for the surface area, at time zero, that the Teflon plug was in contact with the substrate. This initial area, created when the plug was removed just before the experiment, was subtracted from all measured undercut areas obtained from the 35-mm photographic records. The

resulting differences were then normalized by dividing them by the appropriate weight of the deicer. These final results are referred to as adjusted undercut areas.

In order to show the maximum of information in tabular and plotted form, a new variable, "Freezing Mode/Rate," was constructed as shown in Table I-1. there are a total of six levels of this combined variable (3 freezing rates x 3 freezing modes).

Table I-1. Freezing mode/rate codes

Freezing code	Freezing rate	Freezing mode
A	Fast	Bottom-up
B	Fast	Top-down
C	Medium	Bottom-up
D	Medium	Top-down
E	Slow	Bottom-up
F	Slow	Top-down

Plots were developed of the average adjusted undercut area versus time for each of the 24 deicer x substrate combinations (4 deicers x 6 substrates). These plots are shown in Figures I-2 through I-25. The data points are coded by the freezing mode/rate code. The key given in the plots indicates the temperature corresponding to the freezing mode/rate codes for each undercutting experiment.

Chemical Undercutting of Ice on Highway Pavement Materials

The second set of undercutting experiments consisted of determining the time-dependent undercut area produced by three deicers at the ice-substrate interface on highway core samples and laboratory-produced specimens. The three deicers used were ethylene glycol, sodium chloride, and calcium chloride. Six substrates were used in the tests and consisted of core samples taken from four types of highway pavements and two types of laboratory-produced specimens of highway pavement materials. Measurements of the undercutting action of saturated solutions of the deicers were made at three test temperatures of 25°F (–4°C), 15°F (–9°C), and 5°F (–15°C). The undercutting tests with the three deicers were performed with all temperature-substrate combinations.

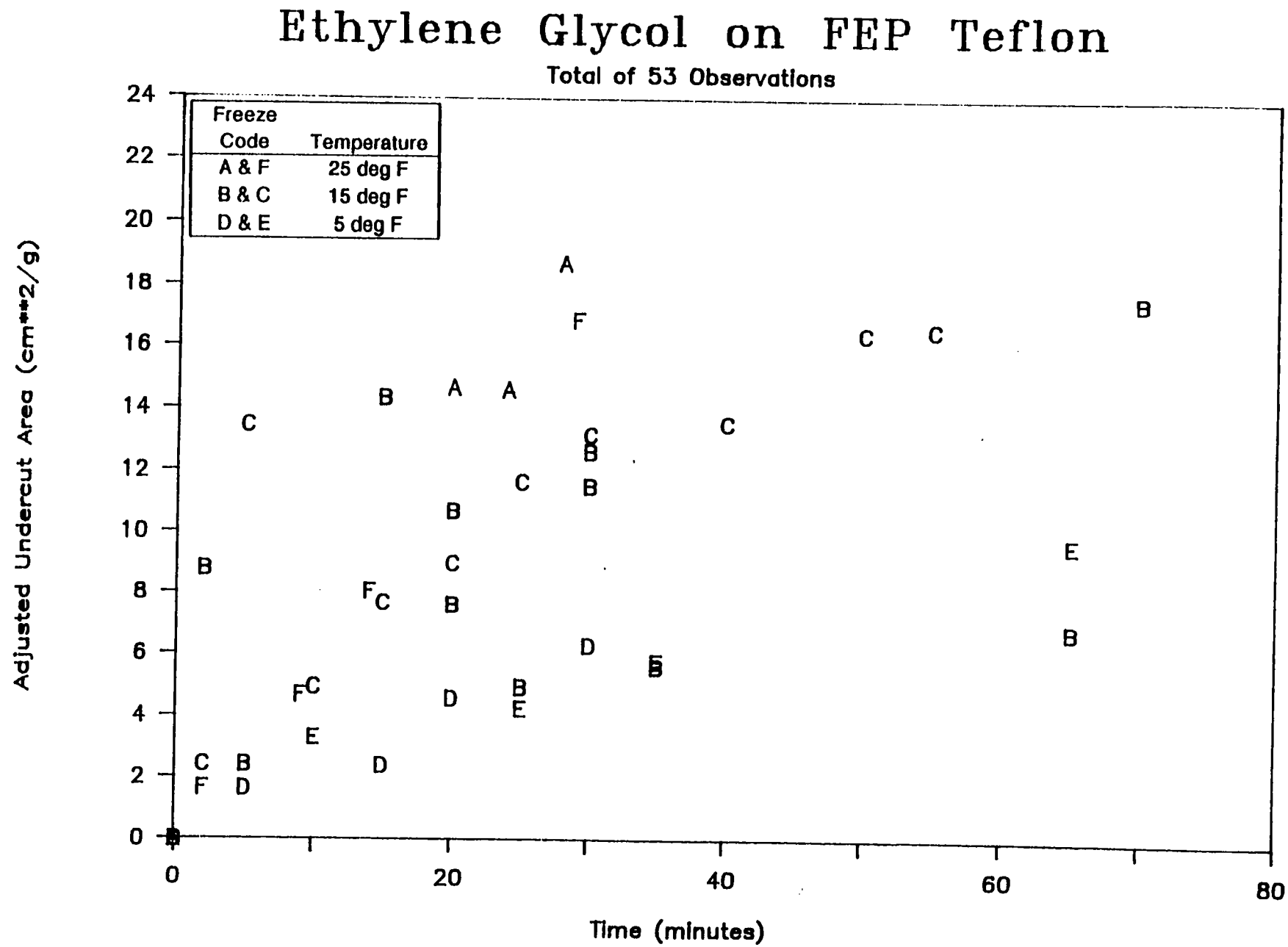
Ethylene Glycol on FEP Teflon
Total of 53 Observations
Freeze Code
Temperature
A & F
25 deg F
B & C
15 deg F
D & E
5 deg F
Adjusted Undercut Area (cm**2/g)
Time (minutes)
0
2
4
6
8
10
12
14
16
18
20
22
24
0
20
40
60
80

Figure I-2

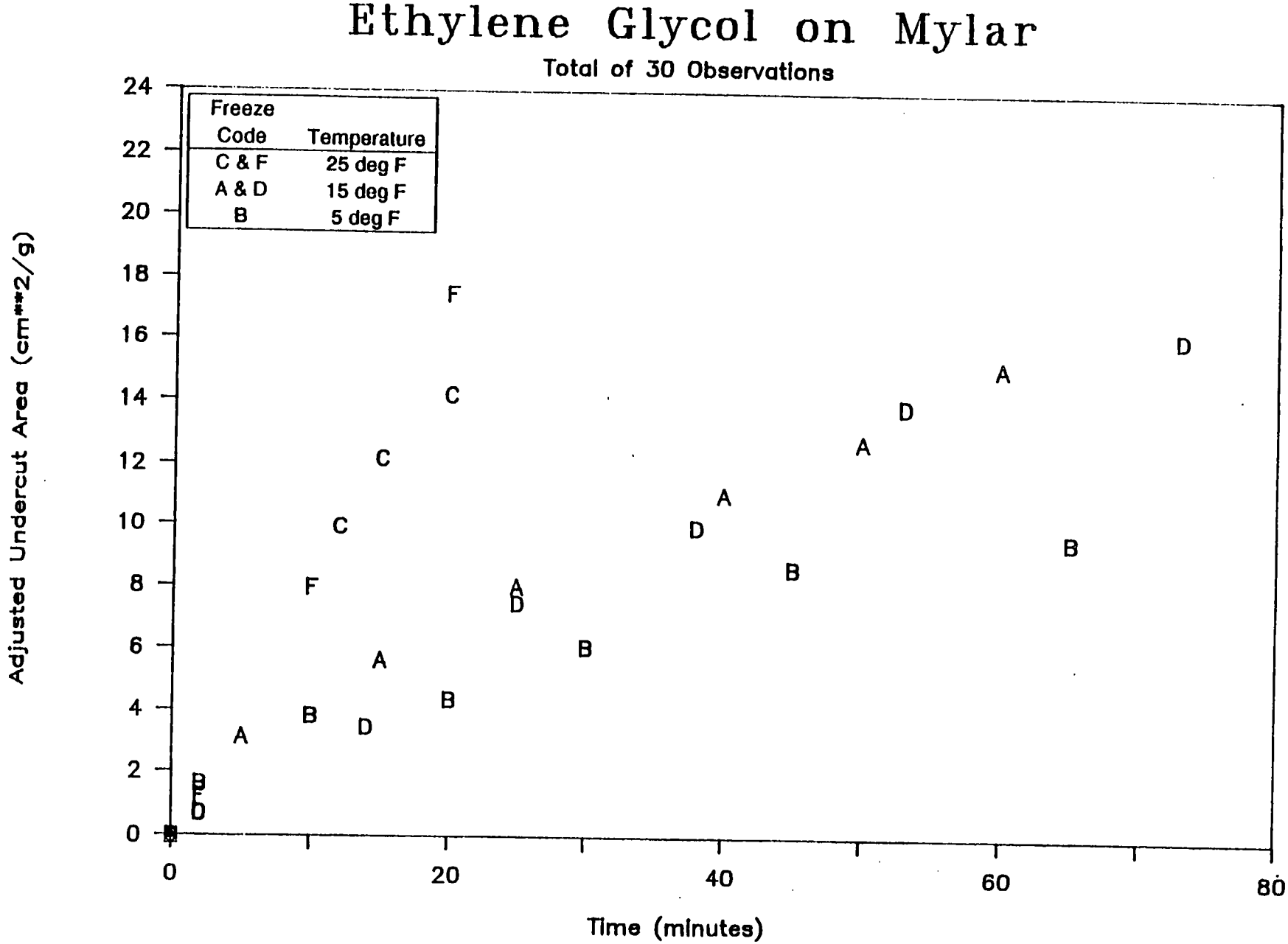
Ethylene Glycol on Mylar
Total of 30 Observations
Freeze Code
Temperature
C & F
25 deg F
A & D
15 deg F
B
5 deg F
Adjusted Undercut Area (cm**2/g)
Time (minutes)
0
2
4
6
8
10
12
14
16
18
20
22
24
0
20
40
60
80

Figure I-3

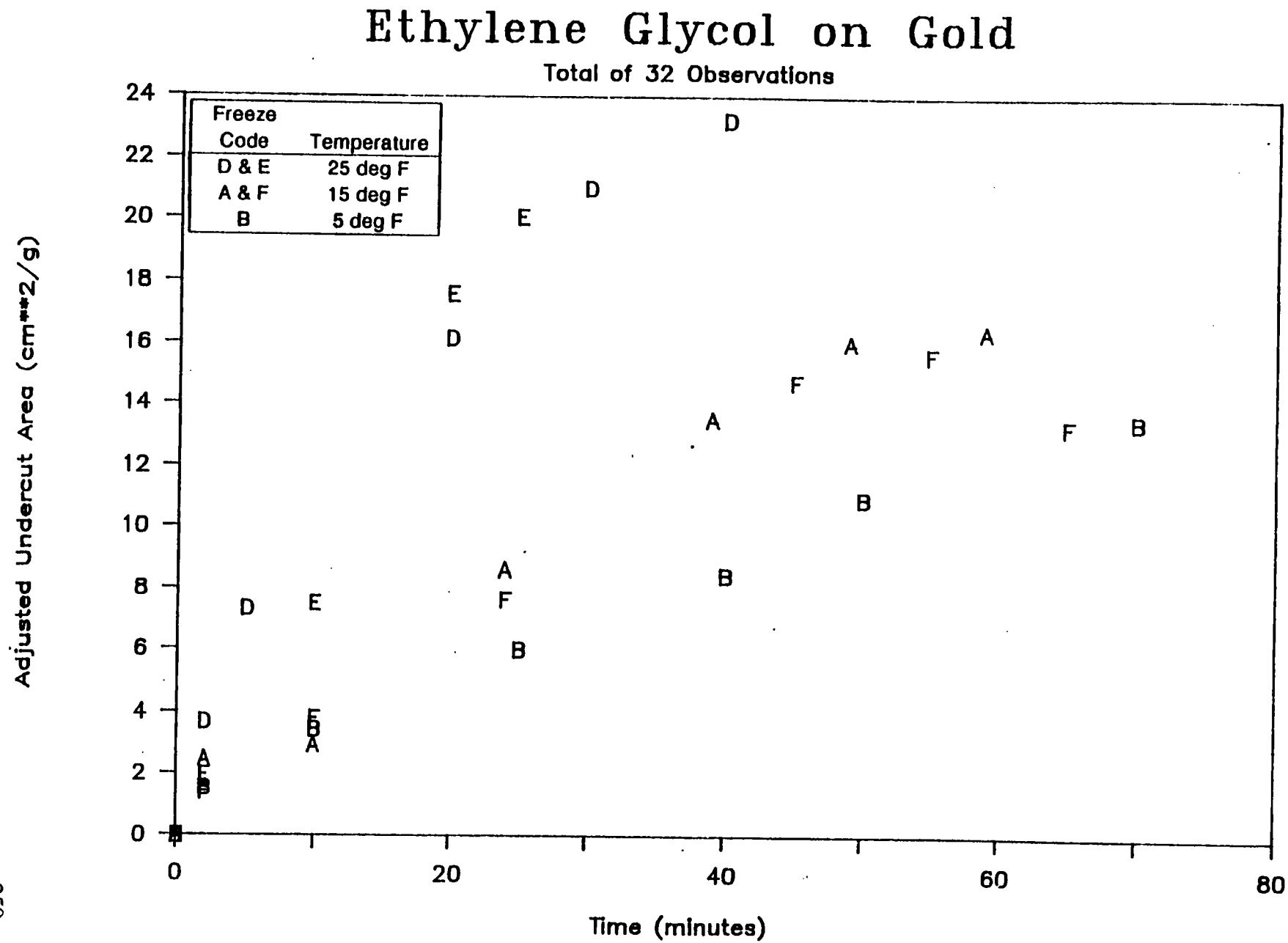
Ethylene Glycol on Gold
Total of 32 Observations
Freeze Code
Temperature
D & E
25 deg F
A & F
15 deg F
B
5 deg F
Adjusted Undercut Area (cm**2/g)
Time (minutes)
0
2
4
6
8
10
12
14
16
18
20
22
24
0
20
40
60
80

Figure I-4

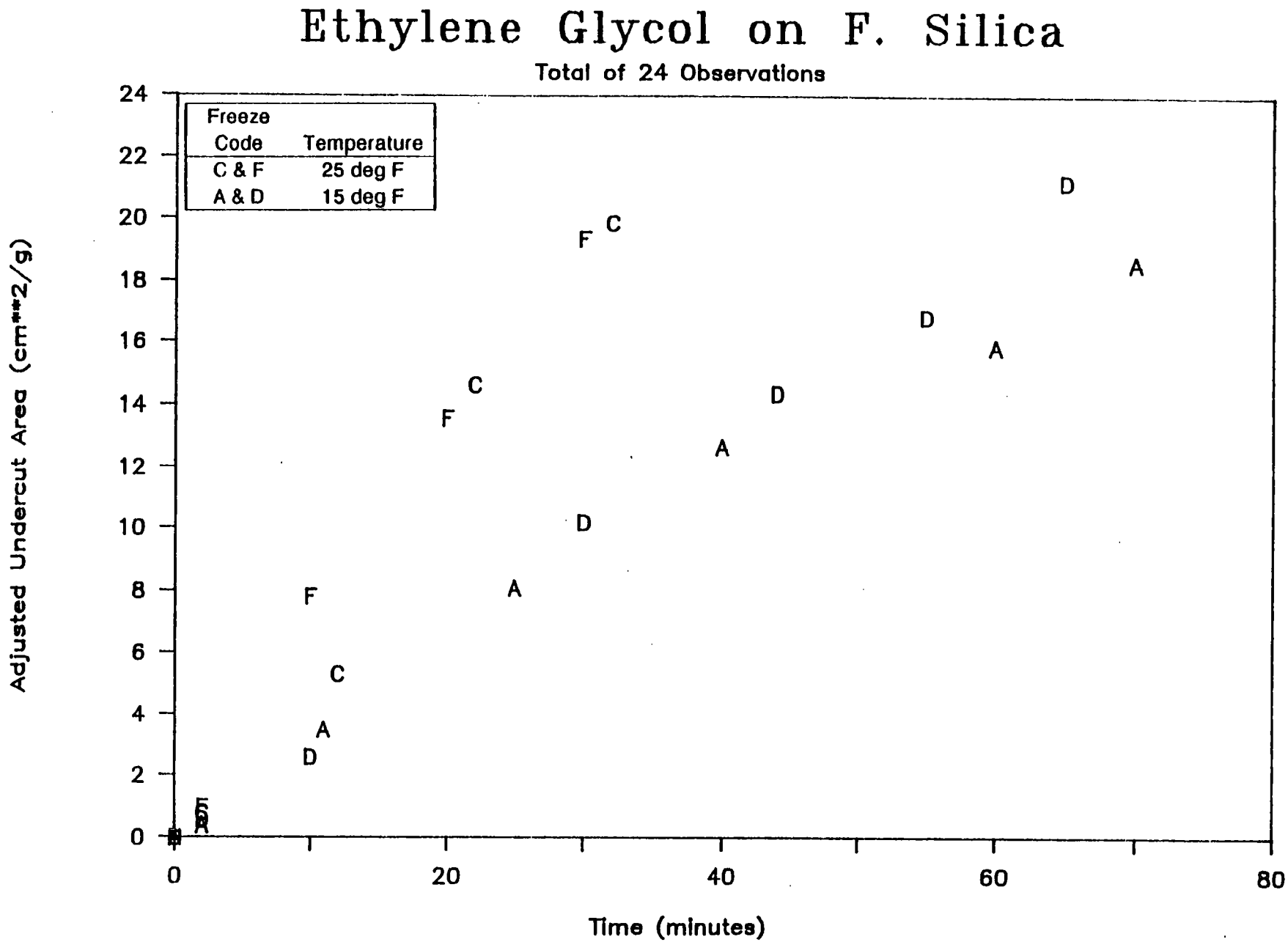
Ethylene Glycol on F. Silica
Total of 24 Observations
Freeze Code
Temperature
C & F
25 deg F
A & D
15 deg F
Adjusted Undercut Area (cm**2/g)
Time (minutes)
0
2
4
6
8
10
12
14
16
18
20
22
24
0
20
40
60
80

Figure I-5

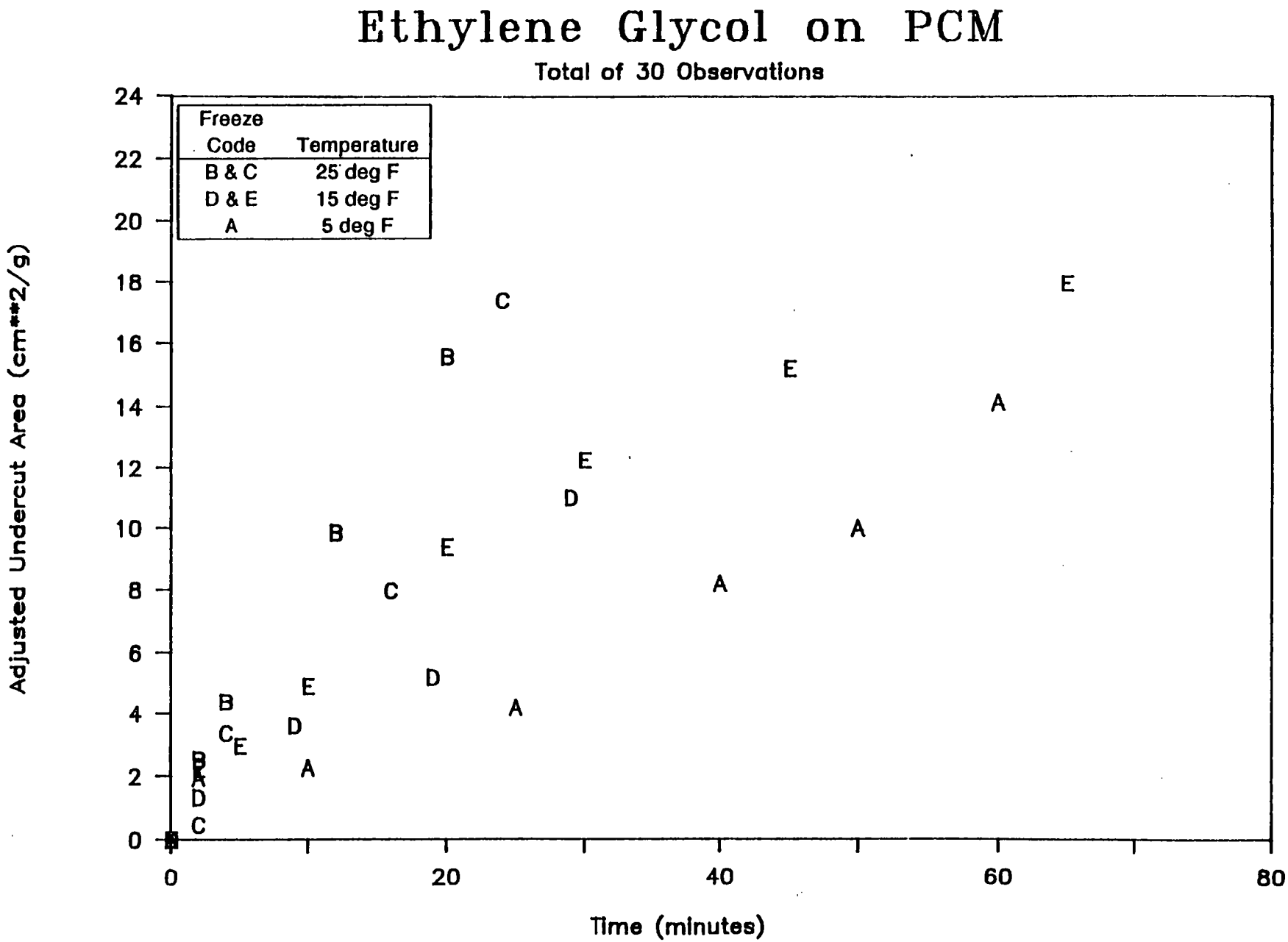
Ethylene Glycol on PCM
Total of 30 Observations
Freeze Code
Temperature
B & C
25 deg F
D & E
15 deg F
A
5 deg F
Adjusted Undercut Area (cm**2/g)
Time (minutes)
0
2
4
6
8
10
12
14
16
18
20
22
24
0
20
40
60
80

Figure I-6

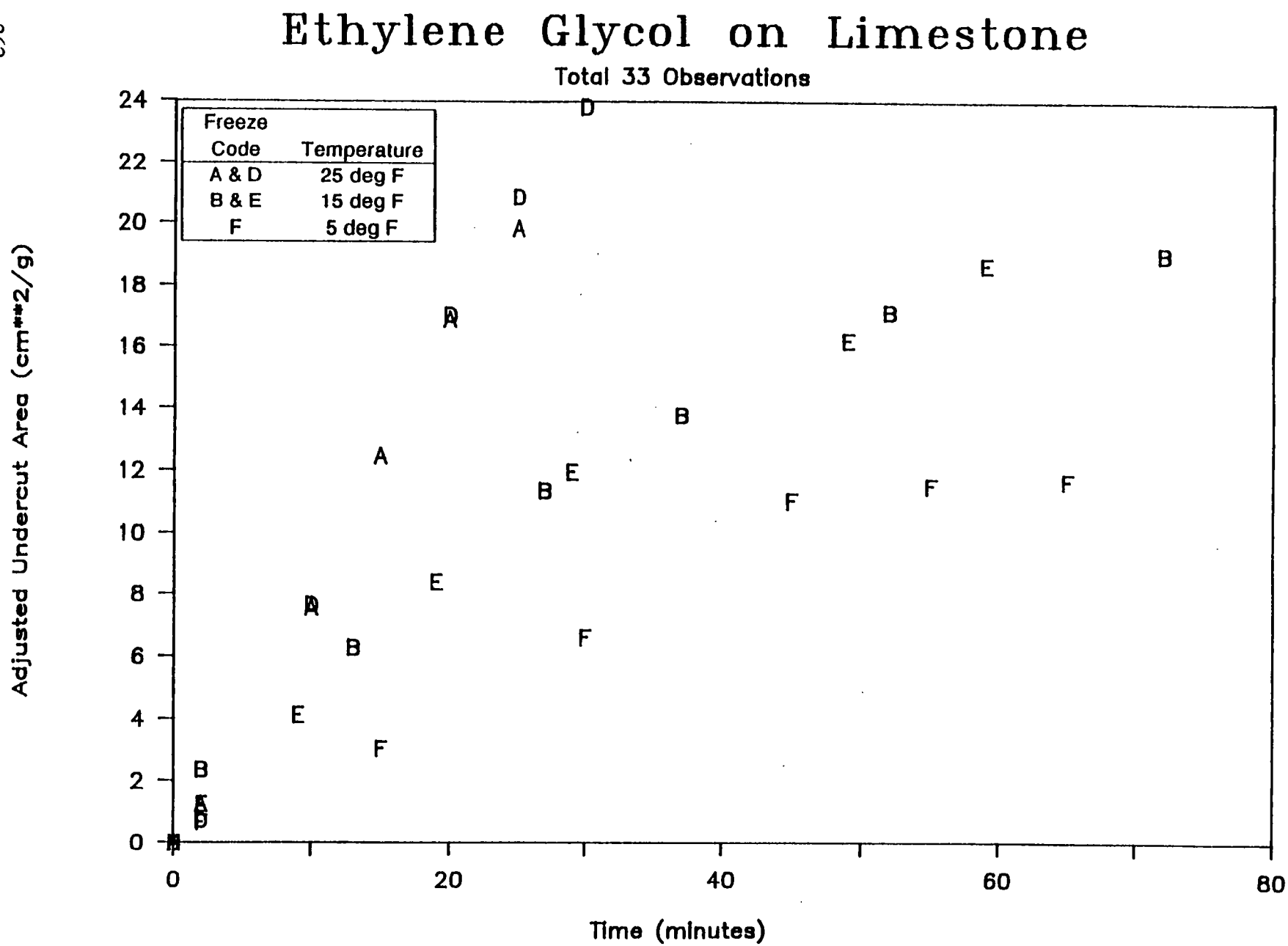
Ethylene Glycol on Limestone
Total 33 Observations
Freeze Code
Temperature
A & D
25 deg F
B & E
15 deg F
F
5 deg F
Adjusted Undercut Area (cm**2/g)
Time (minutes)
0
20
40
60
80
0
2
4
6
8
10
12
14
16
18
20
22
24

Figure I-7

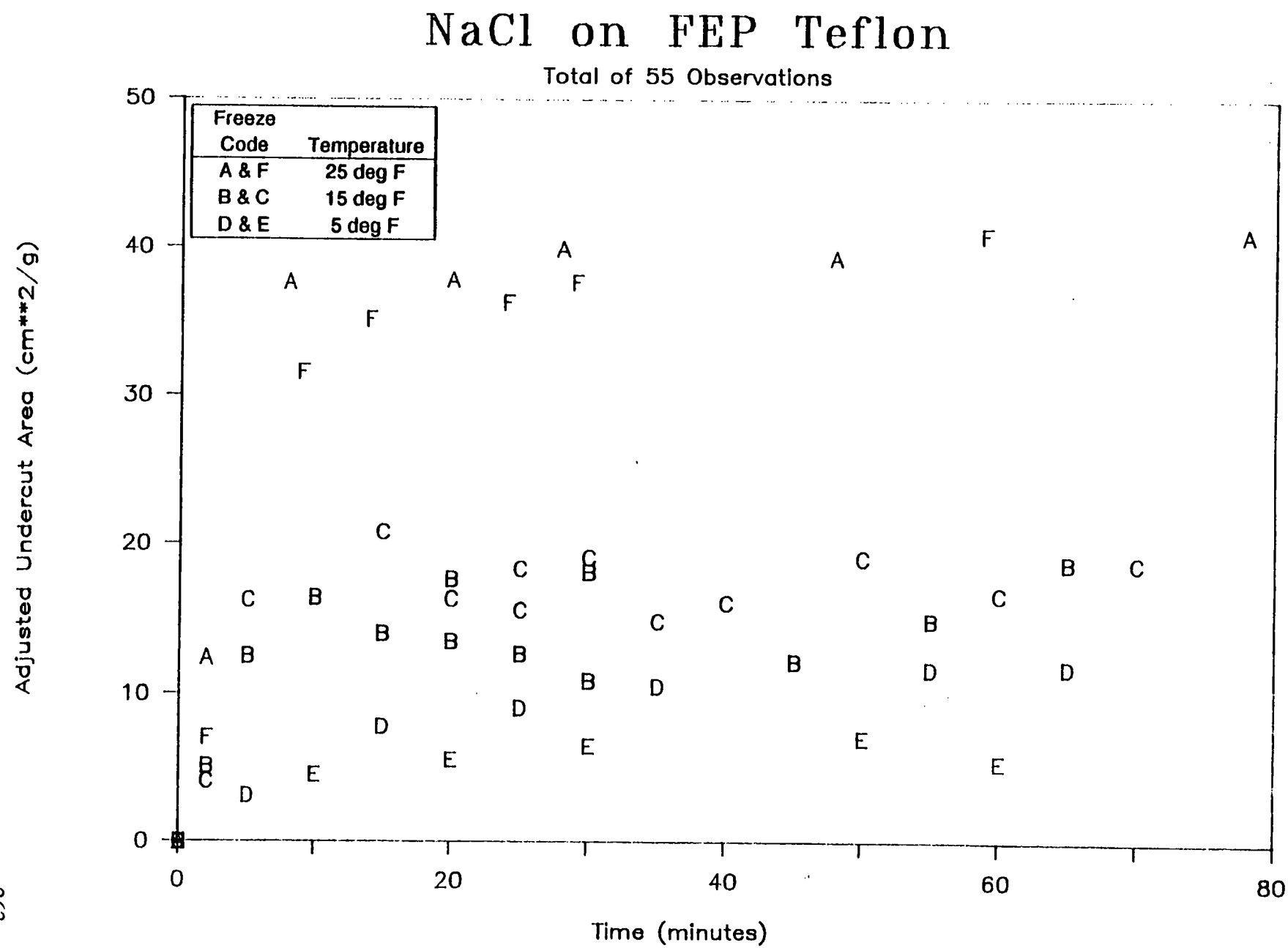
NaCl on FEP Teflon
Total of 55 Observations
Freeze Code
Temperature
A & F
25 deg F
B & C
15 deg F
D & E
5 deg F
Adjusted Undercut Area (cm**2/g)
Time (minutes)
0
10
20
30
40
50
0
20
40
60
80

Figure I-8

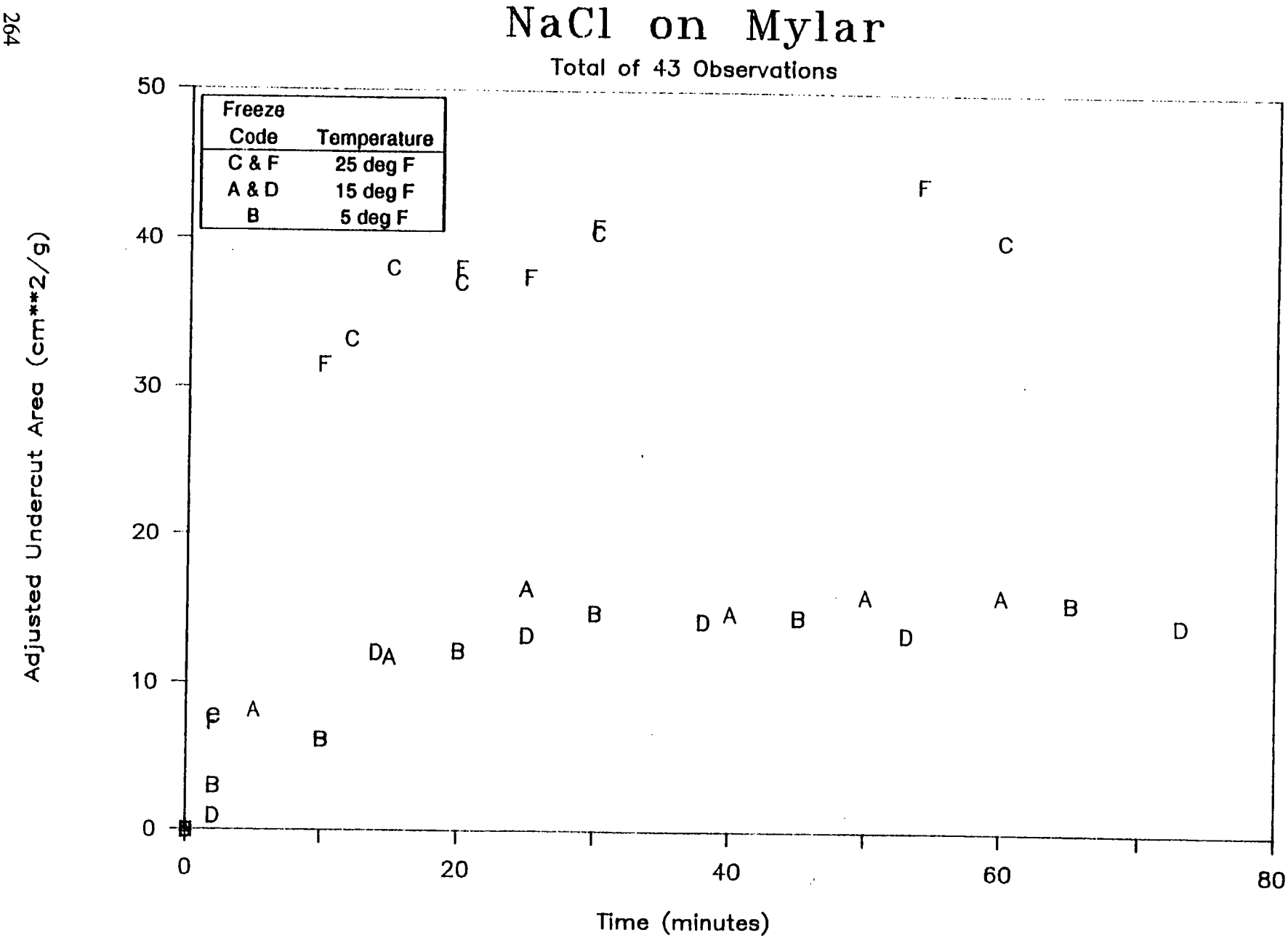
NaCl on Mylar
Total of 43 Observations
Freeze Code
Temperature
C & F
25 deg F
A & D
15 deg F
B
5 deg F
Adjusted Undercut Area (cm**2/g)
Time (minutes)
0
10
20
30
40
50
0
20
40
60
80

Figure I-9

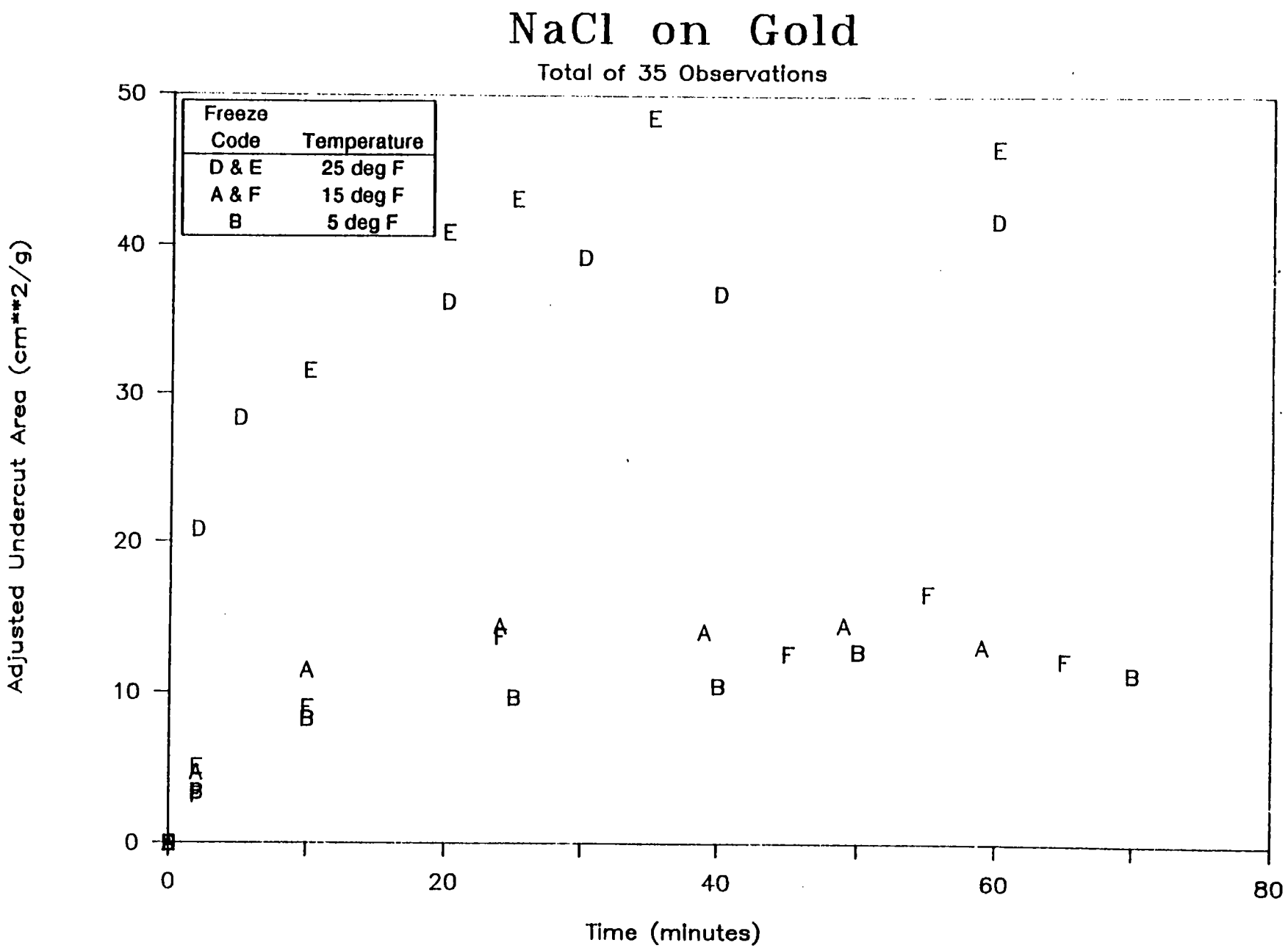
NaCl on Gold
Total of 35 Observations
Freeze Code
Temperature
D & E
25 deg F
A & F
15 deg F
B
5 deg F
Adjusted Undercut Area (cm**2/g)
Time (minutes)
0
10
20
30
40
50
0
20
40
60
80

Figure I-10

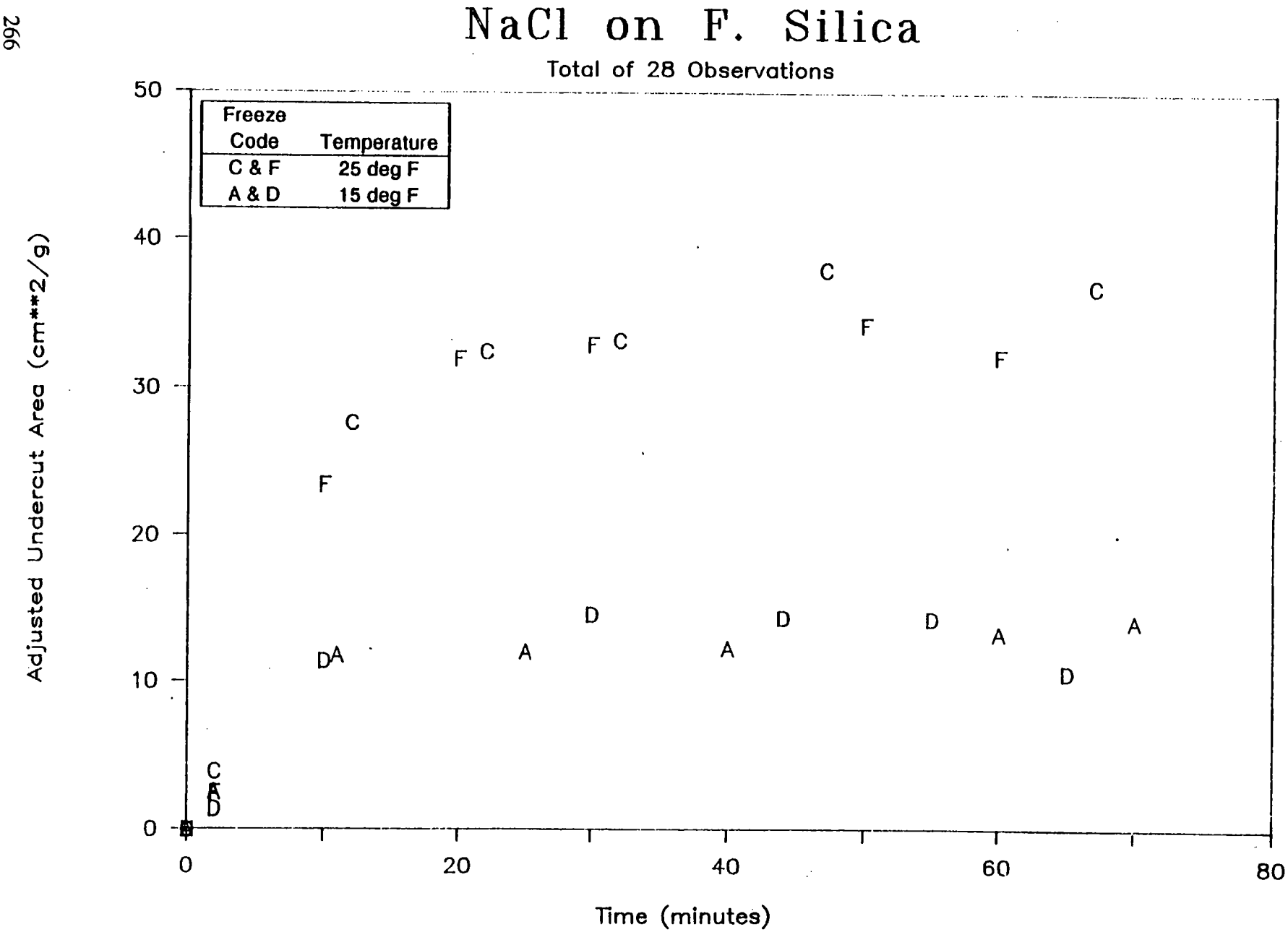
NaCl on F. Silica
Total of 28 Observations
Freeze Code
Temperature
C & F
25 deg F
A & D
15 deg F
Adjusted Undercut Area (cm**2/g)
Time (minutes)
0
10
20
30
40
50
0
20
40
60
80

Figure I-11

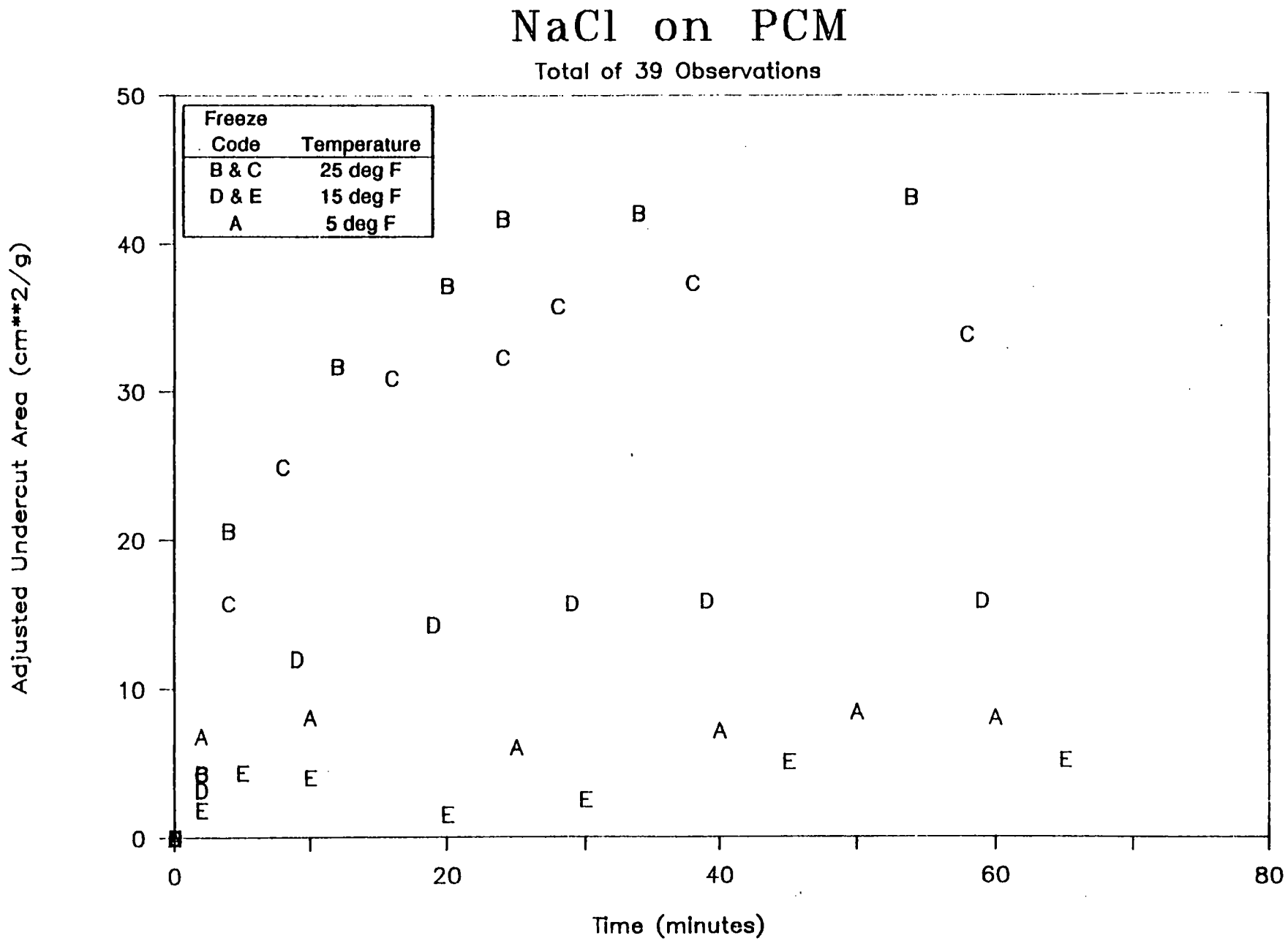
NaCl on PCM
Total of 39 Observations
Freeze Code
Temperature
B & C
25 deg F
D & E
15 deg F
A
5 deg F
Adjusted Undercut Area (cm**2/g)
Time (minutes)
0
10
20
30
40
50
0
20
40
60
80

Figure I-12

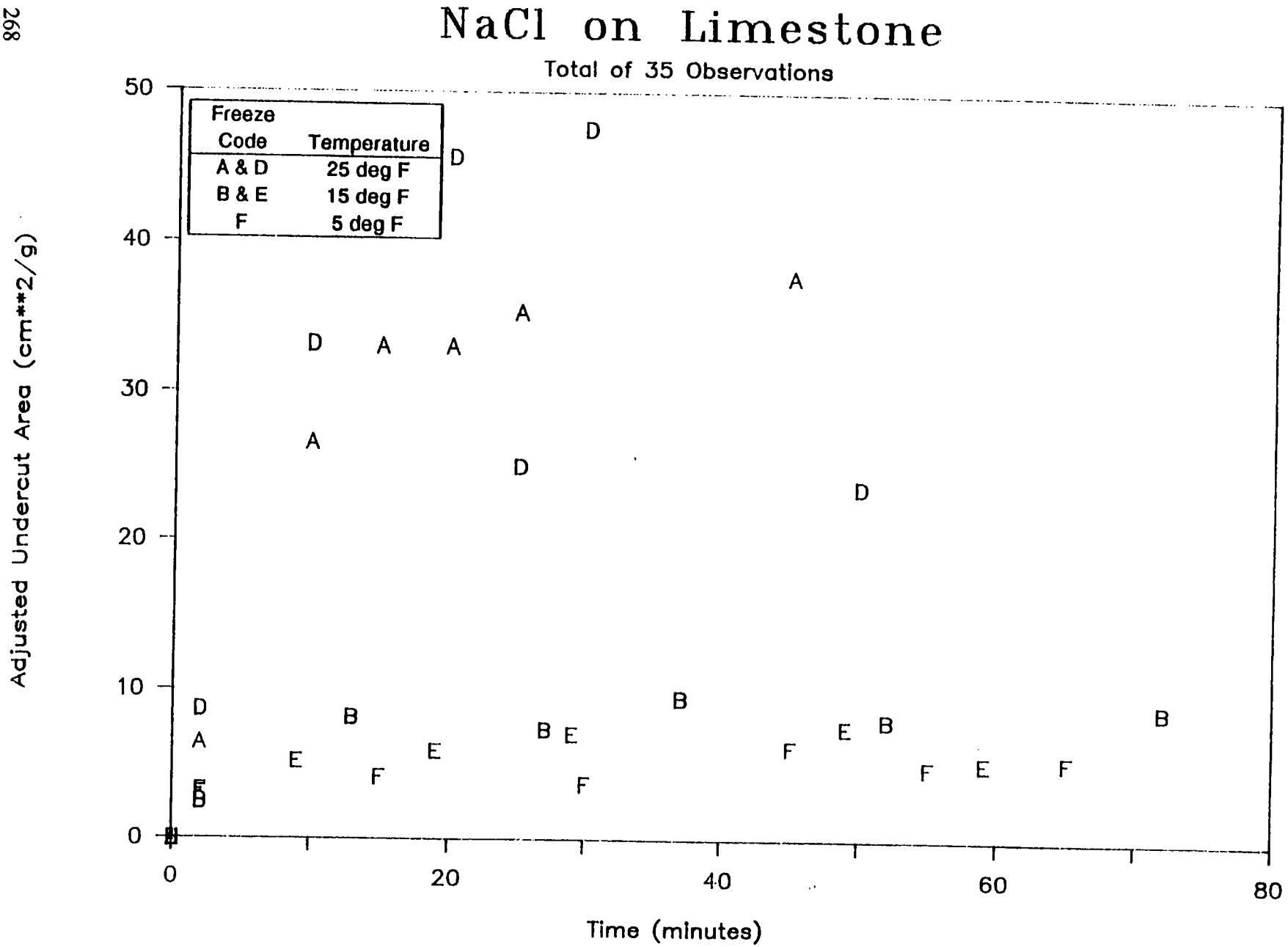
NaCl on Limestone
Total of 35 Observations
Freeze Code
Temperature
A & D
25 deg F
B & E
15 deg F
F
5 deg F
Adjusted Undercut Area (cm**2/g)
Time (minutes)
0
10
20
30
40
50
0
20
40
60
80

Figure I-13

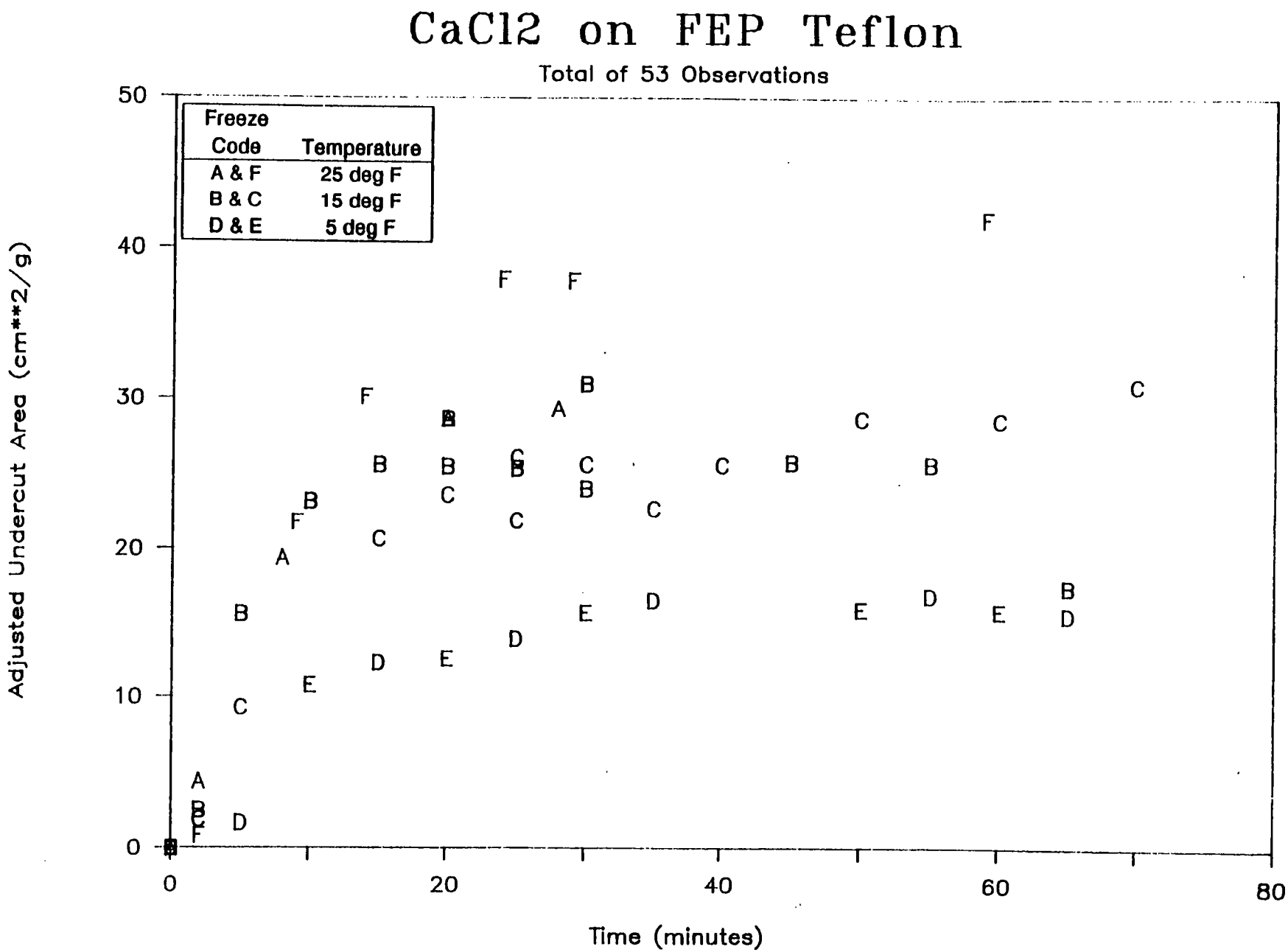
CaCl2 on FEP Teflon
Total of 53 Observations
Freeze Code
Temperature
A & F
25 deg F
B & C
15 deg F
D & E
5 deg F
Adjusted Undercut Area (cm**2/g)
Time (minutes)
0
10
20
30
40
50
0
20
40
60
80

Figure I-14

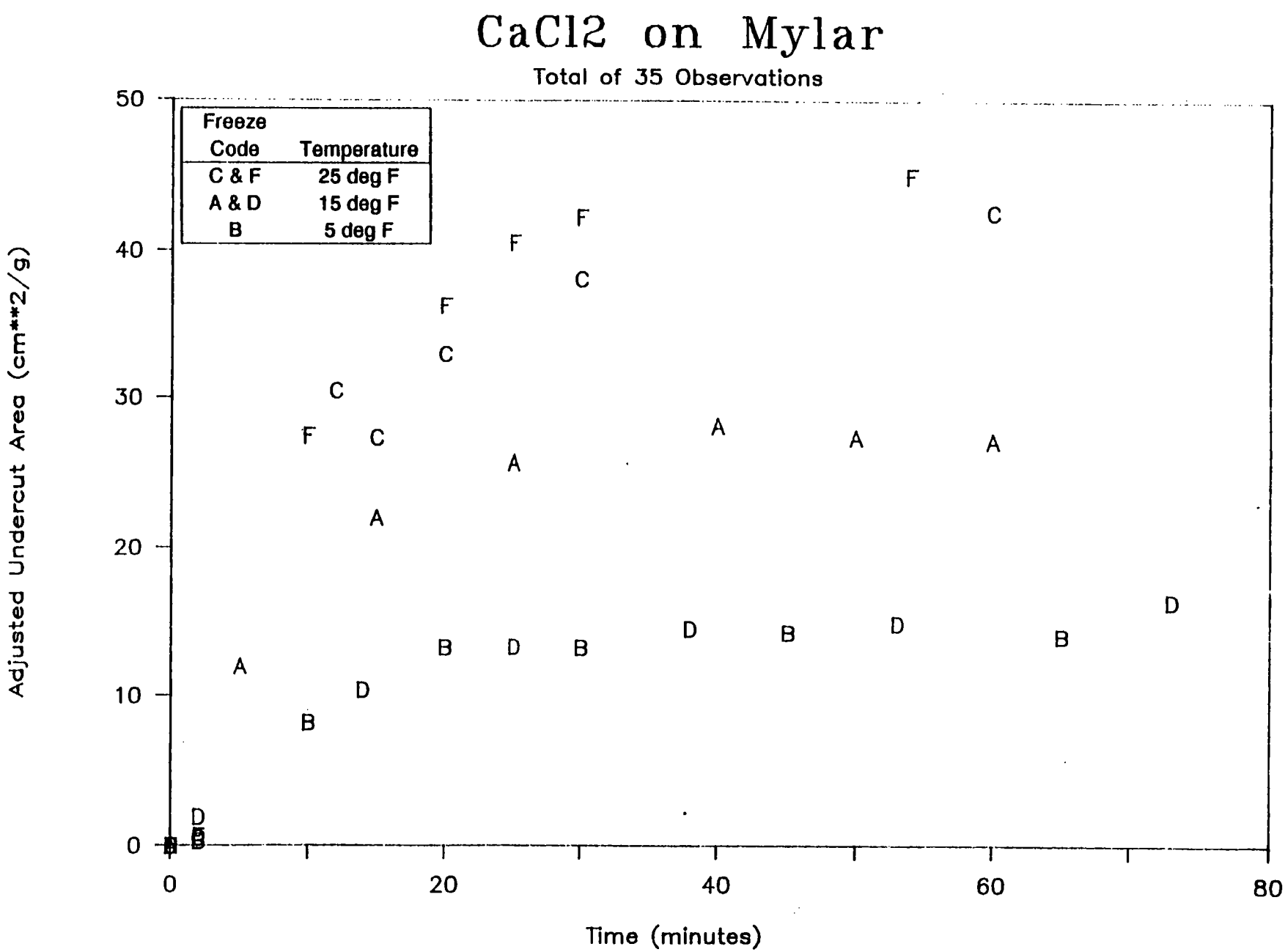
CaCl2 on Mylar
Total of 35 Observations
Freeze Code
Temperature
C & F
25 deg F
A & D
15 deg F
B
5 deg F
Adjusted Undercut Area (cm**2/g)
Time (minutes)
0
10
20
30
40
50
0
20
40
60
80

Figure I-15

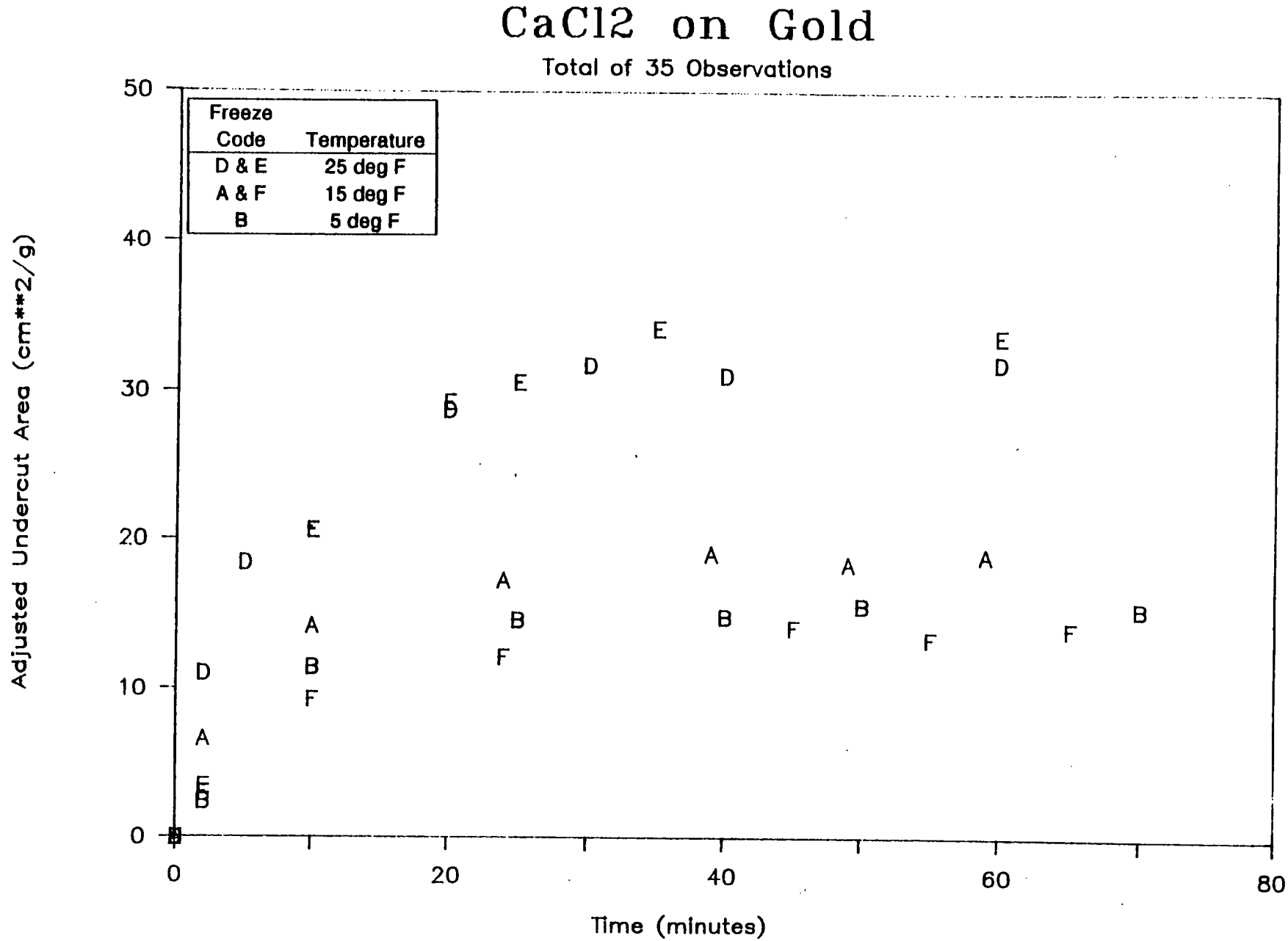
CaCl2 on Gold
Total of 35 Observations
Freeze Code
Temperature
D & E
25 deg F
A & F
15 deg F
B
5 deg F
Adjusted Undercut Area (cm**2/g)
Time (minutes)
0
10
20
30
40
0
20
40
60
80

Figure I-16

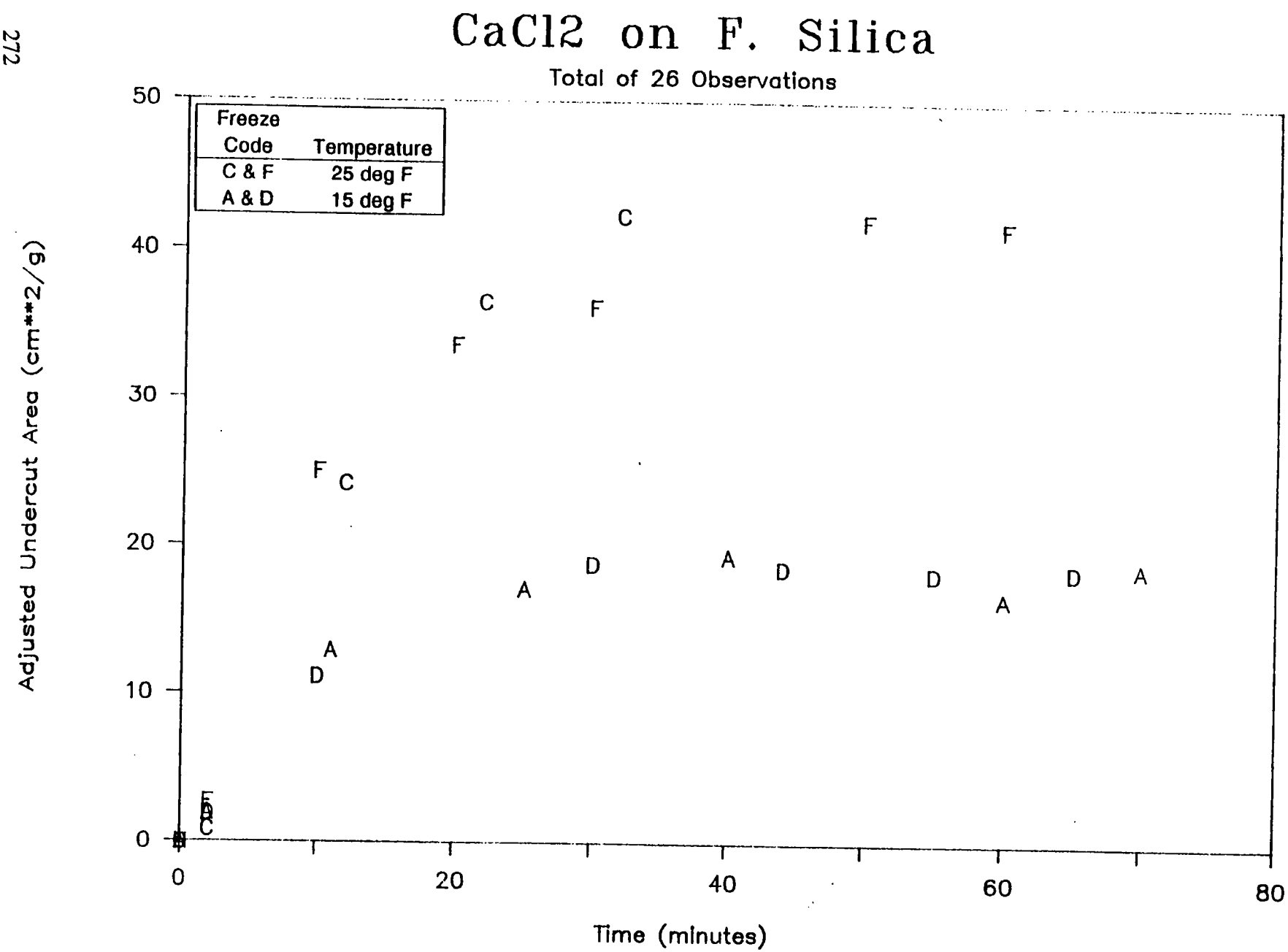
CaCl2 on F. Silica
Total of 26 Observations
Freeze Code
Temperature
C & F
25 deg F
A & D
15 deg F
Adjusted Undercut Area (cm**2/g)
Time (minutes)
0
10
20
30
40
50
0
20
40
60
80

Figure I-17

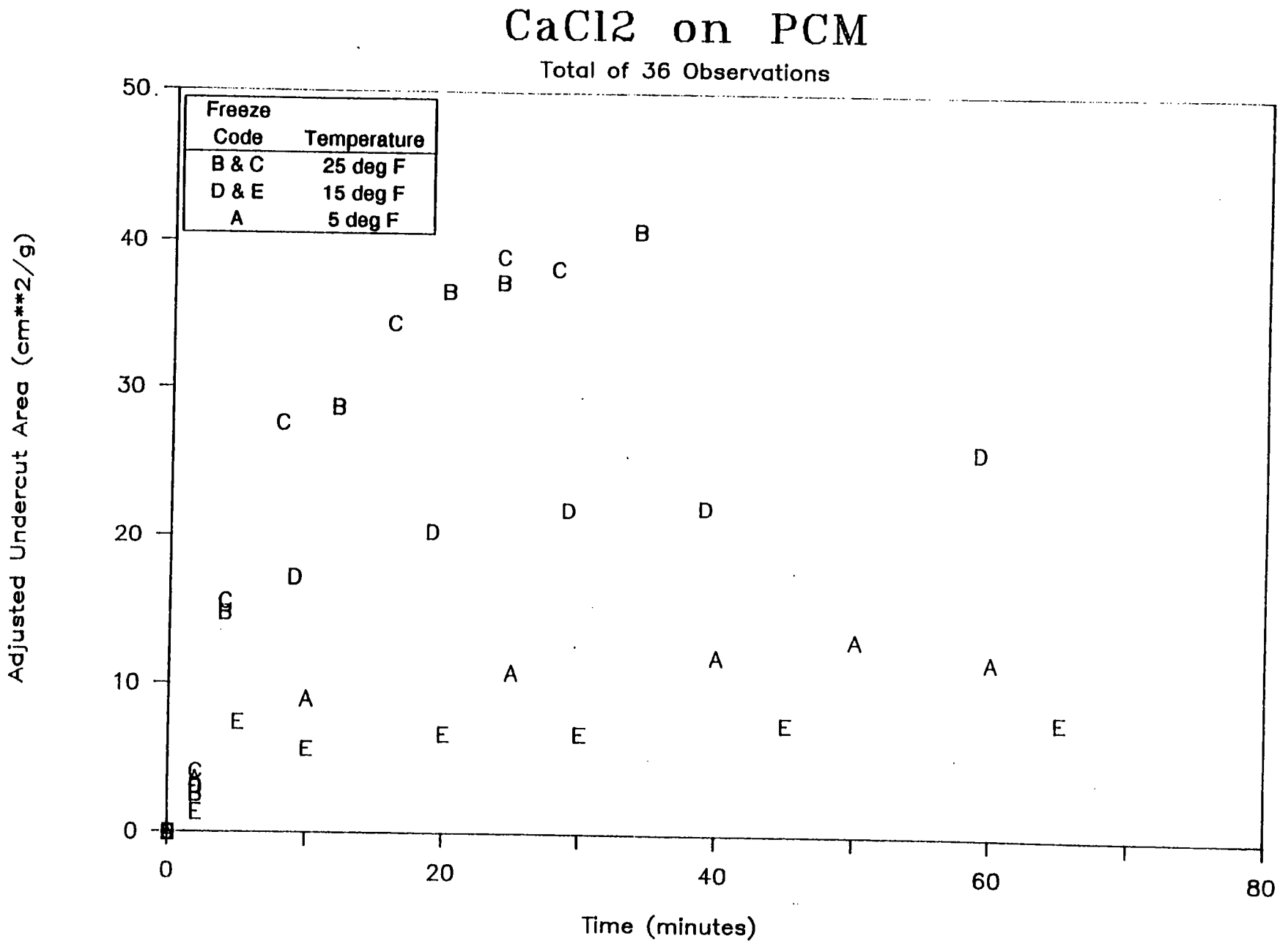
CaCl2 on PCM
Total of 36 Observations
Freeze Code
Temperature
B & C
25 deg F
D & E
15 deg F
A
5 deg F
Adjusted Undercut Area (cm**2/g)
Time (minutes)
0
10
20
30
40
50
0
20
40
60
80

Figure I-18

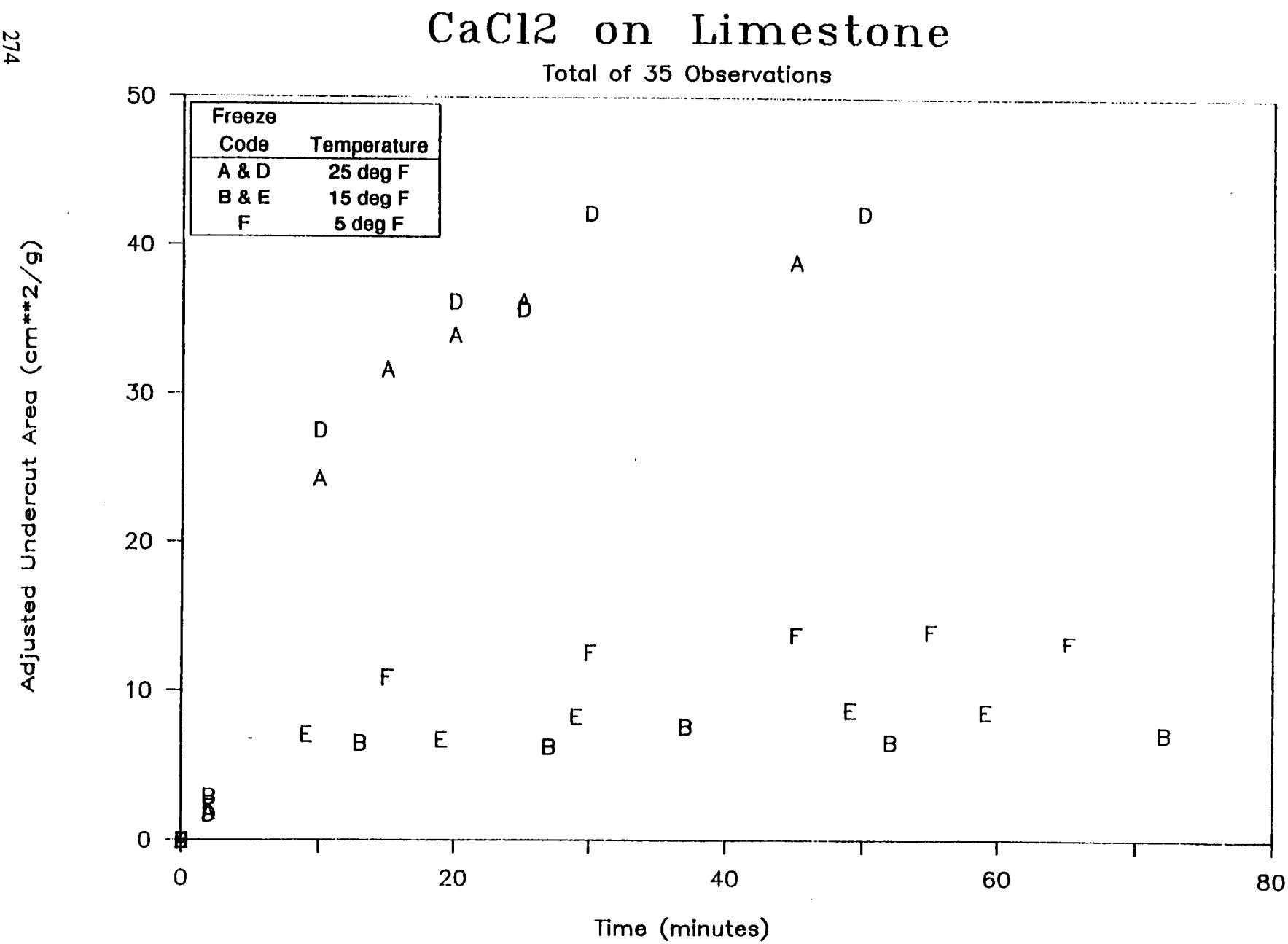
CaCl2 on Limestone
Total of 35 Observations
Freeze Code
Temperature
A & D
25 deg F
B & E
15 deg F
F
5 deg F
Adjusted Undercut Area (cm**2/g)
Time (minutes)
0
10
20
30
40
50
0
20
40
60
80

Figure I-19

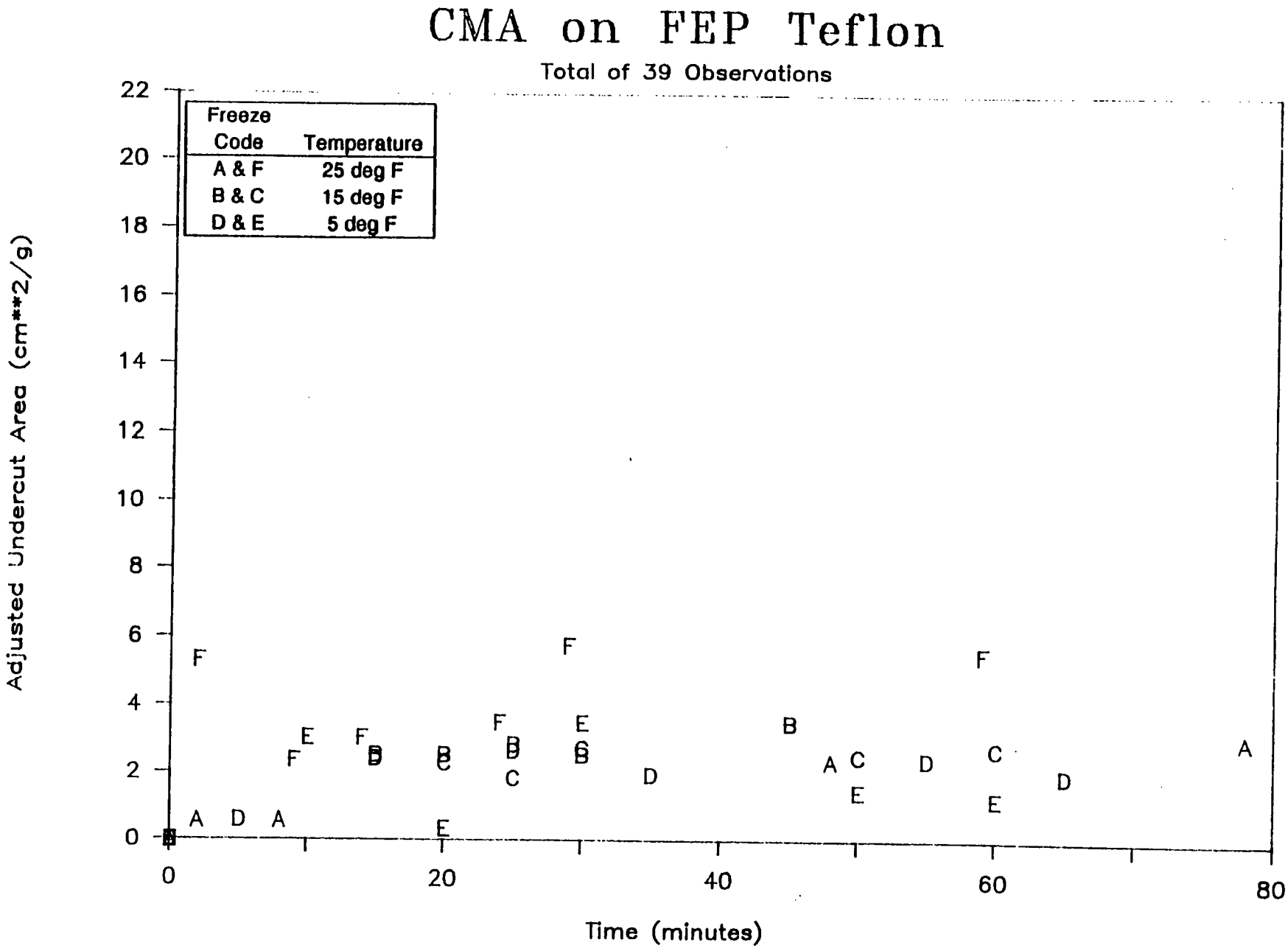
CMA on FEP Teflon
Total of 39 Observations
Freeze Code
Temperature
A & F
25 deg F
B & C
15 deg F
D & E
5 deg F
Adjusted Undercut Area (cm**2/g)
Time (minutes)
0
2
4
6
8
10
12
14
16
18
20
22
0
20
40
60
80

Figure I-20

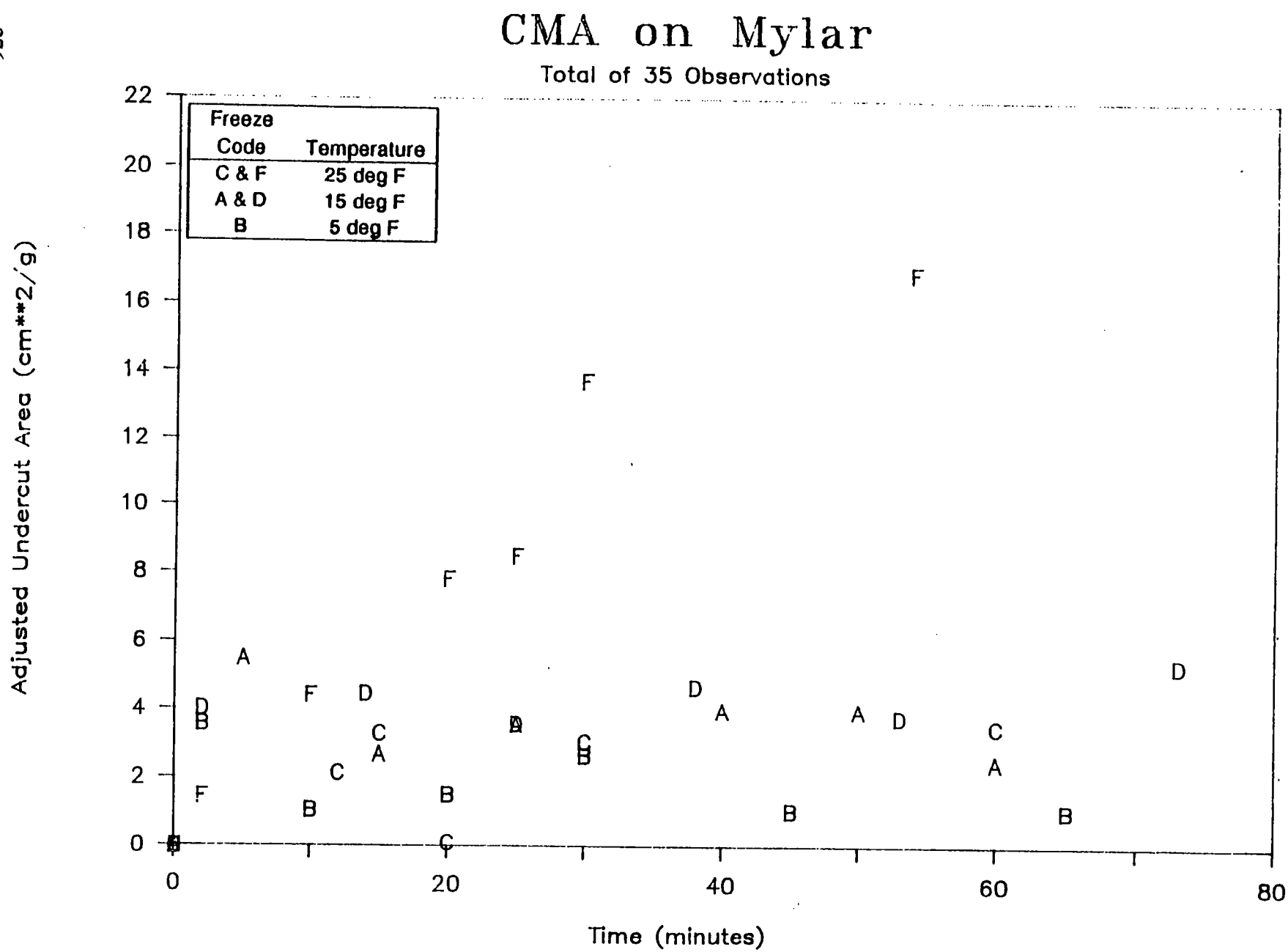
CMA on Mylar
Total of 35 Observations
Freeze Code
Temperature
C & F
25 deg F
A & D
15 deg F
B
5 deg F
Adjusted Undercut Area (cm**2/g)
Time (minutes)
0
2
4
6
8
10
12
14
16
18
20
22
0
20
40
60
80

Figure I-21

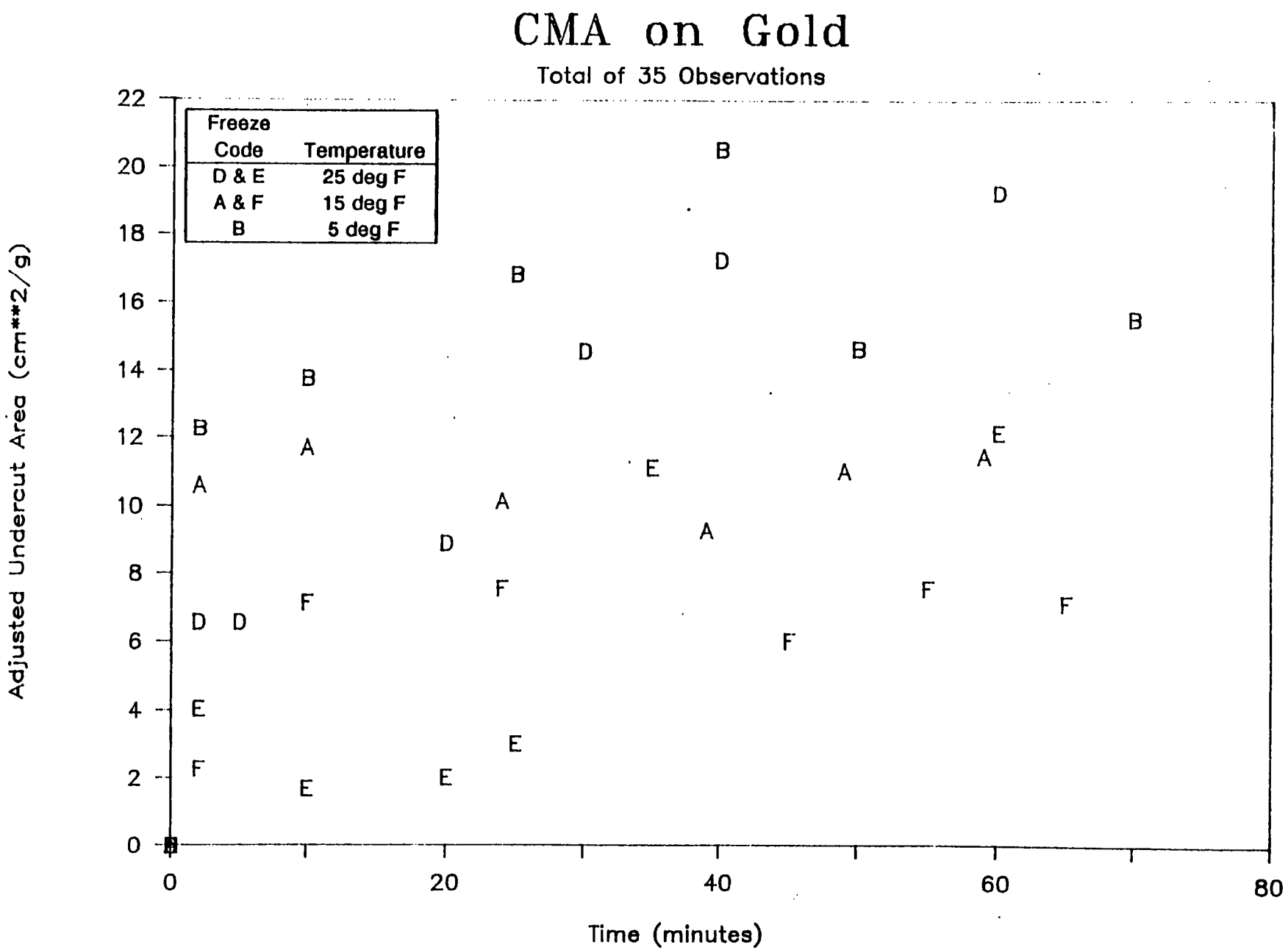
CMA on Gold
Total of 35 Observations
Freeze Code
Temperature
D & E
25 deg F
A & F
15 deg F
B
5 deg F
Adjusted Undercut Area (cm**2/g)
Time (minutes)
0
2
4
6
8
10
12
14
16
18
20
22
0
20
40
60
80

Figure I-22

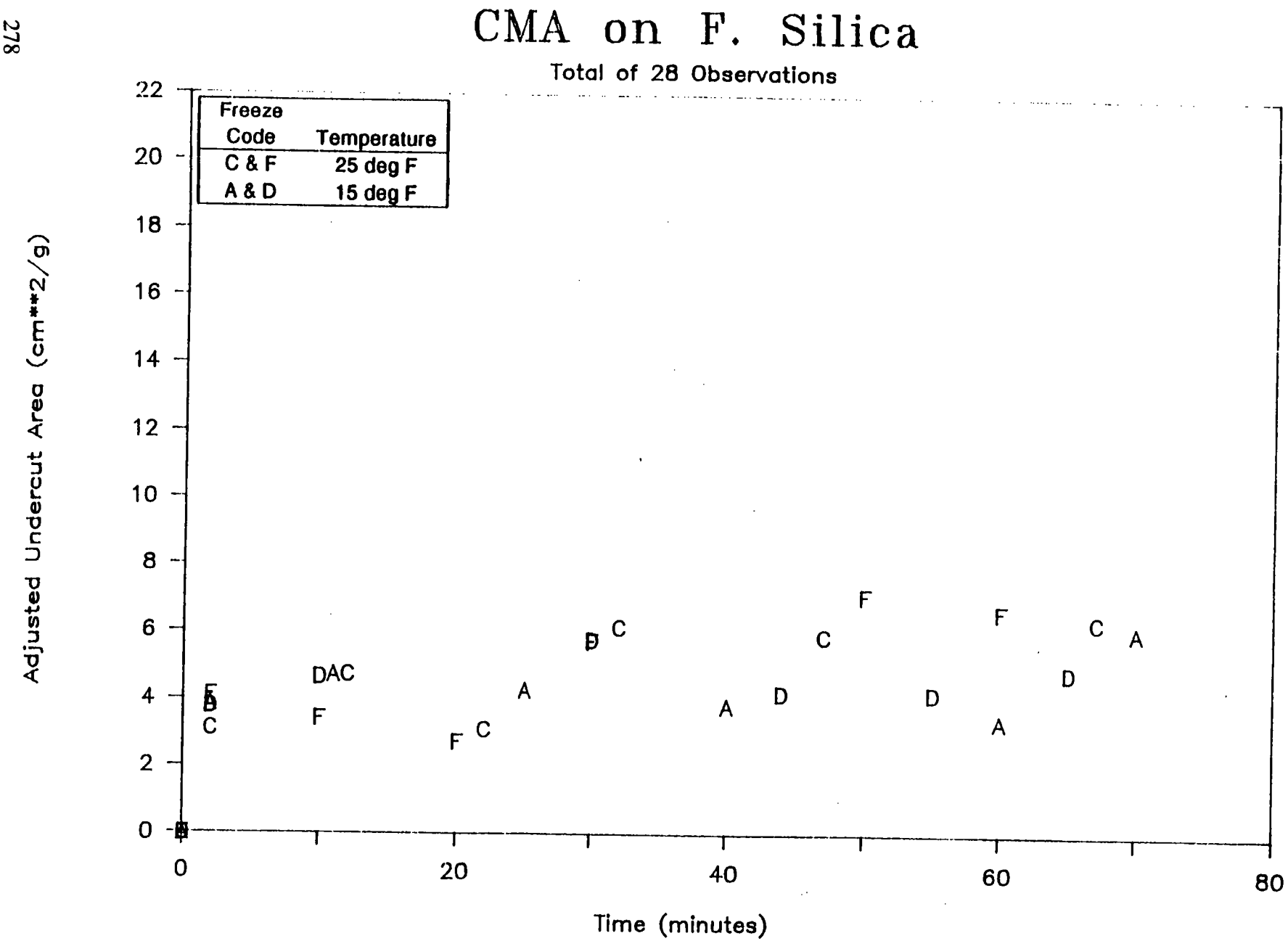
CMA on F. Silica
Total of 28 Observations
Freeze Code
Temperature
C & F
25 deg F
A & D
15 deg F
Adjusted Undercut Area (cm**2/g)
Time (minutes)
0
2
4
6
8
10
12
14
16
18
20
22
0
20
40
60
80

Figure I-23

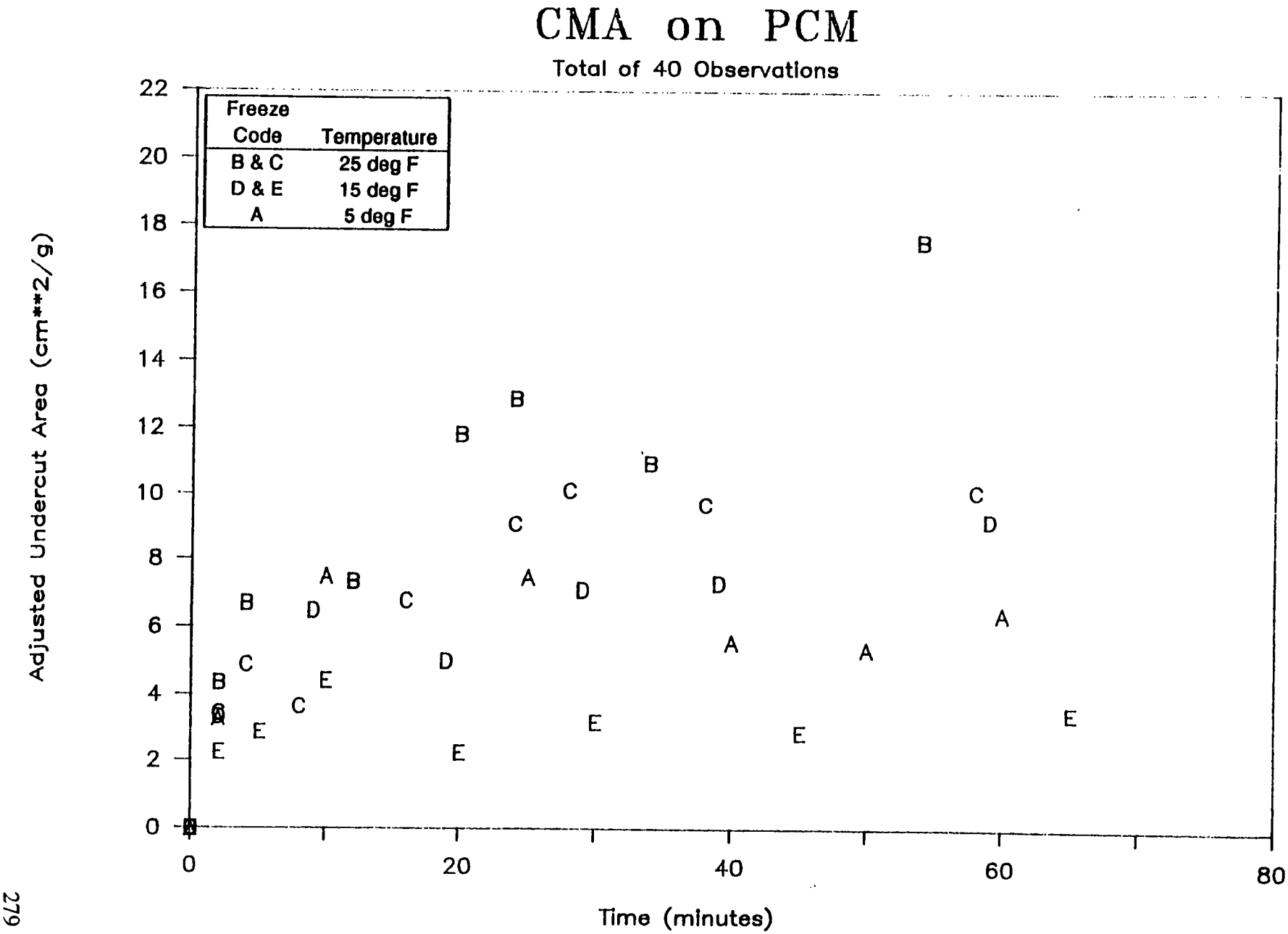
CMA on PCM
Total of 40 Observations
Freeze Code
Temperature
B & C
25 deg F
D & E
15 deg F
A
5 deg F
Adjusted Undercut Area (cm**2/g)
Time (minutes)
0
2
4
6
8
10
12
14
16
18
20
22
0
20
40
60
80

Figure I-24

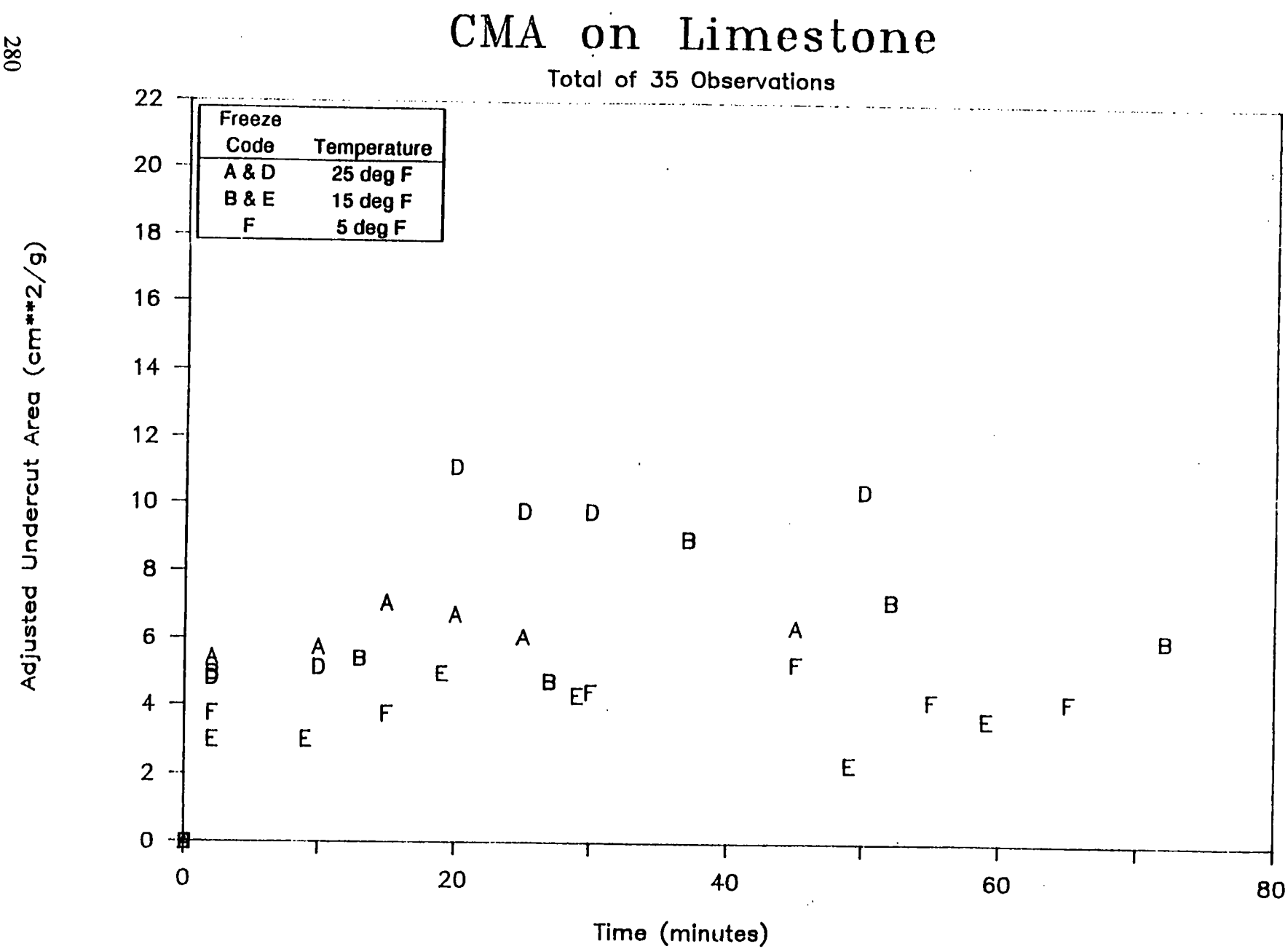
CMA on Limestone
Total of 35 Observations
Freeze Code
Temperature
A & D
25 deg F
B & E
15 deg F
F
5 deg F
Adjusted Undercut Area (cm**2/g)
Time (minutes)
0
2
4
6
8
10
12
14
16
18
20
22
0
20
40
60
80

Figure I-25

Substrate Configurations and Undercutting Test Specimen Preparation

The substrates used in the second set of undercutting tests included portland cement concrete, dense-graded asphalt, open-graded asphalt, and rubber-modified asphalt core samples and laboratory-produced specimens made of portland cement concrete and dense-graded asphalt. The portland cement concrete and dense-graded asphalt core samples were 4-in (10.2-cm) in diameter and were obtained from the Connecticut DOT. The open-graded asphalt core samples were 6-in (15.2-cm) in diameter and were obtained from the New York DOT.

The rubber-modified asphalt (Plusride) core samples were 4-in (10.2-cm) in diameter and were obtained from the Montana Department of Highways and from CALTRANS. All core samples were taken from in-service roads.

The laboratory-produced dense-graded asphalt specimens were 4-in (10.2-cm) in diameter and were supplied by Michigan Technological University through SHRP Contract H-204. These specimens were made in a Marshall test mold using AC-20 asphalt and aggregate obtained from the SHRP Materials Reference Library in Austin, Texas.

The laboratory-produced portland cement concrete specimens had approximate dimensions of 6.5-in (16.5-cm) x 8.5-in (21.6-cm) x 1-in (2.5-cm) deep and were made by SDSM&T. These specimens were made in accordance with the mix design used by the South Dakota DOT for highway (nonbridge deck) pavement construction.

The core samples were of varying length when received. Each core sample was cut to about a 2-in (5.1-cm) length with a diamond saw in a plane parallel to the exposed wearing surface. This produced core samples with one end consisting of the as-received surface and the other end with a relatively smooth, not previously exposed surface.

One end of the laboratory-produced dense-graded asphalt specimens was ground smooth, with a final grinding with 400 grit powder. The other end of the specimens was left in the as-compacted state.

Three of the laboratory-produced portland cement concrete specimens were ground smooth, with a final grinding with 600 grit powder.

All the substrate surfaces used in the second set of undercutting experiments were cleaned prior to growing ice on the surfaces. The substrates were cleaned using the procedures described in Appendix B.

Three undercutting test sites were made on the 4-in (10.2-cm) diameter core samples, and nine sites were made on the 6-in (15.2-cm) core samples. Nine undercutting test sites were made on each of the portland cement concrete slabs.

Ice of 3/16-in (0.48-cm) thickness was formed on the substrates in a prescribed manner. Before growing the ice, the substrates were placed in a refrigerator maintained at 39°F (4°C) and allowed to equilibrate to that temperature for at least 16 hours. Deionized water was also placed in the same refrigerator and allowed to equilibrate to that temperature. The substrates were then transferred to an ice growing chamber inside a walk-in cold room that was maintained at −9°C. The substrates rested on a thick aluminum plate inside the ice growing chamber. When the substrates reached the −9°C temperature, the chilled (4°C) deionized water was added to the substrate surface. Two 100-watt lamps were positioned above the specimens in the chamber and their power was gradually reduced with a Variac. This procedure allowed the ice to grow slowly and from the substrate upward. Tapered holes were produced in the ice during the freezing by use of Teflon plugs resting on the substrate surface. The plugs used were the same as those used during the first set of undercutting experiments. The plugs were held in the correct relative position on the substrate with a ¼-in (0.64-cm) thick acrylic sheet in the same manner as was used in the first undercutting experiments.

After the ice froze, the Teflon plugs were removed from the ice. The substrate-ice samples were then removed from the ice growing chamber and placed in plastic bags. They remained in the plastic bags until the walk-in cold room and the samples equilibrated to the undercutting test temperature.

Fluorescein disodium salt was placed in the cavities formed by the Teflon plugs. The saturated deicing solutions were then added to the cavities and the mixture was stirred until it was of uniform color. Photographs were taken with the aid of a UV-light source at eight predetermined time points over a 1-hour period during the undercutting action. The 35-mm negatives used in the photographic process showed a good contrast between the undercutting areas and the substrate material.

Undercutting tests with the three deicers were performed at each of the three temperatures on each of the six substrates in the as-received, but cleaned condition. Undercutting tests with the three deicers were performed also on the smooth highway core samples and laboratory-produced specimens at 25°F (−4°C) and 5°F (−15°C). Three replicate runs were made for each unique combination of substrate, deicer, and temperature.

The data reduction technique used with the first set of undercutting experimental results was used also with the results from the second set. During the analysis of the undercutting data, the measured areas were adjusted to account for the surface area, at time zero, that the Teflon plug was in contact with the substrate. This area was subtracted from all measured undercut areas obtained from the 35-mm photographic records. The resulting differences were then normalized by dividing them by the appropriate weight of the deicer. These final results are again referred to as adjusted undercut areas. The replicate results were averaged prior to analysis and plotting of the data.

Plots were developed of the average adjusted undercut area versus time for each of the 18 deicers x as-received substrate combinations (3 deicers x 6 substrates). These plots are shown in Figures I-26 through I-43. Also shown in these figures are the results achieved for the smooth substrate surfaces. The data used to generate these figures are given at the end of this appendix.

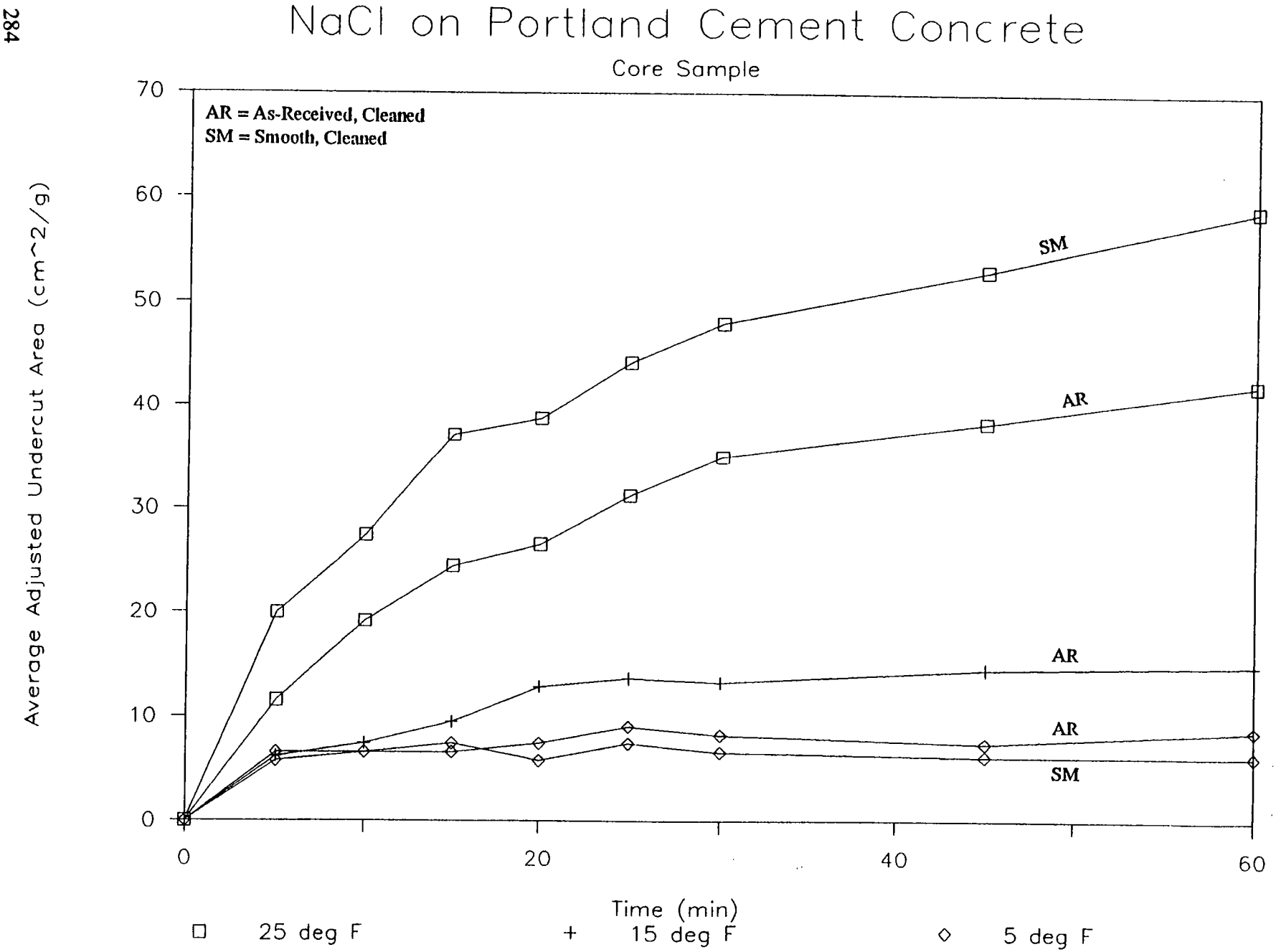
NaCl on Portland Cement Concrete
Core Sample
AR = As-Received, Cleaned
SM = Smooth, Cleaned
Average Adjusted Undercut Area (cm^2/g)
70
60
50
40
30
20
10
0
0
20
40
60
Time (min)
SM
AR
AR
AR
SM
25 deg F
15 deg F
5 deg F

Figure I-26

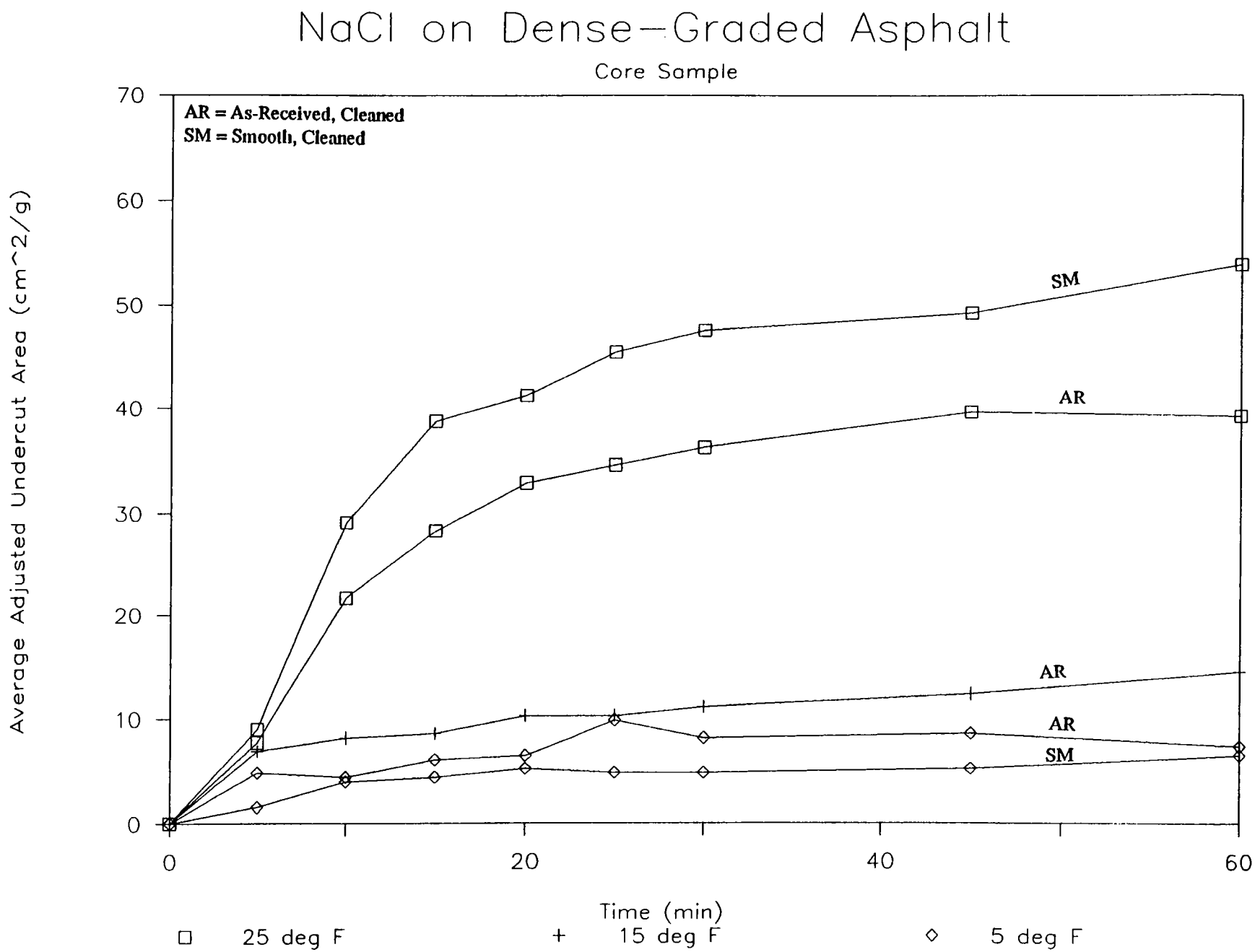
NaCl on Dense-Graded Asphalt
Core Sample
AR = As-Received, Cleaned
SM = Smooth, Cleaned
Average Adjusted Undercut Area (cm^2/g)
70
60
50
40
30
20
10
0
0
20
40
60
Time (min)
SM
AR
AR
AR
SM
□ 25 deg F
+ 15 deg F
◇ 5 deg F

Figure I-27

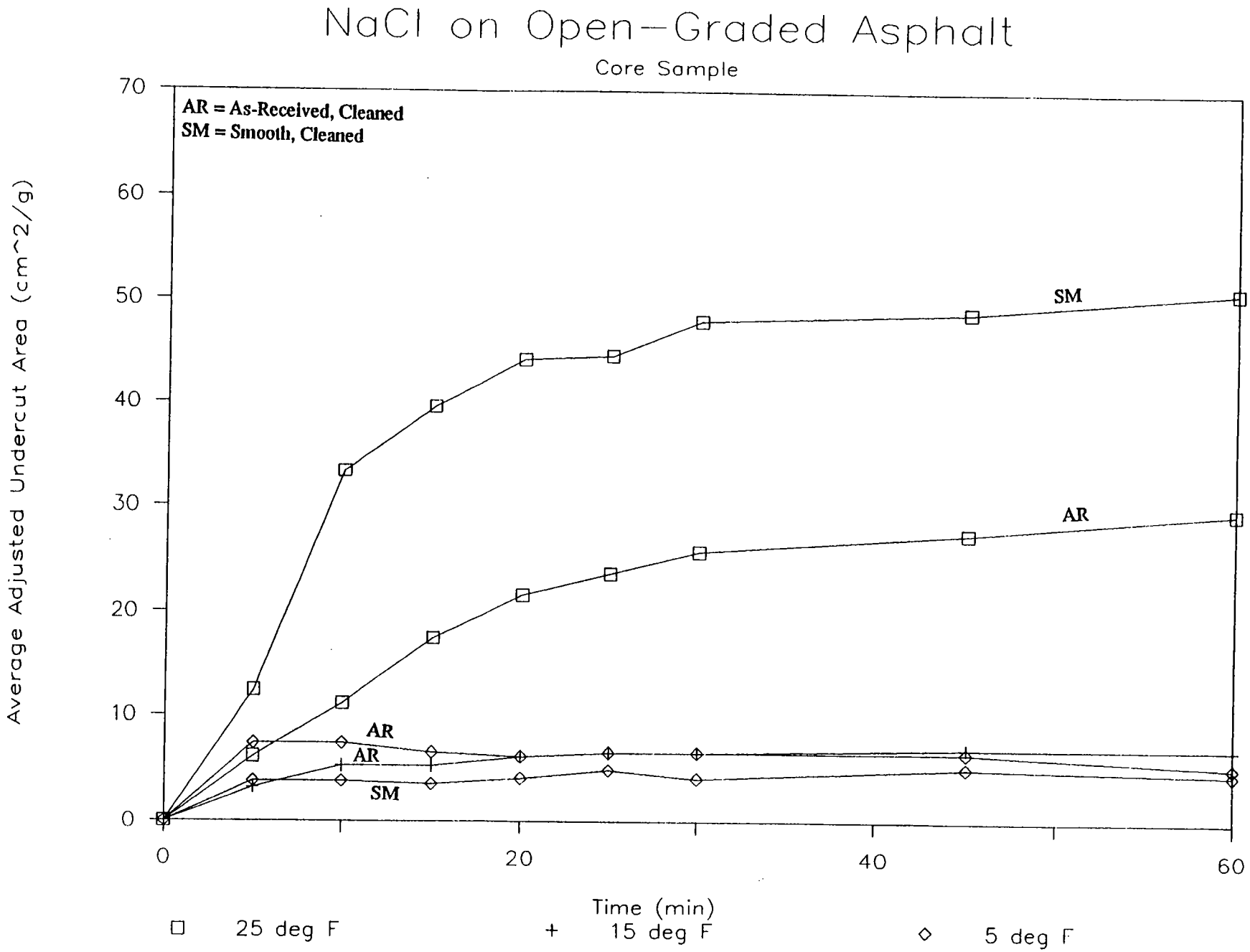
NaCl on Open-Graded Asphalt
Core Sample
AR = As-Received, Cleaned
SM = Smooth, Cleaned
Average Adjusted Undercut Area (cm^2/g)
70
60
50
40
30
20
10
0
0
20
40
60
Time (min)
SM
AR
AR
AR
SM
25 deg F
15 deg F
5 deg F

Figure I-28

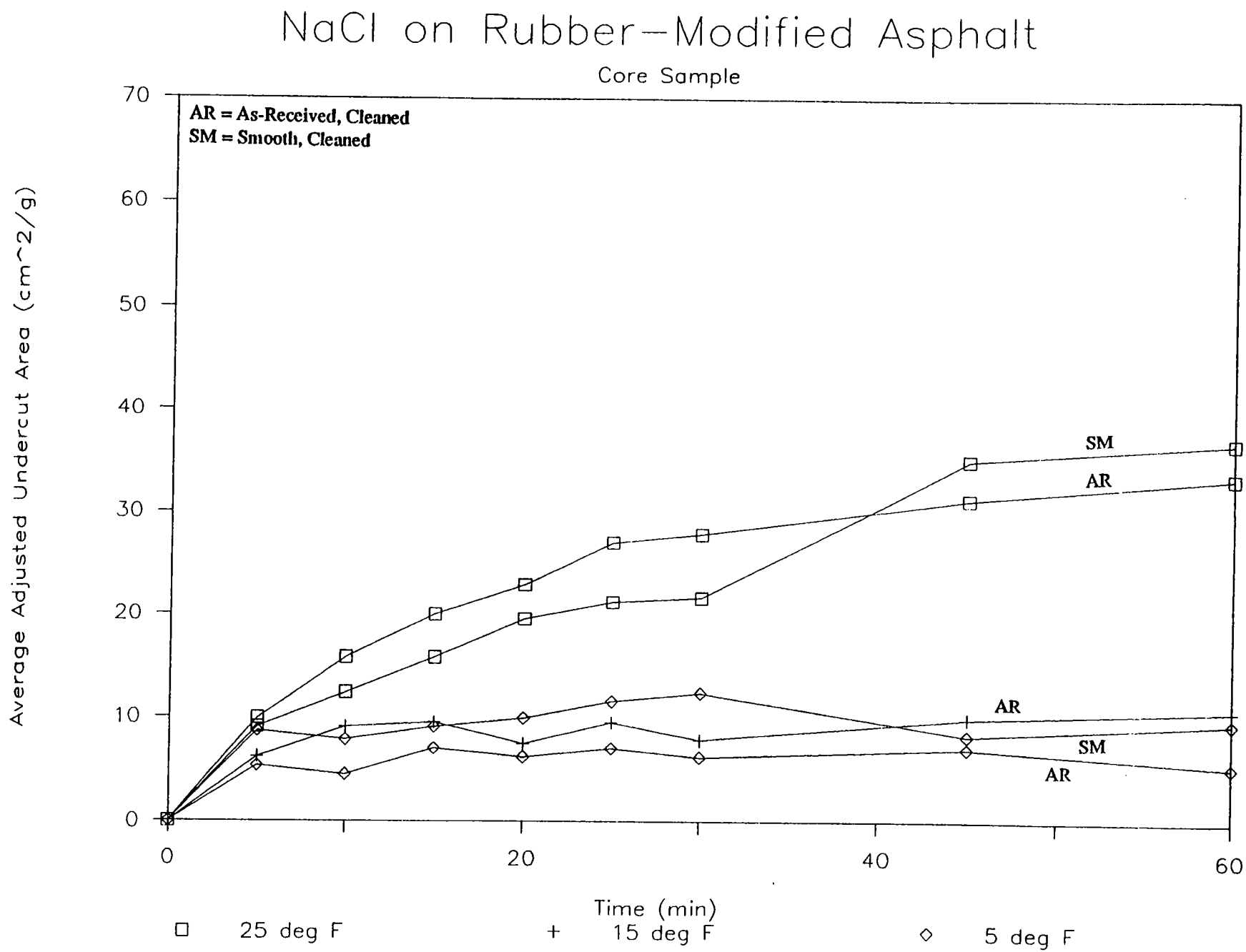
NaCl on Rubber-Modified Asphalt
Core Sample
AR = As-Received, Cleaned
SM = Smooth, Cleaned
Average Adjusted Undercut Area (cm^2/g)
70
60
50
40
30
20
10
0
0
20
40
60
Time (min)
SM
AR
AR
SM
AR
□ 25 deg F
+ 15 deg F
◇ 5 deg F

Figure I-29

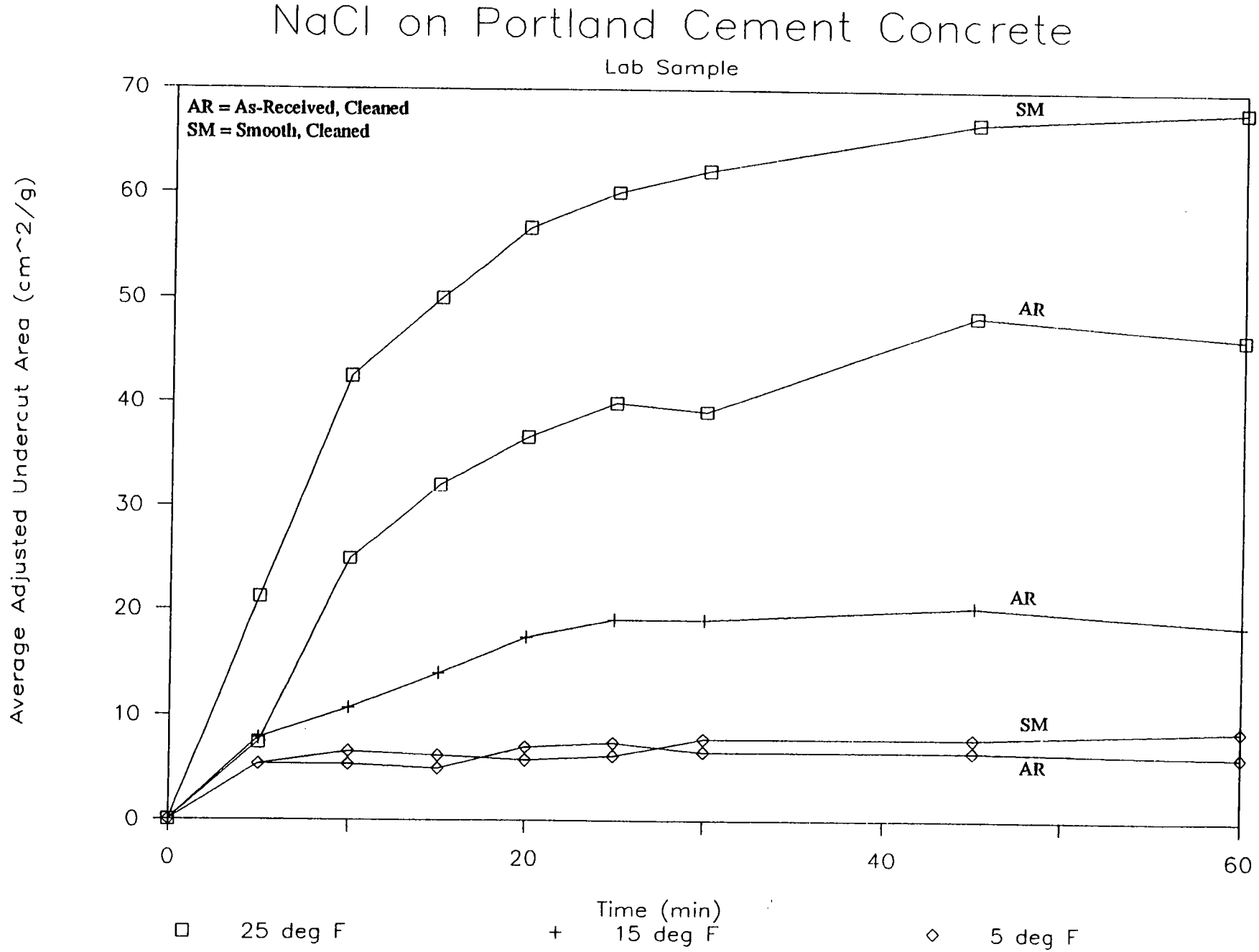
NaCl on Portland Cement Concrete
Lab Sample
AR = As-Received, Cleaned
SM = Smooth, Cleaned
Average Adjusted Undercut Area (cm^2/g)
70
60
50
40
30
20
10
0
0
20
40
60
Time (min)
SM
AR
AR
SM
AR
□ 25 deg F
+ 15 deg F
◇ 5 deg F

Figure I-30

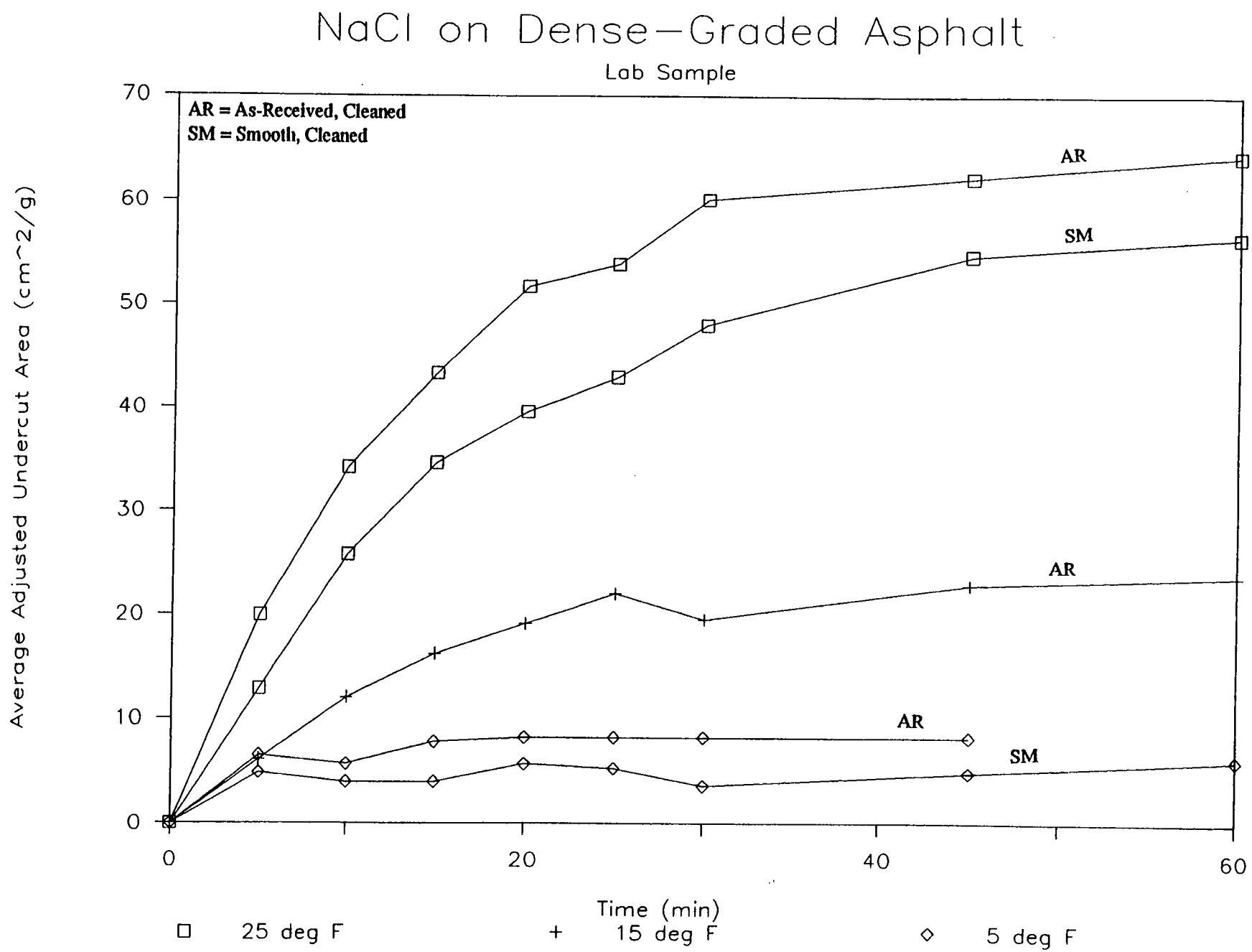
NaCl on Dense-Graded Asphalt
Lab Sample
AR = As-Received, Cleaned
SM = Smooth, Cleaned
AR
SM
AR
AR
SM
Average Adjusted Undercut Area (cm^2/g)
70
60
50
40
30
20
10
0
0
20
40
60
Time (min)
25 deg F
15 deg F
5 deg F

Figure I-31

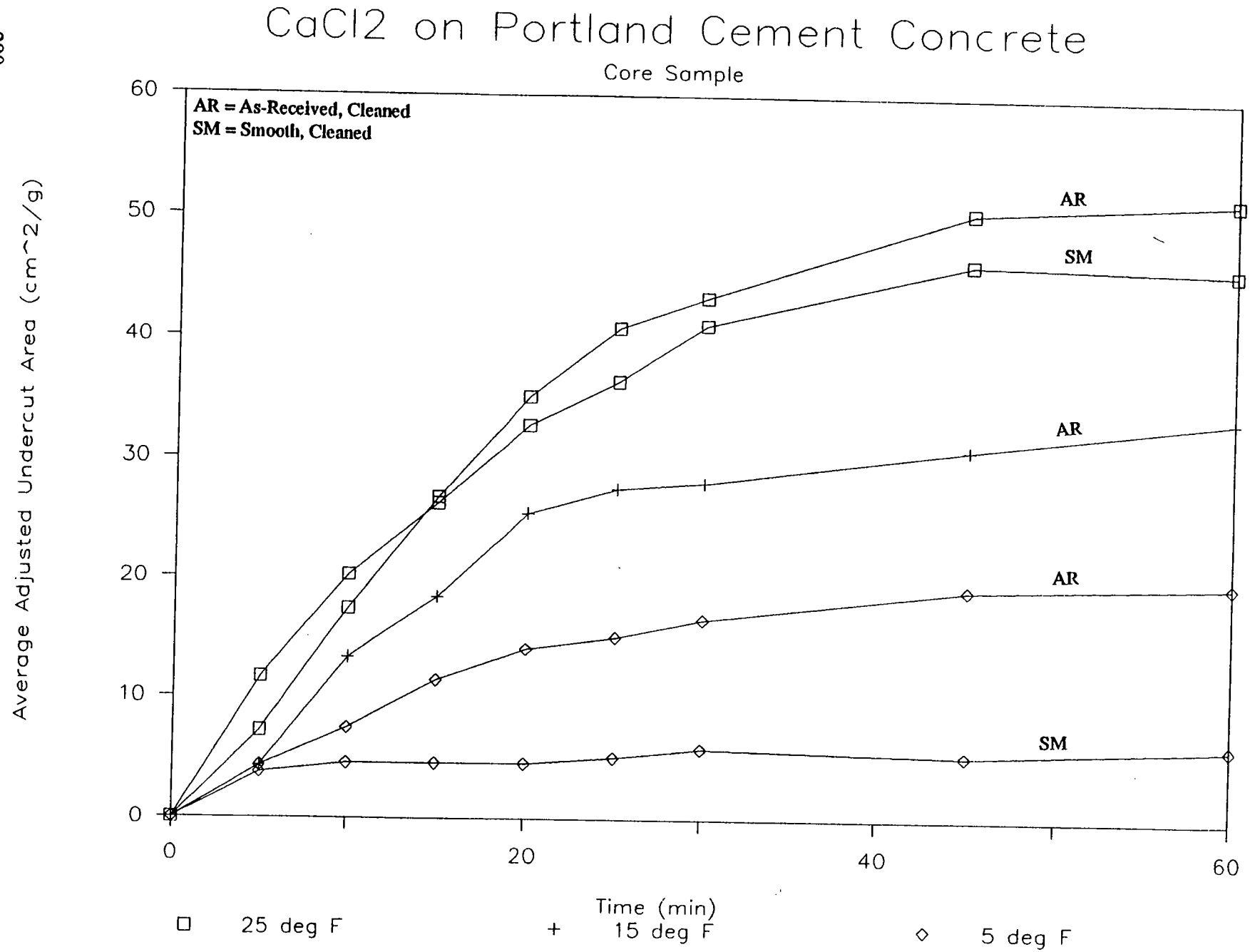
CaCl2 on Portland Cement Concrete
Core Sample
AR = As-Received, Cleaned
SM = Smooth, Cleaned
Average Adjusted Undercut Area (cm^2/g)
60
50
40
30
20
10
0
0
20
40
60
Time (min)
AR
SM
AR
AR
SM
□ 25 deg F
+ 15 deg F
◇ 5 deg F

Figure I-32

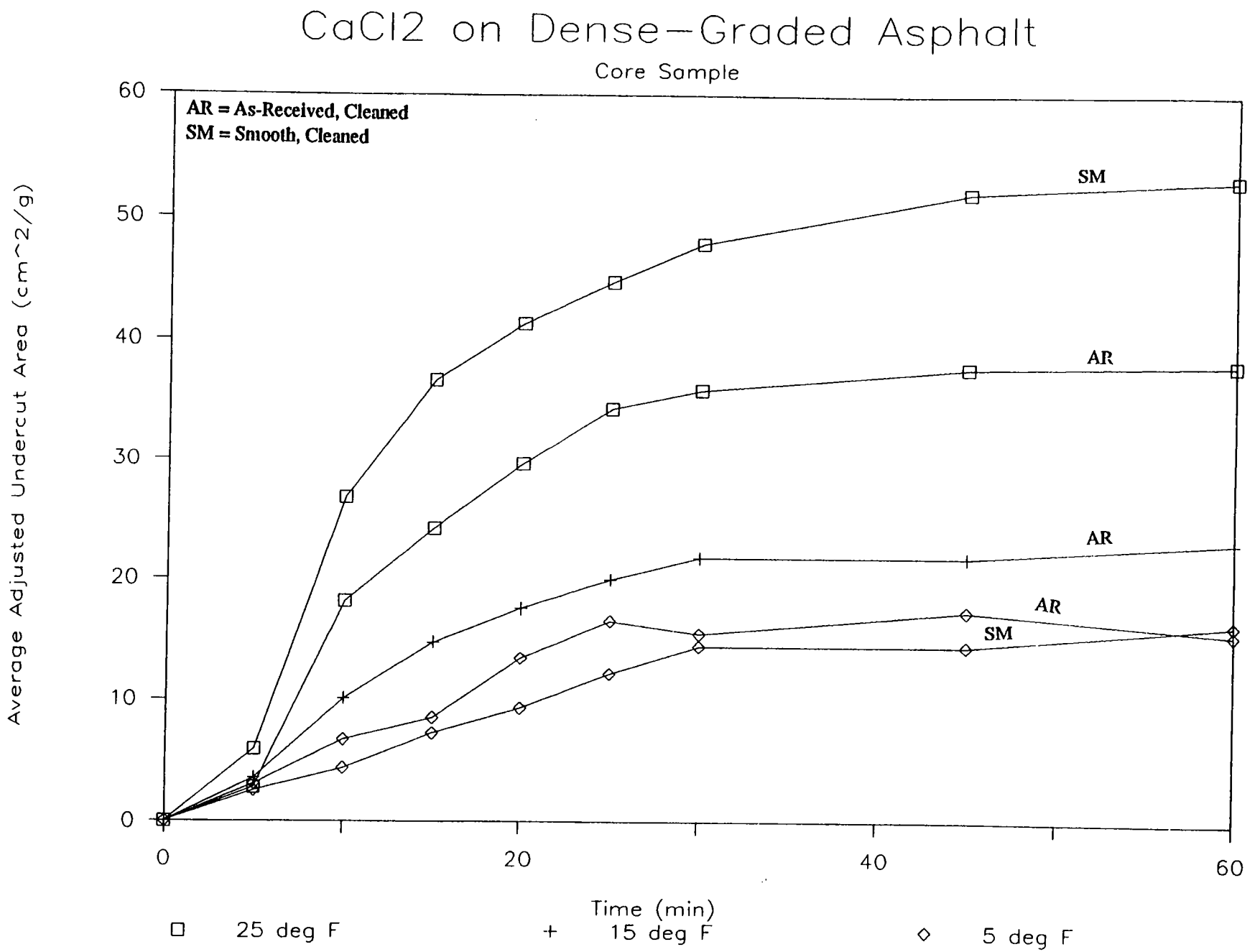
CaCl2 on Dense-Graded Asphalt
Core Sample
AR = As-Received, Cleaned
SM = Smooth, Cleaned
Average Adjusted Undercut Area (cm^2/g)
60
50
40
30
20
10
0
0
20
40
60
Time (min)
SM
AR
AR
AR
SM
25 deg F
15 deg F
5 deg F

Figure I-33

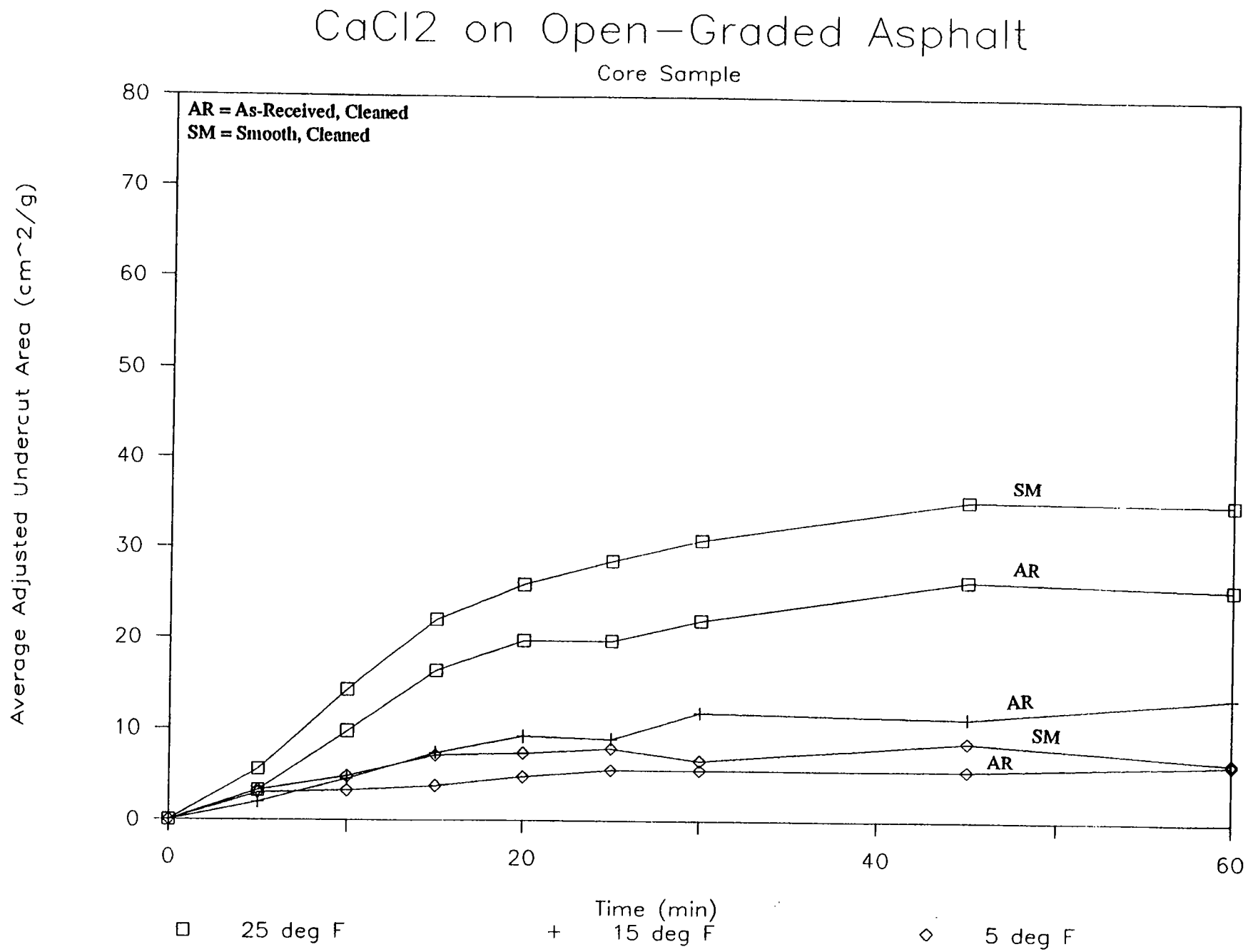
CaCl2 on Open-Graded Asphalt
Core Sample
AR = As-Received, Cleaned
SM = Smooth, Cleaned
Average Adjusted Undercut Area (cm^2/g)
80
70
60
50
40
30
20
10
0
0
20
40
60
Time (min)
SM
AR
AR
SM
AR
25 deg F
15 deg F
5 deg F

Figure I-34

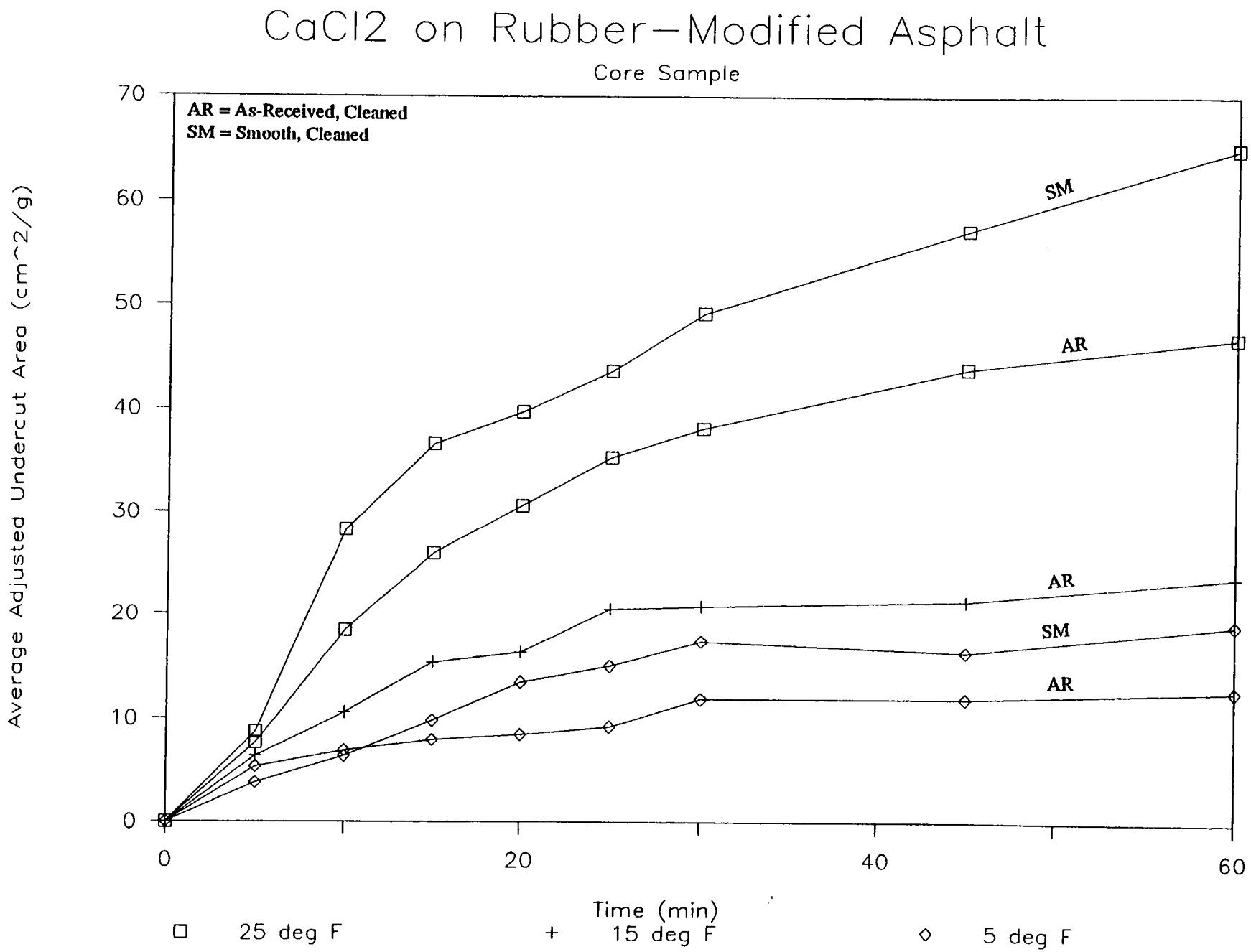
CaCl2 on Rubber-Modified Asphalt
Core Sample
AR = As-Received, Cleaned
SM = Smooth, Cleaned
Average Adjusted Undercut Area (cm^2/g)
70
60
50
40
30
20
10
0
0
20
40
60
Time (min)
SM
AR
AR
SM
AR
25 deg F
15 deg F
5 deg F

Figure I-35

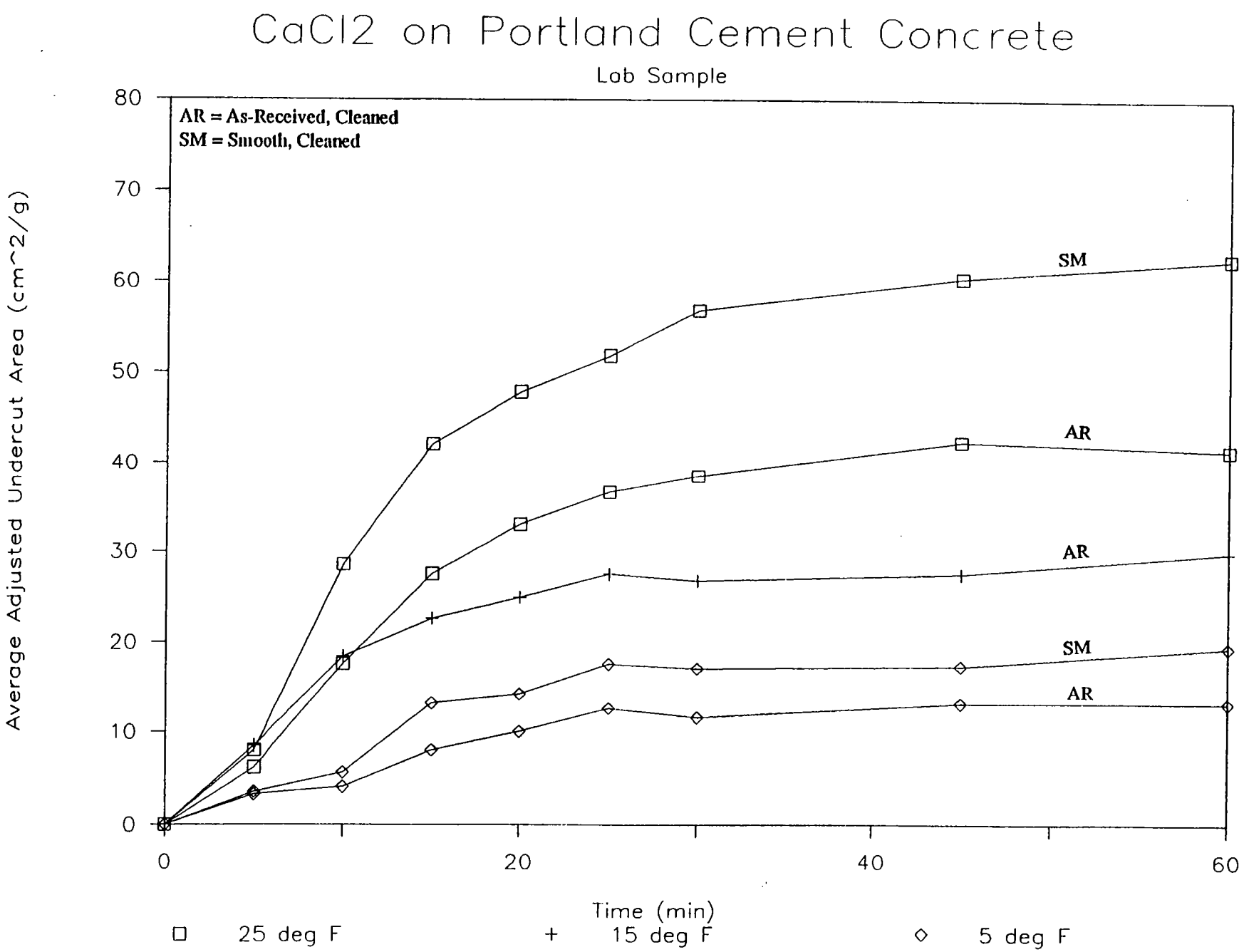
CaCl2 on Portland Cement Concrete
Lab Sample
AR = As-Received, Cleaned
SM = Smooth, Cleaned
Average Adjusted Undercut Area (cm^2/g)
80
70
60
50
40
30
20
10
0
SM
AR
AR
SM
AR
0
20
40
60
Time (min)
25 deg F
15 deg F
5 deg F

Figure I-36

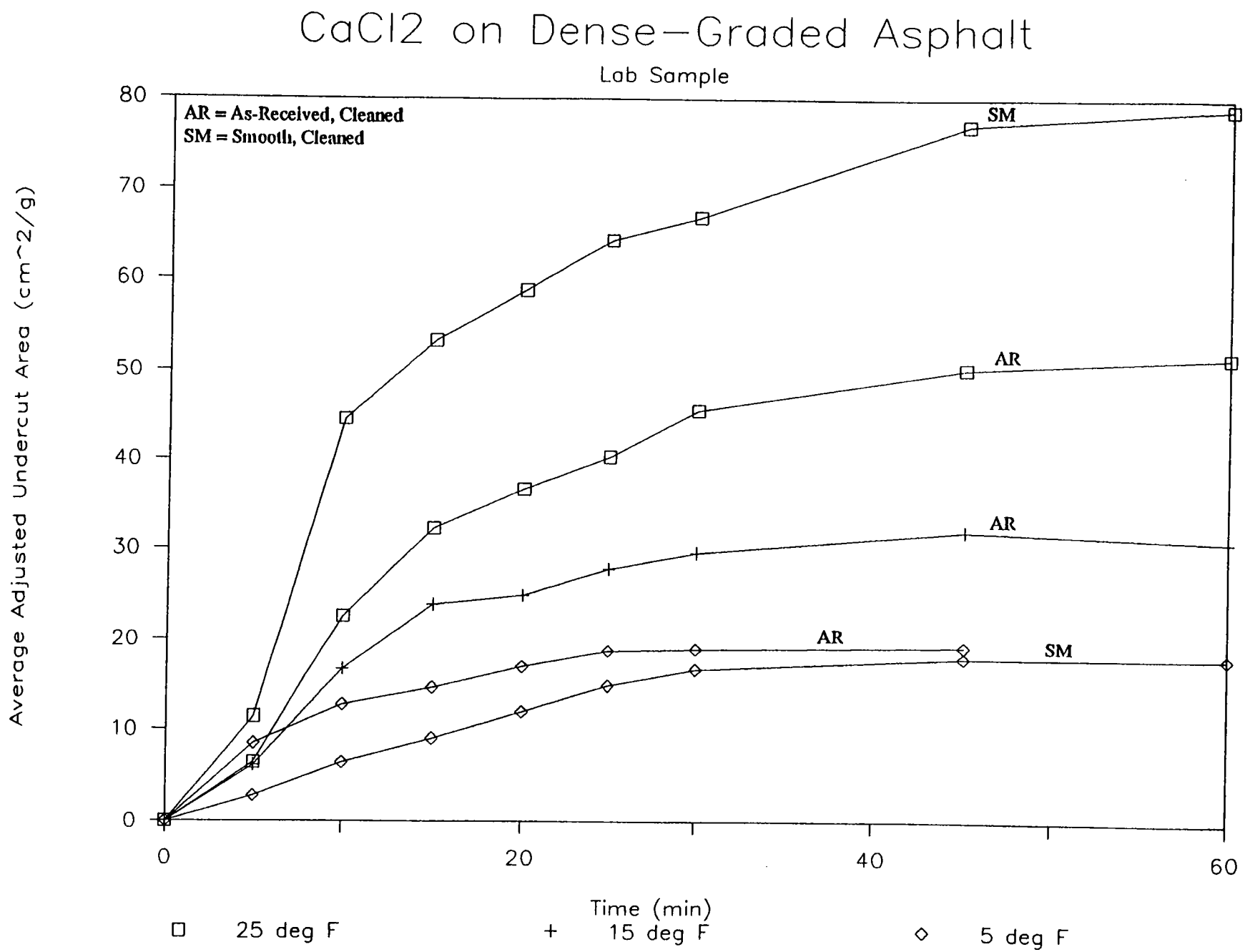
CaCl2 on Dense-Graded Asphalt
Lab Sample
AR = As-Received, Cleaned
SM = Smooth, Cleaned
SM
AR
AR
AR
SM
Average Adjusted Undercut Area (cm^2/g)
0
10
20
30
40
50
60
70
80
0
20
40
60
Time (min)
25 deg F
15 deg F
5 deg F

Figure I-37

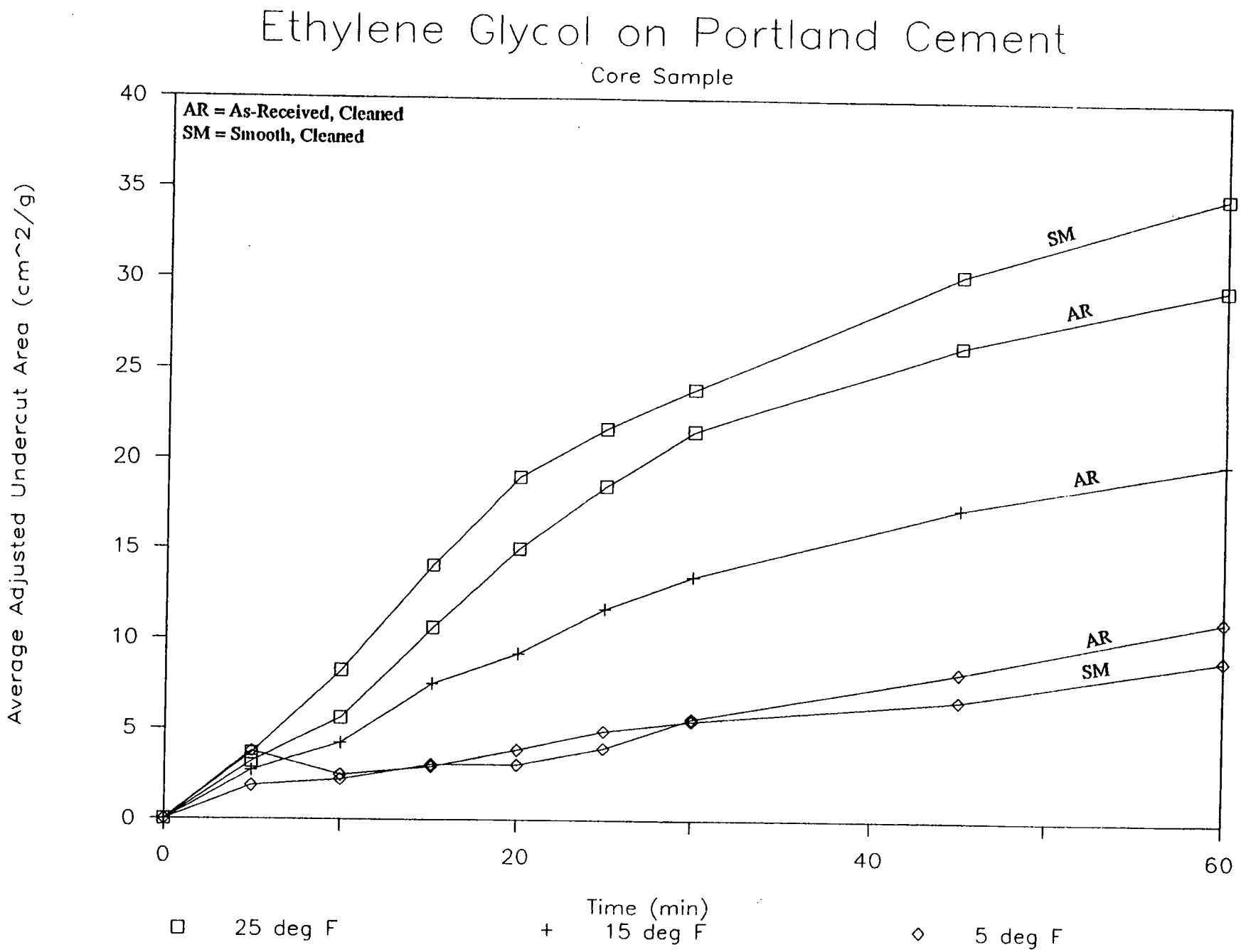
Ethylene Glycol on Portland Cement
Core Sample
AR = As-Received, Cleaned
SM = Smooth, Cleaned
Average Adjusted Undercut Area (cm^2/g)
0
5
10
15
20
25
30
35
40
SM
AR
AR
AR
SM
0
20
40
60
Time (min)
25 deg F
15 deg F
5 deg F

Figure I-38

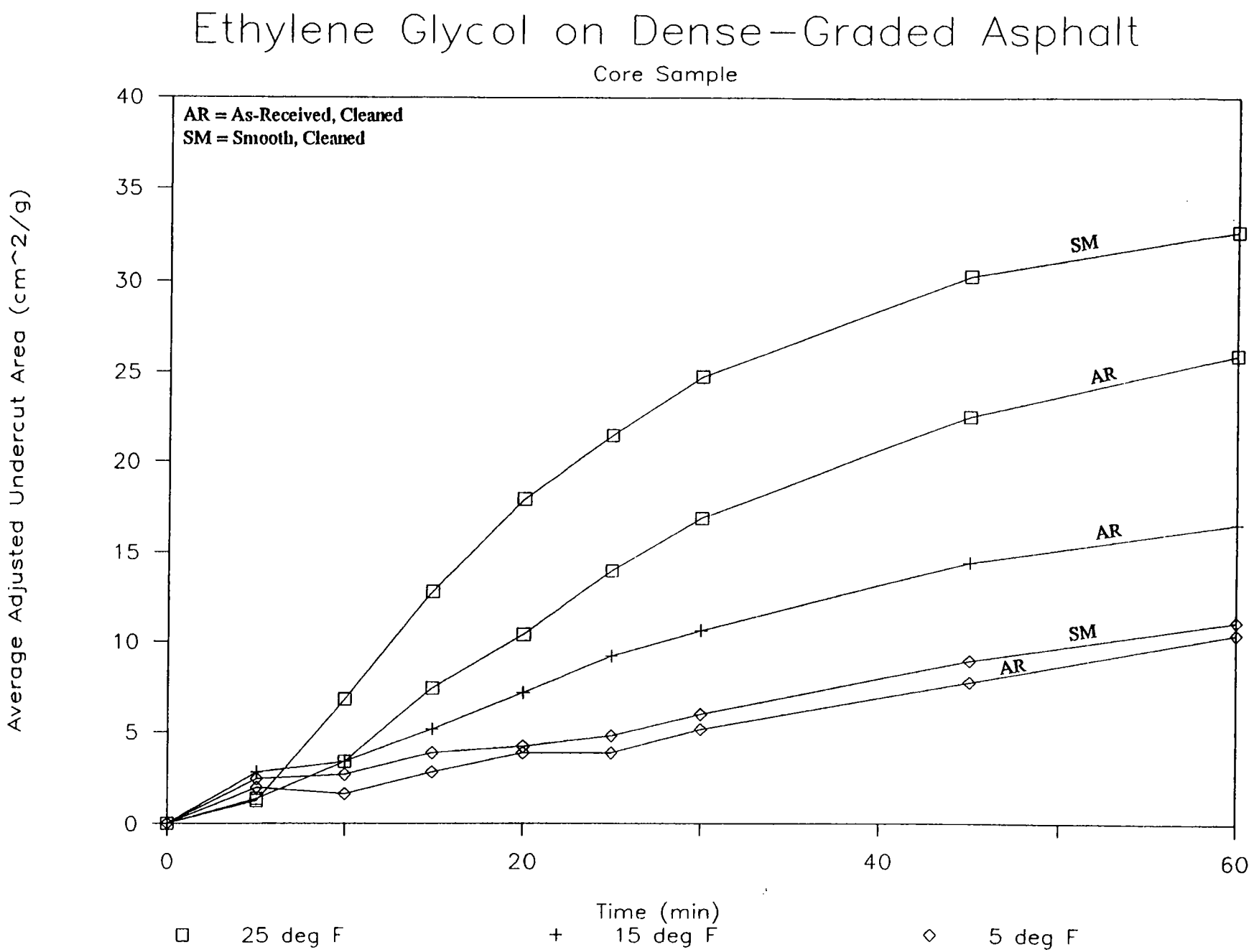
Ethylene Glycol on Dense-Graded Asphalt
Core Sample
AR = As-Received, Cleaned
SM = Smooth, Cleaned
Average Adjusted Undercut Area (cm^2/g)
0
5
10
15
20
25
30
35
40
SM
AR
AR
SM
AR
0
20
40
60
Time (min)
25 deg F
15 deg F
5 deg F

Figure I-39

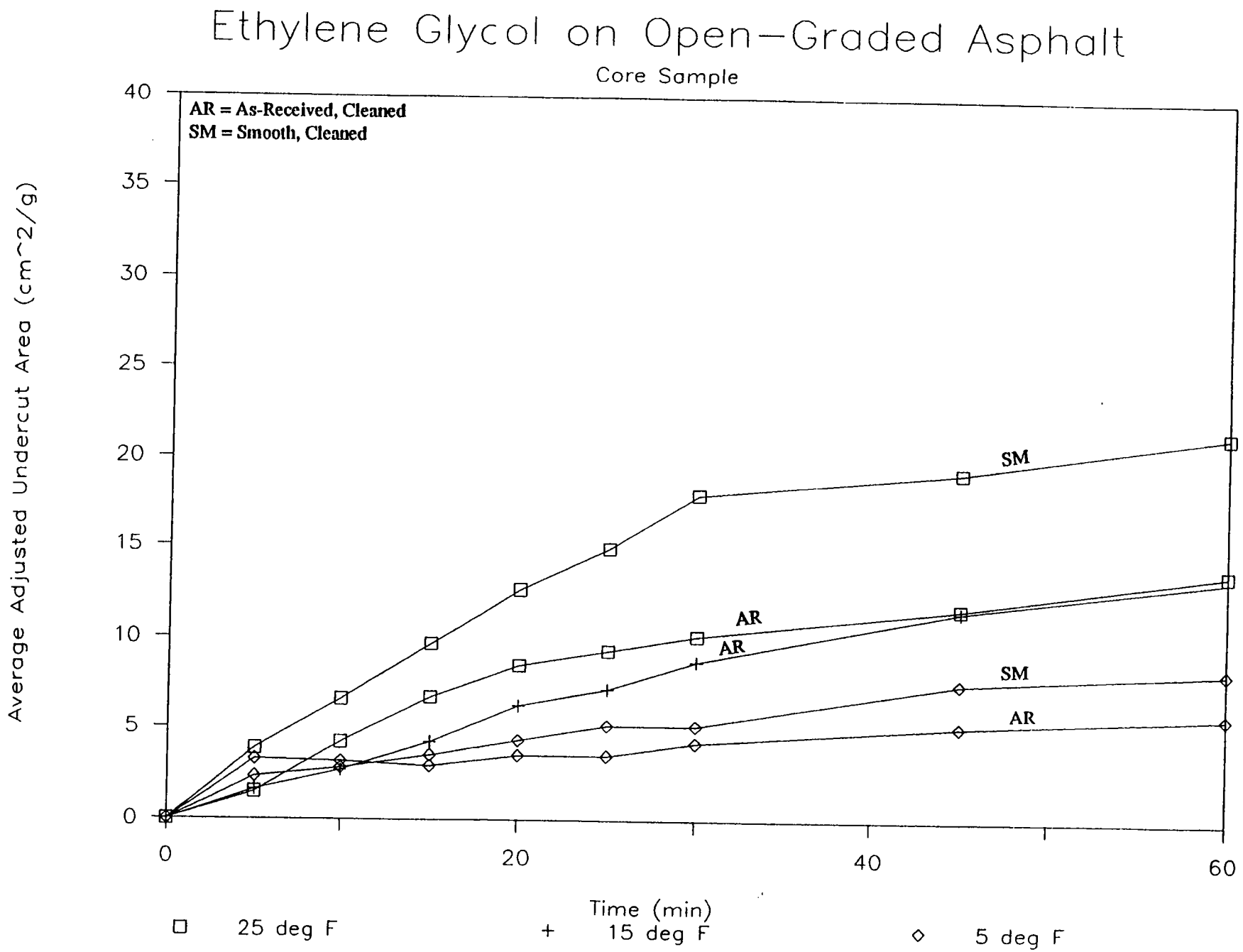
Ethylene Glycol on Open-Graded Asphalt
Core Sample
AR = As-Received, Cleaned
SM = Smooth, Cleaned
Average Adjusted Undercut Area (cm^2/g)
40
35
30
25
20
15
10
5
0
0
20
40
60
Time (min)
SM
AR
AR
SM
AR
25 deg F
15 deg F
5 deg F

Figure I-40

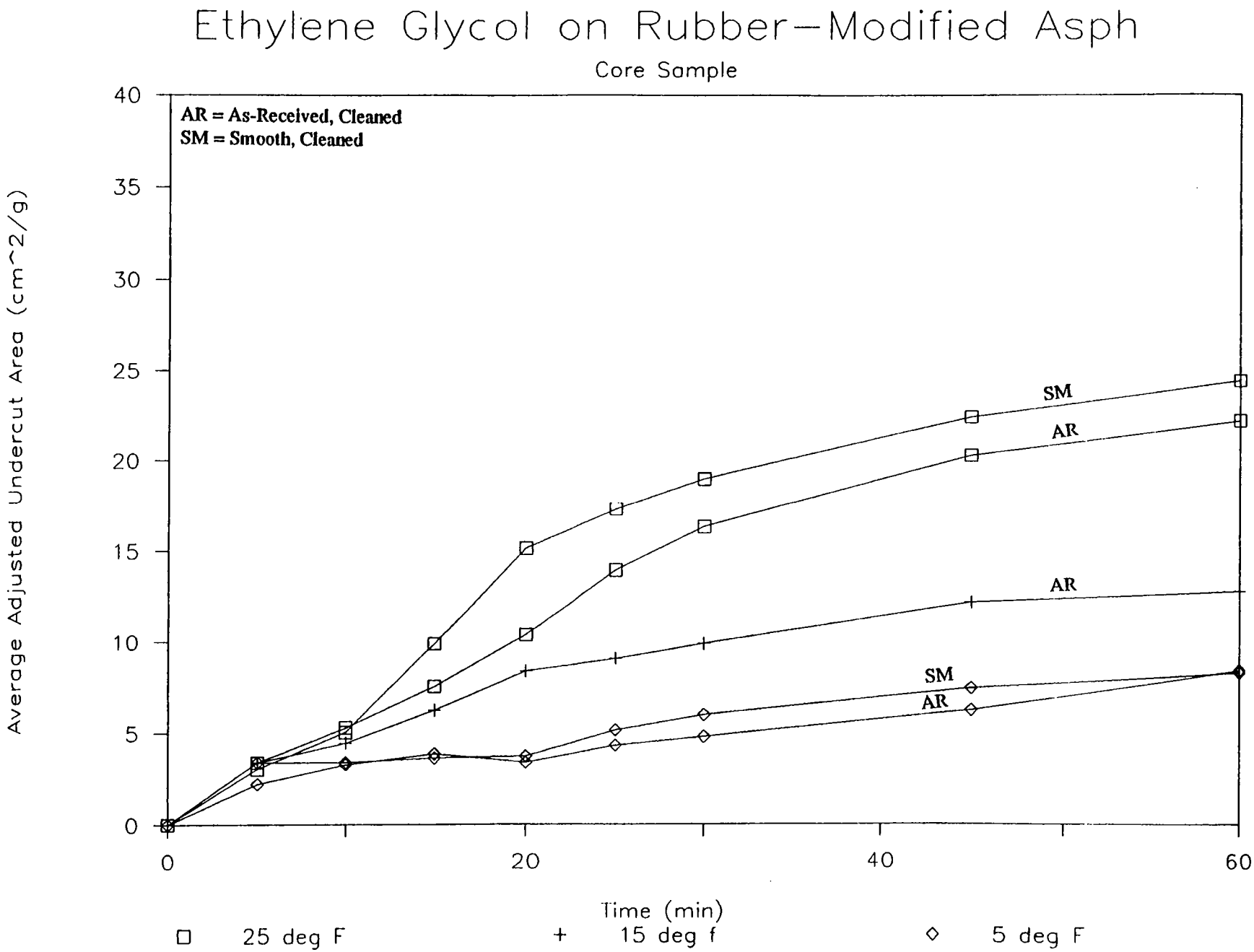
Ethylene Glycol on Rubber-Modified Asph
Core Sample
AR = As-Received, Cleaned
SM = Smooth, Cleaned
Average Adjusted Undercut Area (cm^2/g)
40
35
30
25
20
15
10
5
0
0
20
40
60
Time (min)
SM
AR
AR
SM
AR
25 deg F
15 deg f
5 deg F

Figure I-41

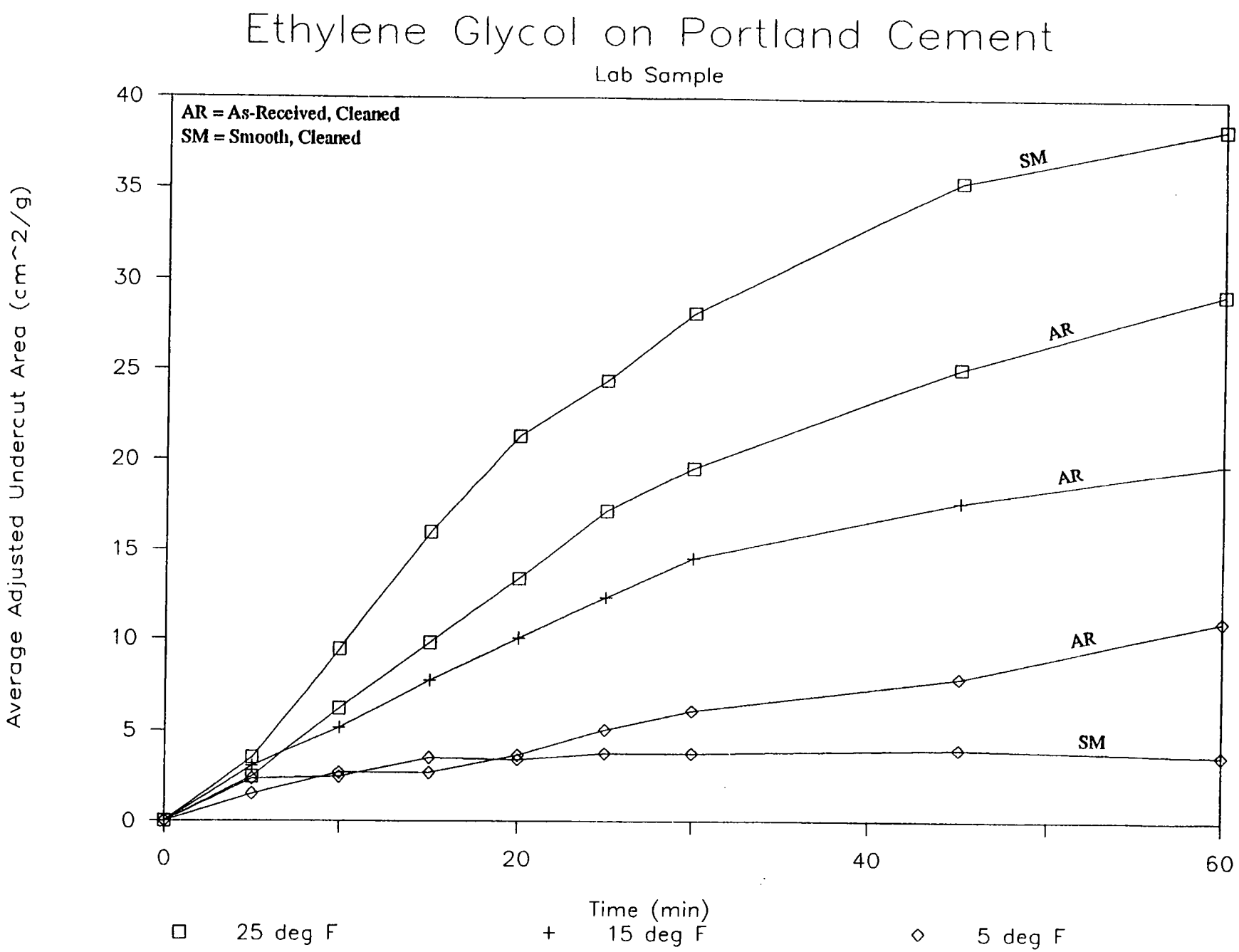
Ethylene Glycol on Portland Cement
Lab Sample
AR = As-Received, Cleaned
SM = Smooth, Cleaned
Average Adjusted Undercut Area (cm^2/g)
Time (min)
SM
AR
AR
AR
SM
25 deg F
15 deg F
5 deg F

Figure I-42

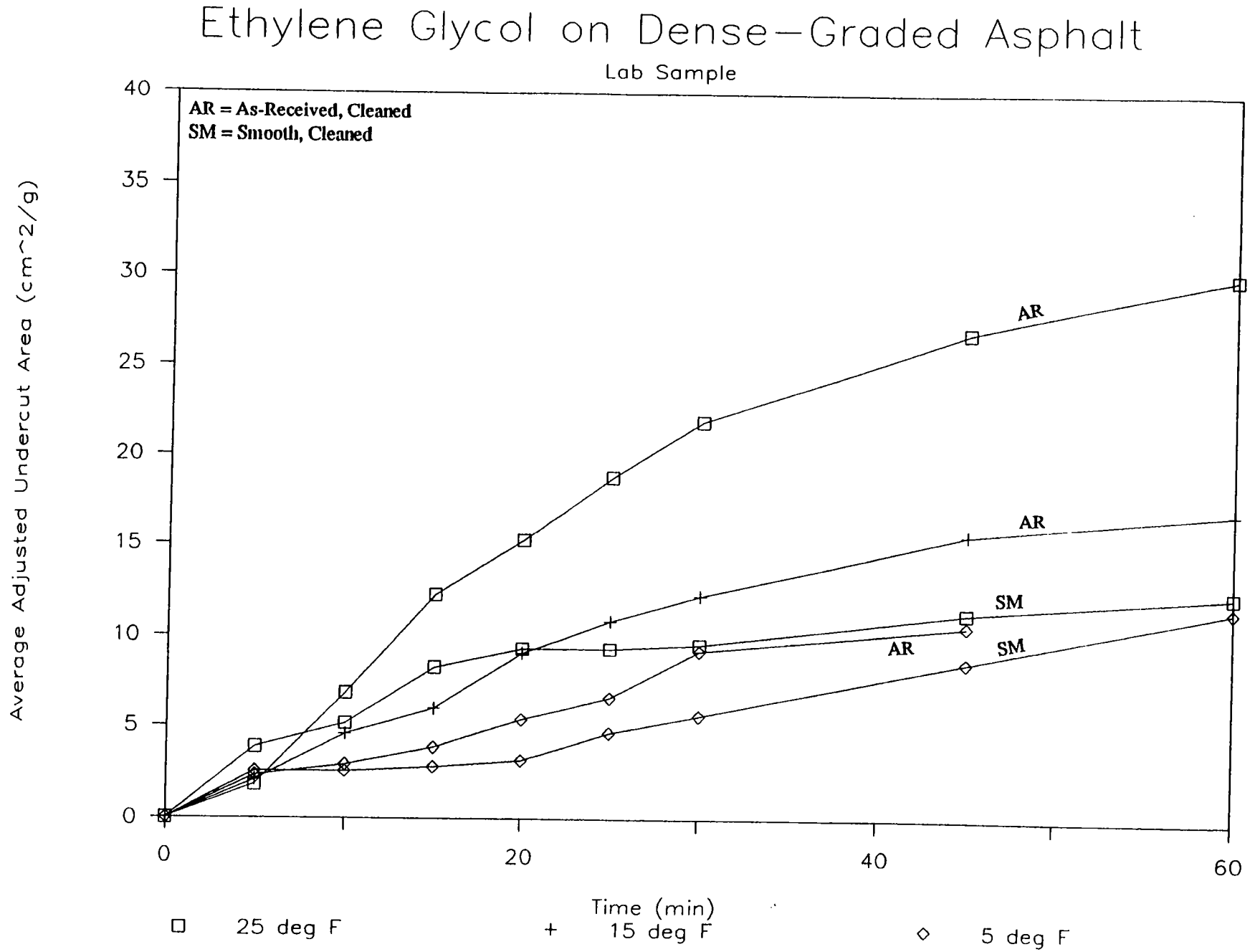
Ethylene Glycol on Dense-Graded Asphalt
Lab Sample
AR = As-Received, Cleaned
SM = Smooth, Cleaned
Average Adjusted Undercut Area (cm^2/g)
40
35
30
25
20
15
10
5
0
0
20
40
60
Time (min)
AR
AR
SM
AR
SM
25 deg F
15 deg F
5 deg F

Figure I-43

19-Mar-90

UNDERCUTTING TESTS - MRI PROJECT NO. 8977-S

SOURCE OF SAMPLE: CONNECTICUT
PAVEMENT TYPE: PORTLAND CEMENT CONCRETE CORE SAMPLE
PAVEMENT SURFACE CONDITION: AS RECEIVED, CLEANED
SAMPLE NO.: 9 CODE: CT509B111
DEICER: NaCl
DEICER WT: 0.0796 g
TEMPERATURE: 25 deg F

ADJUSTED UNDERCUT AREA cm2/g

TIME MIN	Rep 1	Rep 2	Rep 3	Avg	Std Error
0	0.00	0.00	0.00	0.00	0.00
5	7.38	12.41	14.92	11.57	2.22
10	21.20	14.92	21.20	19.11	2.09
15	29.99	17.43	26.22	24.55	3.72
20	32.51	17.43	29.99	26.64	4.66
25	37.53	23.71	32.51	31.25	4.04
30	40.04	24.97	40.04	35.02	5.03
45	43.81	29.99	41.30	38.37	4.25
60	46.32	40.04	40.04	42.14	2.09

SOURCE OF SAMPLE: CONNECTICUT
PAVEMENT TYPE: PORTLAND CEMENT CONCRETE CORE SAMPLE
PAVEMENT SURFACE CONDITION: SMOOTH AND CLEANED
SAMPLE NO.: 9 CODE: CT509C111
DEICER: NaCl
DEICER WT: 0.0796 g
TEMPERATURE: 25 deg F

ADJUSTED UNDERCUT AREA cm2/g

TIME MIN	Rep 1	Rep 2	Rep 3	Avg	Std Error
0	0.00	0.00	0.00	0.00	0.00
5	28.74	19.94	11.15	19.94	5.08
10	36.27	36.27	9.89	27.48	8.79
15	45.07	48.84	17.43	37.11	9.90
20	48.84	52.61	14.92	38.79	11.98
25	53.86	60.14	18.69	44.23	12.90
30	56.37	60.14	27.48	48.00	10.32
45	58.89	71.45	28.74	53.02	12.67
60	62.66	71.45	42.56	58.89	8.55

19-Mar-90

UNDERCUTTING TESTS - MRI PROJECT NO. 8977-S

SOURCE OF SAMPLE: CONNECTICUT
PAVEMENT TYPE: PORTLAND CEMENT CONCRETE CORE SAMPLE
PAVEMENT SURFACE CONDITION: AS RECEIVED, CLEANED
SAMPLE NO.: 10 CODE: CT510B112
DEICER: ETHYLENE GLYCOL
DEICER WT: 0.281 g
TEMPERATURE: 25 deg F

ADJUSTED UNDERCUT AREA cm2/g

TIME MIN	Rep 1	Rep 2	Rep 3	Avg	Std Error
0	0.00	0.00	0.00	0.00	0.00
5	3.16	4.23	2.09	3.16	0.62
10	6.01	5.65	5.29	5.65	0.21
15	10.28	10.63	10.99	10.63	0.21
20	15.97	14.55	14.55	15.02	0.47
25	19.53	17.75	18.46	18.58	0.52
30	23.09	19.88	21.66	21.54	0.93
45	27.00	25.93	26.29	26.41	0.31
60	28.43	28.07	32.34	29.61	1.37

SOURCE OF SAMPLE: CONNECTICUT
PAVEMENT TYPE: PORTLAND CEMENT CONCRETE CORE SAMPLE
PAVEMENT SURFACE CONDITION: SMOOTH AND CLEANED
SAMPLE NO.: 10 CODE: CT510C112
DEICER: ETHYLENE GLYCOL
DEICER WT: 0.281 g
TEMPERATURE: 25 deg F

ADJUSTED UNDERCUT AREA cm2/g

TIME MIN	Rep 1	Rep 2	Rep 3	Avg	Std Error
0	0.00	0.00	0.00	0.00	0.00
5	2.45	4.58	3.87	3.63	0.63
10	6.36	10.63	7.78	8.26	1.26
15	13.48	15.61	13.12	14.07	0.78
20	18.82	20.60	17.75	19.05	0.83
25	20.24	24.87	19.88	21.66	1.60
30	21.66	27.00	23.09	23.92	1.60
45	27.36	34.12	29.49	30.32	2.00
60	32.70	38.75	32.70	34.71	2.02

19-Mar-90

UNDERCUTTING TESTS - MRI PROJECT NO. 8977-S

SOURCE OF SAMPLE: CONNECTICUT
PAVEMENT TYPE: PORTLAND CEMENT CONCRETE CORE SAMPLE
PAVEMENT SURFACE CONDITION: AS RECEIVED, CLEANED
SAMPLE NO.: 11 CODE: CT511B113
DEICER: CaCl2
DEICER WT: 0.1278 g
TEMPERATURE: 25 deg F

ADJUSTED UNDERCUT AREA cm2/g

TIME MIN	Rep 1	Rep 2	Rep 3	Avg	Std Error
0	0.00	0.00	0.00	0.00	0.00
5	5.38	7.73	8.51	7.20	0.94
10	14.77	17.90	19.46	17.38	1.38
15	28.07	28.07	24.16	26.77	1.30
20	32.77	34.33	38.24	35.11	1.63
25	38.24	39.03	45.29	40.85	2.23
30	39.81	42.16	48.42	43.46	2.57
45	48.42	48.42	54.67	50.50	2.09
60	46.85	50.76	57.02	51.54	2.96

SOURCE OF SAMPLE: CONNECTICUT
PAVEMENT TYPE: PORTLAND CEMENT CONCRETE CORE SAMPLE
PAVEMENT SURFACE CONDITION: SMOOTH AND CLEANED
SAMPLE NO.: 11 CODE: CT511C113
DEICER: CaCl2
DEICER WT: 0.1278 g
TEMPERATURE: 25 deg F

ADJUSTED UNDERCUT AREA cm2/g

TIME MIN	Rep 1	Rep 2	Rep 3	Avg	Std Error
0	0.00	0.00	0.00	0.00	0.00
5	13.99	10.07	10.86	11.64	1.20
10	30.42	13.20	17.12	20.25	5.21
15	39.03	16.33	23.38	26.24	6.71
20	49.20	20.25	28.85	32.77	8.58
25	53.11	22.59	33.55	36.42	8.93
30	60.93	25.72	36.68	41.11	10.40
45	64.85	25.72	48.42	46.33	11.34
60	67.98	21.03	48.42	45.81	13.62

19-Mar-90

UNDERCUTTING TESTS - MRI PROJECT NO. 8977-S

SOURCE OF SAMPLE: CONNECTICUT
PAVEMENT TYPE: PORTLAND CEMENT CONCRETE CORE SAMPLE
PAVEMENT SURFACE CONDITION: AS RECEIVED, CLEANED
SAMPLE NO.: 3 CODE: CT503B211
DEICER: NaCl
DEICER WT: 0.0796 g
TEMPERATURE: 15 deg F

ADJUSTED UNDERCUT AREA cm2/g

TIME MIN	Rep 1	Rep 2	Rep 3	Avg	Std Error
0	0.00	0.00	0.00	0.00	0.00
5	7.38	7.38	3.61	6.12	1.26
10	7.38	8.64	6.12	7.38	0.73
15	6.12	14.92	7.38	9.47	2.75
20	9.89	18.69	9.89	12.82	2.93
25	9.89	19.94	11.15	13.66	3.16
30	11.15	18.69	9.89	13.24	2.75
45	9.89	21.20	12.41	14.50	3.43
60	11.15	21.20	12.41	14.92	3.16

SOURCE OF SAMPLE: CONNECTICUT
PAVEMENT TYPE: PORTLAND CEMENT CONCRETE CORE SAMPLE
PAVEMENT SURFACE CONDITION: AS RECEIVED, CLEANED
SAMPLE NO.: 4 CODE: CT504B212
DEICER: ETHYLENE GLYCOL
DEICER WT: 0.281 g
TEMPERATURE: 15 deg F

ADJUSTED UNDERCUT AREA cm2/g

TIME MIN	Rep 1	Rep 2	Rep 3	Avg	Std Error
0	0.00	0.00	0.00	0.00	0.00
5	1.73	2.45	3.87	2.68	0.63
10	4.58	3.87	4.23	4.23	0.21
15	8.14	7.78	6.72	7.55	0.43
20	9.56	9.21	8.85	9.21	0.21
25	9.92	13.48	11.70	11.70	1.03
30	12.41	14.90	13.12	13.48	0.74
45	15.97	19.53	16.68	17.39	1.09
60	17.75	21.66	20.60	20.00	1.17

19-Mar-90

UNDERCUTTING TESTS - MRI PROJECT NO. 8977-S

SOURCE OF SAMPLE: CONNECTICUT
PAVEMENT TYPE: PORTLAND CEMENT CONCRETE CORE SAMPLE
PAVEMENT SURFACE CONDITION: AS RECEIVED, CLEANED
SAMPLE NO.: 5 CODE: CT505B213
DEICER: CaCl2
DEICER WT: 0.1278 g
TEMPERATURE: 15 deg F

ADJUSTED UNDERCUT AREA cm2/g

TIME MIN	Rep 1	Rep 2	Rep 3	Avg	Std Error
0	0.00	0.00	0.00	0.00	0.00
5	4.60	4.60	3.81	4.34	0.26
10	16.33	18.68	4.60	13.20	4.36
15	16.33	28.07	10.86	18.42	5.08
20	22.59	31.98	21.81	25.46	3.27
25	24.94	37.46	20.25	27.55	5.14
30	24.94	37.46	21.81	28.07	4.78
45	24.94	39.03	28.85	30.94	4.20
60	27.29	37.46	35.90	33.55	3.16

SOURCE OF SAMPLE: CONNECTICUT
PAVEMENT TYPE: PORTLAND CEMENT CONCRETE CORE SAMPLE
PAVEMENT SURFACE CONDITION: AS RECEIVED, CLEANED
SAMPLE NO.: 6 CODE: CT506B311
DEICER: NaCl
DEICER WT: 0.0796 g
TEMPERATURE: 5 deg F

ADJUSTED UNDERCUT AREA cm2/g

TIME MIN	Rep 1	Rep 2	Rep 3	Avg	Std Error
0	0.00	0.00	0.00	0.00	0.00
5	4.87	7.38	7.38	6.54	0.84
10	4.87	8.64	6.12	6.54	1.11
15	6.12	7.38	6.12	6.54	0.42
20	7.38	8.64	6.12	7.38	0.73
25	8.64	9.89	8.64	9.05	0.42
30	8.64	7.38	8.64	8.22	0.42
45	6.12	8.64	7.38	7.38	0.73
60	8.64	9.89	7.38	8.64	0.73

19-Mar-90

UNDERCUTTING TESTS - MRI PROJECT NO. 8977-S

SOURCE OF SAMPLE: CONNECTICUT
PAVEMENT TYPE: PORTLAND CEMENT CONCRETE CORE SAMPLE
PAVEMENT SURFACE CONDITION: SMOOTH AND CLEANED
SAMPLE NO.: 6 CODE: CT506C311
DEICER: NaCl
DEICER WT: 0.0796 g
TEMPERATURE: 5 deg F

ADJUSTED UNDERCUT AREA cm2/g

TIME MIN	Rep 1	Rep 2	Rep 3	Avg	Std Error
0	0.00	0.00	0.00	0.00	0.00
5	7.38	4.87	4.87	5.70	0.84
10	7.38	6.12	6.12	6.54	0.42
15	7.38	8.64	6.12	7.38	0.73
20	6.12	6.12	4.87	5.70	0.42
25	8.64	7.38	6.12	7.38	0.73
30	6.12	7.38	6.12	6.54	0.42
45	7.38	6.12	4.87	6.12	0.73
60	4.87	8.64	4.87	6.12	1.26

SOURCE OF SAMPLE: CONNECTICUT
PAVEMENT TYPE: PORTLAND CEMENT CONCRETE CORE SAMPLE
PAVEMENT SURFACE CONDITION: AS RECEIVED, CLEANED
SAMPLE NO.: 7 CODE: CT507B312
DEICER: ETHYLENE GLYCOL
DEICER WT: 0.281 g
TEMPERATURE: 5 deg F

ADJUSTED UNDERCUT AREA cm2/g

TIME MIN	Rep 1	Rep 2	Rep 3	Avg	Std Error
0	0.00	0.00	0.00	0.00	0.00
5	2.45	1.73	1.38	1.85	0.31
10	2.09	2.09	2.45	2.21	0.12
15	2.80	3.16	3.16	3.04	0.12
20	2.45	3.16	3.51	3.04	0.31
25	3.16	3.87	4.94	3.99	0.52
30	4.23	6.01	6.72	5.65	0.74
45	5.65	9.92	9.21	8.26	1.32
60	8.14	12.41	13.12	11.22	1.56

19-Mar-90

UNDERCUTTING TESTS - MRI PROJECT NO. 8977-S

SOURCE OF SAMPLE: CONNECTICUT
PAVEMENT TYPE: PORTLAND CEMENT CONCRETE CORE SAMPLE
PAVEMENT SURFACE CONDITION: SMOOTH AND CLEANED
SAMPLE NO.: 7 CODE: CT507C312
DEICER: ETHYLENE GLYCOL
DEICER WT: 0.281 g
TEMPERATURE: 5 deg F

ADJUSTED UNDERCUT AREA cm2/g

TIME MIN	Rep 1	Rep 2	Rep 3	Avg	Std Error
0	0.00	0.00	0.00	0.00	0.00
5	4.23	2.45	4.58	3.75	0.66
10	2.45	2.09	2.80	2.45	0.21
15	2.80	2.80	3.16	2.92	0.12
20	3.51	3.51	4.58	3.87	0.36
25	4.23	5.65	4.94	4.94	0.41
30	4.23	6.36	6.01	5.53	0.66
45	3.87	10.63	5.65	6.72	2.02
60	4.94	14.55	7.78	9.09	2.85

SOURCE OF SAMPLE: CONNECTICUT
PAVEMENT TYPE: PORTLAND CEMENT CONCRETE CORE SAMPLE
PAVEMENT SURFACE CONDITION: AS RECEIVED, CLEANED
SAMPLE NO.: 8 CODE: CT508B313
DEICER: CaCl2
DEICER WT: 0.1278 g
TEMPERATURE: 5 deg F

ADJUSTED UNDERCUT AREA cm2/g

TIME MIN	Rep 1	Rep 2	Rep 3	Avg	Std Error
0	0.00	0.00	0.00	0.00	0.00
5	3.81	3.81	5.38	4.34	0.52
10	8.51	6.94	6.94	7.47	0.52
15	11.64	9.29	13.20	11.38	1.14
20	13.20	13.99	14.77	13.99	0.45
25	13.20	14.77	17.12	15.03	1.14
30	15.55	16.33	17.90	16.59	0.69
45	19.46	17.12	21.03	19.20	1.14
60	19.46	17.90	21.81	19.72	1.14

19-Mar-90

UNDERCUTTING TESTS - MRI PROJECT NO. 8977-S

SOURCE OF SAMPLE: CONNECTICUT
PAVEMENT TYPE: PORTLAND CEMENT CONCRETE CORE SAMPLE
PAVEMENT SURFACE CONDITION: SMOOTH AND CLEANED
SAMPLE NO.: 8 CODE: CT508C313
DEICER: CaCl2
DEICER WT: 0.1278 g
TEMPERATURE: 5 deg F

ADJUSTED UNDERCUT AREA cm2/g

TIME MIN	Rep 1	Rep 2	Rep 3	Avg	Std Error
0	0.00	0.00	0.00	0.00	0.00
5	3.81	3.81	3.81	3.81	ERR
10	4.60	3.81	5.38	4.60	0.45
15	6.16	3.81	3.81	4.60	0.78
20	6.16	3.81	3.81	4.60	0.78
25	6.16	5.38	3.81	5.12	0.69
30	6.16	6.16	5.38	5.90	0.26
45	5.38	6.16	4.60	5.38	0.45
60	6.16	6.94	5.38	6.16	0.45

20-Mar-90

UNDERCUTTING TESTS - MRI PROJECT NO. 8977-S

SOURCE OF SAMPLE: CONNECTICUT
PAVEMENT TYPE: DENSE-GRADED ASPHALT CORE SAMPLE
PAVEMENT SURFACE CONDITION: AS RECEIVED, CLEANED
SAMPLE NO.: 2 CODE: CT107B111
DEICER: NaCl
DEICER WT: 0.0796 g
TEMPERATURE: 25 deg F

ADJUSTED UNDERCUT AREA cm2/g

TIME MIN	Rep 1	Rep 2	Rep 3	Avg	Std Error
0	0.00	0.00	0.00	0.00	0.00
5	6.12	8.64	8.64	7.80	0.84
10	18.69	22.46	23.71	21.62	1.51
15	22.46	28.74	33.76	28.32	3.27
20	24.97	32.51	41.30	32.92	4.72
25	28.74	32.51	42.56	34.60	4.12
30	29.99	35.02	43.81	36.27	4.04
45	32.51	38.79	47.58	39.62	4.37
60	29.99	41.30	46.32	39.21	4.83

SOURCE OF SAMPLE: CONNECTICUT
PAVEMENT TYPE: DENSE-GRADED ASPHALT CORE SAMPLE
PAVEMENT SURFACE CONDITION: SMOOTH AND CLEANED
SAMPLE NO.: 2 CODE: CT107C111
DEICER: NaCl
DEICER WT: 0.0796 g
TEMPERATURE: 25 deg F

ADJUSTED UNDERCUT AREA cm2/g

TIME MIN	Rep 1	Rep 2	Rep 3	Avg	Std Error
0	0.00	0.00	0.00	0.00	0.00
5	8.64	9.89	8.64	9.05	0.42
10	28.74	29.99	28.74	29.16	0.42
15	37.53	40.04	38.79	38.79	0.73
20	40.04	38.79	45.07	41.30	1.92
25	43.81	42.56	50.09	45.49	2.33
30	45.07	45.07	52.61	47.58	2.51
45	48.84	48.84	50.09	49.26	0.42
60	52.61	52.61	56.37	53.86	1.26

20-Mar-90

UNDERCUTTING TESTS - MRI PROJECT NO. 8977-S

SOURCE OF SAMPLE: CONNECTICUT
PAVEMENT TYPE: DENSE-GRADED ASPHALT CORE SAMPLE
PAVEMENT SURFACE CONDITION: AS RECEIVED, CLEANED
SAMPLE NO.: 8 CODE: CT108B112
DEICER: ETHYLENE GLYCOL
DEICER WT: 0.281 g
TEMPERATURE: 25 deg F

ADJUSTED UNDERCUT AREA cm2/g

TIME MIN	Rep 1	Rep 2	Rep 3	Avg	Std Error
0	0.00	0.00	0.00	0.00	0.00
5	1.02	1.38	1.73	1.38	0.21
10	3.16	4.58	2.45	3.40	0.63
15	7.07	7.78	7.43	7.43	0.21
20	10.63	9.92	10.63	10.39	0.24
25	13.83	13.83	14.19	13.95	0.12
30	18.10	16.33	16.33	16.92	0.59
45	23.44	23.09	20.95	22.49	0.78
60	29.14	25.93	22.73	25.93	1.85

SOURCE OF SAMPLE: CONNECTICUT
PAVEMENT TYPE: DENSE-GRADED ASPHALT CORE SAMPLE
PAVEMENT SURFACE CONDITION: SMOOTH AND CLEANED
SAMPLE NO.: 8 CODE: CT108C112
DEICER: ETHYLENE GLYCOL
DEICER WT: 0.281 g
TEMPERATURE: 25 deg F

ADJUSTED UNDERCUT AREA cm2/g

TIME MIN	Rep 1	Rep 2	Rep 3	Avg	Std Error
0	0.00	0.00	0.00	0.00	0.00
5	1.73	0.67	1.38	1.26	0.31
10	6.36	6.36	7.78	6.84	0.47
15	12.41	13.12	12.77	12.77	0.21
20	17.75	17.39	18.82	17.99	0.43
25	22.02	20.60	21.66	21.43	0.43
30	24.15	23.44	26.65	24.75	0.97
45	29.49	29.49	31.98	30.32	0.83
60	31.27	31.63	35.19	32.70	1.25

20-Mar-90

UNDERCUTTING TESTS - MRI PROJECT NO. 8977-S

SOURCE OF SAMPLE: CONNECTICUT
PAVEMENT TYPE: DENSE-GRADED ASPHALT CORE SAMPLE
PAVEMENT SURFACE CONDITION: AS RECEIVED, CLEANED
SAMPLE NO.: 9 CODE: CT109B113
DEICER: CaCl2
DEICER WT: 0.1278 g
TEMPERATURE: 25 deg F

ADJUSTED UNDERCUT AREA, cm^2/g

TIME MIN	Rep1	Rep2	Rep3	AVG	Std Error
0	0.00	0.00	0.00	0.00	0.00
5	4.60	1.47	2.25	2.77	0.94
10	16.33	18.68	19.46	18.16	0.94
15	18.68	25.72	28.07	24.16	2.82
20	25.72	30.42	32.77	29.64	2.07
25	37.46	28.07	37.46	34.33	3.13
30	38.24	28.85	40.59	35.90	3.59
45	46.07	24.94	42.16	37.72	6.49
60	42.94	28.07	42.94	37.98	4.96

SOURCE OF SAMPLE: CONNECTICUT
PAVEMENT TYPE: DENSE-GRADED ASPHALT CORE SAMPLE
PAVEMENT SURFACE CONDITION: SMOOTH AND CLEANED
SAMPLE NO.: 9 CODE: CT109C113
DEICER: CaCl2
DEICER WT: 0.1278 g
TEMPERATURE: 25 deg F

ADJUSTED UNDERCUT AREA cm2/g

TIME MIN	Rep1	Rep2	Rep3	AVG	Std Error
0	0.00	0.00	0.00	0.00	0.00
5	5.38	7.73	4.60	5.90	0.94
10	25.72	28.07	26.51	26.77	0.69
15	35.11	37.46	37.46	36.68	0.78
20	37.46	42.94	43.72	41.37	1.97
25	42.94	44.50	46.85	44.76	1.14
30	44.50	47.63	51.54	47.89	2.04
45	50.76	52.33	53.11	52.07	0.69
60	47.63	54.67	57.02	53.11	2.82

20-Mar-90

UNDERCUTTING TESTS - MRI PROJECT NO. 8977-S

SOURCE OF SAMPLE: CONNECTICUT
PAVEMENT TYPE: DENSE-GRADED ASPHALT CORE SAMPLE
PAVEMENT SURFACE CONDITION: AS RECEIVED, CLEANED
SAMPLE NO.: 2 CODE: CT101B211
DEICER: NaCl
DEICER WT: 0.0796 g
TEMPERATURE: 15 deg F

ADJUSTED UNDERCUT AREA cm2/g

TIME MIN	Rep 1	Rep 2	Rep 3	Avg	Std Error
0	0.00	0.00	0.00	0.00	0.00
5	6.12	6.12	8.64	6.96	0.84
10	7.38	6.12	11.15	8.22	1.51
15	6.12	9.89	9.89	8.64	1.26
20	8.64	11.15	11.15	10.31	0.84
25	8.64	12.41	9.89	10.31	1.11
30	8.64	13.66	11.15	11.15	1.45
45	9.89	14.92	12.41	12.41	1.45
60	13.66	17.43	12.41	14.50	1.51

SOURCE OF SAMPLE: CONNECTICUT
PAVEMENT TYPE: DENSE-GRADED ASPHALT CORE SAMPLE
PAVEMENT SURFACE CONDITION: AS RECEIVED, CLEANED
SAMPLE NO.: 2 CODE: CT102B212
DEICER: ETHYLENE GLYCOL
DEICER WT: 0.281 g
TEMPERATURE: 15 deg F

ADJUSTED UNDERCUT AREA cm2/g

TIME MIN	Rep 1	Rep 2	Rep 3	Avg	Std Error
0	0.00	0.00	0.00	0.00	0.00
5	3.16	2.45	2.80	2.80	0.21
10	3.16	3.51	3.51	3.40	0.12
15	5.6	4.6	5.3	5.17	0.31
20	8.1	5.6	7.8	7.19	0.78
25	9.6	8.1	9.9	9.21	0.54
30	11.3	9.6	11.0	10.63	0.54
45	15.6	13.5	14.2	14.43	0.63
60	17.0	15.6	17.0	16.56	0.47

20-Mar-90

UNDERCUTTING TESTS - MRI PROJECT NO. 8977-S

SOURCE OF SAMPLE: CONNECTICUT
PAVEMENT TYPE: DENSE-GRADED ASPHALT CORE SAMPLE
PAVEMENT SURFACE CONDITION: AS RECEIVED, CLEANED
SAMPLE NO.: 2 CODE: CT102B213
DEICER: CaCl2
DEICER WT: 0.1278 g
TEMPERATURE: 15 deg F

ADJUSTED UNDERCUT AREA cm2/g

TIME MIN	Rep 1	Rep 2	Rep 3	Avg	Std Error
0	0.00	0.00	0.00	0.00	0.00
5	3.81	2.25	4.60	3.55	0.69
10	10.86	9.29	10.07	10.07	0.45
15	15.55	13.99	14.77	14.77	0.45
20	18.68	17.12	17.12	17.64	0.52
25	20.25	18.68	21.03	19.99	0.69
30	23.38	19.46	22.59	21.81	1.20
45	23.38	21.03	21.03	21.81	0.78
60	23.38	23.38	22.59	23.12	0.26

SOURCE OF SAMPLE: CONNECTICUT
PAVEMENT TYPE: DENSE-GRADED ASPHALT CORE SAMPLE
PAVEMENT SURFACE CONDITION: AS RECEIVED, CLEANED
SAMPLE NO.: 2 CODE: CT104B311
DEICER: NaCl
DEICER WT: 0.0796 g
TEMPERATURE: 5 deg F

ADJUSTED UNDERCUT AREA cm2/g

TIME MIN	Rep 1	Rep 2	Rep 3	Avg	Std Error
0	0.00	0.00	0.00	0.00	0.00
5	2.35	4.87	7.38	4.87	1.45
10	3.61	4.87	4.87	4.45	0.42
15	7.38	7.38	3.61	6.12	1.26
20	6.12	4.87	8.64	6.54	1.11
25	9.89	9.89	9.89	9.89	ERR
30	7.38	7.38	9.89	8.22	0.84
45	6.12	9.89	9.89	8.64	1.26
60	4.87	8.64	8.64	7.38	1.26

20-Mar-90

UNDERCUTTING TESTS - MRI PROJECT NO. 8977-S

SOURCE OF SAMPLE: CONNECTICUT
PAVEMENT TYPE: DENSE-GRADED ASPHALT CORE SAMPLE
PAVEMENT SURFACE CONDITION: SMOOTH AND CLEANED
SAMPLE NO.: 2 CODE: CT104C311
DEICER: NaCl
DEICER WT: 0.0796 g
TEMPERATURE: 5 deg F

ADJUSTED UNDERCUT AREA cm2/g

TIME MIN	Rep 1	Rep 2	Rep 3	Avg	Std Error
0	0.00	0.00	0.00	0.00	0.00
5	1.10	2.35	1.10	1.52	0.42
10	3.61	4.87	3.61	4.03	0.42
15	3.61	4.87	4.87	4.45	0.42
20	4.87	6.12	4.87	5.29	0.42
25	4.87	4.87	4.87	4.87	ERR
30	4.87	4.87	4.87	4.87	ERR
45	6.12	4.87	4.87	5.29	0.42
60	7.38	4.87	7.38	6.54	0.84

SOURCE OF SAMPLE: CONNECTICUT
PAVEMENT TYPE: DENSE-GRADED ASPHALT CORE SAMPLE
PAVEMENT SURFACE CONDITION: AS RECEIVED, CLEANED
SAMPLE NO.: 2 CODE: CT105B312
DEICER: ETHYLENE GLYCOL
DEICER WT: 0.281 g
TEMPERATURE: 5 deg F

ADJUSTED UNDERCUT AREA cm2/g

TIME MIN	Rep 1	Rep 2	Rep 3	Avg	Std Error
0	0.00	0.00	0.00	0.00	0.00
5	2.09	1.73	2.09	1.97	1.39
10	2.09	1.02	1.73	1.62	1.14
15	3.16	2.45	2.80	2.80	1.98
20	4.23	3.51	3.87	3.87	2.74
25	4.23	3.16	4.23	3.87	2.74
30	5.65	4.58	5.29	5.17	3.66
45	8.50	7.07	7.78	7.78	5.50
60	11.70	8.85	10.63	10.39	7.35

20-Mar-90

UNDERCUTTING TESTS - MRI PROJECT NO. 8977-S

SOURCE OF SAMPLE: CONNECTICUT
PAVEMENT TYPE: DENSE-GRADED ASPHALT CORE SAMPLE
PAVEMENT SURFACE CONDITION: SMOOTH AND CLEANED
SAMPLE NO.: 2 CODE: CT105C312
DEICER: ETHYLENE GLYCOL
DEICER WT: 0.281 g
TEMPERATURE: 5 deg F

ADJUSTED UNDERCUT AREA cm2/g

TIME MIN	Rep 1	Rep 2	Rep 3	Avg	Std Error
0	0.00	0.00	0.00	0.00	0.00
5	2.45	2.45	2.45	2.45	ERR
10	2.45	2.45	3.16	2.68	0.24
15	3.87	3.16	4.58	3.87	0.41
20	3.16	4.23	5.29	4.23	0.62
25	4.58	4.94	4.94	4.82	0.12
30	4.94	6.36	6.72	6.01	0.54
45	8.50	8.85	9.56	8.97	0.31
60	9.92	11.70	11.70	11.11	0.59

SOURCE OF SAMPLE: CONNECTICUT
PAVEMENT TYPE: DENSE-GRADED ASPHALT CORE SAMPLE
PAVEMENT SURFACE CONDITION: AS RECEIVED, CLEANED
SAMPLE NO.: 6 CODE: CT106B313
DEICER: CaCl2
DEICER WT: 0.1278 g
TEMPERATURE: 5 deg F

ADJUSTED UNDERCUT AREA cm2/g

TIME MIN	Rep 1	Rep 2	Rep 3	Avg	Std Error
0	0.00	0.00	0.00	0.00	0.00
5	2.25	3.03	3.81	3.03	0.45
10	5.38	6.16	8.51	6.68	0.94
15	9.29	7.73	8.51	8.51	0.45
20	13.99	14.77	11.64	13.46	0.94
25	17.90	17.12	14.77	16.59	0.94
30	16.33	17.12	13.20	15.55	1.20
45	16.33	18.68	17.12	17.38	0.69
60	16.33	17.12	13.20	15.55	1.20

20-Mar-90

UNDERCUTTING TESTS - MRI PROJECT NO. 8977-S

SOURCE OF SAMPLE: CONNECTICUT
PAVEMENT TYPE: DENSE-GRADED ASPHALT CORE SAMPLE
PAVEMENT SURFACE CONDITION: SMOOTH AND CLEANED
SAMPLE NO.: 6 CODE: CT106C313
DEICER: CaCl2
DEICER WT: 0.1278 g
TEMPERATURE: 5 deg F

ADJUSTED UNDERCUT AREA cm2/g

TIME MIN	Rep 1	Rep 2	Rep 3	Avg	Std Error
0	0.00	0.00	0.00	0.00	0.00
5	2.25	2.25	3.03	2.51	0.26
10	4.60	5.38	3.03	4.34	0.69
15	6.16	8.51	6.94	7.20	0.69
20	6.16	12.42	9.29	9.29	1.81
25	10.86	13.99	11.64	12.16	0.94
30	12.42	15.55	15.55	14.51	1.04
45	11.64	18.68	13.20	14.51	2.13
60	16.33	18.68	13.99	16.33	1.36

19-Mar-90

UNDERCUTTING TESTS - MRI PROJECT NO. 8977-S

SOURCE OF SAMPLE: NEW YORK
PAVEMENT TYPE: OPEN-GRADED ASPHALT CORE SAMPLE
PAVEMENT SURFACE CONDITION: AS RECEIVED, CLEANED
SAMPLE NO.: 3 CODE: NY303B111
DEICER: NaCl
DEICER WT: 0.0796 g
TEMPERATURE: 25 deg F

ADJUSTED UNDERCUT AREA cm2/g

TIME MIN	Rep 1	Rep 2	Rep 3	Avg	Std Error
0	0.00	0.00	0.00	0.00	0.00
5	6.12	4.87	7.38	6.12	0.73
10	11.15	11.15	11.15	11.15	ERR
15	17.43	17.43	17.43	17.43	0.00
20	19.94	24.97	19.94	21.62	1.68
25	21.20	28.74	21.20	23.71	2.51
30	22.46	29.99	24.97	25.81	2.22
45	26.22	32.51	23.71	27.48	2.62
60	27.48	32.51	28.74	29.57	1.51

SOURCE OF SAMPLE: NEW YORK
PAVEMENT TYPE: OPEN-GRADED ASPHALT CORE SAMPLE
PAVEMENT SURFACE CONDITION: SMOOTH AND CLEANED
SAMPLE NO.: 3 CODE: NY303C111
DEICER: NaCl
DEICER WT: 0.0796 g
TEMPERATURE: 25 deg F

ADJUSTED UNDERCUT AREA cm2/g

TIME MIN	Rep 1	Rep 2	Rep 3	Avg	Std Error
0	0.00	0.00	0.00	0.00	0.00
5	14.92	12.41	9.89	12.41	1.45
10	33.76	33.76	32.51	33.34	0.42
15	42.56	38.79	37.53	39.62	1.51
20	43.81	43.81	45.07	44.23	0.42
25	45.07	42.56	46.32	44.65	1.11
30	47.58	48.84	47.58	48.00	0.42
45	50.09	50.09	46.32	48.84	1.26
60	51.35	51.35	50.09	50.93	0.42

19-Mar-90

UNDERCUTTING TESTS - MRI PROJECT NO. 8977-S

SOURCE OF SAMPLE: NEW YORK
PAVEMENT TYPE: OPEN-GRADED ASPHALT CORE SAMPLE
PAVEMENT SURFACE CONDITION: AS RECEIVED, CLEANED
SAMPLE NO.: 3 CODE: NY303B112
DEICER: ETHYLENE GLYCOL
DEICER WT: 0.281 g
TEMPERATURE: 25 deg F

ADJUSTED UNDERCUT AREA cm2/g

TIME MIN	Rep 1	Rep 2	Rep 3	Avg	Std Error
0	0.00	0.00	0.00	0.00	0.00
5	1.73	1.02	1.73	1.50	0.24
10	3.16	5.29	4.23	4.23	0.62
15	4.23	8.85	7.07	6.72	1.35
20	5.65	10.63	9.21	8.50	1.48
25	5.65	11.70	10.63	9.33	1.86
30	5.65	12.77	12.05	10.16	2.26
45	6.36	15.61	13.12	11.70	2.76
60	7.43	17.39	16.33	13.72	3.16

SOURCE OF SAMPLE: NEW YORK
PAVEMENT TYPE: OPEN-GRADED ASPHALT CORE SAMPLE
PAVEMENT SURFACE CONDITION: SMOOTH AND CLEANED
SAMPLE NO.: 3 CODE: NY303C112
DEICER: ETHYLENE GLYCOL
DEICER WT: 0.281 g
TEMPERATURE: 25 deg F

ADJUSTED UNDERCUT AREA cm2/g

TIME MIN	Rep 1	Rep 2	Rep 3	Avg	Std Error
0	0.00	0.00	0.00	0.00	0.00
5	3.16	4.23	4.23	3.87	0.36
10	5.29	6.72	7.78	6.60	0.72
15	7.43	11.34	10.28	9.68	1.17
20	6.36	17.39	14.19	12.65	3.28
25	6.36	20.60	17.75	14.90	4.35
30	8.85	23.80	21.31	17.99	4.62
45	9.92	26.29	21.66	19.29	4.87
60	9.56	30.20	24.51	21.43	6.15

19-Mar-90

UNDERCUTTING TESTS - MRI PROJECT NO. 8977-S

SOURCE OF SAMPLE: NEW YORK
PAVEMENT TYPE: OPEN-GRADED ASPHALT CORE SAMPLE
PAVEMENT SURFACE CONDITION: AS RECEIVED, CLEANED
SAMPLE NO.: 3 CODE: NY303B113
DEICER: CaCl2
DEICER WT: 0.1278 g
TEMPERATURE: 25 deg F

ADJUSTED UNDERCUT AREA cm2/g

TIME MIN	Rep 1	Rep 2	Rep 3	Avg	Std Error
0	0.00	0.00	0.00	0.00	0.00
5	3.03	3.03	3.81	3.29	0.26
10	8.51	10.07	10.86	9.81	0.69
15	15.55	16.33	17.12	16.33	0.45
20	18.68	18.68	21.81	19.72	1.04
25	20.25	20.25	18.68	19.72	0.52
30	23.38	20.25	22.59	22.07	0.94
45	31.20	22.59	25.72	26.51	2.52
60	26.51	23.38	27.29	25.72	1.20

SOURCE OF SAMPLE: NEW YORK
PAVEMENT TYPE: OPEN-GRADED ASPHALT CORE SAMPLE
PAVEMENT SURFACE CONDITION: SMOOTH AND CLEANED
SAMPLE NO.: 3 CODE: NY303C113
DEICER: CaCl2
DEICER WT: 0.1278 g
TEMPERATURE: 25 deg F

ADJUSTED UNDERCUT AREA cm2/g

TIME MIN	Rep 1	Rep 2	Rep 3	Avg	Std Error
0	0.00	0.00	0.00	0.00	0.00
5	3.81	6.16	6.94	5.64	0.94
10	5.38	16.33	21.03	14.25	4.64
15	6.16	29.64	30.42	22.07	7.96
20	9.29	34.33	34.33	25.98	8.35
25	9.29	37.46	39.03	28.59	9.66
30	9.29	42.16	41.37	30.94	10.83
45	10.07	54.67	41.37	35.37	13.22
60	9.29	53.89	42.16	35.11	13.35

19-Mar-90

UNDERCUTTING TESTS - MRI PROJECT NO. 8977-S

SOURCE OF SAMPLE: NEW YORK
PAVEMENT TYPE: OPEN-GRADED ASPHALT CORE SAMPLE
PAVEMENT SURFACE CONDITION: AS RECEIVED, CLEANED
SAMPLE NO.: 1 CODE: NY301B211
DEICER: NaCl
DEICER WT: 0.0796 g
TEMPERATURE: 15 deg F

ADJUSTED UNDERCUT AREA cm2/g

TIME MIN	Rep 1	Rep 2	Rep 3	Avg	Std Error
0	0.00	0.00	0.00	0.00	0.00
5	3.61	2.35	3.61	3.19	0.42
10	6.12	4.87	4.87	5.29	0.42
15	4.87	4.87	6.12	5.29	0.42
20	6.12	4.87	7.38	6.12	0.73
25	6.12	6.12	7.38	6.54	0.42
30	7.38	6.12	6.12	6.54	0.42
45	7.38	6.12	7.38	6.96	0.42
60	6.12	8.64	6.12	6.96	0.84

SOURCE OF SAMPLE: NEW YORK
PAVEMENT TYPE: OPEN-GRADED ASPHALT CORE SAMPLE
PAVEMENT SURFACE CONDITION: AS RECEIVED, CLEANED
SAMPLE NO.: 1 CODE: NY301B212
DEICER: ETHYLENE GLYCOL
DEICER WT: 0.281 g
TEMPERATURE: 15 deg F

ADJUSTED UNDERCUT AREA cm2/g

TIME MIN	Rep 1	Rep 2	Rep 3	Avg	Std Error
0	0.00	0.00	0.00	0.00	0.00
5	1.38	1.73	1.73	1.62	0.12
10	2.80	2.45	2.80	2.68	0.12
15	3.87	3.51	5.29	4.23	0.54
20	6.01	5.65	7.07	6.24	0.43
25	6.01	7.07	8.50	7.19	0.72
30	8.14	8.50	9.56	8.73	0.43
45	11.34	10.63	12.77	11.58	0.63
60	14.19	12.05	13.83	13.36	0.66

19-Mar-90

UNDERCUTTING TESTS - MRI PROJECT NO. 8977-S

SOURCE OF SAMPLE: NEW YORK
PAVEMENT TYPE: OPEN-GRADED ASPHALT CORE SAMPLE
PAVEMENT SURFACE CONDITION: AS RECEIVED, CLEANED
SAMPLE NO.: 1 CODE: NY301B213
DEICER: CaCl2
DEICER WT: 0.1278 g
TEMPERATURE: 15 deg F

ADJUSTED UNDERCUT AREA cm2/g

TIME MIN	Rep 1	Rep 2	Rep 3	Avg	Std Error
0	0.00	0.00	0.00	0.00	0.00
5	2.25	3.03	0.68	1.99	0.69
10	4.60	5.38	3.81	4.60	0.45
15	5.38	6.94	10.07	7.47	1.38
20	7.73	6.94	13.20	9.29	1.97
25	7.73	7.73	11.64	9.03	1.30
30	10.07	10.07	15.55	11.90	1.83
45	8.51	8.51	17.12	11.38	2.87
60	12.42	11.64	17.12	13.73	1.71

SOURCE OF SAMPLE: NEW YORK
PAVEMENT TYPE: OPEN-GRADED ASPHALT CORE SAMPLE
PAVEMENT SURFACE CONDITION: AS RECEIVED, CLEANED
SAMPLE NO.: 2 CODE: NY302B311
DEICER: NaCl
DEICER WT: 0.0796 g
TEMPERATURE: 5 deg F

ADJUSTED UNDERCUT AREA cm2/g

TIME MIN	Rep 1	Rep 2	Rep 3	Avg	Std Error
0	0.00	0.00	0.00	0.00	0.00
5	7.38	8.64	6.12	7.38	0.73
10	4.87	9.89	7.38	7.38	1.45
15	8.64	6.12	4.87	6.54	1.11
20	6.12	4.87	7.38	6.12	0.73
25	6.12	7.38	6.12	6.54	0.42
30	4.87	7.38	7.38	6.54	0.84
45	8.64	4.87	6.12	6.54	1.11
60	6.12	4.87	4.87	5.29	0.42

19-Mar-90

UNDERCUTTING TESTS - MRI PROJECT NO. 8977-S

SOURCE OF SAMPLE: NEW YORK
PAVEMENT TYPE: OPEN-GRADED ASPHALT CORE SAMPLE
PAVEMENT SURFACE CONDITION: SMOOTH AND CLEANED
SAMPLE NO.: 2 CODE: NY302C311
DEICER: NaCl
DEICER WT: 0.0796 g
TEMPERATURE: 5 deg F

ADJUSTED UNDERCUT AREA cm2/g

TIME MIN	Rep 1	Rep 2	Rep 3	Avg	Std Error
0	0.00	0.00	0.00	0.00	0.00
5	3.03	3.03	5.38	3.81	0.78
10	3.81	3.81	3.81	3.81	ERR
15	3.03	3.81	3.81	3.55	0.26
20	4.60	3.81	3.81	4.07	0.26
25	4.60	4.60	5.38	4.86	0.26
30	5.38	3.81	3.03	4.07	0.69
45	5.38	4.60	5.38	5.12	0.26
60	6.16	3.03	4.60	4.60	0.90

SOURCE OF SAMPLE: NEW YORK
PAVEMENT TYPE: OPEN-GRADED ASPHALT CORE SAMPLE
PAVEMENT SURFACE CONDITION: AS RECEIVED, CLEANED
SAMPLE NO.: 2 CODE: NY302B312
DEICER: ETHYLENE GLYCOL
DEICER WT: 0.281 g
TEMPERATURE: 5 deg F

ADJUSTED UNDERCUT AREA cm2/g

TIME MIN	Rep 1	Rep 2	Rep 3	Avg	Std Error
0	0.00	0.00	0.00	0.00	0.00
5	2.80	4.23	2.80	3.28	1.04
10	2.45	3.87	3.16	3.16	0.90
15	3.16	2.45	3.16	2.92	0.52
20	3.87	4.23	2.45	3.51	1.20
25	3.87	3.87	2.80	3.51	0.78
30	4.23	4.94	3.51	4.23	0.90
45	4.94	5.65	4.94	5.17	0.52
60	4.94	7.07	5.29	5.77	1.45

19-Mar-90

UNDERCUTTING TESTS - MRI PROJECT NO. 8977-S

SOURCE OF SAMPLE: NEW YORK
PAVEMENT TYPE: OPEN-GRADED ASPHALT CORE SAMPLE
PAVEMENT SURFACE CONDITION: SMOOTH AND CLEANED
SAMPLE NO.: 2 CODE: NY302C312
DEICER: ETHYLENE GLYCOL
DEICER WT: 0.281 g
TEMPERATURE: 5 deg F

ADJUSTED UNDERCUT AREA cm2/g

TIME MIN	Rep 1	Rep 2	Rep 3	Avg	Std Error
0	0.00	0.00	0.00	0.00	0.00
5	1.73	2.09	3.16	2.33	0.43
10	2.09	3.16	3.16	2.80	0.36
15	3.16	3.51	3.87	3.51	0.21
20	4.23	4.94	3.87	4.34	0.31
25	5.65	4.94	4.94	5.17	0.24
30	5.29	5.29	4.94	5.17	0.12
45	7.78	7.07	7.78	7.55	0.24
60	6.72	8.14	9.92	8.26	0.93

SOURCE OF SAMPLE: NEW YORK
PAVEMENT TYPE: OPEN-GRADED ASPHALT CORE SAMPLE
PAVEMENT SURFACE CONDITION: AS RECEIVED, CLEANED
SAMPLE NO.: 2 CODE: NY302B313
DEICER: CaCl2
DEICER WT: 0.1278 g
TEMPERATURE: 5 deg F

ADJUSTED UNDERCUT AREA cm2/g

TIME MIN	Rep 1	Rep 2	Rep 3	Avg	Std Error
0	0.00	0.00	0.00	0.00	0.00
5	2.25	3.81	3.03	3.03	0.45
10	3.03	2.25	4.60	3.29	0.69
15	2.25	5.38	3.81	3.81	0.90
20	3.03	5.38	6.16	4.86	0.94
25	3.81	6.94	6.16	5.64	0.94
30	4.60	5.38	6.94	5.64	0.69
45	2.25	7.73	6.94	5.64	1.71
60	4.60	6.94	7.73	6.42	0.94

19-Mar-90

UNDERCUTTING TESTS - MRI PROJECT NO. 8977-S

SOURCE OF SAMPLE: NEW YORK
PAVEMENT TYPE: OPEN-GRADED ASPHALT CORE SAMPLE
PAVEMENT SURFACE CONDITION: SMOOTH AND CLEANED
SAMPLE NO.: 2 CODE: NY302C313
DEICER: CaCl2
DEICER WT: 0.1278 g
TEMPERATURE: 5 deg F

ADJUSTED UNDERCUT AREA cm2/g

TIME MIN	Rep 1	Rep 2	Rep 3	Avg	Std Error
0	0.00	0.00	0.00	0.00	0.00
5	2.25	3.03	4.60	3.29	0.69
10	4.60	3.03	6.94	4.86	1.14
15	6.16	6.16	9.29	7.20	1.04
20	8.51	6.16	7.73	7.47	0.69
25	10.07	6.94	6.94	7.99	1.04
30	6.94	6.16	6.94	6.68	0.26
45	7.73	7.73	10.86	8.77	1.04
60	6.94	3.81	9.29	6.68	1.59

19-Mar-90

UNDERCUTTING TESTS - MRI PROJECT 8977-S

SOURCE OF SAMPLE: CALIFORNIA
PAVEMENT TYPE: RUBBER-MODIFIED ASPHALT CORE SAMPLE
PAVEMENT SURFACE CONDITION: AS RECIEVED, CLEANED
SAMPLE NO.: 8 CODE: CA408B111
DEICER: NaCl
DEICER WT: 0.0796 g
TEMPERATURE: 25 deg F

ADJUSTED UNDERCUT AREA, cm2/g

TIME MIN	Repl	Rep 2	Rep 3	Avg	Std Error
0	0.00	0.00	0.00	0.00	0.00
5	11.15	9.89	8.64	9.89	0.73
10	14.92	16.17	16.17	15.76	0.42
15	19.94	19.94	19.94	19.94	0.00
20	21.20	23.71	23.71	22.87	0.84
25	22.46	27.48	31.25	27.06	2.55
30	22.46	28.74	32.51	27.90	2.93
45	26.22	32.51	35.02	31.25	2.62
60	23.71	38.79	37.53	33.34	4.83

SOURCE OF SAMPLE: CALIFORNIA
PAVEMENT TYPE: RUBBER-MODIFIED ASPHALT CORE SAMPLE
PAVEMENT SURFACE CONDITION: SMOOTH AND CLEANED
SAMPLE NO.: 8 CODE: CA408C111
DEICER: NaCl
DEICER WT: 0.0796 g
TEMPERATURE: 25 deg F

ADJUSTED UNDERCUT AREA, cm2/g

TIME MIN	Repl	Rep 2	Rep 3	Avg	Std Error
0	0.00	0.00	0.00	0.00	0.00
5	7.38	9.89	9.89	9.05	0.84
10	16.17	9.89	11.15	12.41	1.92
15	14.92	16.17	16.17	15.76	0.42
20	22.46	19.94	16.17	19.52	1.83
25	26.22	18.69	18.69	21.20	2.51
30	28.74	18.69	17.43	21.62	3.58
45	38.79	26.22	40.04	35.02	4.41
60	37.53	27.48	45.07	36.69	5.09

19-Mar-90

UNDERCUTTING TESTS - MRI PROJECT 8977-S

SOURCE OF SAMPLE: CALIFORNIA
PAVEMENT TYPE: RUBBER-MODIFIED ASPHALT CORE SAMPLE
PAVEMENT SURFACE CONDITION: AS RECIEVED, CLEANED
SAMPLE NO.: 9 CODE: CA409B112
DEICER: ETHYLENE GLYCOL
DEICER WT: 0.281 g
TEMPERATURE: 25 deg F

ADJUSTED UNDERCUT AREA, cm2/g

TIME MIN	Rep1	Rep 2	Rep 3	Avg	Std Error
0	0.00	0.00	0.00	0.00	0.00
5	2.80	3.51	3.87	3.40	0.31
10	4.58	6.01	5.29	5.29	0.41
15	6.36	8.85	7.43	7.55	0.72
20	6.72	13.48	10.99	10.39	1.97
25	11.70	16.33	13.83	13.95	1.34
30	13.12	19.53	16.33	16.33	1.85
45	15.97	23.44	21.31	20.24	2.22
60	17.75	26.29	22.38	22.14	2.47

SOURCE OF SAMPLE: CALIFORNIA
PAVEMENT TYPE: RUBBER-MODIFIED ASPHALT CORE SAMPLE
PAVEMENT SURFACE CONDITION: SMOOTH AND CLEANED
SAMPLE NO.: 9 CODE: CA409C112
DEICER: ETHYLENE GLYCOL
DEICER WT: 0.281 g
TEMPERATURE: 25 deg F

ADJUSTED UNDERCUT AREA, cm2/g

TIME MIN	Rep1	Rep 2	Rep 3	Avg	Std Error
0	0.00	0.00	0.00	0.00	0.00
5	2.80	2.09	4.23	3.04	0.63
10	3.87	3.51	7.78	5.06	1.37
15	2.80	14.55	12.41	9.92	3.61
20	8.85	18.10	18.46	15.14	3.15
25	9.21	20.24	22.38	17.27	4.08
30	9.21	23.44	24.15	18.94	4.87
45	9.21	25.58	32.34	22.38	6.87
60	9.56	27.36	36.25	24.39	7.85

19-Mar-90

UNDERCUTTING TESTS - MRI PROJECT 8977-S

SOURCE OF SAMPLE: CALIFORNIA
PAVEMENT TYPE: RUBBER-MODIFIED ASPHALT CORE SAMPLE
PAVEMENT SURFACE CONDITION: AS RECIEVED, CLEANED
SAMPLE NO.: 10 CODE: CA410B113
DEICER: CaCl2
DEICER WT: 0.1278 g
TEMPERATURE: 25 deg F

ADJUSTED UNDERCUT AREA, cm2/g

TIME MIN	Repl	Rep 2	Rep 3	Avg	Std Error
0	0.00	0.00	0.00	0.00	0.00
5	8.51	6.94	7.73	7.73	0.45
10	19.46	21.03	14.77	18.42	1.88
15	28.07	29.64	20.25	25.98	2.90
20	30.42	37.46	24.16	30.68	3.84
25	35.90	41.37	28.85	35.37	3.62
30	39.81	43.72	31.20	38.24	3.70
45	46.07	50.76	35.11	43.98	4.64
60	49.20	53.11	38.24	46.85	4.45

SOURCE OF SAMPLE: CALIFORNIA
PAVEMENT TYPE: RUBBER-MODIFIED ASPHALT CORE SAMPLE
PAVEMENT SURFACE CONDITION: SMOOTH AND CLEANED
SAMPLE NO.: 10 CODE: CA410C113
DEICER: CaCl2
DEICER WT: 0.1278 g
TEMPERATURE: 25 deg F

ADJUSTED UNDERCUT AREA, cm2/g

TIME MIN	Repl	Rep 2	Rep 3	Avg	Std Error
0	0.00	0.00	0.00	0.00	0.00
5	6.16	7.73	12.42	8.77	1.88
10	29.64	25.72	29.64	28.33	1.30
15	38.24	35.11	36.68	36.68	0.90
20	42.16	37.46	39.81	39.81	1.36
25	50.76	39.03	41.37	43.72	3.59
30	50.76	49.98	46.85	49.20	1.20
45	55.46	67.19	49.20	57.28	5.27
60	56.24	62.50	75.80	64.85	5.77

19-Mar-90

UNDERCUTTING TESTS - MRI PROJECT 8977-S

SOURCE OF SAMPLE: MONTANA
PAVEMENT TYPE: RUBBER-MODIFIED ASPHALT CORE SAMPLE
PAVEMENT SURFACE CONDITION: AS RECIEVED, CLEANED
SAMPLE NO.: 2 CODE: MT402B211
DEICER: NaCl
DEICER WT: 0.0796 g
TEMPERATURE: 15 deg F

ADJUSTED UNDERCUT AREA, cm2/g

TIME MIN	Repl	Rep 2	Rep 3	Avg	Std Error
0	0.00	0.00	0.00	0.00	0.00
5	7.38	7.38	3.61	6.12	1.26
10	8.64	8.64	9.89	9.05	0.42
15	8.64	11.15	8.64	9.47	0.84
20	7.38	8.64	6.12	7.38	0.73
25	8.64	9.89	9.89	9.47	0.42
30	7.38	9.89	6.12	7.80	1.11
45	8.64	9.89	11.15	9.89	0.73
60	9.89	11.15	11.15	10.73	0.42

SOURCE OF SAMPLE: MONTANA
PAVEMENT TYPE: RUBBER-MODIFIED ASPHALT CORE SAMPLE
PAVEMENT SURFACE CONDITION: AS RECEIVED, CLEANED
SAMPLE NO.: 3 CODE: MT403B212
DEICER: ETHYLENE GLYCOL
DEICER WT: 0.281
TEMPERATURE: 15 deg F

ADJUSTED UNDERCUT AREA, cm2/g

TIME MIN	Repl	Rep 2	Rep 3	Avg	Std Error
0	0.00	0.00	0.00	0.00	0.00
5	3.87	3.16	3.16	3.40	0.24
10	4.58	3.51	5.29	4.46	0.52
15	6.36	6.01	6.36	6.24	0.12
20	8.14	7.43	9.56	8.38	0.63
25	8.85	9.21	9.21	9.09	0.12
30	9.56	10.28	9.92	9.92	0.21
45	12.77	12.05	11.70	12.17	0.31
60	13.48	13.12	11.70	12.77	0.54

19-Mar-90

UNDERCUTTING TESTS - MRI PROJECT 8977-S

SOURCE OF SAMPLE: MONTANA
PAVEMENT TYPE: RUBBER-MODIFIED ASPHALT CORE SAMPLE
PAVEMENT SURFACE CONDITION: AS RECIEVED, CLEANED
SAMPLE NO.: 4 CODE: MT404B213
DEICER: CaCl2
DEICER WT: 0.1278 g
TEMPERATURE: 15 deg F

ADJUSTED UNDERCUT AREA, cm2/g

TIME MIN	Repl	Rep 2	Rep 3	Avg	Std Error
0	0.00	0.00	0.00	0.00	0.00
5	5.38	6.16	7.73	6.42	0.69
10	9.29	10.07	12.42	10.60	0.94
15	13.20	15.55	17.12	15.29	1.14
20	13.20	16.33	19.46	16.33	1.81
25	17.90	21.81	21.81	20.51	1.30
30	17.90	20.25	24.16	20.77	1.83
45	17.90	21.81	24.16	21.29	1.83
60	21.81	23.38	25.72	23.64	1.14

SOURCE OF SAMPLE: CALIFORNIA
PAVEMENT TYPE: RUBBER-MODIFIED ASPHALT CORE SAMPLE
PAVEMENT SURFACE CONDITION: AS RECIEVED, CLEANED
SAMPLE NO.: 5 CODE: CA405B311
DEICER: NaCl
TEMPERATURE: 5 deg F
DEICER WT: 0.0796 g

ADJUSTED UNDERCUT AREA, cm2/g

TIME MIN	Repl	Rep 2	Rep 3	Avg	Std Error
0	0.00	0.00	0.00	0.00	0.00
5	4.87	6.12	4.87	5.29	0.42
10	6.12	3.61	3.61	4.45	0.84
15	7.38	6.12	7.38	6.96	0.42
20	7.38	4.87	6.12	6.12	0.73
25	8.64	4.87	7.38	6.96	1.11
30	7.38	4.87	6.12	6.12	0.73
45	7.38	6.12	7.38	6.96	0.42
60	3.61	6.12	6.12	5.29	0.84

19-Mar-90

UNDERCUTTING TESTS - MRI PROJECT 8977-S

SOURCE OF SAMPLE: CALIFORNIA
PAVEMENT TYPE: RUBBER-MODIFIED ASPHALT CORE SAMPLE
PAVEMENT SURFACE CONDITION: SMOOTH AND CLEANED
SAMPLE NO.: 5 CODE: CA405C311
DEICER: NaCL
DEICER WT: 0.0796 g
TEMPERATURE: 5 deg F

ADJUSTED UNDERCUT AREA, cm2/g

TIME MIN	Rep1	Rep 2	Rep 3	Avg	Std Error
0	0.00	0.00	0.00	0.00	0.00
5	6.12	11.15	8.64	8.64	1.45
10	4.87	9.89	8.64	7.80	1.51
15	4.87	12.41	9.89	9.05	2.22
20	7.38	11.15	11.15	9.89	1.26
25	8.64	14.92	11.15	11.57	1.83
30	8.64	13.66	14.92	12.41	1.92
45	6.12	8.64	9.89	8.22	1.11
60	7.38	12.41	8.64	9.47	1.51

SOURCE OF SAMPLE: CALIFORNIA
PAVEMENT TYPE: RUBBER-MODIFIED ASPHALT CORE SAMPLE
PAVEMENT SURFACE CONDITION: AS RECIEVED, CLEANED
SAMPLE NO.: 6 CODE: CA406B312
DEICER: ETHYLENE GLYCOL
DEICER WT: 0.281 g
TEMPERATURE: 5 deg F

ADJUSTED UNDERCUT AREA, cm2/g

TIME MIN	Rep1	Rep 2	Rep 3	Avg	Std Error
0	0.00	0.00	0.00	0.00	0.00
5	2.09	2.80	1.73	2.21	0.31
10	3.87	2.80	3.16	3.28	0.31
15	3.87	3.87	3.87	3.87	ERR
20	2.80	4.23	3.16	3.40	0.43
25	3.51	5.29	4.23	4.34	0.52
30	3.87	5.29	5.29	4.82	0.47
45	3.51	7.07	8.14	6.24	1.40
60	4.58	9.56	10.99	8.38	1.94

19-Mar-90

UNDERCUTTING TESTS - MRI PROJECT 8977-S

SOURCE OF SAMPLE: CALIFORNIA
PAVEMENT TYPE: RUBBER-MODIFIED ASPHALT CORE SAMPLE
PAVEMENT SURFACE CONDITION: SMOOTH AND CLEANED
SAMPLE NO.: 6 CODE: CA406C312
DEICER WT: 0.281 g
DEICER: ETHYLENE GLYCOL
TEMPERATURE: 5 deg F

ADJUSTED UNDERCUT AREA, cm2/g

TIME MIN	Repl	Rep 2	Rep 3	Avg	Std Error
5	3.16	4.23	2.80	3.40	0.43
10	2.80	4.23	3.16	3.40	0.43
15	3.51	4.23	3.16	3.63	0.31
20	3.87	3.16	4.23	3.75	0.31
25	4.58	4.94	6.01	5.17	0.43
30	6.01	4.94	7.07	6.01	0.62
45	6.36	6.01	9.92	7.43	1.25
60	7.78	4.94	12.05	8.26	2.07

SOURCE OF SAMPLE: CALIFORNIA
PAVEMENT TYPE: RUBBER-MODIFIED ASPHALT CORE SAMPLE
PAVEMENT SURFACE CONDITION: AS RECIEVED, CLEANED
SAMPLE NO.: 7 CODE: CA407B313
DEICER: CaCL2
DEICER WT: 0.1278 g
TEMPERATURE: 5 deg F

ADJUSTED UNDERCUT AREA, cm2/g

TIME MIN	Repl	Rep 2	Rep 3	Avg	Std Error
0	0.00	0.00	0.00	0.00	0.00
5	5.38	6.16	4.60	5.38	0.45
10	6.94	6.16	7.73	6.94	0.45
15	6.94	7.73	9.29	7.99	0.69
20	7.73	8.51	9.29	8.51	0.45
25	9.29	7.73	10.86	9.29	0.90
30	11.64	10.07	13.99	11.90	1.14
45	13.20	8.51	13.99	11.90	1.71
60	14.77	8.51	14.77	12.68	2.09

19-Mar-90

UNDERCUTTING TESTS - MRI PROJECT 8977-S

SOURCE OF SAMPLE: CALIFORNIA
PAVEMENT TYPE: RUBBER-MODIFIED ASPHALT CORE SAMPLE
PAVEMENT SURFACE CONDITION: SMOOTH AND CLEANED
SAMPLE NO.: 7 CODE: CA407C313
DEICER: CaCl2
DEICER WT: 0.1278 g
TEMPERATURE: 5 deg F

ADJUSTED UNDERCUT AREA, cm2/g

TIME MIN	Repl	Rep 2	Rep 3	Avg	Std Error
0	0	0	0	0	0
5	3.81	4.60	3.03	3.81	0.45
10	6.94	6.16	6.16	6.42	0.26
15	10.86	11.64	6.94	9.81	1.45
20	14.77	13.20	12.42	13.46	0.69
25	17.90	13.99	13.20	15.03	1.45
30	17.90	17.12	17.12	17.38	0.26
45	17.12	18.68	13.20	16.33	1.63
60	20.25	20.25	16.33	18.94	1.30

19-Mar-90

UNDERCUTTING TESTS - MRI PROJECT NO. 8977-S

SOURCE OF SAMPLE: SOUTH DAKOTA
PAVEMENT TYPE: PORTLAND CEMENT CONCRETE LAB SAMPLE
PAVEMENT SURFACE CONDITION: AS RECEIVED, CLEANED
SAMPLE NO.: 3 CODE: SD603B111
DEICER: NaCl
DEICER WT: 0.0796 g
TEMPERATURE: 25 deg F

ADJUSTED UNDERCUT AREA cm2/g

TIME MIN	Rep 1	Rep 2	Rep 3	Avg	Std Error
0	0.00	0.00	0.00	0.00	0.00
5	7.38	7.38	7.38	7.38	ERR
10	29.99	23.71	21.20	24.97	2.62
15	36.27	33.76	26.22	32.09	3.02
20	41.30	37.53	31.25	36.69	2.93
25	43.81	41.30	35.02	40.04	2.62
30	45.07	40.04	32.51	39.21	3.65
45	65.17	42.56	37.53	48.42	8.50
60	52.61	46.32	40.04	46.32	3.63

SOURCE OF SAMPLE: SOUTH DAKOTA
PAVEMENT TYPE: PORTLAND CEMENT CONCRETE LAB SAMPLE
PAVEMENT SURFACE CONDITION: SMOOTH AND CLEANED
SAMPLE NO.: 3 CODE: SD603C111
DEICER: NaCl
DEICER WT: 0.0796 g
TEMPERATURE: 25 deg F

ADJUSTED UNDERCUT AREA cm2/g

TIME MIN	Rep 1	Rep 2	Rep 3	Avg	Std Error
0	0.00	0.00	0.00	0.00	0.00
5	23.71	17.43	22.46	21.20	1.92
10	42.56	41.30	43.81	42.56	0.73
15	51.35	45.07	53.86	50.09	2.62
20	60.14	50.09	60.14	56.79	3.35
25	63.91	56.37	60.14	60.14	2.18
30	63.91	57.63	65.17	62.24	2.33
45	72.71	62.66	65.17	66.84	3.02
60	72.71	65.17	66.43	68.10	2.33

19-Mar-90

UNDERCUTTING TESTS - MRI PROJECT NO. 8977-S

SOURCE OF SAMPLE: SOUTH DAKOTA
PAVEMENT TYPE: PORTLAND CEMENT CONCRETE LAB SAMPLE
PAVEMENT SURFACE CONDITION: AS RECEIVED, CLEANED
SAMPLE NO.: 3 CODE: SD603B112
DEICER: ETHYLENE GLYCOL
DEICER WT: 0.281 g
TEMPERATURE: 25 deg F

ADJUSTED UNDERCUT AREA cm2/g

TIME MIN	Rep 1	Rep 2	Rep 3	Avg	Std Error
0	0.00	0.00	0.00	0.00	0.00
5	1.38	2.80	3.16	2.45	0.54
10	4.58	7.43	6.72	6.24	0.86
15	8.14	10.99	10.28	9.80	0.86
20	12.41	13.48	14.19	13.36	0.52
25	15.26	18.10	18.10	17.16	0.95
30	18.82	19.53	20.24	19.53	0.41
45	24.15	25.22	25.93	25.10	0.52
60	26.65	29.49	31.63	29.26	1.44

SOURCE OF SAMPLE: SOUTH DAKOTA
PAVEMENT TYPE: PORTLAND CEMENT CONCRETE LAB SAMPLE
PAVEMENT SURFACE CONDITION: SMOOTH AND CLEANED
SAMPLE NO.: 3 CODE: SD603C112
DEICER: ETHYLENE GLYCOL
DEICER WT: 0.281 g
TEMPERATURE: 25 deg F

ADJUSTED UNDERCUT AREA cm2/g

TIME MIN	Rep 1	Rep 2	Rep 3	Avg	Std Error
0	0.00	0.00	0.00	0.00	0.00
5	3.51	3.16	3.87	3.51	0.21
10	10.99	7.43	9.92	9.45	1.05
15	18.46	14.19	15.26	15.97	1.28
20	22.38	19.88	21.66	21.31	0.74
25	25.22	22.73	25.22	24.39	0.83
30	29.49	24.87	30.20	28.19	1.67
45	34.83	33.05	38.39	35.42	1.57
60	38.75	35.54	40.88	38.39	1.55

19-Mar-90

UNDERCUTTING TESTS - MRI PROJECT NO. 8977-S

SOURCE OF SAMPLE: SOUTH DAKOTA
PAVEMENT TYPE: PORTLAND CEMENT CONCRETE LAB SAMPLE
PAVEMENT SURFACE CONDITION: AS RECEIVED, CLEANED
SAMPLE NO.: 3 CODE: SD603B113
DEICER: CaCl2
DEICER WT: 0.1278 g
TEMPERATURE: 25 deg F

ADJUSTED UNDERCUT AREA cm2/g

TIME MIN	Rep 1	Rep 2	Rep 3	Avg	Std Error
0	0.00	0.00	0.00	0.00	0.00
5	6.16	6.94	5.38	6.16	0.45
10	17.12	18.68	17.12	17.64	0.52
15	21.81	30.42	30.42	27.55	2.87
20	30.42	31.98	36.68	33.03	1.88
25	33.55	36.68	39.81	36.68	1.81
30	37.46	38.24	39.81	38.50	0.69
45	39.03	42.94	45.29	42.42	1.83
60	35.90	41.37	46.85	41.37	3.16

SOURCE OF SAMPLE: SOUTH DAKOTA
PAVEMENT TYPE: PORTLAND CEMENT CONCRETE LAB SAMPLE
PAVEMENT SURFACE CONDITION: SMOOTH AND CLEANED
SAMPLE NO.: 3 CODE: SD603C113
DEICER: CaCl2
DEICER WT: 0.1278 g
TEMPERATURE: 25 deg F

ADJUSTED UNDERCUT AREA cm2/g

TIME MIN	Rep 1	Rep 2	Rep 3	Avg	Std Error
0	0.00	0.00	0.00	0.00	0.00
5	6.16	7.73	10.07	7.99	1.14
10	28.07	26.51	31.20	28.59	1.38
15	40.59	37.46	48.42	42.16	3.26
20	49.20	39.81	54.67	47.89	4.34
25	49.20	45.29	60.93	51.81	4.70
30	56.24	46.07	67.98	56.76	6.33
45	60.93	49.98	70.32	60.41	5.88
60	63.28	53.11	71.11	62.50	5.21

19-Mar-90

UNDERCUTTING TESTS - MRI PROJECT NO. 8977-S

SOURCE OF SAMPLE: SOUTH DAKOTA
PAVEMENT TYPE: PORTLAND CEMENT CONCRETE LAB SAMPLE
PAVEMENT SURFACE CONDITION: AS RECEIVED, CLEANED
SAMPLE NO.: 1 CODE: SD601B211
DEICER: NaCl
DEICER WT: 0.0796 g
TEMPERATURE: 15 deg F

ADJUSTED UNDERCUT AREA cm2/g

TIME MIN	Rep 1	Rep 2	Rep 3	Avg	Std Error
0	0.00	0.00	0.00	0.00	0.00
5	7.38	9.89	6.12	7.80	1.11
10	12.41	9.89	9.89	10.73	0.84
15	16.17	16.17	9.89	14.08	2.09
20	17.43	19.94	14.92	17.43	1.45
25	17.43	23.71	16.17	19.11	2.33
30	18.69	23.71	14.92	19.11	2.55
45	22.46	22.46	16.17	20.36	2.09
60	18.69	21.20	16.17	18.69	1.45

SOURCE OF SAMPLE: SOUTH DAKOTA
PAVEMENT TYPE: PORTLAND CEMENT CONCRETE LAB SAMPLE
PAVEMENT SURFACE CONDITION: AS RECEIVED, CLEANED
SAMPLE NO.: 1 CODE: SD601B212
DEICER: ETHYLENE GLYCOL
DEICER WT: 0.281 g
TEMPERATURE: 15 deg F

ADJUSTED UNDERCUT AREA cm2/g

TIME MIN	Rep 1	Rep 2	Rep 3	Avg	Std Error
0	0.00	0.00	0.00	0.00	0.00
5	2.80	3.51	2.80	3.04	0.24
10	5.65	5.29	4.58	5.17	0.31
15	8.50	7.43	7.43	7.78	0.36
20	10.28	9.92	9.92	10.04	0.12
25	13.12	12.05	11.70	12.29	0.43
30	15.26	13.12	15.26	14.55	0.71
45	18.46	17.39	17.04	17.63	0.43
60	20.24	18.82	20.24	19.77	0.47

19-Mar-90

UNDERCUTTING TESTS - MRI PROJECT NO. 8977-S

SOURCE OF SAMPLE: SOUTH DAKOTA
PAVEMENT TYPE: PORTLAND CEMENT CONCRETE LAB SAMPLE
PAVEMENT SURFACE CONDITION: AS RECEIVED, CLEANED
SAMPLE NO.: 1 CODE: SD601B213
DEICER: CaCl2
DEICER WT: 0.1278 g
TEMPERATURE: 15 deg F

ADJUSTED UNDERCUT AREA cm2/g

TIME MIN	Rep 1	Rep 2	Rep 3	Avg	Std Error
0	0.00	0.00	0.00	0.00	0.00
5	12.42	6.94	6.16	8.51	1.97
10	20.25	18.68	16.33	18.42	1.14
15	24.16	23.38	20.25	22.59	1.20
20	26.51	24.16	24.16	24.94	0.78
25	30.42	26.51	25.72	27.55	1.45
30	29.64	27.29	23.38	26.77	1.83
45	30.42	28.07	24.16	27.55	1.83
60	32.77	29.64	27.29	29.90	1.59

SOURCE OF SAMPLE: SOUTH DAKOTA
PAVEMENT TYPE: PORTLAND CEMENT CONCRETE LAB SAMPLE
PAVEMENT SURFACE CONDITION: AS RECEIVED, CLEANED
SAMPLE NO.: 2 CODE: SD602B311
DEICER: NaCl
DEICER WT: 0.0796 g
TEMPERATURE: 5 deg F

ADJUSTED UNDERCUT AREA cm2/g

TIME MIN	Rep 1	Rep 2	Rep 3	Avg	Std Error
0	0.00	0.00	0.00	0.00	0.00
5	4.87	6.12	4.87	5.29	0.42
10	6.12	6.12	3.61	5.29	0.84
15	4.87	6.12	3.61	4.87	0.73
20	7.38	7.38	6.12	6.96	0.42
25	7.38	7.38	7.38	7.38	ERR
30	6.12	6.12	7.38	6.54	0.42
45	6.12	7.38	6.12	6.54	0.42
60	6.12	6.12	6.12	6.12	ERR

19-Mar-90

UNDERCUTTING TESTS - MRI PROJECT NO. 8977-S

SOURCE OF SAMPLE: SOUTH DAKOTA
PAVEMENT TYPE: PORTLAND CEMENT CONCRETE LAB SAMPLE
PAVEMENT SURFACE CONDITION: SMOOTH AND CLEANED
SAMPLE NO.: 2 CODE: SD602C311
DEICER: NaCl
DEICER WT: 0.0796 g
TEMPERATURE: 5 deg F

ADJUSTED UNDERCUT AREA cm2/g

TIME MIN	Rep 1	Rep 2	Rep 3	Avg	Std Error
0	0.00	0.00	0.00	0.00	0.00
5	6.12	4.87	4.87	5.29	0.42
10	6.12	7.38	6.12	6.54	0.42
15	7.38	6.12	4.87	6.12	0.73
20	6.12	4.87	6.12	5.70	0.42
25	6.12	6.12	6.12	6.12	ERR
30	8.64	8.64	6.12	7.80	0.84
45	9.89	7.38	6.12	7.80	1.11
60	8.64	7.38	9.89	8.64	0.73

SOURCE OF SAMPLE: SOUTH DAKOTA
PAVEMENT TYPE: PORTLAND CEMENT CONCRETE LAB SAMPLE
PAVEMENT SURFACE CONDITION: AS RECEIVED, CLEANED
SAMPLE NO.: 2 CODE: SD602B312
DEICER: ETHYLENE GLYCOL
DEICER WT: 0.281 g
TEMPERATURE: 5 deg F

ADJUSTED UNDERCUT AREA cm2/g

TIME MIN	Rep 1	Rep 2	Rep 3	Avg	Std Error
0	0.00	0.00	0.00	0.00	0.00
5	1.73	1.73	1.02	1.50	0.24
10	2.45	2.80	2.80	2.68	0.12
15	2.45	2.45	3.16	2.68	0.24
20	2.80	3.51	4.58	3.63	0.52
25	4.58	5.29	5.29	5.06	0.24
30	6.36	6.36	5.65	6.12	0.24
45	7.78	9.21	6.72	7.90	0.72
60	10.99	11.70	10.28	10.99	0.41

19-Mar-90

UNDERCUTTING TESTS - MRI PROJECT NO. 8977-S

SOURCE OF SAMPLE: SOUTH DAKOTA
PAVEMENT TYPE: PORTLAND CEMENT CONCRETE LAB SAMPLE
PAVEMENT SURFACE CONDITION: SMOOTH AND CLEANED
SAMPLE NO.: 2 CODE: SD602C312
DEICER: ETHYLENE GLYCOL
DEICER WT: 0.281 g
TEMPERATURE: 5 deg F

ADJUSTED UNDERCUT AREA cm2/g

TIME MIN	Rep 1	Rep 2	Rep 3	Avg	Std Error
0	0.00	0.00	0.00	0.00	0.00
5	2.09	2.09	2.80	2.33	0.24
10	3.16	2.09	2.09	2.45	0.36
15	4.23	3.51	2.80	3.51	0.41
20	3.87	3.16	3.16	3.40	0.24
25	3.87	3.87	3.51	3.75	0.12
30	3.87	3.51	3.87	3.75	0.12
45	4.58	4.58	2.80	3.99	0.59
60	3.16	4.23	3.51	3.63	0.31

SOURCE OF SAMPLE: SOUTH DAKOTA
PAVEMENT TYPE: PORTLAND CEMENT CONCRETE LAB SAMPLE
PAVEMENT SURFACE CONDITION: AS RECEIVED, CLEANED
SAMPLE NO.: 2 CODE: SD602B313
DEICER: CaCl2
DEICER WT: 0.1278 g
TEMPERATURE: 5 deg F

ADJUSTED UNDERCUT AREA cm2/g

TIME MIN	Rep 1	Rep 2	Rep 3	Avg	Std Error
0	0.00	0.00	0.00	0.00	0.00
5	3.81	3.81	2.25	3.29	0.52
10	3.81	4.60	3.81	4.07	0.26
15	5.38	9.29	9.29	7.99	1.30
20	6.16	10.86	13.20	10.07	2.07
25	9.29	13.99	14.77	12.68	1.71
30	7.73	13.20	13.99	11.64	1.97
45	7.73	14.77	17.12	13.20	2.82
60	9.29	16.33	13.99	13.20	2.07

19-Mar-90

UNDERCUTTING TESTS - MRI PROJECT NO. 8977-S

SOURCE OF SAMPLE: SOUTH DAKOTA
PAVEMENT TYPE: PORTLAND CEMENT CONCRETE LAB SAMPLE
PAVEMENT SURFACE CONDITION: SMOOTH AND CLEANED
SAMPLE NO.: 2 CODE: SD602C313
DEICER: CaCl2
DEICER WT: 0.1278 g
TEMPERATURE: 5 deg F

ADJUSTED UNDERCUT AREA cm2/g

TIME MIN	Rep 1	Rep 2	Rep 3	Avg	Std Error
0	0.00	0.00	0.00	0.00	0.00
5	2.25	4.60	3.81	3.55	0.69
10	6.16	6.16	4.60	5.64	0.52
15	11.64	15.55	12.42	13.20	1.20
20	11.64	16.33	14.77	14.25	1.38
25	14.77	21.03	17.12	17.64	1.83
30	14.77	21.03	15.55	17.12	1.97
45	14.77	19.46	17.90	17.38	1.38
60	17.90	22.59	17.90	19.46	1.56

19-Mar-90

UNDERCUTTING TESTS - MRI PROJECT 8977-S

SOURCE OF SAMPLE: MICHIGAN
PAVEMENT TYPE: DENSE-GRADED ASPHALT LAB SAMPLE
PAVEMENT SURFACE CONDITION: AS RECIEVED, CLEANED
SAMPLE NO.: 7 CODE: MI207B111
DEICER: NaCl
DEICER WT: 0.0796 g
TEMPERATURE: 25 deg F

ADJUSTED UNDERCUT AREA, cm2/g

TIME MIN	Repl	Rep 2	Rep 3	Avg	Std Error
0	0.00	0.00	0.00	0.00	0.00
5	28.74	13.66	17.43	19.94	4.53
10	46.32	23.71	32.51	34.18	6.58
15	60.14	29.99	40.04	43.39	8.86
20	72.71	37.53	45.07	51.77	10.69
25	71.45	40.04	50.09	53.86	9.26
30	87.78	40.04	52.61	60.14	14.29
45	85.27	45.07	56.37	62.24	11.97
60	90.29	45.07	57.63	64.33	13.48

SOURCE OF SAMPLE: MICHIGAN
PAVEMENT TYPE: DENSE-GRADED ASPHALT LAB SAMPLE
PAVEMENT SURFACE CONDITION: SMOOTH AND CLEANED
SAMPLE NO.: 7 CODE: MI207C111
DEICER: NaCl
DEICER WT: 0.0796 g
TEMPERATURE: 25 deg F

ADJUSTED UNDERCUT AREA, cm2/g

TIME MIN	Repl	Rep 2	Rep 3	Avg	Std Error
0	0.00	0.00	0.00	0.00	0.00
5	16.17	16.17	6.12	12.82	3.35
10	31.25	36.27	9.89	25.81	8.09
15	42.56	46.32	14.92	34.60	9.90
20	48.84	53.86	16.17	39.62	11.81
25	53.86	57.63	17.43	42.97	12.82
30	60.14	66.43	17.43	48.00	15.39
45	66.43	67.68	29.99	54.70	12.36
60	66.43	67.68	35.02	56.37	10.68

19-Mar-90

UNDERCUTTING TESTS - MRI PROJECT 8977-S

SOURCE OF SAMPLE: MICHIGAN
PAVEMENT TYPE: DENSE-GRADED ASPHALT LAB SAMPLE
PAVEMENT SURFACE CONDITION: AS RECIEVED, CLEANED
SAMPLE NO.: 8 CODE: MI208B112
DEICER: ETHYLENE GLYCOL
DEICER WT: 0.281 g
TEMPERATURE: 25 deg F

ADJUSTED UNDERCUT AREA, cm2/g

TIME MIN	Repl	Rep 2	Rep 3	Avg	Std Error
0	0.00	0.00	0.00	0.00	0.00
5	1.73	1.73	2.09	1.85	0.12
10	7.78	6.72	6.01	6.84	0.52
15	13.12	11.34	12.41	12.29	0.52
20	15.97	14.55	15.26	15.26	0.41
25	19.53	18.10	18.82	18.82	0.41
30	23.44	21.31	20.95	21.90	0.78
45	27.00	26.65	27.00	26.88	0.12
60	31.63	29.49	28.78	29.97	0.86

SOURCE OF SAMPLE: MICHIGAN
PAVEMENT TYPE: DENSE-GRADED ASPHALT LAB SAMPLE
PAVEMENT SURFACE CONDITION: SMOOTH AND CLEANED
SAMPLE NO.: 8 CODE: MI208C112
DEICER: ETHYLENE GLYCOL
DEICER WT: 0.281 g
TEMPERATURE: 25 deg F

ADJUSTED UNDERCUT AREA, cm2/g

TIME MIN	Repl	Rep 2	Rep 3	Avg	Std Error
0	0.00	0.00	0.00	0.00	0.00
5	3.87	4.94	2.80	3.87	0.62
10	5.65	4.94	4.94	5.17	0.24
15	8.85	7.07	8.85	8.26	0.59
20	9.92	8.14	9.92	9.33	0.59
25	9.92	8.14	9.92	9.33	0.59
30	10.28	8.50	9.92	9.56	0.54
45	12.41	9.92	11.70	11.34	0.74
60	12.77	9.92	14.55	12.41	1.35

19-Mar-90

UNDERCUTTING TESTS - MRI PROJECT 8977-S

SOURCE OF SAMPLE: MICHIGAN
PAVEMENT TYPE: DENSE-GRADED ASPHALT LAB SAMPLE
PAVEMENT SURFACE CONDITION: AS RECIEVED, CLEANED
SAMPLE NO.: 9 CODE: MI209B113
DEICER: CaCl2
DEICER WT: 0.1278 g
TEMPERATURE: 25 deg F

ADJUSTED UNDERCUT AREA, cm2/g

TIME MIN	Repl	Rep 2	Rep 3	Avg	Std Error
0	0.00	0.00	0.00	0.00	0.00
5	7.73	5.38	6.16	6.42	0.69
10	23.38	26.51	17.90	22.59	2.52
15	30.42	35.90	30.42	32.24	1.83
20	32.77	42.16	35.11	36.68	2.82
25	38.24	44.50	38.24	40.33	2.09
30	43.72	49.98	42.94	45.55	2.23
45	47.63	56.24	46.85	50.24	3.01
60	49.20	55.46	49.98	51.54	1.97

SOURCE OF SAMPLE: MICHIGAN
PAVEMENT TYPE: DENSE-GRADED ASPHALT LAB SAMPLE
PAVEMENT SURFACE CONDITION: SMOOTH AND CLEANED
SAMPLE NO.: 9 CODE: MI209C113
DEICER: CaCl2
DEICER WT: 0.1278 g
TEMPERATURE: 25 deg F

ADJUSTED UNDERCUT AREA, cm2/g

TIME MIN	Repl	Rep 2	Rep 3	Avg	Std Error
0	0.00	0.00	0.00	0.00	0.00
5	9.29	12.42	12.42	11.38	1.04
10	35.90	46.07	51.54	44.50	4.58
15	51.54	48.42	60.15	53.37	3.51
20	55.46	54.67	66.41	58.85	3.79
25	60.93	62.50	69.54	64.33	2.65
30	67.19	67.98	65.63	66.93	0.69
45	72.67	78.93	79.71	77.11	2.23
60	78.93	77.37	80.50	78.93	0.90

19-Mar-90

UNDERCUTTING TESTS - MRI PROJECT 8977-S

SOURCE OF SAMPLE: MICHIGAN
PAVEMENT TYPE: DENSE-GRADED ASPHALT LAB SAMPLE
PAVEMENT SURFACE CONDITION: AS RECIEVED, CLEANED
SAMPLE NO.: 1 CODE: MI201B211
DEICER: NaCl
DEICER WT: 0.0796 g
TEMPERATURE: 15 deg F

ADJUSTED UNDERCUT AREA, cm2/g

TIME MIN	Repl	Rep 2	Rep 3	Avg	Std Error
0	0.00	0.00	0.00	0.00	0.00
5	6.12	7.38	4.87	6.12	0.73
10	11.15	11.15	13.66	11.99	0.84
15	16.17	12.41	19.94	16.17	2.18
20	19.94	16.17	21.20	19.11	1.51
25	22.46	17.43	26.22	22.04	2.55
30	19.94	16.17	22.46	19.52	1.83
45	22.46	21.20	24.97	22.87	1.11
60	23.71	22.46	24.97	23.71	0.73

SOURCE OF SAMPLE: MICHIGAN
PAVEMENT TYPE: DENSE-GRADED ASPHALT LAB SAMPLE
PAVEMENT SURFACE CONDITION: AS RECIEVED, CLEANED
SAMPLE NO.: 2 CODE: MI202B212
DEICER: ETHYLENE GLYCOL
DEICER WT: 0.281 g
TEMPERATURE: 15 deg F

ADJUSTED UNDERCUT AREA, cm2/g

TIME MIN	Repl	Rep 2	Rep 3	Avg	Std Error
0	0.00	0.00	0.00	0.00	0.00
5	2.45	1.73	2.09	2.09	0.21
10	4.23	3.87	5.65	4.58	0.54
15	6.01	7.07	4.94	6.01	0.62
20	10.28	10.63	6.36	9.09	1.37
25	12.41	13.48	6.72	10.87	2.10
30	15.97	15.26	5.65	12.29	3.33
45	19.88	20.24	6.72	15.61	4.45
60	23.09	21.31	6.36	16.92	5.30

19-Mar-90

UNDERCUTTING TESTS - MRI PROJECT 8977-S

SOURCE OF SAMPLE: MICHIGAN
PAVEMENT TYPE: DENSE-GRADED ASPHALT LAB SAMPLE
PAVEMENT SURFACE CONDITION: AS RECIEVED, CLEANED
SAMPLE NO.: 3 CODE: MI203B213
DEICER: CaCl2
DEICER WT: 0.1278 g
TEMPERATURE: 15 deg F

ADJUSTED UNDERCUT AREA, cm2/g

TIME MIN	Repl	Rep 2	Rep 3	Avg	Std Error
0	0.00	0.00	0.00	0.00	0.00
5	6.94	6.16	5.38	6.16	0.45
10	17.90	14.77	17.12	16.59	0.94
15	24.16	21.03	26.51	23.90	1.59
20	27.29	21.81	25.72	24.94	1.63
25	30.42	23.38	29.64	27.81	2.23
30	31.20	24.94	32.77	29.64	2.39
45	33.55	26.51	35.90	31.98	2.82
60	31.98	26.51	34.33	30.94	2.32

SOURCE OF SAMPLE: MICHIGAN
PAVEMENT TYPE: DENSE-GRADED ASPHALT LAB SAMPLE
PAVEMENT SURFACE CONDITION: AS RECIEVED, CLEANED
SAMPLE NO.: 4 CODE: MI204B311
DEICER: NaCl
DEICER WT: 0.0796 g
TEMPERATURE: 5 deg F

ADJUSTED UNDERCUT AREA, cm2/g

TIME MIN	Repl	Rep 2	Rep 3	Avg	Std Error
0	0.00	0.00	0.00	0.00	0.00
5	4.87	6.12	8.64	6.54	1.11
10	4.87	4.87	7.38	5.70	0.84
15	9.89	6.12	7.38	7.80	1.11
20	8.64	7.38	8.64	8.22	0.42
25	8.64	7.38	8.64	8.22	0.42
30	7.38	6.12	11.15	8.22	1.51
45	8.64	7.38	8.64	8.22	0.42
60					

19-Mar-90

UNDERCUTTING TESTS - MRI PROJECT 8977-S

SOURCE OF SAMPLE: MICHIGAN
PAVEMENT TYPE: DENSE-GRADED ASPHALT LAB SAMPLE
PAVEMENT SURFACE CONDITION: SMOOTH AND CLEANED
SAMPLE NO.: 4 CODE: MI204C311
DEICER: NaCl
DEICER WT: 0.0796 g
TEMPERATURE: 5 deg F

ADJUSTED UNDERCUT AREA, cm2/g

TIME MIN	Repl	Rep 2	Rep 3	Avg	Std Error
0	0.00	0.00	0.00	0.00	0.00
5	3.61	4.87	6.12	4.87	0.73
10	2.35	4.87	4.87	4.03	0.84
15	3.61	3.61	4.87	4.03	0.42
20	3.61	6.12	7.38	5.70	1.11
25	3.61	3.61	8.64	5.29	1.68
30	2.35	3.61	4.87	3.61	0.73
45	4.87	4.87	4.87	4.87	ERR
60	8.64	4.87	4.87	6.12	1.26

SOURCE OF SAMPLE: MICHIGAN
PAVEMENT TYPE: DENSE-GRADED ASPHALT LAB SAMPLE
PAVEMENT SURFACE CONDITION: AS RECIEVED, CLEANED
SAMPLE NO.: 5 CODE: MI205B312
DEICER: ETHYLENE GLYCOL
DEICER WT: 0.281 g
TEMPERATURE: 5 deg F

ADJUSTED UNDERCUT AREA, cm2/g

TIME MIN	Repl	Rep 2	Rep 3	Avg	Std Error
0	0.00	0.00	0.00	0.00	0.00
5	2.45	2.45	2.09	2.33	0.12
10	2.80	3.51	2.45	2.92	0.31
15	4.23	4.58	2.80	3.87	0.54
20	5.29	6.36	4.58	5.41	0.52
25	6.72	7.43	5.65	6.60	0.52
30	9.21	10.99	7.43	9.21	1.03
45	11.70	11.70	8.50	10.63	1.07
60					

19-Mar-90

UNDERCUTTING TESTS - MRI PROJECT 8977-S

SOURCE OF SAMPLE: MICHIGAN
PAVEMENT TYPE: DENSE-GRADED ASPHALT LAB SAMPLE
PAVEMENT SURFACE CONDITION: SMOOTH AND CLEANED
SAMPLE NO.: 5 CODE: MI205C312
DEICER: ETHYLENE GLYCOL
DEICER WT: 0.281 g
TEMPERATURE: 5 deg F

ADJUSTED UNDERCUT AREA, cm2/g

TIME MIN	Rep1	Rep 2	Rep 3	Avg	Std Error
0	0.00	0.00	0.00	0.00	0.00
5	2.45	2.45	2.80	2.57	0.12
10	2.09	2.80	2.80	2.57	0.24
15	2.09	2.80	3.51	2.80	0.41
20	2.45	3.87	3.16	3.16	0.41
25	3.51	5.65	4.94	4.70	0.63
30	4.94	5.65	6.36	5.65	0.41
45	8.85	8.14	8.85	8.61	0.24
60	10.99	11.70	12.05	11.58	0.31

SOURCE OF SAMPLE: MICHIGAN
PAVEMENT TYPE: DENSE-GRADED ASPHALT LAB SAMPLE
PAVEMENT SURFACE CONDITION: AS RECIEVED, CLEANED
SAMPLE NO.: 6 CODE: MI206B313
DEICER: CaCl2
DEICER WT: 0.1278 g
TEMPERATURE: 5 deg F

ADJUSTED UNDERCUT AREA, cm2/g

TIME MIN	Rep1	Rep 2	Rep 3	Avg	Std Error
0	0.00	0.00	0.00	0.00	0.00
5	6.16	11.64	7.73	8.51	1.63
10	12.42	13.99	11.64	12.68	0.69
15	14.77	16.33	12.42	14.51	1.14
20	17.12	18.68	14.77	16.86	1.14
25	19.46	20.25	16.33	18.68	1.20
30	18.68	21.03	17.12	18.94	1.14
45	19.46	21.03	17.12	19.20	1.14
60					

19-Mar-90

UNDERCUTTING TESTS - MRI PROJECT 8977-S

SOURCE OF SAMPLE: MICHIGAN
PAVEMENT TYPE: DENSE-GRADED ASPHALT LAB SAMPLE
PAVEMENT SURFACE CONDITION: SMOOTH AND CLEANED
SAMPLE NO.: 6 CODE: MI206C313
DEICER: CaCl2
DEICER WT: 0.1278 g
TEMPERATURE: 5 deg F

ADJUSTED UNDERCUT AREA, cm2/g

TIME MIN	Rep1	Rep 2	Rep 3	Avg	Std Error
0	0.00	0.00	0.00	0.00	0.00
5	3.81	2.25	2.25	2.77	0.52
10	6.16	6.16	6.94	6.42	0.26
15	6.94	9.29	10.86	9.03	1.14
20	10.86	12.42	12.42	11.90	0.52
25	12.42	14.77	17.12	14.77	1.36
30	14.77	17.90	17.12	16.59	0.94
45	14.77	21.81	17.12	17.90	2.07
60	16.33	17.90	19.46	17.90	0.90

Appendix J

Figures Cited in Section 2 Concerning the Mathematical Modeling of Physical Processes for Disbonding

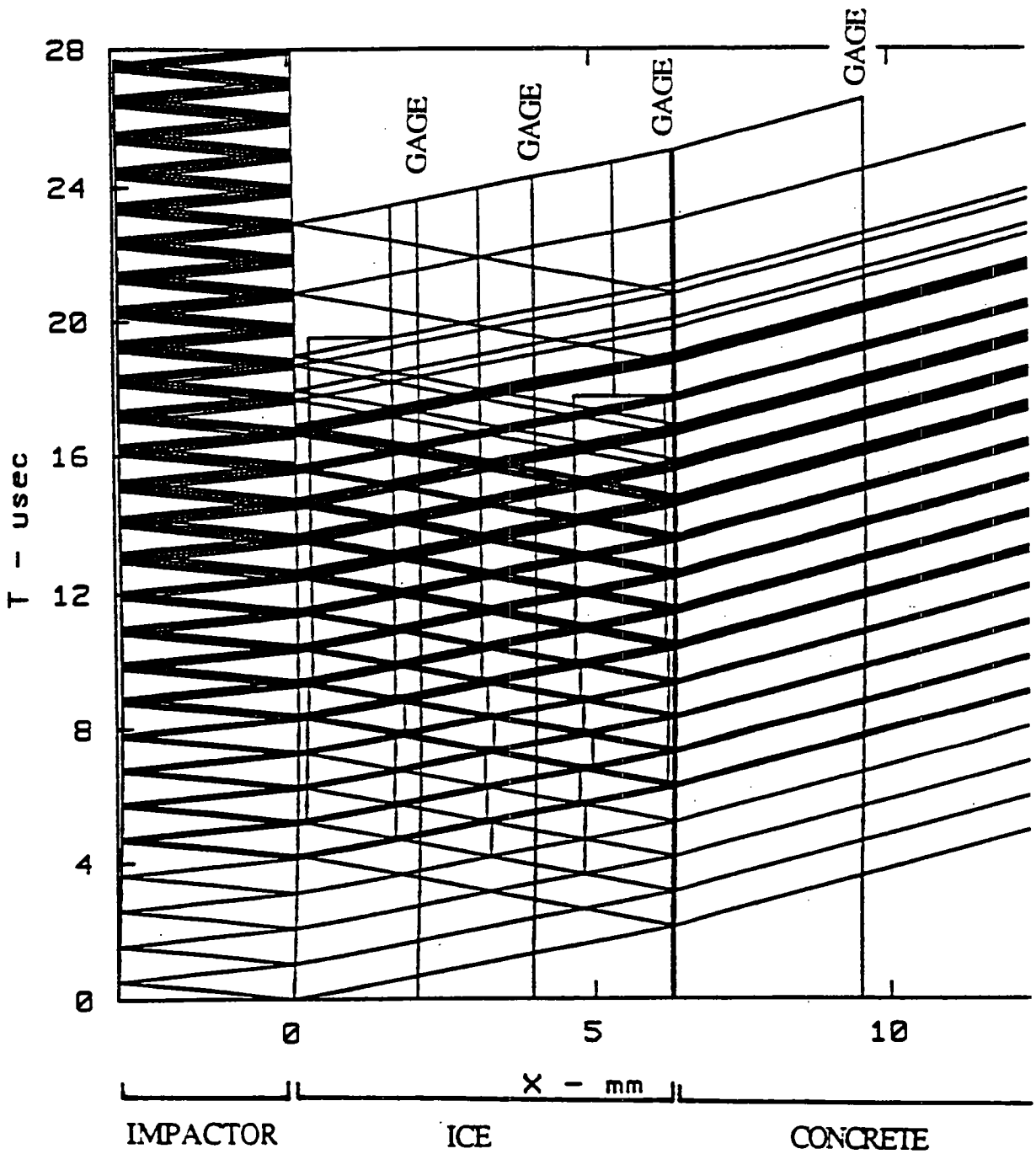

Figure J-1. **Stress waves induced by a steel impactor striking ice on semiinfinite concrete (simulation 1A1). The ice and the ice-concrete interface are not permitted to fail.**

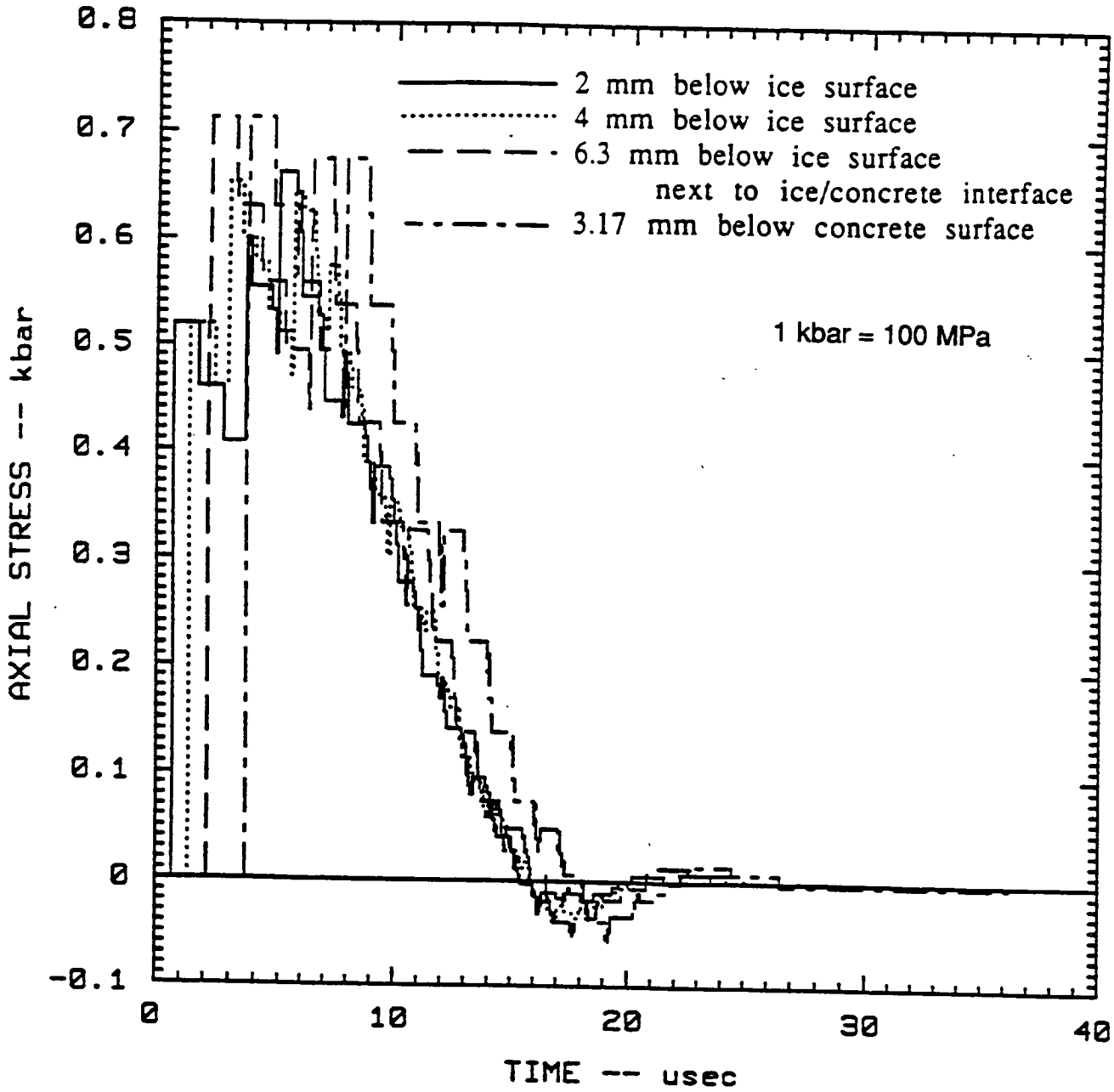

Figure J-2. **Stress histories produced by a steel impactor striking ice on semiinfinite concrete (simulation 1A1). The ice and the ice-concrete interface are not permitted to fail.**

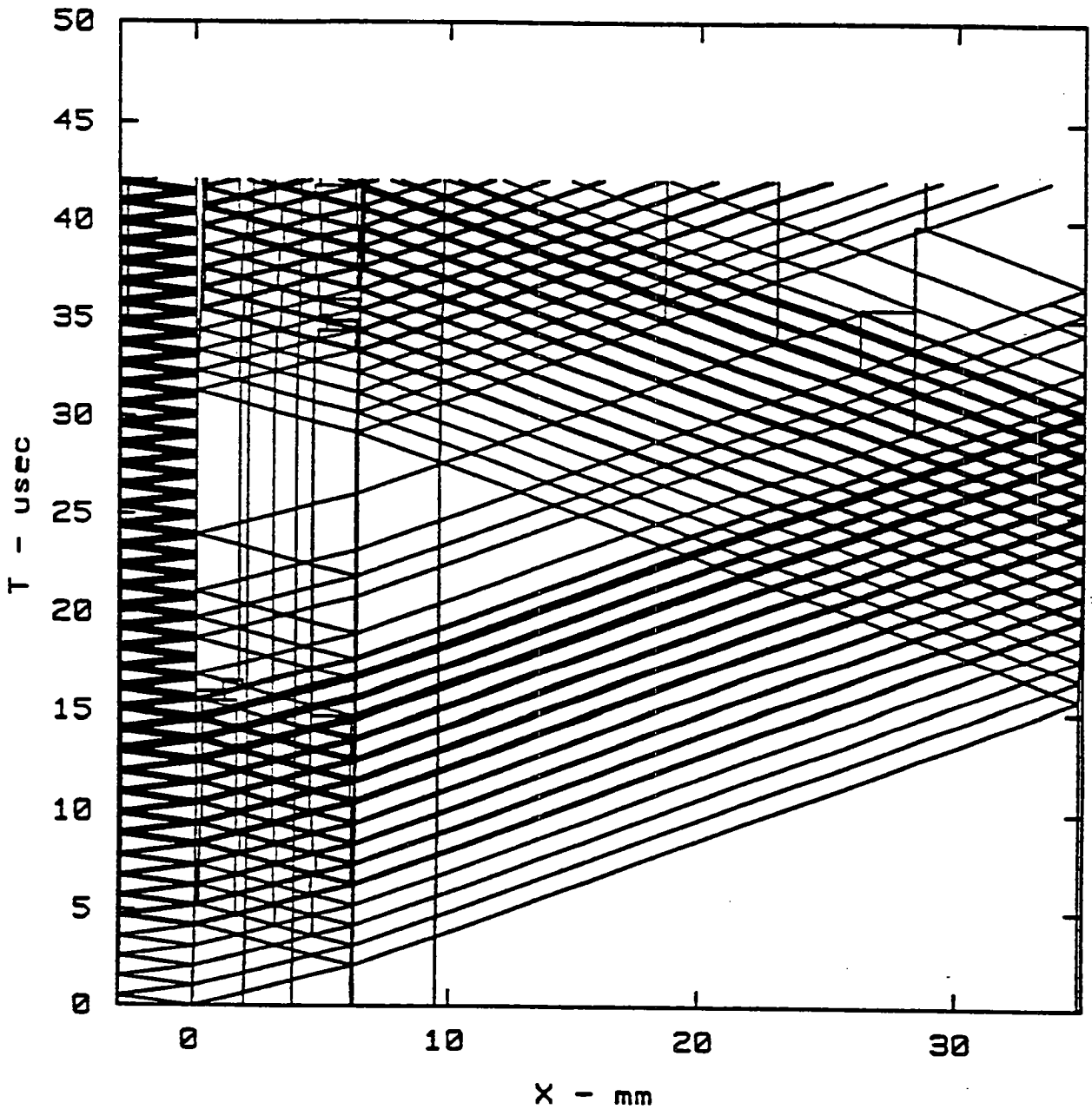

Figure J-3. Stress waves induced by a steel impactor striking ice on 25.4-mm-thick concrete (simulation 1D). The ice and the ice-concrete interface are not permitted to fail.

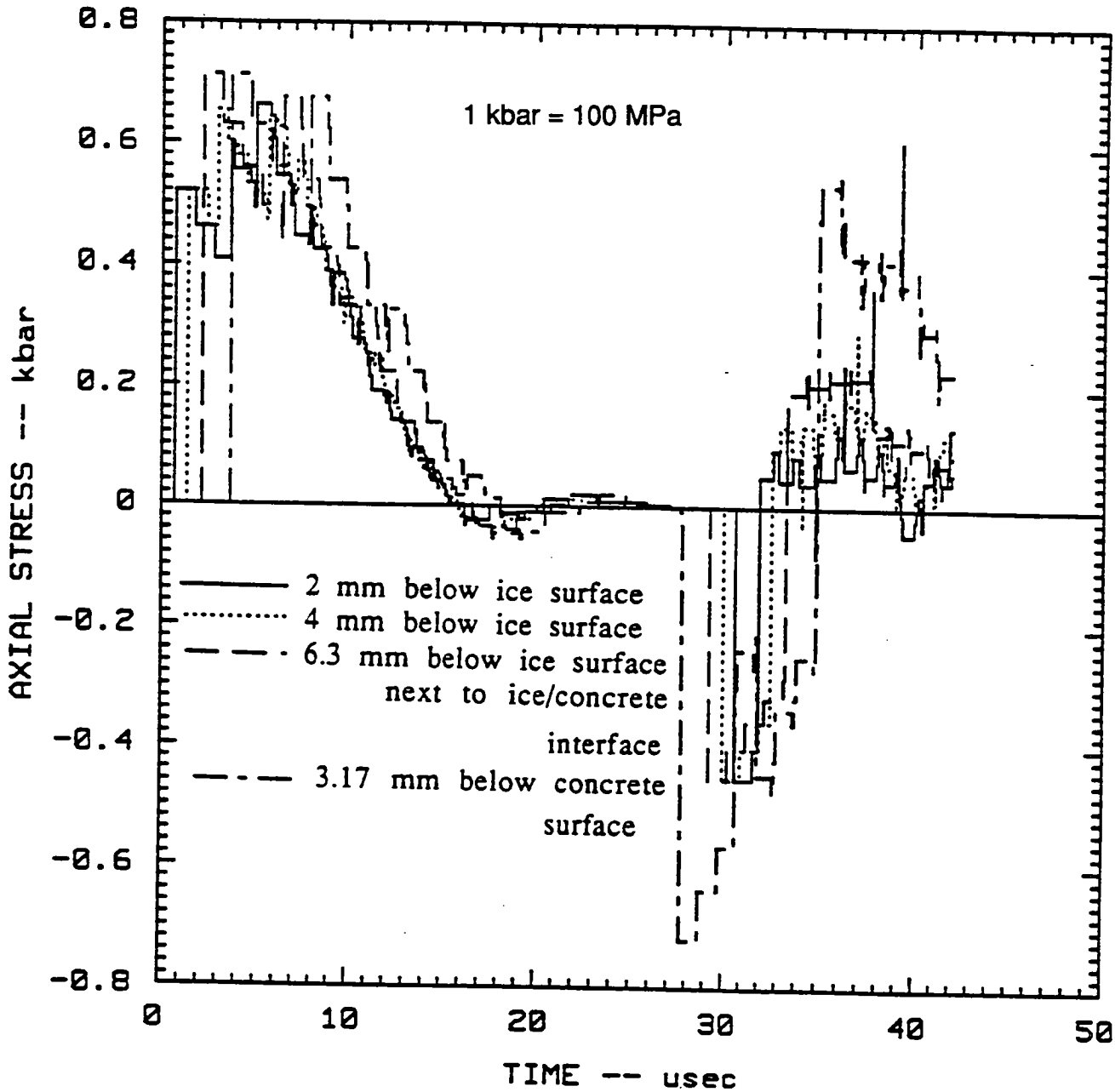

Figure J-4. **Stress histories produced by a steel impactor striking ice on 25.4-mm-thick concrete (simulation 1D). The ice and the ice-concrete interface are not permitted to fail.**

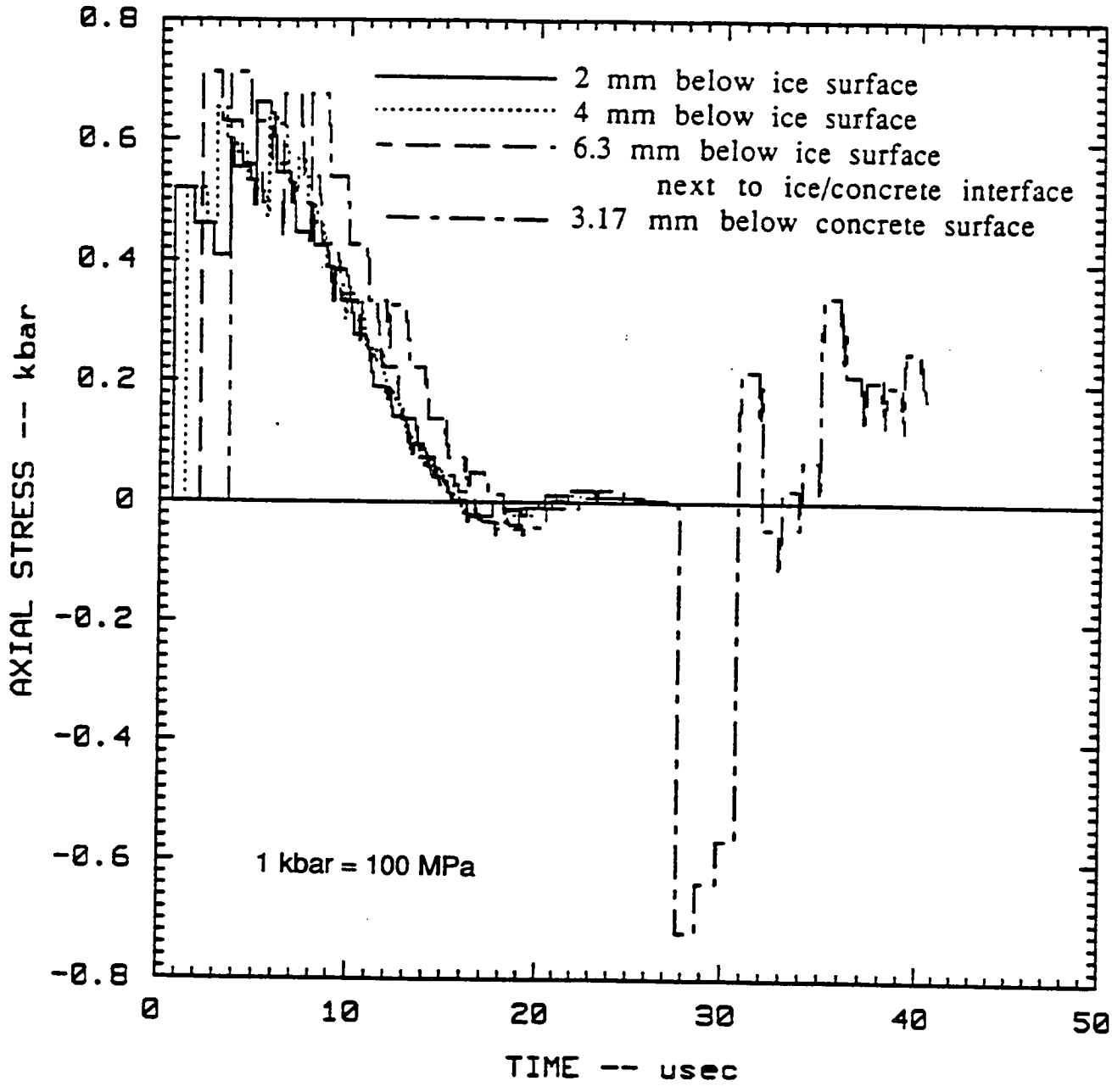

Figure J-5. **Stress histories produced by a steel impactor striking ice on 25.4-mm-thick concrete (simulation 1D1). The ice and the ice-concrete interface fail at a tensile stress of 0.1 kbar.**

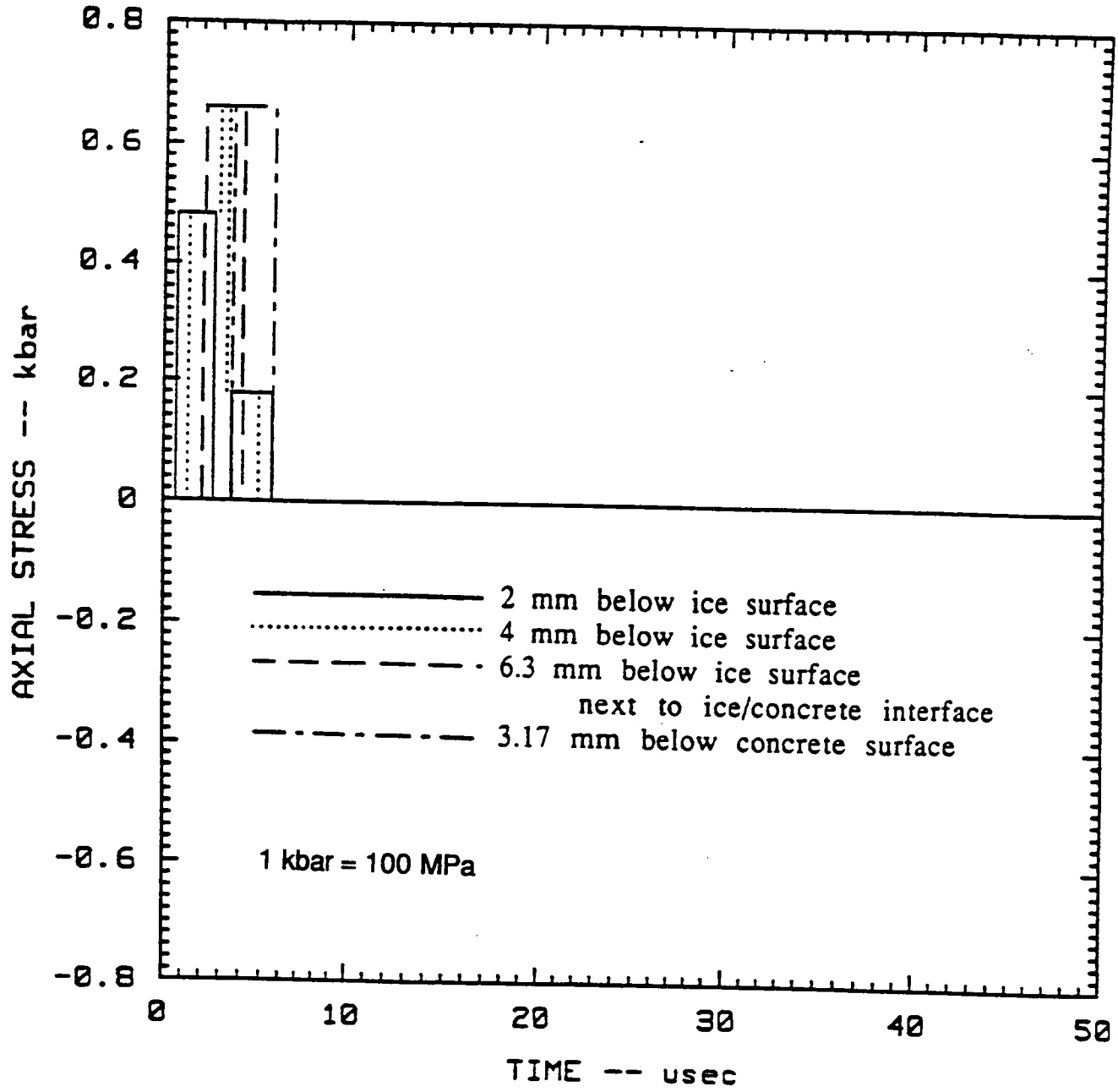

Figure J-6. **Stress histories produced by an ice impactor striking ice on semiinfinite concrete (simulation 2D1). The ice and the ice-concrete interface are not permitted to fail.**

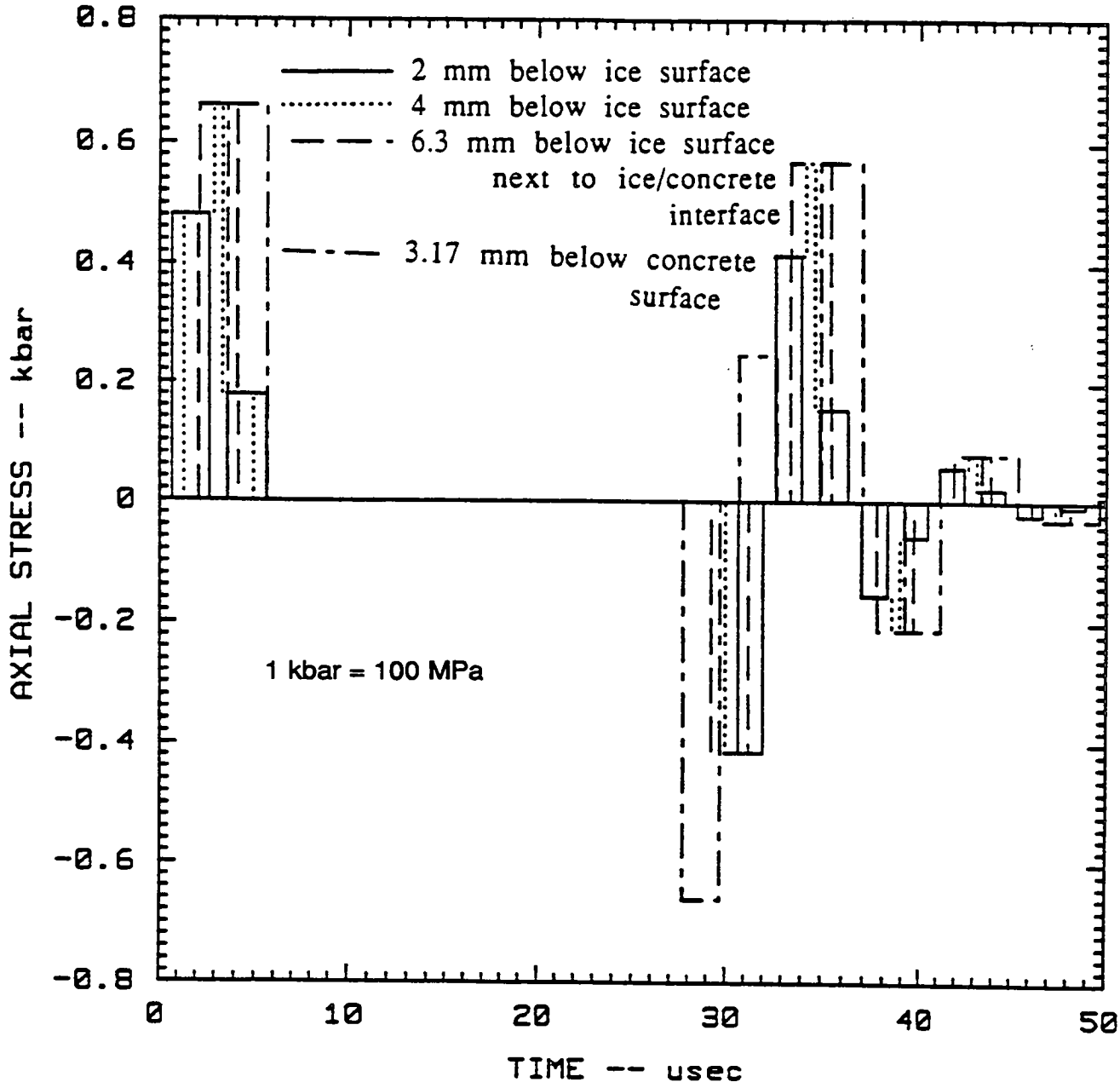

Figure J-7. Stress histories produced by an ice impactor striking ice on 5.4-mm-thick concrete (simulation 3D). The ice and the ice-concrete interface are not permitted to fail.

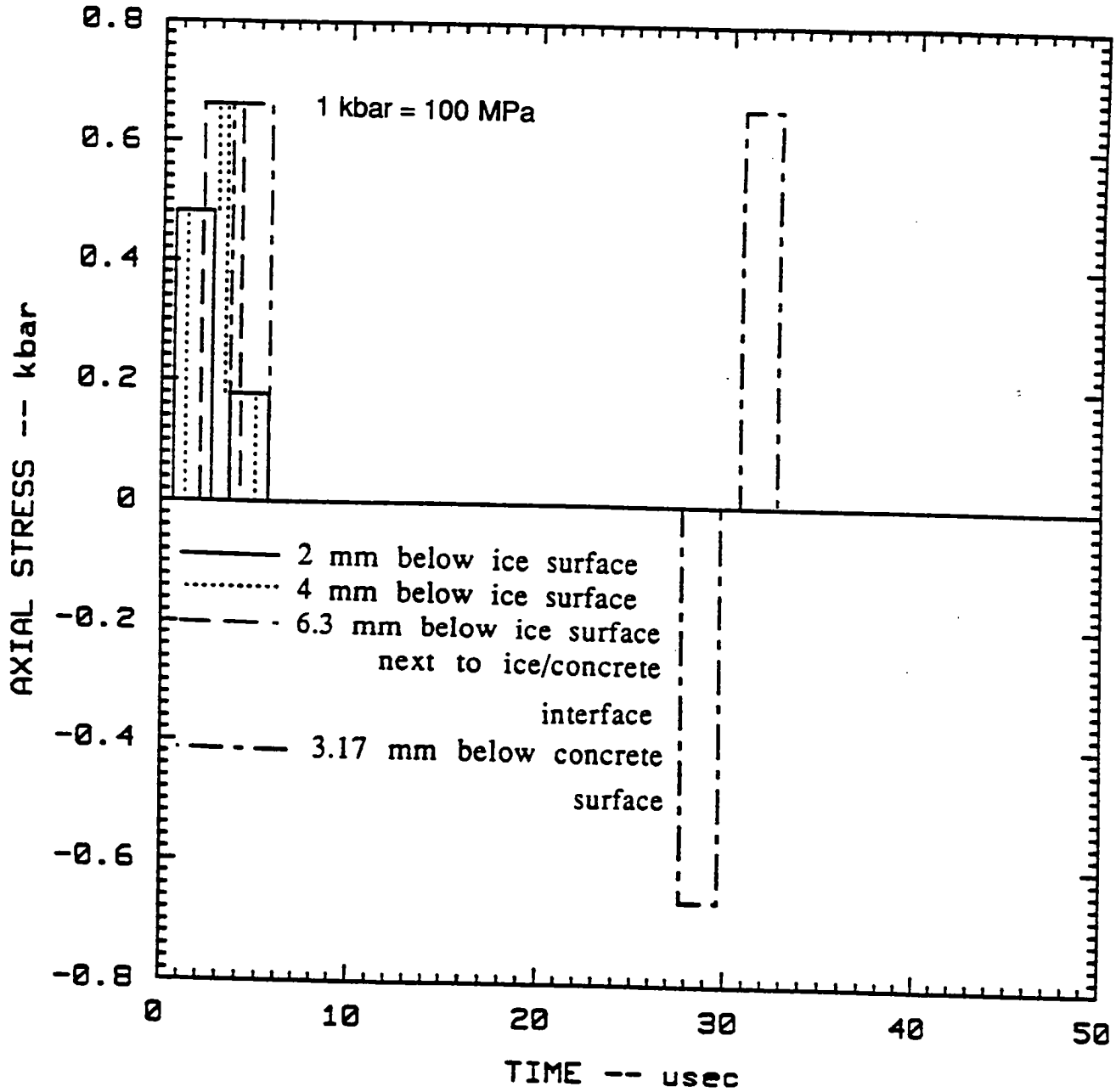

Figure J-8. Stress histories produced by an ice impactor striking ice on 25.4-mm-thick concrete (simulation 4F). The ice and the ice-concrete interface fail at a tensile stress of 0.1 kbar.

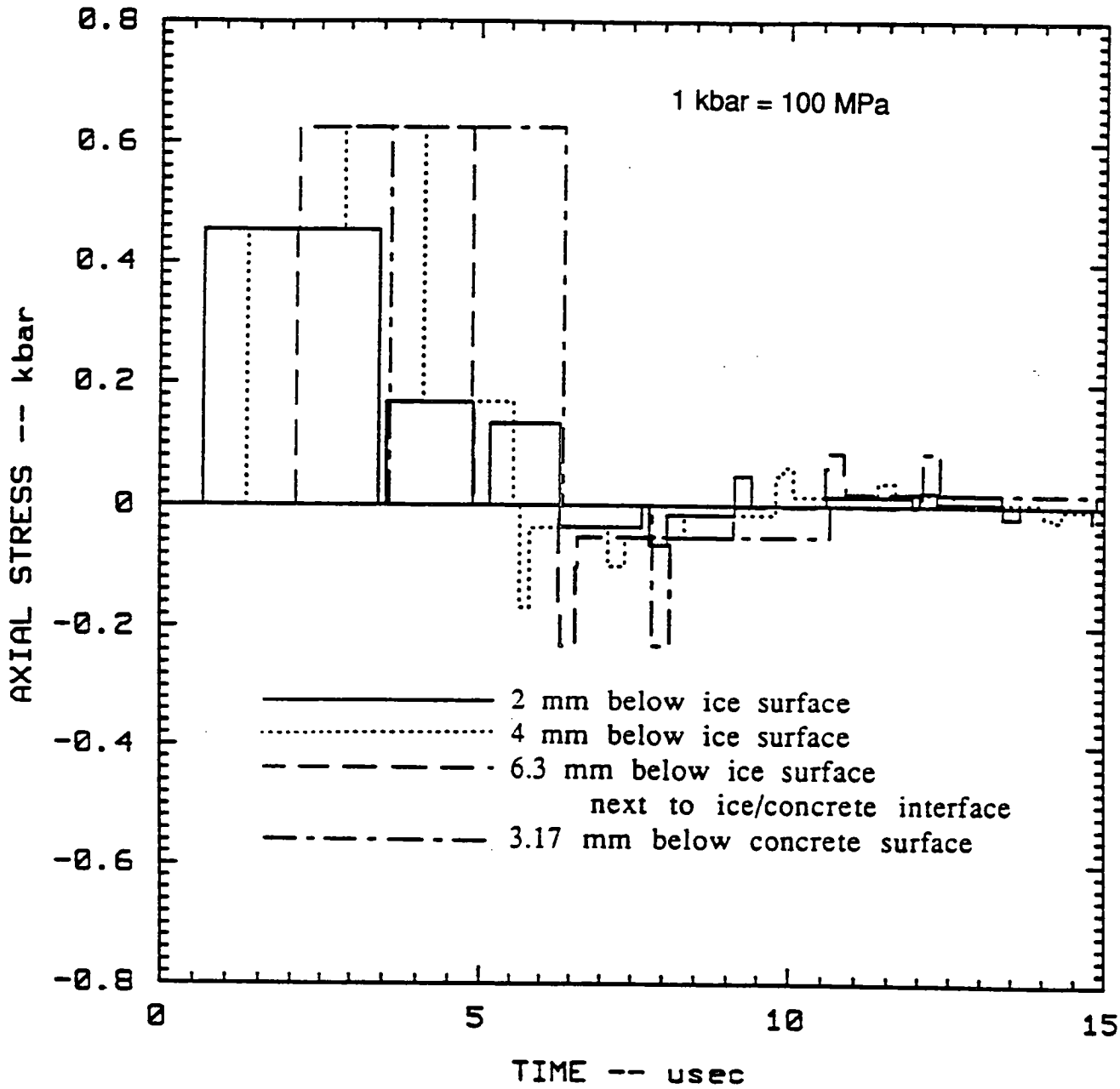

Figure J-9. **Stress histories produced by a nylon impactor striking ice on semiinfinite concrete (simulation 1B1). The ice and the ice-concrete interface are not permitted to fail.**

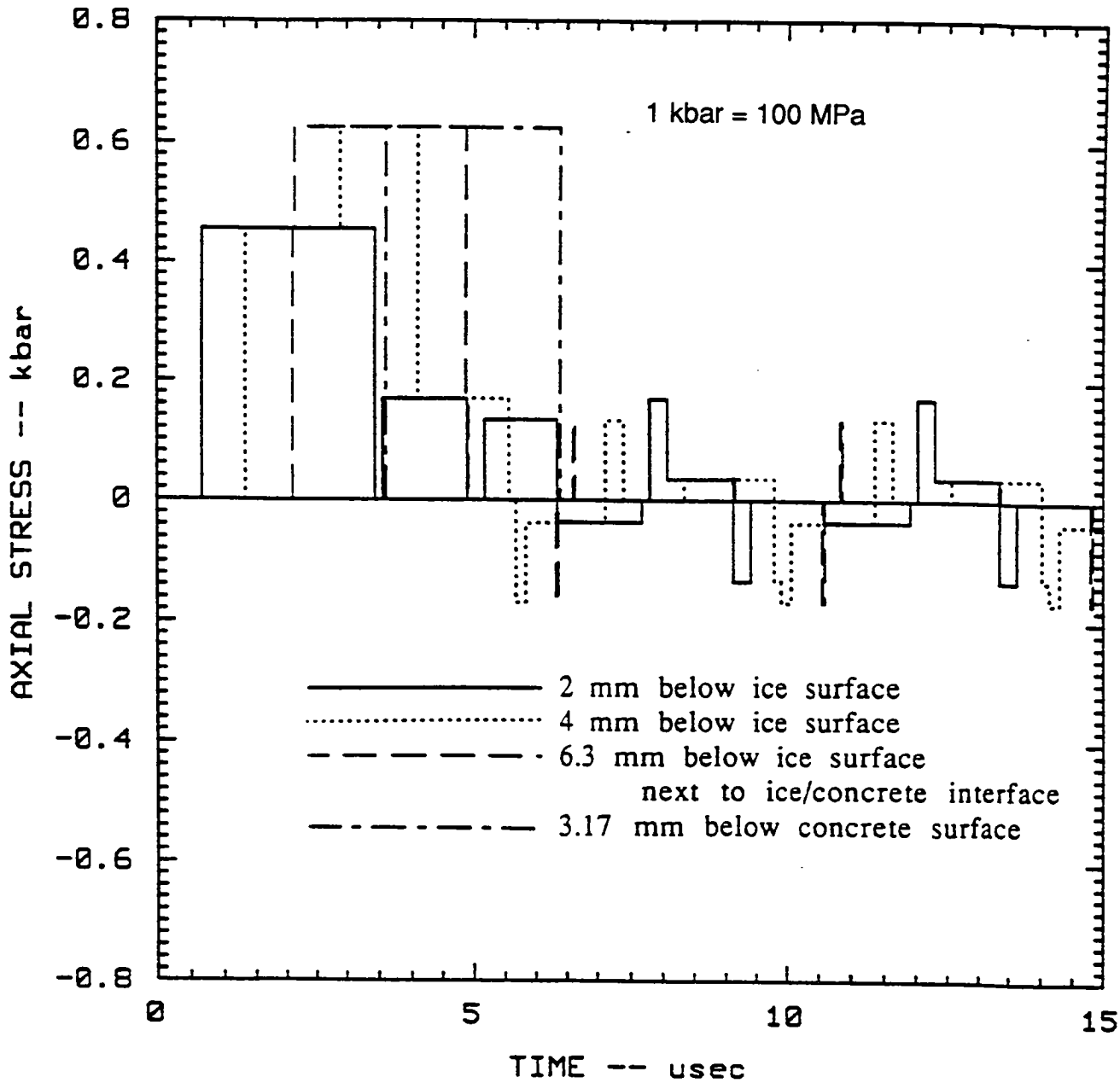

Figure J-10. Stress histories produced by a nylon impactor striking ice on 25.4-mm-thick concrete (simulation 1B2). The ice and the ice-concrete interface are not permitted to fail.

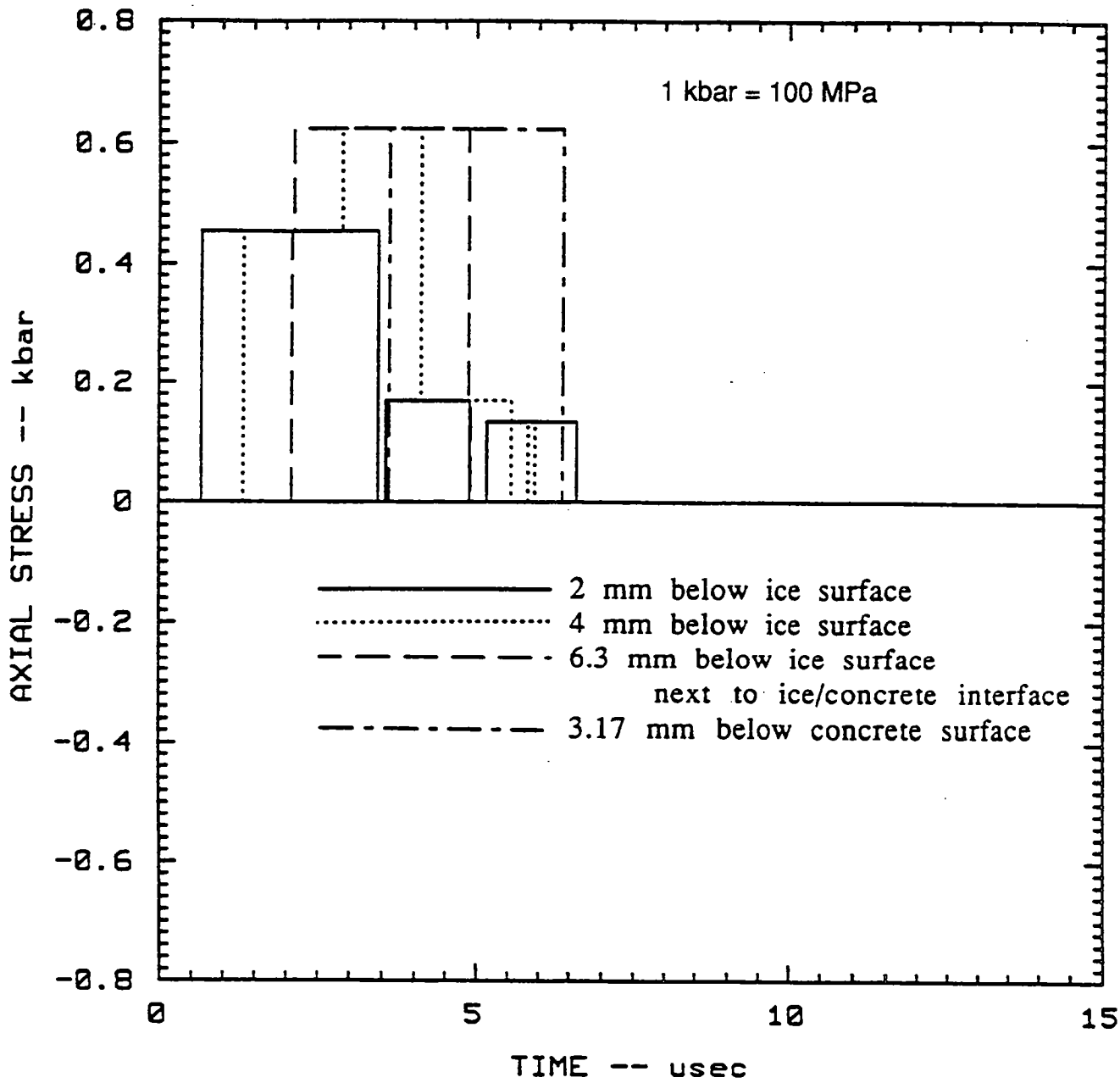

Figure J-11. Stress histories produced by a nylon impactor striking ice on 25.4-mm-thick concrete (simulation 1B3). The ice and the ice-concrete interface fail at a tensile stress of 0.1 kbar.

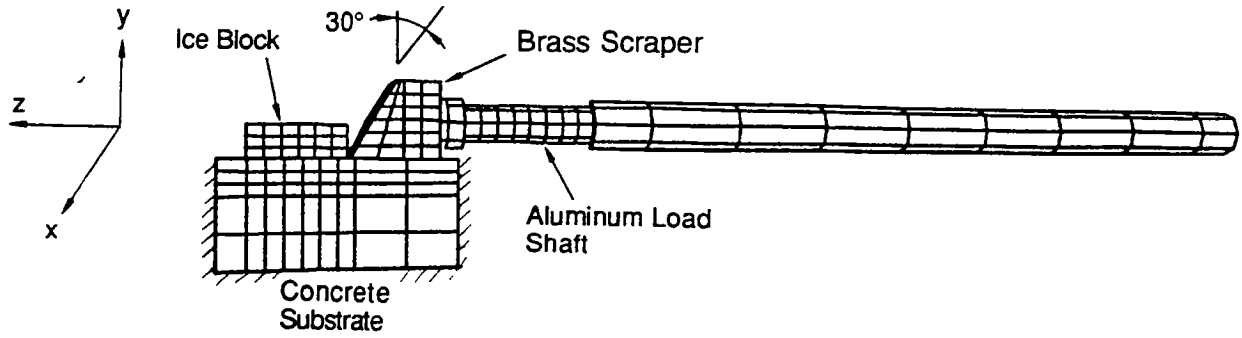

Figure J-12. Finite element mesh of experiment arrangement

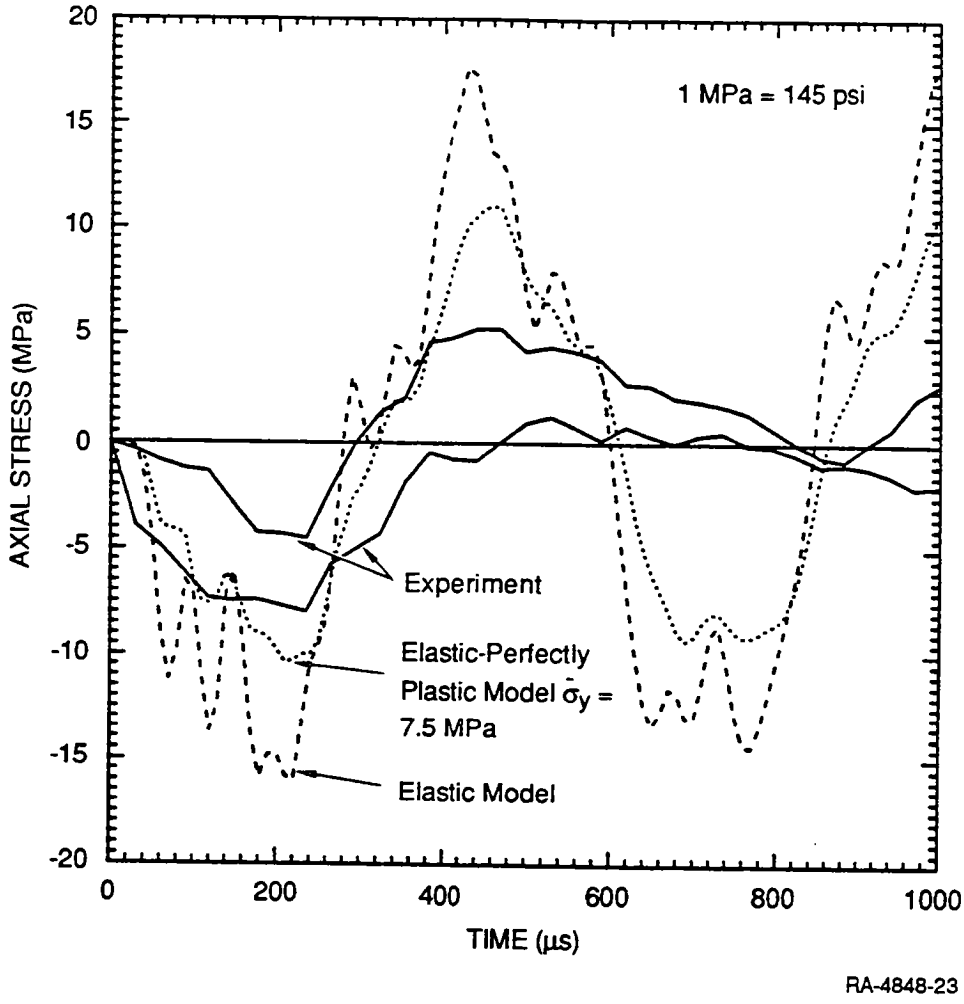

Figure J-13. Comparison of axial stresses in load shaft for different ice material models

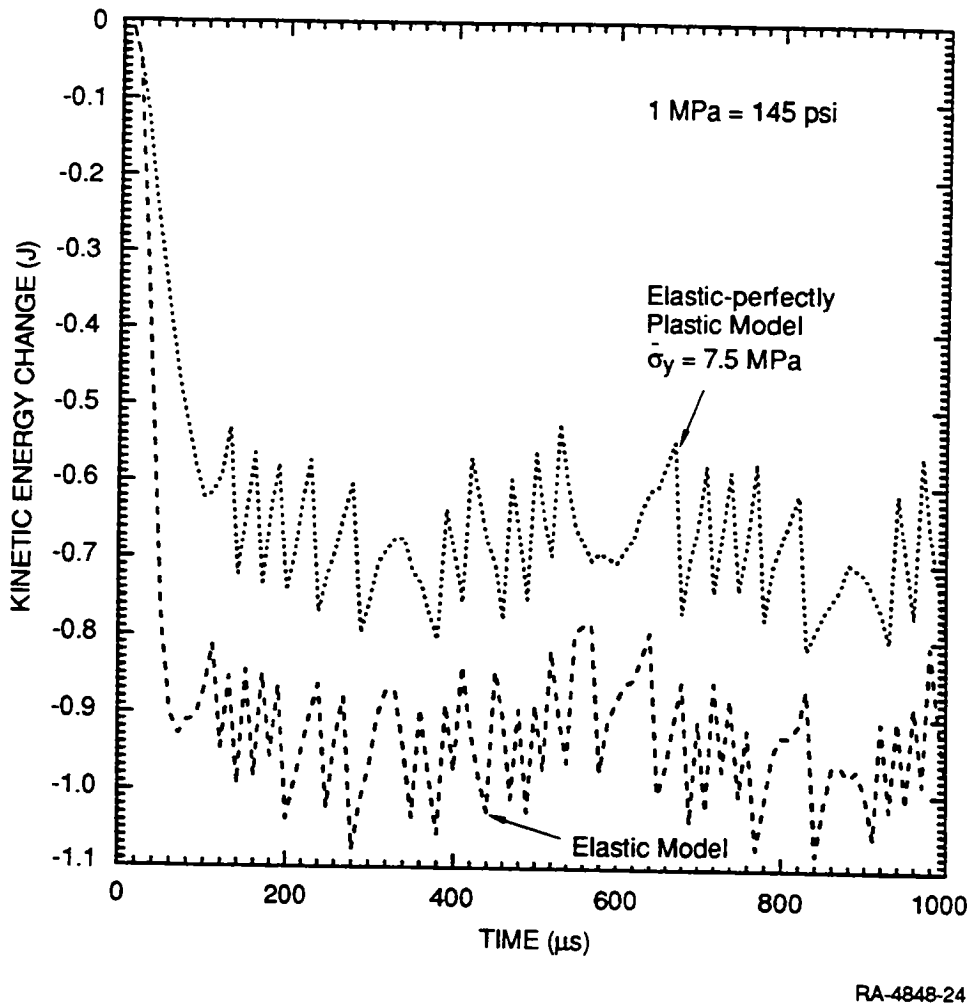

Figure J-14. Comparison of kinetic energy change in scraper-shaft assembly for different ice material models (impact velocity = 6.94 m/sec)

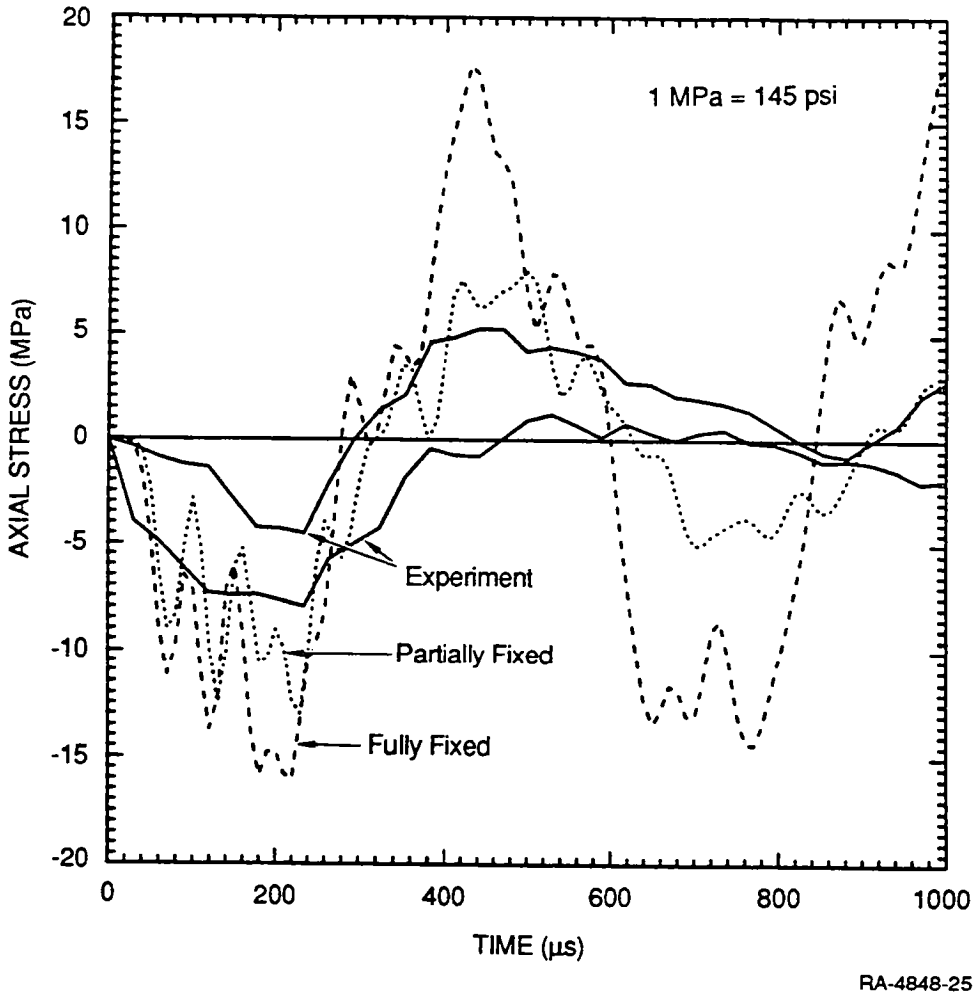

Figure J-15. Comparison of axial stresses in load shaft for different degrees of attachmer between the load shaft and scraper

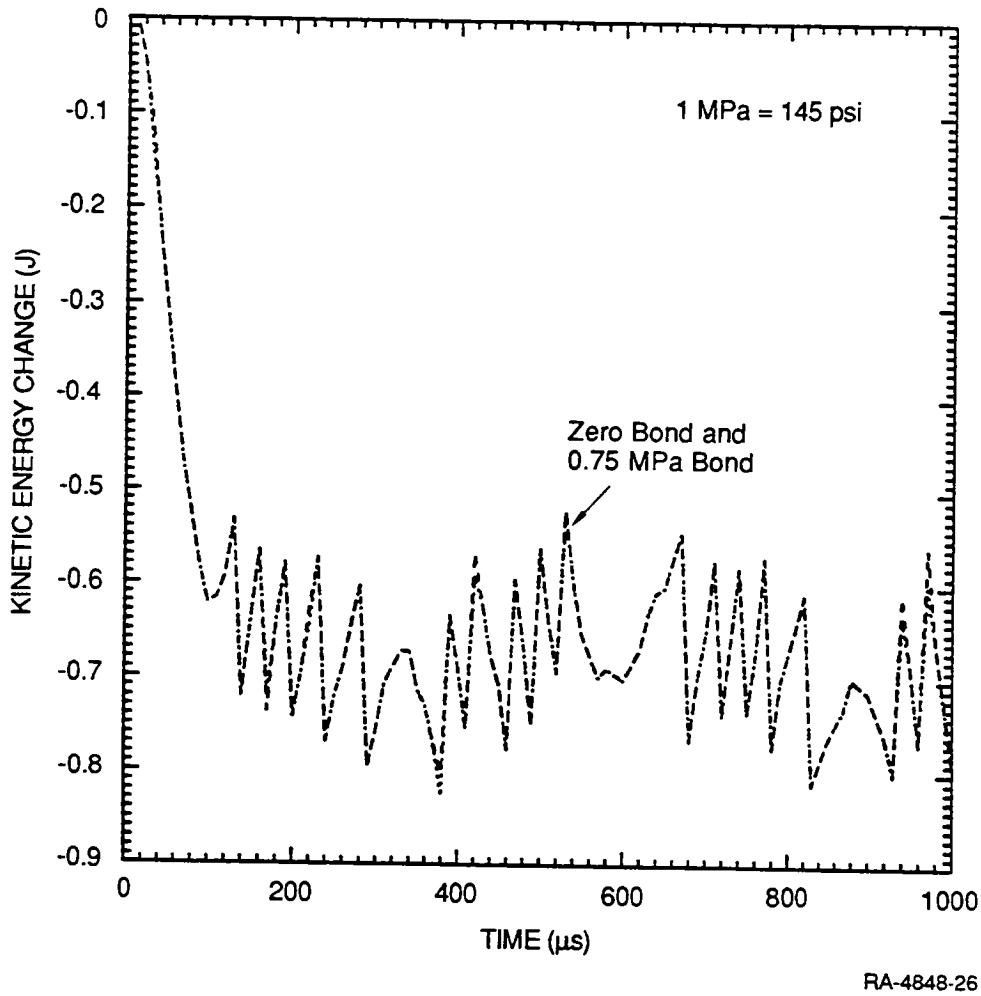

Figure J-16. Comparison of kinetic energy change in scraper-shaft assembly for different ice-concrete bond strengths

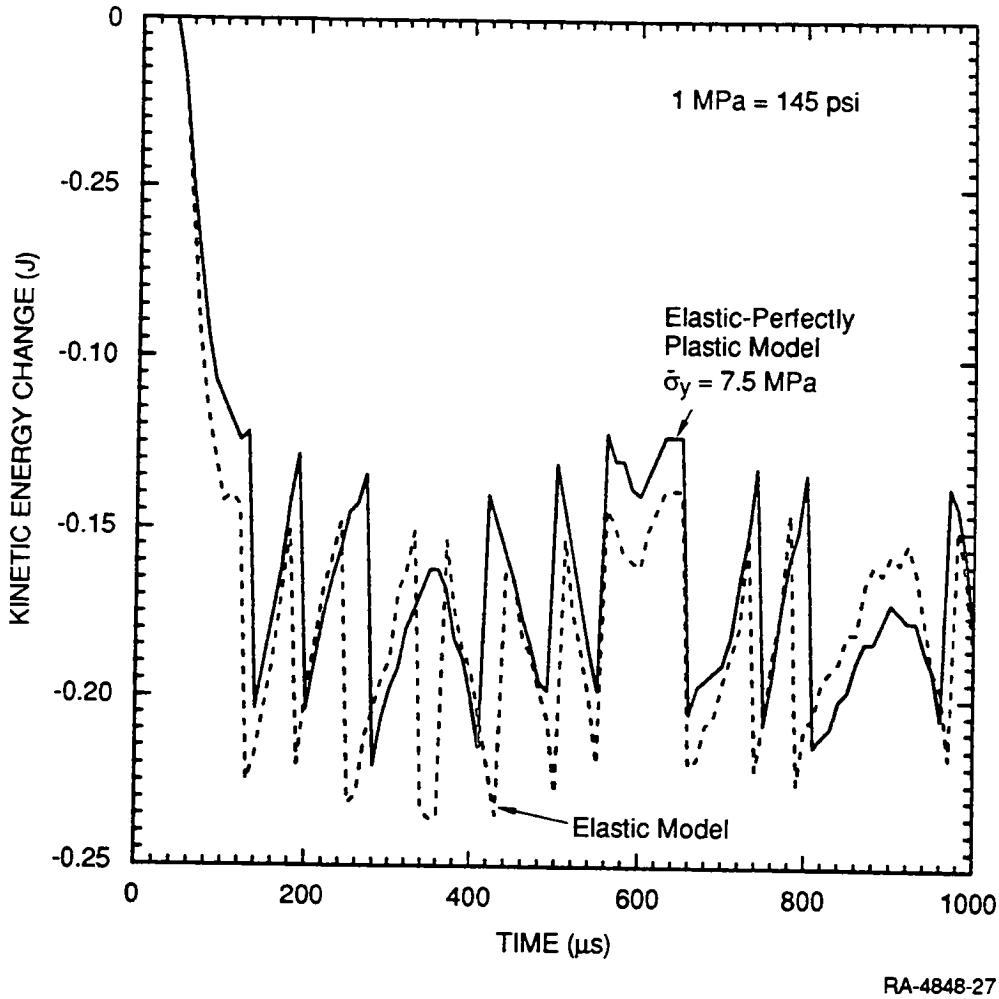

Figure J-17. Comparison of kinetic energy change in scraper-shaft assembly for different ice material models

Velocity = 2.48 m/s

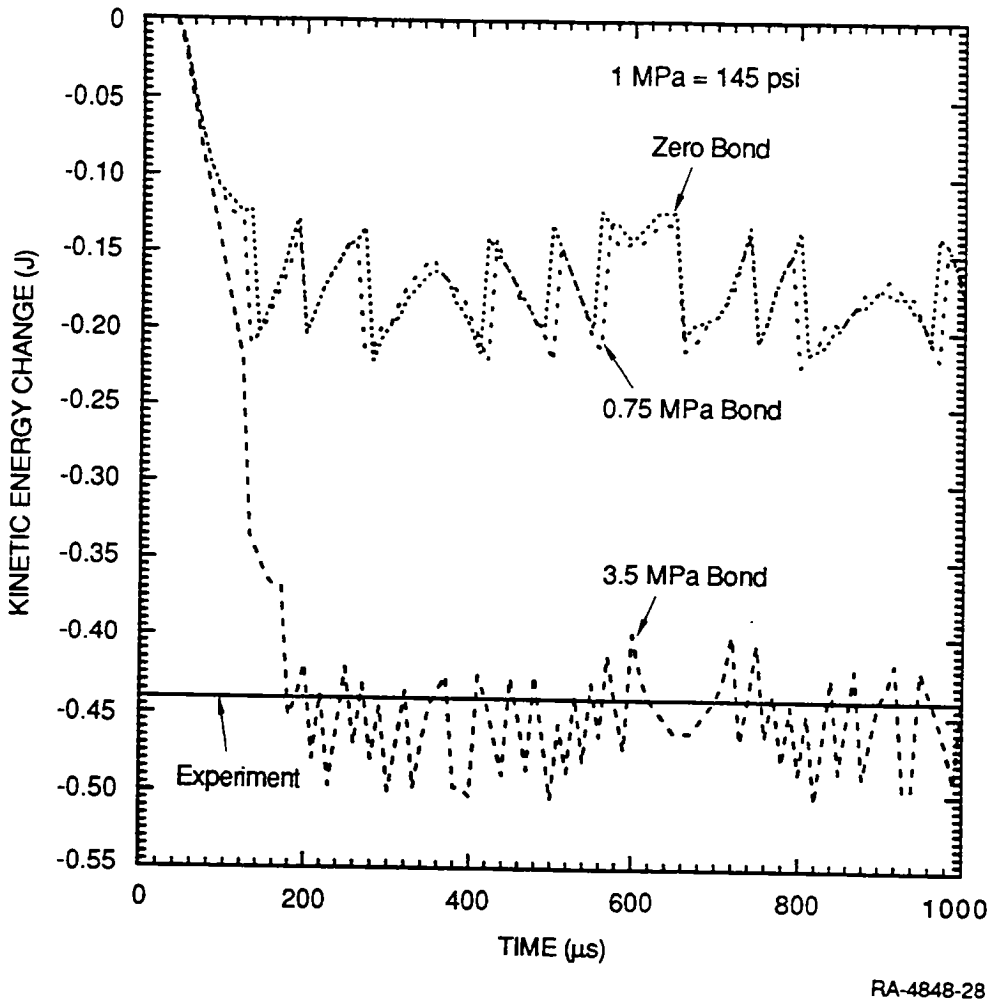

Figure J-18. Comparison of kinetic energy change in scraper-shaft assembly for different ice-concrete bond strengths

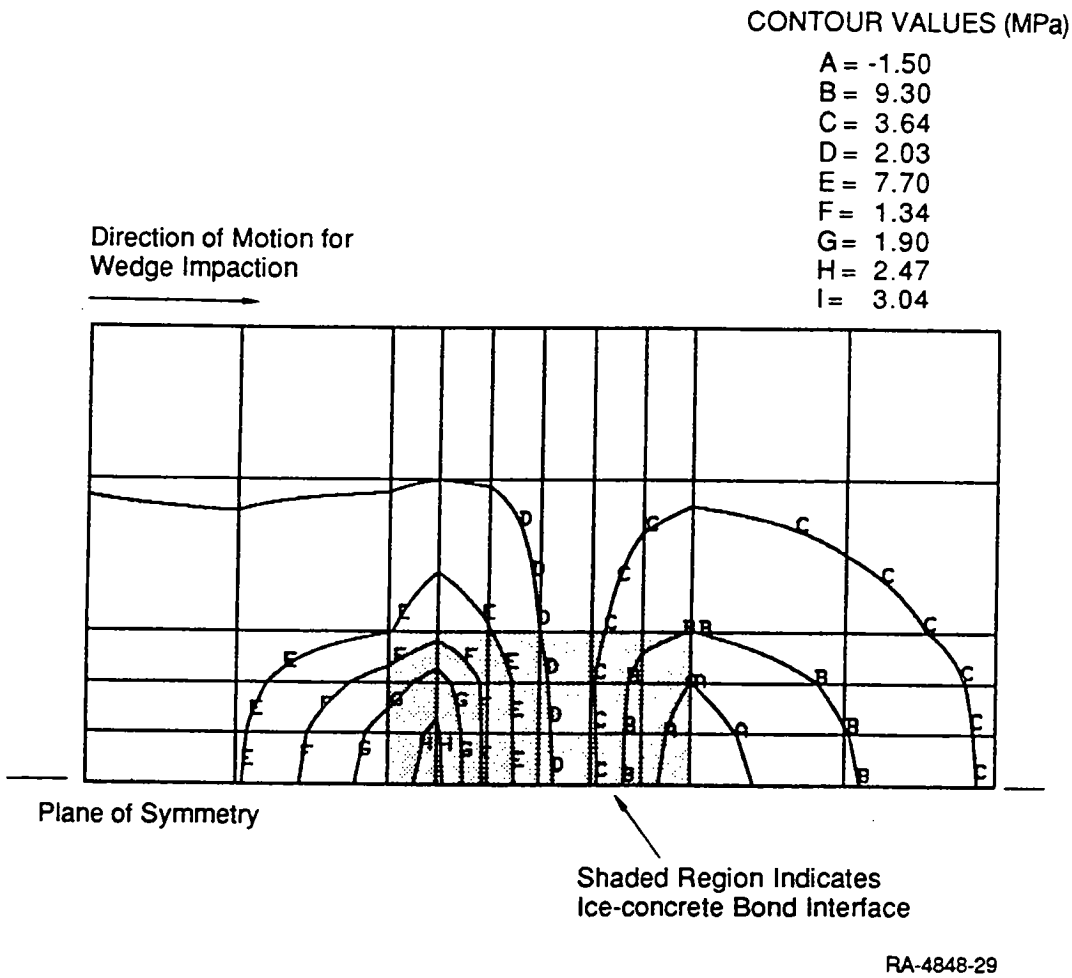

Figure J-19. Representative shear stress in concrete near ice-concrete interface

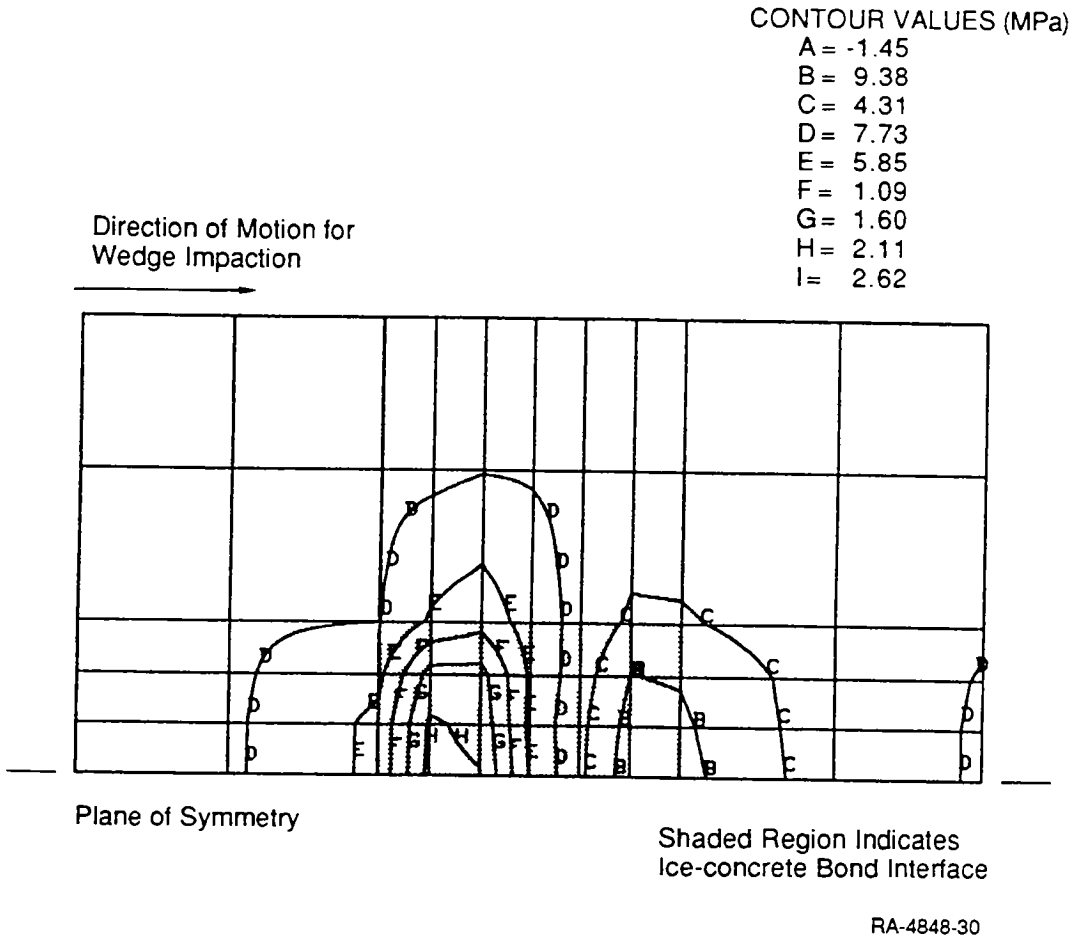

Figure J-20. Representative tensile stress in concrete near ice-concrete interface

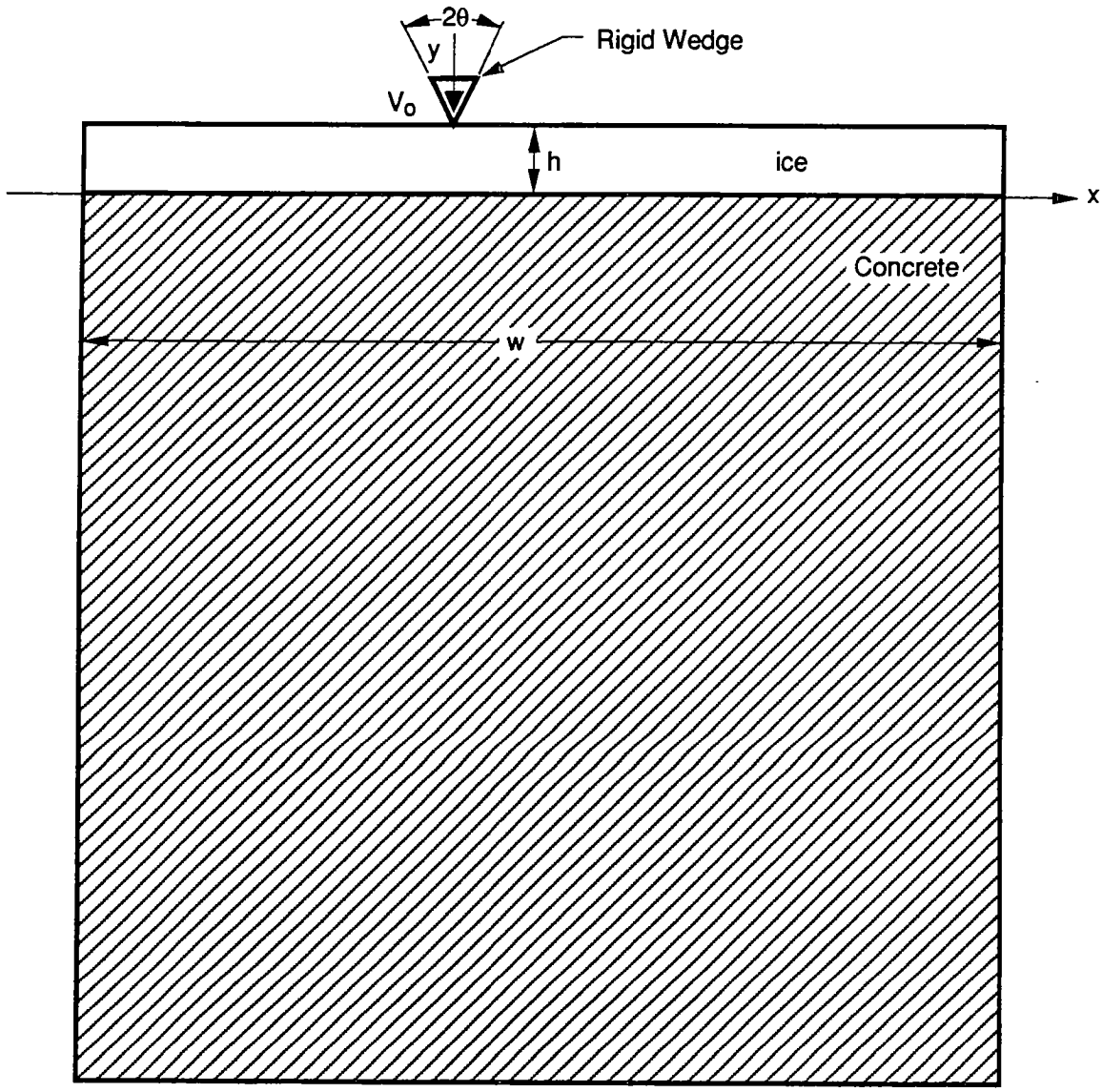

Figure J-21. Schematic representation of two-dimensional analysis of a wedge moving perpendicular to an ice layer on a concrete substrate

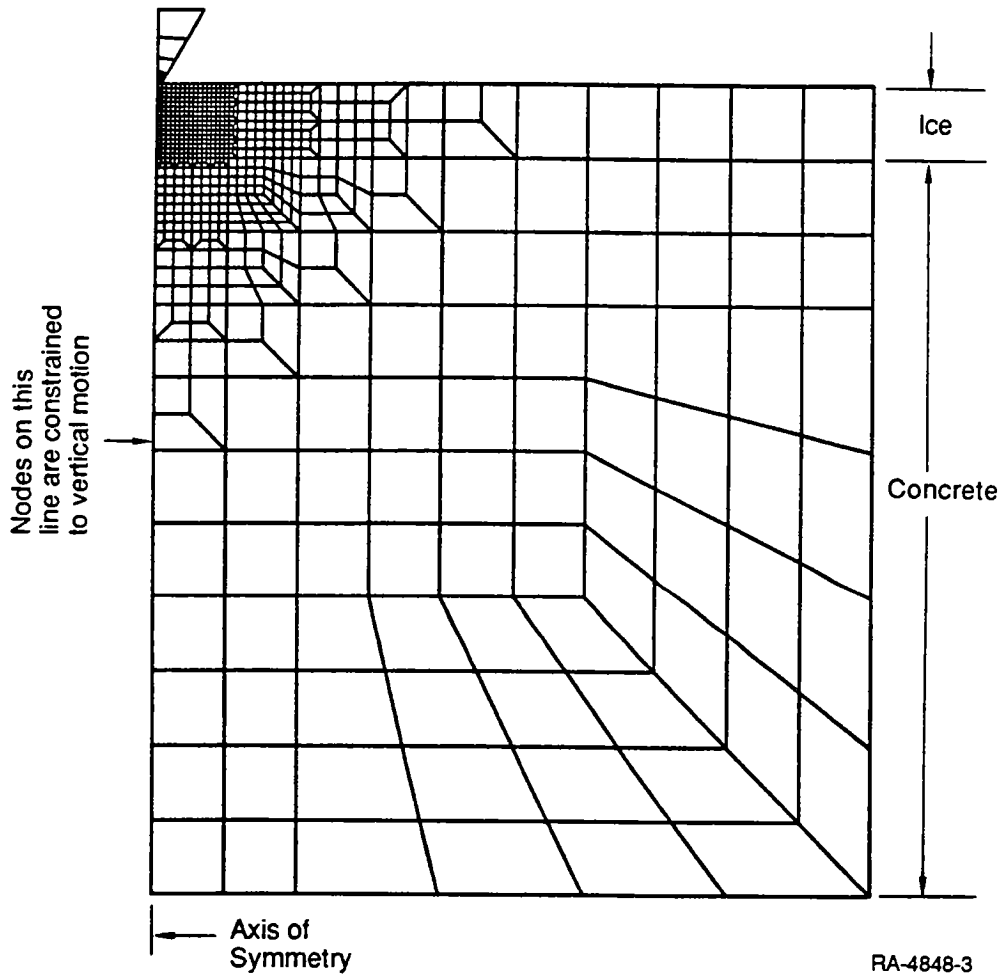

Figure J-22. Finite element mesh of a wedge striking an ice layer on concrete

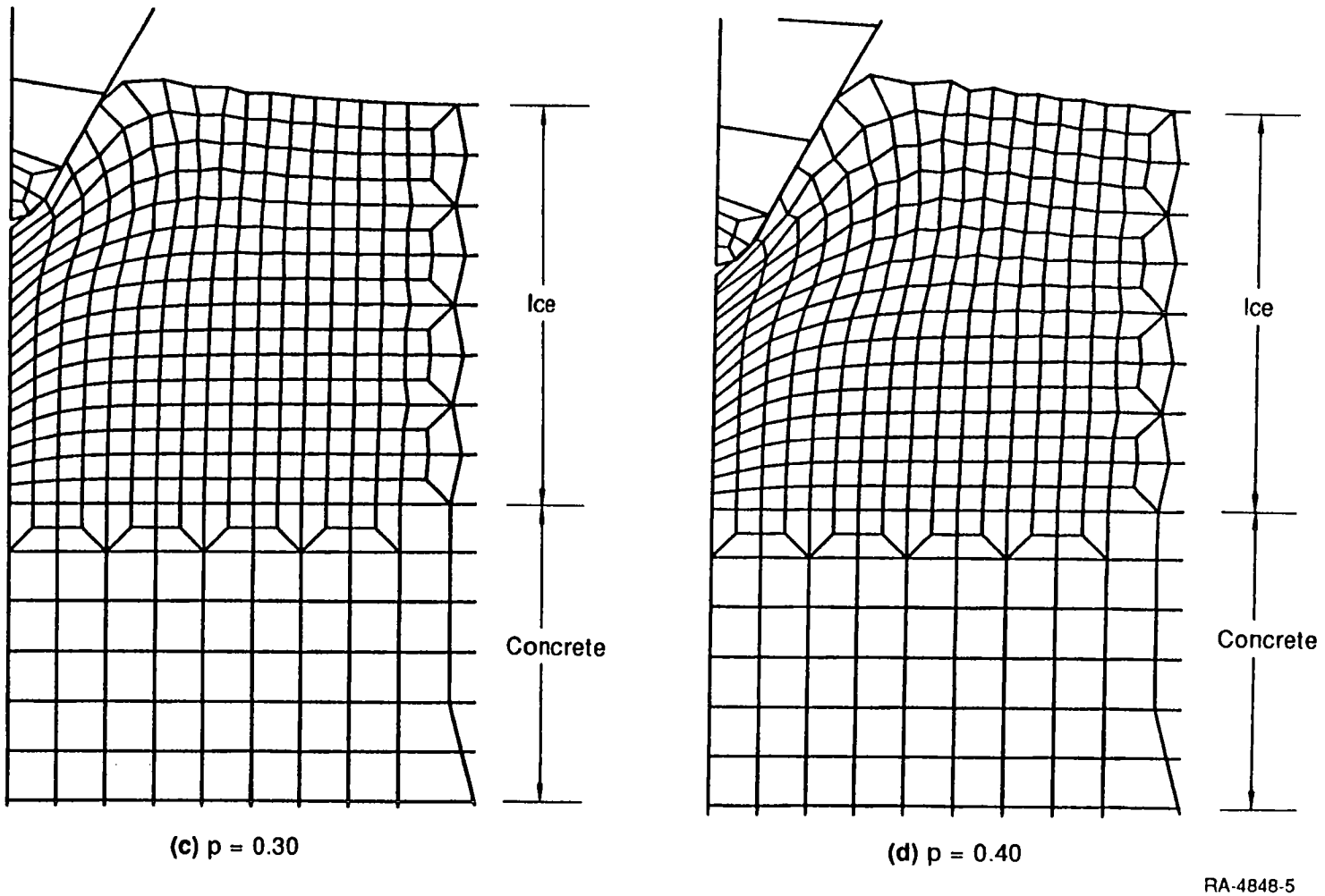

Figure J-23. Finite element mesh distortion from a simulation of the penetration of a wedge into an ice layer on concrete

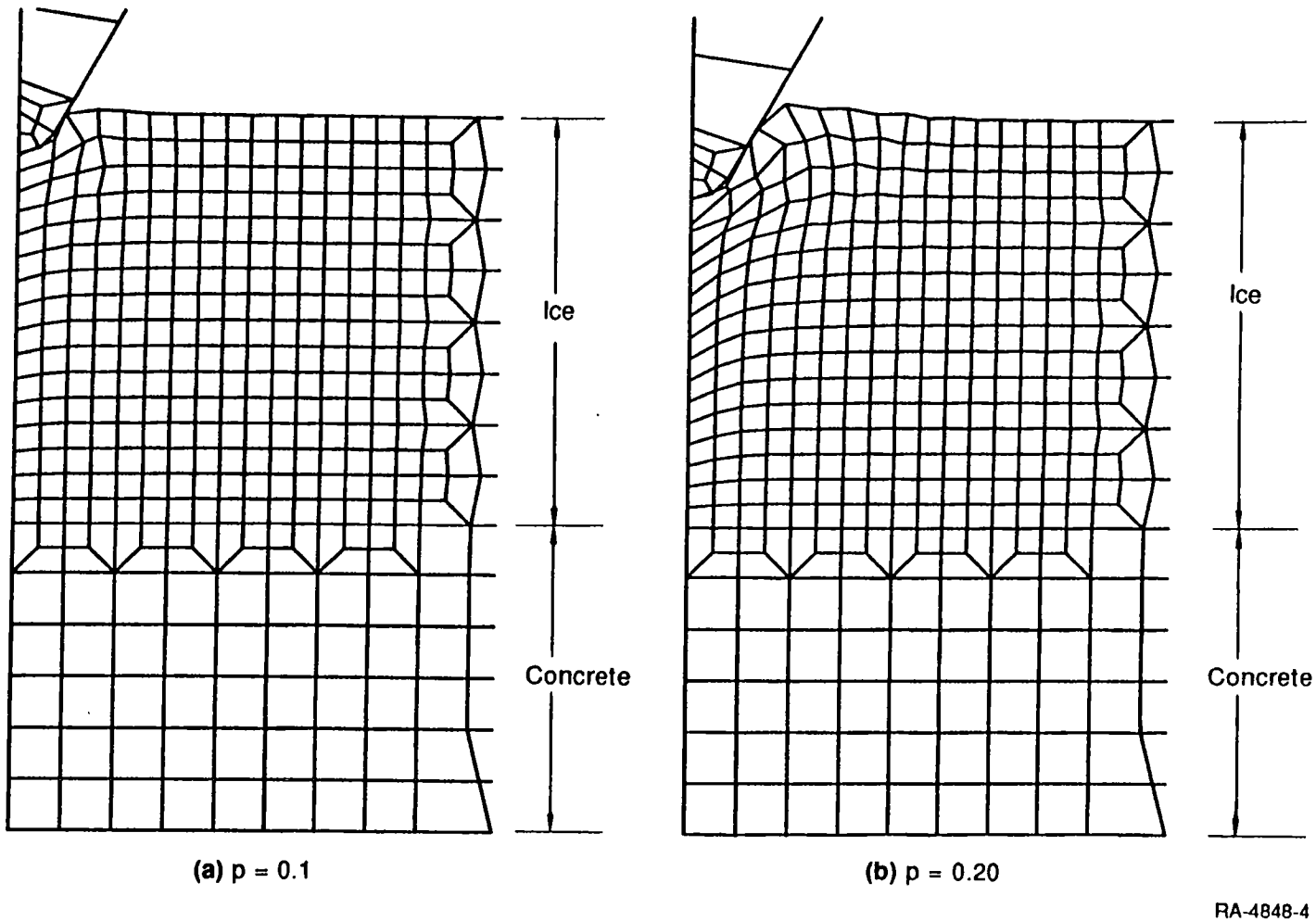

Figure J-23. Finite element mesh distortion from a simulation of the penetration of a wedge into an ice layer on concrete (concluded)

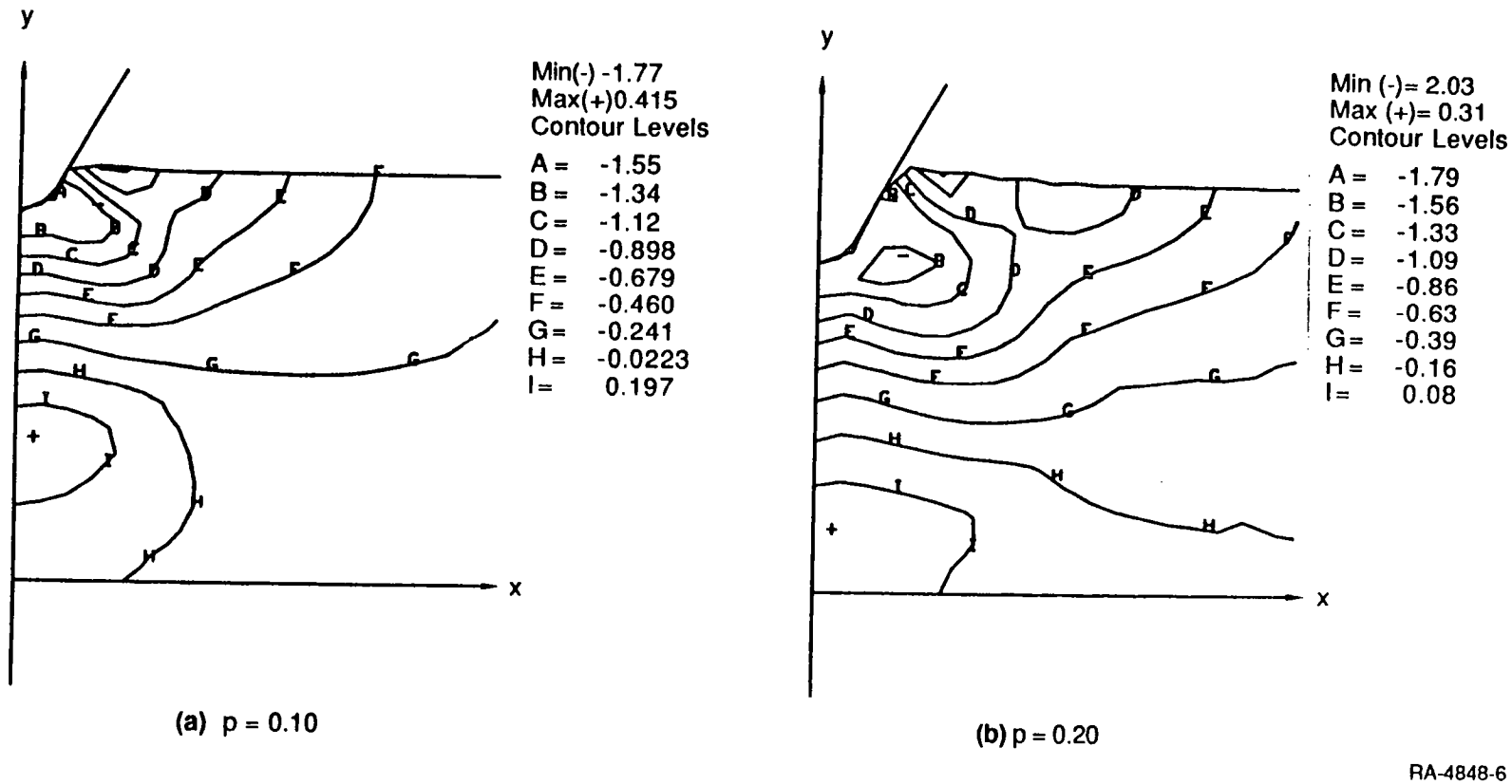

Figure J-24. Contours of horizontal normal stress (S_{xx}/Y) in an ice layer on concrete produced by penetration of a wedge

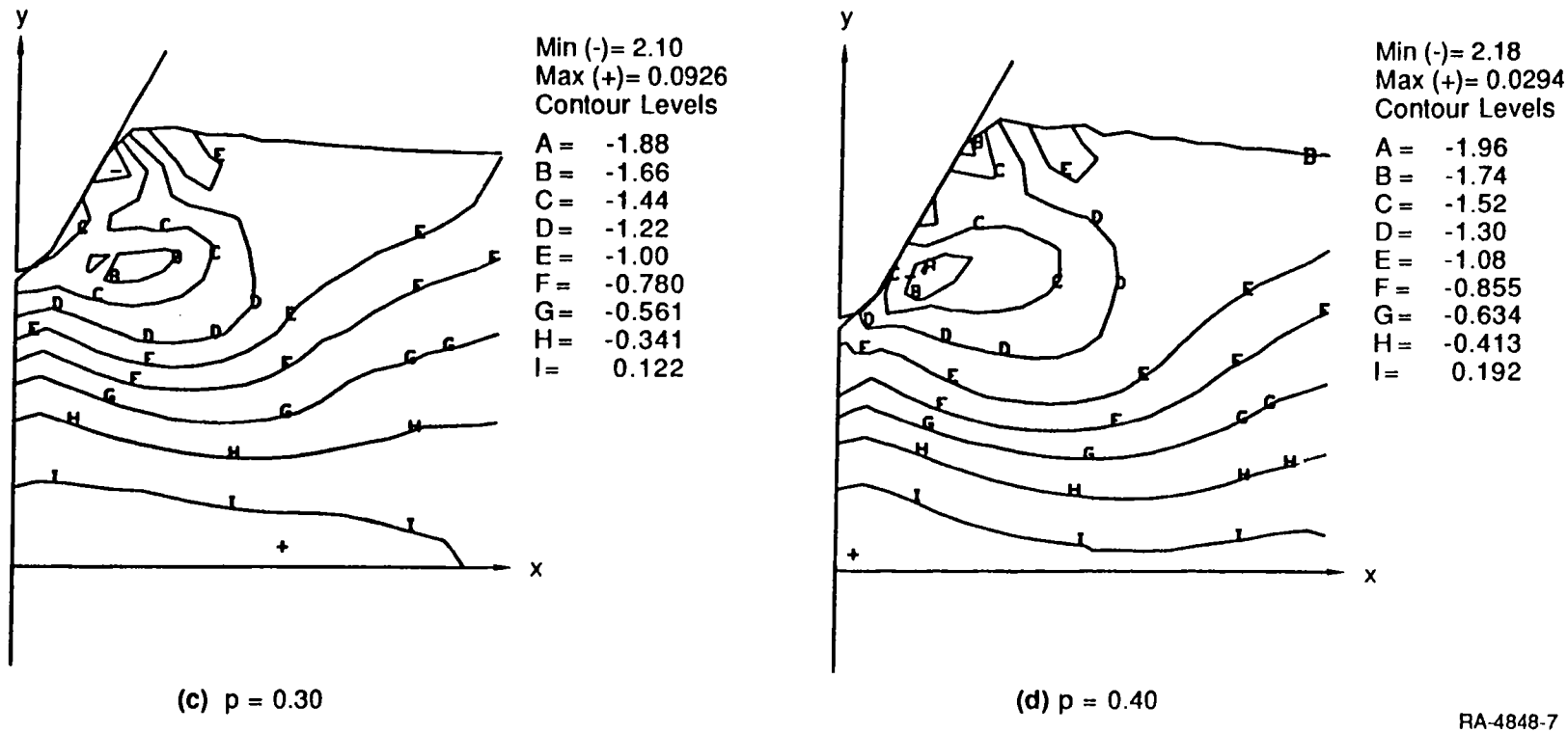

Figure J-24. Contours of horizontal normal stress (S_{xx}/Y) in an ice layer on concrete produced by penetration of a wedge (concluded)

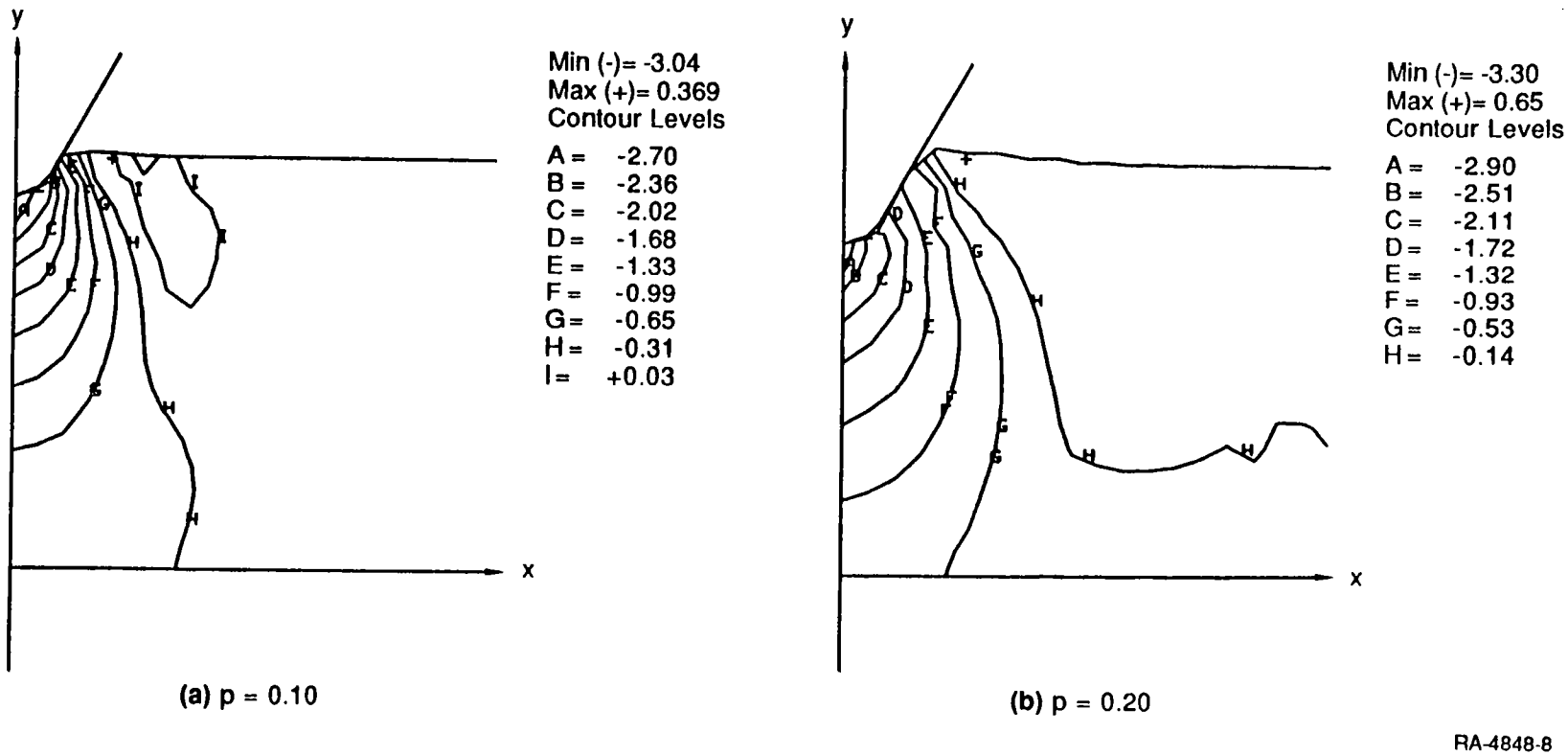

Figure J-25. Contours of vertical normal stress (S_{xx}/Y) in an ice layer on concrete produced by penetration of a wedge

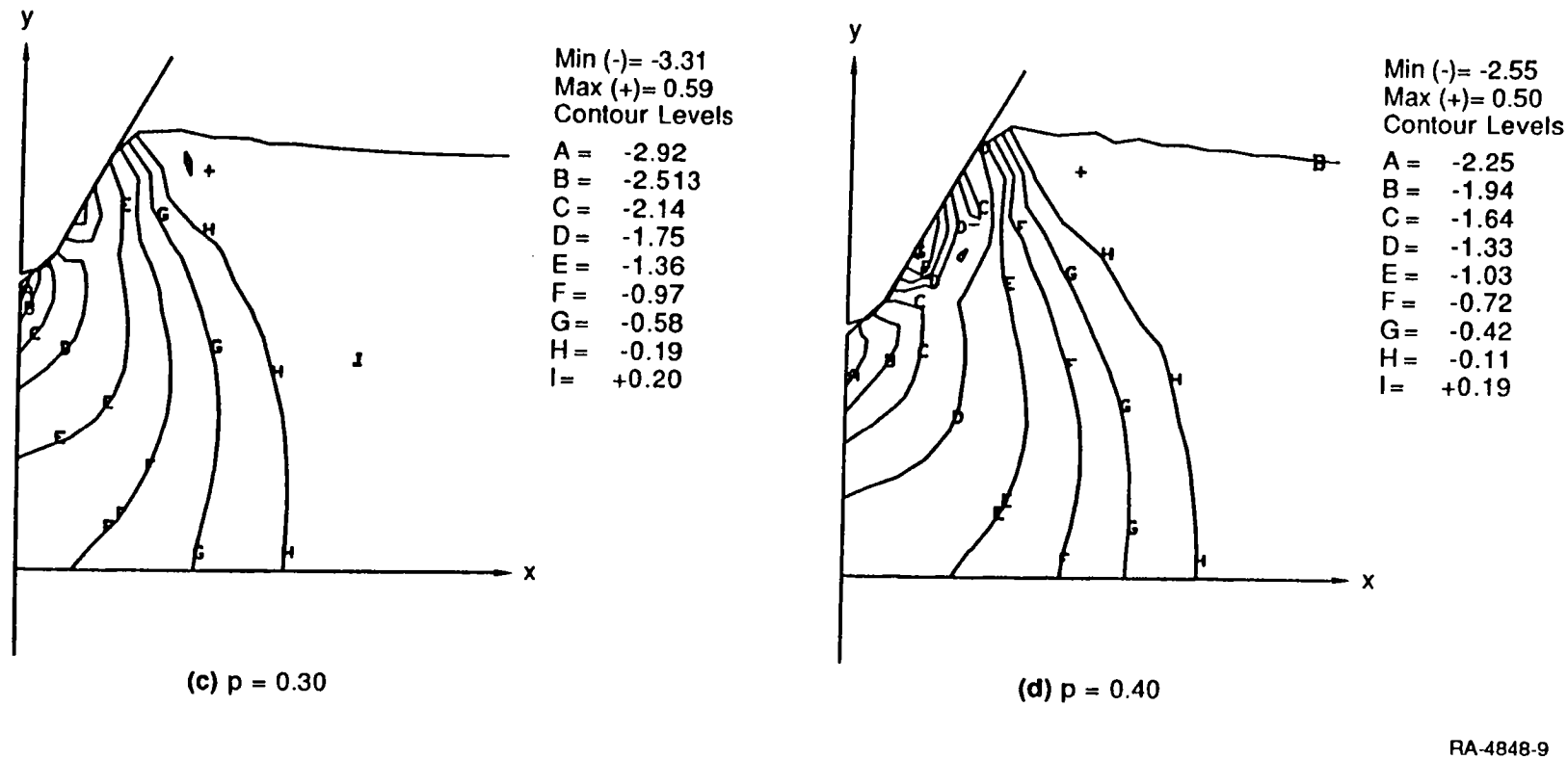

Figure J-25. Contours of vertical normal stress (S_{xx}/Y) in an ice layer on concrete produced by penetration of a wedge (concluded)

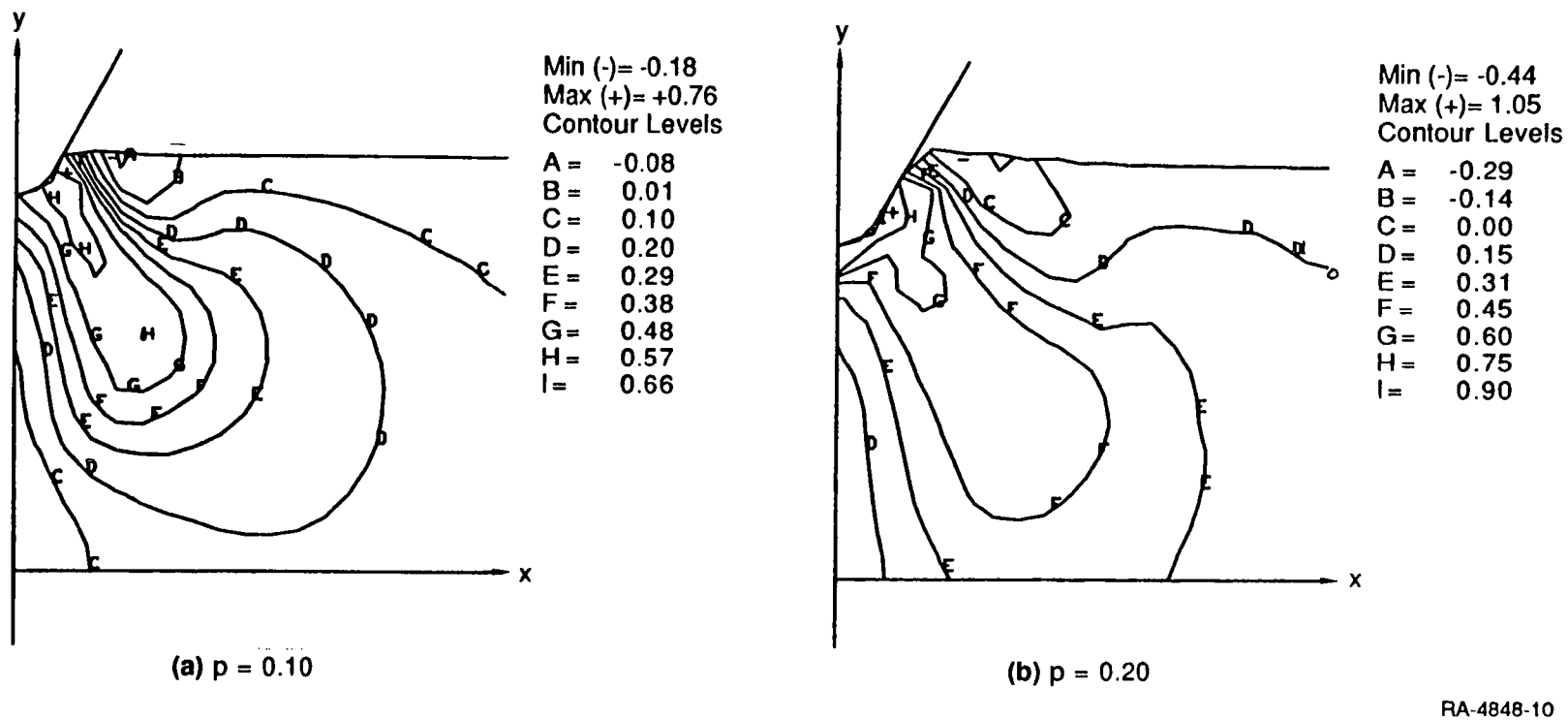

Figure J-26. Contours of shear stress (τ_{xy}/Y) in an ice layer on concrete produced by penetration of a wedge

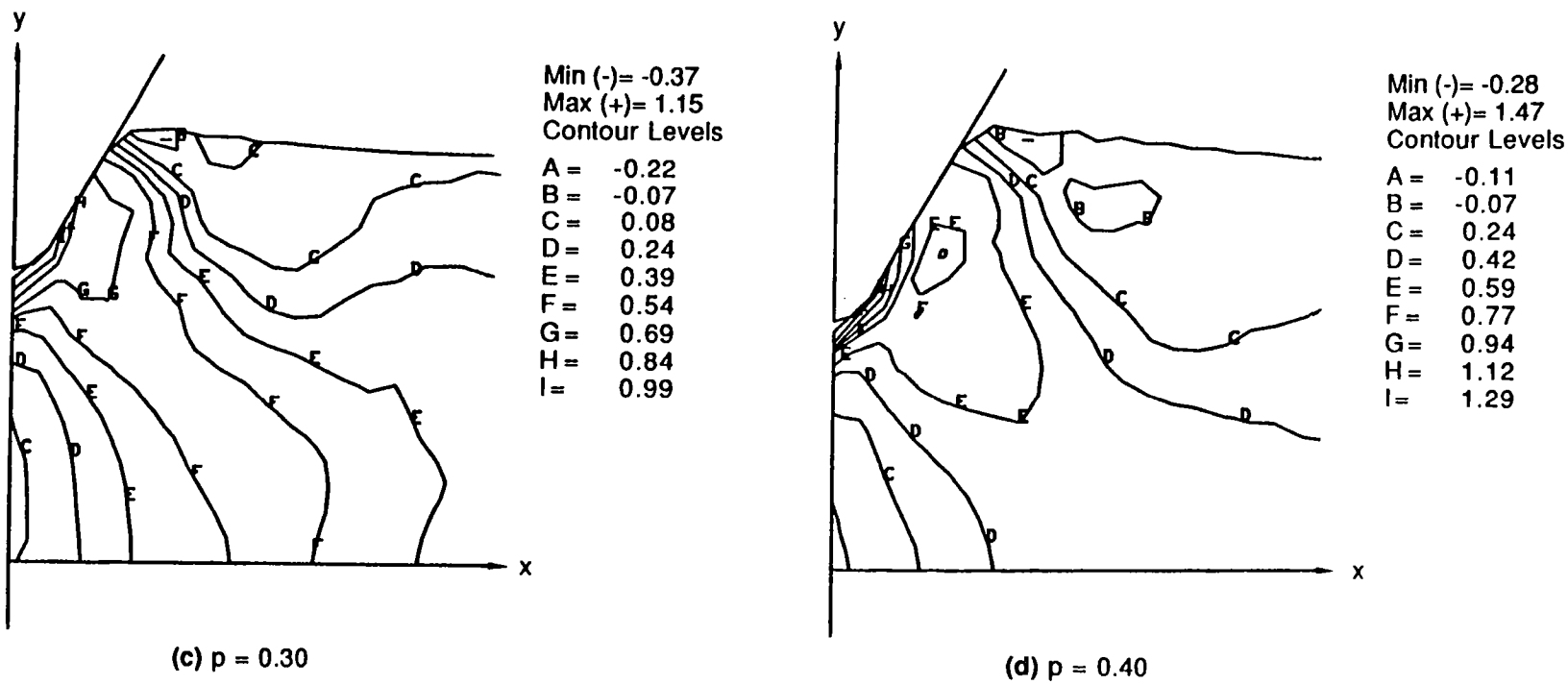

Figure J-26. Contours of shear stress (τ_{xy}/Y) in an ice layer on concrete produced by penetration of a wedge (concluded)

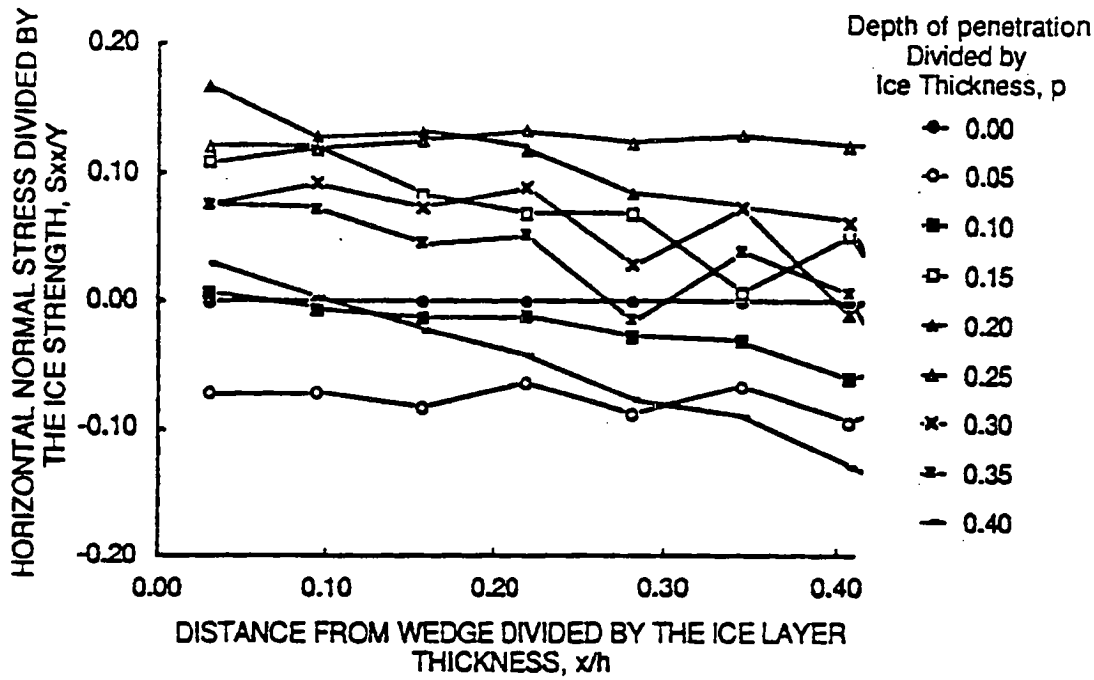

J-27. Horizontal normal stresses on the ice side of the ice/pavement interface

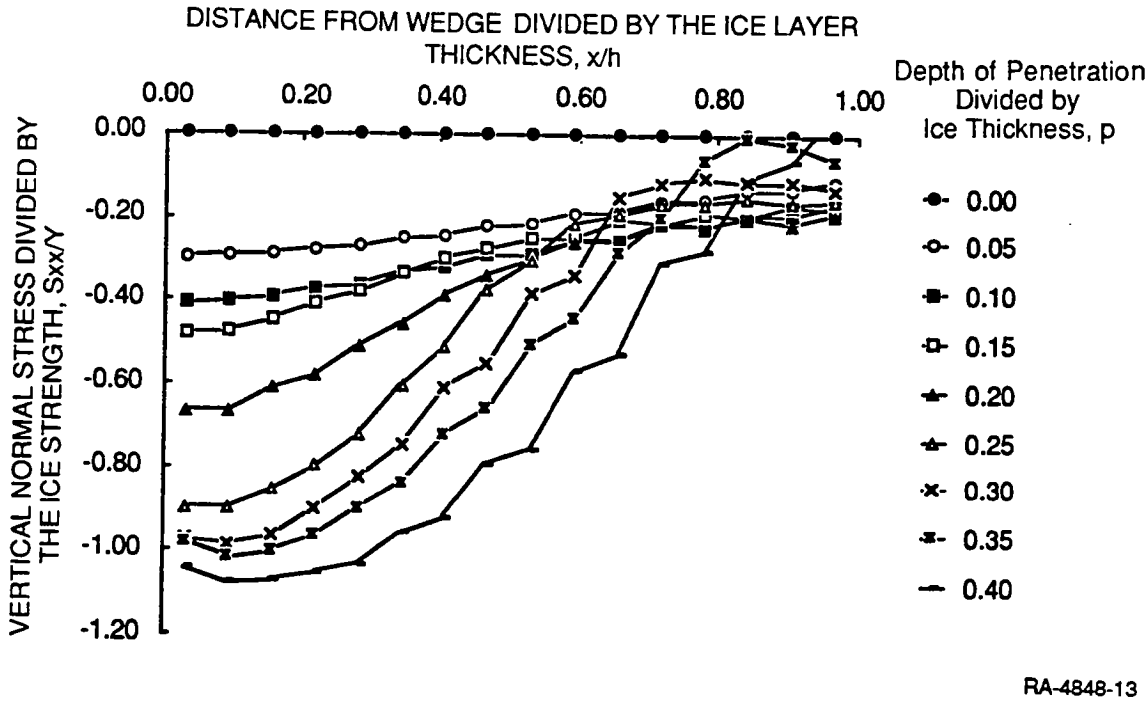

Figure J-28. Vertical normal stress on the ice side of the ice/pavement interface

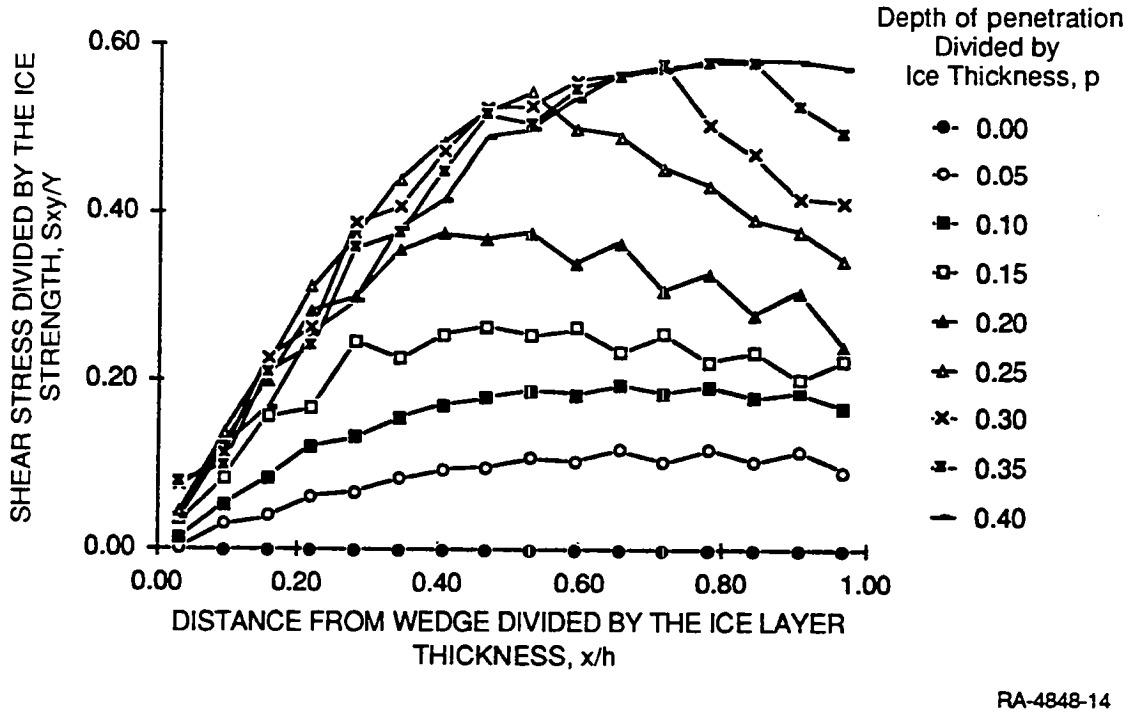

Figure J-29. Shear stress on the ice side of the ice/pavement interface

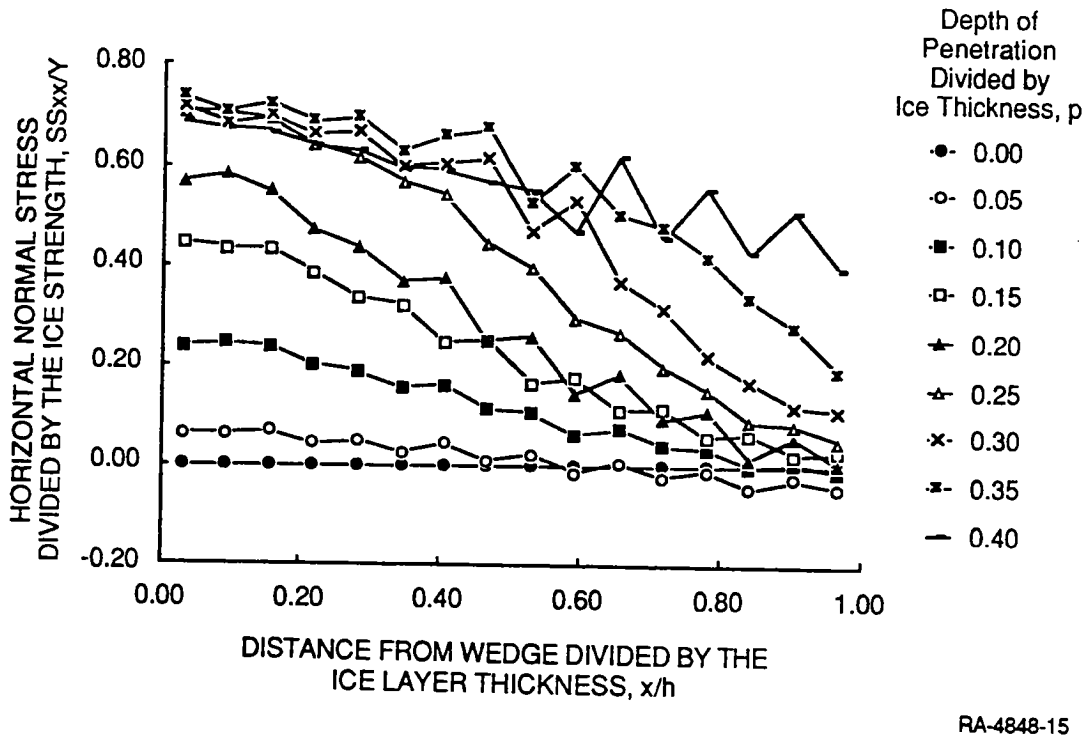

Figure J-30. Horizontal normal stress on the concrete side of the ice/pavement interface

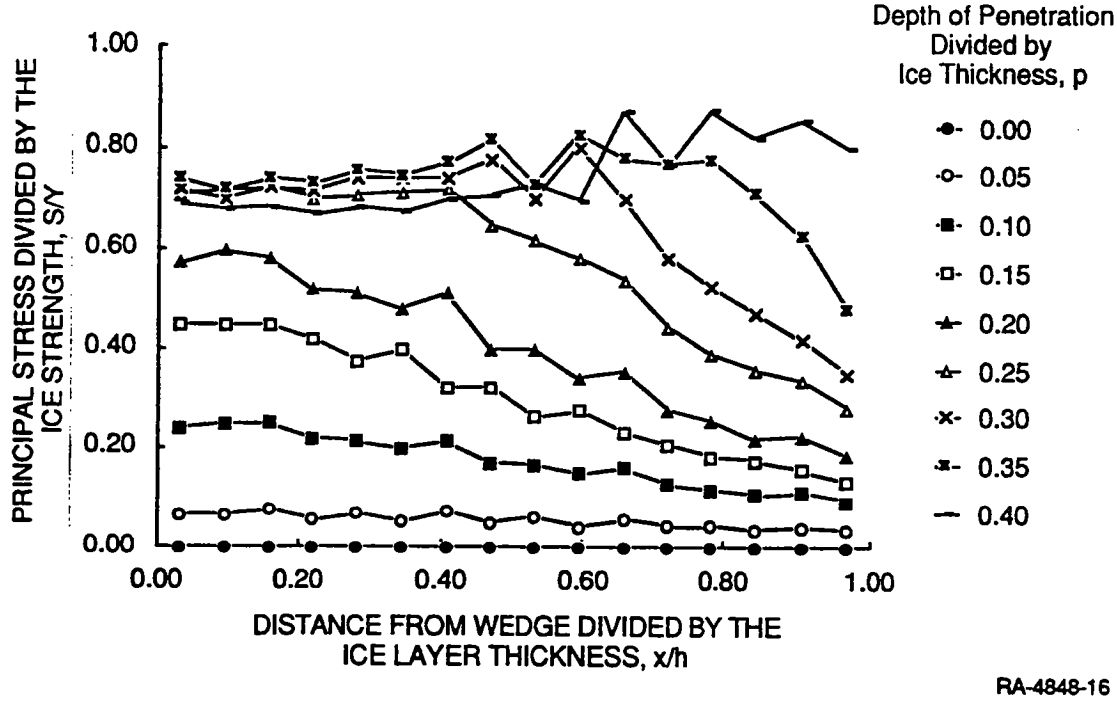

Figure J-31. Principal stress on the pavement side of the ice pavement interface

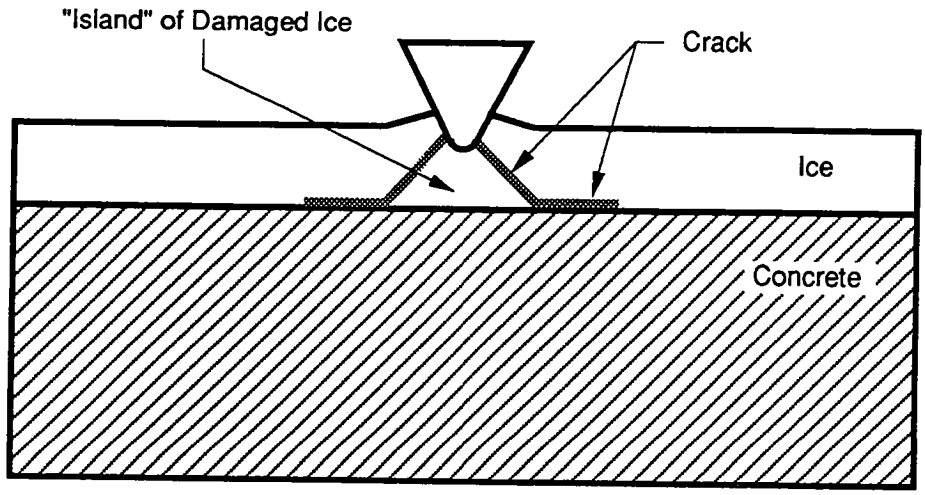

Figure J-32. Schematic of the damage zone in an ice layer from penetration by a wedge

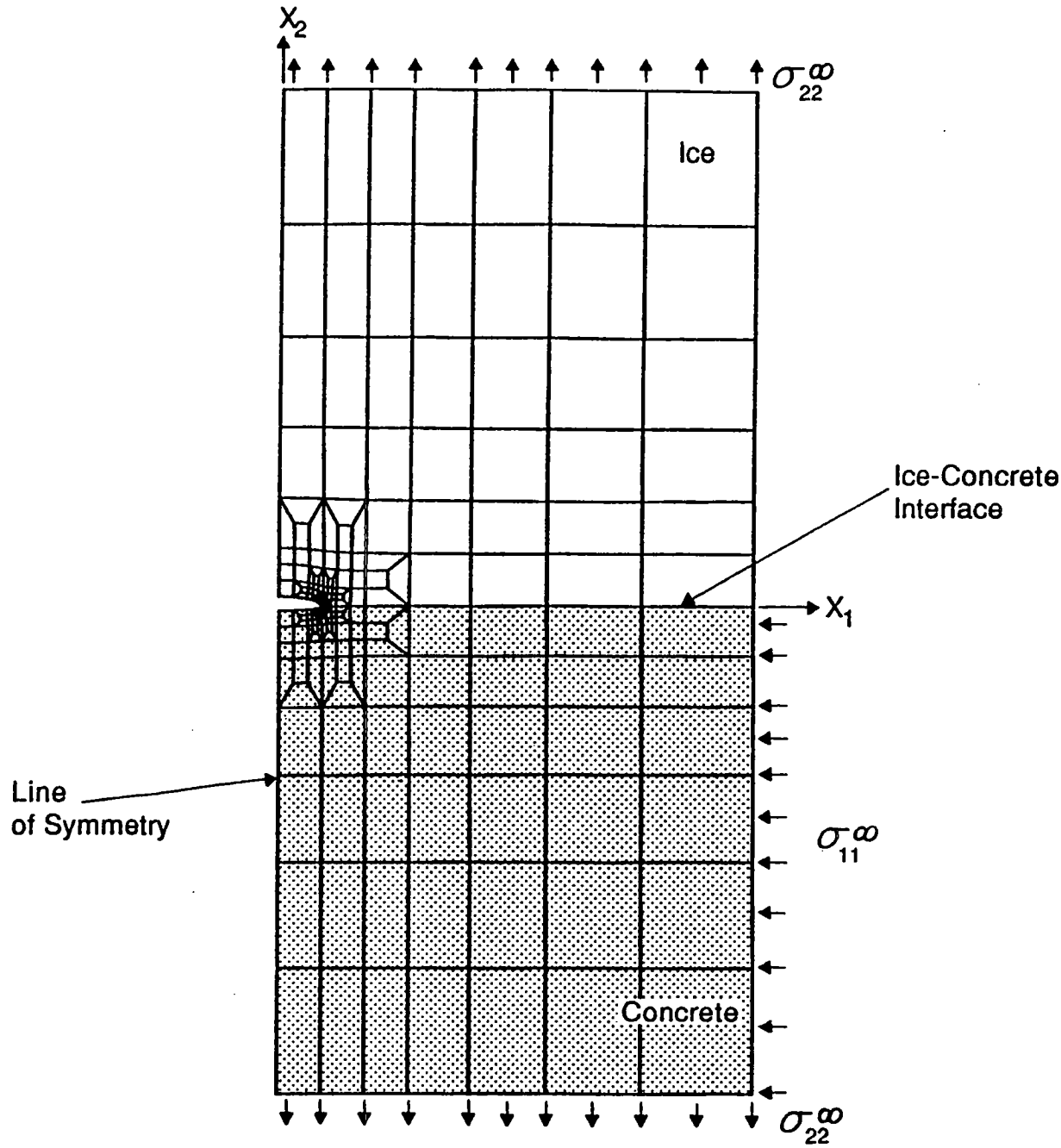

Figure J-33. Rectangular mesh layout for the test problem

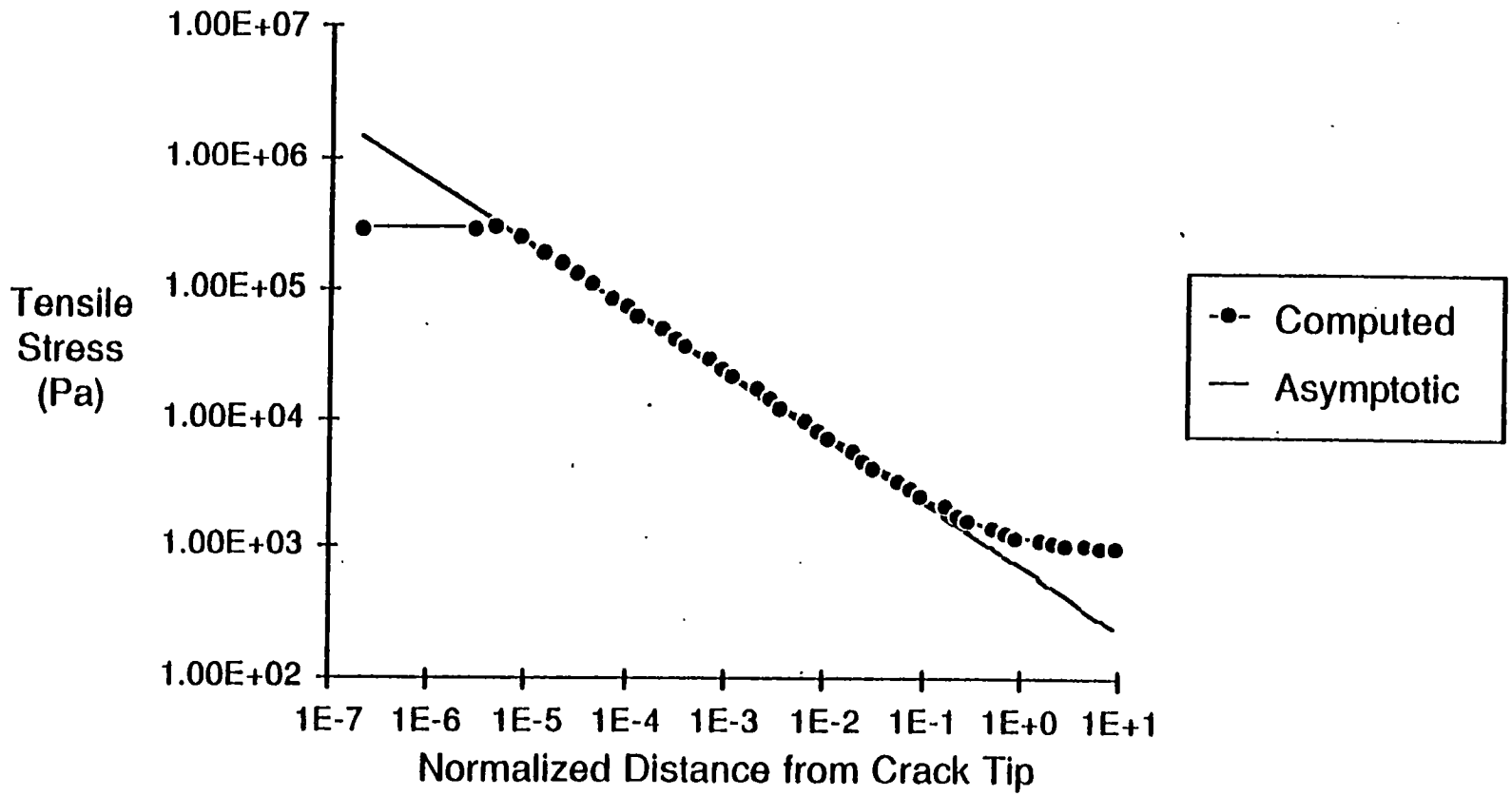

Figure J-34. Bond line stress distribution ahead of crack tip

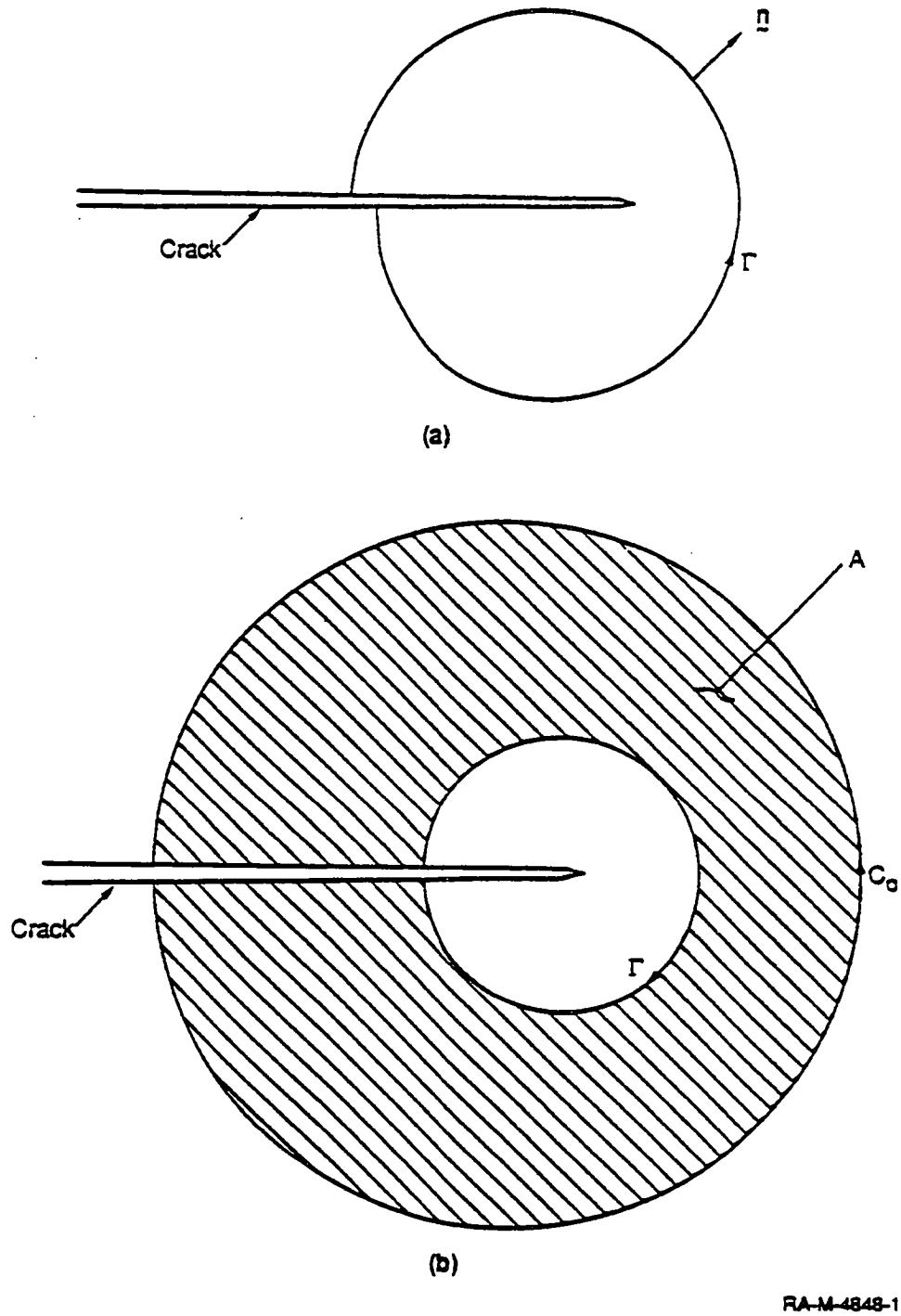

Figure J-35. Contour and domain for J integral computations for (a) line integral representation, (b) area integral representation

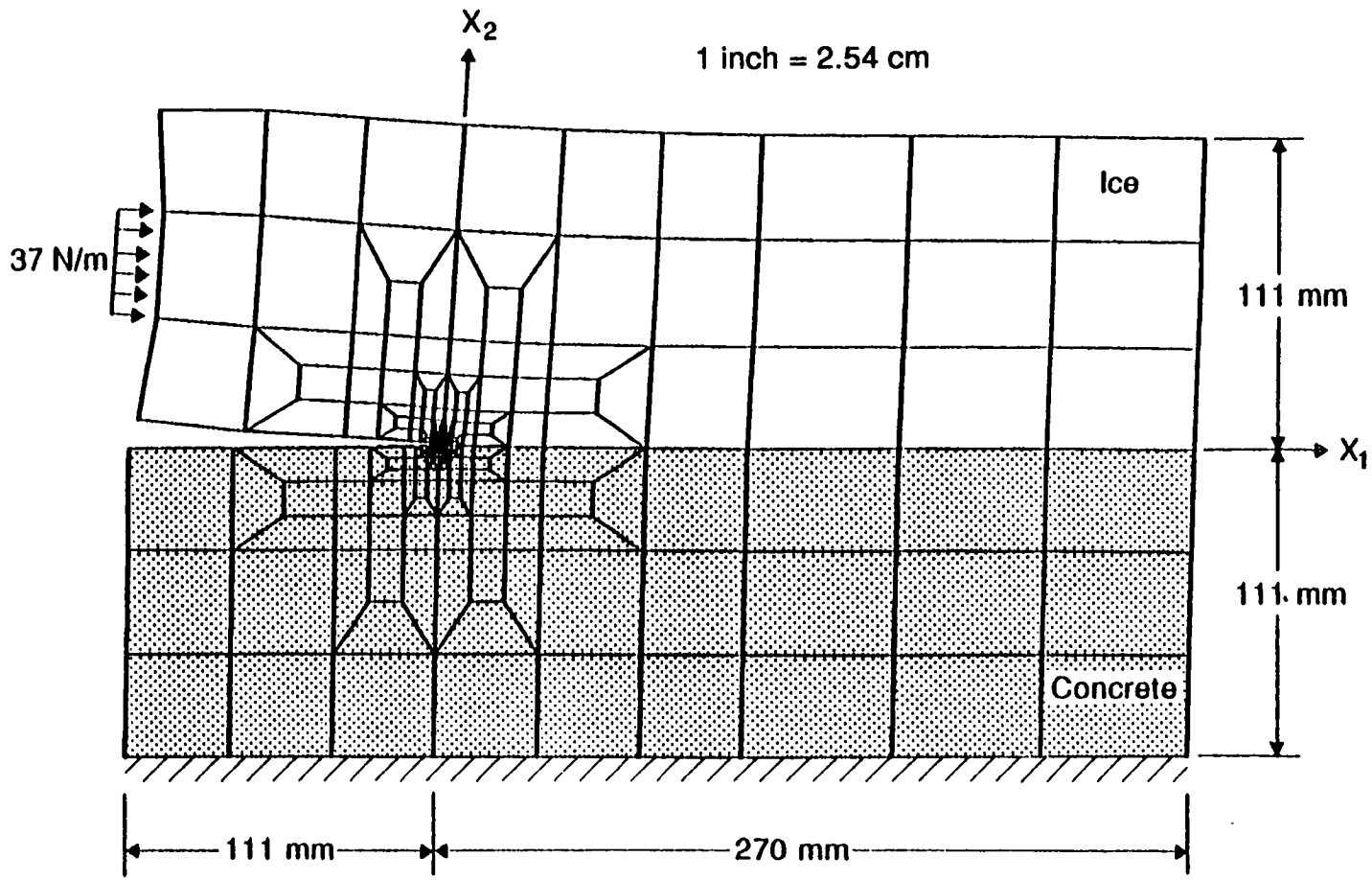

Figure J-36. Rectangular mesh layout for the shear test

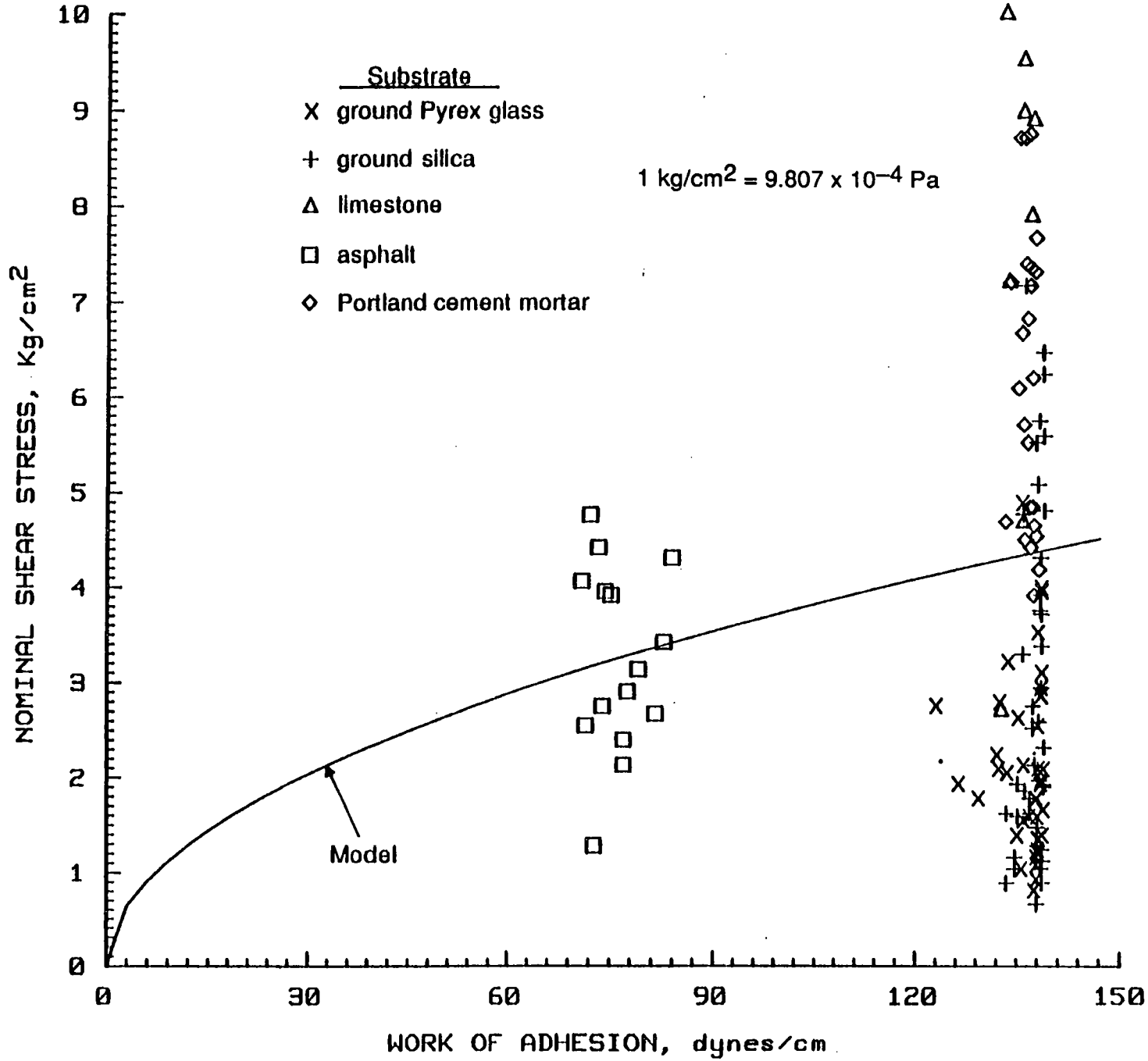

Figure J-37. Comparison of the model with shear test data

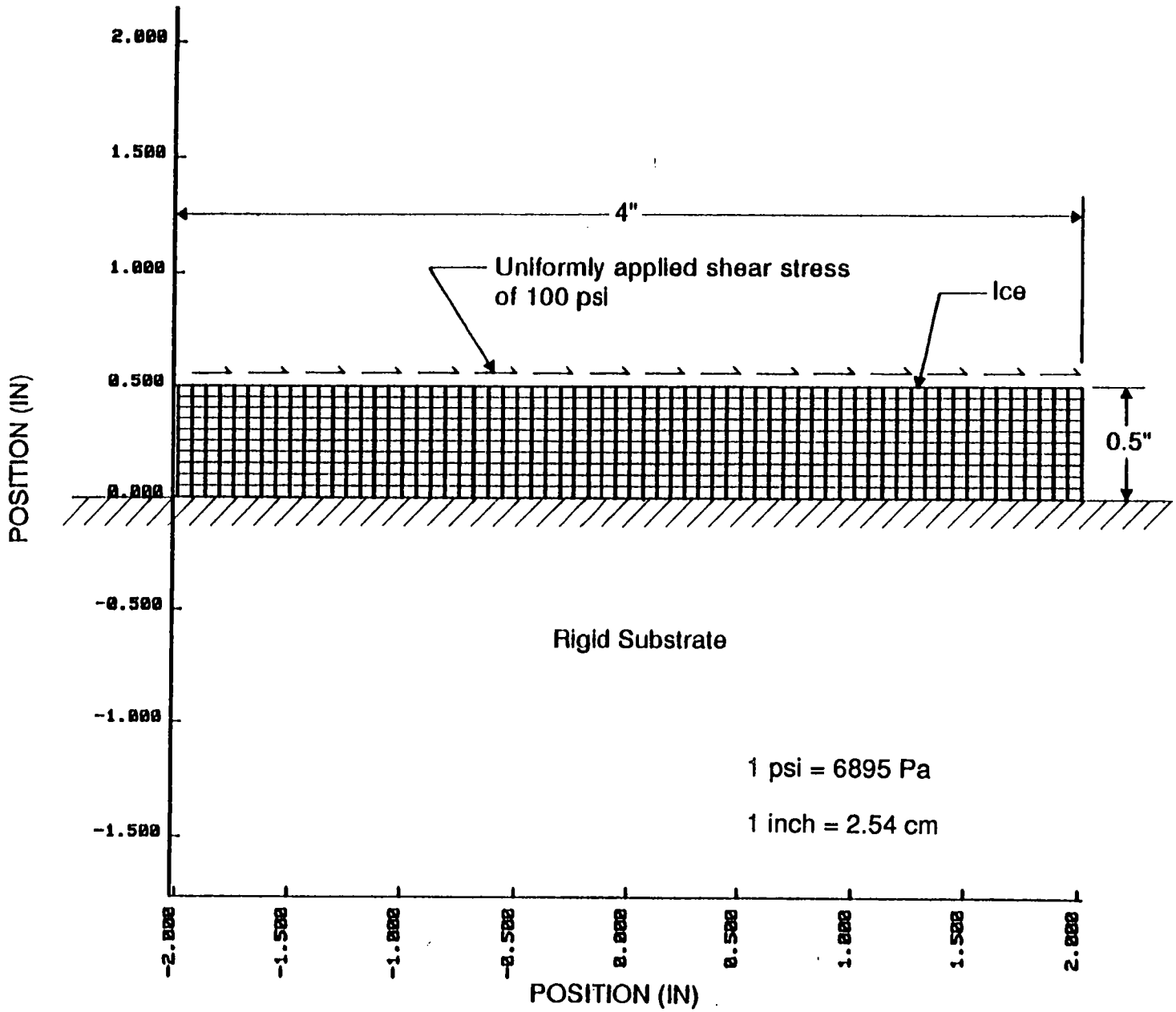

Figure J-38. FEM simulation geometry for ice-substrate shear tests with horizontal load applied to a unchamfered mold

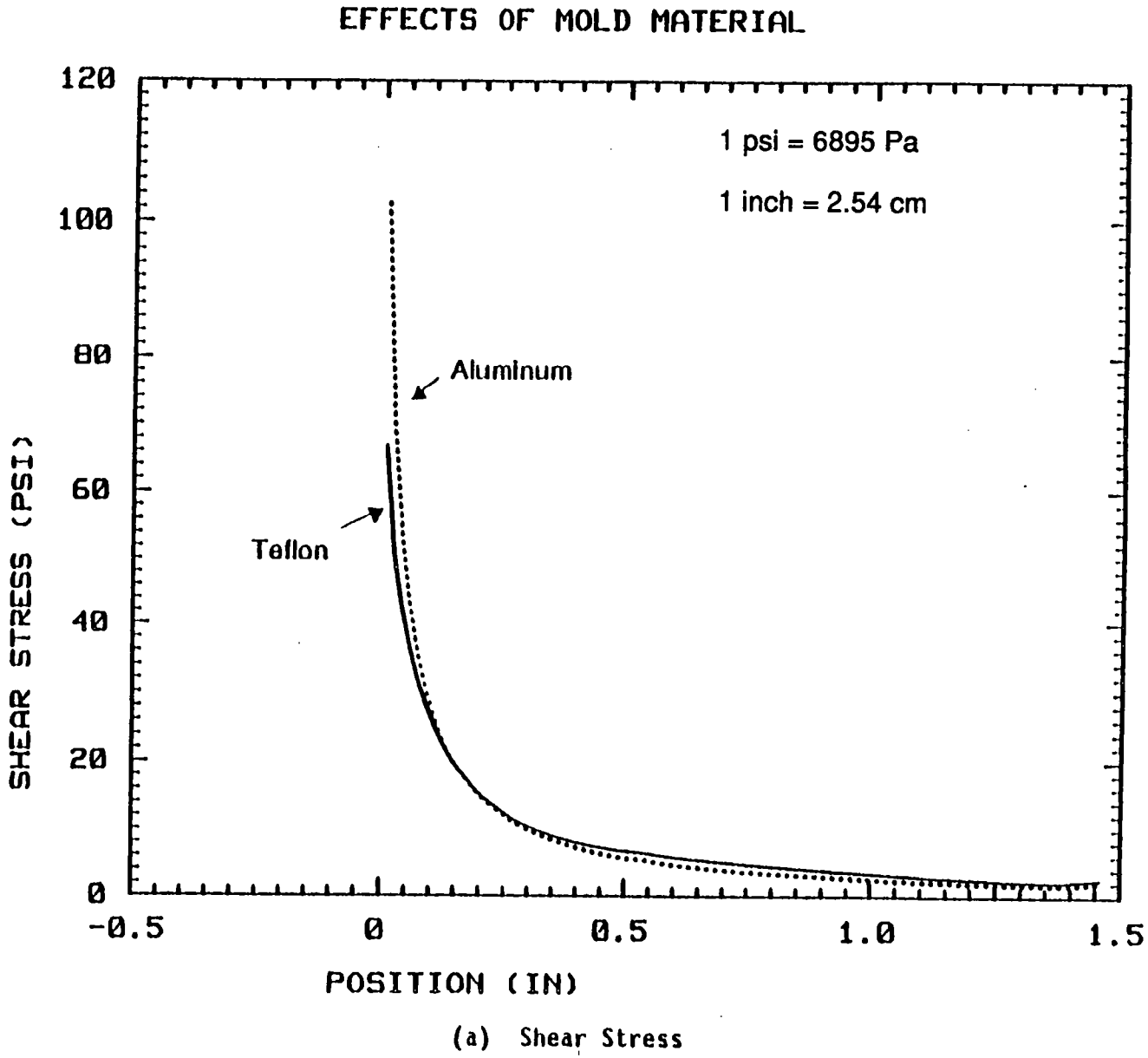

(a) Shear Stress

Figure J-39. Interfacial stresses in the ice induced by a horizontal load applied on an unchamfered mold

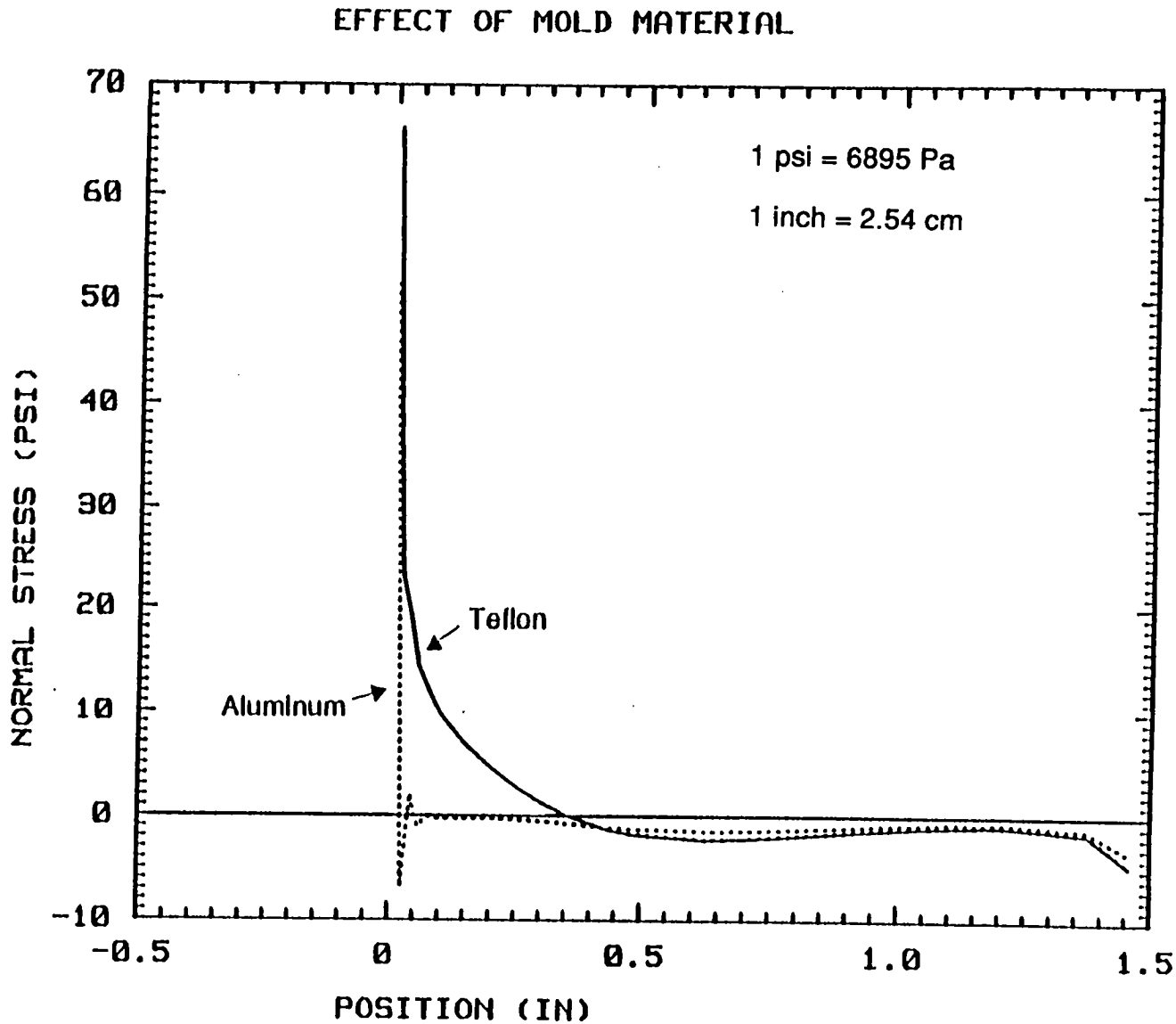

(b) Normal Stress

Figure J-39. Interfacial stresses in the ice induced by a horizontal load applied on an unchamfered mold (concluded)

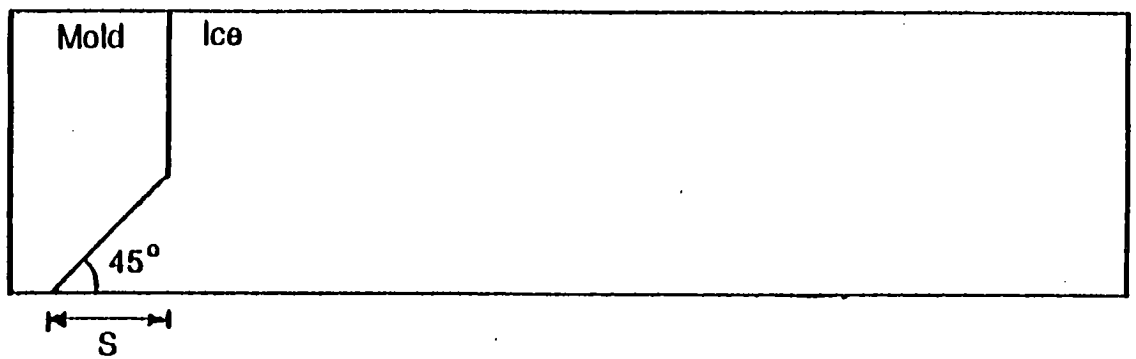

1 inch = 2.54 cm

S = 0 inches for no chamfer
= 0.625 inches for small chamfer
= 0.1875 inches for large chamfer

Unspecified dimensions are the same as in Figure V-6.

Figure J-40. FEM simulation geometry for ice-substrate shear tests with a horizontal load applied to a chamfered mold

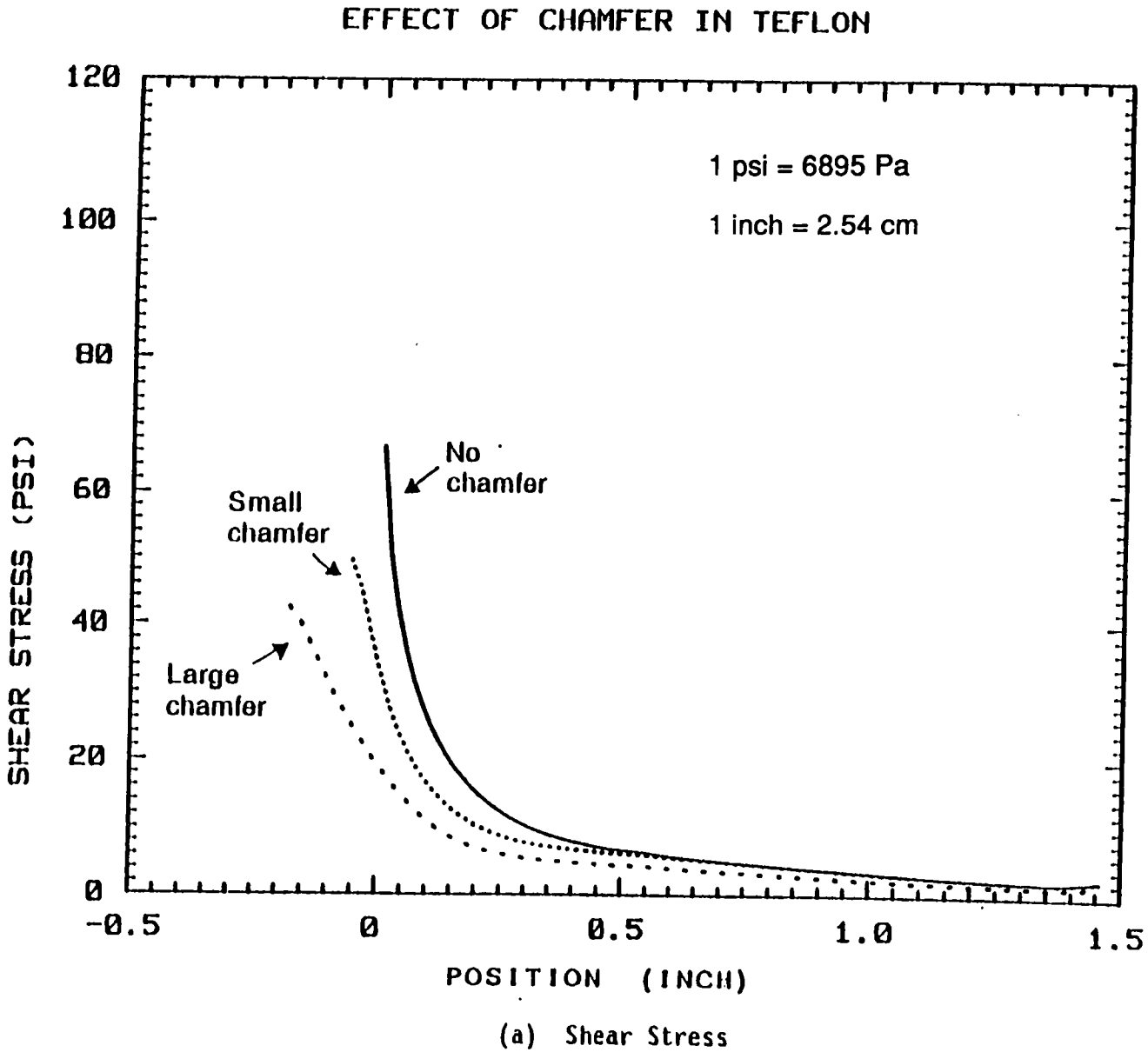

Figure J-41. Interfacial stresses in the ice induced by a horizontal load applied to a chamfered Teflon mold

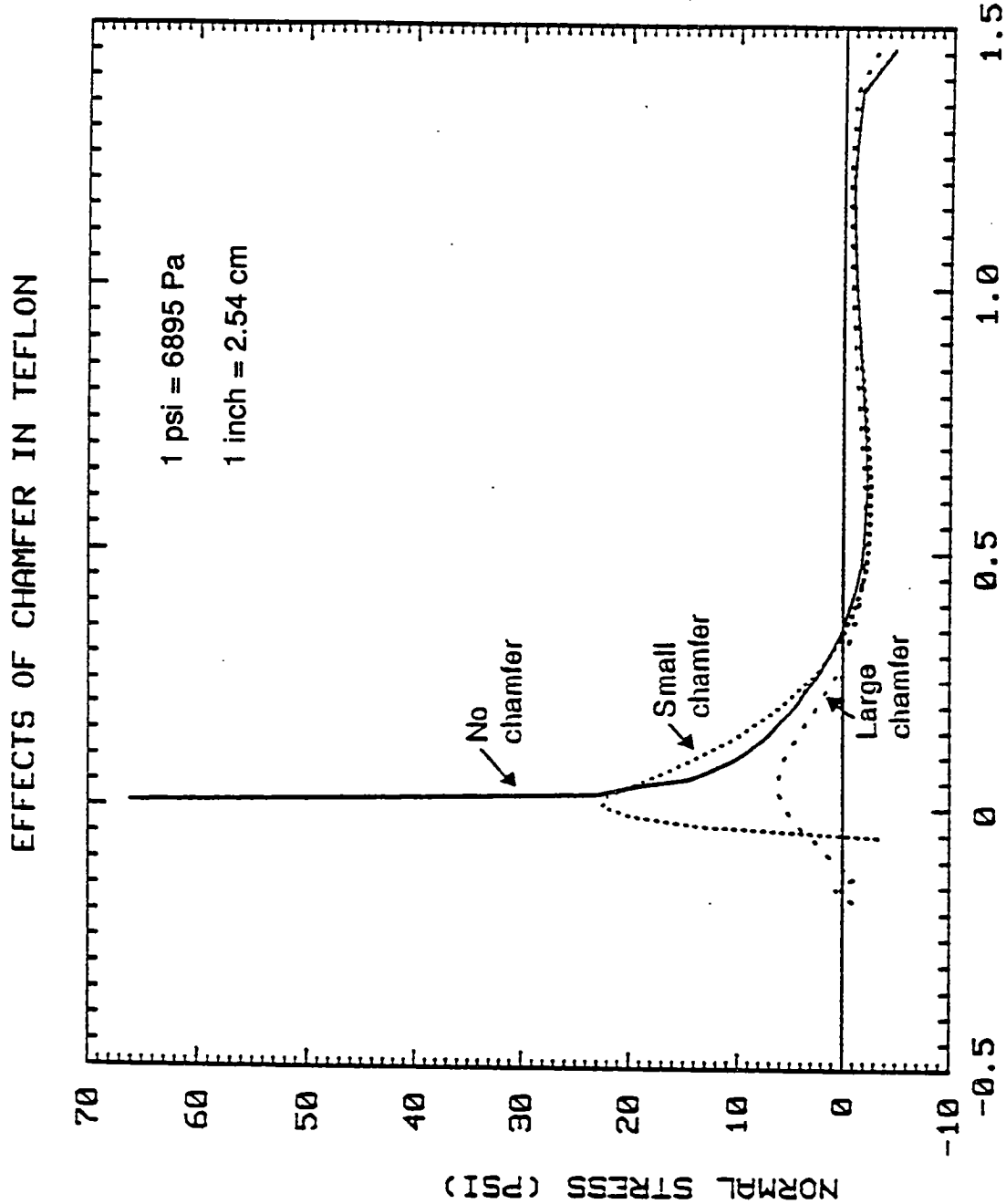

(b) Normal Stress

Figure J-41. Interfacial stresses in the ice induced by a horizontal load applied to a chamfered Teflon mold (concluded)

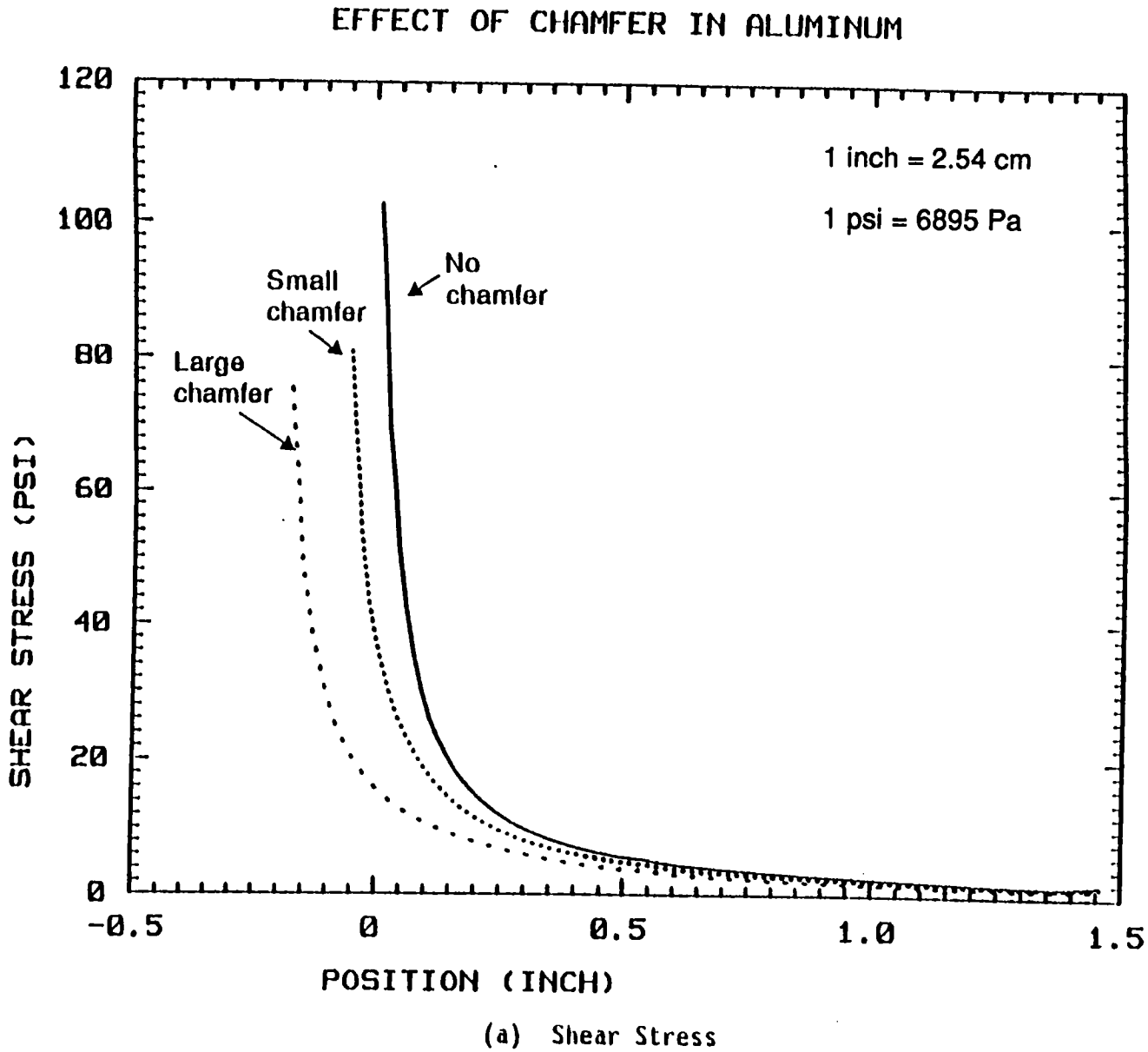

(a) Shear Stress

Figure J-42. Interfacial stresses in the ice induced by a horizontal load applied to a chamfered aluminum mold.

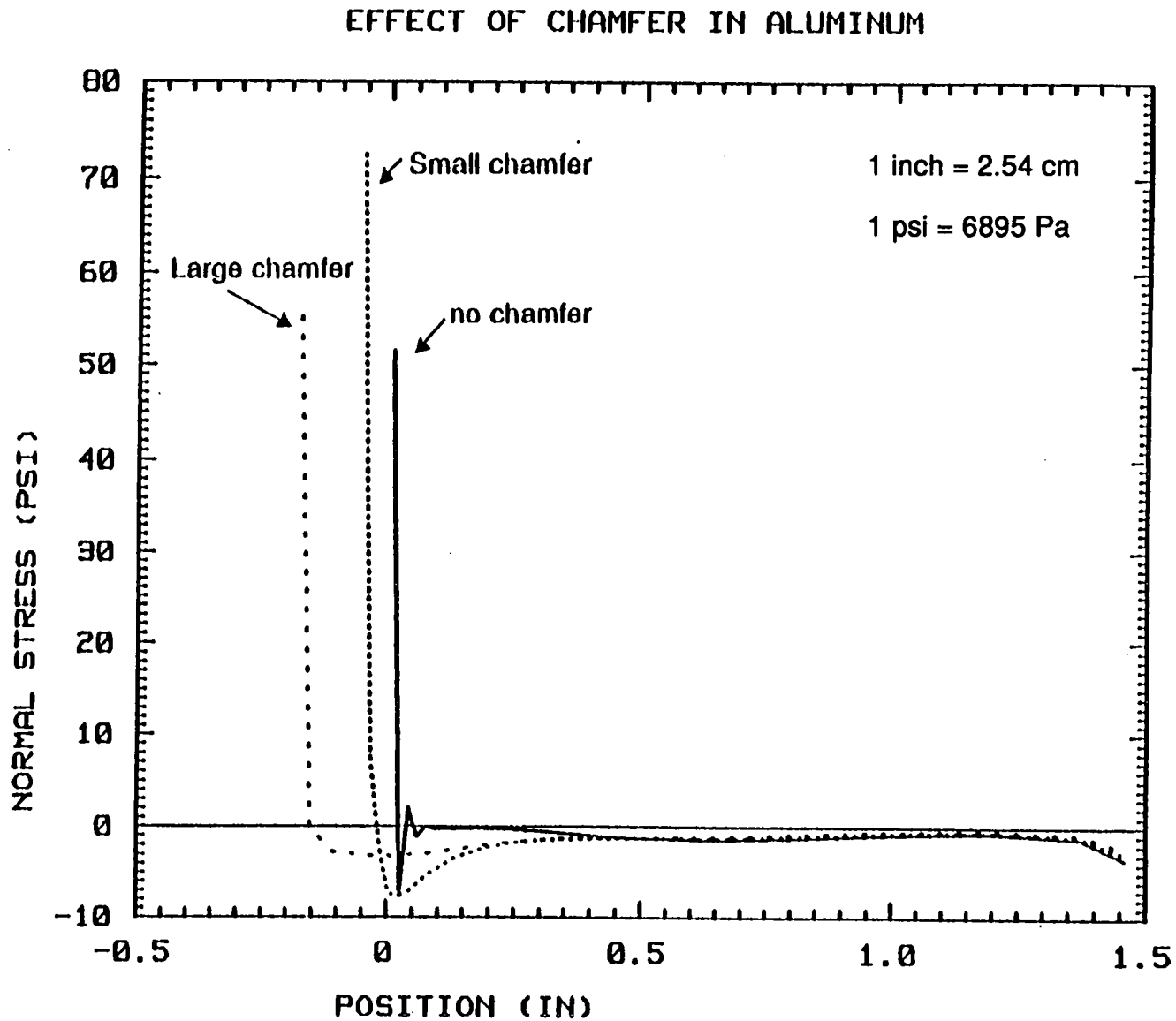

(b) Normal Stress

Figure J-42. Interfacial stresses in the ice induced by a horizontal load applied to a chamfered aluminum mold (concluded)

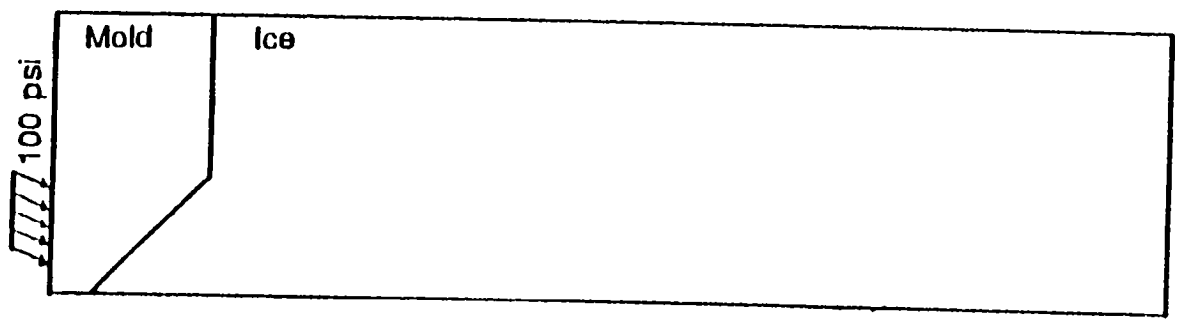

1 psi = 6895 Pa

Unspecified dimensions
are the same as in Figure V-6.

Figure J-43. FEM simulation geometry for ice-substrate shear tests with an angled load (30 degrees below horizontal) applied to a chamfered mold

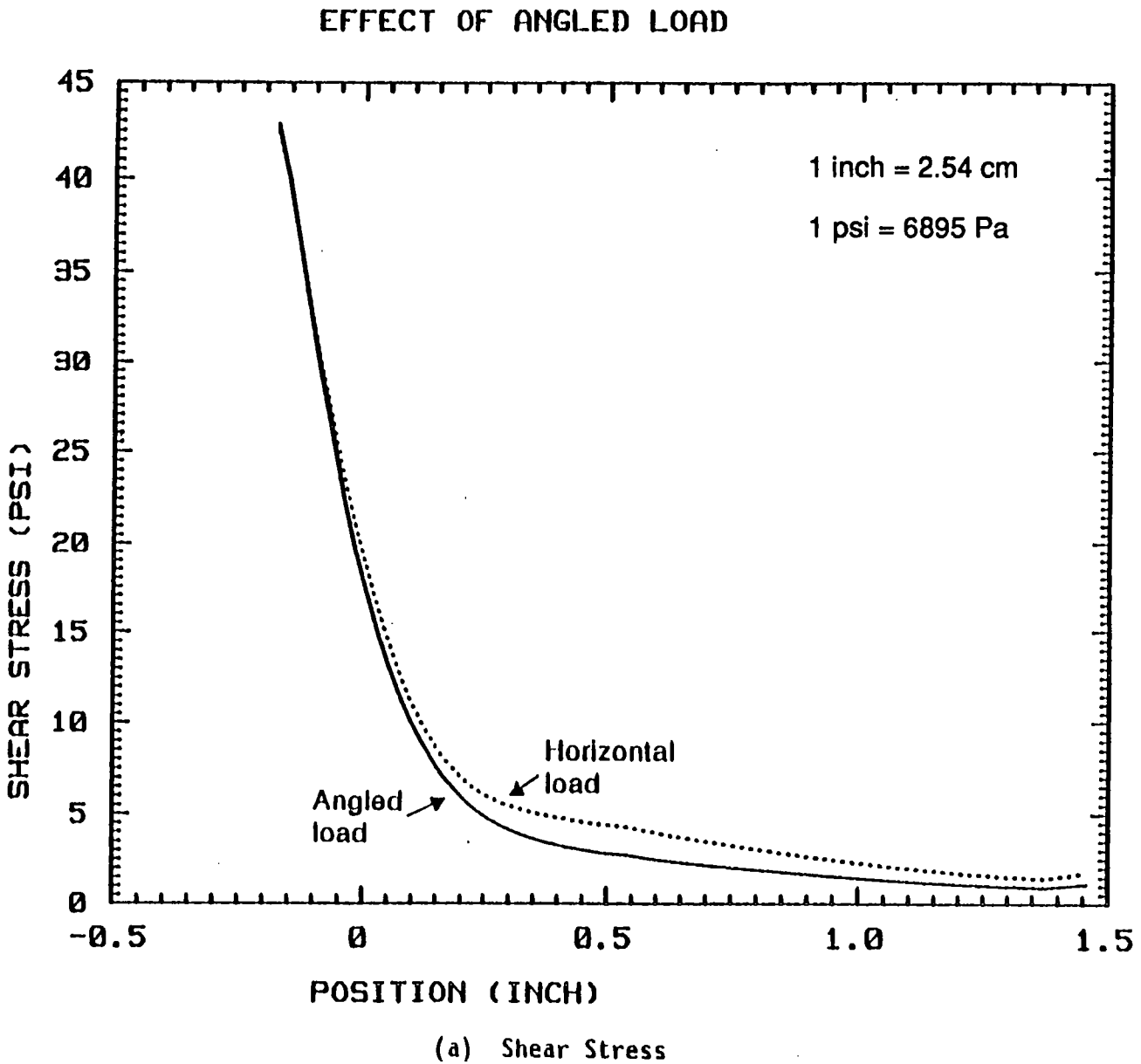

Figure J-44. Interfacial stresses in the ice induced by an angled load (30 degrees below horizontal) applied to a chamfered Teflon mold

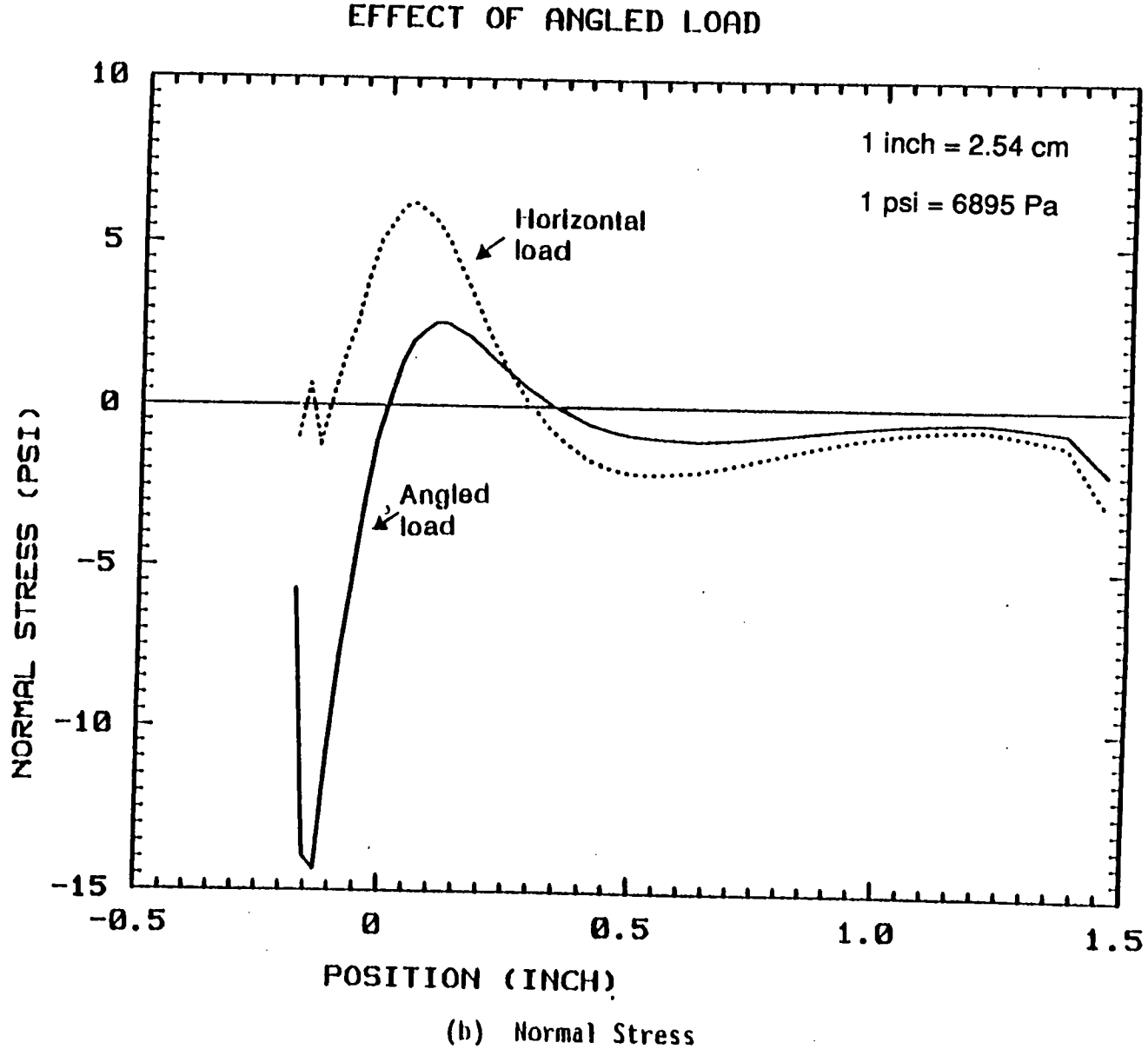

(b) Normal Stress

Figure J-44. Interfacial stresses in the ice induced by an angled load (30 degrees below horizontal) applied to a chamfered Teflon mold (concluded)

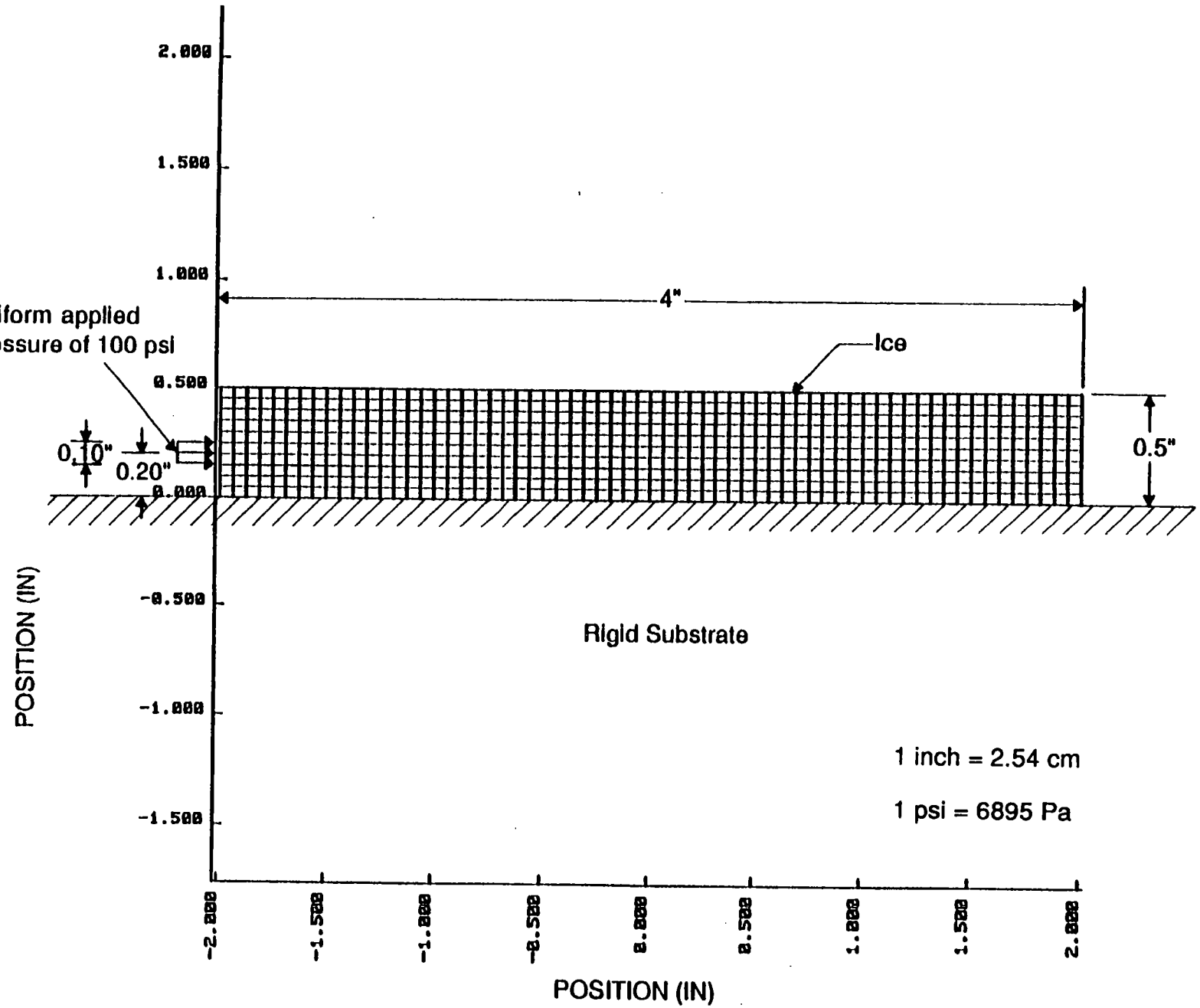

Figure J-45. Uniform shear stress applied to the ice

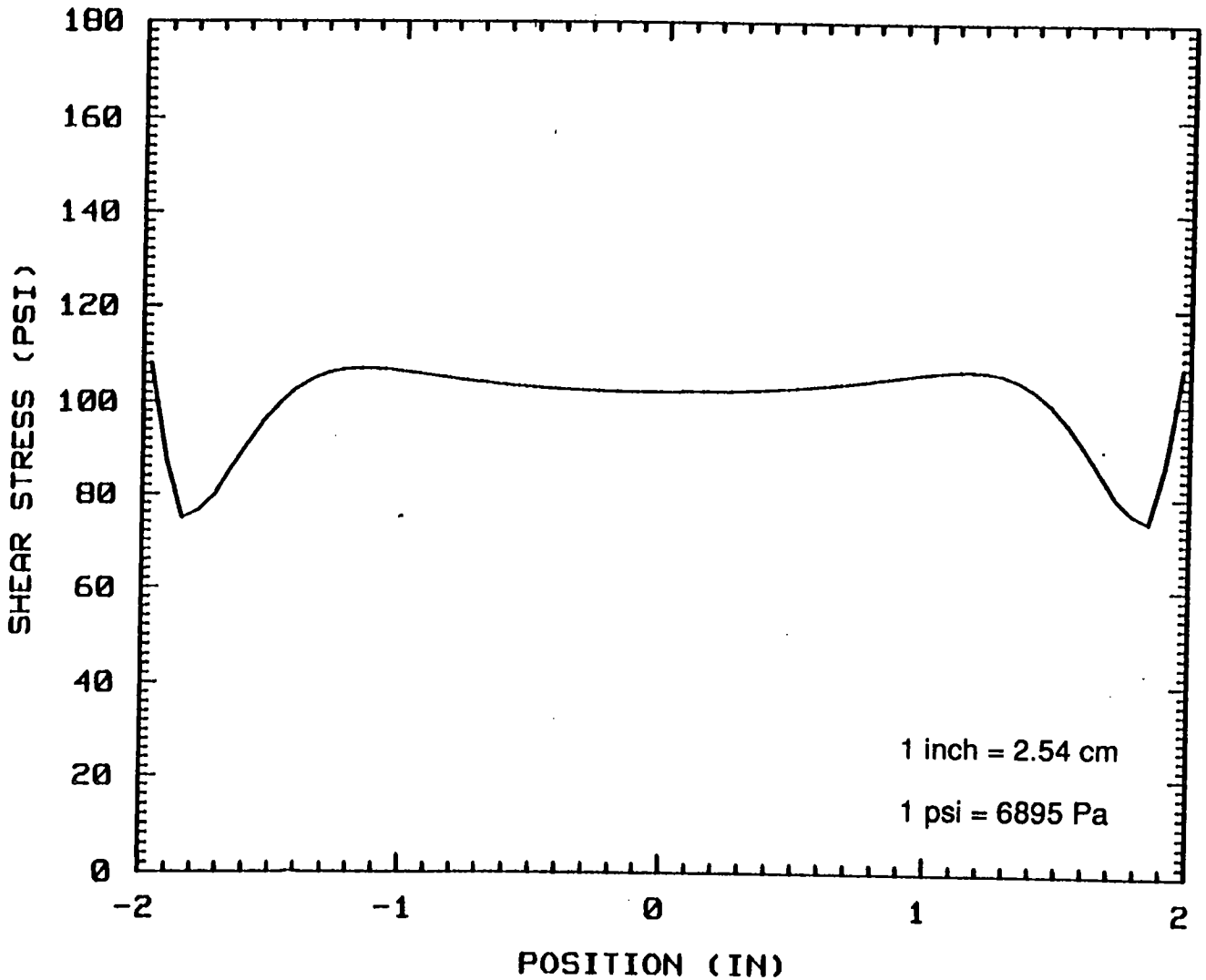

Figure J-46. Ice-pavement interface shear stress for a uniform shear stress applied to the top surface of the ice

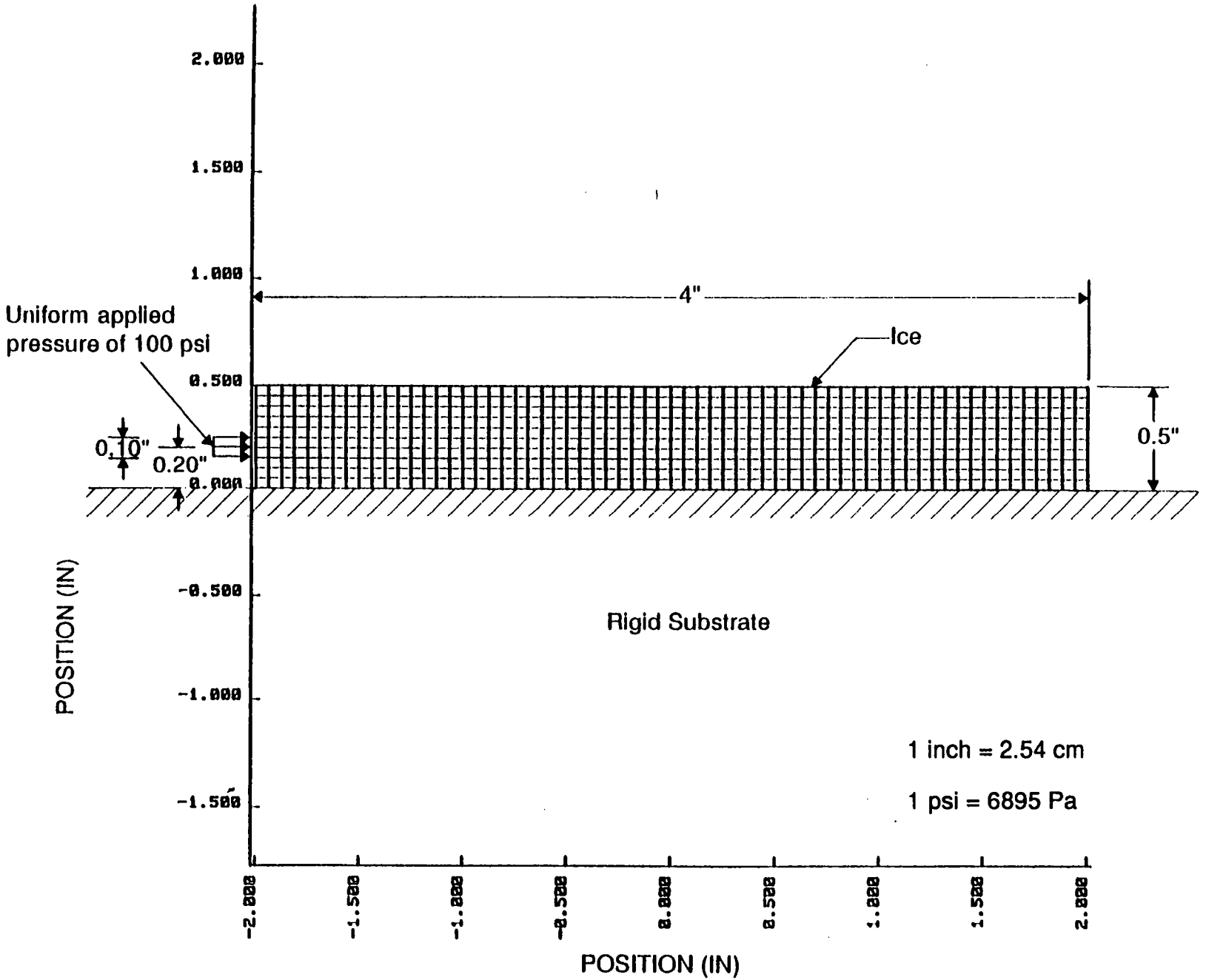

Figure J-47. Uniform pressure applied to edge of ice on a smooth substrate

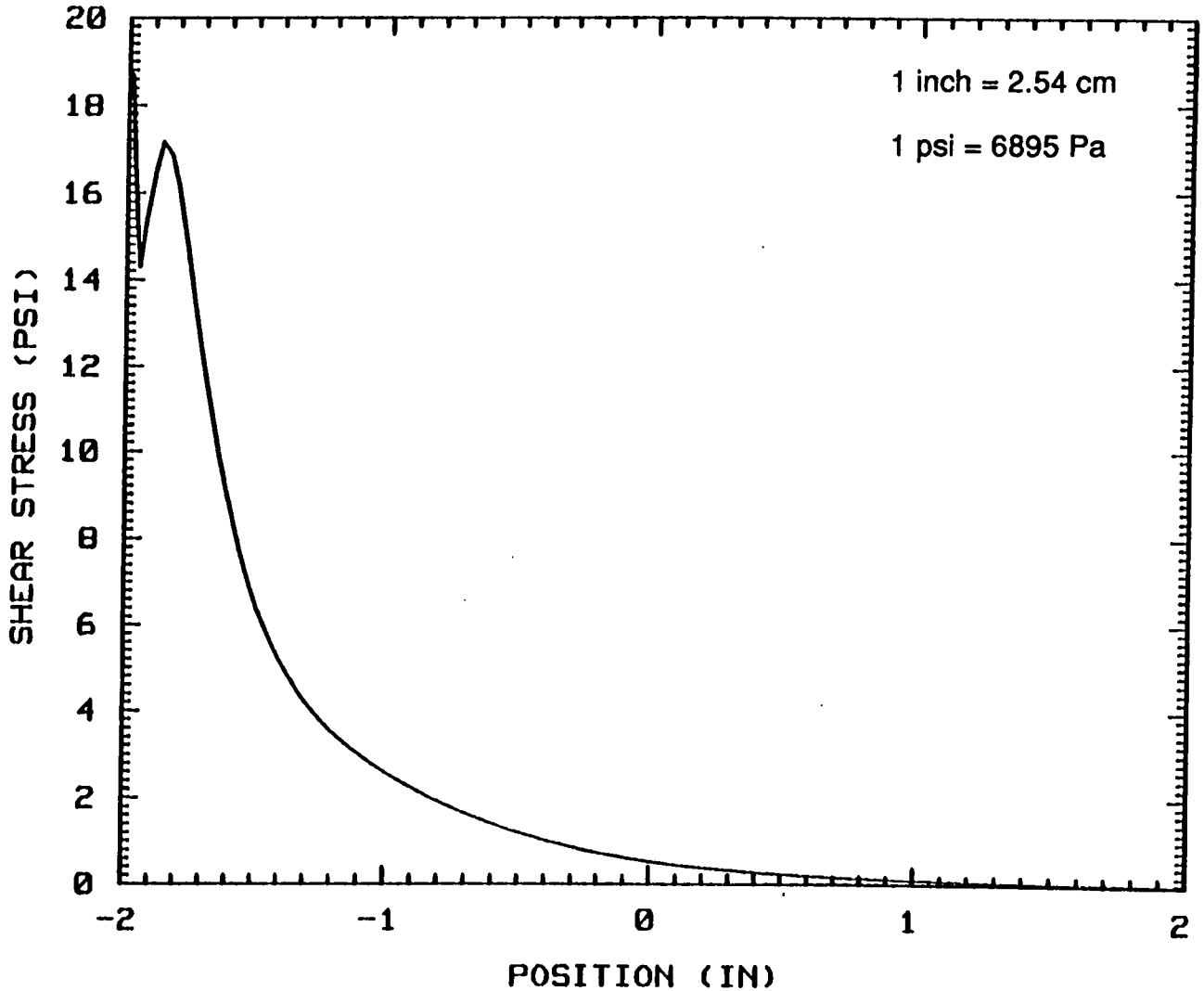

Figure J-48. Interface shear stress from a uniform pressure applied to the vertical surface of the ice at the edge

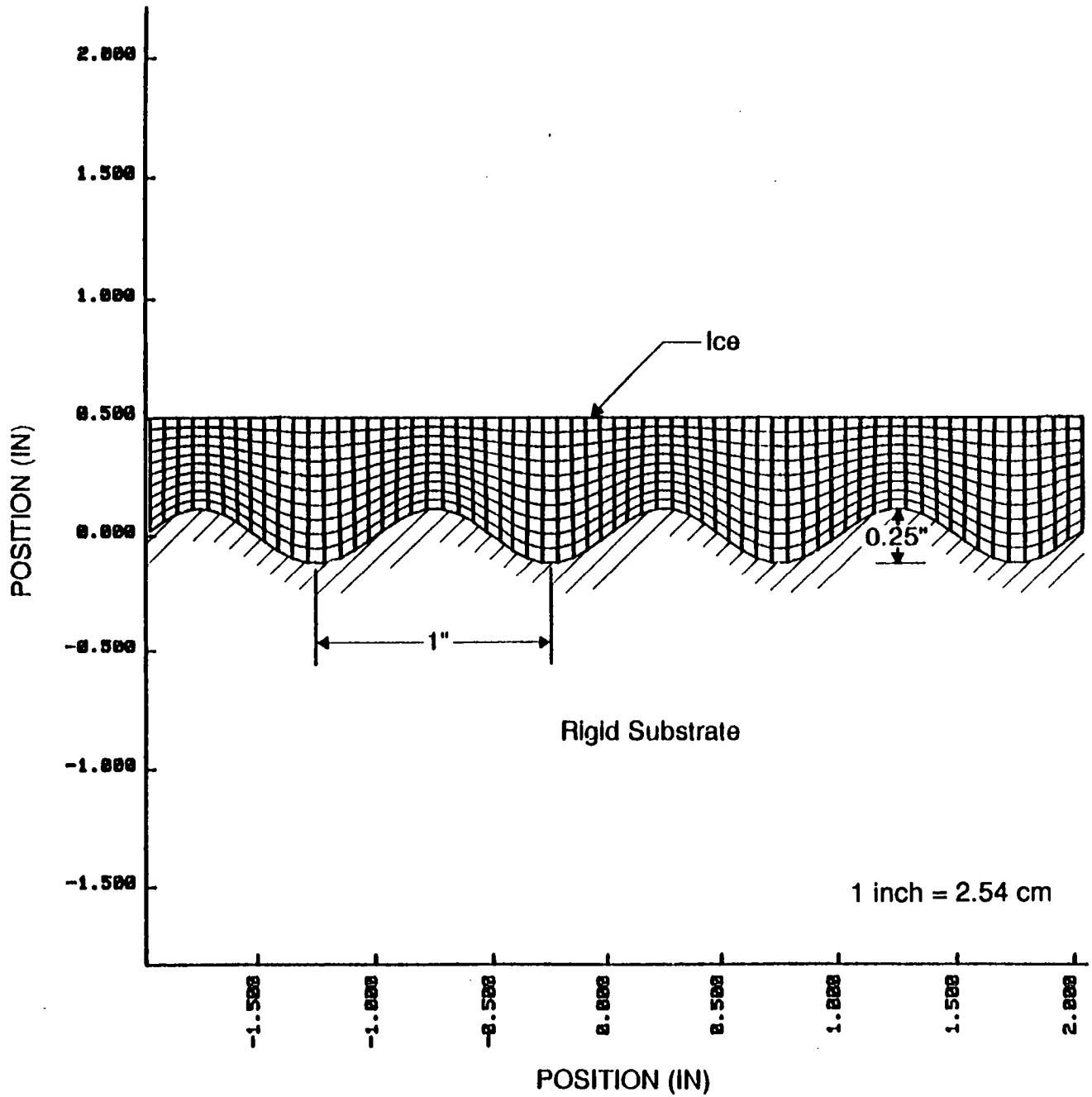

Figure J-49. Profile of ice on a sinusoidal substrate with 2-in wavelength

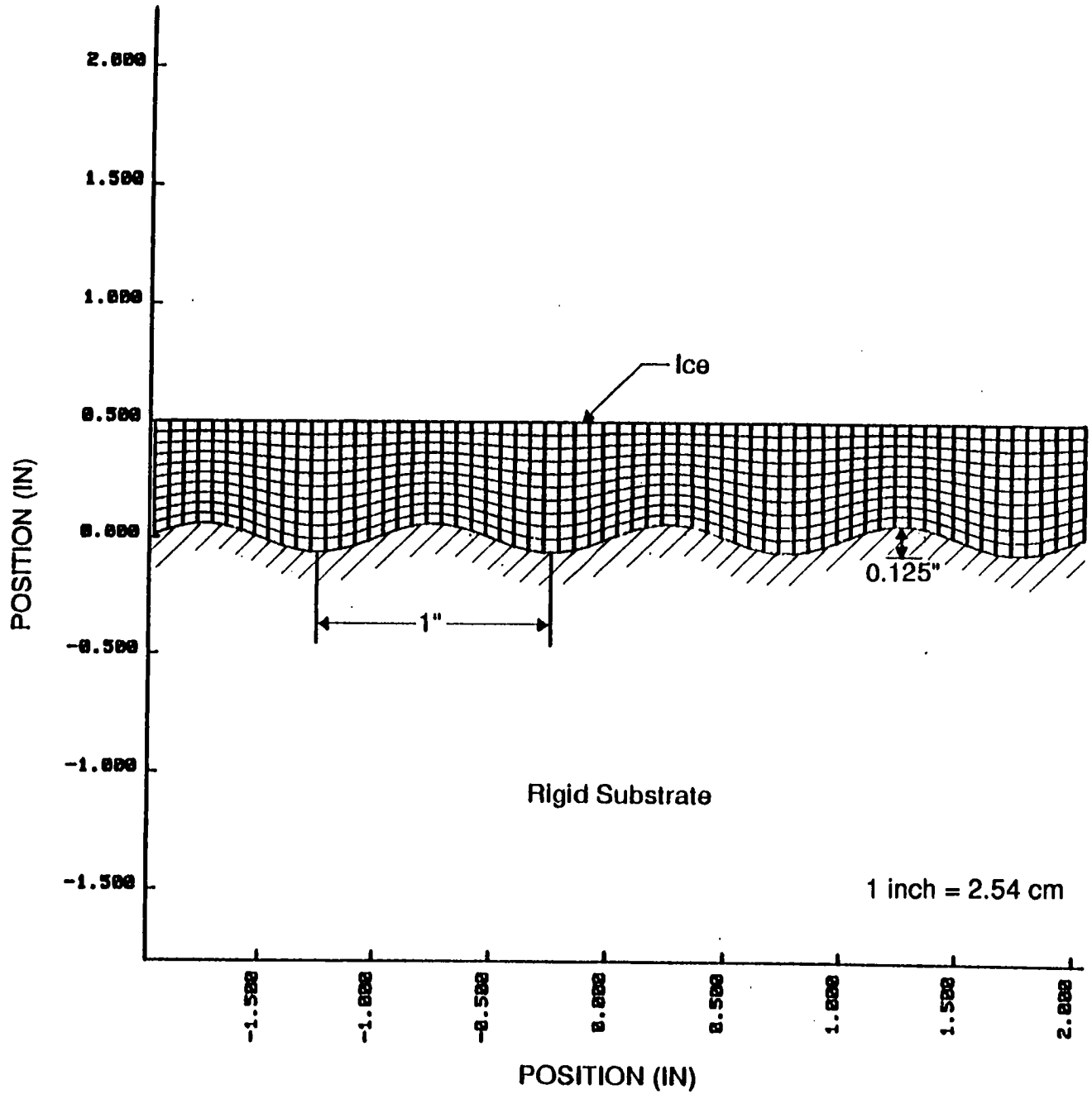

Figure J-50. Profile of ice on a sinusoidal substrate with 1-in wavelength at 0.125-in amplitude

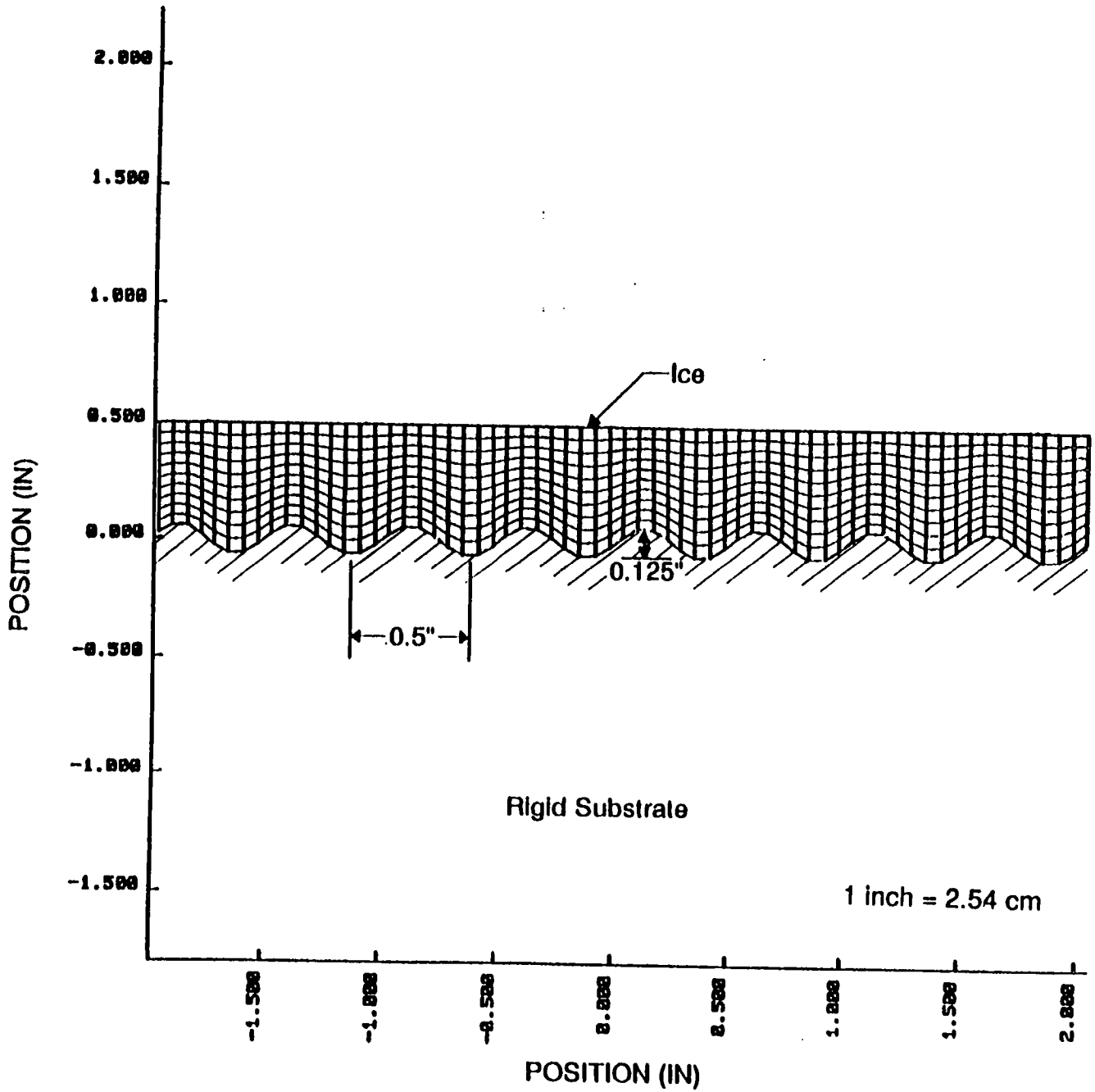

Figure J-51. Profile of ice on a sinusoidal substrate with 0.5-in wavelength and 0.125-in amplitude

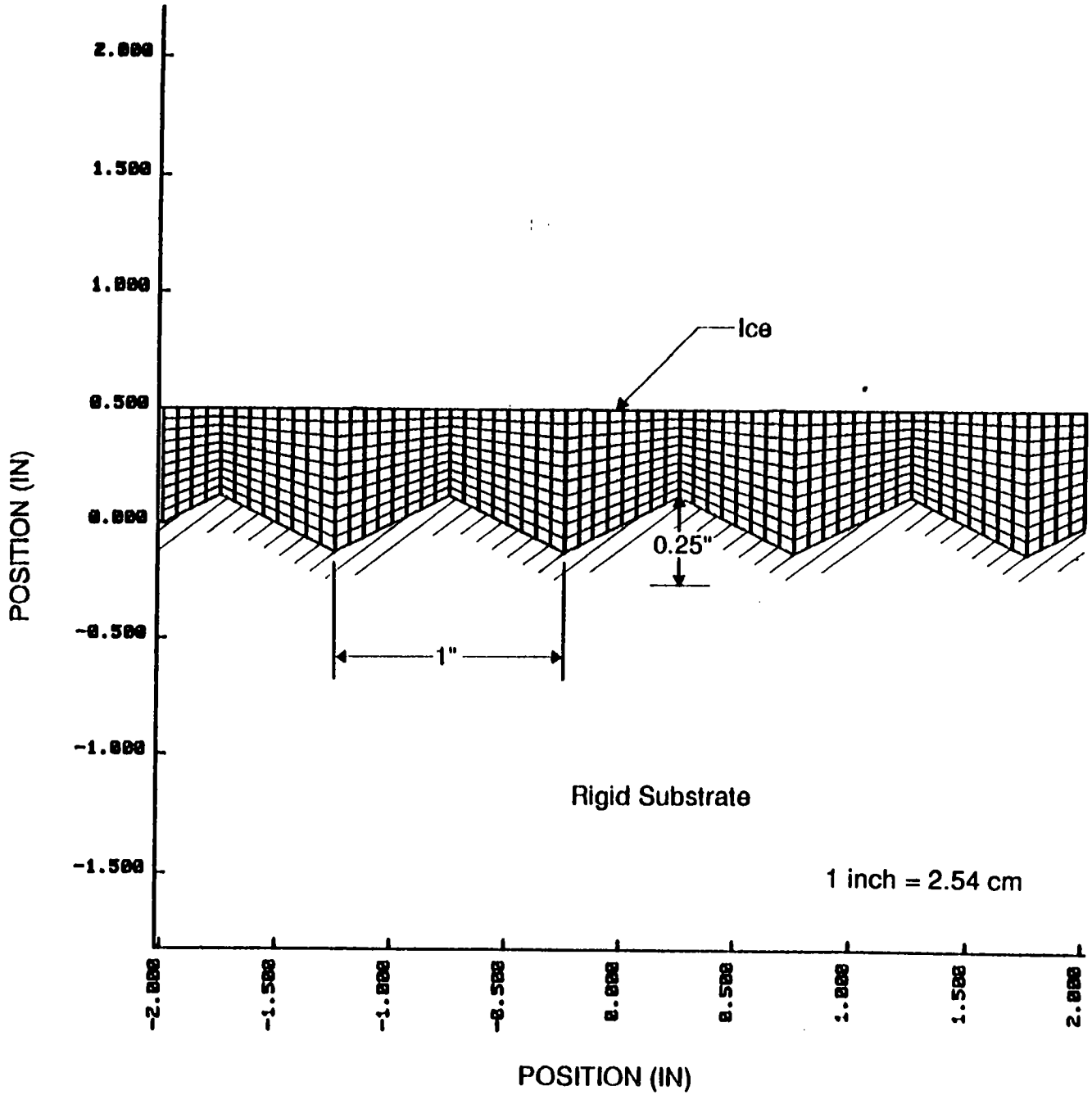

Figure J-52. Profile of ice on a triangular wave substrate

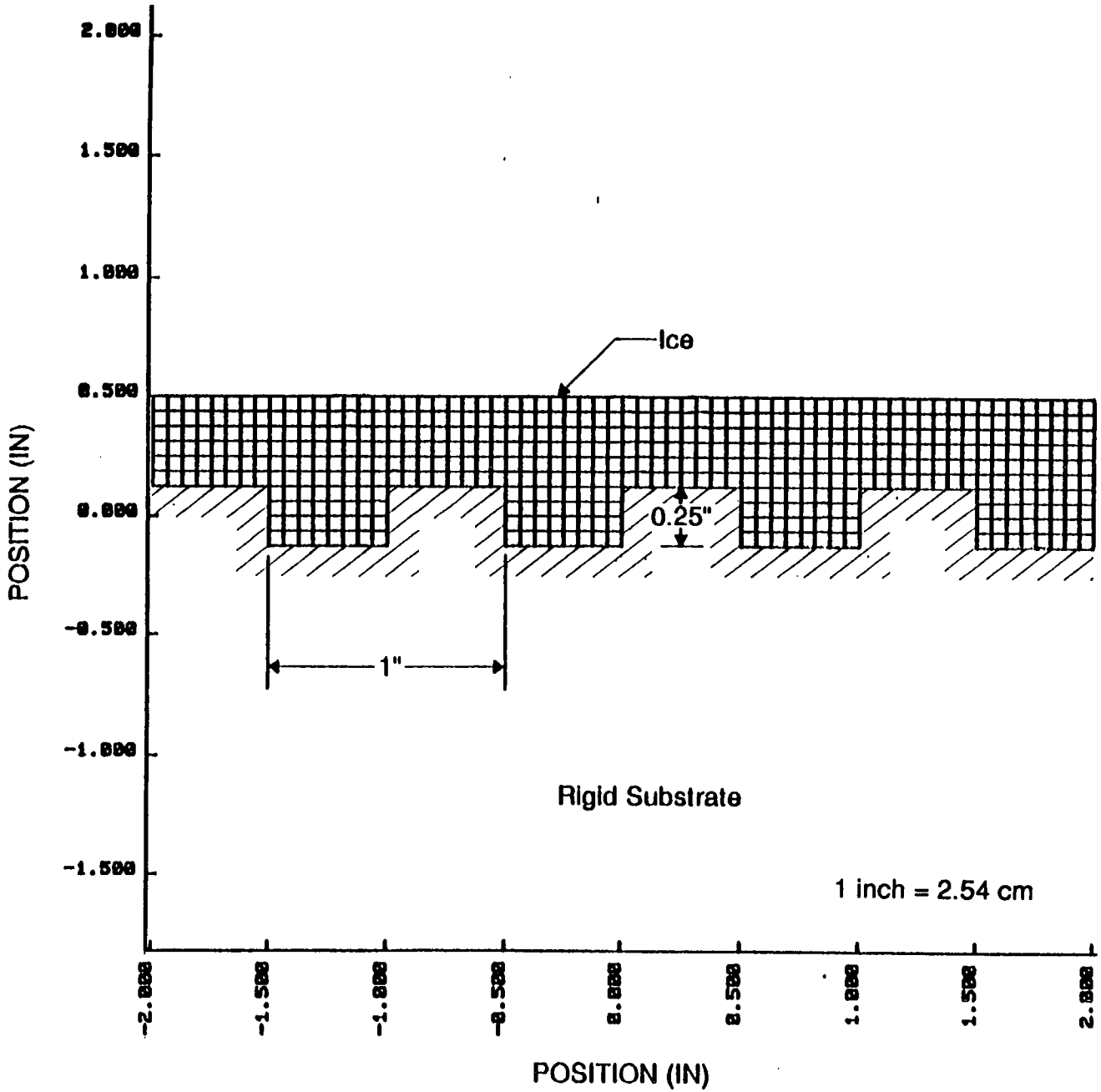

Figure J-53. Profile of ice on a square wave substrate

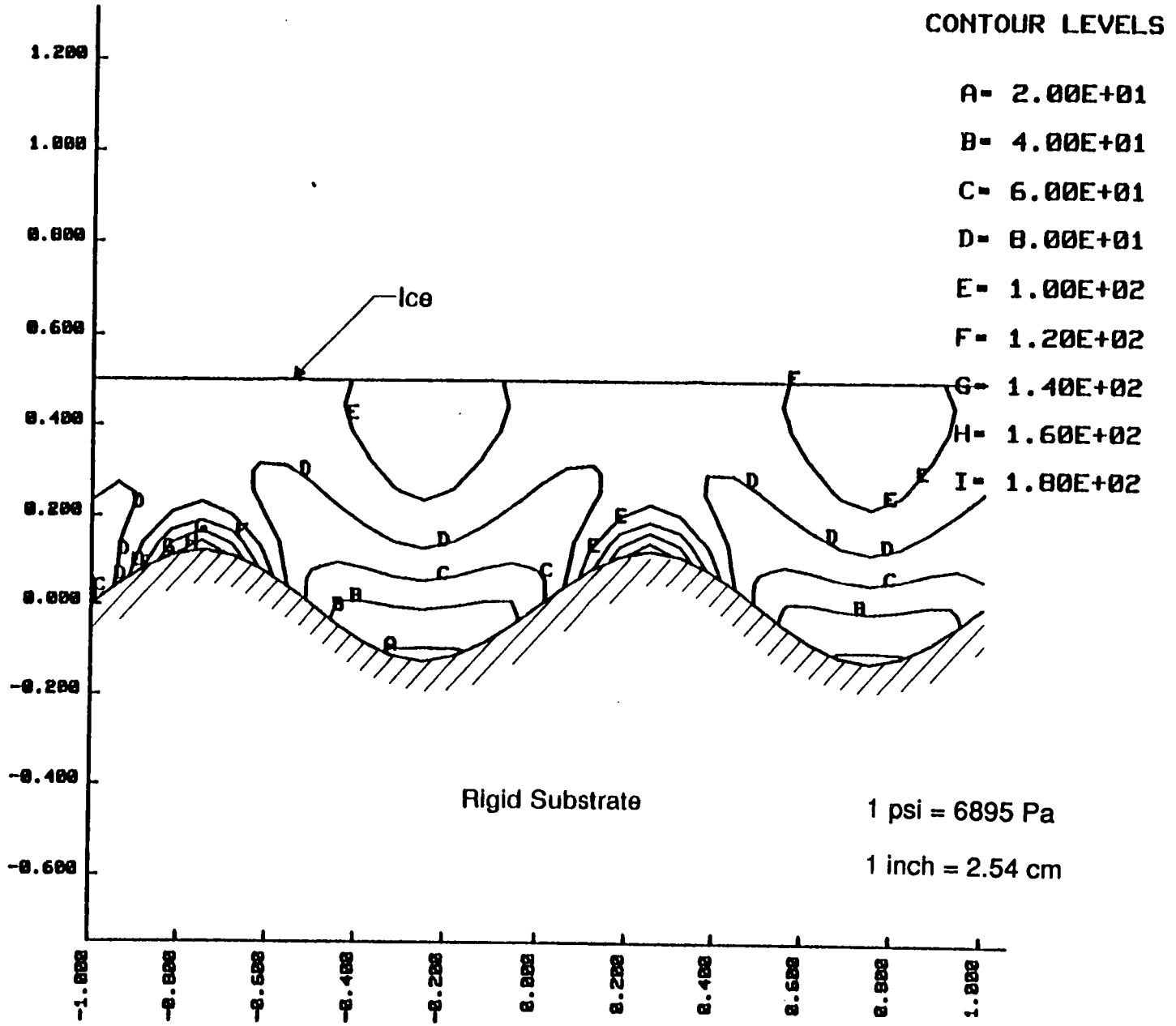

Figure J-54. Contours of shear stress for a rigid substrate with a sinusoidal profile

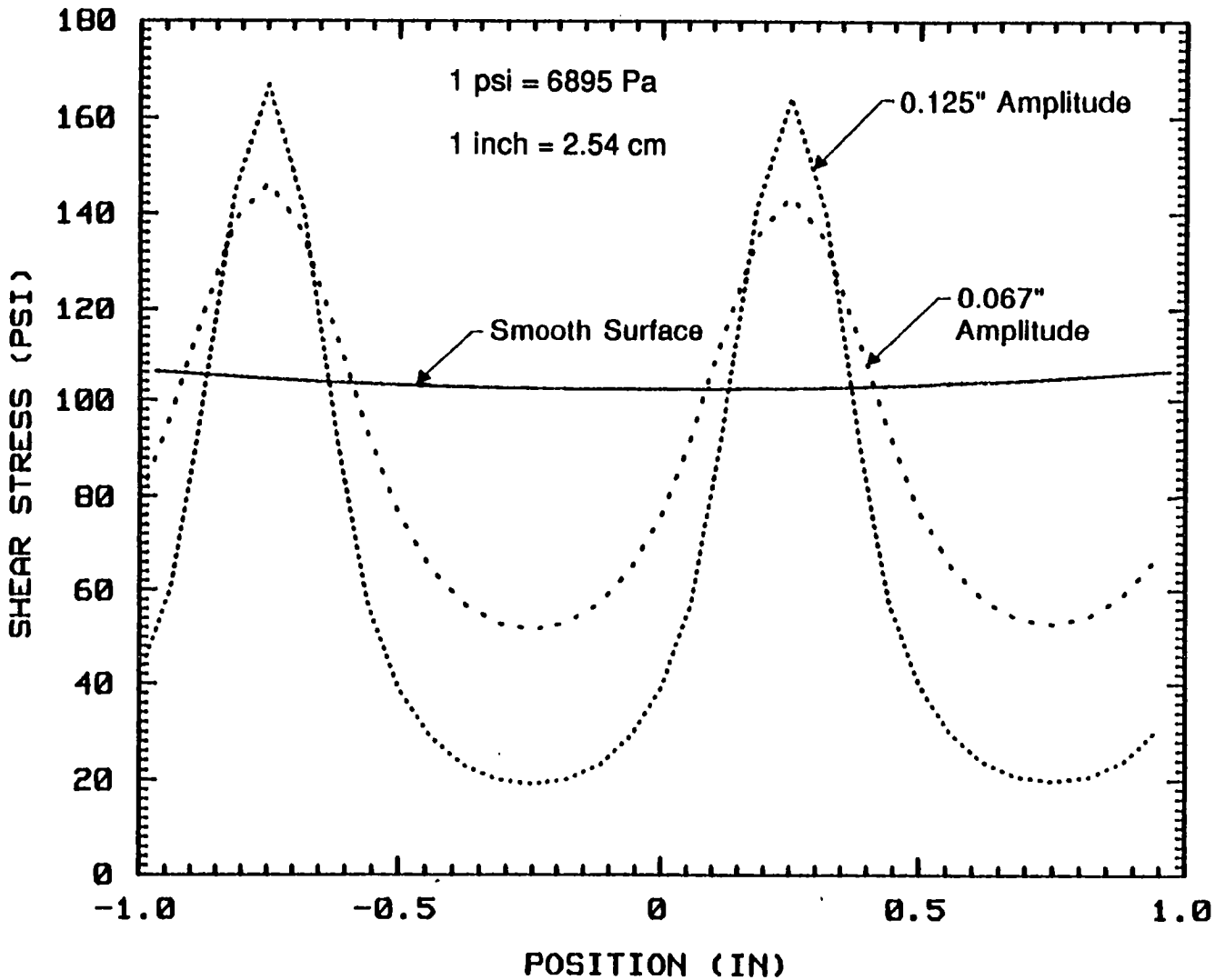

Figure J-55. Sinusoid amplitude on the ice-substrate interfacial shear stress from a uniformly applied shear stress on the top surface of the ice

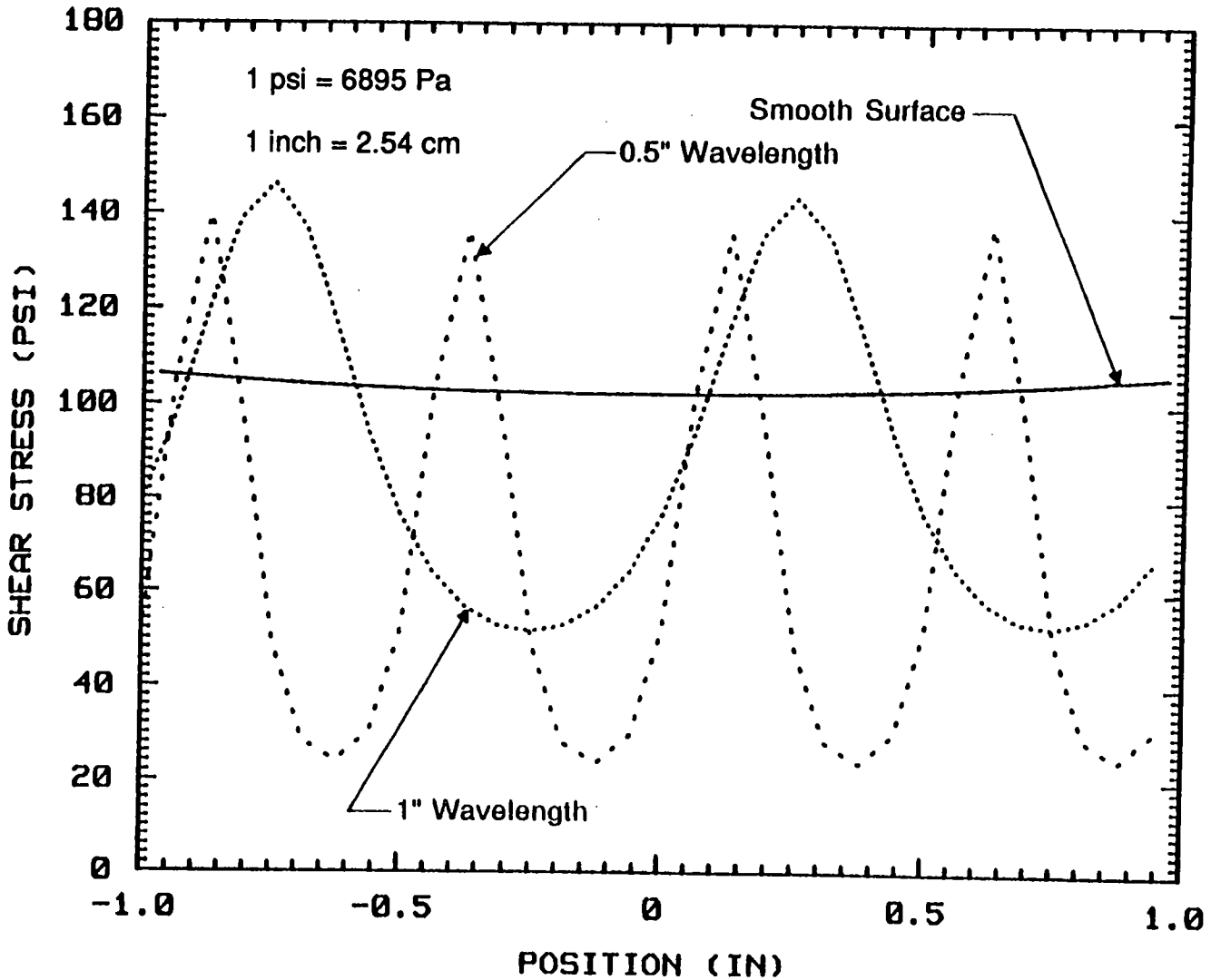

Figure J-56. Effect of sinusoid wavelength on the ice-substrate interfacial shear stress from a uniformly applied shear stress on the top surface of the ice

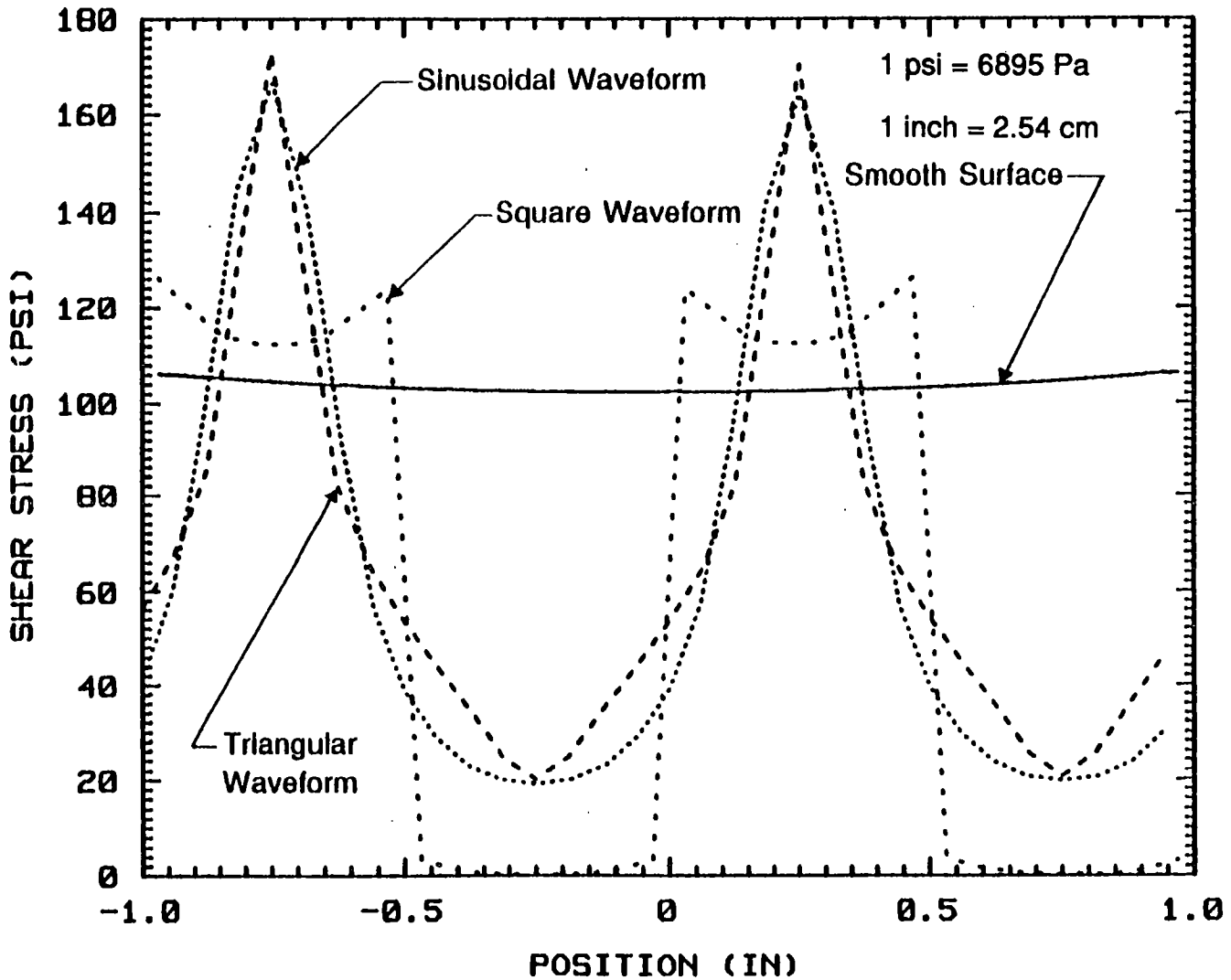

Figure J-57. Effect of waveform on the ice-substrate interfacial shear stress from a uniformly applied shear stress on the top surface of the ice

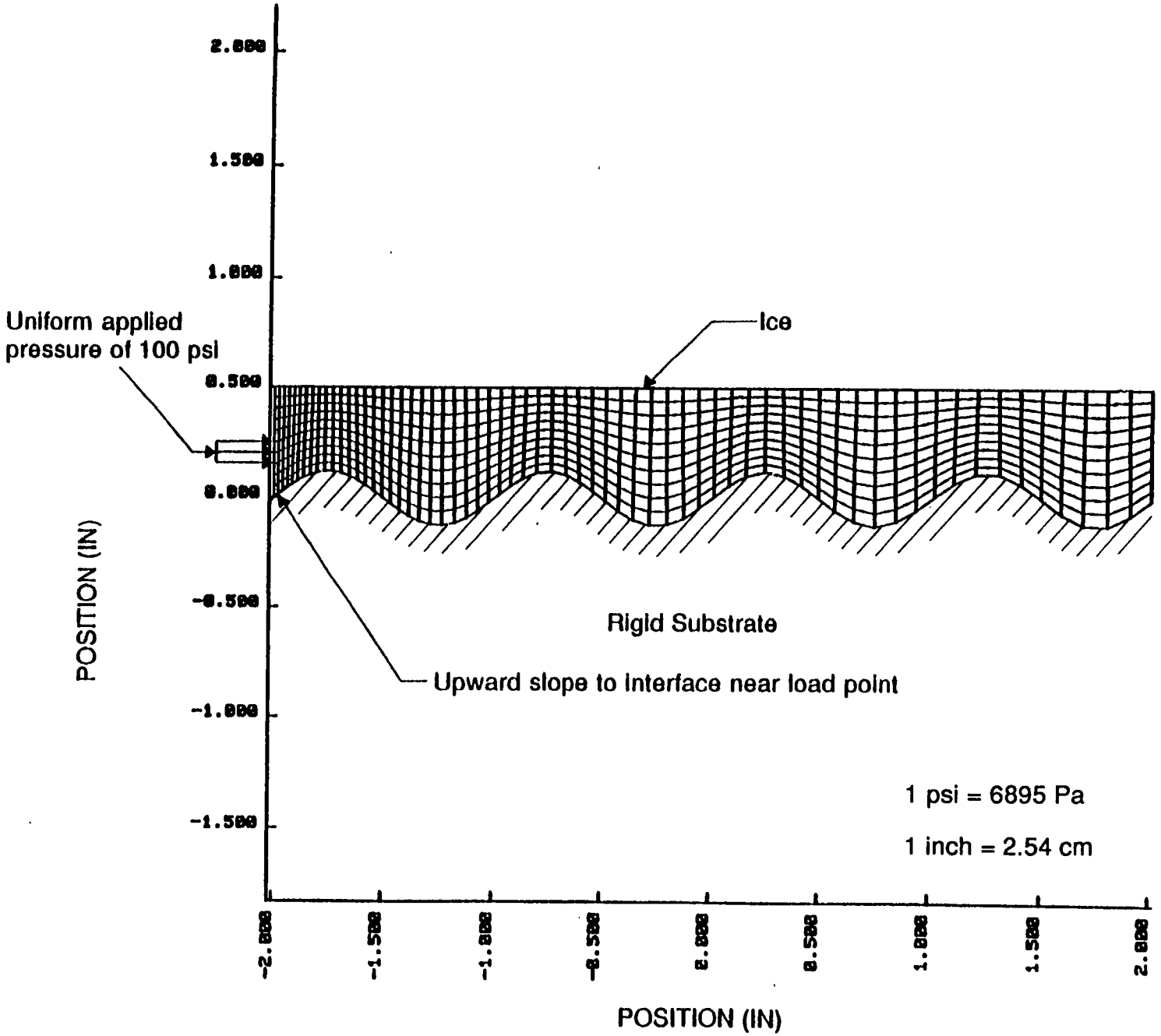

Figure J-58. Modified calculational mesh for edge loading of ice with upward slope to interface near load point

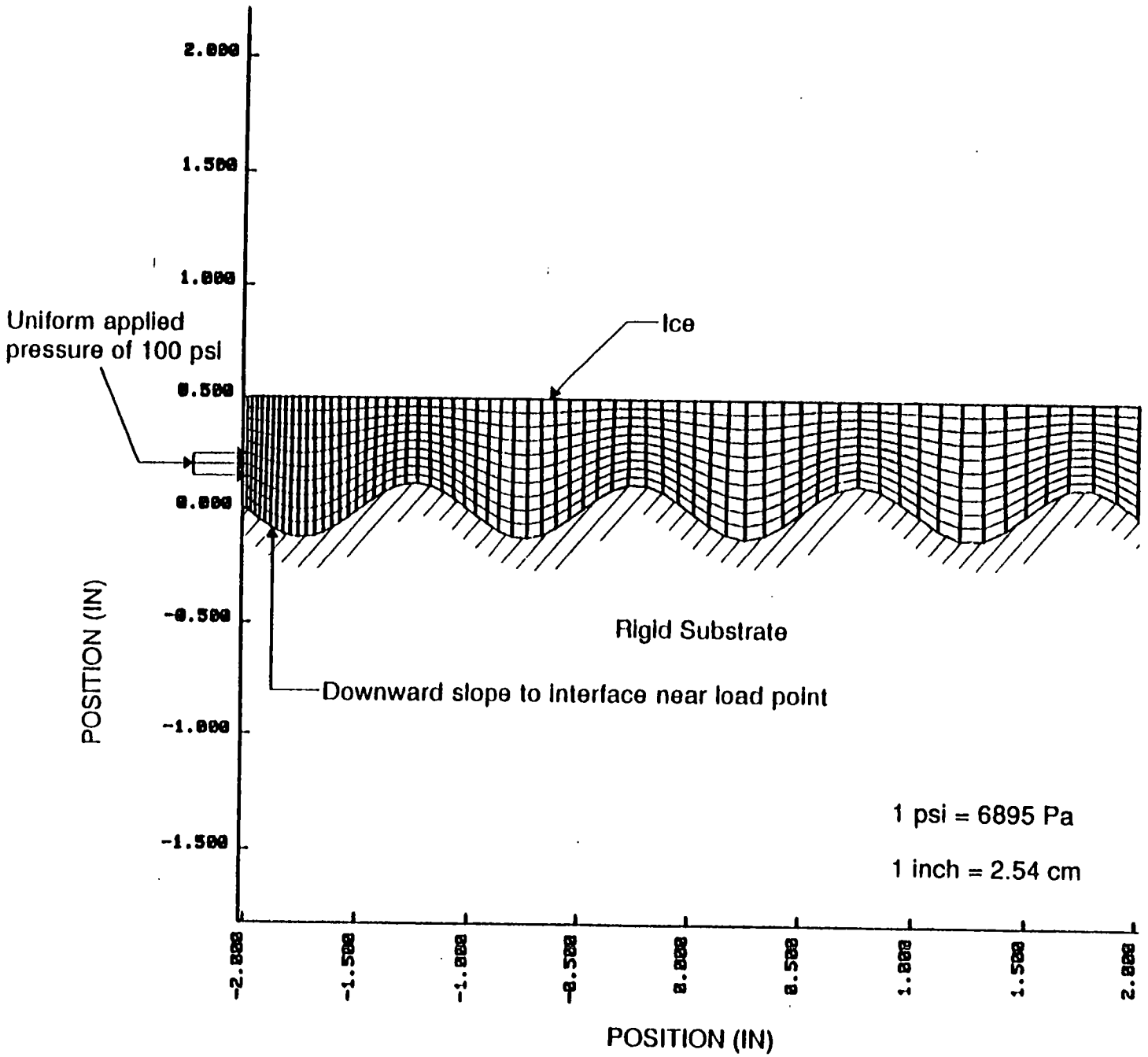

Figure J-59. Modified calculational mesh for edge loading of ice with downward slope to interface near load point

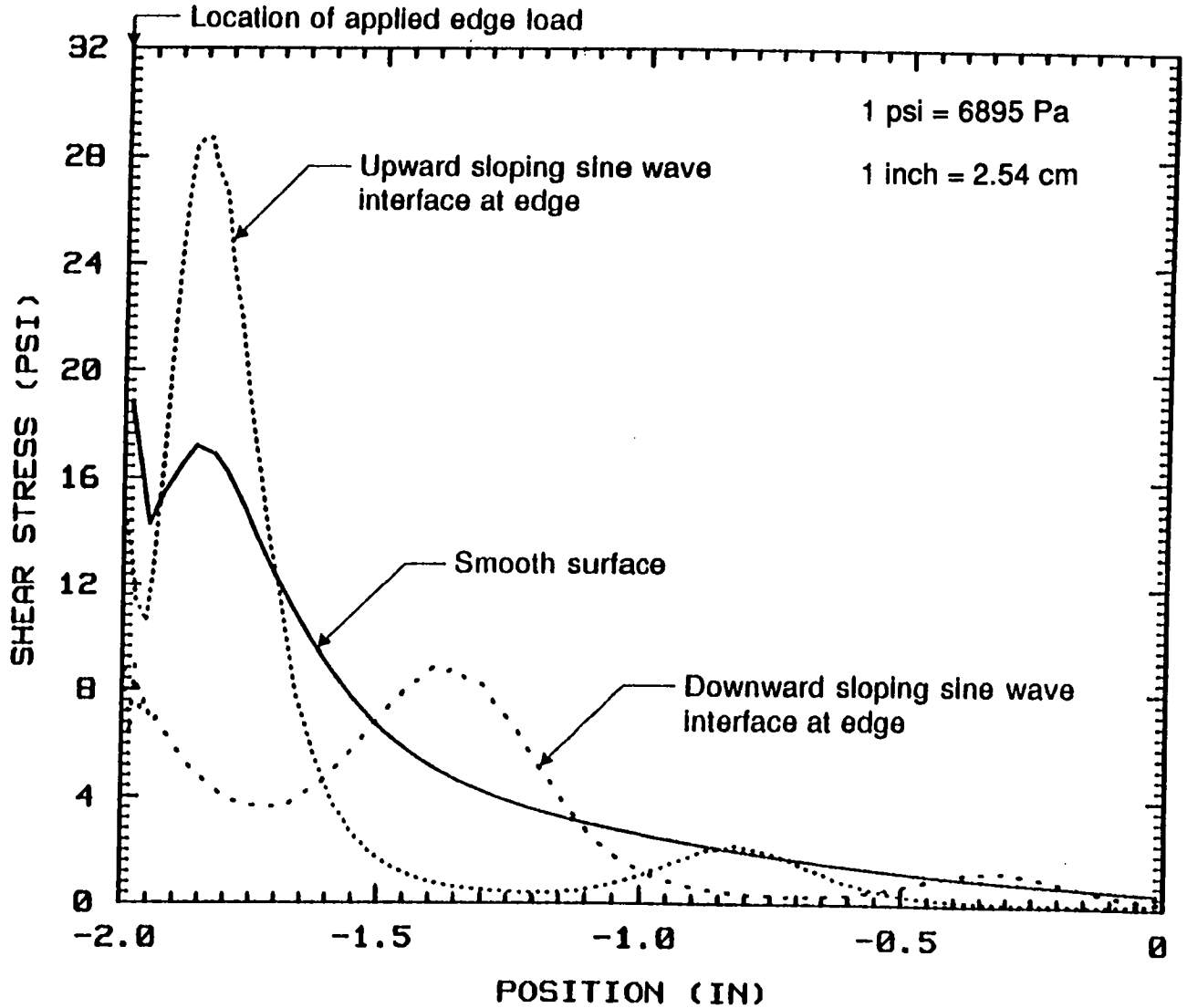

Figure J-60. Effect of interface slope on the ice-substrate interfacial shear stress from edge loading of the ice

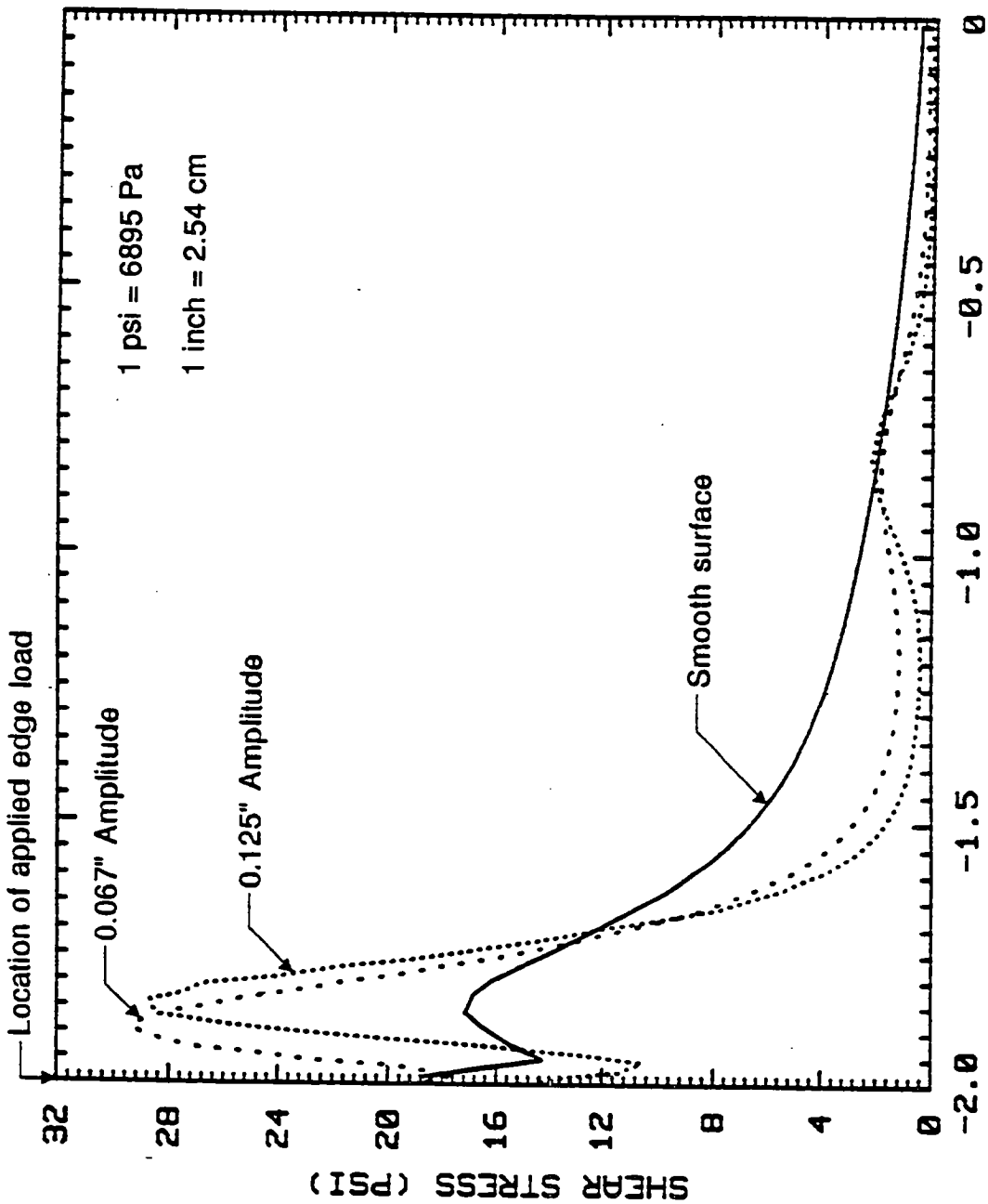

Figure J-61. Effect of substrate profile amplitude on the ice-substrate interfacial shear stress from edge loading of the ice

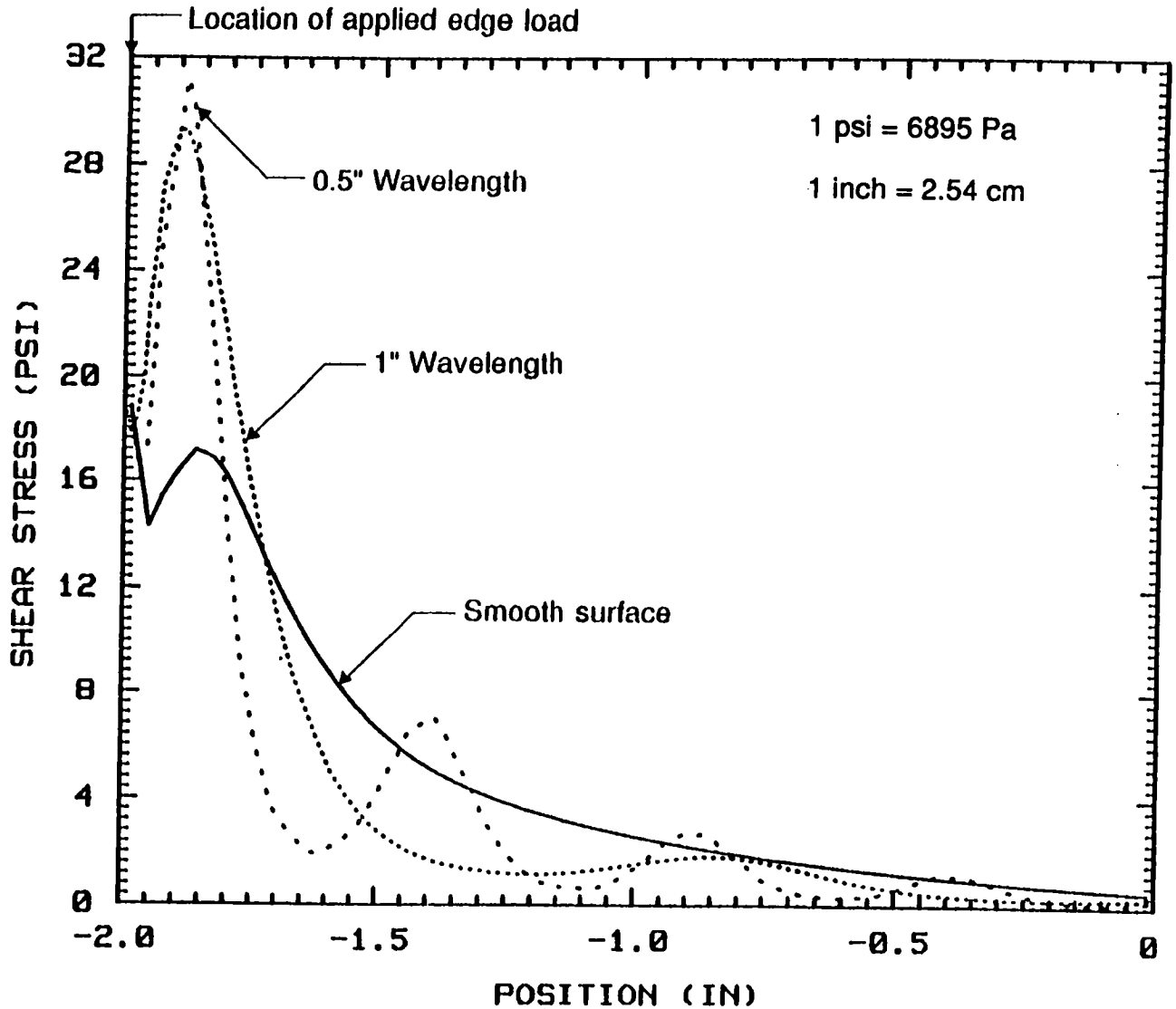

Figure J-62. Effect of substrate profile wavelength on the ice-substrate interfacial shear stress from edge loading of the ice

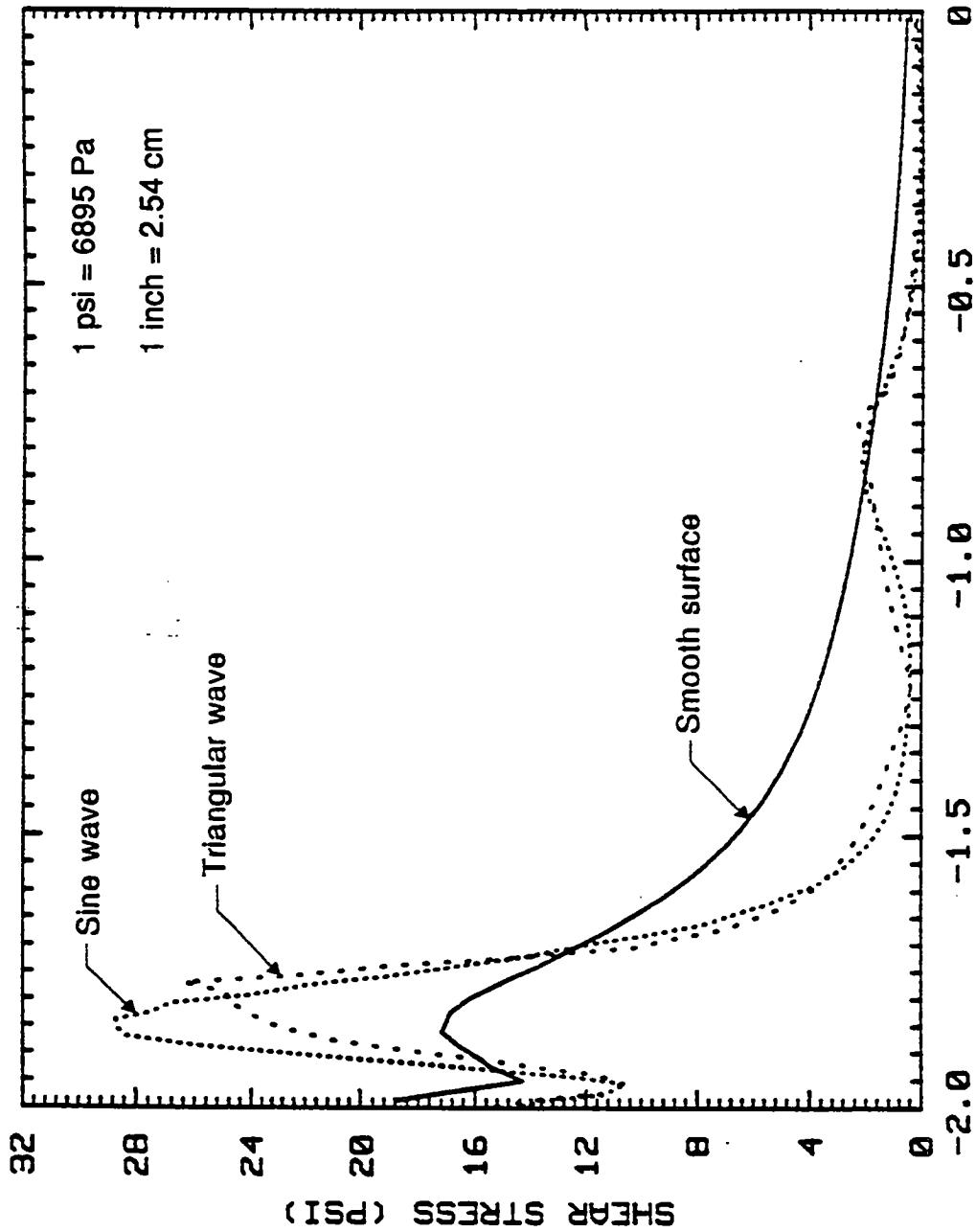

Figure J-63. Effect of waveform on the ice-substrate interfacial shear stress from edge loading of the ice

Appendix K

Verification of the Two-Dimensional Finite Element Analysis of Penetration by the Wedge Indenter

Test Problem Description

This appendix describes a finite element analysis of the wedge indentation of a strip. The results are compared with the known slip line plasticity solution for this situation. This analysis was performed to provide a check on the work described elsewhere in this report for wedge indentation of an ice layer bonded to a concrete substrate.

A schematic of the problem is shown in Figure J-21. Because the problem is horizontally and vertically symmetric, only the upper-right quadrant was analyzed. The mesh is shown in Figure J-22. We chose $2\theta = 60°$, a constant velocity of $V_o = 5$ m/s and $h = 0.3$ cm. Plane strain deformation was enforced. We used the dynamic, explicit finite element code DYNA-2D.[6]

The mesh was rezoned periodically during the calculations to avoid numerical difficulties associated with badly distorted elements, and to further avoid numerical difficulties, the tip of the wedge was blunted slightly to a radius of $h/10 = 0.03$ cm.

The ice was modeled as elastic-plastic using the Von Mises yield criterion. We used a density of 0.898 g/cm^3, Young's modulus of 8.27 GPa, and Poisson's ratio of 0.35. The yield stress was $Y = 100$ MPa and the results for stress were scaled by this number. The tangent modulus was chosen to be very small relative to Young's modulus so as to approximate an elastic-perfectly plastic material. We chose a tangent modulus of 8.27 Mpa. The wedge was assumed to be rigid.

Slip Line Solution

The slip line plasticity solution for this problem is the same as that for the indentation of a strip on a frictionless foundation until the strip lifts away from the foundation. The solution to the strip indentation problem was first obtained by Hill.[7,8] The solution applies to a rigid-perfectly plastic material indented by a sharp, rigid wedge. The solution provides the wedge load for a given depth of penetration and the extent of yielding in the vicinity of the penetrator.

Results and Discussion

The finite element results are compared to the slip line solution in Figures J-23 and J-24. In Figure J-23(a), the stress amplification is plotted as a function of normalized penetration. The stress amplification is defined as the wedge load per unit of original ice surface area indented (F/d in Figure J-23(b)) divided by the yield strength of the ice. In Figure J-24, the normalized effective stress, which is the yield stress in the Von Mises yield criterion, for the element nearest the origin is plotted as a function of the normalized penetration. When yielding at the origin occurs, the cross-section between the wedges in the original problem, Figure J-21, is fully yielded. The penetration required to achieve full yielding in the finite element and slip line solutions are indicated.

The finite element and slip line solutions agree quite well at relative penetrations above about 0.3. They disagree for lower penetrations due to the blunt radius on the tip of the wedge. The blunt tip raises the vertical normal stress component, S_{yy}, below the wedge, amplifying loads required for indentation and causing more extensive yielding than would occur for a sharp wedge.

Conclusions

The finite element results are in reasonable agreement with the known slip line solution for wedge indentation of a strip. This suggests that the FEM analysis can provide reasonably accurate representations of the conditions that are put into the model.

Appendix L

Correct Forms for the Asymptotic Displacement and Displacement Gradient Fields for Bimaterial Interface Crack

In this appendix, we give the correct forms for the asymptotic displacement and displacement gradient fields for the bimaterial interface crack. They were determined from the complex potentials given in (12). Subscript 1 refers to the material in $y > 0$ and subscript 2 refers to the material in $y < 0$. The fields are given for polar coordinates centered on the crack tip with the bond line defined as $\theta = 0$.

The nomenclature and the equations are given on the following pages.

μ = shear modulus

$\kappa = 3 - 4\nu$ (plane strain assumed)

$\varepsilon = ln[(\kappa_1\mu_2 + \mu_1)/(\kappa_2\mu_1 + \mu_2)]$

$$k_1 = \{\sigma_{yy}^{\infty}[\cos(\varepsilon\, ln2a) + 2\,\varepsilon \sin(\varepsilon\, ln2a)] + \sigma_{xy}^{\infty}[\sin(\varepsilon\, ln2a) - 2\,\varepsilon\cos(\varepsilon\, ln2a)]\}\sqrt{\pi}\,\sqrt{a} \Big/ \cosh(\pi\varepsilon)$$

$$k_2 = \{\sigma_{xy}^{\infty}[\cos(\varepsilon\, ln2a) + 2\,\varepsilon \sin(\varepsilon\, ln2a)] - \sigma_{yy}^{\infty}[\sin(\varepsilon\, ln2a) - 2\,\varepsilon\cos(\varepsilon\, ln2a)]\}\sqrt{\pi}\,\sqrt{a} \Big/ \cosh(\pi\varepsilon)$$

a = crack length

$$\sigma_{yy}^{\infty} = (Q_I + 2\,\varepsilon\, Q_{II})/(1 + 4\,\varepsilon^2)\sqrt{\pi}\,\sqrt{a}$$

$$\sigma_{xy}^{\infty} = (Q_{II} - 2\,\varepsilon\, Q_I)/(1 + 4\,\varepsilon^2)\sqrt{\pi}\,\sqrt{a}$$

Q_I = opening mode stress intensity factor (see [1]).

Q_{II} = shearing mode stress intensity factor (see [1]).

For y>0:

$$2\mu_1 u_1 = (r/2)^{1/2}\Big\{(1 + 4\,\varepsilon^2)^{-1}\{e^{\varepsilon(\theta - \pi)}\kappa_1[(k_1 + 2\varepsilon k_2)\cos((\theta/2) - \varepsilon\, lnr) + (k_2 - 2\varepsilon k_1)\sin((\theta/2) - \varepsilon\, lnr)] - e^{-\varepsilon(\theta - \pi)}[(k_1 + 2\varepsilon k_2)\cos((\theta/2) + \varepsilon\, lnr) - (k_2 - 2\varepsilon k_1)\sin((\theta/2) + \varepsilon\, lnr)]\} + \sin\theta\, e^{\varepsilon(\theta - \pi)}[k_1 \sin((\theta/2) + \varepsilon\, lnr) + k_2 \cos((\theta/2) + \varepsilon\, lnr)]\Big\}$$

$$2\mu_1 u_2 = (r/2)^{1/2}\Big\{(1 + 4\,\varepsilon^2)^{-1}\{e^{\varepsilon(\theta - \pi)}\kappa_1[(k_1 + 2\varepsilon k_2)\sin((\theta/2) - \varepsilon\, lnr) - (k_2 - 2\varepsilon k_1)\cos((\theta/2) - \varepsilon\, lnr)] + e^{-\varepsilon(\theta - \pi)}[(k_1 + 2\varepsilon k_2)\sin((\theta/2) + \varepsilon\, lnr) + (k_2 - 2\varepsilon k_1)\cos((\theta/2) + \varepsilon\, lnr)]\} - \sin\theta\, e^{\varepsilon(\theta - \pi)}[k_1 \cos((\theta/2) + \varepsilon\, lnr) - k_2 \sin((\theta/2) + \varepsilon\, lnr)]\Big\}$$

$$2\mu_1 \partial u_1/\partial r = \mu_1 u_1/r + \varepsilon\Big\{(1 + 4\,\varepsilon^2)^{-1}\{e^{\varepsilon(\theta - \pi)}\kappa_1[(k_1 + 2\varepsilon k_2)\sin((\theta/2) - \varepsilon\, lnr) - (k_2 - 2\varepsilon k_1)\cos((\theta/2) - \varepsilon\, lnr)] + e^{-\varepsilon(\theta - \pi)}[(k_1 + 2\varepsilon k_2)\sin((\theta/2) + \varepsilon\, lnr) + (k_2 - 2\varepsilon k_1)\cos((\theta/2) + \varepsilon\, lnr)]\} + \sin\theta\, e^{\varepsilon(\theta - \pi)}[k_1 \cos((\theta/2) + \varepsilon\, lnr) - k_2 \sin((\theta/2) + \varepsilon\, lnr)]\Big\}/(2r)^{1/2}$$

$$2\mu_1 \partial u_2/\partial r = \mu_1 u_2/r + \varepsilon \{ (1 + 4\varepsilon^2)^{-1} \{ e^{\varepsilon(\theta - \pi)} \kappa_1 [-(k_1 + 2\varepsilon k_2)\cos((\theta/2) - \varepsilon \ln r)$$
$$- (k_2 - 2\varepsilon k_1)\sin((\theta/2) - \varepsilon \ln r)] + e^{-\varepsilon(\theta - \pi)}[(k_1 + 2\varepsilon k_2)\cos((\theta/2) + \varepsilon \ln r)$$
$$- (k_2 - 2\varepsilon k_1)\sin((\theta/2) + \varepsilon \ln r)] \} + \sin\theta\, e^{\varepsilon(\theta - \pi)}[k_1 \sin((\theta/2) + \varepsilon \ln r)$$
$$+ k_2 \cos((\theta/2) + \varepsilon \ln r)] \}/(2r)^{1/2}$$

$$2\mu_1 \partial u_1/\partial\theta = (r/2)^{1/2} [\varepsilon \{ (1 + 4\varepsilon^2)^{-1} \{ e^{\varepsilon(\theta - \pi)} \kappa_1 [(k_1 + 2\varepsilon k_2)\cos((\theta/2) - \varepsilon \ln r)$$
$$+ (k_2 - 2\varepsilon k_1)\sin((\theta/2) - \varepsilon \ln r)] + e^{-\varepsilon(\theta - \pi)}[(k_1 + 2\varepsilon k_2)\cos((\theta/2) + \varepsilon \ln r)$$
$$- (k_2 - 2\varepsilon k_1)\sin((\theta/2) + \varepsilon \ln r)] \} + \sin\theta\, e^{\varepsilon(\theta - \pi)}[k_1 \sin((\theta/2) + \varepsilon \ln r)$$
$$+ k_2 \cos((\theta/2) + \varepsilon \ln r)] \}$$
$$+ \{ (1 + 4\varepsilon^2)^{-1} \{ e^{\varepsilon(\theta - \pi)} \kappa_1 [-(k_1 + 2\varepsilon k_2)\sin((\theta/2) - \varepsilon \ln r)$$
$$+ (k_2 - 2\varepsilon k_1)\cos((\theta/2) - \varepsilon \ln r)] + e^{-\varepsilon(\theta - \pi)}[(k_1 + 2\varepsilon k_2)\sin((\theta/2) + \varepsilon \ln r)$$
$$+ (k_2 - 2\varepsilon k_1)\cos((\theta/2) + \varepsilon \ln r)] \} + \sin\theta\, e^{\varepsilon(\theta - \pi)}[k_1 \cos((\theta/2) + \varepsilon \ln r)$$
$$- k_2 \sin((\theta/2) + \varepsilon \ln r)] \}/2 + \cos\theta\, e^{\varepsilon(\theta - \pi)}[k_1 \sin((\theta/2) + \varepsilon \ln r)$$
$$+ k_2 \cos((\theta/2) + \varepsilon \ln r)] \}]$$

$$2\mu_1 \partial u_2/\partial\theta = (r/2)^{1/2} [\varepsilon \{ (1 + 4\varepsilon^2)^{-1} \{ e^{\varepsilon(\theta - \pi)} \kappa_1 [(k_1 + 2\varepsilon k_2)\sin((\theta/2) - \varepsilon \ln r)$$
$$- (k_2 - 2\varepsilon k_1)\cos((\theta/2) - \varepsilon \ln r)] - e^{-\varepsilon(\theta - \pi)}[(k_1 + 2\varepsilon k_2)\sin((\theta/2) + \varepsilon \ln r)$$
$$+ (k_2 - 2\varepsilon k_1)\cos((\theta/2) + \varepsilon \ln r)] \} - \sin\theta\, e^{\varepsilon(\theta - \pi)}[k_1 \cos((\theta/2) + \varepsilon \ln r)$$
$$- k_2 \sin((\theta/2) + \varepsilon \ln r)] \}$$
$$+ \{ (1 + 4\varepsilon^2)^{-1} \{ e^{\varepsilon(\theta - \pi)} \kappa_1 [(k_1 + 2\varepsilon k_2)\cos((\theta/2) - \varepsilon \ln r)$$
$$+ (k_2 - 2\varepsilon k_1)\sin((\theta/2) - \varepsilon \ln r)] + e^{-\varepsilon(\theta - \pi)}[(k_1 + 2\varepsilon k_2)\cos((\theta/2) + \varepsilon \ln r)$$
$$- (k_2 - 2\varepsilon k_1)\sin((\theta/2) + \varepsilon \ln r)] \} + \sin\theta\, e^{\varepsilon(\theta - \pi)}[k_1 \sin((\theta/2) + \varepsilon \ln r)$$
$$+ k_2 \cos((\theta/2) + \varepsilon \ln r)] \}/2 - \cos\theta\, e^{\varepsilon(\theta - \pi)}[k_1 \cos((\theta/2) + \varepsilon \ln r)$$
$$- k_2 \sin((\theta/2) + \varepsilon \ln r)] \}].$$

For $y<0$:

$$2\mu_2 u_1 = (r/2)^{1/2} \{ (1 + 4\varepsilon^2)^{-1} \{ e^{\varepsilon(\theta + \pi)} \kappa_2 [(k_1 + 2\varepsilon k_2)\cos((\theta/2) - \varepsilon \ln r)$$
$$+ (k_2 - 2\varepsilon k_1)\sin((\theta/2) - \varepsilon \ln r)] - e^{-\varepsilon(\theta + \pi)}[(k_1 + 2\varepsilon k_2)\cos((\theta/2) + \varepsilon \ln r)$$

$$- (k_2 - 2\varepsilon k_1)\sin((\theta/2)+\varepsilon \ln r)] \} + \sin\theta\ e^{\varepsilon(\theta + \pi)}[k_1 \sin((\theta/2) +\varepsilon \ln r)$$
$$+ k_2 \cos((\theta/2)+\varepsilon \ln r)] \}$$

$$2\mu_2 u_2 = (r/2)^{1/2} \{ (1 + 4\varepsilon^2)^{-1} \{ e^{\varepsilon(\theta + \pi)}\kappa_2[(k_1 + 2\varepsilon k_2)\sin((\theta/2)-\varepsilon \ln r)$$
$$- (k_2 - 2\varepsilon k_1)\cos((\theta/2)-\varepsilon \ln r)] + e^{-\varepsilon(\theta + \pi)}[(k_1 + 2\varepsilon k_2) \sin((\theta/2)+\varepsilon \ln r)$$
$$+ (k_2 - 2\varepsilon k_1)\cos((\theta/2)+\varepsilon \ln r)] \} - \sin\theta\ e^{\varepsilon(\theta + \pi)}[k_1 \cos((\theta/2) +\varepsilon \ln r)$$
$$- k_2 \cos((\theta/2)+\varepsilon \ln r)] \}.$$

$$2\mu_2 \partial u_1/\partial r = \mu_2 u_1/r + \varepsilon \{ (1 + 4\varepsilon^2)^{-1} \{ e^{\varepsilon(\theta + \pi)}\kappa_2[(k_1 + 2\varepsilon k_2)\sin((\theta/2)-\varepsilon \ln r)$$
$$- (k_2 - 2\varepsilon k_1)\cos((\theta/2)-\varepsilon \ln r)] + e^{-\varepsilon(\theta + \pi)}[(k_1 + 2\varepsilon k_2) \sin((\theta/2)+\varepsilon \ln r)$$
$$+ (k_2 - 2\varepsilon k_1)\cos((\theta/2)+\varepsilon \ln r)] \} + \sin\theta\ e^{\varepsilon(\theta + \pi)}[k_1 \cos((\theta/2) +\varepsilon \ln r)$$
$$- k_2 \sin((\theta/2)+\varepsilon \ln r)] \}/(2r)^{1/2}$$

$$2\mu_2 \partial u_2/\partial r = \mu_2 u_2/r + \varepsilon \{ (1 + 4\varepsilon^2)^{-1} \{ e^{\varepsilon(\theta + \pi)}\kappa_2[-(k_1 + 2\varepsilon k_2)\cos((\theta/2)-\varepsilon \ln r)$$
$$- (k_2 - 2\varepsilon k_1)\sin((\theta/2)-\varepsilon \ln r)] + e^{-\varepsilon(\theta + \pi)}[(k_1 + 2\varepsilon k_2) \cos((\theta/2)+\varepsilon \ln r)$$
$$- (k_2 - 2\varepsilon k_1)\sin((\theta/2)+\varepsilon \ln r)] \} + \sin\theta\ e^{\varepsilon(\theta + \pi)}[k_1 \sin((\theta/2) +\varepsilon \ln r)$$
$$+ k_2 \cos((\theta/2)+\varepsilon \ln r)] \}/(2r)^{1/2}$$

$$2\mu_2 \partial u_1/\partial\theta = (r/2)^{1/2}[\varepsilon \{ (1 + 4\varepsilon^2)^{-1} \{ e^{\varepsilon(\theta + \pi)}\kappa_2[(k_1 + 2\varepsilon k_2)\cos((\theta/2)-\varepsilon \ln r)$$
$$+ (k_2 - 2\varepsilon k_1)\sin((\theta/2)-\varepsilon \ln r)] + e^{-\varepsilon(\theta + \pi)}[(k_1 + 2\varepsilon k_2) \cos((\theta/2)+\varepsilon \ln r)$$
$$- (k_2 - 2\varepsilon k_1)\sin((\theta/2)+\varepsilon \ln r)] \} + \sin\theta\ e^{\varepsilon(\theta + \pi)}[k_1 \sin((\theta/2) +\varepsilon \ln r)$$
$$+ k_2 \cos((\theta/2)+\varepsilon \ln r)] \}$$
$$+ \{ (1 + 4\varepsilon^2)^{-1} \{ e^{\varepsilon(\theta + \pi)}\kappa_2[-(k_1 + 2\varepsilon k_2) \sin((\theta/2)-\varepsilon \ln r)$$
$$+ (k_2 - 2\varepsilon k_1)\cos((\theta/2)-\varepsilon \ln r)] + e^{-\varepsilon(\theta + \pi)}[(k_1 + 2\varepsilon k_2) \sin((\theta/2)+\varepsilon \ln r)$$
$$+ (k_2 - 2\varepsilon k_1)\cos((\theta/2)+\varepsilon \ln r)] \} + \sin\theta\ e^{\varepsilon(\theta + \pi)}[k_1\cos((\theta/2) +\varepsilon \ln r)$$
$$- k_2 \sin((\theta/2)+\varepsilon \ln r)] \}/2 + \cos\theta\ e^{\varepsilon(\theta + \pi)}[k_1 \sin((\theta/2) +\varepsilon \ln r)$$
$$+ k_2 \cos((\theta/2)+\varepsilon \ln r)] \}]$$

$$2\mu_2 \partial u_2/\partial\theta = (r/2)^{1/2}\Big[\varepsilon \Big\{ (1 + 4\varepsilon^2)^{-1} \{ e^{\varepsilon(\theta + \pi)}\kappa_2[(k_1 + 2\varepsilon k_2)\sin((\theta/2)-\varepsilon \ln r)$$
$$- (k_2 - 2\varepsilon k_1)\cos((\theta/2)-\varepsilon \ln r)] - e^{-\varepsilon(\theta + \pi)}[(k_1 + 2\varepsilon k_2)\sin((\theta/2)+\varepsilon \ln r)$$
$$+ (k_2 - 2\varepsilon k_1)\cos((\theta/2)+\varepsilon \ln r)] \} - \sin\theta\ e^{\varepsilon(\theta + \pi)}[k_1 \cos((\theta/2) +\varepsilon \ln r)$$
$$- k_2 \sin((\theta/2)+\varepsilon \ln r)] \Big\}$$
$$+ \Big\{ (1 + 4\varepsilon^2)^{-1} \{ e^{\varepsilon(\theta + \pi)}\kappa_2[(k_1 + 2\varepsilon k_2) \cos((\theta/2)-\varepsilon \ln r)$$
$$+ (k_2 - 2\varepsilon k_1)\sin((\theta/2)-\varepsilon \ln r)] + e^{-\varepsilon(\theta + \pi)}[(k_1 + 2\varepsilon k_2) \cos((\theta/2)+\varepsilon \ln r)$$
$$- (k_2 - 2\varepsilon k_1)\sin((\theta/2)+\varepsilon \ln r)] \} + \sin\theta\ e^{\varepsilon(\theta + \pi)}[k_1 \sin((\theta/2) +\varepsilon \ln r)$$
$$+ k_2 \cos((\theta/2)+\varepsilon \ln r)] \Big\}/2 - \cos\theta\ e^{\varepsilon(\theta + \pi)}[k_1 \cos((\theta/2) +\varepsilon \ln r)$$
$$- k_2 \sin((\theta/2)+\varepsilon \ln r)] \Big\} \Big].$$

References

1. L. David Minsk. A Short History of Man's Attempts to Move Through Snow. *Highway Research Board Special Report 115*, 1970.

2. B. H. Welch et al. Economic Impact of Highway Snow and Ice Control—State of the Art Interim Report. Report No. FHWA-RD-77-20, September 1976.

3. *Strategic Highway Research Program: Research Plans*, TRB, National Research Council, Washington, D.C., May 1986.

4. E. Passaglia and R. A. Haines. The National Cost of Automobile Corrosion. *Automotive Corrosion by Deicing Salts*, NACE, Robert Baboian, Ed., Houston, Texas, 1981.

5. D. M. Murray and U.F.W. Ernst. An Economic Analysis of the Environmental Impact of Highway Deicing. Abt Associates, Inc., Report No. EPA600/2-76-105, May 1976.

6. Reports Presented to TRB Committee on Winter Maintenance (Committee A3C09) at TRB Annual Meeting, Washington, D.C., January 1987.

7. *America's Highways: Accelerating the Search for Innovation*, Transportation Research Board Special Report 202, 1984.

8. R. R. Blackburn, A.D. St. John, and P. J. Hennan. Physical Alternatives to Chemicals for Highway Deicing. Final Report. U.S. Department of Transportation. Contract No. DOT-FH-11-9126, December 1978.

9. E. G. Shafrin and W. A. Zisman. Slowly Advancing Equilibrium Contact Angle Method. *J. Colloid Sci.*, 4, 571, 1949.

10. W. A. Zisman. Relation of Equilibrium Contact Angle to Liquid and Solid Constitution. Advances Chem., Ser. 43, 1, 1964.

11. H. W. Fox and W. A. Zisman. The Spreading of Liquids on Low-Energy Surfaces. II. Modified Tetrafluoroethylene Polymers. *J. Colloid Sci.*, 7, 109, 1952.

12. S. Brunauer, P. H. Emmett, and E. Teller. *J. Amer. Chem. Soc.*, 60, 309, 1938.

13. I. Langmuir. *J. Amer. Chem. Soc.*, 40, 1361, 1918.

14. S. J. Gregg and K.S.W. Sing. *Adsorption, Surface Area, and Porosity*, Academic Press, New York, 1967.

15. U. Buontempo. Infrared Spectra of Amorphous Ice. *Physics Lett.*, 42A, 17-18, 1972.

16. M. S. Bergren, D. Schuh, M. G. Sceats, and S. A. Rice. The OH Stretching Region Infrared Spectra of Low Density Amorphous Solid Water and Polycrystalline Ice Ih. *J. Chem. Phys.*, 69, 3477-3482, 1978.

17. E. Whalley and D. D. Klug. Origin of the High Integrated Infrared Intensity of the O-H Stretching Vibrations of Ice I Relative to the Vapor. *J. Chem. Phys.*, 84, 4807-4809, 1986.

18. N. J. Harrick. Prism Liquid Cell. *Apl. Spectroscopy*, 37, 573-575, 1983.

19. P. V. Hobbs, *Ice Physics*, Clarendon Press, Oxford, 1974.

20. L. W. Gold, Crack Formation in Ice Plates by Thermal Shock, *Can. J. Phys.*, 41, 1712-1728, 1965.

21. M. W. Engle, Heat Transfer from Small Diameter Wires and Thin Films Immersed in Liquid Nitrogen, M.S. Thesis, South Dakota School of Mines and Technology, 1987.

22. L. M. Barker. SWAP-7: A Stress-Wave Analyzing Program. SC-RR-67-143. Sandia Corporation, April 1967.

23. J. Johnson to L. Seaman. Private communication, 1988.

24. M. A. Lange and T. J. Ahrens. The Dynamic Tensile Strength of Ice and Ice-Silicate Mixtures. *Journal of Geophysical Research.* Vol. 88, No. B2, February 10, 1983, pp. 1197-1208.

25. J. O. Hallquist. DYNA-3D User's Manual (Nonlinear Dynamic Analysis of Structures in Three Dimensions. UCID-19592, Rev. 4. Lawrence Livermore National Laboratory, Livermore, CA, April 1988.

26. *Interim Report to SHRP on Project H-203, Ice Pavement Bond Disbonding—Fundamental Study.* For the Period October 8, 1987 to October 7, 1988.

27. J. O. Hallquist. User's Manual for DYNA-2D-An Explicit Two-Dimensional Hydrodynamic Finite Element Code with Interactive Rezoning. UCID-18756. Lawrence Livermore National Laboratory, Livermore, CA, 1984.

28. R. Hill. *The Mathematical Theory of Plasticity.* Clarendon Press. Oxford, U.K., 1950, p. 218.

29. R. Hill. A Theoretical Investigation of the Effect of Specimen Size in the Measurement of Hardness. *Philosophical Magazine.* Vol 41, 1950, pp. 745-753.

30. J. R. Rice. *Journal of Applied Mechanics.* Vol. 55, No. 1, 1988, pp. 98-103.

31. B. Moran and C. F. Shih. *Engineering Fracture Mechanics.* Vol. 27, No. 6, 1987, pp. 615-642.

32. C. F. Shih and R. J. Asaro. *Journal of Applied Mechanics.* Vol. 55, No. 2, 1988, pp. 299-316.

33. K. Y. Lee and H. J. Choi. *Engineering Fracture Mechanics.* Vol. 29, No. 4, 1988, p. 461-472.

34. J. O. Hallquist. NIKE-2D-A Vectorized, Implicit, Finite Deformation, Finite Element Code for Analyzing the Static and Dynamic Response of 2-D Solids. UCID-19677. Lawrence Livermore National Laboratory, Livenmore, CA, 1983.

35. *Interfacial Phenomena—Equilibrium and Dynamic Effects,* C. A. Miller and P. Neogi (1985)

36. *Contact Angle—Wettability and Adhesion,* R. F. Gould, ed. (1964)

37. *Surface and Colloid Science—Volumes 1 & 2,* E. Matjjevic, ed. (1969).

Highway Operations Advisory Committee

Chairman
Dean M. Testa
Kansas Department of Transportation

Vice Chairman
Clayton L. Sullivan
Idaho Transportation Department

Members

Ross B. Dindio
The Commonwealth of Massachusetts Highway Department

Richard L. Hanneman
Salt Institute

Rita Knorr
American Public Works Association

David A. Kuemmel
Marquette University

Magdalena M. Majesky
Ministry of Transportation of Ontario

Michael J. Markow
Cambridge Systematics, Inc.

Gerald M. Miner
Macon, Missouri

Richard J. Nelson
Nevada Department of Transportation

Rodney A. Pletan
Minnesota Department of Transportation

Michel P. Ray
The World Bank

Michael M. Ryan
Pennsylvania Department of Transportation

Bo H. Simonsson
Swedish Road and Traffic Research Institute

Leland Smithson
Iowa Department of Transportation

Arlen T. Swenson
John Deere National Sales Division

Anwar E.Z. Wissa
Ardaman and Associates, Inc.

John P. Zaniewski
Arizona State University

Liaisons

Ted Ferragut
Federal Highway Administration

Joseph J. Lasek
Federal Highway Administration

Frank N. Lisle
Transportation Research Board

Byron N. Lord
Federal Highway Administration

Mohamed Y. Shahin
U.S. Army Corps of Engineers

Harry Siedentopf
Federal Aviation Administration

Jesse Story
Federal Highway Administration

Expert Task Group

Dorothy L. Andres
New Jersey State Department of Transportation

Willard D. Bascom
University of Utah

Bruce Bertram
Salt Institute

Brian Chollar
Federal Highway Administration

Martha Hsu
Maine Department of Transportation

Kazuhiko Itagaki
U.S. Army Corps of Engineers

Maurice Larson
Iowa State University

James N. Moss
Texas State Department of Highways and Public Transportation

Alphonsius Pocius
Specialty Film Division/3M